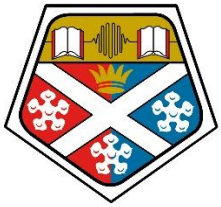

University of Strathclyde Glasgow

Department of Chemical and Process Engineering
University of Strathclyde

Brewing Up Solutions: Developing High-Performance Adsorbents from Spent Coffee Grounds for Carbon Capture

Elliot Ross

Thesis submitted for the degree of Doctor of Philosophy

2025

Declaration

This thesis is the result of the author's original research. It has been composed by the author and has not been previously submitted for examination which has led to the award of a degree.

Elliot Ross

20/06/2025

Acknowledgements

This thesis would not have been possible without the support, encouragement, and kindness of those around me. I'm deeply thankful to everyone who stood by me during this long and difficult journey—your presence made all the difference.

First and foremost, I dedicate this work to my Papa. Without his love, encouragement, and unwavering support, I doubt I'd have ever done this. Everything I've achieved has its roots in the values and strength he passed on to me.

To my supervisor, Professor Ashleigh Fletcher—thank you sincerely. I could not have asked for a better guide through this process. Your expertise is extraordinary, your advice always clear and steady, and your support unfailing. I've learned so much under your supervision, and your example will continue to guide me in whatever comes next.

To my research group—without you, I would have been completely lost. You welcomed me, shared your knowledge and experience, and helped me through every obstacle. Special thanks to Dr Dave Ashworth, the IGA whisperer, who always had the answer to every error code. Thank you also to Dr Jordan Mooney, Dr Umair Jamal, Dr Oluwagbemi Aladeokin, Dr Michaela McFadden, and Dr Aidan Harvey—for being just about the best group anyone could ask for.

To my secondary supervisor, Dr Gavin Craig, thank you for your time and feedback whenever I needed it.

To the technicians—thank you for the essential work that keeps everything running. A special thanks to Ian Airdrie, who always kept one eye on the BET and made sure I could get what I needed done.

Dr Angharad Wood — thank you for standing beside me through the hardest stretches of this journey. Your patience, encouragement, and tireless help with the final stages made this thesis possible. I am so grateful to share this milestone with you.

I would also like to thank the Ronald Miller Foundation for funding my home fees and making this project possible. Your support allowed me to pursue this work.

Finally, to my Mum and Dad—thank you for your unwavering support throughout this journey. Your presence and encouragement have meant more than I can properly express. I'm deeply grateful for everything you've done to help me reach this point.

Abstract

The development of low-cost, regenerable adsorbents for post-combustion carbon capture is critical for realising scalable carbon capture and storage (CCS) technologies. This study investigates the use of spent coffee grounds (SCG), an abundant organic waste stream, as a precursor for producing high-performance biochar-based CO_2 sorbents. Through a systematic Design of Experiments (DoE) framework, SCG-derived biochars were synthesised via physical (CO_2), chemical (KOH, potassium oxalate), and biological (fungal) activation methods, with the aim of optimising porosity, surface chemistry, and CO_2 capture performance under realistic flue gas conditions.

Key findings demonstrate that activation route significantly influences both textural and chemical properties. EX37-850-15-CO_2-600, a nitrogen-rich, microporous sample prepared via single-step CO_2 activation, exhibited the highest low-pressure CO_2 uptake (0.76 mmol g^{-1} at 150 mbar and 60 °C), strong initial enthalpy of adsorption (42.25 kJ mol^{-1}), and the greatest CO_2/N_2 selectivity (up to 44 at 1000 mbar). In contrast, EX53-900-2H-KOX-1:1 (pre-pyrolysed)—produced by potassium oxalate activation—showed superior regenerability under cyclic pressure swing conditions, retaining >95% capacity after 60 cycles with a working capacity of 0.735 mmol g^{-1} between 150–50 mbar. IAST-based binary gas analysis confirmed that nitrogen functionalities play a decisive role in enhancing selectivity beyond what is achievable through porosity alone.

This work represents the first comprehensive comparison of physical, chemical, and biological activation methods applied to SCG under a DoE framework, linking activation parameters to sorbent performance across capacity, selectivity, kinetics, and stability. It highlights a key trade-off between affinity and regenerability, underscoring the importance of aligning sorbent properties with capture process requirements. The findings establish SCG-derived biochars as viable, sustainable alternatives to synthetic sorbents, and offer a pathway for integrating circular economy principles into CCS deployment.

Table of Contents

List of Abbreviations

%MP	Percent Microporosity
AC	Activated Carbon
ACF	Activated Carbon Fibre
ANOVA	Analysis of Variance
ASEAN	Association of Southeast Asian Nations
BBD	Box-Behnken Design
BECCS	Bioenergy with Carbon Capture and Storage
BET	Brunauer–Emmett–Teller
BJH	Barrett–Joyner–Halenda
C	BET Constant (related to adsorption energy)
CCC	Circumscribed Central Composite Design
CCD	Central Composite Design
CCF	Face-centred Central Composite Design
CCI	Inscribed Central Composite Design
CCS	Carbon Capture and Storage
CDR	Carbon Dioxide Removal
CHN	Carbon, Hydrogen, Nitrogen (Elemental Analysis)
CNT	Carbon Nanotube
COF	Covalent Organic Framework
CV	Coefficient of Variance
DF	Degrees of Freedom
DFT	Density Functional Theory
DR	Dubinin–Radushkevich
DoE	Design of Experiments
ESA	Electrical Swing Adsorption
FTIR	Fourier Transform Infrared Spectroscopy
GCF	Green Climate Fund
GO	Grey Oyster
IAST	Ideal Adsorbed Solution Theory
IGA	Intelligent Gravimetric Analyser
IGCC	Integrated Gasification Combined Cycle
IUPAC	International Union of Pure and Applied Chemistry
L-M	Levenberg–Marquardt
MA	Micropore Area
MEA	Monoethanolamine
MOF	Metal–Organic Framework
MSCG	Mycelium impregnated Spent Coffee Grounds
Mt	Million Tonnes
NDC	Nationally Determined Contribution
NLDFT	Non-Local Density Functional Theory
NO_x	Nitrogen Oxides
ODR	Orthogonal Distance Regression
OPC	Ordered Porous Carbon
P/P_o	Relative Pressure
PAN	Polyacrylonitrile
PCC	Post-Combustion Capture
PEI	Polyethyleneimine
PFO	Pseudo-First Order
PSA	Pressure Swing Adsorption
PSO	Pseudo-Second Order
RSM	Response Surface Methodology
RT	Ideal Gas Constant × Temperature
R^2	Coefficient of Determination
S	Surface Area
S(BET)	BET Surface Area
SA	Surface Area
SCG	Spent Coffee Grounds
SEM	Scanning Electron Microscopy
SO_x	Sulphur Oxides
SSA	Specific Surface Area
T	Absolute Temperature
TEPA	Tetraethylenepentamine
TGA	Thermogravimetric Analysis
TSA	Temperature Swing Adsorption
Temp	Temperature
UK	United Kingdom
UNFCCC	United Nations Framework Convention on Climate Change
V_m	Monolayer Capacity
XPS	X-ray Photoelectron Spectroscopy
ZIF	Zeolitic Imidazolate Framework
k_1	PFO Rate Constant
k_2	PSO Rate Constant
min	Minutes
p/p^0	Relative Pressure
q_m	Maximum Adsorption Capacity
syngas	Synthesis Gas
t-plot MA	t-plot Micropore Area
t-plot MV	t-plot Micropore Volume
ΔG	Gibbs Free Energy Change
ΔH	Enthalpy Change
ΔS	Entropy Change

List of Figures

List of Tables

Chapter 1. Introduction

1.1. The State of the World

1.1.1. Climate Change: Impacts and Challenges

The Anthropocene era, defined by humanity's profound influence on the planet, marks an unprecedented chapter in Earth's history. Industrial expansion and fossil fuel combustion have driven atmospheric carbon dioxide (CO_2) concentrations to dangerous levels [1], disrupting natural systems that underpin life. These disruptions manifest as intensifying climate extremes, ocean acidification, collapsing ecosystems, and an accelerating loss of biodiversity [2]. By fundamentally altering the geosphere, hydrosphere, and atmosphere, human activities have triggered a crisis demanding immediate and transformative global action.

Atmospheric and Climatic Disruptions

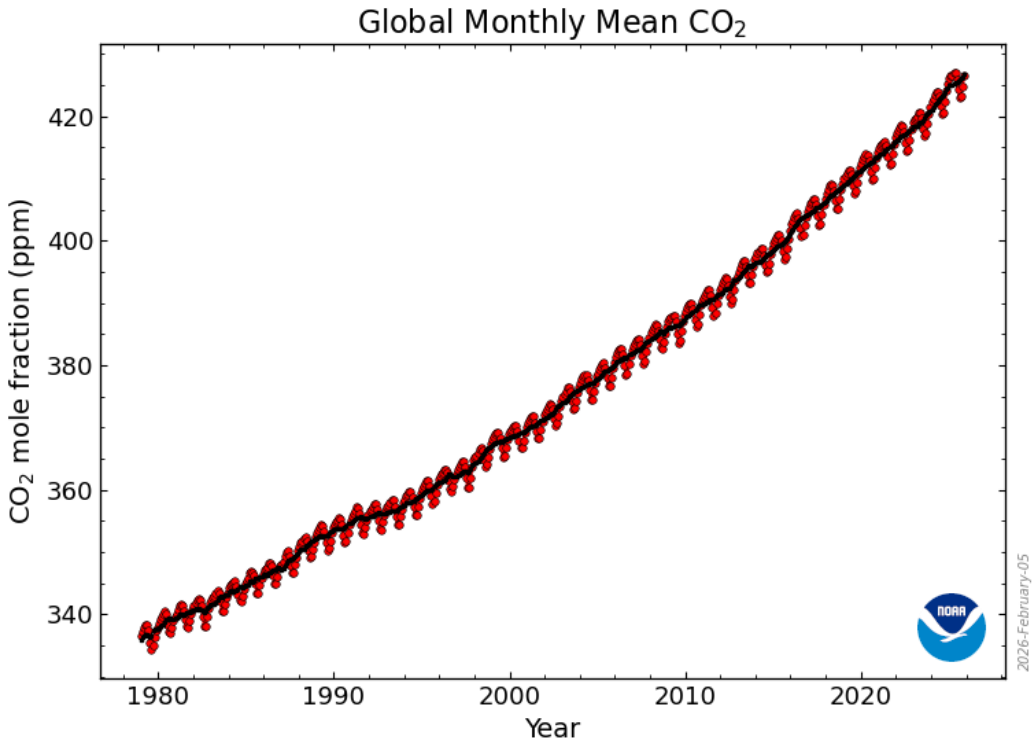

Figure 1 - Global monthly means of Atmospheric carbon dioxide concentrations since 1980. [3]

Since the onset of the Industrial Revolution, atmospheric CO_2 concentrations have risen from approximately 280 ppm to 426.48 ppm (see Figure 1) [3] —the highest level recorded in at least 800,000 years. [4] This dramatic increase has driven a global temperature rise of

approximately 1.1 °C above pre-industrial levels,[4] fundamentally altering Earth's climate system. The consequences are wide-ranging, reinforcing one another to produce a cascade of disruptions across physical and ecological domains.

One of the most visible expressions of this destabilisation is the intensification of extreme weather events. Heatwaves, floods, droughts, and tropical storms are occurring with greater frequency and severity. The 2022 European heatwave, for example, brought widespread drought, wildfires, and agricultural disruption, while Hurricane Ian caused over $100 billion in damages in the south-eastern United States, displacing thousands.[5] In Pakistan, unprecedented monsoon rains inundated one-third of the country, affecting over 33 million people and exacerbating existing public health crises.[6] These events are no longer anomalies—they reflect a shifting climatic baseline.

Rising sea levels further compound these risks. Driven by thermal expansion and accelerating polar ice melt, global sea levels are rising at an increasing rate. The Greenland and Antarctic Ice Sheets together now lose over 500 billion metric tons of ice annually, threatening low-lying island nations with existential risks and exposing coastal megacities to chronic flooding, infrastructure failure, and escalating economic costs.[7]

Ocean acidification represents another, less visible but equally profound consequence of elevated atmospheric CO_2. As the oceans absorb CO_2, surface pH levels decline, weakening the ability of calcifying organisms—such as corals, shellfish, and plankton—to form skeletal structures. This has already led to coral bleaching on the Great Barrier Reef and disrupted shellfish industries in North America.[8] The broader ecological implications are severe, cascading through food webs and undermining the stability of marine ecosystems on which billions depend.

Taken together, these atmospheric and climatic disruptions illustrate the scale, interconnectedness, and urgency of the climate crisis. They do not merely threaten isolated systems; they challenge the resilience of entire ecological and human infrastructures. Addressing this crisis requires deep structural change—one that includes rapid decarbonisation and technologies capable of actively removing CO_2 from the atmosphere.

Ecological and Societal Challenges

The impacts of climate change extend far beyond rising temperatures or shifting weather patterns. They reverberate through ecosystems, economies, and social systems, exposing

the fragility of both natural and built environments. At its core, climate change represents a threat multiplier—deepening existing vulnerabilities and accelerating systemic instability across the globe.

Biodiversity loss is one of the most immediate and irreversible manifestations of ecological disruption. As habitats shift and fragment under the pressures of warming, acidification, and extreme events, many species face extinction faster than they can adapt. Iconic cases such as polar bears in the Arctic and amphibians like the golden toad in Central America illustrate the acute impacts of climate instability and disease spread on vulnerable species. [9] Coral reefs—critical marine biodiversity hotspots—are bleaching with increasing frequency due to ocean warming and acidification, compromising entire marine food webs and the livelihoods they support. [8] These cases reflect a broader trend: nearly 60% of vertebrate populations have declined since 1970, and over a million species are now estimated to be at risk of extinction due to anthropogenic pressures. [2]

Climate change also places profound stress on agricultural systems. Altered precipitation patterns, prolonged droughts, and extreme heat increasingly threaten global food security. Regions such as the Horn of Africa have faced recurrent crop failures, while heatwaves in Europe have reduced staple crop yields by up to 30% in recent years. [10, 11] Beyond climatic factors, unsustainable farming practices have degraded soil health, reducing resilience to further disruption. These effects cascade into food systems, raising prices, intensifying malnutrition, and undermining the livelihoods of farming communities worldwide.

Urban environments are similarly vulnerable. Cities concentrate both populations and infrastructure, making them hotspots of exposure to climate risks such as heatwaves, flooding, and storm surges. Informal settlements in cities like Dhaka and Jakarta regularly experience inundation, with limited resources for adaptation. [6] In wealthier contexts, even well-developed cities like Miami face rising costs from recurrent tidal flooding. Urban planning often fails to keep pace with the scale and pace of change, amplifying existing inequalities in exposure and resilience.

These environmental shocks carry significant economic consequences. Climate-related disasters already cost hundreds of billions annually, with projections reaching $38 trillion per year by 2050 in the absence of substantial mitigation. [12] [13] The economic burden is disproportionately borne by low-income countries—those least responsible for emissions—such as Mozambique, where Cyclone Idai displaced over 1.5 million people and reversed

years of development progress.[8] These losses are not merely financial but structural, disrupting education, healthcare, and governance systems.

The societal implications are equally far-reaching. Climate change is reshaping global migration patterns, with over 20 million people displaced annually by climate-related events.[14] As water becomes scarcer and arable land degrades, competition over resources intensifies, fuelling conflict and political instability in already fragile regions such as the Sahel and the Nile Basin.[7] Health systems are also under strain, with climate-linked increases in heat-related illnesses, respiratory disease, and vector-borne infections like malaria and dengue.[15]

In light of these cascading impacts, calls for climate justice have become more urgent. Wealthier nations—historically responsible for the bulk of emissions—are being pressed to provide financial and technological support to more vulnerable countries. Mechanisms such as the Loss and Damage Fund and the $100 billion annual climate finance commitment under the UNFCCC framework are steps in this direction, though delivery has been uneven.[16]

The complexity of these ecological and societal challenges reinforces the need for an integrated, equitable response. A dual focus on ambitious mitigation and effective adaptation is essential—not only to limit future damage, but to preserve the integrity of the systems upon which human and planetary health depend.

The impacts of climate change extend far beyond atmospheric disruptions, encompassing biodiversity loss, food and water insecurity, and mounting economic and social stresses. In this context, coordinated global policy frameworks—such as the Paris Agreement and Green Climate Fund—have emerged as foundational pillars for collective action, complemented by national and regional initiatives that tailor these ambitions to local contexts.[17–22] In the UK, policy instruments such as the Climate Change Act, the Ten-Point Plan for a Green Industrial Revolution, and industrial carbon capture projects illustrate a pragmatic and collaborative approach to decarbonisation [23–27].

1.1.2. Global Cooperation and Policy

Effectively addressing climate change demands action that is not only ambitious but also unified. Given the transboundary nature of emissions and impacts, no nation can succeed in isolation. Global cooperation and policy coherence have therefore emerged as foundational

pillars in the fight against climate disruption, offering mechanisms to align national interests with collective planetary responsibility.

International frameworks such as the Paris Agreement exemplify this cooperative ethos. As the most significant multilateral accord on climate change to date, the Paris Agreement unites nations under a shared goal: to limit global temperature rise to well below 2 °C, with efforts to cap it at 1.5 °C above pre-industrial levels. By requiring each signatory to submit and periodically update nationally determined contributions (NDCs), the agreement embeds transparency, accountability, and iterative progress into the global response. Crucially, it also provides a platform for capacity building and technology transfer—recognising the differentiated responsibilities and capabilities of developed and developing nations. [17,18]

Complementing this policy framework is the Green Climate Fund (GCF), a key financial mechanism designed to support mitigation and adaptation in vulnerable regions. By mobilising resources from both public and private sectors, the GCF funds a range of initiatives—from renewable energy and climate-resilient agriculture to sustainable urban development—bridging the gap between policy intent and implementation. [19] These investments not only promote low-carbon development but also help build resilience in communities least equipped to confront escalating climate risks.

Regional partnerships further demonstrate the importance of aligning local strategies with global objectives. Initiatives such as the European Green Deal, the African Climate Change Strategy, and the ASEAN Action Plan exemplify how region-specific responses can contribute meaningfully to broader global ambitions. Whether through Europe's focus on carbon neutrality by 2050, Africa's emphasis on climate-resilient development, or ASEAN's regional cooperation in sustainable resource management, these frameworks reflect the diversity of pathways available to meet shared goals. [20–22]

However, the true potential of these agreements lies in their intersection. Aligning international frameworks with national and regional policies enhances coherence, avoids duplication, and amplifies impact. Cooperative strategies enable resource pooling, knowledge sharing, and policy diffusion—mechanisms that are essential for scaling innovation, ensuring equity, and maintaining long-term commitment. In this way, climate governance becomes more than a patchwork of isolated efforts; it evolves into an interconnected system capable of sustained transformation. [17,23]

Looking forward, the scope of climate cooperation must expand beyond emissions reduction to include emerging strategies such as nature-based solutions and circular economy frameworks. These approaches reflect a growing recognition that sustainable development and climate resilience are inseparable. As such, future global policy will increasingly need to embed ecological restoration, resource efficiency, and social equity within its core.

In sum, global cooperation and policy integration are not peripheral to climate action—they are its backbone. The success of international agreements and financial instruments hinges not only on the commitments made, but on the consistency with which they are implemented across scales. Ensuring that governance mechanisms remain adaptive, inclusive, and forward-looking is essential to building a climate-resilient and equitable global future.

1.1.3. UK Efforts to Combat Climate Change

The United Kingdom has positioned itself as a global leader in climate action by combining ambitious policy frameworks with sustained investment in clean technology. Central to this leadership is a strategic approach that integrates legally binding emissions targets, sectoral innovation, and industrial decarbonisation. Key components include the UK's carbon budgeting framework, the Ten-Point Plan for a Green Industrial Revolution, and a strong national focus on developing Carbon Capture, Utilisation, and Storage (CCUS) technologies. [24]

The foundation of the UK's climate strategy lies in the Climate Change Act of 2008, which introduced legally binding carbon budgets to limit greenhouse gas emissions over five-year periods. These budgets—monitored by the independent Climate Change Committee—provide a clear trajectory toward net zero emissions by 2050 and serve as a model for structured, accountable governance internationally. [25]

Building on this foundation, the UK government launched the Ten-Point Plan in 2020, outlining targeted actions to drive a low-carbon economic transition while supporting innovation and job creation. The plan includes initiatives to expand offshore wind, invest in hydrogen technologies, accelerate the adoption of electric vehicles, improve building energy efficiency, develop zero-emission transport, restore natural ecosystems, and advance carbon capture technologies and nuclear innovation. Importantly, it also promotes green finance as a catalyst for sustained private-sector investment. [24]

One of the most notable pillars of this strategy is the UK's investment in carbon capture and storage infrastructure. Leveraging the North Sea's geological storage potential and existing oil and gas infrastructure, the UK is developing a series of industrial CCUS clusters—including the Acorn Project in Scotland, the East Coast Cluster, and HyNet. These clusters are designed to capture CO_2 from hard-to-abate sectors such as steel, cement, and hydrogen production, while taking advantage of shared infrastructure to reduce costs and accelerate deployment. [26]

The Acorn Project exemplifies this cluster approach. Located in northeast Scotland, it repurposes legacy pipelines and offshore storage sites to create a scalable carbon capture system. As part of the broader Scottish Cluster, Acorn aims to capture 5–10 Mt CO_2 annually by 2030 and support Scotland's 2045 net-zero target. In addition to cutting industrial emissions, the project is expected to create regional economic opportunities and serve as a blueprint for similar infrastructure-based decarbonisation strategies. [27]

Through these coordinated efforts, the UK is not only advancing its domestic climate goals but also demonstrating how policy, finance, and innovation can converge to support industrial-scale decarbonisation. Its approach offers a replicable model for countries seeking to meet Paris Agreement targets while maintaining economic competitiveness.

As global emissions continue to rise and hard-to-abate sectors remain a significant challenge, it is increasingly clear that mitigation must extend beyond renewable energy and efficiency alone. Even under the most optimistic deployment scenarios, residual emissions from heavy industry and power generation will persist. Carbon capture technologies—particularly those targeting post-combustion emissions—will therefore play a critical role in achieving climate targets. The following sections explore the principles and potential of these technologies, with a specific focus on solid sorbents for post-combustion CO_2 capture.

1.2. Carbon Capture Technologies

Carbon capture and storage (CCS) is an essential technology for achieving net-zero greenhouse gas emissions, particularly in sectors that are hard to abate, such as heavy industry and energy production. By capturing CO_2 emissions at the source, CCS mitigates their release into the atmosphere, playing a critical role in global climate strategies. This discussion will examine three primary CCS technologies—pre-combustion, oxy-fuel combustion, and post-combustion—evaluating their strengths, limitations, and suitability for specific applications. Each approach offers unique benefits, whether in terms of CO_2

concentration, retrofitting potential, or adaptability to existing industrial systems. Additionally, emerging and hybrid technologies are pushing the boundaries of CCS innovation, seeking to overcome existing economic and technical barriers while enhancing efficiency and scalability.

1.2.1. Pre-Combustion Capture

Pre-combustion CO_2 capture entails recovering CO_2 from a process stream prior to combustion. In this method, the fuel is gasified or partially combusted under elevated pressures (typically 30–70 atm) with a sub-stoichiometric oxygen supply. This generates a synthesis gas (syngas) consisting mainly of carbon monoxide (CO) and hydrogen (H_2) [28,29]. The syngas is then combined with steam and passed through a packed catalyst bed, where the water-gas shift reaction converts CO and water into CO_2 and H_2 (Figure 2).

The primary advantage of pre-combustion capture is the production of high-pressure, high-concentration CO_2, which facilitates separation processes [28,29]. However, significant barriers exist, including high capital investment, the high cost of specialized equipment, limited availability, and the need for extensive support systems, all of which increase technical and economic uncertainties. Pre-combustion methods are particularly suited for integrated gasification combined cycle (IGCC) power plants and hydrogen production facilities, where syngas is a common intermediate.

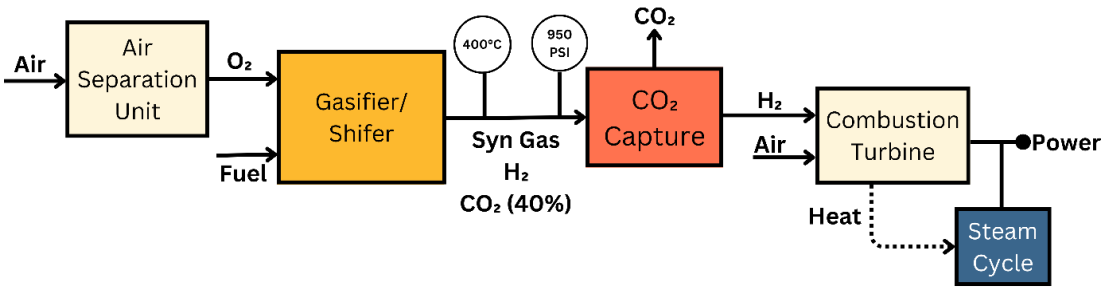

Figure 2 - Simplified schematic of a pre-combustion CO_2 capture system in an IGCC (Integrated Gasification Combined Cycle) power plant, showing key stages: air separation, gasification, shift conversion, CO_2 capture, and power generation. [28]

1.2.2. Oxy-Fuel Combustion

Oxy-fuel combustion restructures the combustion process to generate a flue gas with a high CO_2 concentration [28,29]. This process involves the use of high-purity oxygen (>95%), typically sourced from a cryogenic air separation unit. The oxygen is combined with recycled flue gas to maintain combustion conditions similar to air-fired systems [28,29]. The resulting flue gas is

composed primarily of water and CO_2, which can be easily separated via condensation (Figure 3).

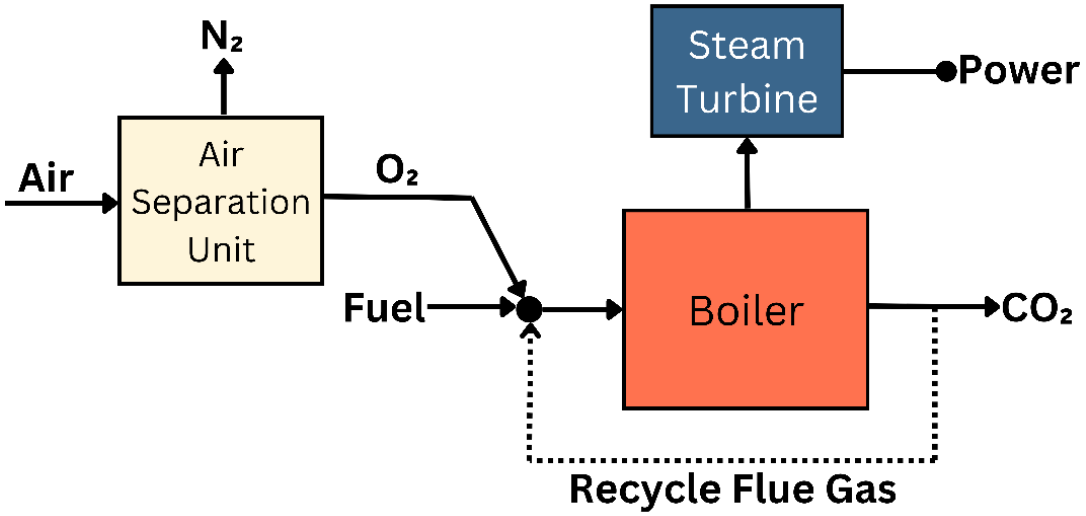

Figure 3 - Simplified schematic of an oxy-fuel combustion system, illustrating oxygen supply via air separation, combustion in a boiler, and power generation through a steam turbine. [28]

Advantages of oxy-fuel combustion include its ability to produce a flue gas with a high CO_2 concentration and its potential for retrofitting existing technologies [28,29]. However, the high cost of oxygen production and the reduction in process efficiency due to the cooling of recycled flue gas pose significant challenges. This method is particularly effective in applications where CO_2 purity is critical, such as enhanced oil recovery or direct storage without further processing.

1.2.3. Post-Combustion Capture

Post-combustion capture involves the separation of CO_2 from flue gases generated after combustion [28,29]. In conventional power plants, flue gases typically contain approximately 8% CO_2 for natural gas and 15% CO_2 for coal, both at atmospheric pressure (Figure 4). The low CO_2 partial pressure complicates the development of cost-effective separation technologies [28,29]. Flue gas streams in post-combustion processes are also typically encountered at moderately elevated temperatures (commonly 40–60 °C after heat recovery), which is an important consideration for adsorbent evaluation and process design.

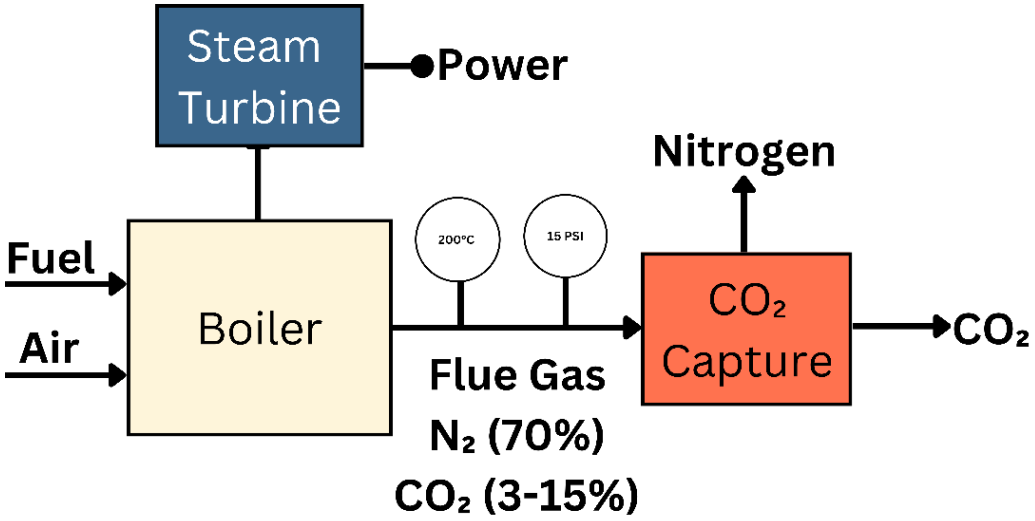

Figure 4 - Simplified schematic of a post-combustion CO_2 capture system, showing CO_2 removal from boiler flue gas prior to release, with power generation via steam turbine.[28]

Despite these limitations, post-combustion capture is regarded as one of the most promising technologies for achieving near-term reductions in CO_2 emissions. Its primary advantage lies in its applicability to retrofitting existing power plants and its suitability for other large-scale stationary point sources, such as steel and cement manufacturing facilities. Additionally, ongoing advancements in solvent-based and solid adsorbent systems have the potential to enhance the cost-effectiveness of this approach [28,29].

Each carbon capture technology presents distinct advantages and limitations depending on the industrial context. Pre-combustion capture is particularly suited to systems where syngas is an intermediate, such as in hydrogen production and IGCC power plants, though its implementation is constrained by high capital costs and complexity. Oxy-fuel combustion offers the benefit of generating high-purity CO_2 streams, yet the associated energy penalty and infrastructure requirements limit its widespread applicability. In contrast, post-combustion CO_2 capture stands out as the most practical and immediately deployable solution for large-scale emission reductions. Its compatibility with existing energy infrastructure, especially in hard-to-abate sectors like power generation, steel, and cement, makes it a critical pathway for near-term decarbonisation. This work therefore focuses on post-combustion capture as the most feasible and impactful approach within current industrial and regulatory frameworks.

1.3. Carbon Capture Techniques

Several approaches for CO_2 separation exist, namely adsorption, absorption, cryogenic and membrane processes. The approach taken is determined by the condition of the gas stream of which the CO_2 is being separated. Factors to be considered are the purity of CO_2, the pressure relative to ambient conditions and the composition of gases.

1.3.1. Absorption

Absorption is a chemical or physical phenomenon in which the molecules, atoms, and ions of the substance being absorbed (sorbate) enter the bulk phase of the material in which it is taken up (sorbent). In the case of CCS absorption techniques, it is CO_2 entering a liquid phase.

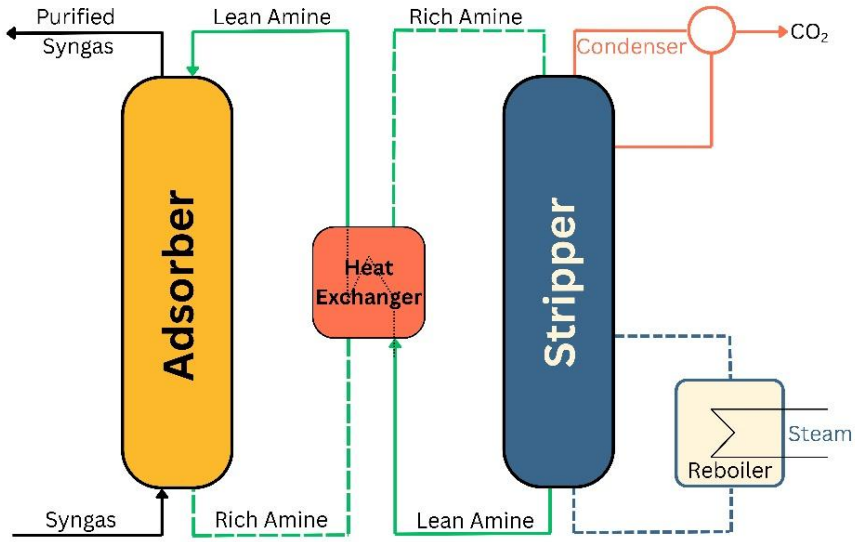

Figure 5 - Flow Diagram of MEA adsorption Capture System [30]

To produce a pure stream of CO_2, a regeneration step is required after absorption. This involves exposing the saturated solvent to elevated temperatures or reduced pressure to liberate the CO_2 from the solution.

Physical absorption operates under Henry's Law, where gas solubility increases with partial pressure. As such, it is effective under high-pressure and high-CO_2 concentration conditions, making it suitable for pre-combustion capture systems. Common physical solvents include Selexol, Rectisol, Purisol, and the Fluor process [29,31]. These solvents generally exhibit low regeneration energy requirements, making the process energetically favourable. However, their effectiveness diminishes at low CO_2 partial pressures, limiting

applicability in post-combustion scenarios. Additionally, physical absorbents tend to suffer from selectivity issues and greater susceptibility to co-absorption of impurities, requiring pre-treatment steps.

Chemical absorption, by contrast, involves CO_2 reacting with sorbents such as aqueous amines (e.g., monoethanolamine, MEA) to form carbamate or bicarbonate species. This method performs well under low-pressure, dilute CO_2 conditions, such as those typical of post-combustion flue gases (see Figure 5). It offers high selectivity and removal efficiency and is the most technologically mature CCS method to date [29,31–33]. However, chemical absorption presents several limitations: the regeneration step is highly energy intensive, often accounting for up to 35% parasitic load in coal-fired power plants; amine degradation leads to solvent loss and the formation of corrosive and toxic by-products; and corrosion of equipment requires costly materials and maintenance.

Despite ongoing improvements in solvent design, such as sterically hindered amines or blended formulations, these drawbacks hinder the economic scalability of amine-based systems. Thus, while chemical absorption remains a benchmark technology, especially for retrofit applications, its widespread deployment is constrained by high operational costs and environmental considerations.

1.3.2. Adsorption

Adsorption is the chemical or physical adhesion of a thin layer of molecules to a surface (shown in Figure 6). In the case of CCS, adsorption involves CO_2 adhering to the surface of a solid material.

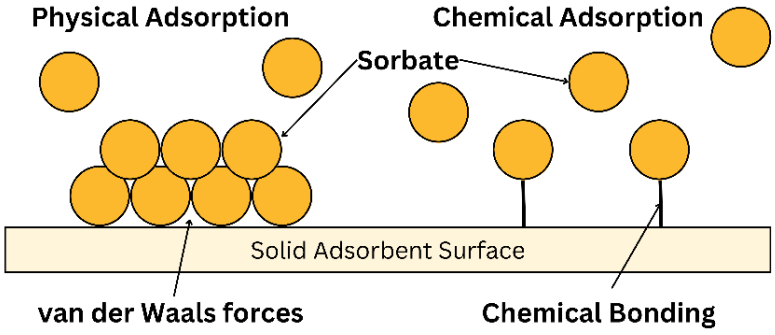

Figure 6 - Principle of Adsorption Illustration.[34]

Physical adsorption (physisorption) relies on Van der Waals interactions between CO_2 molecules and the sorbent surface. Due to their weak binding energies, physisorbents can be regenerated with low energy input, typically via mild temperature or pressure changes. Materials such as activated carbons, zeolites, and metal-organic frameworks (MOFs) have

been extensively investigated for this purpose. [29,31–33] The key advantage of physisorption lies in its reversibility and low thermal budget, which may significantly reduce operational costs.

However, physisorption faces notable limitations in post-combustion applications: selectivity is inherently low due to non-specific interactions, and performance is highly sensitive to flue gas humidity, which often leads to competitive adsorption and pore blockage. Additionally, some physisorbents exhibit slow kinetics or degrade under cycling conditions, especially in the presence of acid gases (SO_x, NO_x). [29,31–33]

Chemical adsorption (chemisorption), by contrast, involves stronger, often covalent interactions between CO_2 and surface functional groups, such as amines, metal oxides, or nitrogen-containing species. This results in higher CO_2 uptake and improved selectivity, especially under low partial pressure conditions relevant to flue gas streams. [35,36] Chemisorbents are more robust to impurities and can be engineered for targeted capture performance.

The downside of chemisorption is its higher regeneration energy, arising from stronger sorbate–sorbent bonds. This trade-off between capacity/selectivity and regeneration cost must be optimised for practical deployment. Moreover, functionalised surfaces can suffer from thermal or oxidative degradation during cycling, limiting long-term stability and increasing maintenance costs.

Regeneration Techniques for Solid Adsorbents

Several regeneration strategies are employed to release CO_2 from adsorbent materials, each with specific advantages and drawbacks depending on the sorbent type, adsorption mechanism, and process conditions:

- **Temperature Swing Adsorption (TSA):** TSA involves heating the sorbent to overcome the adsorption energy and desorb CO_2. It is widely applicable to both physisorbents and chemisorbents and is conceptually simple and scalable. A key limitation of TSA is its slow thermal response, which can result in long cycle times and increased energy consumption due to the need to heat the entire adsorbent bed. Additionally, frequent thermal cycling may induce material degradation or sintering in thermally sensitive sorbents.

- **Pressure Swing Adsorption (PSA):** PSA operates by reducing the system pressure, thereby lowering the partial pressure of CO_2 and promoting desorption. It is rapid and energy-efficient when used with physisorbents under elevated pressure, making it particularly attractive for pre-combustion capture. However, its effectiveness is limited at low CO_2 partial pressures, such as those found in post-combustion flue gas. Moreover, the mechanical demands of repeated pressurisation/depressurisation can increase equipment wear and maintenance requirements.
- **Pressure-Temperature Swing Adsorption (PTSA):** PTSA combines moderate heating with partial pressure reduction to improve desorption efficiency while limiting the energy penalty of pure TSA or PSA modes. This hybrid approach enables faster regeneration and lower regeneration temperatures, making it suitable for sorbents with intermediate adsorption strengths or limited thermal stability.
- **Electrical Swing Adsorption (ESA):** ESA uses resistive or dielectric heating by passing a low-voltage electrical current through conductive or semi-conductive adsorbents. It offers high spatial and temporal control, allowing rapid and selective heating of only the adsorbent surface, thereby minimising energy losses and enabling fast cycle times. This makes ESA a highly promising approach for low-energy, high-frequency adsorption systems. Nonetheless, its applicability is currently restricted by material constraints—only conductive adsorbents can be used—and scaling challenges remain due to the need for precise electrical integration and uniform heating in larger systems. [29,31,37]
- **Microwave-assisted Swing Adsorption (MWSA):** MWSA is an emerging regeneration technique that applies microwave irradiation to heat the sorbent volumetrically and selectively, offering a faster and more energy-efficient alternative to conventional Temperature Swing Adsorption (TSA). Unlike conductive or convective heating, microwaves directly excite polar or conductive regions within the adsorbent, achieving rapid desorption and significantly reducing regeneration times—up to 50 % faster than conventional heating methods for zeolite 13X [38]. The volumetric and selective nature of microwave heating minimises heat losses to reactor walls and may lower the apparent desorption activation energy, enhancing cycling productivity and overall process efficiency.

In summary, the selection of a regeneration method must balance energy efficiency, cycle speed, thermal stability, and equipment complexity. TSA is well-suited for durable, high-capacity sorbents where speed is less critical, PSA excels in high-pressure applications, and ESA holds potential for future low-energy CCS technologies—provided suitable materials and engineering solutions are developed.

1.3.3. Cryogenic Process

Cryogenic separation captures CO_2 by compressing and cooling flue gases to induce phase transitions, allowing CO_2 to condense or solidify while other components remain gaseous (see Figure 7). This method is commercially viable for gas streams with high CO_2 concentrations (typically >50%), such as those from natural gas processing or fermentation, but becomes energetically and economically impractical at the low CO_2 partial pressures characteristic of post-combustion flue gas. [29,31]

Cryogenic separation offers several advantages: it does not require chemical or solid sorbents, thereby reducing issues related to degradation or regeneration; it can operate under atmospheric pressure; and it directly produces liquid CO_2, which simplifies downstream transport and storage logistics. These features make cryogenic methods particularly attractive for integrated capture–transport systems.

However, the process is highly energy-intensive, especially due to the need for gas compression and deep cooling, often below −78.5 °C (the sublimation point of CO_2). This imposes a significant energy penalty, limiting its feasibility for low-concentration, large-volume gas streams such as those from coal or gas-fired power plants. In such contexts, the parasitic energy load can rival or exceed that of chemical absorption. [39]

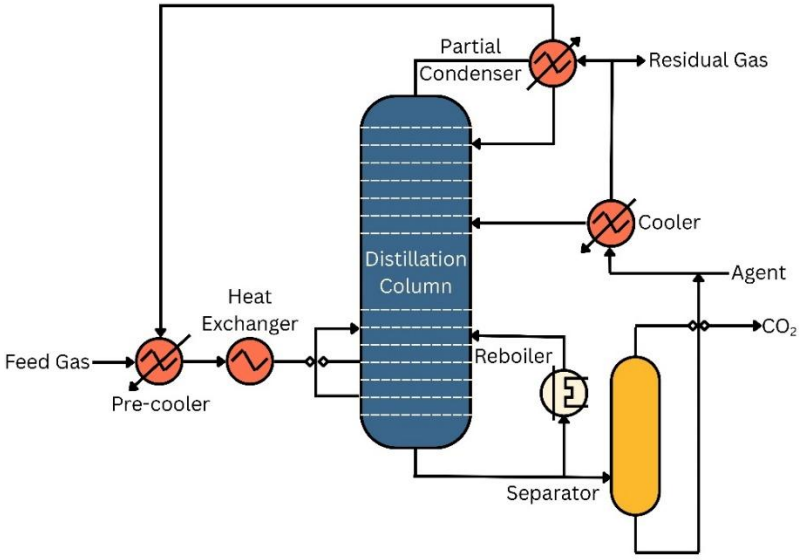

Figure 7 - Flow Diagram of Cryogenic CO_2 Capture [40]

Furthermore, the presence of impurities (e.g., H_2O, SO_2, NO_x) complicates the separation. These components may form ice, clathrates, or corrosive solids during cooling, leading to fouling, plugging, and equipment corrosion. Pre-treatment steps—such as gas drying and impurity scrubbing—are often necessary, increasing system complexity and operational cost. [29,31]

In summary, while cryogenic separation is effective in niche applications with high CO_2 purity and concentration, its application to post-combustion capture is constrained by high energy demand, sensitivity to contaminants, and limited scalability. As such, it is more suited as a complementary technology rather than a primary solution for large-scale CCS.

1.3.4. Membrane Processes

Membrane-based separation technologies function by exploiting the preferential permeation of gas components through a selective barrier (see Figure 8). In carbon capture applications, a high-pressure flue gas stream is applied to one side of the membrane, and carbon dioxide diffuses through more readily than other components due to differences in solubility and diffusivity. This produces a CO_2-enriched permeate stream and a depleted retentate. Various membrane types are in use, including polymeric, ceramic, and mixed-matrix membranes, each offering different trade-offs in terms of permeability, selectivity, thermal stability, and mechanical robustness. [29,31]

Membranes offer several notable advantages. They operate continuously without phase changes or chemical solvents, require relatively small footprints, and are amenable to

modular design, making them attractive for decentralised or retrofit installations. Polymeric membranes are inexpensive and easily manufactured, while ceramic and mixed-matrix membranes can achieve greater chemical resistance and higher temperature operation. These benefits have driven substantial research interest and led to steady improvements in membrane materials and module design. [41]

However, several critical limitations restrict their current viability for large-scale CCS deployment, particularly in post-combustion capture. First, the trade-off between selectivity and permeability remains a central challenge; enhancing one typically compromises the other. This makes it difficult to achieve both high purity and high capture rates under the low CO_2 partial pressures characteristic of power plant flue gas. Second, membrane materials are sensitive to flue gas impurities such as SO_2, NO_x, and water vapour, which can lead to fouling, plasticisation, or chemical degradation, thereby reducing separation performance and operational lifespan. Third, creating the pressure differentials required for separation necessitates gas compression, introducing a non-negligible energy penalty, especially when treating large volumes of low-pressure exhaust gas. Lastly, while membrane technologies have shown promise in pilot-scale studies, the lack of long-term durability data, high material costs for advanced configurations, and concerns over scalability continue to pose barriers to widespread implementation. [41]

Despite these constraints, ongoing advancements in membrane chemistry, structure, and process integration are gradually improving the feasibility of this approach. In particular, hybrid systems that combine membranes with absorption or adsorption processes are being explored to overcome individual weaknesses and enhance overall efficiency. As these technologies mature, membranes may become an increasingly important component of flexible, low-energy carbon capture systems.

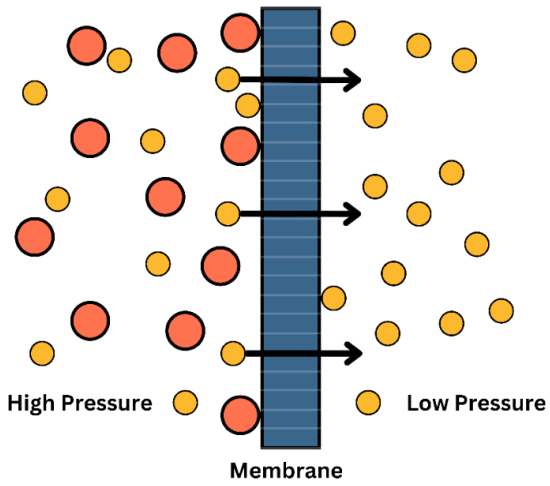

Figure 8 - Principle of gas separation membrane.[42]

Overall, the selection of CO_2 separation techniques is governed by key factors such as CO_2 purity, operating pressure, and gas composition. High-purity, high-pressure streams, such as those found in natural gas processing or pre-combustion systems, can be efficiently treated using cryogenic or membrane-based approaches. In contrast, post-combustion flue gases—typically low in CO_2 concentration, near atmospheric pressure, and rich in impurities—present a more complex challenge. These conditions necessitate technologies capable of maintaining high selectivity and capacity under dilute and variable conditions. While chemical absorption with amines remains the industry benchmark, it is hindered by high regeneration energy requirements, solvent degradation, and environmental constraints. Adsorption-based approaches offer an attractive alternative, with the potential for lower energy penalties and improved material stability. However, current adsorbents often suffer from limited selectivity, insufficient CO_2 capacity at low pressures, or poor long-term performance under realistic conditions.

This study therefore focuses on advancing solid adsorbent systems tailored for post-combustion carbon capture. Specifically, it investigates the development and optimisation of biochar-based adsorbents derived from waste biomass, with targeted activation strategies to enhance CO_2 uptake, selectivity, and regeneration efficiency. By addressing the material-level limitations of current sorbents and aligning with the operational constraints of post-combustion capture, this work aims to contribute to the development of scalable, cost-effective, and sustainable CCS technologies.

1.4. Solid Adsorbents for Post-Combustion Capture

The limitations of existing separation technologies in low-pressure, low-concentration environments have prompted growing interest in alternative materials for post-combustion CO_2 capture. Solid adsorbents, in particular, offer a compelling opportunity to reduce the energy and operational costs associated with solvent-based systems. Their ability to operate through reversible interactions, without the need for bulk liquid regeneration, makes them especially attractive for retrofitting at large stationary sources such as power plants, steelworks, cement kilns, and chemical facilities—industries that collectively contribute over 40% of global CO_2 emissions. [43,44]

However, deploying solid adsorbents at scale presents its own set of challenges. To be viable, these materials must perform efficiently under real flue gas conditions, which typically include dilute CO_2, water vapour, oxygen, and various contaminants. Achieving this requires a careful balance of structural and chemical properties that enable high uptake, fast kinetics, and long-term stability. The following section outlines the key attributes that govern adsorbent performance and discusses how they are measured and evaluated for application in post-combustion carbon capture.

1.4.1. Required Attributes

When assessing solid sorbents for use in post-combustion carbon capture, several attributes are required for them to work effectively and need to be measured. [44–49]

High CO_2 Adsorption Capacity

The CO_2 adsorption capacity of a sorbent—defined as the amount of CO_2 adsorbed per unit mass of material—is a primary metric for assessing sorbent performance in post-combustion applications. This capacity is governed by several physicochemical properties, including surface area, pore size and volume, surface basicity, the presence of functional groups, and the inclusion of alkali or alkaline earth metals [44–46]. Materials with high specific surface areas and well-developed microporosity tend to exhibit greater CO_2 uptake (see relationship in Figure 9), particularly under low partial pressures typical of flue gas environments.

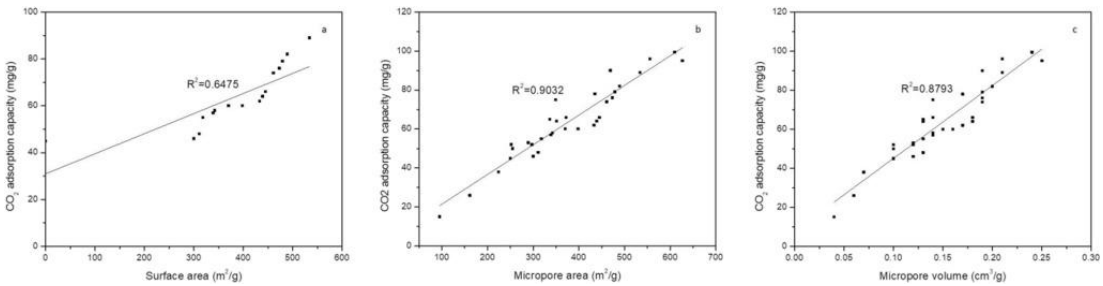

Figure 9 - Relationship between the (a) specific surface area, (b) micropore area, (c) micropore volume, and CO_2 adsorption capacity of biochar [36]

It is well established that the slope of the adsorption isotherm at low pressures indicates the strength of adsorbate–adsorbent interactions. Sorbents that exhibit a steep initial isotherm slope tend to have higher CO_2 affinity and capacity under dilute conditions. Accordingly, isotherms measured at <0.4 bar CO_2, 1–2 bar total pressure, and temperatures below 80 °C are most relevant to post-combustion capture performance.

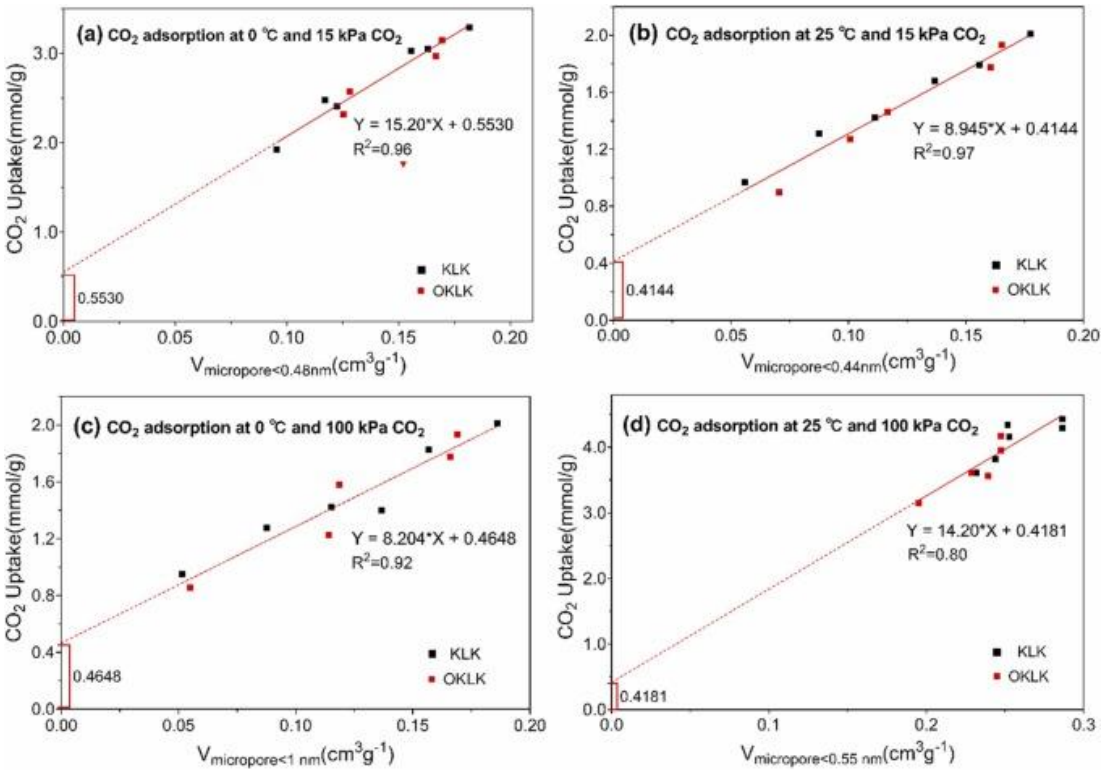

Figure 10 - Relationship between CO_2 uptake and ultra-micropore volume of the Kraft lignin carbons (a) ≤ 0.48 nm, 15 kPa CO_2 and 0 °C; (b)≤ 0.44 nm, 15 kPa CO_2 and 25 °C; (c) ≤ 1 nm, 100 kPa CO_2 and 0 °C; (d) ≤ 0.55 nm, 100 kPa CO_2 and 25 °C [50]

However, many materials underperform due to structural or chemical limitations. Low surface areas or inadequate pore development restrict the number of available adsorption sites. Even in high-surface-area materials, the absence of ultramicropores (pores ≤ 0.7 nm)

can significantly limit CO_2 capacity, as these pores are optimally sized for CO_2 uptake via pore-filling mechanisms under low-pressure conditions (see Figure 10) [50–52]. Materials dominated by mesopores or macropores, although potentially beneficial for diffusion, tend to offer low adsorption densities due to poor confinement effects.

Furthermore, insufficient surface basicity or a lack of heteroatom functional groups reduces interaction strength with CO_2, which is mildly acidic in nature. Carbon-based sorbents that are chemically inert or non-polar often exhibit limited uptake unless their surface chemistry is deliberately tailored. The presence of oxygen-containing groups or residual tars can also interfere with adsorption by occupying active sites or blocking pores.

To enhance CO_2 capacity, research increasingly focuses on optimising microporous structure—especially ultramicropores—and introducing basic functional groups through activation processes or heteroatom doping. These strategies aim to increase both the number and accessibility of high-affinity adsorption sites under relevant operational conditions.

Fast Adsorption/Desorption Kinetics

For a solid sorbent to be viable in post-combustion CO_2 capture, it must exhibit sufficiently rapid adsorption and desorption kinetics. These rates determine how quickly the sorbent can take up and release CO_2, directly influencing the cycle duration of the capture process. Faster kinetics enable shorter adsorption–desorption cycles, which improves throughput, reduces equipment size, and enhances process efficiency in industrial applications.

Kinetic parameters are typically determined using dynamic uptake experiments, such as mass relaxation curves or breakthrough studies, which measure the rate at which the sorbent approaches equilibrium following a step change in pressure or concentration. Materials that reach a high percentage of their total adsorption capacity within a short time—typically on the scale of seconds to a few minutes—are considered preferable for cyclic operation, though exact performance depends on the specific system and conditions used.

Conversely, materials with slow kinetics may limit process efficiency, as longer cycle times reduce the volume of gas that can be treated per unit time and may require larger or parallelised equipment to maintain throughput. Diffusion limitations in narrow pores, poor accessibility of active sites, or overly strong binding interactions can all contribute to slower

uptake and hinder regeneration.

Thus, beyond total adsorption capacity, the speed with which equilibrium is reached is a critical design parameter. Optimising pore architecture and surface accessibility is essential for enhancing kinetics and ensuring the practicality of sorbents in real-world CCS systems. [53]

Selectivity

Selectivity refers to the ability of an adsorbent to preferentially adsorb one component of a gas mixture over others. In the context of post-combustion carbon capture, high CO_2 selectivity is essential because the flue gas is dominated by nitrogen, with typical compositions of 8–10% CO_2, 67–72% N_2, 18–20% H_2O, and 3–5% O_2. Since nitrogen makes up the majority of the flue gas, a sorbent must distinguish CO_2 from N_2 with high efficiency to ensure effective separation and minimise energy-intensive downstream purification.

The most common metric used to assess selectivity is the CO_2/N_2 selectivity, which quantifies how much more readily a material adsorbs CO_2 relative to N_2. While other components like H_2O and O_2 are also present, N_2 is the principal competitor due to its abundance and similar molecular size and volatility. Water vapour, although influential, is often considered separately due to its strong competitive adsorption and interference with CO_2 uptake, particularly on hydrophilic surfaces. In many cases, industrial flue gas streams undergo a dehydration step prior to carbon capture to minimise this interference, allowing studies to focus primarily on the CO_2/N_2 separation challenge.

Selectivity can be predicted from pure gas isotherms using Ideal Adsorbed Solution Theory (IAST), which estimates the adsorption behaviour of gas mixtures based on equilibrium data. The IAST-predicted CO_2/N_2 selectivity S is defined as:

$$S_{CO_2/N_2} = \frac{(q_{CO_2}/q_{N_2})}{(y_{CO_2}/y_{N_2})} \qquad \textit{Equation 1}$$

where q and y are the mole fractions of CO_2 and N_2 in the adsorbed and gas phases, respectively [54]. Higher values indicate stronger preference for CO_2 over N_2. However, it is important to note that IAST calculations assume equilibrium and do not capture dynamic or kinetic effects. In real systems, particularly under flow conditions, actual performance may differ due to diffusion limitations or competitive adsorption. For this reason, fixed-bed reactor measurements are often used to better approximate real-world separation behaviour.

Mechanistically, selectivity can arise from either physisorption or chemisorption. In physisorption, separation is driven primarily by differences in molecular size and polarizability. Since CO_2 is only slightly more polar than N_2, selectivity is generally low unless enhanced by ultramicropores. Pores ≤ 0.7 nm provide tighter confinement, which disproportionately favours the smaller and more quadrupolar CO_2 molecule [55]. In chemisorption, selectivity is enhanced by incorporating basic functional groups, heteroatoms, or metal species into the sorbent surface that interact more strongly with the acidic CO_2 molecule. Nitrogen doping and alkali metal incorporation are common strategies used to improve CO_2 affinity and thus selectivity.

Ultimately, high CO_2/N_2 selectivity is critical for reducing parasitic losses and improving process efficiency in post-combustion carbon capture systems. It ensures that capture systems target the desired component while minimising sorbent saturation and regeneration costs driven by the adsorption of inert or undesired gases.

Low Energy Requirements for Regeneration

The high energy demand of current carbon capture technologies is one of the principal barriers to their large-scale deployment. In particular, amine-based solvent systems used in chemical absorption incur parasitic energy penalties of up to 30–35% of a power plant's output, primarily due to the need to heat large volumes of aqueous solution during solvent regeneration [56]. This imposes a significant operational cost and limits the feasibility of widespread implementation.

Solid sorbents offer a potential solution by reducing the energy required for regeneration. Unlike solvent systems, they do not require the heating of a bulk liquid phase. Instead, regeneration involves desorbing CO_2 from the solid surface, which generally demands lower thermal input. The extent of this energy requirement is closely linked to the heat of adsorption—a measure of the interaction strength between CO_2 molecules and the sorbent surface.

The heat of adsorption is typically determined using the Clausius–Clapeyron equation, applied to adsorption isotherms measured at different temperatures [49,55]. It reflects the energy needed to reverse the adsorption process: materials with higher heats of adsorption bind CO_2 more strongly but may require more energy to regenerate, while those with lower values enable easier desorption but may sacrifice capacity or selectivity. Therefore, an

optimal sorbent balances sufficient binding strength for effective CO_2 uptake with low regeneration energy to maintain economic viability.

Typical values of the heat of CO_2 adsorption vary by material class. For physisorbents such as activated carbons, zeolites, and MOFs, values range from 15–40 kJ/mol, indicating relatively weak interactions and low energy requirements. Amine-functionalised materials and some metal-organic frameworks exhibit intermediate strengths, typically around 40–80 kJ/mol, while strong chemisorbents, including alkali-doped sorbents and metal oxides, can exceed 80 kJ/mol. For instance, Zeolite 13X shows values around 25–40 kJ/mol, amine-grafted silicas around 60–80 kJ/mol, and K_2CO_3-based materials can reach or surpass 100 kJ/mol. These differences guide material selection based on the trade-off between binding strength and regeneration energy. [57]

Operational Stability

The long-term viability of solid sorbents in post-combustion carbon capture hinges on their ability to maintain performance under realistic process conditions. Operational stability encompasses both chemical and mechanical durability. Chemically, sorbents must resist degradation over multiple adsorption–desorption cycles, particularly when exposed to impurities such as SO_2, NO_2, H_2O, and O_2. [36,58] Amine-functionalised materials, for instance, are prone to oxidative breakdown and leaching, whereas carbon-based sorbents and metal oxides tend to offer greater resistance, though data under industrial conditions remain limited. Mechanically, materials must withstand handling, abrasion, and thermal cycling without excessive attrition or fragmentation, which can lead to loss of capacity and increased operational costs. Despite its importance, stability is often underreported in the literature, highlighting the need for standardised testing protocols to support scalable deployment. [59,60]

Cost and Scalability

The economic viability of solid sorbents is tightly linked to both production cost and the scalability of synthesis. While high-performing materials such as MOFs or engineered polymers may offer excellent adsorption metrics, their synthesis often relies on expensive precursors and complex, low-throughput procedures, limiting their practical deployment. In contrast, sorbents produced using low-cost reagents and simple thermal activation methods are more amenable to scale-up and industrial integration. [55,61]

Processes that avoid multi-step chemical treatments, use readily available materials, and eliminate the need for extensive post-processing are particularly attractive. Techno-economic assessments suggest a target production cost of <$10/kg for viable CCS sorbents. These considerations are essential for translating laboratory-scale performance into commercially relevant technologies. [57]

1.5. Solid Adsorbent Landscape for Post-combustion CO_2 Capture

Activated carbons (ACs) and zeolites were among the first solid materials used for CO_2 capture. These materials showed reasonable adsorption capacities and could be regenerated for reuse, but they had limitations like low selectivity and inefficiency in some conditions. To address these issues, researchers have developed more advanced materials, including metal-organic frameworks (MOFs), polymers, and metal oxides. These new materials are designed to improve CO_2 capture by being more effective, stable, and cost-efficient.

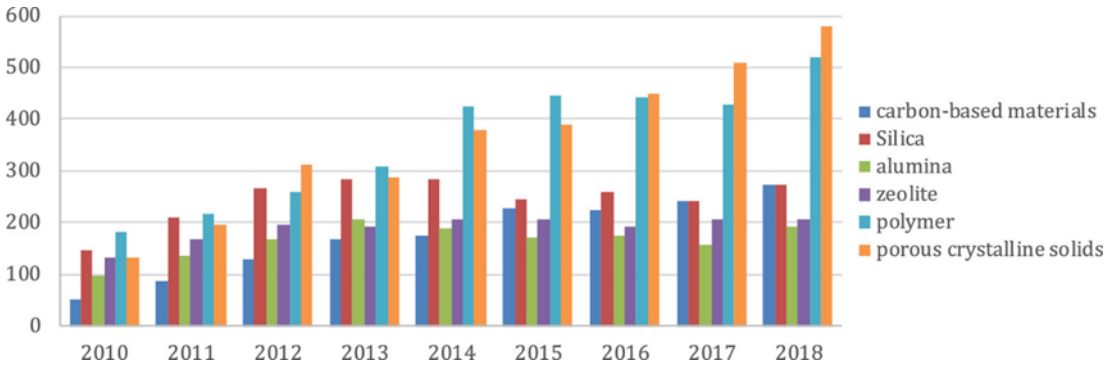

Figure 11 - Research publication trends (2010–2018) for various classes of adsorbent materials used in CO_2 capture. [62]

Research in this area has grown rapidly, with a significant rise in studies published since 2010, as shown in Figure 11. This growth reflects the increasing need for materials that can meet the strict requirements of carbon capture and storage (CCS) technologies, especially post-combustion capture (PCC). Effective adsorbents must have high selectivity for CO_2, require low energy for regeneration, and maintain performance over many cycles of use. As a result, scientists have focused on enhancing the physical and chemical properties of adsorbents to meet these demands.

This section explores the current state of solid adsorbents for CO_2 capture, focusing on key performance factors like adsorption capacity, selectivity, regenerability, and stability. It also discusses challenges like cost and scalability. The following sections will analyse different

types of adsorbents, including carbon-based materials, silica and zeolite systems, porous crystalline solids, and metal oxides, examining their strengths and weaknesses in the context of post-combustion CO_2 capture. [63,64]

1.5.1. Porous Carbon Materials

Porous carbon materials have been integral to human innovation for thousands of years, with their origins traced back to the discovery of charcoal formed from the incomplete burning of wood. Over time, technological advancements have given rise to a wide array of carbon-based materials, including activated carbon, carbon fibres, carbon nanotubes, graphene, and fullerenes. These materials, composed primarily of carbon atoms arranged in diverse configurations, exhibit a range of structures and properties, making them indispensable in fields such as electronics, aerospace, catalysis, energy storage, and environmental technologies.

Among their many uses, adsorption stands out as a particularly significant application. Porous carbons, known for their extensive surface areas and adaptable pore structures, are highly effective as adsorbents. This is especially true for processes like post-combustion CO_2 capture (PCC), where they present an alternative to chemical adsorbents. While chemical adsorbents offer strong CO_2 interactions, porous carbons excel in other areas, such as rapid adsorption kinetics, high stability over repeated cycles, and cost efficiency. These advantages make them a promising option for reducing CO_2 emissions in a practical and sustainable manner.

The production of porous carbons typically involves the carbonization of organic precursors in an inert environment. This process, which includes decomposition, crosslinking, and the release of volatile compounds, results in the formation of a carbon matrix with a porous structure. The simplicity, scalability, and affordability of this method have contributed to the widespread use of porous carbons in various applications.

Carbon-based materials have shown exceptional promise in the field of post-combustion CO_2 capture. Their wide-ranging structural properties, from hierarchical porosity to molecular scale tunability, allow for the efficient adsorption of CO_2 under varied conditions. The development of advanced porous carbons has focused on optimizing these features to enhance performance metrics such as adsorption capacity, selectivity, and cycling stability. The following sections explore the preparation methods, structural features, and specific

advantages of key porous carbon materials, highlighting their roles in advancing post-combustion capture technologies and addressing broader environmental challenges. [62,65]

Activated Carbons

Activated carbons (ACs) are widely recognised as one of the most promising classes of solid sorbents for post-combustion CO_2 capture, owing to their high surface area, tunable porosity, and relatively low production cost. Derived from a wide range of precursors—including biomass, coal, and synthetic polymers—their performance is closely tied to both the nature of the starting material and the activation method employed.[66]

Synthesis typically involves either physical activation using oxidising gases like CO_2 or steam at elevated temperatures, or chemical activation with agents such as KOH, H_3PO_4, or $ZnCl_2$. These processes generate a porous carbon matrix characterised by a high proportion of micro- and mesopores, which is critical for effective gas adsorption. The precursor itself plays a central role in defining the final material's properties; for instance, nitrogen-rich feedstocks or post-treatment methods can introduce basic surface functionalities that enhance CO_2 affinity. Incorporation of heteroatoms—particularly nitrogen—improves selectivity by providing active sites that interact favourably with the quadrupole moment of CO_2.[67]

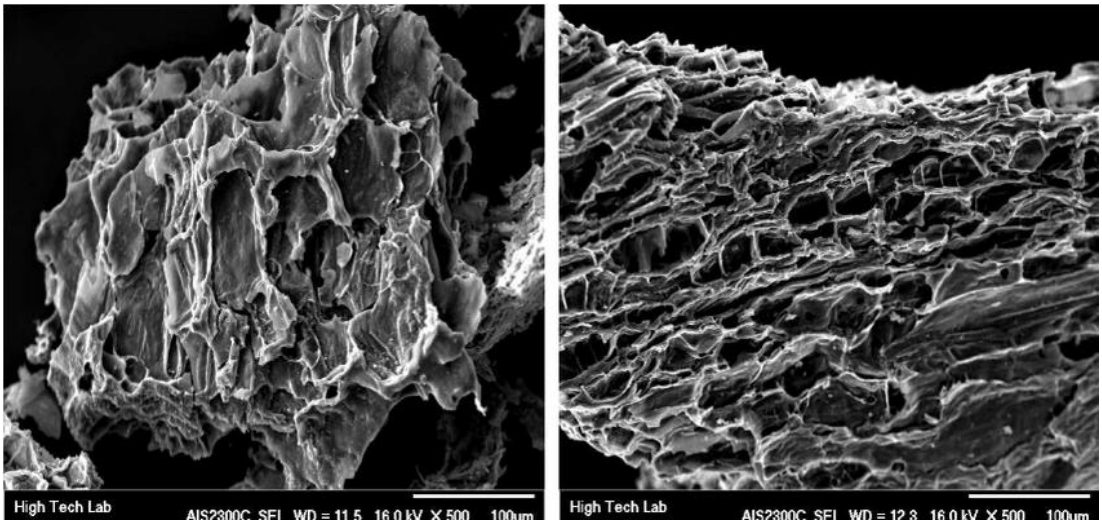

Figure 12 - SEM image of activated carbon derived from benzimidazole-linked polymers [68]

Activated carbons (see Figure 12) have demonstrated high CO_2 uptake capacities, particularly under ambient conditions and low partial pressures typical of flue gas. Chemically activated carbons produced from agricultural waste, such as rice husks, have achieved adsorption capacities exceeding 5 mmol/g at 1 bar and 30°C, a performance

attributed to the synergy between high surface area, optimised pore architecture, and nitrogen functionality. [69] Their adsorption kinetics are generally fast, and the regeneration energy requirements are lower than those of liquid amine systems, making them well-suited for cyclic operation. Furthermore, they exhibit good mechanical and chemical stability across multiple adsorption–desorption cycles, and their production from low-cost precursors supports economic scalability.[67]

Despite these advantages, there are important trade-offs to consider. While their regeneration energy is lower than that of chemical solvents, it can still be non-negligible, especially for carbons with strong CO_2-binding sites. Additionally, achieving precise control over pore size distribution—particularly the formation of ultramicropores critical for low-pressure CO_2 capture—remains technically challenging and may require additional processing steps. Activated carbons are also relatively hydrophobic, which can be advantageous in humid flue gas environments, but this may reduce their performance in applications requiring water co-adsorption. Finally, while their synthesis is more scalable than that of many advanced materials, issues such as precursor variability and environmental impact of chemical activators (e.g. KOH) must be addressed to ensure sustainable production.

Overall, activated carbons offer a compelling balance of performance, cost, and durability, positioning them as strong candidates for industrial post-combustion carbon capture. However, continued research is required to optimise their synthesis and tailor their properties to meet the specific demands of large-scale deployment. The following section explores how biomass-derived variants further enhance the sustainability and circularity of this material class.

Spent Coffee Ground-Derived Activated Carbons

Spent coffee grounds (SCGs) have emerged as a particularly promising biomass precursor for the production of activated carbons for post-combustion CO_2 capture. As one of the most abundantly generated household and commercial food wastes, with global production estimated at approximately 7×10^9 kg annually, SCGs offer a low-cost and widely available feedstock for valorisation. Their relatively high lignin content and low ash composition

favour carbonisation and micropore development, making them structurally suitable for adsorption applications. [70–75]

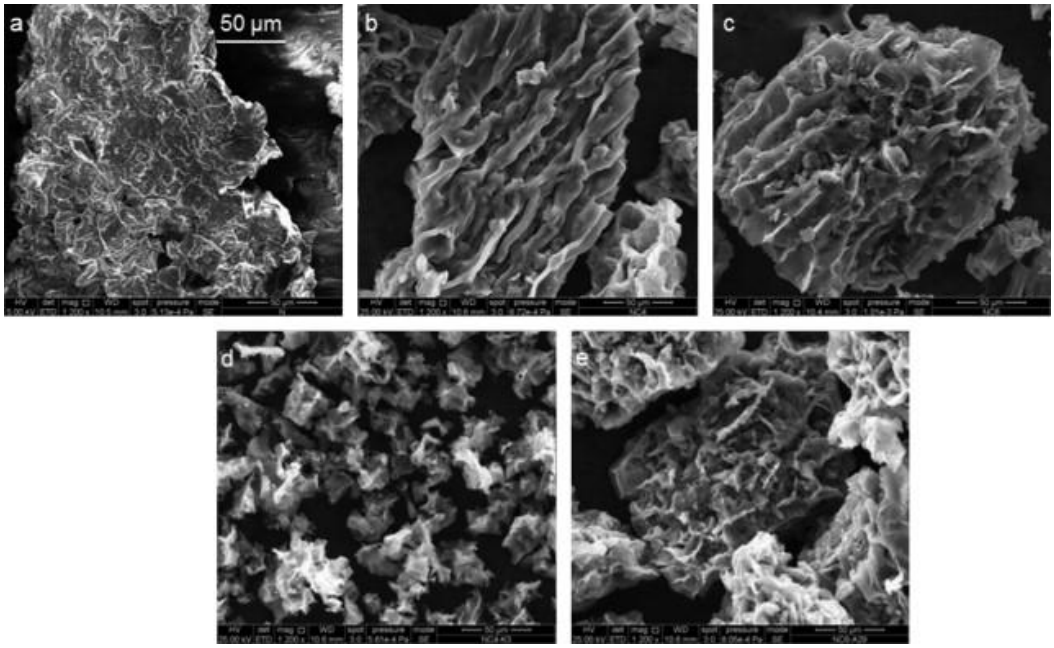

Figure 13 - SEM images of: (a) dried spent coffee grounds (N), (b) char carbonised at 673 K (NCL), (c) char carbonised at 873 K (NCH), (d) carbon activated with KOH (NCLK3), and (e) carbon activated with CO2 (NCHA29).

Similar to other biomass-derived carbons, SCG-based activated carbons are typically synthesised via chemical activation (commonly KOH or K_2CO_3) or physical activation using CO_2. Chemical activation generally produces materials with higher specific surface areas (often exceeding 1500–2000 $m^2 g^{-1}$) and greater total micropore volumes, while CO_2 activation tends to yield narrower micropore size distributions and improved structural control. Both approaches have demonstrated effectiveness for tailoring pore architectures relevant to CO_2 adsorption at low partial pressures. [70–75]

Across multiple studies, CO_2 adsorption performance of SCG-derived activated carbons at 298 K and 1 bar typically falls within the range of 3.0–4.7 mmol g^{-1}, [70–72] with higher capacities (6–7 mmol g^{-1}) reported at 273 K. Performance is consistently correlated with micropore volume rather than total surface area, reinforcing the importance of pore size distribution over absolute surface area. In particular, ultramicropores (<0.7 nm) have been identified as the dominant contributors to CO_2 uptake under flue gas-relevant conditions (≤0.15 bar CO_2), where pore-filling mechanisms and enhanced confinement effects increase adsorption potential. [74,75]

Nitrogen functionalities naturally present in SCGs, or introduced via nitrogen-doping strategies (e.g., melamine or ammonia treatment), have been shown to enhance adsorption affinity and CO_2/N_2 selectivity. Pyridinic and pyrrolic nitrogen species are frequently associated with improved surface basicity and stronger electrostatic interactions with the quadrupole moment of CO_2. However, while nitrogen doping can increase isosteric heat of adsorption and low-pressure uptake, several studies indicate that micropore development remains the primary determinant of overall performance, with surface chemistry acting as a secondary enhancement mechanism. [36]

Reported isosteric heats of adsorption for SCG-derived carbons typically lie between 20–40 kJ mol^{-1}, [71] indicating that adsorption is predominantly physisorptive in nature, albeit strengthened by confinement and surface heteroatom interactions. These moderate adsorption enthalpies are advantageous for cyclic operation, balancing adsorption capacity with manageable regeneration energy requirements.

CO_2/N_2 selectivity values reported in the literature vary significantly depending on activation strategy and calculation method. Chemically activated SCG carbons commonly exhibit selectivities in the range of 13–30 (IAST-derived), [71] while higher values have been reported when calculated from pure-component equilibrium uptake ratios. Physical CO_2 activation has, in some cases, yielded improved selectivity due to enhanced narrow microporosity. Importantly, most studies emphasise the strong dependence of selectivity on ultramicropore volume, with pore size engineering often exerting a greater influence than increases in surface polarity alone. [70–75]

In terms of stability, SCG-derived activated carbons generally demonstrate excellent cyclic durability over multiple adsorption–desorption cycles, with minimal capacity loss reported. Their predominantly physisorptive adsorption mechanism contributes to lower regeneration energy compared to liquid amine systems, while their carbonaceous structure provides chemical and thermal robustness. [71,72,75]

Despite these advantages, several limitations remain. Chemical activation routes, particularly those employing KOH, raise environmental and economic concerns due to chemical consumption, wastewater generation, and corrosion risks. Additionally, achieving consistent pore size distributions at scale remains challenging, and precursor variability may influence reproducibility. While nitrogen doping improves affinity, excessive functionalisation may increase regeneration energy or compromise structural integrity.

Overall, SCG-derived activated carbons represent a highly promising subclass of biomass-based adsorbents for post-combustion CO_2 capture. Their favourable pore-forming characteristics, intrinsic nitrogen content, and global availability position them as attractive candidates for sustainable sorbent development. Continued optimisation of activation strategy and pore size engineering is required to maximise low-pressure performance while maintaining scalability and environmental viability.

Ordered Porous Carbons

Ordered porous carbons (OPCs) are a class of advanced materials developed to address some of the structural and performance limitations associated with conventional activated carbons, particularly for low-pressure CO_2 adsorption. These materials (see Figure 14) feature uniform and tuneable pore networks, offering precise control over surface area and pore size distribution—key factors that influence gas adsorption behaviour. Their structural regularity makes them attractive not only for carbon capture, but also for catalysis, supercapacitors, and gas separation technologies.

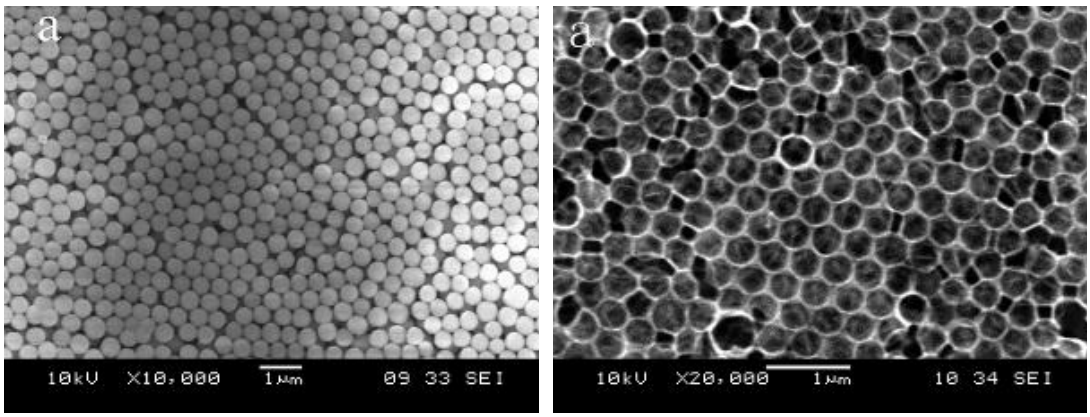

Figure 14 - SEM image of Ordered Porous Carbon CMK-3 [76]

OPCs are commonly synthesised through templating methods. Hard templating uses rigid nanostructured templates such as silica, which are infiltrated with carbon precursors, carbonised, and then removed via chemical etching (e.g. NaOH or HF). Soft templating, by contrast, relies on the self-assembly of block copolymers, enabling the formation of mesostructured carbon without a separate template removal step. Both methods produce carbons with highly ordered mesopores, which facilitate gas diffusion and stand in contrast to the more irregular and heterogeneous porosity of traditional activated carbons. [77,78]

These structural advantages translate into practical benefits for CO_2 capture. OPCs exhibit high adsorption capacities even at low partial pressures, especially when tailored with

micropores and heteroatom dopants. Nitrogen-doped OPCs, for instance, have demonstrated CO_2 capacities of up to 5.8 mmol/g at 1 bar and 25 °C—values that rival or exceed those of many activated carbons. Their mesoporous architecture promotes fast adsorption–desorption kinetics, while their largely carbonaceous composition supports relatively low regeneration energy. Moreover, their stability across multiple cycles and potential for selective adsorption through surface functionalisation make them promising candidates for post-combustion applications. [77]

However, these benefits must be weighed against notable limitations. The synthesis of OPCs, particularly via hard templating, is more complex, time-consuming, and resource-intensive than that of conventional activated carbons. Template removal often involves the use of hazardous chemicals, raising environmental and safety concerns. Even with advances in soft templating, scalability remains a challenge—especially when compared to simpler pyrolysis-based methods. Furthermore, although functionalisation enhances selectivity, it may also reduce thermal stability or complicate regeneration if too strong an interaction with CO_2 is introduced.

OPCs therefore represent a valuable but specialised option within the broader landscape of porous carbons. Their high performance under controlled conditions is well-established, but practical deployment depends on overcoming current challenges in cost, synthesis throughput, and environmental sustainability. Continued research into scalable, benign synthesis routes and structure–performance relationships will be crucial to realising their full potential in carbon capture applications.

Carbon Fibres

Activated carbon fibres (ACFs) represent a class of fibrous adsorbents with compelling potential for post-combustion CO_2 capture. Their unique morphology (see Figure 15)—characterised by a high specific surface area, narrow pore size distribution, and aligned microstructure—enables rapid diffusion and strong adsorption performance, distinguishing them from traditional granular or powdered sorbents.

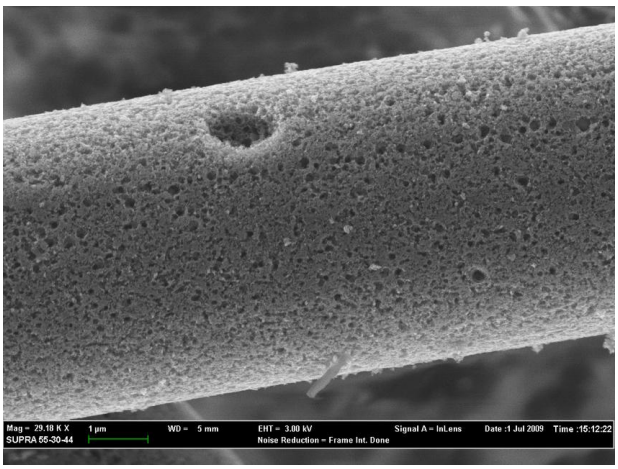

Figure 15 - SEM image of Activated Carbon Fibre "Busofit" [79]

ACFs are typically synthesised by carbonising fibrous precursors such as polyacrylonitrile (PAN), rayon, or pitch, followed by physical or chemical activation. Chemical activation using KOH is particularly effective at enhancing microporosity and surface area, producing materials capable of efficiently capturing CO_2 at low partial pressures [80,81]. Their pore structure is highly accessible, and their uniform fibre orientation contributes to fast adsorption–desorption kinetics—an advantage for cyclic operation in swing adsorption systems.

Chemical modifications further enhance ACF performance. Nitrogen doping introduces basic functional groups that interact favourably with CO_2, increasing both adsorption capacity and selectivity. Hybrid structures incorporating carbon nanotubes (CNTs) have also been explored, which smooth fibre surfaces and add new binding sites, improving uptake and textural uniformity. [82,83] Optimised ACFs have demonstrated CO_2 capacities comparable to or exceeding those of activated carbons, alongside improved separation performance over gases such as CH_4 and N_2. [84,85]

Despite these performance advantages, ACFs face significant barriers to commercial deployment. Their production is more complex and costly than that of traditional carbon sorbents, requiring specialised precursors, controlled fibre processing, and potentially hazardous activation agents. These factors increase material cost and limit scalability, making ACFs more suited to niche applications or high-value separation processes rather than large-scale flue gas treatment. Additionally, while their structural stability and cycling performance are promising, long-term durability under real flue gas conditions—particularly in the presence of impurities—remains underexplored.

In summary, ACFs offer a favourable combination of high uptake, fast kinetics, and tunable selectivity, positioning them as technically attractive materials for CO_2 capture. However, their high production costs and current limitations in large-scale manufacturing constrain their broader industrial applicability. Future efforts should focus on simplifying synthesis pathways and reducing costs to enable their integration into scalable carbon capture systems.

Graphene

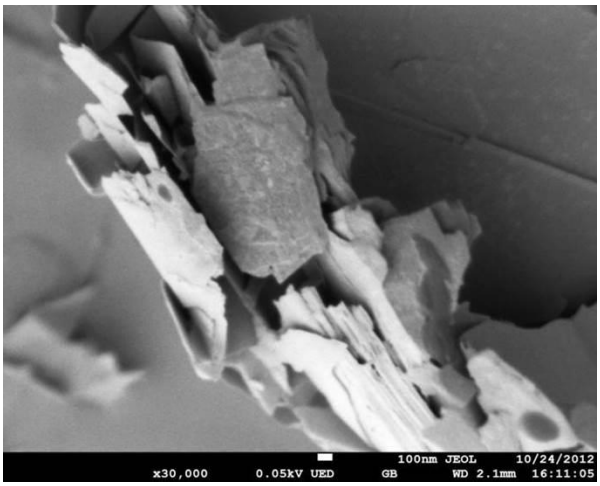

Figure 16 - SEM image of Graphene oxide flakes [86]

Graphene, a two-dimensional allotrope of carbon, has attracted considerable interest in the field of CO_2 capture due to its extraordinary physicochemical properties. With a theoretical surface area of up to 2630 m^2/g, high thermal and electrical conductivity, and excellent mechanical and chemical stability, graphene-based materials offer a compelling platform for adsorption-driven separation technologies. However, translating these properties into practical CO_2 capture applications presents notable challenges.

Graphene is typically synthesised via chemical vapour deposition, exfoliation of graphite, or chemical reduction of graphene oxide (see Figure 16). [87] While these techniques can yield high-quality materials, bulk production often results in agglomeration or restacking of graphene layers, which significantly reduces the accessible surface area and limits adsorption performance. To mitigate this, structural modifications—such as nitrogen or sulphur doping—have been explored to introduce polar functional groups that enhance CO_2 affinity. [87,88] For example, nitrogen-doped graphene synthesised from polypyrrole-functionalised precursors has achieved CO_2 adsorption capacities of up to 4.3 mmol/g at 1 bar and room temperature. [89]

The adsorption behaviour of graphene is predominantly governed by physical interactions, making regeneration energetically favourable. Reported isosteric heats of adsorption range from 25–30 kJ/mol, suggesting a good balance between CO_2 binding strength and ease of desorption. [90,91] Functionalised graphene also exhibits fast kinetics due to its planar architecture, and selectivity can be improved through careful control of pore size and chemical composition. Studies involving polyaniline- or melamine-doped graphene derivatives have shown promising selectivity for CO_2 over N_2 and CH_4, with good cycling stability under moderate conditions.

However, these promising characteristics are tempered by significant practical limitations. Graphene synthesis remains costly and complex, particularly when functionalisation steps are involved. Methods such as chemical activation, doping, or templating can increase material performance but add to production time, cost, and environmental burden. Furthermore, while laboratory-scale results are encouraging, few studies address long-term stability or scalability under real flue gas conditions.

In summary, graphene-based materials offer high potential for CO_2 capture, especially in terms of tunability, selectivity, and regeneration efficiency. Yet, their industrial deployment is currently hindered by synthesis costs and scale-up challenges. Realising their practical value will require the development of cost-effective production methods and further demonstration of performance under industrially relevant operating conditions.

1.5.2. Inorganic Porous Materials

Inorganic porous materials, encompassing silica, alumina, zeolites, and related compounds, represent a versatile class of adsorbents with unique structural and chemical properties. These materials have long been utilized across various industries due to their tuneable porosity, high thermal stability, and chemical robustness. Their applicability to CO_2 capture has garnered significant interest, driven by their diverse range of pore sizes, high surface areas, and capacity for functionalization.

The materials in this category differ greatly in composition and performance, offering a broad spectrum of solutions tailored to specific CO_2 capture scenarios. Silica's easily tuneable mesoporous structure makes it a promising support for functionalization, while alumina's high thermal stability and functionalization potential highlight its applicability under harsh conditions. Zeolites, with their crystalline microporous frameworks, stand out for their molecular sieving capabilities and selective adsorption of CO_2 over other gases.

In this chapter, we explore the preparation, structural features, and CO_2 adsorption performance of these inorganic porous materials. Their advantages, limitations, and roles in advancing post-combustion CO_2 capture technologies will be critically examined.

Silica

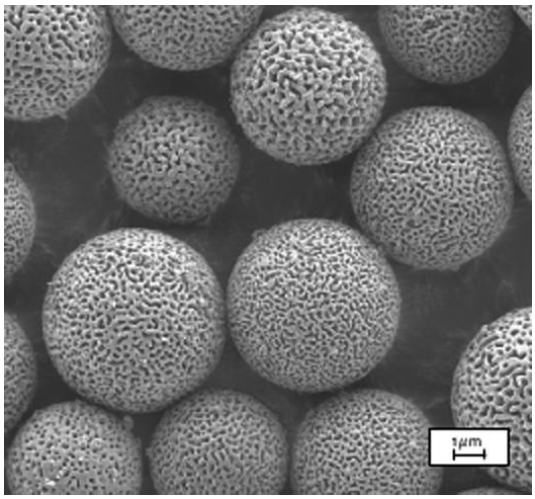

Figure 17 - SEM image of Porous Silica Particles [92]

Silica (see Figure 17) is one of the most abundant and widely studied materials for CO_2 capture, offering a compelling balance of availability, tuneable porosity, and surface modifiability. Its versatility arises from the ease with which it can be structured into mesoporous frameworks and functionalised for enhanced gas interactions. Mesoporous silica, in particular, with pore sizes between 2 and 50 nm, provides a robust platform for tailoring adsorbent performance through structural and chemical design. [44]

Synthesis typically involves templating techniques using surfactants or block copolymers to guide the formation of ordered pore networks, followed by template removal through calcination or solvent extraction. [93] This process yields materials such as MCM-41, SBA-15, and KIT-6, with surface areas exceeding 1200 m^2/g and pore volumes over 1 cm^3/g. [44,94] These frameworks can be further functionalised with amine groups, either via impregnation or grafting. While impregnation is simpler, grafting provides stronger covalent bonding, reducing the risk of amine leaching and improving thermal and cyclic stability. [95]

Amine-functionalised silica has demonstrated high CO_2 adsorption capacities, with reports of up to 5.05 mmol/g at 25 °C and 1 bar using tetraethylenepentamine (TEPA)-modified hierarchical silica. [95] The efficiency of these materials arises from the strong chemisorptive interactions between CO_2 and amine groups, facilitated by the ordered pore structures that

allow rapid gas diffusion and high active site accessibility. Selectivity over N_2 and other gases is also enhanced, making these materials well suited to flue gas separation.

However, the advantages of silica are accompanied by key limitations. Although silica itself is inexpensive and abundant, the preparation of hierarchical structures and the use of complex grafting agents can increase production costs. Furthermore, despite good thermal and oxidative stability, long-term exposure to moisture—particularly steam—can lead to pore collapse or deactivation of functional groups, which poses challenges for sustained performance in humid flue gas environments. Mitigation strategies, such as hydrophobic coatings or optimised pore architectures, are under active investigation but are not yet widely adopted at scale.

In summary, amine-functionalised mesoporous silica offers a promising and versatile platform for post-combustion CO_2 capture. With high uptake, selectivity, and regeneration efficiency, it competes favourably with other advanced adsorbents. Nonetheless, scaling these systems for industrial use requires further development in synthesis scalability, moisture resistance, and process integration to ensure cost-effective and durable performance.

Alumina

Alumina (Al_2O_3) is a thermally stable, widely available material with established industrial relevance and favourable textural properties for gas adsorption. Derived from natural ores such as bauxite through the Bayer process, it has long been used in catalysis and separation processes. In the context of CO_2 capture, mesoporous alumina offers high surface area, moderate affinity for CO_2, and potential for surface modification, positioning it as a competitive adsorbent, especially when functionalised. [63,96]

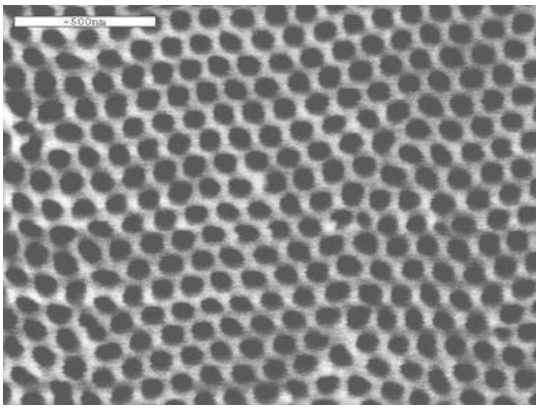

Figure 18 – FE-SEM Image of Porous alumina [97]

Mesoporous alumina (see Figure 18) is typically synthesised from boehmite precursors, producing structures with high crystallinity, large pore volumes, and uniform porosity. These features facilitate gas diffusion and enable high adsorption site accessibility. However, the inherent affinity of unmodified alumina for CO_2 is limited. To address this, functionalisation strategies such as metal oxide doping and organosilane grafting have been developed. For example, doping γ-alumina with La_2O_3 enhances surface basicity and has been shown to increase CO_2 adsorption to 113 µmol/g at 3.5 mol% loading. Other modifications, such as amidoxime or cyanopropyl grafting, have achieved uptake values of up to 3.84 mmol/g at 120 °C. [96,98]

Performance is also strongly influenced by operating conditions. Polyethyleneimine (PEI)-grafted γ-alumina, for instance, has demonstrated a CO_2 uptake of 1.96 mmol/g at 30 °C, while maintaining reasonable stability after mild steam treatment. However, extended exposure to moisture or high-temperature steam can compromise pore structure and reduce long-term adsorption capacity. This highlights a key limitation of alumina-based systems: while chemically robust, they can be vulnerable to hydrothermal degradation depending on surface treatment and process conditions. [99]

Alumina's advantages include its rapid kinetics, good selectivity (particularly when modified with nitrogen-containing groups or metal oxides), and low regeneration energy due to the physisorption-dominated mechanism on many functionalised surfaces. Its low raw material cost and established processing routes also support industrial scalability. Nevertheless, advanced functionalisation steps—especially those involving grafting or multi-stage doping—may introduce complexity and increase production costs.

In summary, alumina offers a promising and versatile platform for CO_2 capture, particularly when engineered with tailored surface chemistries. While not as intrinsically active as some porous carbons or amine-functionalised silicas, its combination of stability, modifiability, and cost-effectiveness makes it a viable option for further development in post-combustion applications—provided challenges related to moisture sensitivity and synthesis complexity are addressed.

Zeolites

Zeolites (Figure 19) are crystalline aluminosilicates with well-defined pore systems formed by interlinked SiO_4 and AlO_4 tetrahedra. Their unique framework creates uniform molecular-sized cavities that host exchangeable cations (e.g. Na^+, Li^+, Ca^{2+}), which balance

the negative framework charge and serve as active sites for gas adsorption. These properties make zeolites highly effective for CO_2 separation, particularly under low-pressure conditions relevant to post-combustion applications. [44,100]

Figure 19 - SEM image of Zeolite [101]

While natural zeolites exist, synthetic analogues are preferred for CO_2 capture due to greater control over composition, porosity, and cation content. Zeolites such as 13X, 5A, Y, ZSM-5, and CHA are commonly produced by hydrothermal treatment of silica and alumina in alkaline media, allowing for tailored Si/Al ratios and cation exchange. Their adsorption mechanism is dominated by ion–dipole interactions between CO_2 and exposed framework cations. Additionally, bi-coordination sites and electrostatic interactions further enhance uptake at low temperatures. [102]

Adsorption performance is strongly influenced by framework composition and cation identity. Zeolites with low Si/Al ratios exhibit higher basicity and stronger electrostatic fields, favouring CO_2 uptake. For example, zeolite 13X can adsorb up to 3.64 mmol/g at 25 °C and 1 atm, while 5A achieves 3.07 mmol/g under similar conditions. [103] Cation exchange is a powerful tool for performance tuning—Li^+-exchanged Y and X zeolites exhibit stronger CO_2 binding, while Ba-modified ZSM-5 offers improved thermal stability and capacity. [104,105] However, CO_2 adsorption tends to decline sharply above 30 °C, and becomes negligible beyond 200 °C, limiting the applicability of many zeolites at higher process temperatures. [106]

A significant challenge for zeolites is their sensitivity to moisture. Water competes for active sites, displacing CO_2 and reducing uptake. Prolonged exposure can also cause framework degradation via dealumination, particularly under acidic or high-temperature conditions. [107] Nonetheless, some alkali-treated zeolites (e.g. Cs- or Na-Y) exhibit enhanced CO_2

performance after water exposure due to the formation of new Brønsted acid sites that improve CO_2 affinity. [106] These findings highlight the potential of surface engineering to mitigate moisture-related limitations.

Zeolites offer notable advantages: they are chemically stable, structurally uniform, and can be synthesised from abundant precursors at industrial scale. Their low cost and high selectivity, especially in cation-exchanged forms, make them attractive for flue gas applications. However, their narrow operating temperature window and vulnerability to moisture remain key barriers to deployment in real-world post-combustion settings.

In summary, zeolites represent a mature and cost-effective platform for CO_2 capture, combining high performance under dry, low-temperature conditions with tunability through cation exchange. Future improvements will depend on addressing humidity tolerance and enhancing thermal robustness through framework and surface modifications.

1.5.3. Porous Crystalline Solids

Porous crystalline solids, such as metal–organic frameworks (MOFs), zeolite imidazolate frameworks (ZIFs), and covalent organic frameworks (COFs), represent a highly promising class of materials for CO_2 capture and storage. These materials are distinguished by their tuneable pore sizes, high surface areas, and exceptional stability, enabling them to selectively adsorb CO_2 under various conditions.

We will be discussing their production, adsorption performance, and assessing them against the required criteria for post-combustion carbon capture (PCC).

Metal–Organic Frameworks (MOFs)

Metal–organic frameworks (MOFs) are a class of porous crystalline materials composed of metal ions or clusters coordinated to organic ligands. Their highly modular architecture offers unmatched control over pore size, chemical functionality, and surface area—features that have positioned MOFs at the forefront of materials research for gas storage and separation, including CO_2 capture. [108–110]

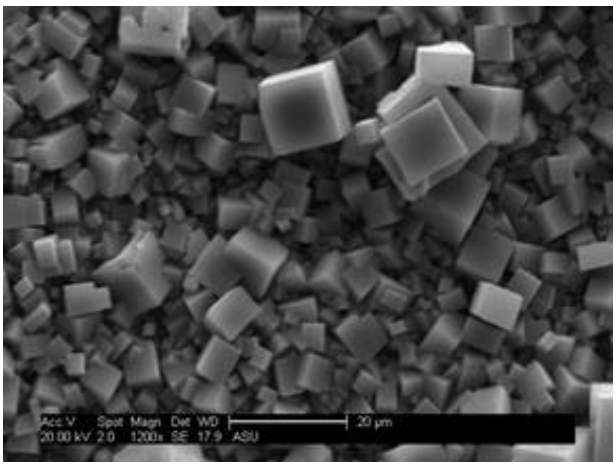

Figure 20 - SEM image of a Metal Organic Framework (MOF) [111]

MOFs (Figure 20) are typically synthesised via solvothermal or hydrothermal methods, enabling precise control over topology and functionalisation. The selection of metal centres (e.g., Mg, Zn, Al) and organic linkers (e.g., carboxylates, imidazolates) allows tuning of adsorption properties. Functionalisation with amines or other polar groups enhances CO_2 selectivity by increasing electrostatic interactions and binding affinity. [112,113] For example, Mg-MOF-74, with open metal sites, demonstrates a dynamic CO_2 capacity of 2.23 mmol/g under practical conditions, while MIL-101 achieves 3.64 mmol/g at 25 °C and 1 atm. [114,115]

Functionalised MOFs, such as MIL-53(Al)-NH_2, improve CO_2/N_2 selectivity through specific interactions with the CO_2 quadrupole moment. Additionally, frameworks incorporating open metal sites or polar linkers enhance uptake at low partial pressures, making MOFs viable for post-combustion scenarios where CO_2 concentrations are low. [116]

Despite their promising adsorption properties, MOFs face significant hurdles in industrial deployment. Many exhibit poor stability under humid conditions—a critical limitation for flue gas capture. Competitive adsorption of water can block active sites or destabilise the framework altogether. Although progress has been made in developing water-tolerant MOFs and hydrophobic surface modifications, their long-term stability in real-world environments remains less robust than that of materials like zeolites.

Thermal and cycling stability is also variable and highly dependent on the specific metal–ligand combination. While some MOFs retain performance over repeated adsorption–desorption cycles under dry conditions, many degrade at temperatures above 150 °C, limiting their use in high-temperature processes. Cost remains another significant barrier. MOF synthesis often involves complex procedures, expensive solvents, and high-purity

reagents, making them costlier to produce than conventional materials such as zeolites or activated carbons. Although solvent-free synthesis and the use of cheaper precursors are under development, scalability remains a major challenge. [117]

In summary, MOFs offer exceptional potential as designer adsorbents with high CO_2 capacities and tunable selectivity. However, their broader application in post-combustion carbon capture is currently constrained by issues related to humidity sensitivity, thermal durability, and synthesis costs. Continued research focused on simplifying production, improving moisture tolerance, and enhancing long-term stability will be critical to realising their promise at scale. [61]

Zeolitic Imidazolate Frameworks (ZIFs)

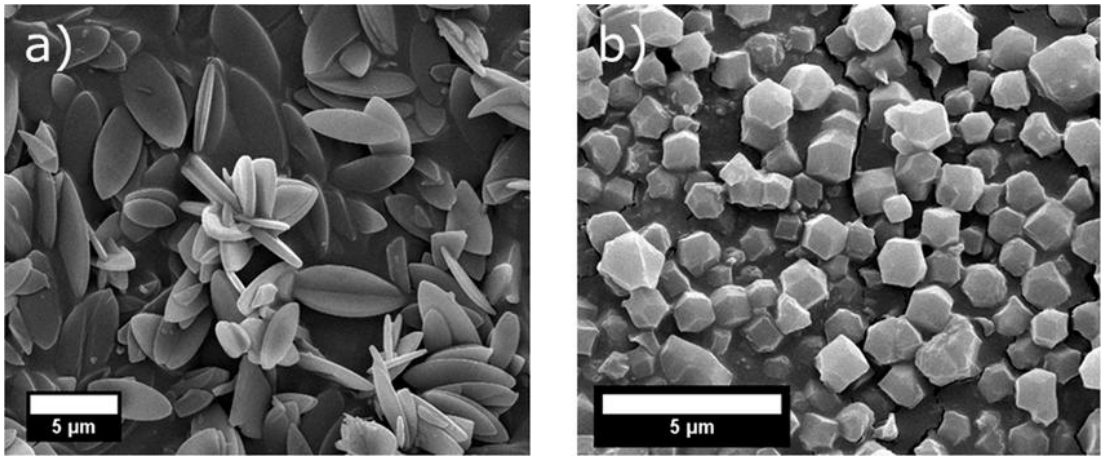

Figure 21 - SEM image of Zeolitic imidazolate frameworks (ZIFs) [118]

Zeolitic imidazolate frameworks (ZIFs) are a subclass of metal–organic frameworks that combine the design flexibility of MOFs with the structural robustness of zeolites. Built from tetrahedrally coordinated metal ions (e.g. Zn^{2+}, Co^{2+}) and imidazolate linkers, ZIFs adopt zeolite-like topologies with tunable pore sizes and high thermal and chemical stability. Their unique properties—particularly high surface area, selective adsorption, and stability under moderate temperatures—have made them promising candidates for post-combustion CO_2 capture. [119–122]

ZIFs (Figure 21) are typically synthesised via solvothermal or hydrothermal methods, though environmentally benign approaches such as aqueous or solvent-free syntheses have gained traction. For example, ZIF-93 has been prepared at room temperature in water, achieving a surface area of 604 m^2/g and demonstrating CO_2 uptake of 1.41 mmol/g. at 1 bar and 303 K. [122] Structural versatility arises from the ability to modify both the metal

centres and organic linkers, and to incorporate functional groups that enhance CO_2 affinity. ZIF-8, constructed from Zn^{2+} and 2-methylimidazolate, is among the most widely studied due to its exceptional stability and gas separation capabilities. Modifications, such as blending with ionic liquids or graphene oxide, have further increased selectivity, though often at the cost of surface area. [123]

ZIFs typically exhibit high selectivity for CO_2 over N_2 and CH_4, facilitated by their narrow pore sizes and polar framework environments. For instance, ZIF-69 has demonstrated CO_2 storage of 82.6 L per litre of material at 0 °C, with exclusion of less polar or bulkier gases. [124] Enhanced CO_2/N_2 and CO_2/CH_4 selectivity has also been achieved by incorporating room-temperature ionic liquids into ZIF-8, increasing selectivity fivefold compared to the unmodified framework. [123]

However, moisture sensitivity remains a key barrier to ZIF implementation in industrial flue gas environments. Water competes for adsorption sites and can destabilise the framework or reduce performance. Although some ZIFs, such as ZIF-8, display moderate hydrophobicity, prolonged exposure to humid conditions often leads to reduced capacity. Recent efforts to mitigate this include hydrophobic functionalisation and hybrid composites (e.g. ZIF–graphene oxide), which aim to preserve adsorption performance under realistic conditions. [125]

ZIFs offer several advantages for post-combustion CO_2 capture. Their thermal stability extends beyond 500 °C, surpassing many other MOFs and comparable to some zeolites. Under dry conditions, they show excellent cycling stability with minimal capacity loss. Moreover, the development of cost-effective synthesis methods, including solvent-free and aqueous processes, has improved their scalability and economic feasibility.

Nonetheless, challenges remain. The trade-off between enhanced functionality and reduced porosity, moisture sensitivity, and potential structural degradation under humid conditions must be addressed. Continued research into stable functionalisation strategies and process-integrated synthesis will be essential for translating the high selectivity and performance of ZIFs into industrial-scale carbon capture systems.

Covalent Organic Frameworks (COFs)

Covalent organic frameworks (COFs) are a class of crystalline porous polymers assembled from lightweight elements (e.g. B, C, N, O) linked through strong covalent bonds. These

materials exhibit low density, high thermal stability, and tunable pore architectures, making them well suited for gas storage and separation applications—including CO_2 capture. [126–128]

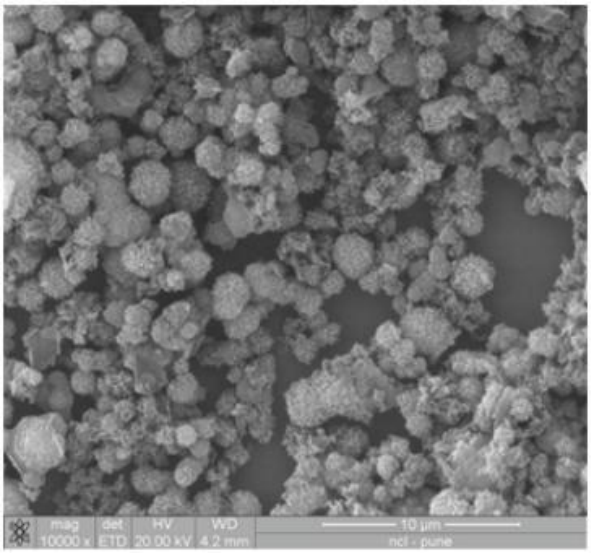

Figure 22 - SEM image of Covalent Organic Framework [129]

COFs (Figure 22) are typically synthesised using solvothermal or ionothermal methods, which allow for precise control over framework geometry, surface area, and chemical functionality. Functional groups (e.g. amines, fluorinated moieties) and metal dopants can be introduced to enhance adsorption capacity and selectivity. [130] For example, COF-102 exhibits a surface area of 3620 m^2/g with a CO_2 uptake of 1.53 mmol/g at 1 bar and 273 K, while TPE-COF-2 achieves 5.34 mmol/g under the same conditions. [128,131] More advanced structures, such as fluorinated or amine-functionalised COFs, further improve CO_2 uptake and selectivity.

Adsorption performance in COFs depends strongly on surface chemistry, pore volume, and accessible adsorption sites. Fluorine-functionalised frameworks like F-DCBP-CTF-1 can reach capacities of 5.98 mmol/g at 273 K and 1 bar, while metal-doped COFs, such as Li@COF-105, have reported capacities as high as 7.81 mmol/g at 25 °C. [132,133] These figures place COFs among the top-performing porous materials under laboratory conditions. Amine-functionalised COFs also show promising CO_2/N_2 and CO_2/CH_4 selectivity, making them attractive for post-combustion flue gas separation. [131,134]

However, a critical limitation for COFs is their sensitivity to moisture. Exposure to water vapour can disrupt framework integrity or occupy adsorption sites, leading to reduced performance. While hydrophobic modifications (e.g. fluorination or alkyl functionalisation)

have improved water resistance, COFs generally remain less robust under humid conditions than inorganic materials like zeolites. The trade-off between enhancing water tolerance and preserving pore accessibility continues to be an area of active research.

On the practical side, COFs are composed of abundant organic precursors, offering potential cost advantages over many metal-containing frameworks. Additionally, emerging solvent-free and low-temperature synthesis methods improve scalability and reduce environmental impact. Nevertheless, large-scale production of high-performance COFs with consistent quality and stability remains a technical challenge. [126–128]

In summary, COFs offer a highly customisable platform for CO_2 capture, with strong performance potential in terms of adsorption capacity, thermal stability, and selectivity. Yet, moisture sensitivity and synthesis complexity currently limit their widespread deployment. Ongoing development of water-resistant, functionally optimised COFs, along with simplified and scalable synthesis routes, will be key to unlocking their practical utility in post-combustion carbon capture systems.

1.5.4. Chemisorbents

Metal Oxides

Metal oxides such as magnesium oxide (MgO) and calcium oxide (CaO) have long been studied for CO_2 capture due to their capacity to react with CO_2 and form thermodynamically stable carbonates. These materials are attractive because of their natural abundance, low toxicity, and low cost. Their fundamental reaction with CO_2 is well understood, and recent research has focused on enhancing their sorption kinetics and reducing the high energy penalties associated with regeneration.

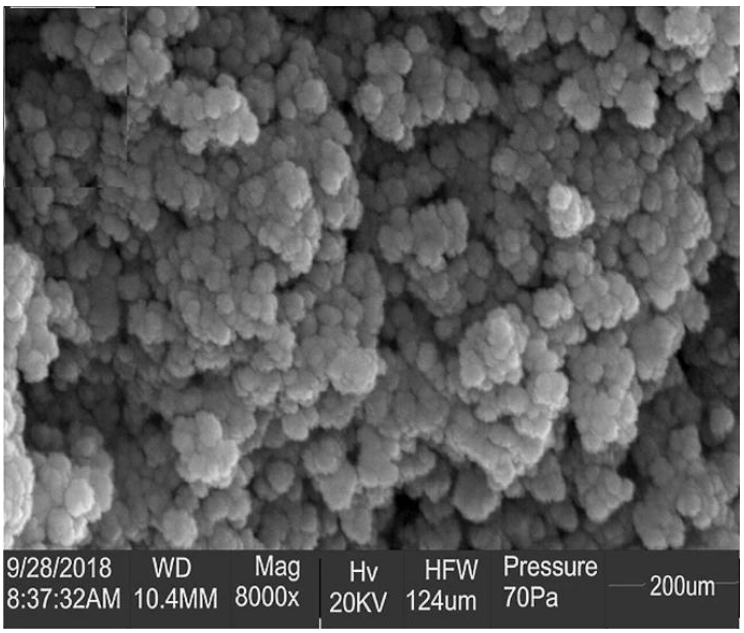

Figure 23 - SEM Image of Magnesium oxide [135]

Typically derived from naturally occurring minerals like magnesite or limestone, MgO (Figure 23) and CaO are prepared via calcination. The resulting material's porosity and surface area depend heavily on synthesis conditions. Mesoporous MgO prepared using carbon templating, for example, has shown significantly improved CO_2 adsorption compared to non-porous forms. [136] Similarly, MgO dispersed on alumina frameworks via coprecipitation methods has demonstrated enhanced performance through increased surface accessibility and improved mass transfer. [137–140]

Surface modification is another effective strategy. Doping with alkali metal salts such as K_2CO_3, Na_2CO_3, or Cs_2CO_3 introduces additional basic sites and surface defects that improve CO_2 uptake. Notably, Cs_2CO_3-doped MgO has reached capacities exceeding 1.9 mmol/g at 573 K, [141,142] while alkali-doped MgO composites have demonstrated even higher capacities—up to 16.8 mmol/g at 300 °C under dry conditions. [143,144]

Despite these advancements, metal oxides face persistent challenges. Their high regeneration temperatures—typically above 400 °C—result in significant energy penalties. Additionally, while some MgO–alumina composites show improved moisture tolerance, many metal oxides are sensitive to water vapour. Moisture competes with CO_2 for active sites and can inhibit adsorption or destabilise carbonate formation. Although alkali-doped variants offer better moisture resistance, maintaining long-term stability in humid flue gas remains an area for further development. [145]

Still, metal oxides offer key advantages for industrial-scale CO_2 capture. Their high selectivity for CO_2 via carbonate formation enables effective separation from other flue gas components such as N_2 and CH_4. Thermal and cycling stability are generally good, particularly for advanced composites. The simplicity of synthesis and abundance of raw materials also contribute to their economic and practical appeal.

In summary, metal oxides—especially when modified for improved porosity and reactivity—are strong candidates for high-temperature post-combustion CO_2 capture. While regeneration energy and water sensitivity remain challenges, ongoing improvements in structure and surface chemistry are helping to address these limitations and expand their applicability in scalable carbon capture systems.

1.5.5. Summary

Porous solids for CO_2 adsorption represent a highly promising avenue for reducing greenhouse gas emissions from post-combustion flue gases. Each class of adsorbent exhibits unique strengths and weaknesses, which must be weighed against the practical demands of industrial applications and their ability to compete with proven aqueous amine systems. This chapter has systematically compared the performance metrics of key sorbent materials, including carbon-based materials, silica and zeolite frameworks, metal–organic frameworks (MOFs), covalent organic frameworks (COFs), and metal oxides. A summary of the performance criteria of these sorbent materials is provided in Table 1.

Activated carbons (ACs), particularly those derived from biomass, offer a unique blend of low cost, high availability, and excellent thermal and chemical stability. Their production aligns with the principles of sustainability and circular economy, leveraging renewable resources such as agricultural and industrial by-products. While their adsorption capacity and selectivity are lower compared to MOFs or zeolites, advances in activation methods and heteroatom doping have shown potential to significantly improve performance. Furthermore, their cyclic stability and resistance to flue gas impurities like SOx and NOx make them an appealing candidate for real-world applications.

Zeolites and other silica-based adsorbents exhibit excellent selectivity and moderate adsorption capacities under dry conditions, but their moisture sensitivity and regeneration energy requirements limit their utility in humid flue gas streams. Similarly, MOFs and COFs present outstanding capacities and tuneable properties; however, their high production

Table 1 - Qualitative comparison of sorbent classes for post-combustion CO_2 capture. High, Moderate, and Low refer to relative performance across key parameters based on typical literature values.

Sorbent	Adsorption Capacity	Kinetics	Regeneration Energy	Selectivity	Cyclic Stability	Thermal Stability	Moisture Sensitivity	Cost	Scalability
Activated Carbons	Moderate	Fast	Low	Moderate	High	High	Low	Low	High
Ordered Porous Carbons	High	Fast	Low	Moderate	High	High	Low	Moderate	Moderate
Carbon Fibres	Moderate	Fast	Low	Moderate	High	High	Low	High	Moderate
Graphene	Moderate	Fast	Low	Moderate	High	High	Low	High	Low
Silica	Moderate	Fast	Low	High	Moderate	High	High	Low	High
Alumina	Moderate	Fast	Low	Moderate	Moderate	High	High	Low	High
Zeolites	High	Fast	Moderate	High	Moderate	High	High	Moderate	High
MOFs	Very High	Fast	Moderate	Very High	Moderate	High	High	High	Low
ZIFs	High	Fast	Moderate	High	Moderate	High	Moderate	High	Low
COFs	High	Fast	Moderate	High	Moderate	High	High	High	Low
Metal Oxides	High	Slow	High	High	Moderate	High	High	Low	High

costs and sensitivity to moisture remain significant barriers to industrial adoption. Advances in functionalization, particularly with amine groups or hydrophobic coatings, are promising but require further scalability assessments.

Metal oxides demonstrate remarkable adsorption capacities at elevated temperatures and have shown promise for high-temperature capture scenarios. Their slow adsorption kinetics and high regeneration energy, however, pose challenges for broader application in post-combustion carbon capture processes.

The development of advanced solid adsorbents for CO_2 capture continues to be an area of intense research. As the global focus on reducing greenhouse gas emissions grows, identifying adsorbents that combine high performance with cost-effectiveness is critical. Biomass-derived activated carbons represent a particularly promising solution, balancing environmental sustainability with practical performance metrics. Future work in this domain should prioritize improving adsorption capacity and selectivity through innovative activation processes and chemical modifications, such as nitrogen doping or surface functionalization.

Emerging computational tools and high-throughput experimental methods offer opportunities to accelerate the discovery of novel adsorbents with tailored properties. Screening large material databases, such as those available for MOFs and COFs, can guide the rational design of adsorbents that meet the specific demands of post-combustion carbon capture.

Furthermore, interdisciplinary collaborations between material scientists, process engineers, and environmental economists are essential to address the scalability and economic feasibility of new technologies. This includes not only reducing production costs but also evaluating the life cycle impacts of adsorbent materials.

In conclusion, while no single material class has yet emerged as the definitive solution for post-combustion carbon capture, the continued integration of novel materials, advanced characterisation techniques, and process optimisation offers a promising path forward. Among these, biomass-derived activated carbons stand out for their favourable performance, low cost, and inherent sustainability. When produced from renewable waste feedstocks and tailored through activation and functionalisation, these materials—commonly referred to as biochar in this context—present a scalable and adaptable platform for industrial carbon capture. The following section explores the role of biochar in

greater detail, highlighting its material properties, processing strategies, and potential to meet the demands of future CCS applications.

1.6. Biochars

Carbon-based materials have been extensively studied, with various high-performing adsorbents having been developed (Figure 24). They provide several advantages over other sorbents, including low-cost precursor materials and synthesis techniques, controllable textural properties (surface area, pore size, and pore volume), modifiable surface chemistry, high hydrophobicity, excellent selectivity, high-temperature, and chemical stability [36]. Biochar is a porous carbonaceous material produced through the thermochemical conversion of organic material in oxygen-depleted conditions known as pyrolysis. As it is produced from natural biomass or agricultural waste, it is a much greener alternative to other sorbents, using renewable precursors and serving as an excellent method for valorising certain waste products.

Biochar has been successfully used in a variety of environmental and commercial applications, such as improving soil quality through carbon sequestration and contamination removal, water purification, catalytic conversion of syngas into biodiesel, and as a material in high-temperature stable supercapacitors [146–148].

Recent data further highlight biochar as one of the most widely adopted methods of carbon dioxide removal (CDR). In 2023, biochar contributed approximately −0.79 $MtCO_2$ per year, making it the largest contributor to novel CDR methods globally, surpassing bioenergy with carbon capture and storage (BECCS) at −0.51 $MtCO_2$ per year, and enhanced rock weathering at −0.03 $MtCO_2$ per year. The growing adoption of biochar reflects its versatility and scalability, with applications spread across multiple regions, unlike BECCS, which is currently concentrated in the US [149].

Biochar's production and use are expected to grow significantly in the coming years, driven by its environmental benefits and broad application potential. Beyond soil improvement and carbon sequestration, biochar can be valorised into value-added products for environmental remediation. Examples include its use as an adsorbent for heavy metals and organic pollutants in water treatment, as a component in green construction materials, and as a feedstock for activated carbon production for gas separation and filtration technologies.

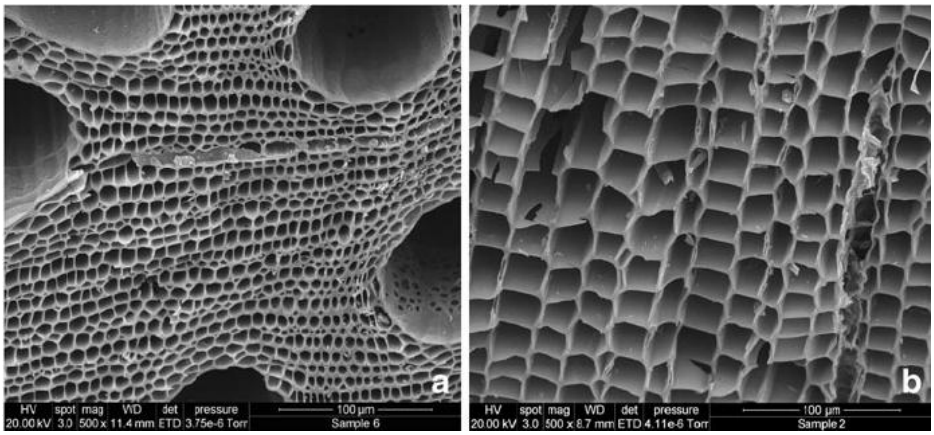

Figure 24 - Example SEM image of biochar a from eucalyptus bark, and b from pine bark, showing intricate porous structure [150]

Engineering the desired physicochemical properties of biochar for use as an adsorbent in post-combustion carbon capture can be achieved through varying the feedstock, pre-treatment of the feedstock, altering the pyrolysis conditions, and applying other modifications to the biochar.

1.6.1. Feedstock

When considering the feedstock for biochar production, there are several factors to account for, the most important being the physical and chemical properties of the char for the application. However, environmental and economic considerations must also be addressed. This work focuses on sustainable and strategic resource recovery, with the aim of valorising local waste products. Consequently, any biomass that would not be considered waste, as well as a large portion of global agricultural waste products, has been excluded.

To keep the cost of production as low as possible, feedstocks that did not already have a market were considered preferential. For example, spent grain waste from brewing was initially evaluated as a potential feedstock, as the alcohol industry is one of Scotland's largest. However, this material already has an established use as cattle feed.

Biomass is broadly categorized into two types: woody and non-woody. Woody biomass, as the name suggests, consists of forestry and tree waste and is characterized by low moisture, low ash, high calorific value, high bulk density, and less voidage. Non-woody biomass includes agricultural crops and residues, animal waste, and urban and industrial solid waste. This category is generally characterized by higher moisture and ash content, lower calorific value, lower bulk density, and higher voidage, though it varies widely due to its broad scope [146].

The environmental implications of feedstock selection are critical. Certain materials, particularly urban or industrial waste, may lead to emissions of harmful compounds during pyrolysis or produce biochars unsuitable for specific applications, such as soil amendment [35,151]. Additionally, sourcing feedstocks from dedicated crops risks competing with food production or contributing to land-use changes such as deforestation, which would undermine the environmental benefits of biochar production. Removing agricultural residues or forest debris as feedstock could also disrupt ecosystems by depleting soil organic matter, which is vital for maintaining soil health, nutrient cycling, and biodiversity [146].

Economic considerations further shape the choice of feedstock. Transportation costs, availability, and seasonality of feedstocks are significant factors. Locally available waste products, such as spent coffee grounds, can reduce logistical expenses. However, feedstocks with high moisture content or large particle sizes often require additional pre-treatment, such as drying or grinding, which increases costs and energy use.[146,147]

Feedstock Properties

Lignin Content

Lignin, an amorphous and hydrophobic polymer with a high molecular weight and numerous functional groups of aromatic substructures, is a key structural material in the support tissues of most plants and a significant component of woody biomass. It is highly resistant to thermal degradation, and feedstocks with high lignin content promote carbonization during pyrolysis, resulting in greater char formation and higher fixed carbon content. [146,147]

Cellulose and Hemicellulose Content

Cellulose and hemicellulose are polysaccharides composed of simple sugar monomers. These compounds decompose at relatively low temperatures, typically below 450 °C, and release pyrolytic vapours that contribute to tar formation. Feedstocks with higher cellulose and hemicellulose content are associated with lower char yields and increased gas and liquid by-products. [146]

Moisture Content

Moisture in biomass significantly affects the pyrolysis process. Higher moisture levels increase the energy required to reach pyrolysis temperatures and inhibit char formation.

Moisture exists in various forms, including liquid water, water vapor, and water adsorbed within the pores of the biomass. Low-moisture feedstocks are more efficient and cost-effective, as they reduce the energy burden during pyrolysis. [146]

Nitrogen Content

The nitrogen content of biomass influences the chemical properties of the resulting biochar. Biomass with higher nitrogen content produces biochar with more nitrogen-containing functional groups, which can enhance adsorption capacity for certain gases such as CO_2 and improve its performance in soil amendment applications. [146,147]

Ash Content

Ash content in feedstocks has a dual role in biochar production. Higher ash content increases pyrolysis yields due to the retention of inorganic constituents. However, it also reduces the specific surface area and adsorption capacity by partially filling or blocking micropores. Wood-derived biochars, with ash content below 7%, are generally more suitable for applications requiring high porosity and surface area compared to non-wood-derived biochars, which can have ash contents exceeding 50%. [151,152]

Applications and Specific Feedstocks

Wood-derived biochars are particularly advantageous for solid adsorbent applications because of their high fixed carbon content, high specific surface area, accessible micropores, and low ash content. [146]

Figure 25 - Spent Coffee Grounds Image generated using OpenAI's DALL·E (GPT-4o) via ChatGPT. Prompt: "A wide-format high-resolution photo of spent espresso pucks and used coffee grounds scattered on a clean white background, suitable for use between lines of text in a Word document. The image should have a clear background and look natural, with slight irregularities and one broken puck."

In this study, biochars are produced from spent coffee grounds (Figure 25), which are among the most common household biomass wastes, with an estimated generation of about 7×10^9 kg/year. Spent coffee grounds have a lignin content exceeding that of some woods and a low ash content, making them particularly suitable for adsorption

applications. Additionally, spent coffee grounds are rich in nitrogen, which can facilitate the enhancement of nitrogen functionalities on the resultant char. This nitrogen originates primarily from the protein, caffeine, and other alkaloid compounds naturally present in coffee beans, which contribute to the incorporation of nitrogen species into the carbon matrix during pyrolysis. Biochars derived from spent coffee grounds have been shown to possess the desired physical properties for such applications. [153–158]

However, their use at scale presents certain challenges. Pre-treatment is required to dry the coffee grounds and ensure uniformity for pyrolysis. Additionally, scalability can be a logistical challenge, as collecting spent coffee grounds from dispersed sources, such as households and cafes, may be complex and resource intensive. Residual oils or soluble compounds in coffee grounds may also influence biochar properties, necessitating further processing in some cases. [153–158]

By addressing these environmental, economic, and technical considerations, this study aims to develop high-performance adsorbents for post-combustion capture applications from spent coffee ground waste, while providing a comprehensive understanding of feedstock selection and optimization for biochar production to ensure sustainability, cost-efficiency, and suitability for a wide range of applications.

1.6.2. Pyrolysis Conditions

The process of biochar production occurs in three distinct stages, each playing a crucial role in determining the final characteristics and applications of the biochar. The first stage, pre-pyrolysis, occurs at temperatures below 200°C and is primarily responsible for the evaporation of moisture and light volatiles, which prepares the biomass for subsequent thermal decomposition. This stage ensures the removal of water content, reducing energy requirements in the later stages and enabling a more controlled pyrolysis process. The second stage, main-pyrolysis, occurs between 200-500°C, where the primary decomposition of cellulose and hemicellulose takes place, releasing a significant amount of volatile matter. This stage is pivotal in creating the basic structural framework of the biochar. Finally, the third stage involves the formation of carbonaceous products as lignin degrades above 500°C, which contributes to the stability and fixed carbon content of the biochar. [146–148]

Altering the pyrolysis conditions—including final temperature, residence time, ramp rate, and gas flow rate—can have substantial effects on the physicochemical properties of the

biochar produced. Understanding and optimizing these parameters are critical for tailoring biochar properties to meet specific application needs.

Final Temperature

The final hold temperature is the most important factor affecting the final properties of the biochar. Higher pyrolysis temperatures result in increased surface area, fixed carbon content, pore structure, pH, and the proportion of alkali functional groups, all of which are beneficial for applications such as adsorption. These properties make high-temperature biochars particularly suitable for environmental remediation, including pollutant adsorption and carbon capture. However, there is a trade-off, as higher temperatures also decrease yield, polarity, hydrophobicity, and the overall number of surface functional groups. [58,146–148,152]

As temperature increases, the release of volatiles promotes the formation of microstructures, such as pores, fissures, and cracks, which enhance surface area. These microstructural changes are critical for applications that require high adsorption capacity. However, beyond 900°C, a decline in pore structure may occur due to structural ordering, pore expansion, merging of adjacent pores, and blocking of pores by melted ash. This phenomenon underscores the importance of balancing pyrolysis temperature to avoid diminishing the functional properties of the biochar. Additionally, higher temperatures are associated with a decrease in heteroatoms and an increase in ash content, which negatively correlates with (O + N)/C, O/C, and H/C ratios. These chemical changes influence the surface reactivity and adsorption characteristics of the biochar. Biochar produced at lower temperatures exhibits high acidity, polarity, low aromatic content, and hydrophobicity, making it suitable for specific soil amendment applications. [146–148,152]

Residence Time

Residence time, the duration the char is held at its final temperature, significantly influences carbonization efficiency and the resultant properties of the biochar. A longer residence time allows for the more thorough removal of volatile matter, increasing both the surface area and fixed carbon content. These improvements enhance the biochar's suitability for high-performance applications, such as gas filtration and catalysis. However, extended residence time has minimal impact on the surface functional groups, which remain largely dictated by feedstock composition and temperature. [146–148,152]

Residence time also affects the thermal stability of the biochar. For instance, prolonged exposure to high temperatures can improve structural integrity, making the biochar more resistant to decomposition during storage or use. This feature is particularly beneficial for long-term carbon sequestration projects, where durability is essential.

Ramp Rate

Ramp rate refers to the rate at which the biomass is heated to the target temperature. While it generally has minor effects compared to temperature and residence time, it can still influence the yield and porosity of the biochar. Faster ramp rates can reduce biochar yield and disrupt structural complexity due to localized melting, phase transitions, and swelling of the cell structure. In contrast, slower ramp rates preserve the biomass's structural integrity, leading to enhanced porosity and better adsorption characteristics. [146–148,152,159]

Optimizing the ramp rate is particularly important for applications requiring precise control over pore size distribution, such as in catalyst support or advanced filtration systems. The ramp rate's interaction with other pyrolysis parameters also offers opportunities for tailoring biochar to specific industrial needs.

N_2 Flow Rate

During pyrolysis, an inert nitrogen (N_2) gas stream is used to create an oxygen-free environment, preventing unwanted combustion reactions. Variations in the flow rate of nitrogen have minimal effects on the physicochemical properties of the final biochar but can influence the process's overall efficiency. Higher N_2 flow rates enhance the removal of volatile matter, potentially reducing biochar yields but improving its purity and adsorption properties. [152,160]

While the effects of N_2 flow rate are less pronounced than those of temperature or residence time, controlling this parameter ensures consistency in the production process. It is particularly relevant in large-scale operations, where maintaining uniformity across batches is critical for industrial applications. Additionally, the choice of carrier gas, whether N_2 or an alternative inert gas, can further influence the process and final biochar properties, presenting opportunities for innovation in pyrolysis technologies.

1.6.3. Environmental Impact and Uses of Biochar

Biochar is a remarkable material with diverse properties and applications, making it a critical tool in addressing climate change and improving resource efficiency. At its core, biochar serves as a highly stable carbon matrix that can sequester carbon dioxide, preventing its release into the atmosphere. Its highly porous structure, thermal stability, and capacity to adsorb water, nutrients, and contaminants enable its use across agriculture, environmental remediation, and industrial applications. With its ability to integrate into various cascading use systems, biochar represents an innovative approach to circular economy principles. This chapter explores how biochar functions as a carbon dioxide removal (CDR) method, its potential economic and practical limitations as a soil amendment, its cascading uses, and its implications for global sustainability. [36,147]

Environmental Impact

Carbon Sequestration and Climate Change Mitigation

Biochar's most significant environmental benefit is its ability to sequester carbon dioxide. By converting biomass into a stable carbon matrix, biochar locks carbon into the soil for centuries, reducing greenhouse gas emissions. This process offsets emissions from organic waste decomposition, which would otherwise release methane (CH_4) and nitrous oxide (N_2O). In 2023, biochar contributed approximately −0.79 $MtCO_2$ per year globally, making it the most widely adopted novel CDR method, surpassing technologies such as BECCS and enhanced rock weathering. This scalability underscores its importance in global climate strategies.

Conventional CDR methods, such as afforestation, reforestation, and forest management, currently dominate carbon dioxide removal efforts, accounting for over 99.9% of all CDR. Between 2013 and 2022, these methods removed an estimated −1,860 $MtCO_2$ per year on average, with alternative models suggesting −2,010 ± 620 $MtCO_2$ annually. While novel approaches like biochar are rapidly gaining attention, conventional methods remain the bulk contributors to global CDR. However, recent trends indicate a slight slowdown in the effectiveness of these traditional strategies, emphasizing the growing importance of scaling novel methods such as biochar to supplement global carbon removal goals. [149]

Resource Efficiency and Waste Valorisation

The production of biochar aligns with principles of a circular economy by converting organic waste into a high-value product. Agricultural residues, forestry by-products, and urban organic waste can be pyrolyzed to create biochar, reducing waste management challenges. Additionally, biochar production captures pollutants during pyrolysis, further minimizing environmental harm. By transforming low-value or waste biomass into a durable material, biochar promotes sustainable resource use and offsets the carbon emissions associated with traditional waste disposal methods, such as landfilling or incineration.

Soil and Ecosystem Health

Biochar's porous structure enhances soil's water retention capacity, aeration, and microbial activity, improving overall soil fertility. By stabilizing nutrients, biochar reduces runoff and leaching, protecting surrounding ecosystems. However, it is crucial to load biochar with nutrients before application, as fresh biochar may adsorb soil nutrients, negatively impacting plant growth in the short term. These attributes make biochar particularly valuable in tropical regions with nutrient-poor soils. Additionally, biochar helps mitigate soil erosion and enhances resilience to extreme weather events by improving soil structure and moisture-holding capacity.

Practical Applications

Agriculture and Soil Management

Biochar's role as a soil amendment is well-documented, particularly in tropical regions where it was historically used to create Terra Preta soils. These ancient soils, enriched with biochar, retained nutrients and fostered microbial activity, providing a model for modern sustainable agriculture. Beyond improving soil fertility, biochar acts as a carrier for plant nutrients, preventing nutrient leaching and enhancing microbial symbiosis. Its potential to increase crop yields and improve soil quality offers significant benefits for smallholder farmers in developing regions. [161]

Water Treatment

Biochar's adsorptive properties enable its use in water purification. It effectively removes heavy metals, pesticides, and organic pollutants, making it valuable in wastewater treatment, aquaculture, and urban water management. In aquaculture systems, biochar can maintain water quality by adsorbing harmful compounds, ensuring healthier

environments for aquatic life. Its application in decentralized water treatment systems also highlights its potential in addressing water scarcity challenges in underserved areas.

Animal Farming

In Europe, approximately 90% of biochar is used in animal farming. As a feed additive, biochar improves digestion, reduces diarrhoea, and decreases methane emissions in livestock. It also acts as a litter additive, reducing odours and improving waste management by stabilizing manure nutrients. Experiments in dairy farming have shown biochar's potential to enhance animal health by reducing gastrointestinal issues and improving feed efficiency. Its versatility in livestock systems makes it an essential tool for sustainable animal farming practices. [162]

Industrial and Construction Applications

Biochar's thermal insulation properties and low thermal conductivity make it an excellent material for green construction. It can be incorporated into plasters and mortars, improving indoor air quality and humidity regulation while reducing the building's carbon footprint. Additionally, biochar is emerging as a component in polymer composites, energy storage systems, and air filtration technologies. For instance, biochar-based insulation materials not only improve energy efficiency but also act as carbon sinks, contributing to net-negative construction practices.

Cascading Use

Given its diverse properties, biochar can be utilized in cascading systems, where it serves multiple functions before being returned to the soil. For example, biochar can first be used for water filtration or as a feed supplement, then composted with organic waste, and finally applied to fields as a soil conditioner. This cascading approach maximizes its economic and environmental benefits. After fulfilling roles in industrial or agricultural systems, biochar's final incorporation into soil ensures long-term carbon sequestration and soil health enhancement.

Challenges and Economic Considerations

Farmers are facing unprecedented economic pressures, with the costs of fertilizers and pesticides rising sharply in recent years. Compared to the price of biochar, which can reach as high as $1,000 per ton, fertilizers and pesticides have also become increasingly unaffordable for many agricultural producers. For example, the price of nitrogen-based

fertilizers has nearly doubled in some regions due to supply chain disruptions and energy cost increases. Pesticide prices have similarly spiked, further squeezing farmers who are already struggling to maintain profitability. Applying 5 tons of biochar per acre, costing upwards of $5,000, adds an additional financial burden that many farmers cannot justify without significant subsidies or long-term benefits. This economic reality underscores the importance of maximizing the utility of biochar through cascading uses before its final incorporation into soil, ensuring that every dollar spent delivers multiple benefits. [36,147,163]

While biochar offers immense potential, its production and application face economic and practical limitations:

- **Production Costs**: High pyrolysis energy requirements and equipment costs make biochar expensive, with prices reaching as high as $1,000 per ton. On average, prices range between $300 and $700 per ton. Applying 5 tons of biochar per acre can exceed the economic return from the land. [163]
- **Logistical Barriers**: Collecting and processing dispersed feedstocks, such as spent coffee grounds or agricultural residues, can be resource-intensive.
- **Environmental Risks**: Overharvesting feedstocks or applying untreated biochar can harm ecosystems, highlighting the need for sustainable practices.

These challenges suggest that biochar should not be added directly to soil without maximizing its utility through cascading uses. Cascading uses allow biochar to fulfil multiple functions, such as water filtration, animal feed supplementation, or composting, before its final incorporation into soil. This approach not only enhances the economic return on investment but also optimizes its lifecycle benefits, ensuring it provides maximum value across its applications. By addressing economic pressures and leveraging biochar's versatility, cascading systems can significantly alleviate cost burdens for farmers and other stakeholders while maximizing environmental impact. Its final application as a soil amendment should follow its deployment in other roles, such as filtration or nutrient stabilization, ensuring economic and environmental efficiency.

Summary

Biochar represents one of the most promising tools for addressing climate change, improving soil health, and supporting sustainable resource management. Its ability to sequester carbon dioxide, enhance soil fertility, and function in diverse applications

underscores its versatility and importance. By incorporating biochar into cascading use systems, its potential can be maximized, ensuring economic viability and environmental impact. However, realizing biochar's full potential requires addressing its production challenges, improving scalability, and fostering innovation. As research and implementation efforts expand, biochar's role in global sustainability efforts is likely to grow, solidifying its position as an invaluable asset for the 21st century.

1.7. Activation Methods

Biochar is a carbonaceous material produced through the thermochemical conversion of biomass under oxygen-limited conditions. While biochar itself possesses inherent properties such as porosity, surface area, and stability, these characteristics often fall short of the requirements for high-performance applications in environmental and industrial contexts. Activated carbon, derived from biochar through activation processes, represents a tailored material with enhanced physicochemical properties. The transformation of biochar into activated carbon involves chemical, physical, or biological methods that significantly increase surface area, refine pore structures—particularly ultra-microporous regions—and modify surface functional groups.

The activation process allows the properties of activated carbon to be tailored for specific applications, such as selectively adsorbing particular pollutants or enhancing catalytic performance. For instance, altering pore size and functional groups can enable the selective adsorption of heavy metals from water, volatile organic compounds from air, or greenhouse gases like CO_2. The ability to engineer activated carbon for targeted performance makes it a versatile material for diverse environmental challenges.

This chapter discusses different activation methods through the lens of their application in transforming biochars into activated carbons suitable for post-combustion CO_2 capture systems. By examining the processes involved in physical, chemical, and biological activation, it highlights how each method influences key material properties such as surface area, pore size distribution, and functional groups. These tailored properties are critical for enhancing the selectivity and capacity of biochar-derived activated carbons, making them effective in addressing the specific challenges of CO_2 adsorption in industrial emissions contexts. [152,164–166]

1.7.1. Physical Activation

Physical activation, also referred to as gaseous activation, involves the use of gaseous oxidizing agents in combination with or during pyrolysis to enhance the physicochemical properties of biochar. This process partially gasifies the carbon skeleton, creating a more developed porous structure suitable for adsorption applications. Physical activation can occur either as a one-step process, where oxidizing agents like steam, carbon dioxide (CO_2), ammonia (NH_3), ozone, or limited air are introduced during pyrolysis, or as a two-step process, where raw biochar is produced first in an inert or oxygen-limited atmosphere and later subjected to thermal treatment in an oxidizing medium. Both methods are commonly employed, depending on the desired properties of the biochar and the specific application. [52,66]

Gaseous Activation Mechanisms

In physical activation, oxidizing agents penetrate the biochar's internal structure and react with its carbon atoms, leading to the opening and widening of previously inaccessible pores. These processes increase the biochar's internal surface area and often introduce oxygen-containing functional groups that serve as active adsorption sites [167] **.**The interplay of chemical and physical processes creates a highly porous material tailored for specific applications. Common activation reactions include:

1. Chemisorption of water or CO_2 on the carbon surface, leading to the formation of surface oxides and subsequent gasification.
2. The water-gas shift reaction, producing CO_2 and hydrogen gas, which further activates the biochar. [168]
3. Removal of trapped tars and volatiles, facilitated by oxidizing agents, enhancing pore development and increasing biochar reactivity [52].

CO_2 Activation

Carbon dioxide activation is a well-established method for enhancing biochar's specific surface area and microporosity. The primary reaction involved is the Boudouard reaction: [66]

$$C + CO_2 \rightarrow 2CO \qquad \textit{Equation 2}$$

This process develops a high density of micropores, making CO_2-activated biochar particularly effective for adsorbing smaller molecules. CO_2 activation not only expands pore structures but also modifies the surface chemistry, creating sites conducive to chemical

bonding. Compared to steam, CO_2 activation typically requires higher temperatures (700-900°C), but it produces biochar with a greater degree of structural uniformity and higher stability [169–171]. For example, CO_2 activation increased surface areas from 249 m^2/g to over 1100 m^2/g at 900°. [172]

In addition to structural benefits, CO_2 activation can enhance selectivity for specific gases like CO_2 and CH_4 by leveraging the carbon matrix's interaction with gas-phase molecules. Combined with other activating agents, CO_2 has shown synergistic effects, further amplifying the adsorption capacity. [173]

Steam Activation

Steam activation is one of the most commonly used methods, known for its ability to enhance both micropores and mesopores. Steam reacts with carbon on the biochar surface to form CO and H_2 via the water-gas shift reaction: [174]

$$C + H_2O \rightarrow CO + H_2 \qquad \textit{Equation 3}$$

Compared to CO_2, steam molecules' smaller size facilitates deeper penetration into the carbon structure, promoting greater pore development. However, steam activation can be more challenging to control, as prolonged exposure or excessive flow rates can lead to overactivation, resulting in pore collapse and reduced adsorption performance [175]. Nonetheless, its adaptability for different scales, from laboratory settings to industrial production, underscores its versatility.

Steam activation is particularly effective for developing mesoporosity, making it suitable for adsorbing larger molecules such as heavy metals and organic pollutants [176]. Recent studies have demonstrated that combining steam activation with chemical agents such as KOH can further enhance biochar's adsorption capacity [177]. Furthermore, steam activation's environmental compatibility, as it uses water vapor rather than hazardous chemicals, positions it as a sustainable choice for large-scale production. [174]

Ammonia Activation

Ammonia (NH_3) activation has recently gained attention for its ability to not only promote pore development and increase specific surface area but also introduce nitrogen-containing functional groups onto the biochar surface. These functional groups improve CO_2 adsorption capacity through chemical interactions, particularly acid-base interactions and hydrogen bonding. Key reactions include:

$$-COO^- + NH_4^+ \rightarrow -CONH_2 + H_2O \quad \textit{Equation 4}$$

$$-OH + NH_3 \rightarrow -NH_2 + H_2O \quad \textit{Equation 5}$$

NH_3 activation has been shown to enhance CO_2 adsorption capacity compared to other physical activation methods due to the combination of increased surface area and the introduction of nitrogen functionalities[35,36,152,178]. Nitrogen doping via NH_3 activation is particularly beneficial for applications requiring selective adsorption of acidic gases. However, NH_3 activation is less effective at developing micropores than CO_2 or steam activation. Studies have demonstrated that combining NH_3 and CO_2 activation produces synergistic effects, leading to substantially increased surface area, enhanced micropore development, and higher densities of nitrogen-containing functional groups [179,180]**.** NH_3 activation also influences the material's thermal stability, as nitrogen functional groups strengthen the overall matrix. This makes NH_3-activated biochar a candidate for high-temperature applications such as catalytic processes and industrial gas separations.

Ozone Activation

Ozone activation, though less common, has gained attention for its ability to functionalize biochar surfaces with oxygen-containing groups such as carboxyl and hydroxyl groups. These groups increase the biochar's polarity and hydrophilicity, improving its adsorption performance for polar compounds like ammonia [181]**.**The process involves exposing biochar to gaseous ozone under controlled conditions, typically followed by thermal desorption to widen pores and remove excess oxygen groups [182]. However, excessive ozone treatment can block micropores and reduce the overall surface area. [183]

Recent advancements in cyclic ozone activation, which alternates between oxidation and thermal treatments, have demonstrated significant increases in biochar's adsorption efficiency [182]**.** Ozone activation's ability to target specific functional group formation makes it a versatile tool for tailoring biochar for specialized applications.

Limited Air Activation

Air activation is an economical approach that uses oxygen to partially oxidize biochar. The primary reactions include:

$$2C + O_2 \rightarrow 2CO$$ *Equation 6*

$$C + O_2 \rightarrow CO_2$$ *Equation 7*

Air activation introduces oxygen functional groups, increases surface area, and enhances mesoporosity. However, it is challenging to control due to the exothermic nature of the reactions, which can lead to overoxidation and reduced yield. Advances in cyclic oxygen chemisorption/desorption have shown promise in overcoming these challenges by precisely regulating activation conditions. [184]

Air-activated biochar has been demonstrated to have improved adsorption capacities for both gases and liquids, with promising applications in environmental remediation [185] . Its cost-effectiveness and scalability make it particularly attractive for large-scale applications.

Summary

Physical activation methods offer diverse pathways for tailoring biochar's physicochemical properties to meet specific application requirements. By selecting appropriate oxidizing agents and optimizing parameters such as temperature, time, and flow rate, biochar can be effectively transformed into high-performance activated carbon suitable for applications such as post-combustion CO_2 capture, heavy metal adsorption, and water purification. Additionally, combining multiple activation techniques, such as NH_3 and CO_2 activation, offers synergistic benefits that can further enhance biochar's versatility for advanced applications.

1.7.2. Chemical Activation

Chemical activation is more widely used than physical activation due to several advantages: it requires lower process times and activation temperatures; produces biochars with larger surface areas; enhances biochar yield; and creates well-developed and uniformly distributed microporous structures. However, chemical activation also has drawbacks, such as the corrosion of apparatus by chemicals, the difficulty of chemical recovery, increased costs, and environmental impacts. Despite these challenges, the versatility and effectiveness of chemical activation make it a preferred method for tailoring biochar to specific applications, including CO_2 adsorption in post-combustion capture systems.

Chemical activating agents can be applied either as a pre-treatment to the biomass before pyrolysis (one-step activation) or as a post-treatment to the biochar after pyrolysis (two-step activation). One-step processes are generally preferred due to their reduced

complexity and energy requirements. The physiochemical properties of the resultant biochar depend significantly on the type of activating agent used, the concentration of the agent, and the activation temperature. Innovations in activation protocols and agent combinations have further expanded the potential applications of chemically activated biochar. [67,152,164,166]

Chemical activation is typically categorized based on the agent used: acid activation, alkali activation, oxidizing agent activation, and metal salt activation.

Acid Activation

Acid activation is a widely studied method for modifying the physicochemical properties of biochar for adsorption applications. Commonly used acidic agents include sulfuric acid, hydrochloric acid, nitric acid, oxalic acid, phosphoric acid, and citric acid. These methods have demonstrated significant increases in surface area and the development of well-structured pores. For instance, phosphoric acid (H_3PO_4) is known to introduce both micropores and phosphorus-containing functional groups, which can enhance the biochar's catalytic and adsorption properties. [67,152,164,166,186]

The modification of reed-derived biochar with hydrochloric acid has been shown to significantly reduce ash content, thereby increasing hydrophobic adsorption sites for organic pollutants like pentachlorophenol [187] Similarly, nitric acid modification introduces functional groups such as carboxylic, phenolic, and lactonic groups, improving the biochar's adsorption capabilities [188]. However, the effect of acid modification on surface area varies based on the acid type and concentration. For example, treatment with 1 M hydrochloric acid increased the surface area of reed-derived biochar from 58.75 to 88.35 m^2/g, while 2% sulfuric acid treatment reduced the surface area of rice straw-derived biochar from 71.35 to 56.9 m^2/g. [189]

For CO_2 adsorption in post-combustion capture systems, acid activation methods have limited applicability due to the acidic functional groups they introduce, which tend to decrease CO_2 adsorption capacity. This limitation highlights the need to carefully evaluate the suitability of acid-modified biochar for carbon capture applications.

Alkali Activation

Alkali activation has been shown to significantly enhance the specific surface area, microporosity, and ultramicroporosity of biochar. The most commonly used agents are

potassium hydroxide (KOH) and sodium hydroxide (NaOH), with KOH being particularly effective for applications requiring high CO_2 adsorption capacity. For example, the surface area and total pore volume of biochar can reach 3263 m^2/g and 1.772 cm^3/g, respectively, after KOH activation [67,152,164,166,190].

Two-step KOH activation generally yields biochars with higher surface areas and total pore volumes compared to one-step processes, although it results in fewer functional groups. The activation process involves reactions such as:

$$2KOH + C \rightarrow K_2O + H_2 + CO \qquad \textit{Equation 8}$$

$$K_2CO_3 \rightarrow K_2O + CO_2 \qquad \textit{Equation 9}$$

These reactions create a pore network and release gases that facilitate pore development. Moreover, metallic elements like potassium can penetrate the carbon framework and, when removed during washing, leave behind expanded lattices, further increasing microporosity. [191] However, excessive KOH can lead to the over-decomposition of biochar, reducing yield and stability.

Sodium hydroxide (NaOH) operates via similar mechanisms but is generally less reactive than KOH. NaOH-treated biochar has shown enhanced sorption capacities for pollutants like phenanthrene and As(V), demonstrating the potential for environmental remediation [192,193]. However, NaOH activation results can vary depending on the feedstock and preparation methods [194]. The alkali-to-char mass ratio is a primary lever for tailoring burn-off and pore development; however, the optimum is feedstock- and condition-dependent. Literature reports effective ranges typically between ~1:1 and 4:1 (KOH:char), with higher ratios increasing burn-off and surface area but potentially compromising yield and mechanical stability [195].

For CO_2 adsorption in post-combustion capture, alkali activation is highly suitable due to its ability to develop micropores and enhance the surface area, which are critical for adsorbing small molecules like CO_2. The introduction of oxygen-containing functional groups also contributes to stronger interactions with CO_2.

Oxidizing Agent Activation

Oxidizing agents, such as hydrogen peroxide (H_2O_2) and potassium permanganate ($KMnO_4$), are less commonly used for biochar activation. These agents primarily introduce oxygen-containing functional groups, enhancing the biochar's hydrophilicity and potential for

adsorption of polar compounds. For instance, H_2O_2 modification increased carboxyl groups in peanut hull-derived biochar, improving its sorption capacity for lead. However, excessive use of H_2O_2 (e.g., over 10%) can reduce adsorption performance for certain pollutants, such as methylene blue. [196–200]

$KMnO_4$ activation can significantly increase both the surface area and adsorption capacity of biochar. For example, hickory wood-derived biochar modified with $KMnO_4$ showed enhanced removal of Pb(II), Cu(II), and Cd(II), with surface areas increasing from 101 to 205 m^2/g. [201]

While oxidizing agent activation enhances oxygen functionality, its suitability for CO_2 adsorption in post-combustion capture is limited. The acidic nature of some oxygen-containing functional groups can reduce the affinity of the biochar for CO_2, making this method less ideal for such applications.

Metal Salt Activation

Metal salt activation involves using salts such as zinc chloride ($ZnCl_2$), ferric chloride ($FeCl_3$), or magnesium chloride ($MgCl_2$) as activating agents. Zinc chloride, a Lewis acid, is particularly effective due to its strong dehydrating ability, which reduces the decomposition temperature of biomass and enhances biochar yield. At temperatures below 700°C, $ZnCl_2$ remains in a liquid state, distributing evenly in the carbon structure and acting as a scaffold for pore formation. When removed, the resulting biochar retains a highly porous structure. [202]

$ZnCl_2$ activation has also been combined with graphitizing agents like $FeCl_3$ to produce biochars with both high porosity and graphitic structures, making them suitable for applications in energy storage. [203]In contrast, H_3PO_4 not only dehydrates but also forms organic phosphate esters, which protect the carbon skeleton and preserve micropores during activation. [204]

Metal salt activation is moderately suited for CO_2 adsorption applications. While it can enhance microporosity and introduce desirable structural properties, the absence of specific functional groups tailored for CO_2 interactions may limit its effectiveness compared to alkali activation.

Emerging Activating Agents

Recent research has explored environmentally friendly activating agents such as potassium bicarbonate ($KHCO_3$) and sodium bicarbonate ($NaHCO_3$). These agents decompose at low temperatures (e.g., 200°C), releasing gases that assist in porosity development, and subsequently react at higher temperatures (e.g., 800°C) to enhance micropore formation. For instance, $KHCO_3$ activation increased the surface area of rice straw-derived biochar to 1962.7 m^2/g compared to 829.7 m^2/g for untreated biochar. [205]

Similarly, oxalates like $K_2C_2O_4$ have shown promise for developing microporous structures. Unlike bicarbonates, oxalates decompose into carbonates and CO, which further react to create highly microporous biochars. [206,207]

Advanced reagents combining multiple functionalities, such as potassium ferrate (K_2FeO_4), are also being investigated. These agents integrate the activating properties of potassium with the catalytic effects of iron, producing biochars with both high surface areas and graphitic structures. [208] Such multifunctional reagents are opening new avenues for biochar applications in catalysis and energy storage.

Chemical activation offers a versatile approach to tailoring biochar for specific applications, including CO_2 adsorption in post-combustion capture systems. Among the discussed methods, alkali activation emerges as the most suitable due to its superior ability to develop microporosity and introduce oxygen-containing functional groups that enhance CO_2 interactions. Acid activation and oxidizing agent activation are less ideal for this application due to the introduction of acidic functional groups that can reduce CO_2 adsorption capacity. Metal salt activation provides moderate suitability by enhancing porosity but lacks targeted functionalization for CO_2.

Emerging activating agents, particularly bicarbonates and oxalates, show promise for optimizing biochar for CO_2 capture. By combining these agents with innovations in activation protocols, the potential for developing highly efficient, cost-effective adsorbents is significant. Future research should focus on fine-tuning activation conditions to maximize CO_2 adsorption capacity while maintaining scalability and environmental sustainability.

1.7.3. Biological Activation

Biological activation involves the use of microorganisms to activate carbon. Microorganisms, such as fungi, bacteria, and enzymes, can break down the biomass

structure, increasing porosity and surface area. This technology offers numerous benefits, including a milder, less energy-intensive, and less toxic approach compared to physical and chemical activation. Additionally, it enables effective valorisation of biomass waste, creating value-added products from waste materials. By leveraging the natural capabilities of microorganisms, biological activation aligns with sustainable and environmentally friendly practices while achieving tailored biochar properties for advanced applications such as CO_2 adsorption.

Fungal Activation

Fungal pre-treatment has demonstrated a significant impact on the pyrolysis performance of biomass, with fungi such as white-rot and brown-rot efficiently breaking down the lignocellulose structure. [209,210] This process reduces the pyrolysis initiation temperature and activation energy required, leading to an increased thermal decomposition rate and promoting the reaction. [211] Fungal pre-treatment depolymerizes the lignocellulose structure, reducing the lignin/cellulose ratio and enhancing delignification over time. [212]

Figure 26 - Hierarchical Structure of Fungal mycelium

White-rot fungi increase the yield of phenols and glucopyranosides while reducing propanol, acetone, and carbon dioxide content in pyrolysis products. [213] Biomass pyrolysis oil pre-treated by white-rot fungi contains a higher concentration of aromatic compounds, while pyrolysis charcoal demonstrates increased porosity. [214] Brown-rot fungi primarily degrade the amorphous cellulose region, whereas white-rot fungi target lignin, facilitating the thermochemical transformation of these components and optimizing pyrolysis outcomes. [215] The sulphur content in pyrolysis oil pre-treated with fungi is significantly reduced, minimizing the risk of SOx gas pollution. [216]

Further kinetic analysis suggests that fungal pre-treatment enhances the production of long-chain hydrocarbons such as desulfurized saponins and 2-methyloxy-4-vinylphenol during pyrolysis. [217]Additionally, the thermal stability of bio-oil and the phenol content are significantly improved when using white-rot and brown-rot fungi for corncob pretreatment.[218] These findings highlight the potential of fungal activation for enhancing the yield and quality of pyrolysis products, as well as providing environmental benefits by reducing pollutant emissions.

Fungi exhibit a complex fractal growth pattern as they colonize and decompose biomass. They develop extensive networks of thread-like structures called hyphae, which infiltrate the biomass and create vast interconnected mycelial networks. These networks possess incredibly high surface areas, allowing fungi to efficiently break down and consume organic material. [219] Research has demonstrated that fungal activation of wheat straw mixed with food waste, followed by carbonization and activation using KOH at 800–900 °C, produced biochar with a surface area of approximately 4000 m^2/g and a pore volume of 2.37 cm^3/g. This biochar exhibited excellent electrochemical performance, with a specific capacitance of 410 F/g in supercapacitors.[220]

Incorporating a branching fractal pattern into the pore structure of solid adsorbents offers potential enhancements for CO_2 adsorption in carbon capture applications. This approach capitalizes on key attributes of fractal geometry: increased surface area, efficient transport pathways, and hierarchical pore distribution. The fractal pattern can generate a hierarchy of pore sizes, striking a balance between large pores for rapid molecular transport and smaller pores for increased surface area. Moreover, the self-similarity in fractals allows for tuning of adsorption properties, optimizing pore structure to match CO_2 molecule size or mechanical and thermal stability parameters.

Despite these promising results, fungal activation faces challenges such as the need for precise cultivation conditions and extended incubation times for industrial applications. [221] Fungal pre-treatment is a slow process requiring precise growth conditions, including sterilization of raw materials to prevent competition from native microorganisms. [222,223] High moisture content may increase bacterial contamination, affecting the efficiency of the process, while low pH and elevated temperatures can inhibit bacterial contamination but reduce fungal enzyme activity. [224] Addressing these limitations requires careful optimization of moisture, pH, and aeration conditions. [225,226]Additionally, advanced heat dissipation

designs are needed to manage the heat generated during fungal metabolism, which may inhibit fungal growth. [225]

Bacterial Activation

Bacteria offer another route for biological activation by leveraging their enzymatic systems to degrade biomass components. Anaerobic digestion, a process involving anaerobic bacteria, has been shown to efficiently convert organic matter in lignocellulosic biomass into biochar precursors. Escherichia coli strains, for instance, have been employed for processing cellulosic feedstock, enhancing biofuel production while simultaneously creating biochar with enhanced properties.

Anaerobic digestion of biomass, such as sugar beet tailings, dairy waste, and bagasse, alters the feedstock's pH and electrochemical properties, resulting in biochars with higher cation and anion exchange capacities, improved hydrophobicity, and increased surface areas. The biochar produced post-anaerobic digestion also exhibited a negative zeta potential, indicative of a high negative surface charge, which enhances its ability to adsorb cations. [227]

Green bacterial activation of lignin-derived biochar has produced carbon with a surface area of 1831 m^2/g and a microporous and mesoporous structure. This biochar demonstrated excellent electrode performance in supercapacitors, achieving 428 F/g at a current density of 1 A/g with 96% stability after 10,000 cycles. Such results highlight the potential of bacterial activation in creating high-performance biochars for energy storage applications. [228]

The advantages of bacterial activation extend to its ability to degrade various biomass types under environmentally friendly conditions. However, challenges such as maintaining anaerobic conditions, controlling contamination, and ensuring consistency in biochar properties need to be addressed to scale bacterial activation for industrial applications.

Enzymatic Activation

Enzymatic activation uses enzymes, such as cellulases and ligninases, to selectively break down biomass components, increasing porosity and surface area. This method is particularly advantageous due to its specificity and mild reaction conditions, which preserve the structural integrity of the biochar.

For example, the removal of lignin and cellulose hydrolysis using cellulase enzymes produced biochar with enhanced microporosity and a larger surface area. Subsequent

vacuum impregnation with paraffin created a three-dimensional porous structure with high energy capacity, demonstrating the potential of enzymatic activation in energy applications.[229] Furthermore, enzyme-mediated breakdown of lignin and cellulose enhances the accessibility of the biomass matrix, facilitating more efficient carbonization and activation.

Studies have shown that enzymatically activated biochars exhibit improved functional group distribution, enhancing their adsorption properties for specific pollutants, including heavy metals and dyes. Additionally, enzymatic methods can be combined with fungal or bacterial processes to create hybrid systems that further optimize biochar properties. However, enzymatic activation is often constrained by the cost of enzyme production and the need for process optimization to achieve scalability.

Biological activation, encompassing fungal, bacterial, and enzymatic methods, represents an innovative and sustainable approach to biochar activation. Each method offers unique advantages in enhancing surface area, pore structure, and functional group distribution, making them highly relevant for CO_2 adsorption applications. Fungal activation's ability to create hierarchical pore structures aligns well with the requirements for high-capacity CO_2 adsorbents. Similarly, bacterial activation can produce biochars with tailored electrochemical properties and enhanced surface areas, making them suitable for dual applications in carbon capture and energy storage. Enzymatic activation, while less explored, holds potential for creating biochars with precise functionalization and high adsorption efficiencies.

A significant benefit of biological activation lies in its ability to integrate with the principles of the circular economy by maximizing resource utilization and creating value-added products. For instance, spent coffee grounds, typically considered waste, can serve as a growth medium for edible fungi, subsequently producing biochar precursors during fungal pre-treatment. This process demonstrates the potential for combining waste valorisation with biochar production, thereby aligning with sustainable practices and economic efficiency. Furthermore, these biological activation methods can be combined with chemical or physical activation techniques to further enhance biochar properties, offering a modular approach to biochar optimization.

Despite the promising results, there is a noticeable lack of research exploring the full potential of biological activation. This area remains relatively underexplored, leaving numerous avenues for future investigation. Opportunities include testing various microbial

strains, optimizing hybrid activation techniques, and identifying new waste materials suitable for biochar production. Expanding research in this field could uncover novel methods to enhance biochar's efficiency for CO_2 adsorption and other applications, reinforcing its role in addressing environmental challenges.

While challenges related to scalability and process control remain, biological activation holds significant potential for developing environmentally friendly, high-performance biochars for post-combustion CO_2 capture and other advanced applications. Continued exploration of hybrid and integrated activation techniques will further enhance the efficacy and sustainability of biochar production, enabling broader environmental and industrial applications.

1.8. Nitrogen Functional Groups

The incorporation of nitrogen (N)-functional groups into biochar provides active sites for the adsorption of CO_2 through both chemical and physical mechanisms. The CO_2 adsorption capacity of biochar is highly correlated with the content of N-functional groups, with studies reporting correlation coefficients (R^2) greater than 0.85. [35,36]

Nitrogen functionalities are proposed to enhance CO_2 adsorption through multiple mechanisms. Covalently tethered nitrogen functional groups act as Lewis basic sites, anchoring acidic CO_2 molecules effectively. [230,231] Another mechanism involves the interaction between the quadrupole moment of CO_2 molecules and the electrostatic field generated by N-doped carbons. [232,233] Hydrogen bonding interactions between CO_2 and surface hydrogen atoms, such as NH and CH groups, have also been suggested. [234] These mechanisms collectively contribute to the improved capacity and selectivity for CO_2 capture in N-doped biochars. These functional groups enhance CO_2 adsorption capacity and selectivity in N-containing carbons via acid-base interactions, quadrupolar interactions, and hydrogen bonding. [35,36]

However, the high temperatures required to develop high surface areas and porosity often lead to significant loss of the original nitrogen content in biomass. To address this, additional treatments or the introduction of extra nitrogen during or after pyrolysis can be employed to produce nitrogen-rich biochars.

1.8.1. Nitrogen Doping

Nitrogen doping (N-doping) involves the incorporation of nitrogen atoms into the carbon structure of biochar to enhance its surface chemistry and adsorption capabilities. This

process is crucial for creating active sites that interact effectively with CO_2 molecules. N-doping methods can be broadly classified into two categories. In in-situ treatment, nitrogen-containing chemicals are added to the biomass before pyrolysis, allowing nitrogen to be integrated into the carbon matrix during the thermal decomposition process. Conversely, post-pyrolysis treatment involves modifying the surface chemistry of biochar after pyrolysis by introducing nitrogen functional groups through chemical reactions. These approaches enable the development of biochar's tailored for specific applications, such as CO_2 capture, by controlling the type and distribution of nitrogen functionalities [35,36,235].

Ammonia Treatment

As previously discussed, the use of ammonia (NH_3) as an activating agent provides a straightforward method for introducing nitrogen functional groups to the surface of biochar. Carbon and oxygen functional groups on the biochar surface can react with NH_3 to form amines, amides, and nitrile acids by releasing water molecules during the reaction [35,36,178,180,236]. This treatment enhances the nitrogen content of biochar, contributing to its suitability for CO_2 adsorption applications.

Inorganic N-Additives

Ammonium salts, such as NH_4NO_3, NH_4OH, NH_4Cl, and NH_4OAc, have been identified as effective, low-cost, and simpler alternatives to ammonia gas treatment. These salts mitigate nitrogen wastage caused by gas purging and reduce inefficiencies associated with solid-gas molecular collisions at the feedstock interface [235].

Nitric acid is another common nitrogen source, often used in combination with sulfuric acid as a post-pyrolysis treatment. Under the presence of sodium disulfate, this method facilitates the nitrification of aromatic carbon in biochar, forming N-functional groups such as amines and –N=O [35,237].

Organic N-Additives

Organic nitrogen additives offer a convenient one-pot method to produce N-doped biochar. These additives, such as urea, melamine, and aniline, contain both nitrogen and carbon, enabling the simultaneous introduction of N atoms in the carbon matrix. However, careful control of reaction temperature is crucial, as organic N-dopants can decompose into different intermediate products under specific thermal conditions [35,36].

Urea, in particular, is a widely used nitrogen source due to its effectiveness, low cost, and renewability. Urea has also been demonstrated to increase the specific surface area and porosity of biochar, further enhancing its CO_2 adsorption capacity. [58] Melamine and alanine have also been effectively used as in-situ nitrogen dopants, providing additional versatility for nitrogen doping applications. [158]

1.8.2. Effect of Feedstock on the Formation of N-Functional Groups

The nitrogen content and type of biomass significantly influence the formation of N-functional groups in biochar. Nitrogenous biomass, such as sludge and microalgae, leads to higher nitrogen content in biochar compared to less nitrogen-rich feedstocks like wood sawdust. For example, the nitrogen content of sludge (approximately 6%) is much higher than that of wood sawdust (around 1%), resulting in biochars with nitrogen contents ranging from 2.1% to 7.1% for sludge-derived biochar and 0.56% to 0.71% for wood sawdust-derived biochar. [238,239]

Microalgae, which are particularly rich in nitrogen, produce biochars with significantly higher nitrogen content compared to other biomass types. For instance, microalgae-derived biochar contains N-functional groups such as pyrrolic-N and pyridinic-N, with nitrogen contents reaching up to 12.93%. [240]

Spent coffee grounds also represent an excellent feedstock for nitrogen-rich biochar production due to their inherently high nitrogen content, typically around 2.5%. The protein and caffeine present in coffee grounds contribute to the formation of N-functional groups such as pyridinic and amine groups during pyrolysis. This makes coffee grounds a sustainable and readily available resource for producing biochar optimized for CO_2 adsorption.

The conversion of nitrogen from feedstock to biochar depends on the type of nitrogen present in the biomass. While some nitrogen species, like protein-N, can form stable N-functional groups in biochar, others, such as amides, may decompose into NH_3 or other volatile compounds during pyrolysis. [241]

Nitrogen-rich biochars can also be prepared by co-processing materials with complementary properties. For example, algae rich in nitrogen can be combined with oxygen-functional group-rich biomass like bamboo to promote the Maillard reaction, increasing nitrogen retention in the biochar. [242] This approach demonstrates the potential

for engineering biochars with enhanced nitrogen functionality by optimizing feedstock combinations.

1.8.3. Effect of Different Nitrogen Functional Groups

Nitrogen-doped biochars contain a variety of functional groups that significantly impact their CO_2 adsorption capacity and selectivity. These functional groups include pyridinic nitrogen, pyrrolic nitrogen, graphitic nitrogen, pyridonic nitrogen, amines (primary, secondary, and tertiary), and oxidized nitrogen species such as nitro and nitroso groups. Each type of functionality interacts differently with CO_2 molecules through mechanisms like Lewis acid-base interactions, hydrogen bonding, or charge transfer. [243–245]

A diagram illustrating these nitrogen functionalities is shown in Figure 27, providing a visual reference for their structures and their specific roles in adsorption processes. The presence and distribution of these functional groups depend on factors such as pyrolysis conditions, feedstock type, and doping methods, which can be tailored to optimize biochar performance for CO_2 capture applications.

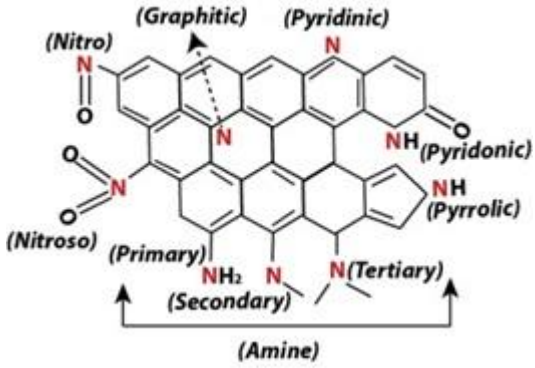

Figure 27 - Different types of possible nitrogen functionalities on carbon surface. [246]

Among these functionalities, pyridinic nitrogen has been identified as one of the strongest contributors to CO_2 adsorption. Pyridinic nitrogen, which is typically located at the edges of graphitic planes, interacts with CO_2 through Lewis acid-base interactions, leading to substantial charge transfer from the nitrogen to the CO_2 molecule. This interaction reduces the bond angle of the CO_2 molecule, enhancing its adsorption onto the biochar surface. [247,248]

Graphitic nitrogen plays a supportive role in CO_2 adsorption but is generally less effective than pyridinic nitrogen. Simulations have shown that biochars containing pyridinic nitrogen achieve adsorption capacities of up to 3.72 mmol/g, compared to 3.39 mmol/g for those

with graphitic nitrogen. The simultaneous presence of both pyridinic and graphitic nitrogen can synergistically improve CO_2 uptake to 4.34 mmol/g, highlighting the importance of optimizing the nitrogen functionalities in biochar. [247]

Pyrrolic nitrogen contributes to CO_2 adsorption primarily through hydrogen bonding interactions. While its binding energy is lower compared to pyridinic nitrogen, pyrrolic nitrogen still offers higher adsorption potential than pristine carbon surfaces. [249] Similarly, amine functionalities, including primary, secondary, and tertiary amines, enhance CO_2 adsorption through hydrogen bonding. These groups exhibit moderate binding energies and can contribute to the selectivity of biochar for CO_2 over other gases. [250]

Pyridonic nitrogen is another highly influential functional group, exhibiting strong hydrogen bonding interactions with CO_2. Its binding energy is comparable to that of pyridinic nitrogen, making it a valuable component for CO_2 adsorption applications. [249] In contrast, oxidized nitrogen functionalities, such as nitro and nitroso groups, exhibit lower binding energies but still enhance the adsorption properties of nitrogen-doped biochars compared to non-doped carbons. [250]

Nitrogen functionalities do more than just enhance CO_2 adsorption; they also influence the separation of CO_2 from other gases, like N_2. Unlike adsorption capacity, CO_2/N_2 selectivity tends to follow a direct relationship with nitrogen content. For example, carbons synthesized from lignin and activated by NH_3 showed monotonic increases in CO_2/N_2 selectivity with rising nitrogen levels. [251] However, it is also noted that excessively high nitrogen content may reduce overall CO_2 uptake due to a decrease in surface area and micropore volume.

The role of microporosity cannot be overlooked. Micropores dominate CO_2 adsorption at low pressures and temperatures, often creating a linear relationship between narrow micropore volume and equilibrium uptake capacity. Mesopores and macropores assist in gas diffusion but do not directly contribute as much to CO_2 binding. Interestingly, studies on urea-derived carbons and algae-derived carbons reveal a strong correlation between CO_2 uptake and specific nitrogen functionalities, such as pyridinic, pyrrolic, and amine groups, at pressures up to 0.5 bar and 25 °C. However, this relationship diminishes at elevated pressures or lower temperatures, demonstrating the complexity of the interaction. [250]

Heat of adsorption studies offer further insights into the role of nitrogen content. Polypyrrole-derived carbons, for instance, exhibit an increase in CO_2 adsorption enthalpy

with higher nitrogen content. This trend flattens at higher nitrogen levels, indicating an energetically homogeneous adsorption surface. [252] Similarly, lignin-derived carbons activated by NH_3 show stable heat of adsorption profiles, a rare characteristic among nitrogen-doped carbons. [251]

The competitive effects of moisture also play a critical role in practical applications. Nitrogen functionalities often increase the hydrophilicity of biochar, which can enhance or hinder CO_2 adsorption depending on environmental conditions. Amine groups, for instance, can form carbamate and bicarbonate species in the presence of moisture, effectively doubling CO_2 adsorption capacity under specific conditions. However, the hydrophilicity may also increase competition between CO_2 and water for adsorption sites, particularly in humid environments. [253,254]

Tailoring nitrogen functionalities through precise doping methods and optimizing pore structures can address these challenges, enabling nitrogen-doped biochars to perform effectively under varying environmental conditions.

1.8.4. Summary

Nitrogen doping offers a transformative approach to enhancing the CO_2 adsorption properties of biochar. Through the introduction of nitrogen functionalities such as pyridinic, pyrrolic, graphitic, and amine groups, biochars can achieve significantly improved adsorption capacities and selectivity for CO_2 over other gases. These functionalities operate through mechanisms including Lewis acid-base interactions, hydrogen bonding, and charge transfer, enabling tailored biochar designs for specific applications.

The choice of feedstock plays a critical role in determining the nitrogen content and functional group distribution within the resulting biochar. Nitrogen-rich feedstocks, such as microalgae and spent coffee grounds, have demonstrated high potential for producing biochars with enhanced nitrogen functionalities. Coupling these feedstocks with optimized pyrolysis conditions and doping methods further enhances the adsorption performance.

Ammonia treatment and the use of inorganic and organic nitrogen additives provide versatile pathways for N-doping, each offering distinct advantages depending on the desired biochar properties. The interplay between microporosity and nitrogen functionality is a key factor, as micropores facilitate adsorption, while nitrogen groups enhance interactions with CO_2. Despite the challenges posed by competitive adsorption with

moisture and the potential trade-offs between nitrogen content and pore structure, tailored biochar designs can mitigate these issues.

Chapter 2. Aims and Objectives

2.1. Background and Problem Statement

Biochar derived from waste biomass, particularly spent coffee grounds (SCG), presents a sustainable route for developing low-cost solid sorbents for post-combustion carbon capture. With rising CO_2 levels and an urgent need for scalable mitigation technologies, the development of materials that are both effective and circular is critical. This study builds on current research by focusing on valorising SCG into high-performance adsorbents through a range of activation strategies. Despite growing interest in biochar-based CO_2 sorbents, gaps remain in understanding how activation conditions influence both textural and chemical properties — and how these, in turn, affect CO_2 selectivity, kinetics, and cyclic stability. Limited data exists on SCG-derived biochars synthesised under controlled design of experiments (DoE), particularly across physical, chemical, and biological activation routes.

2.2. Rationale and Justification

This project aims to develop high-performance SCG-derived adsorbents for post-combustion CO_2 capture through various activation methods, characterise their performance in CO_2 uptake and selectivity, and evaluate their long-term feasibility. The work is justified by:

- the abundance of SCG as a waste stream and its favourable composition.
- the lack of comparative data across activation techniques for this precursor.
- the industrial interest in low-cost, regenerable adsorbents.

The key research questions that the work serves to address are:

- How do different activation routes affect the porosity and surface chemistry of SCG-derived biochars?
- Do selected samples show sufficiently high CO_2 uptake under relevant conditions?
- Can these materials achieve selective CO_2 capture over N_2?
- How stable are high-performing materials over multiple adsorption–desorption cycles?

Which will be answered by undertaking a structured programme of work as detailed below.

2.3. Overall Aim

To synthesise, characterise, and evaluate SCG-derived biochars for post-combustion CO_2 capture, with a focus on textural tuning, adsorption performance, and selectivity under binary gas conditions.

2.4. Specific Objectives

Objective 1: To critically review the literature and identify a suitable biomass precursor and activation methods for developing biochar-based CO_2 adsorbents, informed by compositional attributes and performance criteria.

Objective 2: To synthesise SCG-derived biochars using CO_2, KOH, potassium oxalate, and fungal activation methods.

Objective 3: To determine the influence of synthesis parameters on yield, surface area, pore distribution, and chemical composition.

Objective 4: To evaluate CO_2 adsorption capacity, thermodynamics, and kinetics using gravimetric analysis.

Objective 5: To investigate the cyclic adsorption stability and discuss scalability and feasibility of promising materials.

Objective 6: To assess competitive CO_2/N_2 adsorption behaviour and calculate selectivity using Ideal Adsorbed Solution Theory (IAST), providing insight into adsorbent performance under realistic flue-gas conditions and enabling comparison with state-of-the-art post-combustion CO_2 capture materials.

2.5. Contributions to knowledge

This research is novel in its systematic and comparative evaluation of multiple activation strategies—physical (CO_2), chemical (KOH and potassium oxalate), and biological (fungal pre-treatment)—applied to spent coffee ground (SCG)-derived biochars within a unified Design of Experiments (DoE) framework. Unlike prior studies that typically investigate individual activation routes in isolation, this work directly compares activation severity, yield retention, pore development, surface chemistry, and CO_2 adsorption performance across routes under controlled and statistically structured conditions. This integrated approach enables a clearer understanding of activation–structure–performance relationships and provides practical insight into optimising sorbent design for post-combustion carbon capture.

Furthermore, this study advances the field by combining circular waste valorisation with detailed structure–function analysis, including adsorption capacity, kinetics, thermodynamics, cycling stability, and competitive CO_2/N_2 selectivity assessed through IAST. By explicitly examining the trade-offs between surface chemistry, porosity development, adsorption affinity, and regenerability, the work moves beyond simple capacity reporting and contributes a more mechanistic perspective on designing scalable, PSA-compatible biochar sorbents.

Chapter 3. Adsorption Theory

3.1. Intermolecular Interactions in Surface Systems

Intermolecular forces govern the interactions between molecules and surfaces, playing a foundational role in determining the strength, selectivity, and reversibility of many physical and chemical processes. These interactions range from weak, non-specific attractions to highly directional, selective forces and are critical in fields spanning catalysis, material science, environmental remediation, and molecular recognition. The nature and magnitude of these interactions are dictated by the polarizability, charge distribution, and structural features of the interacting species. This section outlines the primary types of intermolecular forces relevant to surface phenomena, with emphasis on their relative energy contributions and governing principles. [255–257] A detailed overview of these forces—including London dispersion forces, dipole–dipole interactions, hydrogen bonding, quadrupole effects, π–π interactions, and cation–π and anion–π interactions—has been summarised in Appendix A: Intermolecular Interactions, providing additional context on their strengths, roles, and implications for adsorption processes.

3.2. Adsorption Theory

Adsorption is a surface phenomenon in which molecules, atoms, or ions from a gas or liquid phase adhere to a solid or liquid surface, forming a distinct layer. As outlined above, physical processes, which always occur in adsorption systems are underpinned by intermolecular forces. Adsorption contrasts with absorption, where the substance penetrates the bulk material and distributes uniformly, and adsorption is widely utilized in applications such as gas separation, catalysis, and environmental remediation.

Adsorption plays a vital role in contemporary science and engineering, particularly in environmental remediation (e.g., pollutant removal), energy storage (e.g., gas separation), and catalysis. Advanced materials like activated carbon, zeolites, and metal-organic frameworks (MOFs) are engineered to optimize adsorption performance through tailored surface area and porosity.

The study of adsorption dates back centuries. Fontana first observed gas uptake by solids in 1777 [258], while de Saussure (1814) demonstrated that adsorption capacity depends on both gas type and material properties, particularly surface area. In 1843, Mitscherlich highlighted the role of pore structure in adsorption efficiency, and in 1881 [259,260], Kayser formally

introduced the term "adsorption," distinguishing it from absorption [261]. These foundational discoveries established surface area and porosity as key determinants of adsorption capacity.

An adsorption system consists of an adsorbent (the solid or liquid surface) and an adsorbate (the substance being adsorbed). The term adsorptive refers to a substance capable of being adsorbed. These interactions underpin adsorption science, which is broadly classified into physisorption and chemisorption.

The following sections will explore adsorption mechanisms, classification, and models that describe adsorption behaviour, providing a comprehensive framework for its scientific and practical applications.

3.2.1. Adsorption Fundamentals

Within an adsorption system, the interaction involves primarily two components: the adsorbent, the solid or liquid surface that adsorbs another substance, and the adsorbate, the substance being adsorbed. Additionally, the term adsorptive refers to a substance with the potential to be adsorbed. This interplay between adsorbent and adsorbate forms the basis of the adsorption process, where molecules, atoms, or ions adhere to a surface, creating a distinct film or layer.

Adsorption at gas-liquid and gas-solid interfaces involves intermolecular forces that govern how molecules adhere to surfaces, with factors such as surface energy, porosity, and molecular interactions influencing adsorption efficiency. Langmuir's pioneering insights into this interaction revealed that when a gas molecule encounters the surface of a solid or liquid, it does not merely bounce off but momentarily condenses on the surface. This behaviour is dictated by intermolecular forces from surface atoms, which temporarily attract and retain the gas molecule.[262–264]

This molecular condensation, or adsorption, is a precise response to the strength of intermolecular forces. The duration a gas molecule spends anchored to the surface depends on the strength of these forces. In cases where the forces are robust, the gas molecule adheres securely, potentially leading to a surface fully covered by adsorbed molecules. Conversely, when the forces are weaker, the molecule's stay is transient, resulting in partial surface coverage as evaporation rates increase.

A deeper understanding of the adsorption mechanism reveals its dependence on the size of the adsorptive molecule, the pore width of the adsorbent, and the interplay of thermodynamic and kinetic factors governing adsorption. The process is driven by minimization of the system's free energy, where adsorption is favoured when the enthalpic gain from intermolecular interactions outweighs the entropic penalty of restricting molecular movement. Adsorption typically begins in high-energy micropores, where van der Waals forces, electrostatic interactions, or chemical bonding provide strong adsorption sites. As these sites become occupied, adsorption extends to larger, lower-energy mesopores and macropores, provided diffusion does not impose a kinetic limitation on the process.

Adsorption is a dynamic and reversible process, where molecules continuously adsorb and desorb from the surface. The mechanism involves three primary steps. The first is transport, where adsorbate molecules diffuse through the bulk phase (gas or liquid) to reach the adsorbent surface. The rate of transport depends on concentration gradients and diffusion kinetics. Secondly adhesion occurs, where molecules interact with the adsorbent surface through physisorption (e.g. weak van der Waals forces, dipole-dipole interactions, or hydrogen bonding), or chemisorption (e.g. strong covalent or ionic bonding). Adsorption continues until a dynamic balance is reached, where the rate of adsorption equals the rate of desorption, and equilibrium is achieved. At equilibrium, the system has minimized its Gibbs free energy, balancing enthalpic attraction and entropic resistance.

Adsorption efficiency and capacity are governed by key factors such as temperature, pressure, adsorbate concentration, and the chemical properties of the adsorbent. These factors influence the adsorption process by altering the balance between adsorption and desorption rates, ultimately determining the equilibrium state. [257,265] Notable, temperature plays a critical role in adsorption. For physisorption, increasing temperature typically reduces adsorption capacity because higher kinetic energy facilitates desorption. In contrast, chemisorption, which involves stronger chemical bonds, may show increased adsorption at higher temperatures, but only up to a certain point before thermal desorption dominates. Pressure is particularly important in gas-phase adsorption. Higher pressure increases the partial pressure of the adsorbate, enhancing adsorption by driving equilibrium toward greater surface coverage. This relationship is well-described by adsorption isotherms, such as the Langmuir or Freundlich models, which quantify how adsorption capacity changes with pressure. For liquid-phase adsorption, adsorbate

concentration has a similar effect. Higher concentrations increase the number of collisions between adsorbate molecules and the adsorbent surface, raising the likelihood of adsorption. This effect is particularly pronounced when the adsorbent surface offers high-affinity binding sites.

The chemical properties of the adsorbent itself, such as functional groups and active sites, are also crucial. These features enable specific interactions, such as hydrogen bonding, dipole interactions, or covalent bonding, which enhance adsorption strength and selectivity for certain adsorbates. Additionally, surface charge and polarity can influence the adsorbate-adsorbent interaction, further impacting adsorption capacity and efficiency. Understanding the fundamental characteristics and interactions of adsorption enables its wide application in industry and research, including areas such as gas capture, water purification, and catalysis. [262]

3.2.2. Adsorption on Solids and Liquids

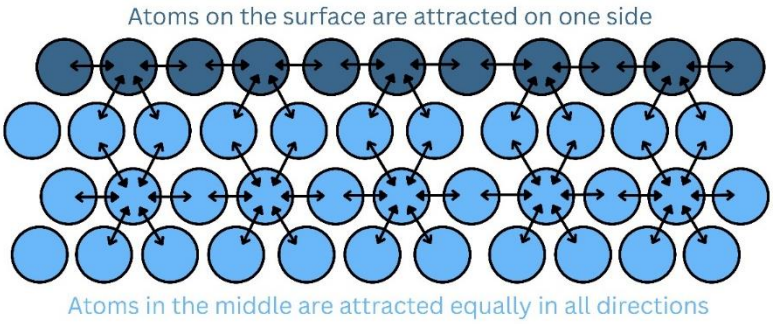

Figure 28 - Surface atoms experience unbalanced forces, creating high-energy sites for adsorption. [266]

Adsorption behaviour differs between solids and liquids due to the distinct intermolecular forces governing surface interactions. In solid-phase adsorption, van der Waals forces, electrostatic interactions, and, in some cases, covalent or ionic bonding dictate how molecules adhere to the surface. In liquid-phase adsorption, additional factors such as solvation effects and hydrogen bonding influence the extent and nature of adsorption, as the surrounding liquid medium competes with the adsorbate for surface sites. [263,265] For liquids, the process of adsorption is intricately linked to the concept of surface tension, a phenomenon arising from unbalanced forces acting upon the molecules located at the liquid's surface (Figure 28). Unlike their counterparts within the liquid's bulk, which experience uniform attraction from surrounding molecules, surface molecules encounter attraction from one side only. This imbalance generates surface tension, creating a distinct

interfacial region where adsorption can occur. This differential attraction draws molecules inwards, fostering a condition ripe for adsorption as external substances interact with these surface molecules.[267] In solids, adsorption is primarily governed by unbalanced intermolecular forces at the surface, often referred to as surface energy. Unlike bulk atoms, which experience balanced interactions in all directions, surface atoms retain excess attractive forces due to missing neighbouring atoms. These unsatisfied forces create high-energy adsorption sites where gas molecules can be temporarily attracted and retained upon contact. The extent and duration of adsorption depend on multiple factors, including the nature of the adsorptive, the characteristics of the adsorbent, temperature, pressure, and specific surface properties of the solid. Features such as capillary forces within porous materials and surface heterogeneities, including functional groups or irregularities, further influence adsorption strength and capacity.

Both scenarios underscore the pivotal role of surface properties in dictating adsorption behaviour. While the driving forces behind adsorption in liquids and solids share fundamental similarities, the outcomes and dynamics of the process are shaped by the medium's physical state and its inherent material properties. This complexity highlights the need for tailored approaches in studying and optimizing adsorption processes to meet specific application requirements.

3.2.3. Types of Adsorption

Adsorption processes are broadly categorised into two mechanisms based on the nature of interaction between the adsorbate and the adsorbent: physical adsorption (physisorption) and chemical adsorption (chemisorption). [260,265] This distinction (see Figure 29) is critical for both theoretical interpretation and practical application, influencing material selection, energy requirements, and process reversibility.

Physisorption is a universal phenomenon that occurs whenever a gas or liquid comes into contact with a solid surface. It is governed by weak intermolecular forces—typically van der Waals or London dispersion interactions—and does not involve the formation of chemical bonds. As a result, physisorption is generally reversible, occurs over a wide range of temperatures and pressures, and can lead to the formation of multilayers. It is exothermic and is accompanied by a decrease in system entropy as adsorbate molecules adopt an ordered configuration on the surface. Chemisorption, by contrast, involves the formation of stronger, often covalent or ionic, bonds between the adsorbate and specific sites on the

adsorbent surface. This mechanism is typically more selective and results in the formation of a monolayer. Due to the strength and specificity of the interactions, chemisorption is associated with greater enthalpic changes and is often irreversible under moderate conditions. These attributes make chemisorption particularly relevant to catalytic and sensing applications, where the formation and disruption of chemical bonds are central to function. The two mechanisms are not mutually exclusive: physisorption often precedes chemisorption, serving as an initial step that brings molecules close enough for bond formation to occur. A more detailed discussion of each mechanism follows below.

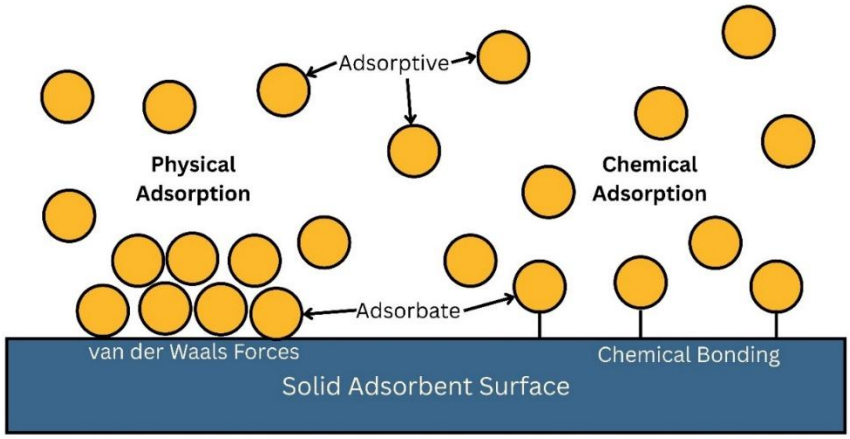

Figure 29 - Illustrative comparison of physical and chemical adsorption on a solid surface, governed by van der Waals forces and chemical bonding, respectively. [268]

Physisorption

Physisorption, characterized by the absence of chemical bond formation, is a process where molecules adhere to a surface through physical interactions. Governed by dynamic equilibria, molecules alternate between adsorption and desorption without the specificity of chemical reactions. This phenomenon is primarily driven by weak intermolecular interactions, including Van der Waals forces, hydrogen bonding, and π-π interactions. Among these, Van der Waals forces—such as London dispersion forces, dipole-dipole interactions, and dipole-induced dipole interactions—are the most predominant contributors to physisorption, facilitating the transient electrical moments that underpin the adsorption process. These interactions influence how molecules are attracted to the adsorbent and retained on its surface.

The process's efficiency is closely tied to the adsorbent's physical properties—surface area, pore size, and distribution—dictating the prevalence and extent of adsorption sites.

Physisorption is distinctive for its capability to form multi-layered adsorbates under optimal conditions, typically favoured by an increase in pressure or a decrease in temperature. The heat of adsorption in physisorption is notably low, generally ranging from 20–40 kJ/mol and rarely exceeding 80 kJ/mol. This low energy requirement highlights the reversible nature of physisorption, which is leveraged in applications such as Pressure Swing Adsorption (PSA) and Temperature Swing Adsorption (TSA), where changes in pressure or temperature effectively induce desorption. [265]

Thermodynamically, physisorption is inherently exothermic, the release of heat stemming from the system's decrease in entropy as the adsorbate organises upon the surface. This thermodynamic behaviour means that the quantity of adsorbate secured by the adsorbent is sensitive to the system's temperature. According to Le Chatelier's principle [269], a decrease in temperature typically enhances the amount of substance adsorbed, highlighting the critical role of thermal conditions in physisorption processes.

Incorporating these thermodynamic principles, physisorption emerges as a process of significant practical utility, with applications ranging from gas storage to separation technologies, governed by the delicate balance of forces and conditions that drive molecular interactions at surfaces.

Chemisorption

Chemisorption is a distinctive adsorption mechanism primarily due to the involvement of a chemical reaction between the adsorbate and the adsorbent. This interaction is characterized by the formation of strong chemical bonds at the surface, which are significantly more robust than the forces at play in physical adsorption processes. The essence of chemisorption lies in the exchange of electrons between the adsorbate and the adsorbent, leading to the creation of new compounds through valence bonds. The strength of these chemical bonds is highlighted by the high heats of adsorption observed in chemisorption, typically ranging from 80 kJ/mol to 800 kJ/mol. This strong bond formation necessitates considerable energy for bond breaking, or desorption, underscoring the energetically intensive nature of chemisorption. [260,265] Unlike physical adsorption, which can cover the entire surface with multiple layers of adsorbate, Chemisorption is highly selective and localized; it occurs specifically at certain active sites on the surface and only if those sites are not already occupied by another species. As a result, chemisorption typically forms a single layer of adsorbate on the adsorbent surface. However, scenarios exist where an

adsorbent chemisorbs an adsorptive to form a single layer, and then physical adsorption (physisorption) occurs atop this layer, creating hybrid cases of adsorption.

One of the hallmark characteristics of chemisorption is its potential irreversibility. The nature of the adsorptive may change after desorption, rendering the adsorbed species potentially non-recoverable. This aspect is due to the chemical reaction's direction and nature, which may not always be reversible. Furthermore, chemisorption involves an energy change that can be either exothermic or endothermic, as a chemical reaction, with the initial step requiring activation energy. [265]

In terms of analytical evaluation, chemisorption is often described using the Langmuir isotherm, which models' adsorption as a process where a fixed number of active sites on the adsorbent surface interact with adsorbate molecules. An isotherm is a mathematical relationship that describes how the amount of adsorbate bound to the surface varies with concentration (or pressure) at a constant temperature. In the Langmuir model, adsorption is assumed to occur at specific, energetically uniform sites capable of forming covalent bonds with the adsorbate, reflecting the strong and localized nature of chemisorption. Following this framework, when an adsorbate molecule interacts with the adsorbent surface, two possible outcomes are observed. In an elastic rebound, the molecule collides with the surface and bounces back without energy transfer, resulting in no adsorption. In contrast, an inelastic collision involves energy transfer, allowing the molecule to temporarily adhere to the surface in a weakly bound precursor state. From this state, the molecule may migrate to a stronger binding site where chemisorption occurs, forming stable covalent or ionic bonds.

The likelihood of a molecule reacting with the surface depends significantly on the chemical species involved. The Gibbs energy equation offers a quantitative measure of this interaction:

$$\Delta G = \Delta H - T\Delta S \qquad \textit{Equation 10}$$

For chemisorption to be spontaneous, the free energy change (ΔG) must be negative. This is typically achieved through a negative enthalpy change (ΔH), which reflects the exothermic nature of bond formation, compensating for the decrease in entropy (ΔS) as the system becomes more ordered upon adsorption. However, in some cases, endothermic chemisorption can occur if the entropy loss is offset by sufficient energy input, emphasizing the diversity of chemisorption scenarios. [270]

Differentiating between physisorption and chemisorption in terms of potential energy, the included diagram in Figure 30 illustrates these interactions. The transition from physisorption to chemisorption, as depicted in the diagram, involves crossing an energy barrier that represents the activation energy. In cases where the activation energy is absent or minimal, such as with certain simple gases, direct chemisorption can occur without significant energy input. This transition highlights the importance of energy barriers in determining the feasibility and rate of adsorption. Such interactions exemplify the efficiency of chemisorption under ideal conditions, where the strength of the resulting chemical bonds significantly enhances surface reactivity. [271] Consequently, chemisorption plays a pivotal role in numerous industrial processes, such as catalysis and material surface modification, owing to its unique characteristics of strong bond formation, selectivity, and energy efficiency. This detailed understanding underscores its importance in advancing technologies reliant on adsorption-based mechanisms, particularly in addressing challenges like efficient chemical transformations and enhanced material performance.

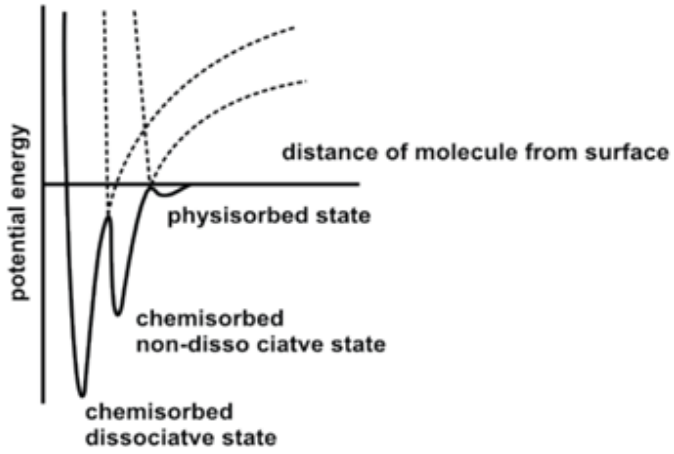

Figure 30 - Potential energy diagram illustrating physisorption and chemisorption states. [272]

3.3. Porosity

Porosity, which refers to the presence of void spaces or pores within a material, plays a crucial role in adsorption by influencing the available surface area and determining the material's effectiveness in capturing specific molecules. These voids significantly influence the material's structural and functional properties, particularly its capacity to act as an adsorbent. Adsorption is a surface phenomenon, meaning that the availability of surface area, largely governed by porosity, determines the adsorption performance of a material.

Porous materials are widely used in applications such as catalysis, separation, and purification processes due to their ability to adsorb specific molecules effectively.

3.3.1. Classification of Pores by Size

Pores are categorized based on their dimensions, as defined by the International Union of Pure and Applied Chemistry (IUPAC). The classification is essential for understanding adsorption mechanisms and tailoring materials for specific applications:

Table 2 – Classification of Pore Sizes

Pore Type	Pore Width	Characteristics
Macropores	> 50 nm	Facilitate bulk transport of matter to smaller pores; contribute to material strength and structural stability.
Mesopores	2–50 nm	Enable diffusion and adsorption of larger molecules; essential for multilayer adsorption mechanisms.
Micropores	< 2 nm	Provide high surface area; ideal for adsorbing small molecules through molecular sieving.
Ultra-Micropores	< 0.7 nm	Enable enhanced adsorption of very small gas molecules, such as hydrogen or helium, resulting in efficient gas storage.

Pore Types and Configurations

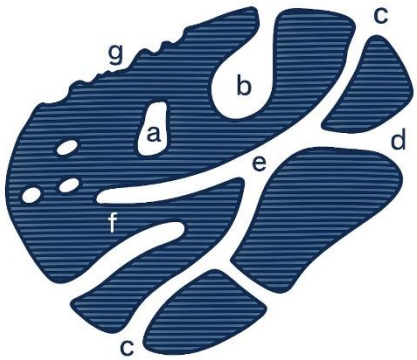

Figure 31 - Schematic of pore types in porous solids: (a) closed pores, (b, f) blind pores, (c, d, e) transport pores, and (g) surface roughness. [273]

Different regions can be identified in porous materials, including closed pores **(**Figure 31**, a)**, which are isolated from external surfaces and have no interaction with external fluids. They do not contribute to adsorption but play an important role in determining the material's bulk density, mechanical strength, and thermal conductivity. Open pores are connected to external surfaces and significantly influence adsorption, sub-categories are blind pores **(b,**

f), which are Connected to the external surface at only one end, limiting their accessibility, and transport pores **(c, d, e)**, by contrast, these are open at both ends, enabling the flow of matter between external and internal surfaces. These pores also connect to the inner microporosity, enhancing adsorption efficiency. Finally, there is surface roughness **(g)**, comprising regions that are wider than they are deep, defined as external surfaces. These areas are not classified as porosity but contribute to the external surface area. The total surface area of a porous solid comprises both external and internal surfaces.

Mechanisms of Adsorption in Pores

Adsorption mechanisms differ depending on pore size and structure, which govern how adsorbate molecules interact with the material:

- **Micropores:** These pores fill first due to their high surface energy and strong adsorbate-adsorbent interactions. Molecules entering micropores experience overlapping potential fields from the pore walls, which results in strong confinement effects and efficient packing of small molecules like CO_2 or CH_4. The small dimensions also reduce the diffusion path, enabling rapid adsorption.
- **Mesopores:** Adsorption in mesopores begins with the formation of a monolayer on the pore walls. As the adsorbate concentration increases, additional molecular layers build upon the initial monolayer, leading to multilayer adsorption. At higher pressures, capillary condensation occurs, filling the pore volume, especially in smaller mesopores where the adsorptive forces are stronger.
- **Macropores:** These primarily act as conduits for transporting adsorbates to smaller pores. While limited adsorption occurs on their surfaces, they reduce diffusion limitations and improve the overall kinetics of the adsorption process.

Understanding these mechanisms is critical for designing materials with optimized pore structures for specific applications, such as gas storage, separation, or pollutant removal. This understanding will also aid in the next section, which discusses isotherm types.

Relationship Between Porosity and Surface Area

Porosity and surface area are closely related, as the total surface area of a porous material comprises contributions from both internal and external surfaces. Materials with a high internal surface area, such as zeolites and aerogels, exhibit exceptional adsorption

capabilities. However, external surface area also plays a role in certain applications, especially when rapid adsorption or diffusion is required.

The relationship between surface area and particle size is inverse; smaller particle sizes typically yield higher surface areas. This makes particle size reduction a common approach to enhance adsorption efficiency. When particles aggregate, some of the external surface area converts into internal surface area, further increasing adsorption potential.

3.3.2. Porosity and Small Molecule Adsorption Enhancement

Porosity plays a critical role in determining the adsorption behaviour of porous materials, particularly in applications involving small gas molecules. The size, distribution, and connectivity of pores influence both the accessibility of adsorption sites and the strength of adsorbate–adsorbent interactions. Microporous (<2 nm) and ultramicroporous (<0.7 nm) structures are especially effective for small molecule adsorption due to their high surface area and capacity to generate confined environments that enhance intermolecular interactions.

In the context of CO_2 capture, two key mechanisms contribute to enhanced selectivity in microporous and ultramicroporous materials: molecular sieving and increased surface interaction.

The molecular sieving effect arises from the precise control of pore dimensions, which enables preferential adsorption of CO_2 molecules while excluding slightly larger gases such as N_2 and O_2.[274] This selectivity is facilitated by differences in kinetic diameters—3.30 Å for CO_2, compared to 3.64 Å for N_2 and 3.45 Å for O_2—and is most pronounced in pores narrower than 0.7 nm.[275,276] This mechanism is particularly advantageous for post-combustion capture, where CO_2 must be separated from dilute gas mixtures.

Enhanced surface interaction is the second key contributor to selectivity. In narrow pores, the potential fields from opposing pore walls overlap, intensifying van der Waals forces and inducing additional polarization effects. These confined conditions increase the adsorption energy of CO_2 relative to other gases, improving uptake at low pressures.[277,278]

Together, these mechanisms explain the strong performance of microporous and ultramicroporous materials in selective CO_2 capture. A detailed understanding of porosity and its influence on adsorption dynamics is therefore essential for the rational design of efficient adsorbents for gas separation, storage, catalysis, and environmental remediation.

3.4. Thermodynamics of Adsorption

Adsorption is a thermodynamically driven process where molecules from a gas or liquid phase adhere to a solid surface. The feasibility and extent of adsorption are determined by the changes in Gibbs free energy (ΔG), enthalpy (ΔH), and entropy (ΔS) of the system. Thermodynamic principles provide insight into adsorption mechanisms, equilibrium conditions, and energy interactions between the adsorbate and adsorbent. [265,279]

A system reaches adsorption equilibrium when the chemical potential of the adsorbed phase equals that of the free phase. Adsorption can be classified into two primary types: physisorption and chemisorption. Physisorption is governed by weak van der Waals forces and is typically reversible, whereas chemisorption involves stronger chemical bonds and may be irreversible. The thermodynamics of adsorption determine the stability, efficiency, and applicability of adsorption in various scientific and industrial processes.

3.4.1. Fundamental Thermodynamic Relations

Gibbs free energy (G) is a thermodynamic potential that determines whether a process occurs spontaneously. The Gibbs free energy change is given by:

$$\Delta G = \Delta H - T\Delta S \qquad \textit{Equation 11}$$

where:

- ΔG = Gibbs free energy change, indicating spontaneity of adsorption.
- ΔH = Enthalpy change, representing the heat absorbed or released.
- T = Absolute temperature (K).
- ΔS = Entropy change, quantifying the disorder in the system.

For adsorption to be thermodynamically favourable, ΔG must be negative. The balance between ΔH and $T\Delta S$ dictates the extent and nature of adsorption. Physisorption is always exothermic, with a small ΔH (-10 to -40 kJ/mol) and a slightly negative ΔS, due to the weak interactions between the adsorbate and the surface. Chemisorption, however, may be either exothermic or endothermic. In exothermic cases, bond formation stabilizes the system, releasing energy ($\Delta H < 0$). In endothermic chemisorption, bond formation requires activation energy, meaning heat must be supplied ($\Delta H > 0$). [279]

Thermodynamically, physisorption is inherently exothermic, as the release of heat results from the system's decrease in entropy as the adsorbate organizes upon the surface. This

thermodynamic behaviour means that the quantity of adsorbate secured by the adsorbent is sensitive to the system's temperature. According to Le Chatelier's principle [269], a decrease in temperature typically enhances the amount of substance adsorbed, highlighting the critical role of thermal conditions in physisorption processes. Chemisorption, in contrast, can be either exothermic or endothermic, depending on the nature of the chemical bonds formed. If the adsorbate forms a strong, stable bond with the surface, heat is released, making the process exothermic. However, in cases where bond formation requires energy input—such as breaking pre-existing bonds at the surface—chemisorption can be endothermic.[279]

Additionally, the driving force for adsorption can be quantified through adsorption isotherms, which relate pressure and concentration to adsorption capacity. Understanding adsorption energy distributions helps predict surface behaviour and optimize adsorption applications.

Entropy (*S*) is a measure of disorder or randomness in a system. In adsorption, entropy typically decreases because adsorbed molecules become more ordered on the surface compared to their free phase. The entropy change is expressed as:

$$\Delta S=\Delta QT \qquad \textit{Equation 12}$$

where *ΔQ* is the heat exchanged and *T* is the temperature. Since adsorption constrains molecular movement, *ΔS* is usually negative, particularly for physisorption.

In contrast, chemisorption may involve bond formation that can sometimes increase system entropy. If adsorption leads to dissociation of a molecule into multiple smaller fragments, entropy may increase, partially offsetting the enthalpic component in the Gibbs free energy equation. [265,279]

Enthalpy (*H*) is the total heat content of a system and plays a critical role in adsorption processes. It accounts for the heat released or absorbed during adsorption. The enthalpy change is given by:

$$\Delta H = U + P\Delta V \qquad \textit{Equation 13}$$

where *U* is the internal energy, *P* is pressure, and *ΔV* is the change in volume. In physisorption, *ΔH* is small and negative, whereas in chemisorption, it varies significantly depending on bond formation and breaking.

Since chemisorption involves bond rearrangement, its activation energy is typically higher than that of physisorption. This makes chemisorption slower than physisorption at lower temperatures but more stable at higher temperatures. [265,279]

In closed systems, the internal energy (*U*) and Helmholtz free energy (*A*) play key roles in adsorption thermodynamics. The Helmholtz energy is defined as:

$$A = U - TS \qquad \textit{Equation 14}$$

where *U* represents the total energy of the system. Helmholtz energy is crucial in adsorption studies under conditions where volume is held constant.

The relation between Helmholtz energy and work done on the system allows for the prediction of adsorption at different thermodynamic conditions. This is especially relevant in nanoporous materials, where surface effects dominate over bulk properties. [265,279]

3.4.2. Heats of Adsorption and Energy Considerations

The heat of adsorption, ΔH_{ads}, is a key thermodynamic parameter that determines the strength and nature of the interaction between the adsorbate and the adsorbent. Chemisorption is characterized by higher adsorption enthalpies due to the formation of strong chemical bonds, typically in the range of 100–400 kJ/mol. In contrast, physisorption is governed by weak van der Waals forces, with lower adsorption enthalpies, usually between 10–50 kJ/mol. The magnitude of ΔH_{ads} provides insight into the adsorption mechanism and influences the selection of adsorbents for specific applications. Additionally, the nature of the adsorbate-adsorbent interactions can determine the reversibility of adsorption and the energy required to desorb the species. [265,279]

The adsorption enthalpy can be experimentally determined using calorimetric methods or estimated through the Clausius-Clapeyron equation [280]:

$$\frac{d(\ln P)}{dT} = \frac{-\Delta H}{RT^2} \qquad \textit{Equation 15}$$

where:

- *P* is the equilibrium pressure, which represents the pressure at which adsorption and desorption rates are equal.
- *T* is the absolute temperature, measured in kelvin (K).
- *R* is the universal gas constant, approximately 8.314 J/(mol·K).

- *ΔH* is the heat of adsorption, which quantifies the energy change associated with the adsorption process.

3.4.3. Adsorption Equilibrium

Adsorption equilibrium is reached when the rate of adsorption equals the rate of desorption, meaning there is no net exchange of adsorbate molecules between the surface and the surrounding medium. At equilibrium, the chemical potential of the adsorbed phase equals that of the free phase, ensuring a stable distribution of molecules between these states. Understanding adsorption equilibrium is crucial for optimizing industrial processes.

The equilibrium condition can be expressed as:

$$\mu_{ads} = \mu_{gas} \qquad \textit{Equation 16}$$

where:

- μ_{ads} is the chemical potential of the adsorbed phase,
- μ_{gas} is the chemical potential of the gas phase.

Factors influencing adsorption equilibrium include temperature, pressure (or concentration for liquid-phase adsorption), and the nature of the adsorbent-adsorbate interactions. The balance between these factors determines the extent of adsorption and the surface coverage at a given set of conditions.

Thermodynamically, adsorption equilibrium is governed by Gibbs free energy changes. The condition for spontaneous adsorption is:

$$\Delta G = \Delta H - T\,\Delta S < 0 \qquad \textit{Equation 17}$$

where:

- *ΔG* is the Gibbs free energy change,
- *ΔH* is the enthalpy change associated with adsorption,
- *T* is the absolute temperature,
- *ΔS* is the entropy change.

A negative *ΔG* indicates a favourable adsorption process. Exothermic adsorption (negative *ΔH*) is typically more favourable at lower temperatures, while endothermic adsorption (positive *ΔH*) may be enhanced by increasing temperature.

The equilibrium adsorption capacity is often measured through adsorption isotherms, which describe how the amount adsorbed varies with pressure or concentration at constant temperature. These relationships provide insight into the strength of adsorbate-adsorbent interactions and the capacity of the adsorbent for a given species.

A thorough understanding of adsorption equilibrium is essential for designing and optimizing adsorption-based technologies, ensuring efficient separation, purification, and catalytic performance across various applications. Additionally, equilibrium considerations help predict adsorption efficiency in real-world systems where surface effects and thermodynamic constraints play a crucial role.

3.5. Adsorption Isotherms

Adsorption isotherms represent the relationship between the amount of adsorbate adsorbed by a solid surface and the pressure (or concentration) of the adsorbate at constant temperature. These curves are crucial for understanding and quantifying adsorption processes, enabling the characterization of porous materials and the evaluation of surface properties such as surface area, pore size distribution, and adsorption capacity. Adsorption isotherms are widely used in fields ranging from material science and catalysis to environmental engineering and energy storage.

To construct an adsorption isotherm, the amount of gas adsorbed by a solid is measured as a function of its equilibrium pressure. This can be achieved using two principal methods: the manometric method and the gravimetric method. The manometric method determines the adsorbed quantity by monitoring pressure changes in a confined volume using the ideal gas law, while the gravimetric method directly measures the change in the weight of the adsorbent during adsorption. Both techniques have specific advantages and are selected based on the experimental conditions, such as the nature of the gas and the temperature of adsorption.

For gases like nitrogen, argon, and krypton at cryogenic temperatures, the manometric method is commonly employed due to its high accuracy. This approach involves admitting a known volume of pure gas into a sample cell containing the adsorbent and measuring the pressure drop as the gas adsorbs onto the surface. Calibration of the system, including accurate determination of dead space and careful control of temperature, is critical for reliable results. Similarly, gravimetric methods are particularly useful for vapours and allow for direct measurement of adsorbate mass changes.

The isotherms generated provide insights into the adsorption mechanism and are classified into different types based on their shape, as defined by the International Union of Pure and Applied Chemistry (IUPAC). [281] These classifications correlate with the surface properties and pore structure of the adsorbent, offering a foundation for further analysis of material behaviour.

In practice, constructing adsorption isotherms requires specialized equipment capable of spanning a broad pressure range, often involving ultra-low pressures for micropore analysis. Attention to experimental details, such as equilibration times, purity of the adsorptive gas, and proper calibration of pressure transducers, ensures accurate representation of the adsorption process. These considerations are vital, particularly when analysing nonporous materials for applications like gas storage, separation, or catalysis.

In summary, adsorption isotherms are a fundamental tool in the study of physisorption, providing a quantitative framework to assess the interaction between gases or vapours and solid surfaces under controlled conditions. Their measurement and interpretation remain central to the development and optimization of advanced adsorbent materials.

3.5.1. Classification of Adsorption Isotherms

Adsorption isotherms are categorized into six distinct types as defined by the International Union of Pure and Applied Chemistry (IUPAC). These classifications provide crucial insight into the adsorption mechanisms and the structural properties of the adsorbent material, including porosity, surface characteristics, and adsorption capacity. The types of isotherms (Types I–VI) are distinguished by their characteristic shapes and are typically plotted as the amount adsorbed (e.g., in moles per gram of adsorbent) against the relative pressure (p/p_0), where p_0 is the saturation pressure of the adsorptive at a given temperature. These classifications provide a framework for understanding the behaviour of adsorbents under different conditions and are visually represented in Figure 32, with their significance discussed below. [281]

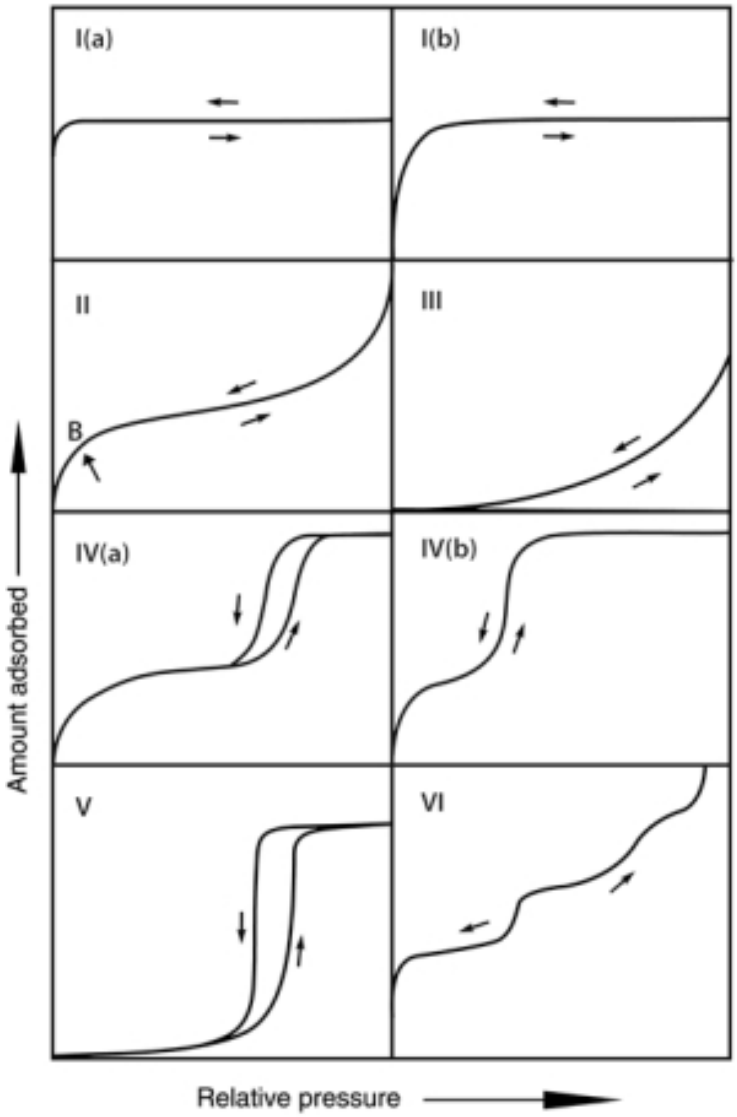

Figure 32 - IUPAC classification of adsorption isotherms (Types I–VI), illustrating characteristic uptake behaviour across pore types and interaction strengths.[282]

Type I Isotherm

Type I isotherms are typical of microporous materials with limited external surface area, such as activated carbons, zeolites, and molecular sieves. They exhibit a steep uptake at low relative pressures due to strong adsorbent–adsorbate interactions in narrow micropores. The adsorption reaches a plateau, determined by micropore volume rather than surface area, indicating that micropore filling is the dominant mechanism.

- *Type I(a)*: Associated with materials having ultramicropores (<1 nm), which exhibit high adsorption at very low pressures.

- *Type I(b)*: Corresponds to materials with wider micropores or narrow mesopores (<2.5 nm), resulting in broader uptake ranges.

This isotherm type is crucial for evaluating micropore volume and is particularly relevant for adsorbents used in gas storage and separation applications.

Type II Isotherm

Type II isotherms describe physisorption on nonporous or macroporous solids. They show an initial sharp rise as a monolayer forms, followed by a smoother increase corresponding to multilayer adsorption. The "knee" marks the point of monolayer completion. These isotherms are common in materials with extensive external surface area and are used to determine specific surface area via BET analysis. They are important for characterising materials used in catalysis or bulk adsorption processes.

Type III Isotherm

Type III isotherms occur when adsorbate–adsorbent interactions are weak. No clear monolayer is formed; instead, molecules cluster at favourable sites, leading to a concave isotherm that does not approach saturation even at high pressures. This behaviour is typical of nonporous or macroporous solids with low surface energy and is indicative of adsorption dominated by weak van der Waals forces. This type provides insight into materials with limited adsorption affinity, such as poorly activated or hydrophobic surfaces.

Type IV Isotherm

Type IV isotherms are characteristic of mesoporous materials, such as silica gels, mesoporous molecular sieves, and oxide catalysts. Adsorption initially proceeds via monolayer and multilayer formation, followed by capillary condensation in the mesopores, which causes a sharp rise in uptake at intermediate pressures.

- *Type IV(a)*: Displays hysteresis due to capillary condensation in mesopores larger than ~4 nm (for N_2 at 77 K). The hysteresis loop is sensitive to pore shape and connectivity.
- *Type IV(b)*: Exhibits reversible behaviour in narrower mesopores or cylindrical/conical pores closed at one end, where capillary condensation is less pronounced.

Type IV isotherms are essential for identifying mesopore size distributions and are widely used in characterising adsorbents for catalysis, pollutant removal, and water adsorption.

Type V Isotherm

Type V isotherms resemble Type III at low pressures due to weak adsorbent–adsorbate interactions but show a stronger uptake at higher pressures due to cooperative interactions or pore filling. This behaviour is often observed in water adsorption on hydrophobic materials with micropores or mesopores. The shape of the isotherm provides insights into hydrophobicity, pore accessibility, and clustering behaviour in water vapour adsorption applications.

Type VI Isotherm

Type VI isotherms exhibit a stepwise pattern indicative of layer-by-layer adsorption on uniform, nonporous surfaces. Each step corresponds to the completion of an adsorbed layer, with sharp transitions occurring at discrete pressure intervals. This behaviour is observed for rare gas adsorption (e.g. argon, krypton) on graphitised carbon at cryogenic temperatures. These isotherms reveal surface uniformity and well-defined adsorption sites, making them valuable for studying precision adsorbents in surface science and sensor design.

The IUPAC classification of adsorption isotherms serves as a foundational tool for analysing adsorption mechanisms and deducing structural and surface properties of materials. By recognising the isotherm type, researchers can infer porosity, surface energy, and interaction strength—guiding the optimisation of adsorbents for applications in gas storage, separation, catalysis, and environmental remediation.

3.5.2. Adsorption Hysteresis

Adsorption hysteresis refers to the phenomenon where the adsorption and desorption branches of an isotherm do not coincide, forming a reproducible loop. This behaviour is most commonly observed in the multilayer range of physisorption isotherms and is closely linked to capillary condensation within mesoporous and microporous materials. The shape, size, and characteristics of hysteresis loops depend on the geometry of the pores, network effects, and the mechanisms underlying adsorption and desorption. These loops serve as crucial indicators of material properties, aiding in the classification and characterization of adsorbents. The various types of hysteresis loops are depicted in Figure 33. [281]

Hysteresis loops primarily arise due to delayed condensation and metastable states within adsorbed layers. For open-ended pores, such as cylindrical ones, condensation is delayed because the adsorbed multilayer does not immediately achieve thermodynamic equilibrium during the adsorption process. On the other hand, the desorption branch corresponds to a liquid-vapor transition that tends to be in equilibrium. This discrepancy creates the characteristic hysteresis loop.

In complex pore structures, hysteresis can also be influenced by network effects and pore-blocking mechanisms. For instance, in ink-bottle-shaped pores, wide cavities connected to the external surface via narrow necks can trap liquid condensate during desorption. The cavities remain filled until the narrow necks are emptied at lower vapor pressures, a phenomenon known as pore blocking. Such effects depend on the neck size and its distribution, offering detailed insights into the pore structure. However, if the neck diameter is below a critical size (e.g., 5–6 nm for nitrogen at 77 K), cavitation—the spontaneous formation and growth of gas bubbles in the metastable liquid—becomes the dominant desorption mechanism. Unlike pore-blocking-controlled evaporation, cavitation does not provide quantitative information about neck size distributions.

The IUPAC classification of hysteresis loops, refined to reflect recent research, categorizes them into six main types (H1–H5). Each type is associated with particular pore structures and adsorption mechanisms. These categories, depicted in Figure 33, are summarized below:

- **Type H1**: Characterized by steep and narrow loops, Type H1 is typically observed in materials with uniform mesopores. Examples include templated silicas (e.g., MCM-41, SBA-15), ordered mesoporous carbons, and controlled pore glasses. The minimal network effects and delayed condensation contribute to the distinct loop shape, which can also occur in ink-bottle pores where the neck size distribution matches the cavity size distribution. [281]
- **Type H2**: Found in materials with complex pore networks, where pore-blocking and percolation effects dominate.
    - **H2(a)**: Exhibits steep desorption branches caused by narrow pore necks or cavitation. This behaviour is seen in silica gels and certain mesoporous silicas (e.g., SBA-16).

- **H2(b)**: Associated with a broader neck size distribution, this subtype is observed in mesocellular silica foams and some hydrothermally treated mesoporous materials.

- **Type H3**: The adsorption branch of H3 loops resembles a Type II isotherm, while the desorption branch terminates abruptly, often at cavitation-induced pressures. These loops are associated with aggregates of plate-like particles and materials containing macropores not fully filled with condensate.
- **Type H4**: A combination of Types I and II, H4 loops show significant low-pressure uptake due to micropore filling. These loops are typically found in materials like zeolites, mesoporous carbons, and aggregated crystals with a mix of micro- and mesopores.
- **Type H5**: Rare and distinctive, H5 loops are linked to materials with open and partially blocked mesopores, such as plugged hexagonal silicas. These loops provide insights into irregular pore structures.

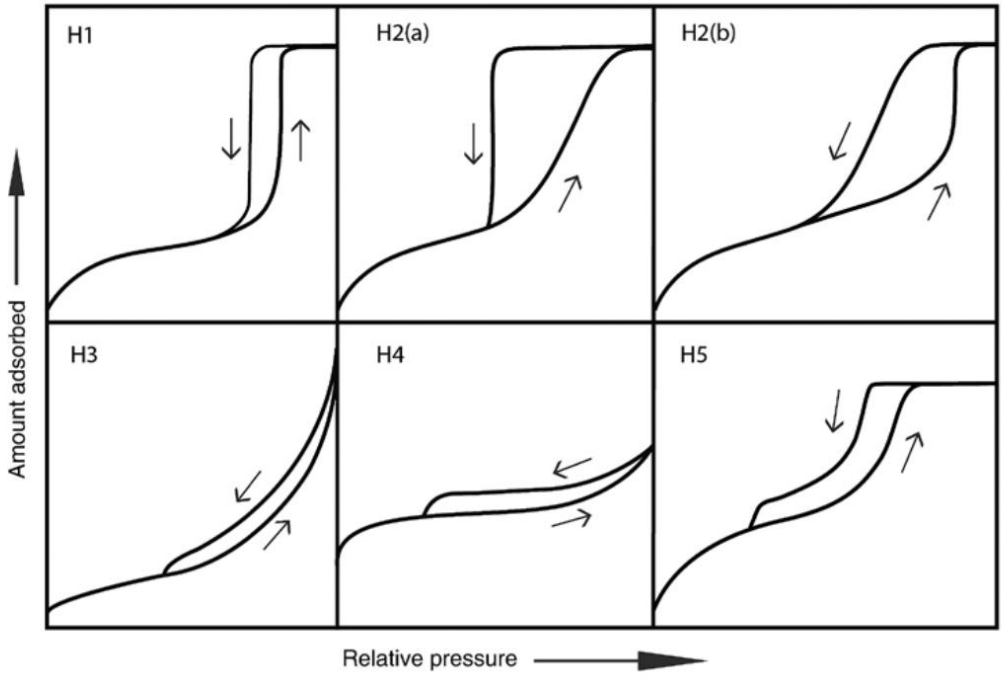

Figure 33 - IUPAC classification of hysteresis loop types (H1–H5), reflecting pore structure, connectivity, and desorption mechanisms in mesoporous materials.[282]

Understanding adsorption hysteresis is essential for accurately characterizing porous materials, particularly mesoporous and microporous adsorbents. The analysis of hysteresis loops provides several practical insights:

- **Pore Size and Geometry**: The type and shape of the loop reveal information about the pore geometry, such as whether the pores are cylindrical, slit-shaped, or ink-bottle-like.
- **Network Effects**: Hysteresis analysis can identify the connectivity and accessibility of pores, which are critical for understanding material performance.
- **Cavitation and Pore Blocking**: Identifying these effects helps determine whether quantitative information about pore neck size and distribution can be reliably extracted.

By linking hysteresis loops to structural properties, researchers can fine-tune adsorbents for a wide range of applications, including catalysis, gas separation, and energy storage. The refined IUPAC classification of hysteresis types, as illustrated in Figure 33, remains a cornerstone in the field of adsorption science. It provides a robust framework for analysing and optimizing materials for diverse industrial and environmental uses. [281]

3.6. Gas-Solid Adsorption Models

A variety of surface features of solid materials can be determined by observing adsorption processes, as uptake depends on variables such as surface energy distribution, surface area, porosity, adsorptive properties, temperature, and pressure.

Gas-solid adsorption models provide methods to explain and obtain information on adsorbent-adsorptive interactions. These models rely on specific assumptions and are classified into monolayer and multilayer systems.

This section will first discuss monolayer adsorption models, including the Langmuir, Freundlich, Tóth, and Sips isotherms, followed by multilayer models such as the BET model. These models will be evaluated based on their underlying assumptions, mathematical formulations, applicability to real-world adsorption systems, and their respective limitations.[283]

3.6.1. Monolayer Models

Gas-solid adsorption can be thermodynamically described under conditions of constant temperature and pressure. In such a system, gas-phase species near a solid surface act as

adsorptives, forming a thin layer of adsorbed molecules on the surface of the adsorbent. The density of the adsorbed gas varies as a function of distance from the surface, and at equilibrium, the pressure of the adsorbed gas is assumed to be in equilibrium with the partial pressure of the gas phase.

A monolayer refers to a single, uniform layer of adsorbed molecules covering the surface of the adsorbent. In this state, each adsorption site on the surface is occupied by only one molecule, with no stacking of additional layers. Monolayer adsorption is fundamental to many theoretical adsorption models and is particularly relevant in describing gas-solid interactions at low to moderate pressures.

At low relative pressures, adsorption behaviour can often be described by Henry's Law, which states that the concentration of the adsorbed phase is directly proportional to the pressure of the system:

$$C_A = K_H P \qquad \textit{Equation 18}$$

where:

- C_A is the concentration of the adsorbed species on the surface,
- K_H is Henry's constant,
- P is the pressure of the system.

However, at higher pressures, adsorption deviates from Henry's Law, necessitating more sophisticated models.

Langmuir Adsorption Isotherm Model

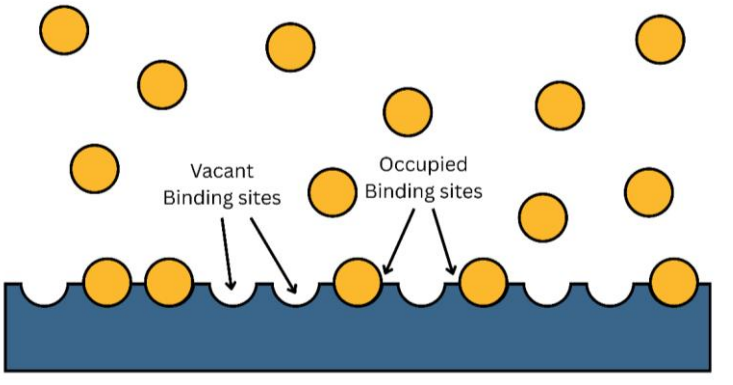

Figure 34 - Schematic of the Langmuir adsorption model, showing monolayer adsorption on discrete binding sites with vacant and occupied surface positions. [284]

The Langmuir adsorption isotherm model, proposed by Irving Langmuir in 1916, describes the adsorption of gases on solid surfaces under the assumption of monolayer adsorption (see Figure 34). Langmuir's contributions to surface chemistry, including his studies on oil films and adsorption, led to his Nobel Prize in Chemistry in 1932 [262–264].

The Langmuir model is based on several key assumptions that define its applicability:

1. **Homogeneous Surface**: The adsorbent surface consists of energetically equivalent sites, implying that all adsorption sites are identical in size, shape, and energy.
2. **Finite Number of Sites**: There is a fixed number of adsorption sites available on the surface, meaning that adsorption is limited to monolayer coverage.
3. **Dynamic Equilibrium**: The system maintains a balance between adsorption and desorption of gas molecules, following the reaction:

$$A + B \rightleftharpoons AB \qquad \textit{Equation 19}$$

where A represents a gas molecule, B is an available adsorption site, and AB denotes the adsorbed gas on the solid surface [264].

4. **Monolayer Adsorption**: Adsorption is restricted to a single molecular layer, with no further adsorption occurring beyond the monolayer.
5. **No Lateral Interactions**: Adsorbed molecules do not interact with each other, meaning that adsorption at one site does not influence neighbouring sites.

The Langmuir isotherm is derived from kinetic principles, where the rates of adsorption (r_{ads}) and desorption (r_{des}) are defined as:

$$r_{ads} = k_{ads} P_A [S_{active}] \qquad \textit{Equation 20}$$

$$r_{des} = k_{des} [S_{occup}] \qquad \textit{Equation 21}$$

where:

- k_{ads} and k_{des} are the adsorption and desorption rate constants,
- P_A is the partial pressure of gas A,
- $[S_{active}]$ is the number of available adsorption sites,
- $[S_{occup}]$ is the concentration of adsorbed molecules per unit area.

At equilibrium, $r_{ads} = r_{des}$, leading to the expression for the equilibrium constant K_{eq}:

$$\mathrm{Keq} = \frac{k_{ads}}{k_{des}} = \frac{[S_{occup}]}{P_A[S_{active}]} \qquad \textit{Equation 22}$$

Defining the total number of adsorption sites $[S_{Total}]$ as:

$$[S_{Total}] = [S_{active}] + [S_{occup}] \qquad \textit{Equation 23}$$

and introducing the fractional surface coverage θ:

$$\theta = \frac{[S_{occup}]}{[S_{Total}]} \qquad \textit{Equation 24}$$

we obtain the Langmuir adsorption isotherm equation:

$$\theta = \frac{K_L P_A}{1 + K_L P_A} \qquad \textit{Equation 25}$$

where K_L is the Langmuir constant, related to adsorption energy [264].

Expressing the equation in terms of gas concentration (C), using the ideal gas law $\mathrm{C} = \mathrm{P}/\mathrm{RT}$, and incorporating $K_L = K_{eq}RT$, we get:

$$\theta = \frac{bC}{1 + bC} \qquad \textit{Equation 26}$$

where $b = K_L$ is related to the adsorption affinity [263].

Despite its usefulness, the Langmuir model has several limitations:

1. **Valid Only for Monolayer Adsorption**: It does not account for multilayer adsorption, making it unsuitable for high-pressure conditions.
2. **Assumes Homogeneous Surfaces**: In reality, most adsorbents have heterogeneous surfaces, making models like Freundlich or Sips more appropriate in such cases.
3. **No Lateral Interactions**: The assumption that adsorbed molecules do not interact is unrealistic, especially at high coverages where intermolecular forces become significant.
4. **Ideal Gas Assumption**: The model assumes ideal gas behaviour, which may not hold at high pressures where deviations occur [285]

To address these limitations, extensions such as the BET model (for multilayer adsorption) and Sips model (for heterogeneous adsorption) have been developed. [285]

Freundlich Adsorption Isotherm Model

The Freundlich adsorption isotherm model, proposed by Herbert Freundlich in 1909, is an empirical equation describing the adsorption of gases onto solid surfaces. Unlike the Langmuir model, which assumes a homogeneous surface with fixed adsorption sites, the Freundlich model accounts for surface heterogeneity and variable adsorption energies [265,286].

The Freundlich isotherm is expressed as:

$$\frac{x}{m} = K_F P^{1/n} \qquad \textit{Equation 27}$$

where:

- $\frac{x}{m}$ is the amount of adsorbate per unit mass of adsorbent,
- *P* is the equilibrium pressure of the adsorbate,
- K_F is the Freundlich adsorption capacity constant,
- *n* is an empirical parameter indicating adsorption intensity [286].

For low-pressure conditions, adsorption increases linearly with pressure when $1/n \approx 1$. At higher pressures, the adsorption process slows down, but unlike the Langmuir model, it does not reach a saturation point.

A log-log plot of the Freundlich equation:

$$\log\left(\frac{x}{m}\right) = \log K_F + \frac{1}{n}\log P \qquad \textit{Equation 28}$$

yields a straight line, making it useful for experimental data fitting.

While both Langmuir and Freundlich models describe adsorption behaviour, they differ fundamentally in their assumptions:

- **Langmuir Model**: Assumes a homogeneous surface with a finite number of adsorption sites and monolayer coverage.
- **Freundlich Model**: Assumes a heterogeneous surface where adsorption sites have varying affinities, and multilayer adsorption is possible.

At low pressures, both models exhibit a nearly linear relationship with pressure:

$$x/m \propto P$$ *Equation 29*

However, at high pressures, the Langmuir model predicts saturation, whereas the Freundlich model continues increasing without an upper limit, following a logarithmic trend.

Despite its empirical usefulness, the Freundlich isotherm has some limitations:

1. **Fails at High Pressures**: The model does not predict saturation, leading to deviations from experimental data when monolayer adsorption dominates.
2. **Lack of Theoretical Basis**: Unlike Langmuir, which is derived from kinetic principles, Freundlich's equation is purely empirical.
3. **No Defined Monolayer Capacity**: The model does not distinguish between monolayer and multilayer adsorption, making it unsuitable for monolayer-dominated adsorption systems.

The Freundlich model remains widely used in adsorption studies, especially for describing heterogeneous surface interactions, but alternative models such as the Langmuir-Freundlich hybrid or BET isotherm are preferred when higher accuracy is required. [265]

Temkin Adsorption Isotherm Model

The Temkin adsorption isotherm model, developed by M.I. Temkin and V. Pyzhev, is an empirical adsorption model that describes adsorption on heterogeneous surfaces while considering the influence of adsorbate-adsorbate interactions. Unlike the Langmuir and Freundlich models, the Temkin model assumes that adsorption energy is distributed uniformly across adsorption sites rather than being constant or varying arbitrarily. [283,287]

The Temkin isotherm equation in its non-linearized form is given as:

$$q_e = \frac{RT}{b}\ln(K_T P_e)$$ *Equation 30*

where:

- q_e is the amount of adsorbate per unit mass of adsorbent,
- R is the universal gas constant (8.314 J/mol·K),
- T is the absolute temperature (K),
- b is a parameter related to adsorption energy (J/mol),

- K_T is the Temkin adsorption equilibrium constant (1/Pa),
- P_e is the equilibrium partial pressure of the adsorbate [288].

The parameter b in the model represents the change in adsorption energy, which can be expressed as:

$$b = \frac{\Delta E}{\Delta H} \qquad \textit{Equation 31}$$

where:

- *ΔE* is the change in adsorption energy (J/mol),
- *ΔH* is the change in heat of adsorption (J/mol).

A positive value of *b* indicates an exothermic adsorption process, while a negative value of *b* suggests an endothermic process.

There are three key assumptions of the Temkin model:

1. **Uniform Energy Distribution**: Unlike Langmuir, which assumes fixed adsorption energy, Temkin considers a continuous energy distribution of adsorption sites.
2. **Adsorption Energy Decreases Linearly**: The heat of adsorption decreases linearly with increasing surface coverage, rather than logarithmically as in the Freundlich model.
3. **Excludes Extremely High or Low Concentrations**: The model disregards adsorption behaviour at very high or very low adsorbate concentrations.

And the advantages of using the Temkin model include the fact that, unlike Langmuir, the model accounts for indirect interactions affecting adsorption energy, there is more Realistic modelling of Certain Heterogeneous Surfaces, which provides a better description of adsorption when energy distribution is uniform, and the model performs well when adsorption energy varies slightly across sites in medium pressure ranges. However, there are limitations of the Temkin model, such as the model assumes a strictly linear decrease in adsorption energy, which may not always be accurate, it does not account for extreme variations in adsorption site energy for highly heterogeneous surfaces, and it is limited to moderate coverage, working best for intermediate adsorption and is less accurate at very low or very high pressures. Due to its unique energy distribution profile, the Temkin model

is widely applied in gas-solid adsorption studies, particularly in catalysis and surface chemistry, where adsorbate-adsorbate interactions influence adsorption behaviour.

Tóth Adsorption Isotherm Model

The Tóth adsorption isotherm model, proposed by J. Tóth in 1971, is an empirical equation that enhances the Langmuir model by improving accuracy in predicting experimental adsorption values. It is particularly useful for describing adsorption on heterogeneous surfaces across a broad range of adsorbate concentrations.[283,289–291]

The Tóth model accounts for sub-monolayer coverage and assumes an asymmetrical quasi-Gaussian energy distribution, which extends towards lower adsorption energies. This makes it more applicable to systems where adsorption sites have varying affinities [289].

The Tóth isotherm equation is given as:

$$q_e = \frac{q_m K_T P_e}{(1 + (K_T P_e)^{n_T})^{1/n_T}} \qquad \textit{Equation 32}$$

where:

- q_e is the amount of adsorbate per unit mass of adsorbent,
- q_m is the maximum adsorption capacity,
- K_T is the Tóth isotherm constant,
- P_e is the equilibrium partial pressure of the adsorbate,
- n_T is the heterogeneity parameter. [289]

The heterogeneity parameter n_T influences the adsorption behaviour:

- When $n_T = 1$, the Tóth equation reduces to the Langmuir isotherm, indicating a homogeneous surface.
- When $n_T < 1$, the system exhibits high surface heterogeneity, meaning adsorption sites have a broad range of energies.
- When $n_T > 1$, the system behaves similarly to Langmuir but retains some degree of heterogeneity.

This flexibility makes the Tóth model a bridge between Langmuir and Freundlich, combining their strengths while avoiding their limitations.

The Tóth model offers several advantages over traditional isotherm models. It improves the accuracy of experimental data fitting by addressing deviations observed in both the Langmuir and Freundlich models. This is particularly beneficial for systems with heterogeneous surfaces, where adsorption site energies are not uniform. By incorporating an asymmetrical energy distribution, the model captures a broader range of adsorption behaviours. Additionally, unlike the Freundlich model, which does not predict saturation, the Tóth model approaches a monolayer capacity at high pressures, making it more realistic for many practical applications.

However, the Tóth model also presents some limitations. As an empirical model, it lacks a rigorous theoretical foundation, which may restrict its interpretative value in mechanistic studies. The heterogeneity parameter n_T, though critical to the model's performance, is often challenging to determine accurately through experimental methods. Furthermore, the model does not fully account for pore-filling mechanisms, limiting its suitability for materials with significant microporosity, where adsorption occurs through volume-filling rather than surface-layer formation. [283]

Sips Adsorption Isotherm Model

The Sips adsorption isotherm model, also known as the Langmuir-Freundlich isotherm, is a hybrid model that combines the characteristics of both Langmuir and Freundlich isotherms. It was developed to describe adsorption on heterogeneous surfaces while addressing the limitations of the Freundlich model at high adsorbate concentrations. [283,292]

At low concentrations, the Sips model behaves like the Freundlich isotherm, capturing surface heterogeneity. At high concentrations, it predicts monolayer adsorption, similar to the Langmuir isotherm, ensuring that adsorption capacity is limited and does not increase indefinitely. [292]

The Sips isotherm equation is expressed as:

$$q_e = \frac{q_m (K_S P_e)^{n_s}}{1 + (K_S P_e)^{n_s}} \qquad \textit{Equation 33}$$

where:

- q_e is the amount of adsorbate per unit mass of adsorbent,
- q_m is the maximum adsorption capacity,
- K_S is the Sips isotherm constant,

- P_e is the equilibrium partial pressure of the adsorbate,
- n_s is the Sips isotherm exponent, indicating surface heterogeneity.[292]

The Sips model offers several advantages by integrating features of both the Langmuir and Freundlich isotherms. It corrects the unbounded increase in adsorption predicted by the Freundlich model at high pressures, thus ensuring more realistic behaviour under saturation conditions. At low concentrations, the model retains Freundlich-like characteristics, effectively accounting for surface heterogeneity. This dual capability allows the Sips model to accurately describe adsorption systems across a broad pressure range and provides improved data fitting in practical applications where both heterogeneous surfaces and finite adsorption capacities are present.

Nonetheless, the Sips model has inherent limitations. As an empirical construct, it lacks a theoretical foundation rooted in thermodynamics, which may limit its explanatory power in mechanistic adsorption studies. Estimating model parameters—particularly the heterogeneity exponent n_s and the equilibrium constant K_S—can be experimentally challenging and may introduce uncertainty in data interpretation. Additionally, the model may not reliably capture adsorption behaviour under extreme pressure conditions, either very low or very high, where deviations from idealised assumptions become significant. Despite these constraints, the Sips model remains widely applied in systems requiring an accurate description of adsorption over variable surface energies and concentration regimes.[283]

3.6.2. Multilayer Adsorption

Multilayer adsorption occurs when adsorbate molecules continue to accumulate beyond the first monolayer, forming successive layers on the surface of the adsorbent. This phenomenon becomes significant at higher partial pressures, where deviations from monolayer adsorption models, such as the Langmuir isotherm, are observed. These deviations arise because monolayer models assume a fixed number of adsorption sites, whereas multilayer adsorption allows for the formation of additional layers as adsorption sites become occupied.

At low pressures, adsorption primarily occurs on the homogeneous surface sites of the adsorbent, as described by monolayer models. However, as pressure increases, the thermal energy of gas molecules decreases, leading to enhanced interactions between the adsorbate molecules and the surface. As a result, additional molecules adsorb onto the

previously adsorbed layer rather than directly onto the solid surface, forming a multilayer structure. This process is characteristic of Type II and Type IV isotherms, which indicate distinct stages of adsorption behaviour.

One key feature of multilayer adsorption is the variation in adsorption energy across different layers. The first layer interacts directly with the adsorbent surface and typically exhibits the highest adsorption energy. However, in subsequent layers, the adsorption energy approaches that of bulk condensation, meaning the heat of adsorption in these layers is comparable to the heat of liquefaction.

Multilayer adsorption can occur on various adsorbents under appropriate temperature and pressure conditions, making it essential for accurately describing adsorption in systems where high-pressure adsorption dominates. Models that account for multilayer adsorption, such as the BET (Brunauer-Emmett-Teller) isotherm, extend beyond monolayer assumptions to provide a more comprehensive representation of adsorption behaviour in such cases.

BET Adsorption Isotherm Model

The Brunauer-Emmett-Teller (BET) adsorption isotherm model, developed by Brunauer, Emmett, and Teller in 1938, extends Langmuir theory to describe multilayer adsorption. Unlike the Langmuir model, which assumes monolayer adsorption, the BET model accounts for the formation of multiple adsorbed layers at higher pressures, making it fundamental for understanding gas adsorption on solid surfaces and surface area determination. [270,283,285]

Key Assumptions of the BET Model

The BET model is based on the following assumptions:

1. **Multilayer Formation**: Adsorption occurs in multiple layers, allowing an infinite number of layers to form at saturation pressure, similar to condensation.
2. **Adsorption Site Availability**: Each adsorbed molecule serves as a new adsorption site for subsequent layers.
3. **Dynamic Equilibrium**: Molecules in the upper layers are in equilibrium with the gas phase, meaning the rates of adsorption and desorption are equal.
4. **No Lateral Interactions**: Adsorbed molecules do not interact with each other within the same layer.

5. **Layer-Dependent Heat of Adsorption**:
    - The first layer has a distinct adsorption energy (gas-solid interaction).
    - Subsequent layers experience adsorption energy equal to the heat of liquefaction [285].

The BET equation is given as:

$$\theta = \frac{V}{V_m} = \frac{C\frac{P}{P_0}}{\left(1-\frac{P}{P_0}\right)\left(1+(C-1)\frac{P}{P_0}\right)} \qquad \textit{Equation 34}$$

where:

- θ is fractional surface coverage (number of adsorbed layers)
- *V* is the volume of adsorbed gas at pressure P
- V_m is the monolayer adsorption volume,
- *P* is the equilibrium pressure,
- P_0 is the saturation pressure,
- *C* is the BET constant, related to the heat of adsorption. [285]

The BET model is widely used to determine specific surface area by constructing a BET plot, from which monolayer capacity (V_m) can be obtained. The total surface area *S* is then calculated using:

$$S = \frac{V_m N_A A_m}{M} \qquad \textit{Equation 35}$$

where:

- A_m is the cross-sectional area of the adsorbed molecule (e.g., 16.2 Å² for nitrogen),
- N_A is Avogadro's number,
- *M* is the mass of the adsorbent.

The BET constant *C* is linked to the heat of adsorption (H_{Ads}) and heat of liquefaction (H_{Liq}):

$$C = e^{\frac{H_{Ads} - H_{Liq}}{RT}}$$ *Equation 36*

A higher *C* value indicates stronger adsorbate-adsorbent interactions, whereas lower values suggest weaker binding. The BET constant also influences the shape of the isotherm:

- If C is high (~80 or more), a sharp knee appears in the isotherm, indicating clear monolayer formation.
- If C is low (<50), monolayer and multilayer adsorption overlap, making monolayer capacity less distinct.
- If C is very low (<2), the BET method is generally not applicable.

The choice of adsorptive gas significantly affects BET surface area determination. The most commonly used adsorptive is nitrogen (N_2) at 77 K, due to its availability, well-characterized properties, and widespread acceptance. However, alternative gases such as argon (Ar) at 87 K) and krypton (Kr) at 77 K are also used under specific conditions.

- Nitrogen (N_2) at 77 K: The standard adsorptive for BET analysis. However, its quadrupole moment leads to specific interactions with certain surfaces, potentially affecting accuracy.
- Argon (Ar) at 87 K: A preferred alternative for microporous materials, as it lacks a quadrupole moment, reducing interaction effects. It also provides higher resolution adsorption isotherms in microporous materials.
- Krypton (Kr) at 77 K: Used for very low surface area materials, as it has a significantly lower saturation pressure, leading to improved sensitivity in detecting small surface areas.
- Carbon Dioxide (CO_2) at 273 K: Utilized for micropore analysis since it can access pores as small as 0.4 nm, which nitrogen and argon cannot effectively probe at cryogenic temperatures. [281]

The BET model offers several notable advantages, particularly in extending the Langmuir theory to account for multilayer adsorption. This makes it especially useful at higher relative pressures, where monolayer assumptions no longer apply. It remains the standard method for calculating the specific surface area of porous materials and is widely adopted in both academic and industrial research. Moreover, the flexibility of the BET model allows

for the use of various adsorptive gases depending on the material system, enhancing its applicability across different types of porous solids.

However, the BET model also presents important limitations. It is generally unsuitable for microporous materials, where adsorption occurs via pore-filling mechanisms rather than surface-layer formation, leading to inaccuracies in surface area estimation. [293] Additionally, the model assumes non-interacting adsorbed molecules, an approximation that breaks down at very high pressures where capillary condensation or lateral interactions can occur. Furthermore, when nitrogen is used as the adsorptive gas, its quadrupole moment can influence adsorption behaviour on certain surfaces, potentially distorting the interpretation of results. [281] Despite these limitations, the BET model remains foundational in adsorption science, especially for the characterisation of mesoporous materials and determination of surface area.

Application of the BET Model to Microporous Materials

Microporous materials often present unique challenges when applying classical adsorption models such as the BET theory. According to IUPAC classifications, microporous adsorbents generally display Type I isotherms. However, in many real-world cases, these materials exhibit a mix of characteristics—sometimes blending features of Type I with those of Type II (or even Type IV if mesoporosity is present). This hybrid behaviour is significant because it implies that adsorption in micropores is not limited solely to discrete sites as assumed in the Langmuir model; instead, pore filling is a dominant process. Unlike conventional adsorption on nonporous or mesoporous surfaces, molecules may accumulate within the micropores in a continuous fashion, and the adsorbate may not remain in constant equilibrium with the gas phase.

Despite these complexities, the BET model is frequently used to estimate surface areas through determination of the “monolayer capacity.” In microporous systems, however, this estimation must be interpreted with caution. The traditional notion of a well-defined monolayer becomes ambiguous since the adsorbed phase might include both a true monolayer over non-microporous areas and additional uptake due to micropore filling. For this reason, some researchers refer to the measured capacity as the “BET strong retention capacity,” which encompasses both the monolayer coverage of accessible external surfaces and the contribution from micropores. [281,293]

A critical aspect of applying the BET analysis to microporous materials is the objective selection of the relative pressure range used to fit the BET equation. Typically, for many materials, a relative pressure (P/P_o) window of about 0.05 to 0.3 is chosen because, in these regions, the BET plot is expected to be linear. However, in microporous materials, the isotherm may show several distinct linear segments within this range due to the heterogeneous nature of the pore structure. This variability can lead to subjective decisions if one relies solely on visual inspection. [293]

To address this, Rouquerol and colleagues proposed a more systematic method to determine the correct pressure interval. The method involves two key criteria:

1. **Positive Intercept Criterion:** When fitting the BET plot, the intercept obtained must be positive. A negative intercept would imply an unphysical negative value for the constant C (related to adsorption energy), thereby invalidating the fit.
2. **Continuous Increase in the Adjusted Term:** One should plot the term $v(P_0 - P)$ as a function of the relative pressure P/P_0. The selected pressure interval should extend only up to the last point where this term exhibits a continuous, positive increase. This approach helps avoid including data points where the assumptions of the BET model break down.

Once a range is selected based on these criteria, two consistency checks should be performed to validate the analysis:

- The partial pressure corresponding to the calculated monolayer capacity must lie within the selected range.
- An independent estimation of the relative pressure can be obtained from the BET constant C, and this value should agree (within about 10%) with the experimentally determined partial pressure at which the monolayer capacity is observed.

Due to the complexities mentioned above, the “BET monolayer capacity” derived from microporous materials does not represent a pure monolayer coverage in the classical sense. Rather, it reflects a combination of the adsorption on non-microporous surfaces and the additional uptake within the micropores. In practice, researchers often use complementary techniques such as the αs-method or t-plot analysis to separate these contributions. By first determining the non-microporous surface area and then subtracting

this from the overall BET-derived capacity, one can estimate the micropore volume more accurately. [293]

3.6.3. Micropore Filling Models

Micropore filling models describe adsorption in materials with narrow micropores rather than assuming a monolayer or multilayer adsorption mechanism. Unlike the Langmuir or BET models, which focus on surface coverage, micropore filling models account for adsorption as a volume-filling process governed by the adsorption potential field rather than site-specific interactions. These models are particularly applicable to activated carbons, zeolites, and metal-organic frameworks (MOFs), where micropores provide significant adsorption capacity.

The fundamental distinction between micropore filling models and conventional adsorption models is that adsorption in microporous materials does not occur through discrete molecular layers but instead results from strong potential energy gradients within confined pore spaces. This leads to an adsorption process that depends on the adsorption potential rather than direct molecule-surface interactions.

Dubinin-Radushkevich (DR) Adsorption Isotherm Model

The Dubinin-Radushkevich (DR) adsorption isotherm model is derived from Polanyi's potential theory of adsorption and is widely used to describe the adsorption of vapours on microporous adsorbents over a broad range of pressures up to saturation [294]. This model is particularly relevant for microporous materials, where adsorption occurs via pore filling rather than layer-by-layer adsorption. The DR equation provides a quantitative framework for understanding how enhanced dispersion forces, due to the close proximity of micropore walls, influence adsorption at low relative pressures. [295]

Polanyi's adsorption model explains gas-solid adsorption based on an adsorption potential field rather than direct surface interactions. The model assumes that gas molecules near an adsorbent surface experience a spatially dependent potential field, independent of molecular interactions, leading to adsorption as a function of potential energy rather than pressure. [296]

The adsorption process is governed by changes in chemical potential, given by:

$$d\mu = -S_m dT + V_m dP + dU_m \qquad \textit{Equation 37}$$

where:

- μ is the chemical potential,
- S_m is the molar entropy,
- V_m is the molar volume,
- U_m is the molar internal energy.

At equilibrium, the chemical potential of a molecule at a distance xx from the surface equals that at an infinite distance. By integrating this relationship under constant temperature conditions, the adsorption potential is expressed as:

$$A = RT \ln\left(\frac{P_0}{P}\right) \qquad \textit{Equation 38}$$

where:

- A is the adsorption potential,
- P_0 is the saturation pressure of the adsorbate,
- P is the equilibrium pressure,
- R is the universal gas constant,
- T is the absolute temperature.

This equation indicates that adsorption is influenced by relative pressure rather than absolute pressure, making it particularly relevant for microporous materials, where adsorption occurs via pore filling rather than surface coverage.

Polanyi's potential theory forms the basis for adsorption models that describe micropore filling rather than monolayer adsorption. It provides a framework for understanding adsorption energy distributions in porous materials and is the foundation for the Dubinin-Radushkevich (D-R) equation, which quantifies microporous adsorption.

The theory of volume filling of micropores is based on two key assumptions:

1. **Affinity Coefficient and Characteristic Curves:** The adsorption energy of different adsorbates can be related using an affinity coefficient β, which allows adsorption data for different gases on the same adsorbent to be superimposed. This relationship is given by: [294,295,297]

$$E = \beta E_{\text{ref}} \qquad \textit{Equation 39}$$

where:

- E is the free energy of adsorption,
- E_{ref} is the adsorption energy of a reference adsorbate (commonly benzene or nitrogen).

This assumption enables the comparison of adsorption behaviour across different adsorbate-adsorbent systems by normalizing adsorption energy values.

2. **DR Characteristic Equation:** The volume of adsorbate adsorbed at a given pressure follows:

$$V = V_0 \exp\left(-K\left(\frac{A}{E}\right)^2\right) \qquad \textit{Equation 40}$$

where:

- V_0 is the total available micropore volume,
- K is a structural constant,
- A is the adsorption potential.

This equation describes how micropore volume fills as a function of adsorption potential, emphasizing that microporous adsorption does not follow a traditional monolayer or multilayer model but is instead governed by energy gradients within the pore network.

DR Equation for Microporous Adsorption

Combining the previous relationships, the DR equation is obtained as:

$$V = V_0 \exp\left(-K\left(\frac{RT\ln(P_0/P)}{E}\right)^2\right) \qquad \textit{Equation 41}$$

where:

- P_0 is the saturation pressure,
- P is the equilibrium pressure,
- R is the universal gas constant,
- T is the absolute temperature.

This equation shows that adsorption is fundamentally controlled by temperature and the ratio of equilibrium pressure to saturation pressure, rather than absolute pressure alone.
294,295

Although the DR equation effectively describes micropore filling, it exhibits deviations from experimental data under certain conditions. Specifically, it does not accurately capture Henry's Law behaviour at low P/P_0 values, where deviations from linearity occur due to:

- Capillary condensation effects in transitional pores,
- Multilayer formation on macropore walls,
- Variations in adsorbate-adsorbent interactions not accounted for in the DR model.

Another limitation of the DR equation is its reliance on a single characteristic energy for adsorption, which assumes a uniform adsorption potential within micropores. In reality, many microporous materials exhibit a distribution of adsorption sites with different energetic characteristics, leading to discrepancies between predicted and experimental adsorption behaviour. [295,298,299]

Despite these limitations, the DR equation remains widely used for characterizing microporous materials and predicting adsorption capacity.

3.6.4. Comparative Analysis of Adsorption Models

Adsorption models serve as essential tools for understanding gas-solid interactions, surface properties, and adsorption mechanisms. Each model differs in its assumptions, complexity, and applicability to specific adsorption systems. This section compares the monolayer, multilayer, and micropore filling models discussed earlier, emphasizing their theoretical foundations, key assumptions, number of parameters, and practical applications.

Table 3 - Comparison of Model Assumptions

Model	Surface Homogeneity	Monolayer or Multilayer	Adsorbate-Adsorbate Interaction	Adsorption Energy Distribution
Langmuir	Homogeneous	Monolayer	No interaction	Constant adsorption energy
Freundlich	Heterogeneous	Monolayer (empirical)	Indirect interactions	Decreases logarithmically
Temkin	Heterogeneous	Monolayer	Indirect interactions	Decreases linearly
Tóth	Heterogeneous	Monolayer	No direct assumption	Varies across sites
Sips	Heterogeneous	Monolayer	No direct assumption	Combination of Langmuir & Freundlich
BET	Homogeneous	Multilayer	No interaction (within layer)	First layer distinct, subsequent layers

				equal to heat of liquefaction
DR	Heterogeneous	Micropore filling	No direct interaction	Defined by adsorption potential

The number of parameters in an adsorption model determines its flexibility and complexity. Models with fewer parameters offer simplicity and ease of use, whereas models with more parameters provide greater accuracy in fitting experimental data but require careful parameter estimation. [283]

Table 4 - Number of Parameters in Each Model

Model	**Number of Parameters**	**Key Parameters**
Langmuir	2	Adsorption constant (K), Monolayer capacity (qm)
Freundlich	2	Freundlich constant (KF), Exponent (n)
Temkin	2	Temkin constant (KT), Heat of adsorption parameter (b)
Tóth	3	Tóth constant (KT), Maximum capacity (qm), Heterogeneity parameter (nT)
Sips	3	Sips constant (KS), Maximum capacity (qm), Exponent (nS)
BET	2	BET constant (C), Monolayer capacity (qm)
DR	2	Structural constant (K), Characteristic energy (E)

Table 5 - Practical Applicability of Adsorption Models

Model	**Best for Low-Pressure Adsorption**	**Best for High-Pressure Adsorption**	**Suitable for Microporous Materials**	**Common Applications**
Langmuir	Yes	No	No	Catalysis, gas separation
Freundlich	Yes	Partially	No	Adsorption on heterogeneous surfaces
Temkin	Yes	No	No	Surface interactions in catalysis
Tóth	Yes	Yes	No	Gas adsorption in porous materials
Sips	Yes	Yes	No	Adsorption on heterogeneous surfaces
BET	No	Yes	Limited	Surface area analysis
DR	No	Yes	Yes	Microporous materials, gas storage

Summary of Model Selection

- For monolayer adsorption on homogeneous surfaces, the Langmuir model is appropriate due to its simplicity and theoretical foundation.
- For adsorption on heterogeneous surfaces, the Freundlich, Temkin, and Tóth models provide better fits, with Sips offering a hybrid approach.
- For multilayer adsorption, the BET model is widely used, particularly for surface area analysis.
- For microporous materials, the Dubinin-Radushkevich (DR) model effectively describes micropore filling.

Understanding the assumptions and limitations of these models is essential for selecting the most appropriate approach to describe adsorption behaviour. Depending on the system under study, the choice of model will influence data interpretation and experimental conclusions. A detailed description of the statistical error functions and model-fitting algorithms—crucial for robust parameter estimation and isotherm comparison—has been provided in Appendix C: Model Fitting Algorithms and Error Functions, ensuring the main body remains focused on the comparative analysis of the isotherm models while offering comprehensive methodological details for those interested.

Chapter 4. Adsorption Analysis & Characterisation

4.1. Nitrogen Adsorption/Desorption

The accurate measurement of adsorption isotherms is fundamental for characterizing porous materials, determining surface areas, and understanding adsorption mechanisms. Among the various gas adsorption techniques, nitrogen physisorption at cryogenic temperatures (77 K) is one of the most widely used methods for assessing the textural properties of adsorbents, including surface area, pore volume, and pore size distribution. This method is particularly relevant for studying mesoporous and microporous materials, where adsorption behaviour deviates from simple monolayer models.

Nitrogen adsorption and desorption measurements are based on monitoring the amount of gas adsorbed onto a solid surface at different equilibrium pressures. The resulting adsorption isotherm provides critical insights into the surface properties of the material, while the desorption branch reveals information about pore connectivity and hysteresis effects. This technique is essential for validating adsorption models and optimizing material design for applications such as gas storage, catalysis, and separation processes.

Nitrogen adsorption-desorption experiments typically involve exposing a solid sample to nitrogen gas under controlled temperature and pressure conditions. As the pressure increases, nitrogen molecules interact with the surface and internal structure of the adsorbent, gradually forming an adsorbed layer. The amount of nitrogen adsorbed is measured at various equilibrium pressures, generating an adsorption isotherm that characterizes the material's porosity and adsorption capacity.

The desorption process occurs by gradually reducing the pressure, allowing previously adsorbed nitrogen molecules to desorb from the surface. The difference between adsorption and desorption behaviour, known as hysteresis, provides valuable information about the material's pore structure, particularly in mesoporous materials where capillary condensation occurs.

The interpretation of nitrogen adsorption-desorption data relies on established isotherm models, such as the Brunauer-Emmett-Teller (BET) model for surface area determination and the Barrett-Joyner-Halenda (BJH) method for pore size distribution analysis. These techniques are widely used to classify materials according to their textural properties and

adsorption performance, supporting the development of advanced adsorbents for industrial applications.

While nitrogen physisorption is invaluable for understanding the physical characteristics of porous materials, its applicability is limited when describing adsorption in microporous systems where pore-filling rather than surface coverage dominates. To account for these effects, theories such as Polanyi's adsorption potential theory and the Dubinin-Radushkevich (D-R) equation provide a more suitable framework for describing adsorption in microporous materials. These advanced models extend beyond surface-based approaches by incorporating adsorption potential and energy distribution concepts, allowing for a more accurate description of gas-solid interactions in materials with fine pore structures. The following sections will explore these theoretical foundations and their relevance to adsorption modelling.

4.2. Surface Characterization Tools

The adsorption models discussed in the previous section are fundamental for obtaining equilibrium data that characterize solid sorbents. These models provide insight into key structural parameters such as pore size, pore volume, surface area, and microporosity for a given adsorbate. Understanding these properties is crucial for evaluating sorbent performance in various applications.

This section outlines the primary experimental techniques used to characterize porous materials, focusing on how adsorption models are applied to extract structural information. Methods such as the Brunauer-Emmett-Teller (BET) approach for surface area determination, the t-method for micropore analysis, and techniques for assessing pore volume and pore size distribution will be discussed. Additionally, the limitations and assumptions inherent in these techniques will be highlighted to ensure accurate interpretation of results.

4.2.1. Surface Area Analysis: The BET Method

Surface area analysis is a critical step in characterizing porous materials, as it provides insights into the available surface for adsorption, reaction sites, and overall material properties. The Brunauer-Emmett-Teller (BET) method is one of the most widely used techniques for this purpose, offering a means to quantify surface area based on gas adsorption isotherms. This approach extends the Langmuir model to multilayer adsorption and is particularly useful for mesoporous and macroporous materials. However, careful

consideration must be given to the selection of experimental parameters, including the appropriate pressure range and the influence of microporosity, to ensure accurate and meaningful results. The following section provides a step-by-step guide on how BET surface area is determined, along with considerations for microporous materials and the method's inherent limitations.[281,293,300]

Discussion on Limitations

- **Overestimation in Microporous Materials:** The BET model assumes that adsorption occurs in layers, which is not valid in highly microporous materials where adsorption occurs primarily through pore-filling mechanisms rather than layer formation. As a result, the BET method can significantly overestimate the true surface area of microporous materials. [293]
- **Potential Variability in Pressure Range Selection:** Although the Rouquerol criteria provide a systematic approach to selecting the appropriate pressure range, variability can still arise due to differences in experimental conditions, data interpretation, and material properties. If the selected pressure range does not strictly adhere to these criteria, the calculated monolayer capacity may not accurately reflect the actual surface area.
- **Quadrupole Effects:** Nitrogen, the most commonly used adsorptive, has a quadrupole moment, which can lead to specific interactions with polar surfaces. This can introduce errors in surface area calculations, making it necessary to consider alternative adsorptives such as argon in certain cases.
- **Not Suitable for Very High or Low C Values:** The BET model relies on the assumption that the BET constant (C) is within a reasonable range. If C is extremely high (>150), strong adsorbate-adsorbent interactions can cause deviation from multilayer behaviour, making BET assumptions invalid. Conversely, if C is too low (<2), weak adsorption results in poorly defined monolayer formation, leading to unreliable surface area estimates.

By following these steps and considering microporosity contributions, BET surface area analysis provides a robust but carefully interpreted measurement of porous materials. While widely used, it is crucial to be aware of the inherent limitations to avoid misinterpretation of the results.

4.2.2. Determination of Pore Volume and Pore Size Distribution

The characterization of porous materials requires an accurate determination of their pore volume and pore size distribution, which are critical parameters influencing adsorption, diffusion, and catalytic behaviour. The most commonly employed method for determining these properties in mesoporous materials is the Barrett-Joyner-Halenda (BJH) method, introduced in 1951. This method relies on the desorption branch of the nitrogen adsorption isotherm and is widely applied for mesoporous materials, though it is not suitable for micropore analysis due to its underlying assumptions.

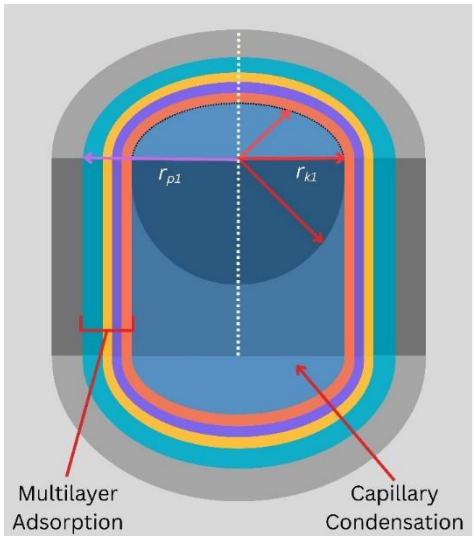

Figure 35 - Schematic of multilayer adsorption and capillary condensation in a mesopore, illustrating Kelvin radius (r_{k1}) and pore radius (r_{p1}) used in BJH pore size analysis.[301]

Understanding pore volume and pore size distribution is essential for applications in catalysis, gas storage, and separation processes. The BJH method utilizes capillary condensation and evaporation phenomena to derive meaningful pore structural information. The approach assumes a network of cylindrical pores (see Figure 35) and is limited primarily to mesoporous materials (2–50 nm). However, additional corrections and alternative models, such as Density Functional Theory (DFT) methods, may be required for microporous and macroporous materials.[301–303]

Key Assumptions of the BJH Method

1. **Cylindrical Pore Geometry:** The BJH model assumes that pores are cylindrical, which may not fully represent real materials with complex pore shapes.

2. **Capillary Condensation and Evaporation:** The model assumes that capillary condensation occurs during adsorption and that desorption follows a reverse process.
3. **Physisorption and Capillary Effects:** Adsorbed molecules remain due to two mechanisms: (a) physisorption on the pore walls and (b) capillary condensation within the inner pore volume.
4. **Desorption Branch Analysis:** The method primarily utilizes the desorption branch of the nitrogen adsorption isotherm, as it provides a better representation of pore size distribution in mesoporous materials.

Discussion on Limitations

- **Not Applicable to Micropores:** The BJH method is based on capillary condensation, which does not occur in micropores (<2 nm). For microporous materials, other methods such as the t-plot method or NLDFT (Non-Local Density Functional Theory) must be used.
- **Dependence on Desorption Data:** The use of the desorption branch can introduce errors due to assumptions about pore emptying mechanisms, which may not always be valid. In some cases, delayed evaporation effects can result in an underestimation of pore sizes.
- **Assumption of Cylindrical Pores:** The model assumes cylindrical pore geometry, which may not accurately represent complex pore structures present in real materials.
- **Sensitivity to Experimental Conditions:** The derived pore size distribution can be affected by measurement parameters, including equilibration time, pressure stability, and instrumental resolution.

By following these steps, the BJH method provides a practical approach for determining pore volume and pore size distribution in mesoporous materials. However, careful consideration of its assumptions and limitations is necessary to ensure accurate interpretation of results.

4.2.3. Micropore Analysis: The t-Method

The t-method is a widely used technique for analysing microporosity in porous materials based on gas adsorption data. It allows for the determination of the micropore volume,

micropore surface area, and external (non-microporous) surface area by evaluating the statistical thickness of an adsorbed gas layer. This method is particularly useful for isotherms that display micropore filling at low relative pressures alongside multilayer adsorption at higher pressures (commonly observed in materials that exhibit Type I behaviour or a combination of Type I/IV features). [304–306]

Principle of the t-Method

When a gas is adsorbed onto a solid surface, it forms a film whose thickness t increases with relative pressure (P/P_0). The fundamental assumption of the t-method is that the film thickness increases uniformly with increasing P/P_0. An empirical equation is used to calculate this statistical thickness. For nitrogen adsorption at 77 K, several models exist for estimating t. Commonly used equations include those proposed by de Boer and the Harkins-Jura equation. For high-surface-area carbonaceous materials, the ASTM standard D-6556-01 is often employed. One representative equation is:

$$t = \left(\frac{0.43}{(\log P_0/P)^2} + 0.33\right) \qquad \textit{Equation 42}$$

where:

- t is the statistical thickness of the adsorbed layer (in Å),
- P/P^0 is the relative pressure (with log taken as base 10).

By plotting the volume of liquid adsorbed (V_{liq}) against t, a $V - t$ plot is generated. For a nonporous or external surface, this plot is linear; deviations from linearity (e.g., a positive intercept when extrapolated) indicate the presence of micropore filling.

Considerations and Limitations

- **Selection of the Linear Region**: Accurate determination depends on correctly identifying the region where the V–t plot is linear (i.e., where multilayer adsorption dominates). Misidentification can lead to errors in estimating micropore volume.
- **Calibration**: The t-curve is typically calibrated using a nonporous reference material. Consistency between the t-method and BET surface area measurements can serve as a validation check.
- **Data Quality at Low Relative Pressures**: Sufficient data at very low P/P_0 is crucial for accurately capturing the micropore filling behavior.

- **Inapplicability to Macroporous Materials**: The t-method is not suitable for materials dominated by macropores (>50 nm) since these do not exhibit micropore filling.
- **Alternative Models**: In cases of complex pore structures or ambiguous micropore characterization, complementary techniques such as NLDFT (Non-Local Density Functional Theory) or the Horvath-Kawazoe (HK) model may be more appropriate.

The t-method is a powerful and widely used tool for micropore analysis. By carefully selecting the linear region of the V–t plot, one can estimate the micropore volume and surface area, providing valuable insights into the material's porosity. However, the method's accuracy relies on the validity of the chosen t-curve, the quality of the low-pressure data, and proper calibration against a nonporous reference. For a comprehensive porosity analysis, the t-method is often used in conjunction with BET, NLDFT, or HK models.

4.3. CO_2 Adsorption Characterisation and Analysis

The adsorption of CO_2 was studied using an Intelligent Gravimetric Analyzer (IGA), a high-precision gravimetric adsorption system that allows real-time measurement of gas adsorption as a function of applied pressure. The IGA operates by stepwise increasing the pressure and holding it constant until full equilibration is achieved, ensuring that the boundary conditions remain stable throughout the measurement process.

Unlike volumetric adsorption methods, where the system equilibrates by allowing pressure fluctuations, gravimetric analysis maintains a constant pressure while monitoring the mass change of the adsorbent material. This approach provides highly accurate adsorption isotherms by recording the amount of CO_2 adsorbed at various pressures and temperatures.

The adsorption isotherm generated through IGA measurements enables a direct comparison of CO_2 uptake across different materials under controlled conditions. It also allows for the study of adsorption selectivity when gas mixtures are employed, provided the appropriate setup is used. Additionally, kinetic parameters can be extracted by analysing the mass variation over time as the system reaches equilibrium at each pressure step. This data is essential for understanding both adsorption and desorption rates, which are critical for evaluating the efficiency of the material in practical applications.

The IGA also facilitates the investigation of material stability through cycling capacity tests, where multiple adsorption-desorption cycles are conducted to assess the longevity and potential degradation of the adsorbent over time. These experiments are crucial for determining the feasibility of the material in industrial applications where repeated adsorption cycles are required.

The following subsections will delve into key aspects of CO_2 adsorption analysis, including adsorption capacity, adsorption models, kinetic models, thermodynamics, activation energy, and cyclic stability providing a comprehensive characterization of the adsorption process.

4.3.1. CO_2 Adsorption Capacity

The ability of a material to adsorb CO_2 is a key determinant of its suitability for applications such as carbon capture, gas separation, and storage. Understanding adsorption capacity is essential for designing efficient materials that can maximize CO_2 uptake while maintaining stability and recyclability over multiple adsorption-desorption cycles. Factors influencing CO_2 adsorption capacity include surface area, pore size distribution, chemical functionality, and temperature and pressure conditions.

Adsorption is a dynamic process influenced by thermodynamic and kinetic parameters. The interaction between CO_2 molecules and the adsorbent surface dictates the extent and efficiency of adsorption, making it imperative to analyse capacity under various controlled conditions. Standardized measurement techniques ensure comparability across different materials and experimental setups, enabling systematic evaluation of their performance.

CO_2 adsorption capacity is a critical parameter for evaluating the performance of adsorbent materials. It quantifies the amount of CO_2 that a material can adsorb under specified conditions of temperature and pressure. The capacity is commonly expressed in millimoles of CO_2 per gram of adsorbent (mmol/g), which provides a standardized basis for comparison across different materials and studies.

Temperature Conditions

The adsorption capacity was measured at three standard temperatures**:** 0°C, 25°C, and 60°C. These temperatures were selected for the following reasons:

- 0°C: Represents low-temperature adsorption, useful for assessing performance under cryogenic or sub-ambient conditions, and for extracting kinetic information

when higher temperatures lead to adsorption processes that occur too rapidly to be accurately measured.

- 25°C: Standard room temperature, providing a baseline for adsorption under typical ambient conditions, which correspond to an atmospheric pressure of approximately 1 atm (1013 mbar). This temperature is commonly used in adsorption studies as it allows for direct comparison under standard temperature and pressure (STP) conditions, ensuring consistency in reported adsorption capacities.
- 60°C: Higher temperature condition relevant for industrial applications, such as post-combustion CO_2 capture, where flue gases are at elevated temperatures. At low pressures of 80–150 mbar, this represents the partial pressure of CO_2 typically found in flue gas conditions (8–15%).

The variation in adsorption capacity with temperature provides insights into the thermal dependence of the adsorption process, crucial for optimizing adsorbent materials for specific applications. Additionally, these measurements allow the construction of isosteres, which are necessary for thermodynamic calculations covered in section 4.3.4. This facilitates the determination of parameters such as adsorption enthalpy, providing a deeper understanding of the energetics governing the adsorption process.

Pressure Range

The CO_2 adsorption isotherms were measured over a wide pressure range to maximize the information extracted from the experiments. Prior to measurement, the samples were degassed using a turbo pump to 10^{-6} -10^{-7} mbar to ensure the removal of residual gases and surface contaminants. The isotherms were then conducted up to 19,500 mbar, the maximum operational pressure of the IGA.

Although pressures this high may seem excessive for adsorbents intended for post-combustion carbon capture, where CO_2 partial pressures are significantly lower, extending the pressure range allows for a more comprehensive analysis. This approach enables the extraction of additional isostere information for thermodynamic analysis and provides further insights into adsorption kinetics. By studying adsorption behaviour across a broad pressure spectrum, a deeper understanding of adsorption mechanisms and potential industrial applicability can be achieved.

Enhancing CO_2 Adsorption Through Physisorption Interactions

Tailoring the adsorbent surface to optimize physisorption interactions can significantly enhance CO_2 adsorption. By modifying surface chemistry to promote specific intermolecular forces, such as London dispersion, dipole-dipole, or π-π interactions, adsorbents can achieve improved affinity for CO_2 molecules. For example, introducing nitrogen-containing groups (e.g., pyridinic or graphitic nitrogen) onto carbon-based adsorbents can enhance dispersion and dipole-induced dipole interactions, increasing the adsorbent's effectiveness.

Nitrogen functional groups are particularly effective for physisorption because they can alter the electronic environment of the adsorbent, making it more favourable for weak, non-covalent interactions with CO_2. Additionally, these groups can contribute to π-π interactions when CO_2 interacts with aromatic surfaces, further enhancing adsorption. This approach avoids introducing stronger, irreversible interactions, ensuring the process remains within the realm of physisorption and retains its characteristic reversibility and low energy requirements. [257,265]

4.3.2. Adsorption Kinetics

Adsorption kinetics is a fundamental aspect of gas adsorption processes, particularly for post-combustion carbon capture applications. Understanding the rate at which CO_2 is adsorbed onto a material is essential for optimizing adsorbent performance in industrial settings. The kinetic behaviour is governed by factors such as pore structure, diffusion mechanisms, and the strength of interaction between gas molecules and the adsorbent surface.

In post-combustion carbon capture, adsorption kinetics dictates the feasibility of rapid CO_2 uptake under fluctuating gas flow conditions. Slow adsorption rates can limit efficiency—necessitating larger adsorbent beds and longer contact times—while fast kinetics enhance throughput and reduce operational costs. Typically, the adsorption curve shows a rapid initial uptake (driven by a high diffusion driving force) followed by a gradual approach to equilibrium. This curve's shape reflects an interplay between mass transfer resistance and the availability of adsorption sites; the steep initial slope represents fast surface adsorption, while the plateau indicates saturation as sites become occupied.

Operating conditions such as pressure, temperature, and gas flow rate significantly affect the observed kinetics. Elevated pressures may enhance the driving force for adsorption,

while higher temperatures can accelerate diffusion but sometimes decrease equilibrium uptake due to enhanced desorption. Variations in these parameters often shift the balance between rapid surface uptake and slower internal diffusion, which is reflected in changes to the rate constants and stretching exponents.

Kinetic models are not limited to batch adsorption experiments; they also inform the design and analysis of dynamic systems such as fixed-bed columns. Parameters derived from kinetic model fitting can be used to predict breakthrough curves, which capture the combined effects of external mass transfer, intra-particle diffusion, and equilibrium adsorption. This integration enables more accurate design and optimization of adsorption units for industrial-scale CO_2 capture.

Kinetic models describe the time-dependent behaviour of adsorption processes by providing rate equations that relate the amount of adsorbate adsorbed at any time (q_t) to the equilibrium amount (q_e) and other parameters, such as rate constants. These models help determine whether the adsorption process is controlled by chemical reaction rates, diffusion processes, or a combination of mechanisms. Because real adsorption processes are often complex and may involve multiple steps (e.g., rapid surface adsorption followed by slower intra-particle diffusion), various models have been developed. These range from simple pseudo-first order (PFO) or pseudo-second order (PSO) models to more advanced models (e.g., DE, SE, LDF, and DSE) that capture the heterogeneous and multi-stage nature of adsorption.

Pseudo-First Order (PFO) Model

The PFO model assumes that the rate of adsorption is directly proportional to the number of available adsorption sites. It was originally proposed by Lagergren and is often applied when physical adsorption (physisorption) is dominant. [307]

The differential equation is given by:

$$\frac{dq_t}{dt} = k_1 (q_e - q_t) \qquad \textit{Equation 43}$$

where:

- q_t is the amount adsorbed at time t,
- q_e is the equilibrium amount,
- k_1 is the pseudo-first order rate constant.

Integrated Form:

Assuming $q_t = 0$ at $t = 0$, integration yields:

$$q_t = q_e \left(1 - e^{-k_1 t}\right) \qquad \textit{Equation 44}$$

This equation shows an exponential approach to equilibrium. The PFO model is suitable for systems dominated by physical adsorption processes where a simple exponential uptake is observed.

Pseudo-Second Order (PSO) Model

The PSO model assumes that the adsorption rate is proportional to the square of the difference between the equilibrium and the current adsorption amounts. This model is often used when chemical interactions (chemisorption) are significant or when the rate-limiting step is more complex. [307]

The differential equation is:

$$\frac{dq_t}{dt} = k_2 \left(q_e - q_t\right)^2 \qquad \textit{Equation 45}$$

where k_2 is the pseudo-second order rate constant.

Rearrangement and integration yield:

$$\frac{t}{q_t} = \frac{1}{k_2 \, q_e^2} + \frac{t}{q_e} \qquad \textit{Equation 46}$$

This linear form is used to fit experimental data and extract q_e and k_2.

The PSO model is applied when adsorption involves stronger interactions or when experimental data suggest a non-exponential decay, often indicative of chemisorption or complex kinetics.

In real systems, adsorption is rarely perfectly described by a single kinetic order. The term “pseudo” is used because these models are simplified representations of more complex phenomena. Often, the overall adsorption process involves multiple steps:

Multiple Stages: For example, an initial rapid surface adsorption followed by slower intra-particle diffusion.

Combination of Mechanisms: Such as film diffusion, pore diffusion, and chemical interactions occurring simultaneously.

Heterogeneous Behaviour: Deviations from ideal kinetics may be better captured by more advanced models.

Advanced Kinetic Models

For systems with complex or multi-stage adsorption behaviour—where a single pseudo-first order model is insufficient to capture the full kinetics observed in experiments—more sophisticated models are employed. These advanced models are essentially built upon the pseudo-first order framework but are extended with additional exponential terms or stretching parameters to account for multiple adsorption stages (such as an initial rapid surface adsorption followed by slower intraparticle diffusion) and kinetic heterogeneity. The following models, which extend the pseudo-first order concept to describe more complex processes, are commonly used: [308–310]

Double Exponential (DE) Model

The DE model represents the overall adsorption kinetics as the sum of two independent exponential processes. It captures two distinct phases—a fast initial uptake and a slower process (e.g., diffusion into pores).

$$\frac{M_t}{M_e} = A_1\left(1 - e^{-k_1 t}\right) + (1 - A_1)\left(1 - e^{-k_2 t}\right) \qquad \textit{Equation 47}$$

where:

- M_t is the adsorbed amount at time t,
- M_e is the equilibrium adsorbed amount,
- A_1 is the fraction of the process following the fast kinetics,
- k_1 and k_2 are rate constants for the fast and slow processes, respectively.

Use the DE model when experimental data clearly show two distinct kinetic phases.

Stretched Exponential (SE) Model

The SE model modifies the simple exponential (or PFO) model by introducing a “stretching” exponent (β\betaβ) to account for a distribution of rate constants, which reflects heterogeneity in adsorption sites or diffusion paths. [311,312]

$$\frac{M_t}{M_e} = 1 - \exp\left(-k\, t^{\beta}\right) \qquad \textit{Equation 48}$$

- k is the effective rate constant,
- β (with $0 < \beta \leq 1$) is the stretching exponent.
  When $\beta = 1$, the model reduces to the simple first-order (PFO) model.

Use the SE model when the adsorption kinetics deviate from a simple exponential behaviour, indicating a spread in kinetic processes.

Linear Driving Force (LDF) Model

The LDF model is a simplified, first-order approximation that assumes the rate of adsorption is directly proportional to the difference between the equilibrium uptake and the current uptake.

$$\frac{M_t}{M_e} = 1 - \exp(-k\, t) \qquad \textit{Equation 49}$$

This form is mathematically equivalent to the simple PFO model and is widely used for engineering design purposes.

The LDF model is particularly useful when a single mass transfer mechanism dominates and simplicity is desired for process calculations, such as in fixed-bed adsorber design.

Double Stretched Exponential (DSE) Model

The DSE model extends the SE concept to systems exhibiting two overlapping adsorption processes, each characterized by its own rate constant and stretching exponent. [311,312]

$$\frac{M_t}{M_e} = A_1\left(1 - \exp\left(-k_1\, t^{\beta_1}\right)\right) + (1 - A_1)\left(1 - \exp\left(-k_2\, t^{\beta_2}\right)\right) \qquad \textit{Equation 50}$$

where:

- A_1 is the fractional contribution of the first process,
- k_1 and k_2 are the rate constants,
- β_1 and β_2 are the stretching exponents.

The DSE model is suitable when experimental data indicate that two distinct yet heterogeneous processes contribute to overall kinetics (e.g., a rapid surface adsorption combined with a slower diffusion-limited uptake).

Model Selection Discussion

While advanced models like the DE and DSE can capture the dual-phase and heterogeneous nature of adsorption more accurately, they also require estimation of more parameters. In practice, simpler models (such as SE or LDF) are often preferred when they provide an adequate fit, in keeping with the principle of model parsimony. The choice of model ultimately depends on the experimental data and the complexity of the adsorption process.

Fitting the Kinetic Curve

To accurately fit the kinetic data:

- **Data Selection:** Only data from the Intelligent Gravimetric Analyzer (IGA) recorded after system stabilization (both during adsorption and desorption) are used.
- **Equilibrium Determination:** The adsorption curve may exhibit a slight relaxation effect after the peak uptake; therefore, the highest stable mass uptake value is chosen as the equilibrium point for fitting. M_e.
- **Model Fitting:** Kinetic models are fitted using software (e.g., Origin) with appropriate fitting functions (e.g., SWeibull1 for the SE model, ExpAssoc for the DE model).
- **Validation:** The fit is validated by ensuring that 99% of the residuals lie within ±0.02 of the fitted curve. When several models meet this criterion, the simplest model is selected to avoid overfitting.

Extracted Information from Kinetic Analysis

Kinetic analysis provides valuable insights into the adsorption mechanism. The derived rate constants and exponents reveal how adsorption kinetics change with operating conditions (such as pressure and temperature) and indicate the dominant mechanisms (surface adsorption versus diffusion). These kinetic parameters are also essential for estimating activation energies via Arrhenius-type analyses, thereby further informing the design and optimization of industrial CO_2 capture systems.

The rate constants (k) and exponents (β) in these models provide insight into the underlying diffusion processes. For instance, if β deviates from unity, it suggests that a simple molecular diffusion process is not solely responsible—indicating contributions from

intra-particle diffusion, film diffusion, or a combination of both. This linkage helps connect the kinetic parameters to the physical mass transfer phenomena in the sorbent.[307]

4.3.3. Activation Energy

Activation energy (Ea) in the context of gas adsorption represents the energy barrier that molecules must overcome to diffuse into and interact with the adsorbent surface (See Figure 36). In post-combustion carbon capture, where CO_2 is separated from flue gas streams, understanding the activation energy is crucial for evaluating the kinetics of adsorption and optimizing materials for rapid and efficient capture. Lower activation energies indicate easier diffusion and faster adsorption rates, whereas higher values suggest the presence of steric hindrances, electrostatic interactions, or pore-structure constraints that slow the uptake process. [313–316]

Characterizing activation energy allows for a deeper understanding of the diffusion mechanisms and interactions governing CO_2 adsorption. It provides insight into how materials behave under different pressures and temperatures, helping to assess whether adsorption is kinetically or thermodynamically controlled. Additionally, activation energy values can be used to compare materials, offering a metric to predict the performance of sorbents under real-world operating conditions.

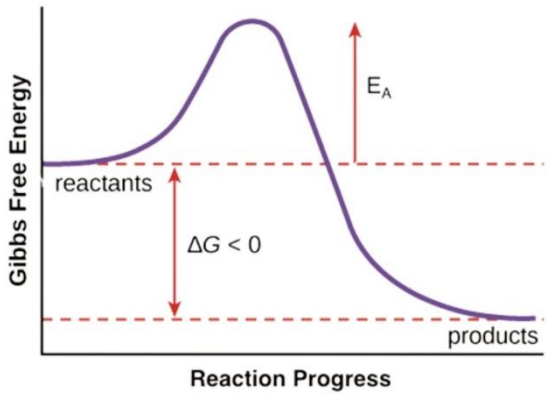

Figure 36 - Gibbs free energy profile showing activation energy (E_a) and the negative free energy change (ΔG) for a spontaneous adsorption process. [317]

Calculation of Activation Energy from Kinetic Data

The activation energy for CO_2 adsorption can be determined using the Arrhenius equation:

$$k = Ae^{-E_a/RT} \qquad \textit{Equation 51}$$

where:

- k is the rate constant obtained from the kinetic model (typically from the Stretched Exponential (SE) model in this study),
- A is the pre-exponential factor,
- E_a is the activation energy (J/mol or kJ/mol),
- R is the universal gas constant (8.314 J/mol·K), and
- T is the absolute temperature (K).

By rearranging the equation and taking the natural logarithm:

$$\ln k = \ln A - \frac{E_a}{R}\frac{1}{T} \qquad \textit{Equation 52}$$

A plot of $\ln k$ versus $1/T$ (an Arrhenius plot) yields a straight line, where the slope corresponds to $-E_a/R$, allowing for the determination of activation energy. This method is applied over a range of pressures (e.g., 0–1000 mbar) by evaluating adsorption kinetics at different temperatures, providing a pressure-dependent activation energy profile.

Activation Energy Trends and Implications for Carbon Capture

Activation energy values vary depending on the physical and chemical properties of the adsorbent material. For CO_2 adsorption on carbonaceous materials, values generally range from a few kJ/mol for physisorption-dominated processes to significantly higher values when chemisorption or steric hindrances play a role.

In post-combustion carbon capture, activation energy trends provide valuable insight into the practical applicability of an adsorbent. For instance:

- **Low activation energies** suggest minimal resistance to diffusion, allowing rapid uptake at low pressures, which is advantageous for practical carbon capture applications where adsorption needs to be fast and reversible.
- **Increasing activation energy with pressure** may indicate steric hindrances, electrostatic interactions, or the transition from surface adsorption to pore-diffusion-dominated mechanisms.
- **Functional group contributions**, such as nitrogen-containing moieties, can influence activation energies by enhancing CO_2 interactions through electrostatic attraction or hydrogen bonding.

In some cases, higher activation energies may correspond to additional diffusion barriers, such as steric effects from functionalized pore entrances or molecule alignment requirements for successful adsorption. In contrast, large pore structures may exhibit "free diffusion," reducing activation energy contributions from mass transport limitations. [313,314]

Interpretation of Activation Energy Results

The activation energy values extracted from kinetic data provide a means to distinguish between diffusion-limited and thermodynamically controlled adsorption processes. A lower activation energy coupled with high adsorption capacity suggests an efficient material suitable for practical deployment in industrial settings. Additionally, comparing activation energy with adsorption isotherm data can reveal whether adsorption uptake is limited by kinetic factors or equilibrium constraints.

By analysing activation energy trends in conjunction with temperature-dependent adsorption data, it becomes possible to fine-tune adsorbent formulations for optimized CO_2 capture. This characterization is particularly useful for evaluating sorbents across different operating conditions, ensuring that materials are well-suited for dynamic adsorption/desorption cycles necessary in post-combustion capture technologies.[315,316]

The determination of activation energy is a crucial step in characterizing CO_2 adsorption kinetics, offering insights into diffusion limitations, surface interactions, and overall performance of adsorbent materials. By leveraging kinetic data and applying the Arrhenius approach, activation energy analysis allows for material comparison and optimization, ensuring that adsorbents are both effective and practical for large-scale carbon capture applications.

4.3.4. Thermodynamics of Adsorption

Relevance of Thermodynamic Quantities to Post-Combustion Carbon Capture

Thermodynamic analysis is crucial for understanding and optimizing CO_2 adsorption in post-combustion carbon capture applications. The key thermodynamic quantities—Gibbs free energy (ΔG), enthalpy (ΔH), and entropy (ΔS)—govern the spontaneity, heat effects, and disorder associated with adsorption. Building on the fundamental principles introduced in the earlier in section 3.4, these parameters help determine whether CO_2 adsorption is efficient under real-world flue gas conditions and how temperature affects adsorption capacity. [257,265,279,297]

For CO_2 capture, the enthalpy of adsorption (ΔH) provides insight into the strength of interactions between CO_2 and the adsorbent. Since post-combustion capture typically operates under low CO_2 partial pressures and varying temperatures, understanding these thermodynamic parameters allows for the design of optimal adsorbents that maximize capacity and regeneration efficiency.[265,279]

Thermodynamic Theory of Adsorption

The thermodynamics of adsorption can be understood through the fundamental equation:

$$\Delta G = \Delta H - T\Delta S \qquad \textit{Equation 53}$$

where:

- ΔG is the Gibbs free energy change, indicating the spontaneity of the adsorption process.
- ΔH is the enthalpy change, representing the heat absorbed or released.
- T is the absolute temperature (K).
- ΔS is the entropy change, measuring the disorder in the system.

For CO_2 adsorption:

- Physisorption is always exothermic (ΔH < 0) with weak van der Waals interactions and a slightly negative ΔS due to reduced molecular motion upon adsorption.
- Chemisorption can be exothermic or endothermic, depending on the nature of the chemical bond formation between CO_2 and the adsorbent surface.

The heat of adsorption (ΔH) is a key indicator of interaction strength between CO_2 and the adsorbent and can be extracted using the **Clausius-Clapeyron equation**: [280]

$$\frac{d \ln P}{dT} = \frac{-\Delta H}{RT^2} \qquad \textit{Equation 54}$$

where:

- P is the equilibrium pressure.
- R is the universal gas constant (8.314 J/mol·K).
- T is the absolute temperature.
- ΔH is the enthalpy of adsorption.

A negative ΔH confirms an exothermic adsorption process, supporting the practical requirement for effective CO_2 capture at moderate temperatures.

Calculation of Thermodynamic Properties from Isostere Analysis

To determine the thermodynamic parameters of CO_2 adsorption, adsorption isotherms were measured at three different temperatures: 0°C, 25°C, and 60°C. The isostere approach, which involves extracting equilibrium adsorption data at constant surface coverage, enables the calculation of ΔH and ΔS.

There are two primary methods to extract isostere information from adsorption isotherms:

1. Linear Data Interpolation: Selecting equilibrium adsorption values at fixed surface coverages and interpolating between experimental data points.
2. Model-Based Method: Fitting an appropriate adsorption model (see section on model fitting) to the data and extracting isosteres from the fitted model.

In this study, the model-based method was chosen to ensure consistency and smooth interpolation across a range of pressures and temperatures. The number of extracted isostere points is limited to n-1, where n is the number of available data points. This constraint arises to prevent over-interpolation of the data and to ensure that each isostere is based on a reliable difference between data points rather than artificially smoothed trends.

The n-1 extracted data points are evenly distributed between the lowest recorded uptake on the highest-adsorbing isotherm (0°C) and the highest recorded uptake on the lowest-adsorbing isotherm (60°C). These selected data points are then applied to the isotherm models to determine the corresponding equilibrium pressures at each temperature, ensuring consistency in the isostere construction.

Isosteric Enthalpy and Entropy of Adsorption

The isosteric enthalpy (ΔH_i) and entropy (ΔS_i) of adsorption were calculated at constant CO_2 uptake using:

$$\ln P = -\frac{\Delta H_i}{R}\frac{1}{T} + C \qquad \textit{Equation 55}$$

where P is the equilibrium pressure at a given molar uptake of gas, T is the absolute temperature, and R is the gas constant.

The calculated ΔH_i values for CO_2 adsorption fall within the range of -30 to -25 kJ/mol, higher than the enthalpy of vaporization (15.326 kJ/mol at -57.5 °C). This suggests that the adsorption mechanism is governed by interactions beyond simple condensation, primarily influenced by microporous structures and nitrogen functionalities incorporated from melamine.

The entropy of adsorption (ΔS_i) decreases as CO_2 concentration increases, consistent with thermodynamic theory. A more negative ΔS_i indicates increased molecular ordering upon adsorption, reducing the degrees of freedom of adsorbed species relative to the gas phase.[279]

Influence of Nitrogen Functionality and Adsorption Regeneration

The presence of nitrogen functional groups, introduced via melamine, affects the adsorption energetics. Pyridinic nitrogen's in the structure contribute to enhanced CO_2 interactions, while amines may have steric hindrances limiting their contribution. Despite increased nitrogen content, adsorption energies remain within the range typical of physisorption, enabling effective regeneration by pressure swing desorption. The ability to desorb CO_2 with minimal thermal input suggests an energy-efficient capture process compared to conventional amine scrubbing, which requires high regeneration temperatures. [35]

The thermodynamics of CO_2 adsorption is critical for understanding adsorption efficiency and material performance in post-combustion carbon capture. By analysing isosteric heat and entropy changes through isostere extraction from adsorption isotherms, a comprehensive thermodynamic profile can be established. The results confirm that CO_2 adsorption is driven by physisorption mechanisms enhanced by nitrogen functionalities. The low regeneration energy observed further supports the potential application of these materials in large-scale CO_2 capture systems.

4.3.5. Cyclic Stability Testing

Introduction to Cyclic Stability Testing

Cyclic stability testing is essential for evaluating the long-term performance of CO_2 adsorbents in post-combustion carbon capture applications. Over multiple adsorption-desorption cycles, materials typically exhibit an initial variation in adsorption capacity, followed by stabilization in the charge and discharge cycles. This stabilization indicates that

the material has reached a steady-state performance, where its working capacity can be reliably assessed.

In industrial settings, the difference in CO_2 uptake between the high-pressure and low-pressure regions during cyclic operation defines the working capacity of the adsorbent. This is a crucial parameter for determining the efficiency of an adsorbent in a pressure swing adsorption (PSA) or temperature swing adsorption (TSA) system. The working capacity can be mathematically expressed as:

$$W = q_{high} - q_{low} \qquad \textit{Equation 56}$$

where:

- W is the working capacity (mmol/g),
- q_{high} is the CO_2 uptake at the upper operating pressure,
- q_{low} is the CO_2 uptake at the lower operating pressure.

A stable working capacity over repeated cycles is necessary for adsorbents to be viable in industrial applications. Materials that show a significant decline in working capacity over time may suffer from pore blocking, structural degradation, or loss of active sites, making them less suitable for long-term use.

Importance of Cyclic Stability in Post-Combustion Carbon Capture

Cyclic stability testing provides key insights into the robustness and regenerability of an adsorbent. Several factors influence the long-term stability of CO_2 adsorption materials:

- Structural Integrity: The material must retain its porosity and surface area over multiple cycles.
- Chemical Stability: The adsorption sites should remain active without degradation or poisoning.
- Regenerability: Efficient desorption should be achievable under practical conditions with minimal energy input.

For post-combustion carbon capture, adsorbents must withstand repeated cycles under fluctuating temperature and pressure conditions while maintaining high working capacity. The stabilization of charge and discharge cycles over multiple iterations confirms that the adsorbent can be used effectively in industrial applications without significant degradation.

Cyclic stability testing is crucial for determining the feasibility of an adsorbent in CO_2 capture applications. The stabilization of adsorption-desorption cycles ensures predictable performance, and the working capacity provides a direct measure of how much CO_2 can be captured and released per cycle. Adsorbents with high and stable working capacities over many cycles are ideal candidates for large-scale deployment in industrial carbon capture systems.

4.4. Competitive Adsorption

4.4.1. Relevance of Competitive Adsorption to Post-Combustion Carbon Capture

Post-combustion carbon capture involves the selective removal of CO_2 from flue gases that predominantly consist of nitrogen (N_2) along with minor components. Unlike single-component adsorption studies, competitive adsorption experiments simulate real gas mixtures and yield insights into both the efficiency and specificity of a sorbent. In industrial applications, sorbents must capture CO_2 effectively while minimizing N_2 uptake, making an understanding of competitive adsorption behaviour crucial for optimizing material performance.

In many post-combustion systems, the flue gas typically contains approximately 15% CO_2 and 85% N_2. This composition necessitates the development of sorbents with high CO_2 selectivity. In this context, Ideal Adsorbed Solution Theory (IAST) provides a useful framework by relating pure component adsorption data to the performance of gas mixtures.

4.4.2. Ideal Adsorbed Solution Theory (IAST) Overview

IAST is a thermodynamic method used to predict the equilibrium composition of the adsorbed phase in a gas mixture from pure component isotherms. It assumes that the adsorbed phase behaves as an ideal solution—analogous to Raoult's Law for vapor–liquid equilibria—and that the pure component isotherms accurately represent adsorption behaviour. A key concept in IAST is the spreading pressure (ω), which represents the excess free energy per unit area (J/m^2) of the adsorbed film. Calculated from the pure component isotherms via an integration based on the Gibbs–Duhem equation, spreading pressure links the microscopic adsorption properties to the macroscopic equilibrium of the adsorbed mixture. [318–321]

4.4.3. Limitations and Considerations

While IAST is a powerful tool for predicting competitive adsorption equilibria, several limitations should be noted [321]:

- **Assumption of Ideal Mixing:**

  IAST assumes that the adsorbed phase behaves as an ideal solution. This simplification may not hold for sorbents with heterogeneous surfaces or when strong specific interactions are present.

- **Quality of Pure Component Data:**

  The accuracy of IAST predictions relies heavily on the quality of the pure component isotherm fits. Inaccuracies in these fits can lead to significant errors in the predicted mixture behaviour.

- **Extension to Multicomponent Systems:**

  Although IAST is most straightforward for binary systems, real flue gases often contain additional components (e.g., H_2O, SO_2). Extending IAST to multicomponent mixtures requires additional considerations or alternative models.

- **Kinetic Limitations:**

  IAST is based solely on equilibrium thermodynamics and does not account for kinetic factors such as mass transfer limitations or non-equilibrium effects. These factors can be significant in dynamic processes like pressure swing adsorption (PSA) or temperature swing adsorption (TSA).

- **Numerical Complexity:**

  The system of nonlinear equations generated by IAST must be solved iteratively, and the convergence and accuracy depend on the numerical methods employed.

4.4.4. Summary and Practical Implications

The IAST framework provides a rigorous thermodynamic approach for predicting the performance of sorbents in separating CO_2 from N_2. By using pure component isotherm data to calculate spreading pressures and solving for the adsorbed phase composition, IAST enables the estimation of adsorption capacities and selectivity. The selectivity equation (Appendix B: Adsorption Characterisation and Techniques) offers a quantitative measure of the sorbent's preferential adsorption behaviour. Despite its assumptions and numerical complexities, IAST remains an invaluable tool for screening and designing sorbents for post-combustion carbon capture. When integrated with experimental competitive adsorption data and kinetic studies, IAST leads to a comprehensive understanding of sorbent

performance—ultimately guiding the development of high-performance materials for large-scale CCS applications.[322,323]

$$S_{CO_2/N_2} = \frac{(q_{CO_2}/q_{N_2})}{(y_{CO_2}/y_{N_2})} \qquad \textit{Equation 57}$$

4.5. Fourier Transform Infrared (FTIR) Spectroscopy

Fourier Transform Infrared (FTIR) Spectroscopy is a widely used analytical tool for investigating molecular structures by detecting infrared absorption patterns. It is particularly valuable in adsorbent research, where surface chemistry plays a crucial role in adsorption behaviour and material reactivity. By providing insights into chemical changes during pyrolysis and activation, FTIR helps optimize materials for industrial applications. FTIR spectroscopy is based on the absorption of infrared radiation by molecules, causing vibrational transitions that correspond to specific energy levels. When IR radiation interacts with a material, certain frequencies are absorbed while others pass through, generating a unique absorption spectrum. This spectrum provides structural information based on the vibrational motion of molecular bonds.

The FTIR spectrum can be divided into two key regions: the functional group region (above 1450 cm^{-1}), where distinct vibrations provide structural insights, and the fingerprint region (below 1450 cm^{-1}), which contains complex absorption patterns unique to each material. These characteristics allow FTIR to serve as a powerful tool for material identification and characterization. [324]

- **Stretching vibrations** (see Figure 37) involve changes in bond length.
- **Bending vibrations** involve bond angle variations.

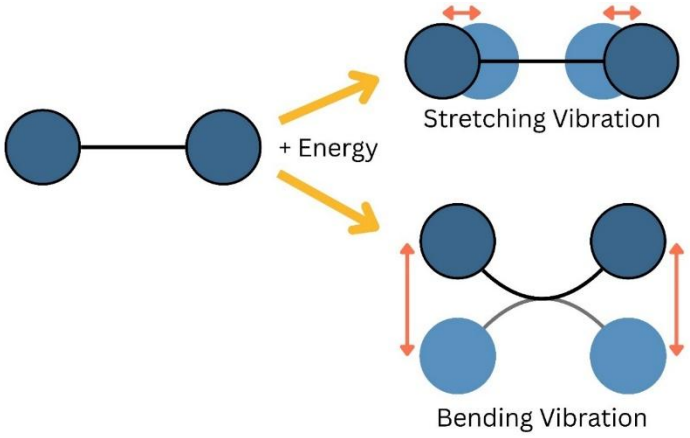

Figure 37 - Molecular vibrational modes induced by infrared absorption: stretching and bending vibrations. [325]

4.5.1. Fourier Transform and Instrumentation

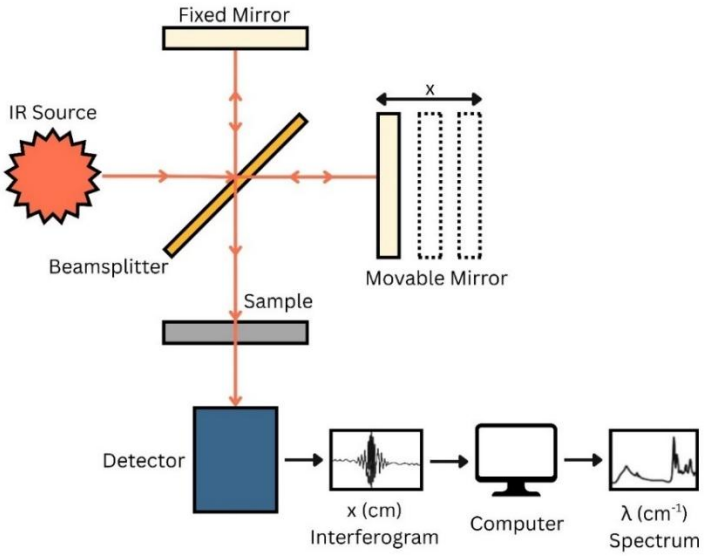

Figure 38 - Schematic of an FTIR spectrometer [326]

FTIR spectrometers (see Figure 38) utilize an interferometer, typically a Michelson interferometer, to collect spectral data efficiently. The system splits an IR beam into two paths—one directed at a fixed mirror and the other at a moving mirror—before recombining them to generate an interferogram. Unlike dispersive IR spectroscopy, which measures individual wavelengths sequentially, FTIR captures all wavelengths simultaneously, significantly improving speed, sensitivity, and resolution. The Fourier Transform (FT) is then applied to convert the interferogram into an absorption spectrum, allowing for clear identification of vibrational modes. [324]

- Infrared source (broadband radiation).
- Beam splitter and mirrors (interferometer).
- Detector (e.g., DTGS or MCT for different sensitivities).
- Sample handling (ATR, transmission, or reflectance techniques).

Germanium (Ge) ATR for Dark Carbon Materials

Attenuated Total Reflectance (ATR) FTIR is commonly used for analysing solid materials, but highly absorbing samples like biochar and activated carbon can obscure spectral details when using standard ATR crystals such as ZnSe and diamond. Germanium (Ge) ATR overcomes this limitation due to its higher refractive index (n ≈ 4.0), [327] which reduces infrared penetration depth to ~0.6–1.0 µm. This minimizes excessive absorption, prevents

peak distortions, and improves spectral clarity, allowing for more accurate functional group identification. Additionally, Ge ATR is less sensitive to surface roughness, making it ideal for porous materials like biochar, where consistent sample contact is challenging. By enhancing signal quality and reducing distortions, Ge ATR provides clearer and more reliable FTIR data for studying biochar adsorption mechanisms and surface modifications. [328,329]

The Fourier Transform plays a crucial role in converting the raw interferogram into a meaningful absorption spectrum. The interferogram initially records intensity variations as a function of mirror displacement. However, this signal is complex and not directly interpretable. The Fourier Transform decomposes the interferogram into individual sinusoidal wave components, mapping them to their respective frequencies to produce a spectrum. Each absorption peak corresponds to a molecular vibration at a specific wavenumber, providing structural insights into the material.

4.5.2. Limitations and Considerations

Despite its advantages, FTIR analysis comes with certain limitations:

- Water interference can mask peaks in the OH and CO regions.
- Peak overlap complicates analysis in complex mixtures.
- IR-inactive molecules (e.g., N_2, O_2) do not produce detectable vibrations.
- Quantification requires calibration, as absorbance is not always directly proportional to concentration.

FTIR spectroscopy is an indispensable tool in biochar and adsorbent research, offering valuable molecular-level insights into surface functionalities, adsorption properties, and chemical modifications. The Fourier Transform method allows for efficient spectral analysis, while the use of Ge ATR enhances measurements for highly absorbing materials like carbon-based adsorbents. By refining FTIR methodologies, researchers can improve material characterization and optimize biochar for carbon capture and environmental applications.

4.6. X-ray Photoelectron Spectroscopy (XPS): Principles and Applications

4.6.1. Introduction

X-ray Photoelectron Spectroscopy (XPS), also known as Electron Spectroscopy for Chemical Analysis (ESCA), is a surface-sensitive technique used to determine the elemental composition, chemical states, and electronic states of materials. XPS plays a critical role in

adsorbent and biochar research, where surface chemistry governs adsorption efficiency and reactivity. It is widely applied in material characterization, particularly for carbon-based materials, catalysts, and thin films. XPS offers several advantages, including high surface sensitivity (~1–10 nm depth), identification of chemical states of elements, and quantitative analysis of surface composition, making it an indispensable tool for analysing functionalized surfaces and adsorbent materials. [330,331]

4.6.2. Fundamental Principles

XPS is based on the photoelectric effect, where X-ray irradiation causes core electrons to be ejected from atoms in a sample. The energy of these emitted photoelectrons is measured, and their binding energy (BE) is determined using the equation:

$$BE = h\nu - KE - \phi \qquad \textit{Equation 58}$$

where $h\nu$ is the X-ray photon energy, KE is the kinetic energy of the emitted electron, and ϕ is the work function of the spectrometer. The binding energy is characteristic of specific elements and their chemical environments, enabling elemental and chemical state analysis.

XPS primarily probes the top 1–10 nm of a material's surface, making it highly sensitive to surface modifications and functional groups relevant to adsorption processes.

4.6.3. Instrumentation

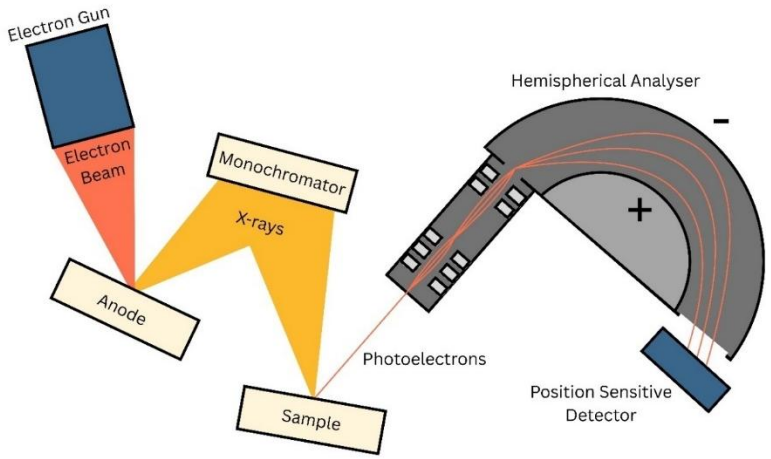

Figure 39 - Schematic of an XPS system showing X-ray generation, photoelectron emission, and energy analysis via a hemispherical analyser. [332]

A standard XPS (see Figure 39) system consists of:

- X-ray Source – Typically Al Kα (1486.6 eV) or Mg Kα (1253.6 eV) radiation is used.
- Electron Energy Analyzer – Measures the kinetic energy of photoelectrons.

- Vacuum Chamber – Maintains ultra-high vacuum (UHV) (~10^{-9} mbar) to prevent electron scattering.
- Charge Compensation System – Reduces charging effects in non-conductive materials.

4.6.4. Data Interpretation

XPS spectra consist of characteristic binding energy peaks, allowing for elemental identification and quantification. The precise location and shape of these peaks provide detailed insights into a material's chemical state and surface interactions.

Chemical shifts occur due to variations in an element's oxidation state or bonding environment, providing critical information about functional groups on a material's surface. Peaks corresponding to oxygen, nitrogen, and carbon in biochar can indicate the presence of hydroxyl (-OH), carboxyl (-COOH), and other functional groups relevant to adsorption and surface reactivity.

Multiplet splitting arises when unpaired electrons in transition metal elements interact with spin-orbit coupling, leading to multiple peaks for a single element. This provides insights into complex oxidation states and electronic configurations. Satellite peaks occur due to inelastic scattering events or shake-up processes, where some of the photoelectron energy is transferred to another electron, creating additional spectral features. These secondary peaks offer valuable information on the electronic environment of an element and help differentiate between similar chemical states.

By distinguishing between bulk composition and surface functional groups, XPS is particularly useful for analysing materials modified through functionalization or chemical treatments. This capability enables researchers to optimize adsorption sites and tune surface properties for specific applications, such as carbon capture and catalysis. [330,331]

4.6.5. Limitations

Despite its advantages, XPS has several limitations that must be considered. One of the primary drawbacks is the requirement for ultra-high vacuum (UHV), which restricts its application to vacuum-compatible samples and excludes in-situ or high-pressure environments. This limits the ability to study samples under real-world operational conditions.

Another limitation is its inability to detect hydrogen (H) and helium (He), as these elements lack core-level electrons that interact with X-rays in a measurable way. This makes it difficult to analyse hydrogen-containing functional groups directly, often requiring complementary techniques such as infrared spectroscopy.

XPS is also surface-sensitive, meaning it provides information about only the top 1–10 nm of a material. While this is advantageous for studying coatings and surface chemistry, it does not reflect bulk composition. Depth profiling techniques, such as ion sputtering, can be employed to analyse deeper layers, but these methods may cause sample damage or alter chemical states.

Finally, quantitative analysis in XPS requires careful calibration. Peak intensities must be corrected using sensitivity factors, and overlapping peaks must be resolved through peak fitting and deconvolution techniques to ensure accurate compositional analysis. [330,331]

4.7. Elemental Analysis

CHNX combustion analysis is a widely used technique for determining the carbon (C), hydrogen (H), nitrogen (N), oxygen (O), and heteroatom (e.g., sulfur, halogens) content of a sample. This method is particularly valuable in biochar and adsorbent research, where elemental composition provides insights into material properties, combustion efficiency, and adsorption potential. The C/H/O ratio is critical for evaluating carbonization extent, surface functionality, and stability in applications such as carbon capture and pollutant removal. The presence of heteroatoms such as sulfur and halogens can also influence adsorption behaviour and material reactivity, making their quantification important for environmental and catalytic applications. [333–336]

CHNX analysis is based on complete combustion of the sample in a high-purity oxygen environment. The elements present are converted into gaseous compounds, which are detected and quantified:

- Carbon (C) → CO_2 (carbon dioxide)
- Hydrogen (H) → H_2O (water vapor)
- Nitrogen (N) → N_2 (molecular nitrogen) or NO_x (oxides of nitrogen)
- Oxygen (O) → Measured indirectly

The gases are separated and quantified using infrared (IR) absorption or thermal conductivity detectors (TCDs). The percentage of each element is calculated using the equation:

$$\%X = \frac{m_X}{m_{sample}} \times 100 \qquad \textit{Equation 59}$$

where m_X is the mass of the detected element (C, H, N, O, or S) and m_{sample} is the total sample mass.

Oxygen is typically measured indirectly by calculating the difference between the total sample mass and the sum of detected carbon, hydrogen, and nitrogen content:

$$O\% = 100\% - (C\% + H\% + N\% + Ash\%) \qquad \textit{Equation 60}$$

where Ash% represents the residual inorganic content, which is determined separately through thermogravimetric analysis (TGA) or direct ash measurement.

4.7.1. Applications in Biochar and Adsorbent Research

CHNX analysis provides essential information for evaluating biochar and carbon-based adsorbents. The carbon content of a material indicates the degree of carbonization and potential for long-term stability in adsorption applications. A higher carbon percentage generally suggests a more thermally stable material with a greater proportion of graphitic structures, which can enhance adsorption efficiency and durability. [336]

The hydrogen-to-carbon (H/C) ratio serves as a measure of aromaticity and thermal stability. Lower H/C values correspond to materials with higher aromatic character, indicative of advanced carbonization and greater structural stability. This is particularly useful in biochar applications where high thermal stability is required for long-term environmental applications such as soil amendment or carbon sequestration.

The nitrogen content in biochar and adsorbents can provide insights into potential surface functionalities, including amines, pyrroles, and pyridinic nitrogen species. These functional groups can enhance adsorption performance, particularly for acidic gases like CO_2, by increasing surface reactivity and selectivity.

The oxygen-to-carbon (O:C) ratio is an indicator of the presence of oxygenated functional groups such as hydroxyl, carboxyl, and lactone groups. These groups influence hydrophilicity, surface reactivity, and potential for chemical interactions with adsorbates.

Understanding the O/C ratio is crucial for tailoring biochar and adsorbents for specific applications, such as water purification, gas separation, and catalysis.

Finally, the sulfur content can provide information on the presence of sulfur-containing functional groups, which can significantly impact catalytic properties and adsorption selectivity. Sulfur-functionalized carbon materials are often used in applications such as heavy metal adsorption and catalytic reactions, making its quantification important in materials research. [333–336]

4.7.2. Limitations of CHNX Analysis

- Does not provide chemical state information – Only quantifies elemental content, requiring complementary techniques (e.g., XPS, FTIR) to determine functional groups.
- Indirect oxygen determination – Less precise than direct oxygen measurement via pyrolysis-based techniques or oxygen analysers.
- Sample homogeneity – Inaccurate results may occur if the sample is not well-mixed or contains high inorganic content.

CHNX combustion analysis is a fundamental tool for characterizing biochar and carbon-based adsorbents, offering precise quantification of carbon, hydrogen, nitrogen, oxygen, and heteroatom content. By understanding elemental composition, researchers can optimize material properties for adsorption, catalysis, and carbon sequestration applications.

4.8. Proximate Analysis

Proximate analysis is a standardized method for determining the moisture, volatile matter, fixed carbon, and ash content of solid materials. It is widely used in biochar, biomass, and solid fuel research, providing critical insights into thermal stability, combustion behaviour, and adsorption potential. The results help optimize material properties for applications in carbon capture, filtration, and catalysis. [337,338]

4.8.1. Thermogravimetric Analysis (TGA) and Its Role in Proximate Analysis

Thermogravimetric analysis (TGA) measures mass loss as a function of temperature and time under controlled atmospheric conditions. It provides key insights into material decomposition, moisture content, volatile release, and thermal stability. The technique also enables the study of decomposition kinetics through derivative thermogravimetry (DTG),

which identifies distinct thermal events by measuring the rate of mass change with temperature.

A typical TGA system (see Figure 40) consists of a microbalance with a sensitivity of 0.1 µg, a furnace capable of operating at temperatures up to 1500–1700°C, and crucibles made of materials such as alumina or mullite. The system operates in a controlled atmosphere, either inert or oxidative, to study thermal decomposition mechanisms. Factors such as sample size, heating rate, buoyancy effects, electrostatic forces, and gas flow rates must be optimized to ensure accurate measurements.

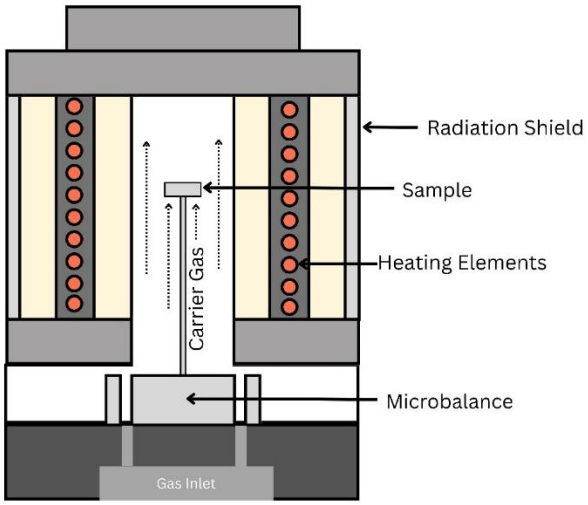

Figure 40 - Schematic of a thermogravimetric analyser (TGA) setup showing sample heating, carrier gas flow, and mass measurement via microbalance.[339]

4.8.2. Components of Proximate Analysis

Proximate analysis fractionates a sample into four key components, determined through controlled heating in a thermogravimetric analyser or muffle furnace.

1. Moisture Content

Moisture content refers to the mass loss when a sample is heated at 105°C in an inert atmosphere until constant weight is achieved. High moisture content reduces combustion efficiency and affects adsorption properties in biochar applications.

The percentage of moisture content is calculated as:

$$MC(\%) = \frac{m_i - m_f}{m_i} \times 100 \qquad \textit{Equation 61}$$

where:

- m_i is the initial mass before drying (g)
- m_f is the final mass after drying (g)

2. Volatile Matter

Volatile matter represents the mass loss when a pre-dried sample is heated at approximately 900°C in an inert atmosphere for a short duration. It consists mainly of organic volatiles and light hydrocarbons, influencing biochar porosity, surface area, and reactivity. High volatile content suggests increased gas yield during pyrolysis and greater reactive surface sites.

The percentage of volatile matter is calculated as:

$$VM(\%) = \frac{m_f - m_c}{m_i} \times 100 \qquad \textit{Equation 62}$$

where:

- m_f is the mass after drying (g)
- m_c is the mass after volatile matter burn-off (g)

3. Fixed Carbon

Fixed carbon is the solid carbonaceous residue remaining after the release of volatile matter. It indicates thermal stability, carbonization degree, and long-term adsorption potential in biochar materials.

The percentage of fixed carbon is determined indirectly as:

$$FC(\%) = 100 - (MC + VM + Ash) \qquad \textit{Equation 63}$$

where MC, VM, and Ash represent the respective percentages of moisture, volatile matter, and ash content.

4. Ash Content

Ash content refers to the non-combustible inorganic residue left after complete combustion at approximately 750°C in air. A high ash content may indicate mineral impurities, which influence adsorption efficiency, catalytic activity, or structural integrity of biochar and carbon-based adsorbents.

The percentage of ash content is calculated as:

$$Ash(\%) = \frac{m_a}{m_i} \times 100 \qquad \text{Equation 64}$$

where:

- m_a is the mass of ash after combustion (g)
- m_i is the initial mass of the sample (g)

4.8.3. Applications in Biochar and Adsorbent Research

TGA-based proximate analysis is widely used to evaluate biochar and carbon-based adsorbents, aiding in the optimization of adsorption efficiency, combustion properties, and stability. Biochar with high fixed carbon and low volatile matter is preferred for long-term carbon sequestration and adsorption applications. Conversely, biochar with high volatile matter exhibits greater surface functionality, improving interactions with contaminants or gases. Ash content analysis helps assess mineral composition, which influences catalysis, porosity, and adsorption selectivity.

TGA provides deeper insights into material thermal decomposition mechanisms by identifying characteristic degradation temperatures associated with moisture loss, volatile release, and residual carbon oxidation. The DTG curve, in particular, distinguishes different stages of decomposition, making it a valuable tool for biochar optimization, thermal stability assessment, and kinetic modelling. [340]

4.8.4. Limitations of Proximate Analysis

- Proximate analysis does not distinguish individual chemical compounds, necessitating complementary techniques such as FTIR, XPS, or Raman spectroscopy for functional group identification.
- Volatile matter measurements may include moisture, potentially leading to overestimation if samples are not pre-dried.
- Ash composition is not identified in proximate analysis and requires techniques like XRF or ICP-OES for detailed elemental analysis.

Proximate analysis provides essential thermal and compositional insights into biochar and carbon-based materials, influencing adsorption capacity, reactivity, and energy applications. By determining moisture, volatile matter, fixed carbon, and ash content, researchers can optimize biochar for carbon capture, environmental remediation, and energy storage applications. The integration of TGA and DTG techniques enhances the

accuracy and reliability of these measurements, offering a comprehensive approach to material characterization.

Chapter 5. Design of Experiment (DoE)

Experimentation is central to scientific inquiry and process optimisation. It involves systematically manipulating variables to observe and analyse their effects on defined outcomes. In engineering, chemistry, and industrial research, experimental approaches enable researchers to understand complex systems, identify causal relationships, and improve product or process performance.

Traditional experimentation often relies on a *one-variable-at-a-time* (OVAT) approach, where each factor is varied individually while others are held constant. While intuitive, this method is inefficient and fails to capture interactions between variables—factors which may jointly influence the outcome in ways that OVAT cannot detect. Additionally, OVAT designs often require a large number of experiments to explore the parameter space, increasing cost and time without guaranteeing optimal insights.

Design of Experiments (DoE) offers a statistically rigorous alternative. DoE is a structured, multivariate approach that allows simultaneous variation of multiple factors. It enables the identification of main effects, interactions, and nonlinearities, all while reducing the number of experimental runs required. By applying statistical models, DoE supports robust, data-driven decision-making, especially in systems where performance depends on several controllable inputs.

The objectives of DoE typically fall into three categories:

- **Screening**: Identifying which among many potential factors significantly affect a response.
- **Optimisation**: Determining the factor settings that maximise or minimise the desired outcome.
- **Robustness**: Assessing the stability of a process under varying conditions, including the influence of nuisance variables.

Through these objectives, DoE helps researchers efficiently explore experimental space, extract meaningful patterns, and develop reproducible, scalable solutions.

Core Principles of Experimental Design

Design of Experiments (DoE) is underpinned by three fundamental principles that ensure the validity, reliability, and statistical rigour of experimental results: randomisation,

replication, and blocking. These principles are critical in minimising bias, accounting for variability, and isolating the true effects of experimental factors.

i) Randomisation involves the random assignment of experimental runs and treatments to mitigate the effects of uncontrolled or unknown sources of variation. By eliminating systematic bias—whether due to environmental drift, equipment variation, or experimenter influence—randomisation supports the application of valid statistical analyses. Modern DoE software, automates random run orders using built-in random number generators, ensuring an unbiased execution of the experimental design.

ii) Replication refers to repeating experimental conditions across independent runs to estimate the variability inherent in the process. It provides a measure of experimental error, strengthens the statistical power of hypothesis testing, and enhances the robustness of conclusions. Replication is distinct from repeated measurements, which involve repeated observations under identical conditions to evaluate measurement precision. In the context of this study, replication was used selectively due to material and time constraints, with a focus on optimising experimental breadth within available resources.

iii) Blocking is a technique used to account for nuisance variables—factors that are not of primary interest but may influence the response. Experimental units are grouped into blocks with similar characteristics, allowing variation due to these nuisance factors to be isolated and minimised within each block. For example, biochar derived from different biomass batches could introduce variation due to precursor heterogeneity. While formal blocking was not employed in this study, some experimental groupings (e.g. by activation method) implicitly served to separate major sources of variation.

Together, these principles form the foundation of effective experimental design, enhancing the clarity and interpretability of results, particularly in systems where multiple variables interact in complex ways.

A clear understanding of the variables involved is essential to any well-structured experimental design. ***Factors*** refer to the independent variables deliberately manipulated to observe their influence on one or more response variables. These may be numerical (e.g., temperature, activation time) or categorical (e.g., activation method). Each factor is tested at specific ***levels***, which define the values or settings assigned during the experiment. For instance, temperature may be varied across low, centre, and high levels based on practical and literature-informed constraints.

Response variables—also called dependent variables—are the measurable outcomes affected by the factors. In this study, responses such as biochar yield, BET surface area, micropore area, micropore volume, and microporosity percentage were selected for their relevance to CO_2 adsorption performance.

Constants are parameters intentionally held fixed throughout all experimental runs to isolate the effects of the studied factors. Examples include the type of precursor material or the sample mass used per activation.

Finally, ***nuisance variables*** are factors that are not of direct interest but may still affect the response. These include uncontrolled variables (like ambient humidity), controlled variables (such as precursor batch), and noise variables (such as instrument fluctuations). While not always directly accounted for, their influence should be minimised or acknowledged in both the design and interpretation phases.

Experimental Design Procedure

The effective application of Design of Experiments (DoE) requires a systematic approach that balances research objectives with practical constraints. The following steps outline the standard procedure followed in planning and executing a statistically sound experimental design.

Define the Experimental Objectives

Begin by clearly articulating the purpose of the experiment. This typically involves identifying the key research question and determining which process parameters are expected to influence performance. Objectives may include identifying significant factors, exploring interactions, or optimising outcomes for a specific application.

Select the Response Variables

Response variables should be directly linked to the goals of the experiment and should be measurable with sufficient accuracy and repeatability. It is common to evaluate more than one response if multiple properties are relevant to performance. Care should also be taken to ensure appropriate calibration of measurement tools and consistency in data acquisition.

Identify Factors and Choose Appropriate Levels

Factors are the independent variables manipulated during the experiment. These must be selected based on their theoretical or practical relevance to the process under study. Levels

should be chosen to span a meaningful range without compromising safety, data quality, or process feasibility. The range should be wide enough to reveal trends, but not so broad that experimental failure or irrelevance occurs at the extremes.

Choose an Experimental Design Strategy

The selection of a suitable design depends on the objective:

- For **screening** a large number of variables, fractional factorial designs allow efficient identification of significant factors.
- For **optimisation** and interaction modelling, response surface methods such as central composite designs (CCD) or Box-Behnken designs are more appropriate.

The choice should also consider available resources, anticipated complexity, and whether the response is expected to exhibit curvature.

Conduct the Experiment

Once the design is finalised, runs should be executed according to the randomised run order. Consistency in experimental procedure is essential. Conducting pilot runs can help identify issues with material behaviour, equipment reliability, or data acquisition prior to full-scale execution.

Analyse the Data Statistically

Following data collection, statistical methods are applied to interpret the influence of each factor. Common techniques include ANOVA, regression analysis, and residual diagnostics. These analyses help identify main effects, interactions, and potential non-linear behaviour. Graphical tools such as contour plots or surface plots may also be used to visualise trends and assess model fit.

Draw Conclusions and Validate Findings

Based on the analysis, conclusions can be drawn about the influence of process variables and, where relevant, the conditions that optimise the response. If optimisation was the goal, verification runs should be carried out at the predicted optimum to confirm performance. This step provides confidence in the model and its applicability to real-world scenarios.

Factorial Designs

Factorial designs form the foundation of many experimental strategies in process optimisation. They systematically evaluate how multiple factors affect one or more response variables by testing combinations of factor levels. These designs are especially powerful for identifying interactions—cases where the effect of one factor depends on the level of another.

Full Factorial Design

In a full factorial design, all possible combinations of factor levels are tested. This allows for the estimation of both main effects and interactions with complete coverage of the experimental space. For example, a three-factor experiment where each factor is tested at two levels (coded as -1 for low and +1 for high) results in $2^3 = 8$ unique combinations. A typical design matrix is shown in **Error! Reference source not found.**.

Each row represents an experimental run with a unique combination of factor levels. This structure enables a complete analysis of main effects (e.g., the average change in response when X_1 shifts from -1 to +1) and interaction effects (e.g., how the combined change in X_1 and X_2 influences the response differently than either factor alone). The effects are typically estimated using contrast methods or regression modelling.

While highly informative, full factorial designs grow exponentially in size as more factors are added. This makes them well-suited for studies involving up to three or four factors, but less practical beyond that point without automation or high-throughput capabilities.

Run	X_1	X_2	X_3
y_1	+1	+1	+1
y_2	+1	+1	-1
y_3	+1	-1	-1
y_4	+1	-1	+1
y_5	-1	+1	+1
y_6	-1	+1	-1
y_7	-1	-1	-1
y_8	-1	-1	+1

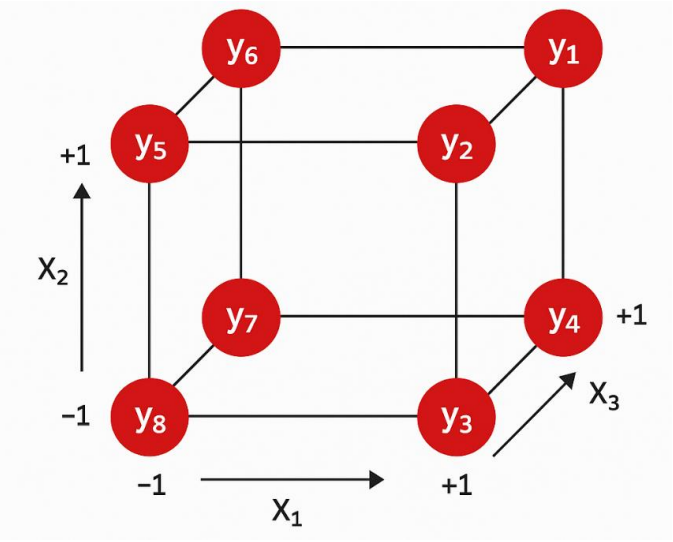

Figure 41 - Design matrix for a 2^3 full factorial experiment.

Fractional Factorial Design

When resource limitations prevent testing every combination, fractional factorial designs offer a more efficient alternative. These designs use only a carefully selected subset of the full factorial runs, allowing estimation of main effects and lower-order interactions while assuming higher-order interactions are negligible.

For example, a 2^{5-1} design includes 16 runs—half the number required by a full five-factor design. This reduction in experimental burden is particularly useful during early-stage screening, where the goal is to identify the most influential factors rather than fully characterise all interactions.

The trade-off is confounding—certain effects cannot be independently resolved because they are mathematically aliased with others in the design. The resolution of the design describes the extent of this confounding. Higher-resolution designs (e.g., Resolution V) separate main effects and two-factor interactions, whereas lower-resolution designs may confound even the main effects with two-factor terms.

Fractional factorial designs are often used as a precursor to more detailed studies, providing a data-driven basis for focusing future optimisation efforts on a smaller set of impactful variables.

Response Surface Methodology (RSM)

Response Surface Methodology (RSM) is a collection of statistical and mathematical techniques used for developing, improving, and optimising processes. It is particularly useful when the relationship between the response variable and the experimental factors is suspected to be nonlinear. Unlike factorial designs, which are limited to estimating main and interaction effects, RSM can model curvature by fitting second-order polynomial equations to the data.

RSM is typically employed after screening experiments have identified the most influential factors. By using surface plots, contour plots, and response models, it becomes possible to visualise how changes in factor levels affect the response, and to identify the optimum conditions within the experimental domain.

Two common RSM designs are the **Box-Behnken Design (BBD)** and the **Central Composite Design (CCD)**. Each has its own advantages depending on the nature of the experiment and constraints of the system.

Box-Behnken Design (BBD)

The Box-Behnken design is an efficient, three-level factorial design that avoids extreme conditions by excluding combinations where all factors are at their highest or lowest levels. This makes it particularly suitable for situations where such extremes are either infeasible or undesirable due to safety, cost, or stability concerns.

BBDs are rotatable or near-rotatable and require fewer experimental runs than comparable CCDs. The design points lie on the midpoints of the edges of the factor space and at the centre point. As a result, they are well suited for fitting quadratic models while maintaining experimental efficiency.

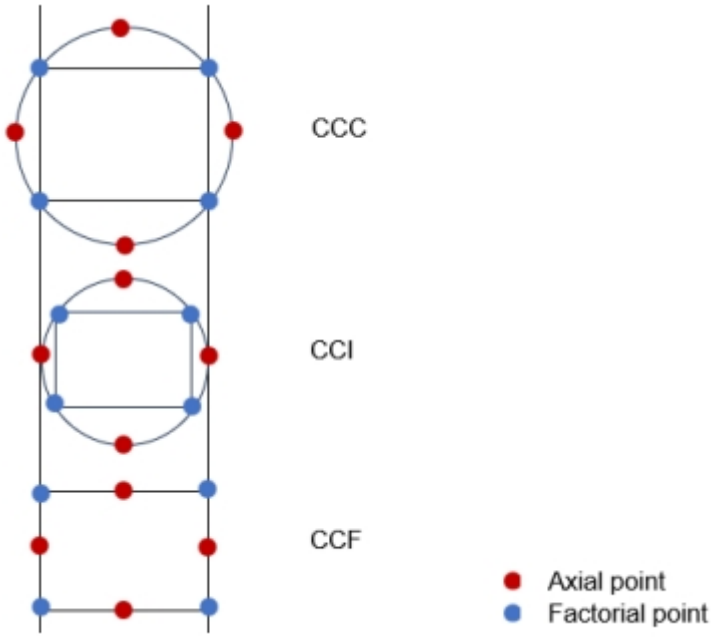

Figure 42 – CCC, CCI, and CCF experimental design schematic.

Central Composite Design (CCD)

The Central Composite Design extends a two-level factorial design by adding centre points and axial (or star) points. This allows for the estimation of both interaction and curvature effects, making it highly versatile for process optimisation. CCDs can be configured in different forms depending on the design constraints:

- **Circumscribed (CCC)**: The axial points extend beyond the factorial region. This design explores the widest process space but may include levels outside the practical operating range.

- **Face-centred (CCF)**: The axial points are set at ±1, aligning with the faces of the cube. This design is more conservative and is ideal when factor ranges are tightly constrained.
- **Inscribed (CCI)**: The factorial points are scaled to fit within the bounds of the axial region. This is suitable when the experimental space is strictly limited, and only interior points are feasible.

To achieve **rotatability**—a property that ensures uniform prediction variance at equal distances from the centre—the axial distance α is calculated using the following equation:

$$\alpha = \sqrt[4]{2^k} \qquad \textit{Equation 65}$$

where k is the number of factors.

Each CCD variant offers trade-offs between experimental flexibility, process coverage, and practical feasibility. The choice depends on factors such as available equipment, safety limits, and the precision required in optimisation.

In summary, (DoE provides a powerful framework for exploring, modelling, and optimising complex systems in a structured and statistically sound manner. By incorporating principles such as randomisation, replication, and blocking—and by carefully selecting factors, levels, and response variables—DoE enables researchers to extract meaningful insights with fewer experimental runs than traditional approaches. While limitations may arise from resource constraints or unbalanced designs, the core methodology remains highly adaptable and robust. The tools and concepts described here underpin the experimental planning and analysis presented in later chapters, providing a rationale for the conditions tested and the interpretations drawn.

Chapter 6. Experimental Procedures

6.1. Materials and Equipment

6.1.1. Biomass Sources

Spent coffee grounds (SCG) of the Strath Blend, consisting of 100% Arabica beans, were sourced from the University Union Café roasters. The material was collected as waste espresso grounds, corresponding to a fine espresso grind size. The roast level was not specified by the supplier. SCG were collected in batches of approximately 2 kg and stored in sealed containers prior to drying and further processing.

6.1.2. Reagents and Chemicals

High-purity nitrogen (oxygen-free nitrogen, 99.998% purity, 230 bar) and carbon dioxide (99.80% purity, 50 bar) gases were supplied by BOC (*UK*). Potassium oxalate monohydrate (99%, ACS reagent grade) was obtained from Thermo Scientific (*UK*), while potassium hydroxide (technical grade, >95%, powder form) was supplied by Sigma-Aldrich (*UK).* Deionized water, produced using Millipore ElixR 5 system by passing distilled water through an ion-exchange resin system, was utilized throughout all washing procedures.

6.2. Experimental Setup

6.2.1. Pyrolysis Reactor Configuration

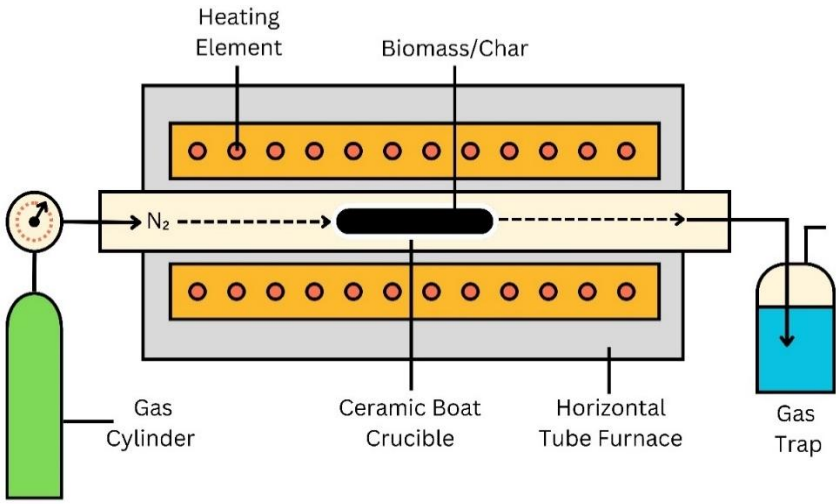

Figure 43 – Horizontal tube furnace schematic.

All pyrolysis procedures were carried out using a Carbolite Eurotherm MTF-12-38-250 horizontal tubular furnace (see Figure 43). Samples were placed in alumina (99.8%) boat crucibles (70 mm × 14 mm × 10 mm) positioned centrally within the reactor tube. The

furnace allowed precise temperature control and a controlled atmosphere, maintained by a continuous gas flow rate of 100 mL/min, unless otherwise specified.

To prevent atmospheric contamination and safely manage gaseous by-products, the outlet of the reactor tube was connected to a water gas trap. This setup served a dual purpose: (i) to maintain a slight positive pressure within the system, preventing back diffusion of air into the furnace tube, and (ii) to capture condensable or potentially harmful gaseous species generated during pyrolysis. The trap contained a small volume of deionised water, which acted as a physical barrier and preliminary scrubbing medium, ensuring safe venting of residual gases to the atmosphere.

6.2.2. Activation Systems Setup

The activation processes, including use of CO_2, potassium hydroxide (KOH), potassium oxalate, and fungal activation, utilized the same Carbolite Eurotherm furnace setup described in Section 5.1.1. Activation atmospheres were maintained by regulated gas flow (nitrogen or CO_2), as required for each activation method. Alumina boat crucibles were employed consistently across all activation experiments to ensure experimental uniformity.

6.3. Methodologies

6.3.1. Spent Coffee Grounds Collection and Pre-treatment

Spent coffee grounds (SCG) were dried at 100 °C in a Memmert UFE-400 oven until a consistent mass was achieved, then stored in an air-tight glass container. All subsequent pyrolysis procedures utilized a Carbolite Eurotherm tube furnace with controlled conditions, maintaining a nitrogen atmosphere (100 mL/min flow rate) unless otherwise specified.

6.3.2. Pyrolysis of Untreated SCG

Approximately 2-4 g of dried coffee grounds were placed into an alumina boat crucible, which was then positioned inside the tube furnace, and the exact mass recorded for each run. After sealing the furnace, nitrogen was flushed through the system at 100 mL/min for a minimum of 15 min to purge any oxygen. Samples were then heated at a ramp rate of 20 °C/min to predetermined temperatures, maintained for specified durations.

6.3.3. CO_2 Activation of SCG-Derived Biochars

Preparation of CO_2-activated biochars followed the pyrolysis procedure described above, with the exception that nitrogen was replaced with CO_2 at a flow rate of either 100 or 600 mL/min. Activation temperatures and hold times were systematically varied and recorded.

6.3.4. Potassium Hydroxide (KOH) Activation

KOH-activated biochars were prepared through a two-stage process. Initially, SCG underwent pre-pyrolysis at 600 °C under a nitrogen flow rate of 100 mL/min for 1 h. The resulting char was ground and mixed with KOH at defined mass ratios. The mixture was placed into alumina crucibles, returned to the furnace, sealed, and purged with N_2. Samples were subsequently heated at 20 °C/min to specified activation temperatures, maintained for predetermined durations. Following activation, biochars were repeatedly washed with deionized water until neutral pH was reached and dried at 100 °C for 12 h.

6.3.5. Potassium Oxalate Activation

Dried SCG were ground and uniformly mixed with potassium oxalate at predetermined mass ratios. The mixtures were placed in alumina boat crucibles, sealed within the furnace under a nitrogen flow of 100 mL/min, heated at 20 °C/min to the final activation temperatures, and held for predetermined times. The resultant biochars were washed extensively with distilled water until neutral pH was obtained, then dried at 100 °C for 12 h.

6.3.6. Fungal Activation

The procedure for SCG fungal activation utilized sterile procedures within a laminar flow hood. The fungus *Pleurotus ostreatus* was sourced from a verified supplier. Agar plate preparation and contamination checks for visible mould were performed using the following method: malt extract agar (Thermo Scientific™) was prepared by dissolving 50 g in a litre of distilled water, with the mixture autoclaved at 115 °C for 15 min, before pouring into sterile Petri dishes. These plates were inoculated with fungal culture and incubated at room temperature, regularly monitored for contamination. Rye grain spawn preparation involved dry rye grains (2.5 kg) being soaked in water for 24 h, then boiled until sufficiently soft (~2 h), drained and dried. Sterile rye grains were inoculated with fungal cultures from agar plates and incubated until fully colonized (2-3 wk). The next stage required freshly collected SCG to be combined with hay, previously soaked to improve water retention, and amended with 1 wt.% $CaCO_3$ (calcium source). This substrate was sterilized and inoculated using colonized rye grain spawn, then incubated until fully colonized (2-3 weeks).

Next, fully colonized substrate bags were cut with a sterile scalpel to promote fruiting under controlled conditions. Following the first mushroom flush, fungal-inoculated coffee grounds were harvested for pyrolysis. Finally, harvested fungal-activated substrates were loaded into alumina crucibles and pyrolyzed under standard conditions (N_2 atmosphere, 100 mL/min flow rate, heating ramp of 20 °C/min) at predetermined temperatures and hold times.

6.4. Characterization of Precursors and Biochars

The characterization of both the precursor material (spent coffee grounds, SCG) and the derived biochars was conducted using a variety of techniques to evaluate key structural and chemical properties. These methods provided insight into the changes in physical characteristics, functional groups, and elemental composition as a result of the pyrolysis and activation processes.

6.4.1. Proximate Analysis (Moisture, Ash, Volatile Matter, Fixed Carbon)

Proximate analysis was carried out to determine the moisture, ash, volatile matter, and fixed carbon content of the biochar samples. Approximately 5–10 mg of crushed sample was placed in a crucible and analysed using a NETZSCH STA 449 F3 Jupiter system. The analysis followed the procedure detailed in the British Standard (BS1016) method. The sample was first stabilized under a nitrogen flow at 50 mL/min and heated to 120 °C to determine moisture content. Subsequently, the sample was heated to 920 °C and held for 3 min under nitrogen to determine the volatile matter content. After cooling, the temperature was adjusted to 820 °C under pressurized air for the determination of the fixed carbon and ash content.

Thermogravimetric experiments were conducted to determine the thermal behaviour of the biochar samples. Curves corresponding to mass change (TG), derivative thermogravimetric (DTG), and differential scanning calorimetry (DSC) of the biochar samples were obtained under a nitrogen (N_2) environment by exposing the samples to ramped temperatures increasing from room temperature to 920 °C, before switching to an air environment at 820 °C (oxygen present). The obtained curves allowed the division of the combustion process into three distinct stages. Example of these experiments can be seen in

Appendix D: Thermogravimetric Analysis (TGA) Proximate Analysis Curves .

First Stage: Moisture Evaporation (~120 °C**)** The first stage of the thermal process occurred at approximately 120 °C, corresponding to the evaporation of moisture from the biochar

samples. This stage was identified by a significant mass loss in the TG curve, which was corroborated by an endothermic peak in the DSC curve and a corresponding peak in the DTG curve. The mass loss during this stage indicates the removal of physically adsorbed water. The moisture content varied among the samples, ranging from 0.66% to 15.53%.

Second Stage: Decomposition of Volatile Matter (~920 °C**)** The second stage was observed at approximately 920 °C, where the decomposition of volatile matter took place. This stage was characterised by a marked decline in the TG curve, representing the thermal degradation of organic components in the biochar. The DTG curve displayed a prominent peak at this temperature, indicating the rate of mass loss due to the volatilisation of organic compounds. The DSC curve exhibited an endothermic reaction, which is consistent with the decomposition of volatile matter. The volatile matter content varied significantly among the samples, ranging from 14.12% to 80.03%.

Third Stage: Combustion of Fixed Carbon (~820 °C**)** The third stage commenced when the N_2 flow was replaced with air at approximately 820 °C, allowing oxygen to contact the sample and initiate the combustion of fixed carbon. This transition resulted in a sharp mass decrease in the TG curve, signifying the oxidation of the remaining carbonaceous material. The DTG curve showed a peak corresponding to the rapid combustion process, while the DSC curve displayed an exothermic peak due to the oxidation reaction. The fixed carbon content varied among the samples, with the highest being 74.49% and the lowest 18.57%.

Ash Content: Following the combustion of fixed carbon, the remaining mass constitutes the ash content of the biochar samples. The ash content varied among the samples, ranging from 0.75% to 20.39%. The ash content provides an indication of the inorganic residue left after complete combustion, which is an important parameter for assessing the quality and purity of biochar.

These stages highlight the thermal stability and decomposition characteristics of the biochar samples, providing crucial insights into their behaviour under different thermal conditions. Understanding these physiochemical properties is essential for optimising the production and application of biochar in various fields.

6.4.2. Elemental Analysis (C, H, N, Content)

Elemental analysis was conducted to determine the carbon (C), hydrogen (H), and nitrogen (N) content of both the SCG precursor and the derived biochars. A Perkin Elmer 2400 CHN analyser was used for this purpose, with approximately 0.1 g of each sample combusted at 1800 °C. The resulting gases were analysed to quantify the relative elemental composition. This analysis provided insight into the elemental composition and the changes induced by pyrolysis and activation processes.

6.4.3. Fourier Transform Infrared Spectroscopy (FTIR) Analysis

FTIR spectroscopy was employed to identify functional groups and assess the chemical transformations occurring during pyrolysis by analysing both SCG and biochar samples. Two different FTIR systems were used to ensure comprehensive characterization: a Bruker TENSOR 27 FTIR spectrometer with an Attenuated Total Reflectance (ATR) accessory and an Agilent 4300 handheld FTIR spectrometer equipped with a Germanium ATR crystal attachment.

For benchtop analysis, FTIR spectra were collected using the Bruker TENSOR 27 spectrometer. The ATR accessory enabled direct sampling of solid materials. Spectra were recorded in the range of 400–4000 cm^{-1} with a resolution of 4 cm^{-1}, and 64 scans were performed for each sample. This method allowed for the identification of key functional groups, providing insight into the chemical structure of the precursor and pyrolyzed materials.

To complement this analysis, a portable Agilent 4300 FTIR spectrometer was also used, particularly for in-situ and rapid characterization. The instrument was set up in a benchtop configuration with a pressure tower attachment to ensure proper contact between the sample and the ATR crystal. The ATR crystal surface and pressure tower tip were cleaned with acetone prior to use and between each measurement to prevent contamination. A background spectrum was collected before analysis, which was automatically subtracted from subsequent measurements by the Agilent software.

A small amount of the sample was placed directly on the Germanium ATR crystal and compressed using the pressure tower to ensure uniform contact. Each measurement was performed in triplicate, and an average spectrum was generated to improve reproducibility. The use of both FTIR systems allowed for robust spectral acquisition and enhanced reliability in identifying functional groups across different sample types.

6.4.4. X-ray Photoelectron Spectroscopy (XPS) Analysis

XPS was employed to investigate the surface composition and chemical bonding states of SCG and biochar samples. Analysis was performed using a ThermoFisher™ K-Alpha X-ray Photoelectron Spectrometer. A small amount of sample was placed on the XPS sample holder and exposed to a monochromatic X-ray source. The resulting spectra were analysed to determine the elemental composition (atom %) and the chemical bonding states on the surface of the materials. XPS provided valuable information about the surface functional groups and elemental distribution in the biochars, which can be correlated with their potential for CO_2 adsorption.

6.4.5. BET Surface Area and Porosity Measurement by Nitrogen Adsorption

The textural properties, including specific surface area and porosity, of SCG and biochar samples were characterized by nitrogen adsorption using the Micromeritics ASAP 2420 V2.09 system (Figure 44). Surface area, pore volume, and average pore size were determined via analysis of the cryogenic nitrogen adsorption/desorption isotherm at -196 °C. The resulting data provided insights into specific surface area as well as micro-, meso-, and macropore volumes, which are critical parameters for evaluating the material's potential for CO_2 adsorption.

Prior to analysis, approximately 2 g of each sample underwent a degassing cycle to remove any residual solvents or surface contaminants. Degassing was performed under vacuum conditions (10 µmHg), initially at 50 °C for 30 min, followed by 120 °C for 40 min. Once degassed, the samples underwent a 49-point adsorption cycle over the relative pressure range of 0.01 to 1, followed by a 30-point desorption cycle from 1 to 0.1. Throughout the experiment, sample temperature was maintained at -196 °C using a liquid nitrogen bath.

Figure 44 - Micromeritics ASAP 2420 Surface Area and Porosity Analyser. [341]

Nitrogen adsorption isotherms were analysed using the Brunauer-Emmett-Teller (BET) model, which, for unrestricted multilayer formation, is expressed as:

$$\frac{\mathrm{p}}{\mathrm{n}(\mathrm{p}_0 - \mathrm{p})} = \frac{1}{\mathrm{n}_\mathrm{m}\,\mathrm{c}} + \frac{\mathrm{c} - 1}{\mathrm{n}_\mathrm{m}\,\mathrm{c}} \cdot \frac{\mathrm{p}}{\mathrm{p}_0} \qquad \textit{Equation 66}$$

where p_o is the saturation vapor pressure, n is the molar adsorption uptake at pressure p (mmol g^{-1}), n_m represents complete monolayer coverage (mmol g^{-1}), and c is a dimensionless constant related to adsorption energy.

BET surface area calculations were performed using adsorption data within the relative pressure (P/P_0) range of 0.05 to 0.35. The linear region used for BET fitting was selected based on application of the Rouquerol criteria, which ensure the validity of the BET model by identifying a physically meaningful range where $n(1 - P/P_0)$ increases monotonically with P/P_0 and the calculated n_m is positive.

The total pore volume (V_{total}) was estimated from the amount of nitrogen adsorbed at $P/P_0 = 0.99$. Micropore area and micropore volume were determined using the t-plot method, which differentiates microporous and non-microporous contributions to total surface area by analysing statistical thickness variations of the adsorbed nitrogen layer.

6.5. CO_2 Adsorption Capacity and Kinetics Assessment

6.5.1. Gravimetric Adsorption Analysis (IGA Method)

CO_2 adsorption capacity and kinetic studies were conducted using an Intelligent Gravimetric Analyzer (IGA), specifically IGA models 001 and 003 supplied by Hiden Isochema Ltd. Adsorption experiments were performed under both static and dynamic conditions using CO_2 as the primary adsorbate. The system (Figure 45) comprised a high-precision microbalance, a controlled gas handling system supplied by high-purity gas cylinders or a mass flow controller (MFC), and a temperature-controlled chamber. The adsorption setup was automated via IGASwin software, which controlled gas dosing, pressure regulation, and real-time data collection.

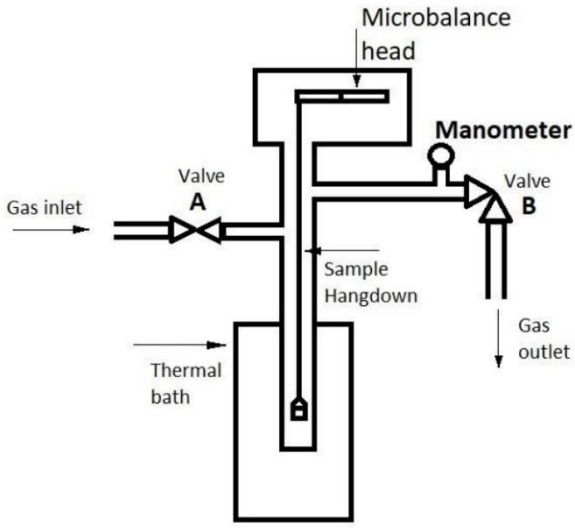

Figure 45 – IGA Schematic [342]

Sample Degassing and Analysis Protocol

Prior to adsorption measurements, all biochar samples underwent degassing to remove surface contaminants and moisture. Each sample (approximately 40–60 mg) was placed in a sample holder suspended from a tungsten wire attached to the microbalance. The reactor chamber was sealed before initiating the degassing process. Degassing was conducted in a Hiden Isochema standard furnace at 120 °C under vacuum conditions of 10^{-6}–10^{-7} mbar. A rotary vacuum pump was used initially, followed by a turbomolecular pump to achieve the desired pressure. The temperature was increased at a ramp rate of 3 °C/min, and the degassing process continued for 12 h until a stable sample mass was observed. After degassing, the sample temperature was adjusted using a thermo-stirrer unit, which

maintained a set temperature with a precision of ±0.1 °C. Once equilibrium was reached, the dry mass was recorded, and the chamber was pressurized to the initial adsorption conditions.

Conditions for Adsorption Capacity Assessment

Adsorption isotherms were measured under static conditions, with CO_2 adsorption experiments performed at 0 °C and 60 °C using an ethylene-glycol bath and a water bath, respectively. The chamber pressure was systematically increased from 0 to 19500 mbar, with desorption following the same steps in reverse. The adsorption data were analysed in IGASwin software, which logged mass uptake, pressure, and temperature variations throughout the experiment.

Cycling Adsorption Studies

Cyclic adsorption-desorption studies were performed to assess the stability and regeneration potential of the biochar materials. These studies were carried out at 60 °C in a static mode, using a wet sample mass of 40-60 mg. The pressure was increased to 1000 mbar at a ramp rate of 100 mbar/min, followed by equilibration for 15 min. Subsequently, the pressure was reduced to 50 mbar at the same ramp rate, with an additional 15-min equilibration. A total of 60 cycles were performed.

6.5.2. Competitive Adsorption and Selectivity Analysis (CO_2-N_2 Mixtures)

Experimental Conditions

Competitive adsorption studies were conducted using a binary gas mixture of CO_2 (15%) and N_2 (85%) at 60 °C, with pressure varying from 0 to 1000 mbar in 100 mbar increments. The gas mixture was introduced into the reactor chamber using the mass flow controller (MFC), ensuring precise control over flow rates and composition. No calibration was performed for the competitive adsorption experiments, as previous studies have demonstrated that the effect of gas flow on mass measurements is negligible at the low flow rate of 100 mL/min used in this study. Given this negligible effect, buoyancy corrections were considered unnecessary, and the experimental setup was deemed sufficient for assessing comparative adsorption trends across biochar samples. [343]

Chapter 7. Effects of Operating Parameters on Biochar Yield and Textural Properties

Activation processes play a crucial role in tailoring the properties of biochar for CO_2 adsorption applications. In this study, four activation methods—KOH, CO_2, fungal, and potassium oxalate (KOx)—were initially screened to assess their effectiveness in modifying biochar properties. Based on these preliminary experiments, KOx activation was selected for further optimisation using a central composite design (CCD) approach, as it showed the most promising characteristics for CO_2 adsorption. The optimisation focused on determining the influence of key experimental factors, including temperature, hold-time, and activation mass ratio, on response variables.

To systematically evaluate the effects of these factors across all activation methods, statistical analysis was conducted using regression modelling and analysis of variance (ANOVA). These analyses allowed for the identification of significant factors and their interactions, providing insight into how processing conditions influence key response variables. The selected response variables—yield, BET surface area, micropore area, micropore volume, and microporosity percentage—were chosen due to their strong correlation with CO_2 adsorption performance. While additional characterisation techniques such as CHN analysis, TGA, and XPS could have provided further insights, these were not pursued due to cost constraints. By applying statistical methods across all activation techniques, it should be possible to elucidate relationships between process parameters and material properties, guiding development of optimised biochars for CO_2 capture.

KOH Activation

The KOH activation experiments were designed to systematically investigate the effects of temperature, activation ratio, and hold-time on key biochar properties relevant to CO_2 adsorption. The initial focus was on temperature and KOH-to-biochar mass ratio, as these factors were expected to have the most significant influence on porosity development and adsorption capacity.

Factor Selection and Justification

Temperature: A five-level design was implemented, covering a broad range of activation temperatures. This factor was presumed to be the most significant in determining porosity and adsorption properties, as thermal activation directly influences the extent of

carbonisation and the development of microporous structures. The selected temperature range was chosen to capture the full extent of thermal decomposition and pore development, ranging from low, associated with partial activation, to higher temperatures, where excessive burn-off might occur.

Activation Mass Ratio (KOH:Biochar): Two levels (1:1 and 1:8) were selected to represent low and high chemical loadings. The lower ratio aimed to assess extent of activation with minimal reagent use, whereas the higher ratio provided conditions for extensive pore formation through more aggressive chemical activation.

Hold-Time: Initially, hold-time was not considered a variable, as literature suggested that extended retention at activation temperature enhances carbon stability and surface area. A fixed duration of 120 min was set to ensure full reaction completion. However, after initial screening and comparisons with other activation methods, a shorter hold-time (15 min) was introduced as a factor. This decision allowed for testing the practical limits of activation time, particularly at elevated temperatures, where prolonged heating could lead to excessive material degradation.

This experimental framework effectively captures the major effects of temperature and activation ratio, while also allowing for a secondary assessment of hold-time at extreme conditions. However, because hold-time was introduced later, the design does not represent a full-factorial DOE. Initially, retention time was excluded based on literature reports suggesting that prolonged hold-times promoted volatile removal and the formation of stable, fixed carbon structures. It was assumed that allowing sufficient time for the reaction to reach completion would more clearly isolate the effects of activation temperature and KOH loading. However, preliminary results revealed that under the harsh chemical conditions of KOH activation, extended retention could lead to over-activation and destruction of microporous structures, an effect similarly observed during CO_2 activation. Consequently, hold-time was retroactively included as a factor to investigate these degradation phenomena. As a result, the design is unbalanced, with temperature explored at multiple levels while hold-time and activation ratio remain at two levels each. This imbalance may affect the statistical power of certain interaction terms, meaning that while main effects can be well analysed, interaction effects between factors should be interpreted with caution.

The results from this study provide a robust basis for identifying significant activation parameters, but further refinements in future work could explore intermediate hold-times or a more even distribution of factor levels to better resolve second-order effects. Additionally, further optimisation could be conducted to refine activation conditions and enhance adsorption performance. The detailed summary of the experimental factors and their corresponding results, including yield, BET surface area, micropore area, and micropore volume, is presented in Table 6 to illustrate the observed trends across different experimental conditions.

ANOVA

Analysis of Variance (ANOVA) is a statistical method used to test whether differences between group means are statistically significant by comparing the variance attributed to experimental factors with the residual variance of the dataset. It enables identification of which factors meaningfully influence a response variable while accounting for experimental variability.

Analysis of Variance (ANOVA) was employed to determine the statistical significance of key experimental factors—temperature, hold-time, and activation ratio (biochar:KOH mass ratio)—on the response variables of yield, BET surface area, and micropore characteristics. The purpose of this section is to evaluate those factors that have a statistically significant influence and to quantify how much of the observed variability in the response variables can be explained by the experimental factors.

The ANOVA table presents F-values and p-values, which determine the statistical significance of each factor. A high F-value and a p-value below 0.05 indicate that the factor has a meaningful effect on the response variable. Residual analysis is included to validate the assumptions of ANOVA and assess the reliability of the model. Four residual plots—normal probability plot, residuals vs. fitted values, histogram of residuals, and residuals vs. order—are examined to check for normality, homoscedasticity, and randomness in residual distribution. Ensuring these assumptions are met strengthens confidence in the statistical conclusions.

Temperature did not emerge as a significant factor for yield ($p = 0.424$), which is somewhat unexpected given its role in thermal degradation. However, the pre-pyrolysed nature of the biochar may explain this result, as most mass loss occurs during pyrolysis rather than

activation. Consequently, activation may not induce substantial additional mass loss, leading to insignificant yield variations.

In contrast, hold-time was found to be a significant factor ($p = 0.012$), with lower hold-times (15 min) leading to significantly higher yield compared to longer hold-times (120 min). This aligns with expectations, as prolonged activation at high temperatures facilitates further degradation and mass loss. The activation mass ratio (KOH:biochar) was not significant for

Table 6 - Experimental conditions and corresponding textural properties of KOH-activated biochars, illustrating the main effects of temperature, hold-time, and activation ratio on yield, BET surface area, micropore Area, micropore volume and % microporosity.

Biochar ID	Final Temp (°C)	Hold-Time (mins)	Biochar:KOH Ratio	Yield (%)	BET Surface Area (m^2/g)	Micropore Area (m^2/g)	Micropore Volume (cm^3/g)	% Microporosity
EX42-700-15-KOH-1:1	700	15	1:1	10.83	1085	943	0.361	86.9
EX41-1000-15-KOH-1:1	1000	15	1:1	22.75	22	11.25	0.004	49.2
EX26-500-2H-KOH-1:1	500	120	1:1	20.82	262	224	0.115	85.4
EX27-700-2H-KOH-1:1	700	120	1:1	17.29	845	745	0.385	88.1
EX23-800-2H-KOH-1:1	800	120	1:1	13.64	1185	1066	0.551	89.9
EX25-900-2H-KOH-1:1	900	120	1:1	11.04	1217	996	0.511	81.8
EX44-700-15-KOH-1:8	700	15	1:8	61.85	28	24	0.009	86.7
EX43-1000-15-KOH-1:8	1000	15	1:8	44.24	478	415	0.159	0
EX28-500-2H-KOH-1:8	500	120	1:8	19.01	2	3	0.002	N/A
EX29-700-2H-KOH-1:8	700	120	1:8	4.296	2862	193	0.084	6.7
EX30-800-2H-KOH-1:8	800	120	1:8	5.098	3196	0	0	0
EX31-900-2H-KOH-1:8	900	120	1:8	1.374	3204	0	0	0
EX31-900-2H-KOH-1:8	900	120	1:8	1.836	2513	0	0	0

Table 7 - ANOVA results for the effects of temperature, hold-time, and KOH:biochar ratio on yield and textural properties of KOH-activated biochars.

Response	Factor	DF	F-Value	P-Value	R^2	Adjusted R^2	Predicted R^2
Yield	Temp	4	1.09	0.424	35.22	2.84	0
Yield	Hold-Time	1	9.08	0.012	45.22	40.24	9.08
Yield	KOH:Biochar	1	0.13	0.727	1.15	0	0
BET Surface Area	Temp	4	2.27	0.150	53.18	29.77	0
BET Surface Area	Hold-Time	1	3.8	0.077	25.66	18.9	3.77
BET Surface Area	KOH:Biochar	1	2.31	0.157	17.34	9.82	0
t-plot Micropore Area	Temp	4	0.29	0.874	12.81	0	0
t-plot Micropore Area	Hold-Time	1	0	0.971	0.01	0	0
t-plot Micropore Area	KOH:Biochar	1	10.35	0.008	48.49	43.81	26.37
t-plot Micropore Volume	Temp	4	0.3	0.867	13.2	0	0
t-plot Micropore Volume	Hold-Time	1	0.14	0.711	1.29	0	0
t-plot Micropore Volume	KOH:Biochar	1	11.07	0.007	50.15	45.62	28.57
% Microporosity	Temp	4	0.41	0.797	17	0	0
% Microporosity	Hold-Time	1	0.4	0.542	3.48	0	0
% Microporosity	KOH:Biochar	1	21.17	0.001	65.81	62.7	53.03

yield ($p = 0.727$), suggesting that within the tested range, the extent of chemical activation did not substantially impact overall mass retention.

Despite temperature being expected to be the dominant factor, it was not found to be statistically significant ($p = 0.150$). The variability in surface area across different temperatures suggests that other factors, such as the interaction between temperature and mass ratio, may play a role in surface development. The highest BET surface areas were observed at 800 °C and 900 °C, particularly for the high mass ratio (1:8), where extensive pore development is expected due to the aggressive activation conditions. The hold-time factor was also found to be insignificant ($p = 0.077$), though shorter hold-times trended towards lower surface areas. Temperature was not a significant factor for micropore area ($p = 0.874$) or micropore volume ($p = 0.867$), possibly due to inconsistencies in pore formation at different activation conditions. However, activation mass ratio was highly significant for both micropore area ($p = 0.008$) and micropore volume ($p = 0.007$), with higher KOH loadings leading to a decrease in microporosity. This suggests that excessive KOH may facilitate mesopore development rather than strictly enhancing micropore formation, potentially altering the adsorption characteristics of the resulting biochar.

Hold-time did not significantly influence micropore characteristics ($p = 0.971$ for micropore area and $p = 0.711$ for micropore volume), suggesting that once initial pore formation occurs, extended hold-times do not enhance microporosity significantly. While activation mass ratio had the strongest impact on % microporosity ($p = 0.001$), with lower KOH:biochar ratios leading to significantly higher microporosity. This suggests that higher KOH loadings may favour mesoporosity development rather than strictly microporosity. Temperature and hold-time, in contrast, were not significant for microporosity ($p = 0.797$ and $p = 0.542$, respectively).

The imbalanced design, with temperature having more levels than the other factors, likely contributed to the limited statistical significance observed for certain parameters. With only two levels for hold-time and activation ratio, the ability to detect nuanced trends in these factors was restricted. A more balanced experimental design, such as a full factorial design incorporating additional levels for hold-time and activation ratio, may have provided a clearer picture of their influence and improved the robustness of statistical conclusions. Additionally, the fact that the biochar was pre-pyrolysed before activation likely muted the expected impact on yield, as the major mass loss had already occurred. This highlights the importance of considering the full thermal history of the material when designing activation studies.

While temperature did not emerge as a significant factor for most responses, activation mass ratio played a critical role in defining microporosity. The significance of hold-time for yield further reinforces the impact of prolonged activation on mass loss. These findings suggest that optimising KOH activation requires careful balancing of activation time and chemical ratio to achieve desired porosity characteristics without excessive material loss. Further optimisation studies with a more balanced design could provide deeper insights into the interplay of these factors.

General Factorial regression

To further analyse the impact of temperature, hold-time, and activation ratio on the key response variables, a General Factorial Regression approach was applied. This statistical method allows for the evaluation of both main effects and interaction effects, providing insight into whether the combined influence of factors contributes to variations in yield, BET surface area, micropore area, micropore volume, and % microporosity.

Unlike ANOVA, which primarily assesses factor significance by comparing means across discrete levels, General Factorial Regression models the relationship between factors and responses through regression equations. This approach enables the quantification of how changes in temperature, hold-time, and activation ratio influence each response variable and determines whether interactions between factors significantly contribute to the observed trends.

To systematically present the findings, this section will first walk through an example analysis, demonstrating how non-significant terms are identified and removed to refine the regression equation. The process will illustrate how terms with high p-values are eliminated, resulting in a final model that retains only significant predictors. Following this, a summary table will be provided, consolidating the regression results for all response variables. This structured approach will allow for a clear comparison of the statistical models, highlighting the most influential factors and identifying areas where the experimental design may have limited the detection of significant effects.

t-plot MA Full Model

Table 8 - ANOVA summary for the full General Factorial Regression model of micropore area (t-plot MA), including main and interaction effects.

Source	DF	Adj SS	Adj MS	F-Value	P-Value
Model	11	2191292	199208	*	*
Linear	6	1002282	167047	*	*
Temp	4	306949	76737	*	*
Hold-Time	1	223	223	*	*
KOH:Biochar	1	711192	711192	*	*
2-Way Interactions	5	839956	167991	*	*
Temp*KOH:Biochar	4	686669	171667	*	*
Hold-Time*KOH:Biochar	1	33689	33689	*	*
Error	1	0	0		
Total	12	2191292			

Table 9 - Model summary for the full General Factorial Regression of micropore area.

S	R-sq	R-sq(adj)	R-sq(pred)
0	100.00%	100.00%	*

The initial full model included temperature, hold-time, and activation ratio, along with their interaction effects. However, the model could not be estimated properly because the degrees of freedom for the error term were zero. This issue arises due to the imbalanced

experimental design, where temperature has five levels while hold-time and activation ratio only have two levels each. This imbalance leads to an overfitting problem where the number of parameters in the model exceeds the number of independent data points available to estimate them, making it mathematically impossible to calculate meaningful statistics. As a result, interaction terms such as Temp * Hold-Time, Temp * KOx:Biochar, and Hold-Time * KOx:Biochar had to be removed.

The ANOVA for results of the full model are presented in Table 8, highlighting the overfitting issue, with the error term having zero degrees of freedom. Table 9 provides the model summary, which indicates an artificially high R-squared value (100%), a clear indication of an over-parameterised model.

t-plot MA No Interactions

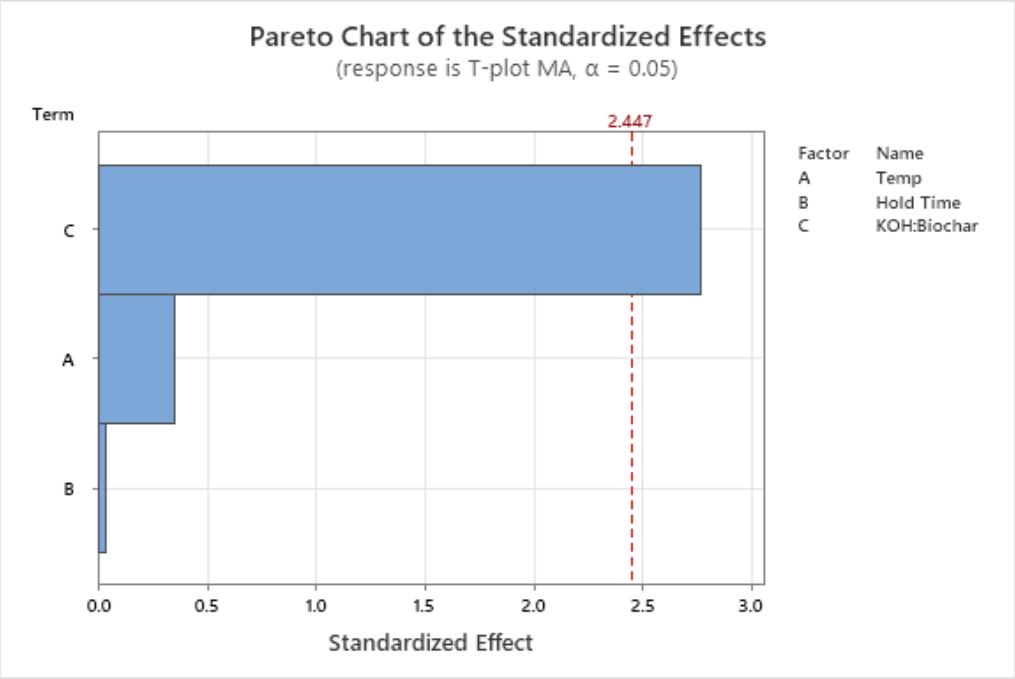

Figure 46 - Pareto chart of standardised effects for micropore area (t-plot MA) at α = 0.05. Only the activation ratio (KOH:Biochar) exceeds the significance threshold, indicating its dominant influence.

Once the interaction terms were eliminated, a simpler model was generated that included only the main factors (temperature, hold-time, and activation ratio). However, after removing the problematic interactions, only activation ratio (KOH:Biochar) emerged as statistically significant, as shown in the Analysis of Variance ($p = 0.033$). Temperature ($p = 0.734$) and hold-time ($p = 0.969$) remained insignificant. The model summary in Table 11 reports an adjusted R-squared value of 23.34%, indicating that the main factors accounted

for a modest proportion of the variance in micropore area, with over three-quarters of the variability attributable to factors not captured by the model.

Table 10 - ANOVA results for the simplified regression model excluding interaction terms.

Source	DF	Adj SS	Adj MS	F-Value	P-Value
Model	6	1351337	225223	1.61	0.289
Linear	6	1351337	225223	1.61	0.289
Temp	4	283962	70991	0.51	0.734
Hold-Time	1	223	223	0.00	0.969
KOH:Biochar	1	1070327	1070327	7.65	0.033
Error	6	839956	139993		
Lack-of-Fit	5	839956	167991	*	*
Pure Error	1	0	0		
Total	12	2191292			

Table 11 - Model summary for the simplified General Factorial Regression of micropore area using only main effects.

S	R-sq	R-sq(adj)	R-sq(pred)
374.156	61.67%	23.34%	0.00%

Regression Equation

t-plot MA = 356 - 235 Temp_500 + 120 Temp_700 + 184 Temp_800 + 80 Temp_900 - 150 Temp_1000 + 7 Hold-Time_15 - 7 Hold-Time_120 + 291 KOH:Biochar_1 - 291 KOH:Biochar_8

t-plot MA Reduced GFR

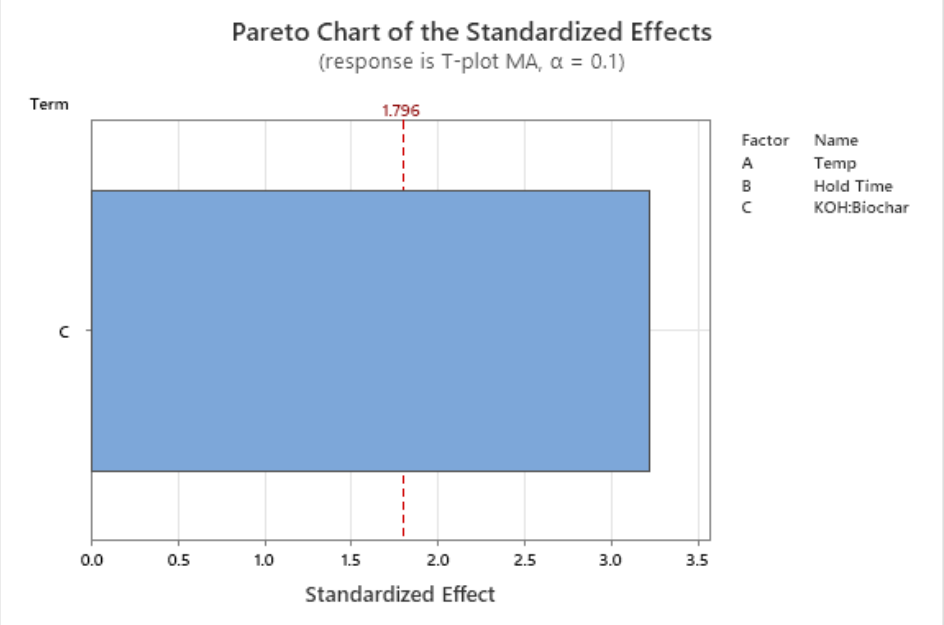

Figure 47 - Pareto chart of standardised effects for micropore area (t-plot MA) at α = 0.10. Activation ratio remains the only significant factor, reinforcing its primary role in determining microporosity.

Table 12 - ANOVA results for the reduced regression model including only activation ratio (KOH:biochar) as a predictor of micropore area.

Source	DF	Adj SS	Adj MS	F-Value	P-Value
Model	1	1062521	1062521	10.35	0.008
Linear	1	1062521	1062521	10.35	0.008
KOH:Biochar	1	1062521	1062521	10.35	0.008
Error	11	1128772	102616		
Lack-of-Fit	10	1128772	112877	*	*
Pure Error	1	0	0		
Total	12	2191292			

Table 13 - Model summary for the reduced model, highlighting improved adjusted R^2 and modest predictive capability (predicted R^2 = 26.37%).

S	R-sq	R-sq(adj)	R-sq(pred)
320.337	48.49%	43.81%	26.37%

Regression Equation

t-plot MA = 377.6 + 286.7 KOH:Biochar_1 - 286.7 KOH:Biochar_8

Since only activation ratio was significant, a reduced model (Table 12) was created where temperature and hold-time were excluded. This resulted in a much simpler regression equation, demonstrating that, as the activation ratio increases (more KOH relative to biochar), the micropore area decreases significantly. Table 12 confirms the statistical significance of activation ratio with a p-value of 0.008. The model summary in Table 13 provides the adjusted R-squared value of 43.81%, indicating the proportion of variation explained by the model. The predicted R-squared (26.37%) suggests that the model has some predictive capability, though it is still relatively low.

Figure 46 and Figure 47 present Pareto charts of the standardised effects for the reduced models, with significance thresholds at $\alpha = 0.05$ and $\alpha = 0.1$, respectively. These charts illustrate the dominance of the activation ratio (KOH:Biochar) over other factors, reinforcing its primary role in determining micropore area. The Pareto charts confirm that temperature and hold-time do not have significant effects in this context.

Box-Cox Transformations and Their Role in Model Refinement

Box-Cox transformations were applied to all response variables to determine whether model accuracy could be improved by stabilising variance and improving the normality of residuals. This transformation, which adjusts the response variable using an optimal power

parameter (λ), helps linearise relationships between factors and responses, potentially enhancing model interpretability and predictive power. The optimal λ is determined by maximising the log-likelihood function, selecting the transformation that best normalises the data. While transformations improved some models, others could not be transformed, due to the presence of zero or negative values, limiting their applicability. In cases where the optimal λ produced an impractical or difficult-to-interpret transformation, simpler models without transformations were preferred to ensure clarity and avoid overfitting.

Stepwise Selection and Its Role in Model Refinement

Stepwise selection is an automated regression technique used to streamline the model refinement process by iteratively adding or removing predictors based on statistical significance. It helps identify the most influential factors while eliminating non-contributory terms, ensuring a more parsimonious and interpretable model.

This method follows predefined significance thresholds, typically $\alpha = 0.15$ for inclusion and removal. The algorithm begins with an initial model and evaluates the contribution of each predictor. Variables that improve model fit are added, while those with minimal impact are removed. The process continues until no further adjustments enhance the model.

Stepwise selection effectively automates the refinement process discussed earlier, reducing the risk of overfitting while maintaining a balance between model complexity and accuracy. However, it has limitations, such as sensitivity to collinearity and the potential omission of meaningful interactions. Despite these constraints, it was valuable in this study for isolating key influences on biochar properties while simplifying the final regression models.

However, there are limitations to this approach when applied to this dataset. The imbalanced design of experiments reduces the ability to effectively model interaction effects, making it difficult to capture more complex relationships between the factors. Additionally, the relatively low adjusted and predicted R-squared values indicate that other, unaccounted-for variables may also be influencing micropore development. Future studies could benefit from a full-factorial design with additional levels for activation ratio and hold-time, which would provide a more balanced dataset for statistical analysis and improve the robustness of interaction effect estimations.

Overall, this refinement process demonstrates how General Factorial Regression can be used to systematically identify and remove non-significant terms, ultimately leading to a

simpler and more interpretable model that highlights the key factor influencing micropore area—the activation ratio.

Table 14 - Summary of reduced factorial regression models for key response variables. Significant predictors were retained through stepwise regression.

Response	Regression Equation	R^2 (%)	Adjusted R^2 (%)	Significant Terms
Yield	Yield = 22.70 + 12.21 Hold-Time_15 - 12.21 Hold-Time_120	45.22	40.24	Hold-Time
BET SA	BET SA = 1025 - 622 Hold-Time_15 + 622 Hold-Time_120 - 463 KOH:Biochar_1 + 463 KOH:Biochar_8	40.94	29.12	Hold-Time, KOH:Biochar
t-plot MA	t-plot MA = 377.6 + 286.7 KOH:Biochar_1 - 286.7 KOH:Biochar_8	48.49	43.81	KOH:Biochar
t-plot MV	t-plot MV = 0.1789 + 0.1425 KOH:Biochar_1 - 0.1425 KOH:Biochar_8	50.15	45.62	KOH:Biochar
%MP	%MP = 46.78 + 33.44 KOH:Biochar_1 - 33.44 KOH:Biochar_8	65.81	62.7	KOH:Biochar

The factorial regression models highlight key factors affecting biochar properties. Table 14 presents significant variables after removing non-contributory terms. The KOH:Biochar ratio is the dominant factor influencing microporosity (%MP), total pore volume (t-plot MV), and micropore area (t-plot MA). Yield and BET surface area (BET SA) are significantly impacted by hold-time and KOH:Biochar ratio, as identified through stepwise regression.

For yield, stepwise regression identified hold-time as the only significant factor, with an adjusted R^2 of 40.24%. Although transformations were tested to improve model fit, the simpler stepwise model was selected as it avoids overfitting and provides a more interpretable equation. The transformed model initially produced an artificially high adjusted R^2 of 99.96%, which strongly indicated overfitting. Given the relatively small dataset and the risk of inflating statistical significance, the more conservative stepwise model was deemed more appropriate.

Similarly, BET SA required adjustments to improve model interpretability. While factorial regression initially suggested temperature as a significant factor, the stepwise model retained only hold-time and KOH:Biochar ratio, producing an adjusted R^2 of 29.12%. Transformations were tested, but the resulting optimal λ (-2.08) was impractical to apply.

The final model offers a more straightforward representation of the key influences on surface area development.

For micropore area (t-plot MA), micropore volume (t-plot MV), and microporosity (%MP), the KOH:Biochar ratio was the only statistically significant factor. While chemical activation is expected to strongly influence pore development, it is surprising that temperature and hold-time did not emerge as significant contributors. The models exhibit adjusted R^2 values between 43.81% and 62.7%, reinforcing the role of activation ratio in determining microporosity. However, the absence of expected temperature and hold-time effects suggests potential nonlinear relationships or interactions that were not captured by the factorial approach, warranting further investigation with alternative modelling techniques.

A key limitation of this study is the imbalanced experimental design. Temperature had five levels, while hold-time and activation ratio had only two, leading to overfitting in some cases, particularly for micropore area. This resulted in artificially high R^2 values (100%) in full factorial models, requiring the removal of interaction terms and limiting the ability to analyse complex factor relationships.

Additionally, low adjusted and predicted R^2 values in some models suggest missing influential variables. The categorical approach of the factorial regression simplifies trends, potentially missing nonlinear dependencies, particularly in BET SA. Future research should consider response surface methodology (RSM) or multiple linear regression using continuous variables to enhance modelling accuracy.

The next section explores regression models incorporating continuous variables and interaction terms. Multiple linear regression with interactions will provide deeper insights into biochar properties, addressing the shortcomings of the factorial regression by capturing overlooked factor influences and interactions.

General Linear Regression analysis

Building upon the findings from the General Factorial Regression approach, this section presents the application of general linear regression to the KOH-activated biochar samples. While factorial regression provided an initial assessment of factor significance, it was inherently limited by the discrete nature of its factor levels and the constraints of the experimental design. In contrast, multiple linear regression treats temperature, hold-time, and activation ratio as continuous variables, allowing for a more refined and flexible analysis of their effects on the response variables.

The process of generating and refining the regression models follows the same principles as in the previous section. Initially, full models incorporating all main effects and interaction terms are developed. Terms with high p-values are systematically removed to refine the models, retaining only those factors that significantly impact the response variables. Given that this process mirrors the approach taken in the General Factorial Regression section, a worked example will not be included here. Instead, the focus will be on summarising the final reduced models and their implications.

Table 15 presents the reduced regression models for key response variables, highlighting the significant factors influencing yield, BET surface area, micropore area, micropore volume, and microporosity. These refined models provide a clearer understanding of how activation conditions shape the structural properties of biochar, informing potential process optimisations for CO_2 adsorption applications.

Table 15 - Reduced general linear regression models for key response variables treating activation parameters as continuous variables.

Response	Regression Equation	R^2 (%)	Adjusted R^2 (%)	Significant Terms
Yield	Yield = 38.41 - 0.2326 Hold-Time	45.22	40.24	Hold-Time
BET SA	BET SA = -9429 + 28.94 Temp - 1.39 Hold-Time - 670 KOH:Biochar - 0.01954 Temp² + 0.685 Temp*KOH:Biochar + 2.992 Hold-Time*KOH:Biochar	94.74	89.48	Temp, KOH:Biochar, Temp², Temp*KOH:Biochar, Hold-Time*KOH:Biochar
t-plot MA	t-plot MA = 746 - 81.9 KOH:Biochar	48.49	43.81	KOH:Biochar
t-plot MV	t-plot MV = 0.3621 - 0.0407 KOH:Biochar	50.15	45.62	KOH:Biochar
%MP	%MP = 89.8 - 9.55 KOH:Biochar	65.81	62.70	KOH:Biochar

The reduced general linear regression models provide an improved but still limited understanding of the effects of activation parameters on biochar properties. Notably, the BET model identified temperature, KOH:Biochar, Temp², Temp*KOH:Biochar, and Hold-Time*KOH:Biochar as significant factors, whereas the General Factorial Regression analysis only found Hold-Time and KOH:Biochar to be significant. This represents a significant improvement in capturing the complexity of the relationships between activation parameters and BET surface area. However, other key parameters, such as temperature, remain statistically insignificant for yield, contradicting established literature.

The regression model indicates that increasing hold-time reduces yield ($p = 0.012$), consistent with expectations that prolonged activation enhances mass loss. The adjusted R^2

(40.24%) suggests moderate explanatory power, an improvement over the previous factorial approach. However, temperature remains insignificant, which may indicate either an insufficient experimental range or missing interaction effects.

The model for BET surface area (BET SA) demonstrates a significantly higher explanatory power (adjusted R^2 = 89.48%), capturing critical interactions and nonlinear effects. the model incorporates significant terms, including quadratic temperature effects (p = 0.004), interactions between temperature and activation ratio (p = 0.018), and hold-time and activation ratio (p = 0.005). The negative quadratic temperature coefficient indicates an optimal activation temperature beyond which surface area decreases, likely due to significant structural degradation. The activation ratio (KOH:Biochar) also plays a critical role, with interaction effects suggesting a complex dependence on multiple factors.

Micropore area and volume both correlate negatively with activation ratio (KOH:Biochar), suggesting excessive KOH loading reduces microporosity, possibly due to over-etching favouring mesopore formation. However, temperature remains insignificant, despite its expected role in porosity development. Adjusted R^2 values (43.81% and 45.62%) indicate moderate explanatory power but fail to fully capture process complexity.

Microporosity (%MP) is significantly influenced by activation ratio (p = 0.001), with an adjusted R^2 of 62.70%, the highest among the response variables. The negative coefficient suggests that higher KOH loadings shift pore development toward mesopores. However, the absence of a temperature effect remains a major limitation.

Despite the improvement in the yield model, the results remain constrained by an imbalanced experimental design, lack of interaction terms, and oversimplified linear relationships. Temperature, a critical factor in activation, is unexpectedly insignificant across all models, likely due to untested nonlinear dependencies or insufficient factor resolution. Additionally, low predicted R^2 values indicate poor generalisability.

CO_2 Activation

The CO_2 activation experiments were conducted to evaluate the effects of temperature, hold-time, and CO_2 flow rate on key biochar properties relevant to CO_2 adsorption. The primary objective was to understand how these factors influence yield, BET surface area, micropore area, micropore volume, and microporosity percentage.

Factor Selection and Justification

Temperature: Activation temperature plays a critical role in determining porosity and surface area. A range of 500 °C to 900 °C was selected to examine the extent of thermal decomposition and micropore formation, with the expectation that higher temperatures promote porosity development but may also reduce yield due to increased burn-off.

Hold-Time: Two hold-times (15 and 120 min) were tested to assess the impact of prolonged exposure to activation conditions. Extended hold-times allow for greater structural modification but may lead to excessive material loss.

Table 16 - Summary of synthesis conditions and textural properties for CO_2-activated biochars across varying temperatures, hold-times, and CO_2 flow rates.

Biochar Identification	Final Temp (°C)	Hold-Time (mins)	CO_2 Flow Rate (mL/m)	Yield (%)	BET Surface Area (m^2/g)	t-plot Micropore Area (m^2/g)	t-plot Micropore Volume (cm^3/g)	% micro-porosity
EX40-700-15-CO_2-100	700	15	100	23.61	0.6	0	0	0
EX39-700-15-CO_2-600	700	15	600	23.03	0.6	0	0	0
EX38-850-15-CO_2-100	850	15	100	15.70	723	614	0.236	84.9
EX37-850-15-CO_2-600	850	15	600	15.1	737	621	0.239	84.3
EX15-500-2H-CO_2-100	500	120	100	25.59	0.1	5	0.002	0
EX16-700-2H-CO_2-100	700	120	100	23.73	1.7	0	0	0
EX18-800-2H-CO_2-100	800	120	100	5.92	535	366	0.189	68.4
EX17-900-2H-CO_2-100	900	120	100	4.35	580	445	0.229	0
EX20-500-2H-CO_2-600	500	120	600	24.39	5	9	0.005	N/A
EX21-700-2H-CO_2-600	700	120	600	21.23	208	181	0.093	87
EX22-800-2H-CO_2-600	800	120	600	5.08	506	361	0.186	71.3

CO_2 Flow Rate: Two levels of CO_2 flow rate (100 mL/min and 600 mL/min) were included to determine how gas flow influences activation efficiency and pore formation. Higher flow rates can enhance gas-solid interactions but may also lead to inconsistent activation.

This study presents another imbalanced experimental design, with temperature explored at multiple levels, while hold-time and CO_2 flow rate were limited to two levels each. This

imbalance impacts the ability to assess interactions comprehensively. However, the design still allows for the identification of major trends and key factor effects.

The experimental results, summarised in Table 16, provide insights into the relationships between processing conditions and biochar properties. To further analyse these effects, ANOVA, General Factorial Regression, and General Linear Regression were applied. These statistical methods identify significant factors, quantify their impact, and refine the models to provide a clearer understanding of activation outcomes.

ANOVA

Table 17 - ANOVA results for CO_2-activated biochars.

Response	Factor	DF	F-Value	P-Value	R^2	Adjusted R^2
Yield	Temp	4	199.1	0	99.25	98.75
Yield	Hold-Time	1	0.44	0.522	4.71	0
Yield	CO_2 Flow Rate	1	0.06	0.815	0.64	0
BET SA	Temp	4	44.35	0	96.73	94.55
BET SA	Hold-Time	1	0.25	0.629	2.7	0
BET SA	CO_2 Flow Rate	1	0.01	0.941	0.06	0
t-plot MA	Temp	4	37.66	0	96.17	93.62
t-plot MA	Hold-Time	1	0.48	0.504	5.11	0
t-plot MA	CO_2 Flow Rate	1	0	0.981	0.01	0
t-plot MV	Temp	4	25.7	0.001	94.49	90.81
t-plot MV	Hold-Time	1	0.06	0.805	0.71	0
t-plot MV	CO_2 Flow Rate	1	0	0.947	0.05	0
%MP	Temp	4	3.09	0.105	67.34	45.57
%MP	Hold-Time	1	0.13	0.725	1.44	0
%MP	CO_2 Flow Rate	1	0.81	0.391	8.27	0

Green shading indicates statistically significant results (P < 0.05).

The ANOVA analysis (ANOVA

Table 17) highlights the dominant role of temperature in determining biochar properties during CO_2 activation. Temperature significantly influenced yield ($p < 0.001$), BET surface area ($p < 0.001$), micropore area ($p < 0.001$), and micropore volume ($p < 0.001$), while hold-time and CO_2 flow rate had no statistically significant effects on any response variable. This suggests that within the tested conditions, structural changes in biochar were primarily driven by thermal activation rather than extended exposure or increased gas flow.

Yield showed a strong inverse relationship with temperature, where higher activation temperatures led to greater mass loss, likely due to increased carbon volatilisation.

However, hold-time and CO_2 flow rate did not significantly impact yield, indicating that prolonged heating or enhanced CO_2 diffusion had minimal additional effects on mass retention.

Surface area and microporosity also followed a temperature-dependent trend, with the highest BET surface areas and micropore formation observed at 800–850 °C. Lower temperatures (500–700 °C) resulted in minimal porosity, reinforcing the necessity of high temperatures for effective CO_2 activation. Despite this strong influence, some models exhibited relatively lower adjusted R^2 values, suggesting that additional unaccounted factors, such as heating rate or inherent biochar properties, could be influencing pore formation.

A key limitation of this approach is the imbalanced experimental design, where temperature had five levels, while hold-time and CO_2 flow rate were only tested at two levels each. This reduces the ability to detect interactions, which may explain why hold-time and flow rate showed no significant effects. Additionally, ANOVA treats variables as categorical, potentially oversimplifying nonlinear relationships that could be better captured through regression with continuous variables. Despite these limitations, the findings fromANOVA

Table 17 confirm that temperature is the primary driver of biochar activation under CO_2, with hold-time and flow rate playing minor roles within the tested range. Future studies could address these constraints by employing RSM or a full-factorial design to better capture complex interactions and nonlinear effects.

General Factorial regression

Table 18 - Reduced General Factorial Regression models for CO_2-activated biochars.

Response	Regression Equation	R^2 (%)	Adjusted R^2 (%)	Significant Terms
Yield	Yield = 14.515 + 10.475 Temp_500 + 8.385 Temp_700 - 9.010 Temp_800 + 0.885 Temp_850 - 10.735 Temp_900 + 0.571 CO_2 Flow Rate_100 - 0.571 CO_2 Flow Rate_600	99.72	99.43	Temp, CO_2 Flow Rate
BET SA	BET SA = 377.1 - 374.5 Temp_500 - 324.4 Temp_700 + 143.4 Temp_800 + 352.7 Temp_850 + 202.8 Temp_900	96.73	94.55	Temp
t-plot MA	t-plot MA = 295.7 - 288.7 Temp_500 - 250.4 Temp_700 + 67.8 Temp_800 + 322.0 Temp_850 + 149.3 Temp_900	96.17	93.62	Temp

t-plot MV	t-plot MV = 0.1361 - 0.1327 Temp_500 - 0.1129 Temp_700 + 0.0513 Temp_800 + 0.1013 Temp_850 + 0.0929 Temp_900	94.49	90.81	Temp
%MP	%MP = 35.2 - 35.2 Temp_500 - 13.5 Temp_700 + 34.6 Temp_800 + 49.4 Temp_850 - 35.2 Temp_900	67.34	45.57	Temp

The stepwise regression models effectively identified the key factors influencing biochar properties during CO_2 activation (Table 18). Across all responses, temperature emerged as the dominant variable, significantly affecting yield, BET surface area, micropore area, micropore volume, and microporosity percentage.

For yield, higher temperatures (≥800 °C) drastically reduced mass retention, which aligns with expectations that increased thermal degradation leads to greater carbon loss. The stepwise model retained both temperature and CO_2 flow rate as significant, though the positive effect of flow rate on yield is unexpected. Typically, higher CO_2 flow rates would enhance activation by facilitating volatile removal, potentially leading to further mass loss rather than retention. This anomaly may be due to experimental variability or secondary interactions not captured in the model, warranting further investigation.

BET surface area and micropore area followed a similar trend, where activation at 850 °C resulted in the highest surface area and pore development. The statistical analysis showed that temperature significantly contributed to the variance in BET surface area (R^2 = 96.73%) and micropore area (R^2 = 96.17%). Lower temperatures (500–700 °C) yielded minimal porosity, likely due to insufficient activation energy. Micropore volume also exhibited strong temperature dependence, with high temperatures enhancing pore formation (R^2 = 94.49%). While the 800–900 °C range maximised micropore development, the lower significance of hold-time and CO_2 flow rate suggests that the process is primarily governed by thermal energy rather than prolonged exposure or gas availability. For microporosity percentage, temperature remained the primary influence (R^2 = 67.34%), though the relatively lower adjusted R^2 suggests that additional factors, such as the intrinsic structure of the biochar or secondary reactions, may also play a role.

A key limitation of this study is the imbalanced experimental design, where temperature was tested at five levels, but hold-time and CO_2 flow rate were limited to two. This design constraint limited the detection of interaction effects and may have oversimplified complex relationships. Additionally, the exclusion of non-significant factors in stepwise regression

improves model interpretability but may overlook subtle contributions from secondary variables.

Overall, these findings confirm that temperature is the primary driver of porosity development in CO_2 activation, while hold-time and CO_2 flow rate have comparatively minor impacts.

General Linear Regression analysis

Discussion of General Linear Regression Results

The general linear regression models provide further insight into the impact of temperature, hold-time, and CO_2 flow rate on biochar properties during CO_2 activation (Table 19). Across all responses, temperature remained the most influential factor, reinforcing findings from previous statistical analyses.

Table 19 - Reduced general linear regression models for CO_2-activated biochars using continuous variables.

Response	Regression Equation	R^2 (%)	Adjusted R^2 (%)	Predicted R^2 (%)	Significant Terms
Yield	Yield = 69.6 - 0.0631 Temp - 0.0918 Hold-Time	85.25	79.35	64.89	Temp, Hold-Time
BET SA	BET SA = -1403 + 2.361 Temp	71.34	66.56	0	Temp
t-plot MA	t-plot MA = -1119 + 1.882 Temp	68.72	63.51	0	Temp
t-plot MV	t-plot MV = -0.455 + 0.000778 Temp	70.74	65.87	0	Temp
%MP	%MP = -436 + 0.611 Temp + 2.748 Hold-Time - 0.00315 Temp*Hold-Time	89.79	82.13	0	Temp, Hold-Time, Temp*Hold-Time

For yield, temperature had a significant negative correlation, with increasing temperature leading to a reduction in mass retention (R^2 = 85.25%). Hold-time also contributed significantly, with longer hold-times reducing yield further. However, CO_2 flow rate was not retained in the model, suggesting its effect on yield was negligible when considered in a continuous variable framework.

BET surface area and micropore area exhibited a strong temperature dependence (R^2 = 71.34% and 68.72%, respectively), indicating that higher temperatures enhance porosity development. However, the predictive R^2 values were low, suggesting that additional factors may contribute to surface area formation beyond temperature alone. For micropore volume, temperature remained the sole significant predictor (R^2 = 70.74%), further

reinforcing that thermal energy drives micropore formation. Neither hold-time nor CO_2 flow rate significantly contributed to micropore volume development, indicating that prolonged activation time or increased gas flow may not substantially alter pore structure. In the case of microporosity percentage, both temperature and hold-time emerged as significant factors (R^2 = 89.79%), with a notable interaction between the two. The inclusion of this interaction term suggests that the effect of temperature on microporosity is influenced by hold-time, likely due to extended exposure promoting structural rearrangements within the biochar matrix. However, the high variance inflation factor values indicate multicollinearity, which could impact model stability and interpretation. A key limitation of these models is the relatively low predictive R^2 values for some responses, particularly BET surface area and micropore area. This suggests that unaccounted variables, such as biochar precursor properties or reaction atmosphere conditions, may be influencing the results. Additionally, the presence of large residuals in certain models suggests that outlier effects may be influencing parameter estimates.

Overall, the general linear regression models confirm that temperature is the primary driver of biochar activation in CO_2 environments, while hold-time plays a secondary role in certain properties like microporosity. The findings also highlight potential limitations in modelling interactions between factors.

Fungal Activation Using Grey Oyster Mushrooms

Fungal activation using *Pleurotus ostreatus* (Grey Oyster mushrooms) was explored as a biological method to enhance biochar porosity. The mushrooms were cultivated on SCG, allowing mycelium growth to modify the biochar precursor before pyrolysis. This approach leverages enzymatic degradation and biological oxidation, potentially increasing pore development and altering the chemical structure of the resulting biochar.

Table 20 - Synthesis conditions and measured properties of fungal-activated biochars. Temperature and hold-time were varied to assess their effects on yield, BET surface area, and microporosity.

Biochar Identification	Final Temp (°C)	Hold-Time (mins)	Yield (%)	BET Surface Area (m^2/g)	t-plot Micropore Area (m^2/g)	t-plot Micropore Volume (cm^3/g)
EX75-500-15-GO	500	15	8.86	0.9995	4.2935	0.001519
EX77-900-15-GO	900	15	9.95	22.5043	24.2943	0.009025
EX78-500-2H-GO	500	120	10.44	2.3735	3.223	0.001222

EX79-700-15-GO	700	15	11.35	5.3459	10.7097	0.003872
EX80-900-2H-GO	900	120	11.87	2.7301	0.6988	0.000321
EX81-700-2H-GO	700	120	14.61	2.9536	18.5623	0.00622
EX82-700-15-GO	700	15	13.01	14.8915	17.2	0.006327
EX83-500-60-GO	500	60	21.09	8.0426	8.756	0.00323
EX84-900-60-GO	900	60	9.67	0.0037	0	0

Unlike chemical or gas activation methods, fungal activation does not allow direct control over activation intensity. Therefore, this study focused on two factors: temperature and hold-time, each at three levels. Temperature influences the degree of carbonisation and potential pore formation, while hold-time determines the extent of thermal modification.

The experimental matrix, shown in Table 20, outlines the conditions used in this study. The response variables measured include biochar yield, BET surface area, micropore area, and micropore volume, providing insight into the effectiveness of fungal pre-treatment in biochar activation.

This study aims to evaluate the impact of temperature and hold-time on fungal-activated biochar properties and compare the results with other activation methods. Statistical analyses, including ANOVA and regression modelling, will be performed to determine the significance of process variables and their influence on biochar characteristics.

ANOVA

Table 21 - ANOVA results for fungal-activated biochars.

Response	Factor	DF	F-Value	P-Value	R^2 (%)	Adjusted R^2 (%)
Yield	Temp	2	0.47	0.645	13.62	0
Yield	Hold-Time	2	1	0.421	25.07	0.1
BET SA	Temp	2	0.27	0.771	8.31	0
BET SA	Hold-Time	2	1.29	0.341	30.11	6.82
t-plot MA	Temp	2	1.11	0.389	27.03	2.7
t-plot MA	Hold-Time	2	1	0.42	25.08	0.11
t-plot MV	Temp	2	1.15	0.378	27.72	3.63
t-plot MV	Hold-Time	2	1.06	0.403	26.16	1.55

General Regression Analysis

Table 22 - General factorial regression models for fungal-activated biochars.

Response	Regression Equation	R^2 (%)	Adjusted R^2 (%)	Significant Terms
Yield	Yield = 13.00 + 0.47 Temp_500 + 2.03 Temp_700 - 2.50 Temp_900 - 2.71 Hold-Time_15 + 3.40 Hold-Time_60 - 0.69 Hold-Time_120	50.69	1.39	None
BET SA	BET SA = 5.84 - 2.03 Temp_500 - 0.55 Temp_700 + 2.58 Temp_900 + 5.24 Hold-Time_15 - 2.09 Hold-Time_60 - 3.15 Hold-Time_120	37.5	0	None
t-plot MA	t-plot MA = 9.02 - 3.60 Temp_500 + 4.29 Temp_700 - 0.69 Temp_900 + 4.03 Hold-Time_15 - 2.50 Hold-Time_60 - 1.53 Hold-Time_120	38.8	0	None
t-plot MV	t-plot MV = 0.00353 - 0.00154 Temp_500 + 0.00100 Temp_700 + 0.00054 Temp_900 + 0.00140 Hold-Time_15 - 0.00142 Hold-Time_60 + 0.00002 Hold-Time_120	41.62	0	None

General Linear Regression

Fungal activation using Grey Oyster mushrooms was investigated as a biological pre-treatment method for enhancing biochar porosity. However, statistical analysis revealed that neither temperature nor hold-time had a significant effect on any of the measured properties, including yield, BET surface area, micropore area, and micropore volume. ANOVA results (Table 21) showed high p-values across all responses, indicating no statistically significant relationships. Similarly, general regression and linear regression models demonstrated low R^2 values and failed to identify any significant terms. This suggests that fungal activation was not effective in substantially modifying biochar properties compared to conventional chemical or gas activation methods. While some variation in BET surface area and microporosity was observed, these changes were inconsistent and likely influenced by experimental variability rather than controlled process factors. The inability to regulate activation intensity in fungal treatment may have contributed to its limited impact.

Table 23 - General linear regression models for fungal-activated biochars using continuous variables.

Response	Regression Equation	R^2 (%)	Adjusted R^2 (%)	Significant Terms
Yield	Yield = 16.64 - 0.00742 Temp + 0.0144 Hold-Time	15.31	0	None
BET SA	BET SA = 3.3 + 0.0115 Temp - 0.0786 Hold-Time	33.27	11.03	None
t-plot MA	t-plot MA = 8.4 + 0.0073 Temp - 0.0631 Hold-Time	14.76	0	None

t-plot MV	t-plot MV = 0.00113 + 0.000005 Temp - 0.000016 Hold-Time	16.73	0	None

Overall, fungal activation using *Pleurotus ostreatus* showed minimal effectiveness in enhancing biochar porosity, and further studies may need to explore alternative biological pre-treatments or combinations with chemical activation to achieve meaningful structural modifications.

Potassium Oxalate Activation

This study investigated biochar activation using potassium oxalate (KOx) with temperature, hold-time, and KOx impregnation ratio as the primary factors. The initial design followed a full factorial approach at high and low levels for each factor. Additional experimental points, including centre points and axial extensions, were introduced to capture potential curvature and refine the response surface. This structure closely resembles a central composite design (CCD), allowing for the assessment of both linear and quadratic effects in the response variables. While the design enables response surface modelling, some limitations exist. The selection of additional points was influenced by practical constraints rather than strict statistical spacing, leading to deviations from a standard CCD. Additionally, the presence of missing data in some conditions may affect the robustness of model predictions. However, the dataset provides a broad coverage of activation conditions, allowing for regression analysis and response surface exploration to assess the influence of process parameters on yield, BET surface area, microporosity, and pore volume.

ANOVA

Table 24 - ANOVA results for KOx-activated biochars.

Response	Factor	DF	F-Value	P-Value	R^2 (%)	Adjusted R^2 (%)
Yield	Temp	6	1.84	0.187	52.54	24.06
Yield	Hold-Time	5	1.56	0.25	41.47	14.87
Yield	KOx:Biochar	3	1.05	0.405	19.45	0.86
BET SA	Temp	6	2.12	0.14	56	29.6
BET SA	Hold-Time	5	0.68	0.647	23.67	0
BET SA	KOx:Biochar	3	1.69	0.219	28.03	11.42
t-plot MA	Temp	6	2.13	0.139	56.13	29.8
t-plot MA	Hold-Time	5	0.82	0.562	27.08	0
t-plot MA	KOx:Biochar	3	1.63	0.231	27.34	10.58
t-plot MV	Temp	6	2.29	0.118	57.93	32.68
t-plot MV	Hold-Time	5	0.88	0.524	28.63	0

t-plot MV	KOx:Biochar	3	1.84	0.19	29.8	13.61
%MP	Temp	6	0.41	0.854	19.87	0
%MP	Hold-Time	5	1.85	0.183	45.69	21.01
%MP	KOx:Biochar	3	0.88	0.475	16.95	0

The results of the ANOVA analysis (Table 24) indicate that none of the tested factors—temperature, hold-time, or KOx:biochar ratio—were statistically significant in influencing biochar yield, BET surface area, micropore area, micropore volume, or microporosity percentage. Despite variations in BET surface area and microporosity across different conditions, the high variability in the data prevented clear trends from emerging. Notably, higher activation temperatures (900–1200 °C) generally corresponded to increased surface area and microporosity, but the lack of statistical significance suggests that other uncontrolled factors may have influenced the results.

Overall, while potassium oxalate activation produced some promising surface area and microporosity values, the lack of statistical significance in the process parameters suggests that the activation mechanism requires further investigation to optimise conditions effectively**.**

General Factorial Regression

The results presented in Table 26 indicate that temperature is the only significant factor influencing BET surface area, micropore area, and micropore volume, while yield and % microporosity showed no significant trends. The moderate R^2 values (56–58%) suggest that temperature affects porosity development, but the low adjusted R^2 values (30–33%)

Table 25 - Synthesis conditions and textural properties of KOx-activated biochars.

Biochar Identification	Final Temp (°C)	Hold-Time (mins)	Biochar:KOx Mass Ratio	Yield (%)	BET Surface Area (m^2/g)	t-plot Micropore Area (m^2/g)	t-plot Micropore Volume (cm^3/g)	% Micro-porosity
EX45-900-2H-KOx-1:1	900	120	KOx 1:1	15.41	1472	1232	0.477	83.6
EX46-500-2H-KOx-1:1	500	120	KOx 1:1	21.01	19	17	0.006	87.5
EX47-900-15-KOx-1:1	900	15	KOx 1:1	N/A	N/A	N/A	N/A	N/A
EX48-500-15-KOx-1:1	500	15	KOx 1:1	22.33	5	2	0.001	48.2
EX49-900-15-KOx-1:8	900	15	KOx 1:8	22.35	160	100	0.040	62.4
EX50-500-15-KOx-1:8	500	15	KOx 1:8	16.42	159	128	0	80
EX51-900-2H-KOx-1:8	900	120	KOx 1:8	0	N/A	N/A	N/A	N/A
EX52-500-2H-KOx-1:8	500	120	KOx 1:8	21.76	40	12	0.005	28.9
EX56-1000-2H-KOx-1:1	1000	120	KOx 1:1	12.66	1570	1082	0.431	68.9
EX45-900-2H-KOx-1:1	900	120	KOx 1:1	6.19	1579	851	0.352	53.9
EX58-1100-30-KOx-1:1	1100	30	KOx 1:1	19.75	774	732	0.278	94.5
EX59-700-68-KOx-1:4.5	700	68	KOx 1:4.5	22	504	450	0.172	89.2
EX60-1200-68-KOx-1:4.5	1200	68	KOx 1:4.5	14.94	1307	1061	0.413	81.2
EX61-400-68-KOx-1.45	400	68	KOx 1:4.5	21.22	19	7	0.003	36.1
EX62-700-5-KOx-1:4.5	700	5	KOx 1:4.5	27.23	5	0	0	0
EX63-700-68-KOx-1:4.5	700	68	KOx 1:4.5	22.42	558	509	0.194	91.2

EX64-700-180-KOx-1:4.5	700	180	KOx 1:4.5	18.83	847	758	0.290	89.4
EX65-700-68-KOx-1:10	700	68	KOx 1:10	23.89	599	497	0.192	82.8

indicate substantial unexplained variability, likely due to missing factors or experimental noise. The lack of significance for hold-time and KOx:Biochar ratio is unexpected, suggesting that these factors either have a minimal effect within the tested range or that their influence is nonlinear and not captured by the current model.

Table 26 - General factorial regression models for KOx-activated biochars.

Response	Regression Equation	R^2 (%)	Adjusted R^2 (%)	Significant Factors
Yield	Yield = 17.54 + 3.68 Temp_400 + 2.84 Temp_500 + 5.33 Temp_700 - 6.56 Temp_900 - 4.88 Temp_1000 + 2.21 Temp_1100 - 2.60 Temp_1200	52.54	24.06	None
BET Surface Area (BET SA)	BET SA = 719 - 699 Temp_400 - 663 Temp_500 - 216 Temp_700 + 84 Temp_900 + 851 Temp_1000 + 55 Temp_1100 + 588 Temp_1200	56.00	29.60	Temperature
Micropore Area (t-plot MA)	t-plot MA = 559 - 552 Temp_400 - 519 Temp_500 - 116 Temp_700 - 13 Temp_900 + 524 Temp_1000 + 173 Temp_1100 + 503 Temp_1200	56.13	29.80	Temperature
Micropore Volume (t-plot MV)	t-plot MV = 0.2164 - 0.214 Temp_400 - 0.2134 Temp_500 - 0.0468 Temp_700 + 0.0006 Temp_900 + 0.214 Temp_1000 + 0.062 Temp_1100 + 0.197 Temp_1200	57.93	32.68	Temperature
% Microporosity (%MP)	%MP = 66.1 - 30.0 Temp_400 - 4.9 Temp_500 + 4.5 Temp_700 - 16.1 Temp_900 + 2.9 Temp_1000 + 28.4 Temp_1100 + 15.1 Temp_1200	19.87	0.00	None

A key limitation is that interaction terms were removed due to insignificance, meaning no strong combined effects between temperature, hold-time, and KOx ratio were detected. While this is a standard outcome in statistical modelling, it suggests that temperature alone dictates porosity changes under these conditions. The imbalance in factor levels (e.g., seven levels for temperature but none for hold-time and KOx ratio in the final models) may have reduced the ability to detect significant effects for these variables. Additionally, the lack-of-fit in the BET SA model ($p = 0.011$) suggests that a simple linear approach may not fully capture the activation process. To address these limitations and gain deeper insight into the relationships between activation parameters and biochar properties, more advanced regression techniques, such as nonlinear regression or RSM, will be explored in the following section. These approaches will help refine the predictive models and improve understanding of how KOx activation conditions influence porosity development. While temperature significantly affects biochar porosity, the models fail to capture key activation

effects and have low predictive power. Future studies should refine experimental designs, improve statistical models, and explore alternative activation mechanisms to optimise KOx activation for CO_2 adsorption applications.

General Regression Analysis

Table 27 - General regression models incorporating linear, interaction, and quadratic terms for KOx-activated biochars.

Response	Regression Equation	Adjusted R^2 (%)	Significant Factors
Yield	Yield = 14.40 + 0.0123 Temp + 0.195 Hold-Time - 0.000349 Temp*Hold-Time	50.07	Temp*Hold-Time Interaction (p = 0.022)
BET SA	BET SA = -1132 + 1.622 Temp - 1.92 Hold-Time + 228.1 KOx:Biochar + 0.01353 Temp*Hold-Time* - *0.274 Temp*KOx:Biochar - 0.974 Hold-Time*KOx:Biochar	79.32	Temp (p = 0.054), KOx:Biochar (p = 0.034), Temp*KOx:Biochar (p = 0.037)
t-plot MA	t-plot MA = -1131 + 2.010 Temp + 2.53 Hold-Time + 122.9 KOx:Biochar - 0.215 Temp*KOx:Biochar	67.61	Temp (p = 0.001), Temp*KOx:Biochar (p = 0.064)
t-plot MV	t-plot MV = -0.434 + 0.000770 Temp + 0.001073 Hold-Time + 0.0413 KOx:Biochar - 0.000076 Temp*KOx:Biochar	70.02	Temp (p = 0.001), Hold-Time (p = 0.046)
%MP	%MP = -27 + 0.081 Temp + 1.26 Hold-Time + 5.9 KOx:Biochar - 0.000019 $Temp^2$ - 0.00049 $Hold\text{-}Time^2$ + 0.31 $KOx:Biochar^2$ - 0.00106 Temp*Hold-Time* - *0.0065 Temp*KOx:Biochar - 0.0857 Hold-Time*KOx:Biochar	0.00	None

The regression analysis identified temperature as the only significant factor affecting BET surface area, micropore area (t-plot MA), and micropore volume (t-plot MV). Neither hold-time nor the KOx:biochar ratio had a statistically significant impact on any response. Furthermore, no factors were significant for yield or %MP, suggesting that their variation may be driven by uncontrolled variables or nonlinear effects not captured by the models.

Although interaction and quadratic terms were explored, they did not substantially improve model performance, indicating that a more complex modelling approach may be needed. The relatively low adjusted R^2 values for most models suggest that additional process variables or nonlinear dependencies should be considered in future work. Response surface methods or mechanistic modelling could provide a more accurate description of KOx activation and its effects on biochar properties.

Compared to factorial regression, regression analysis offered better model performance by treating temperature as a continuous variable, allowing for a clearer identification of trends. The stepwise regression approach further improved model fit, particularly for BET

surface area and micropore-related responses. However, yield and %MP remained poorly explained, with no significant predictors emerging, reinforcing the need for alternative modelling approaches. While regression modelling improved factor identification, its limitations remain evident, particularly where model fit is weak. Further optimisation, incorporating additional variables or nonlinear modelling techniques, may be necessary to better capture the complexity of KOx activation and its influence on biochar properties.

Contour plots

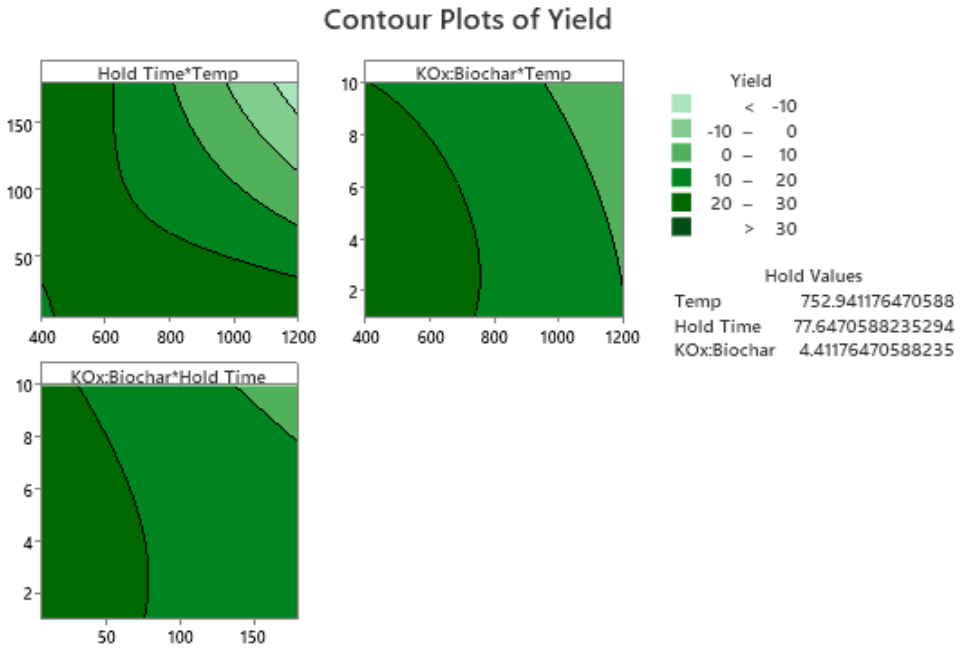

Figure 48 - Contour plots showing the effect of temperature, hold time, and KOx:biochar ratio on biochar yield.

The following contour plots (Figure 48 - Figure 52) visualise how temperature, hold time, and KOx:biochar ratio interact to influence key performance metrics. These visualisations provide a qualitative overview of trends across the experimental domain and help identify regions associated with favourable outcomes.

Figure 48 displays contour plots for **yield**. A clear gradient is visible, with higher yields observed at lower temperatures and shorter hold times. The smooth transitions across the surface suggest a systematic relationship between processing conditions and char mass recovery. KOx:biochar ratio also shows a modest influence, with yield decreasing slightly as reagent dosage increases.

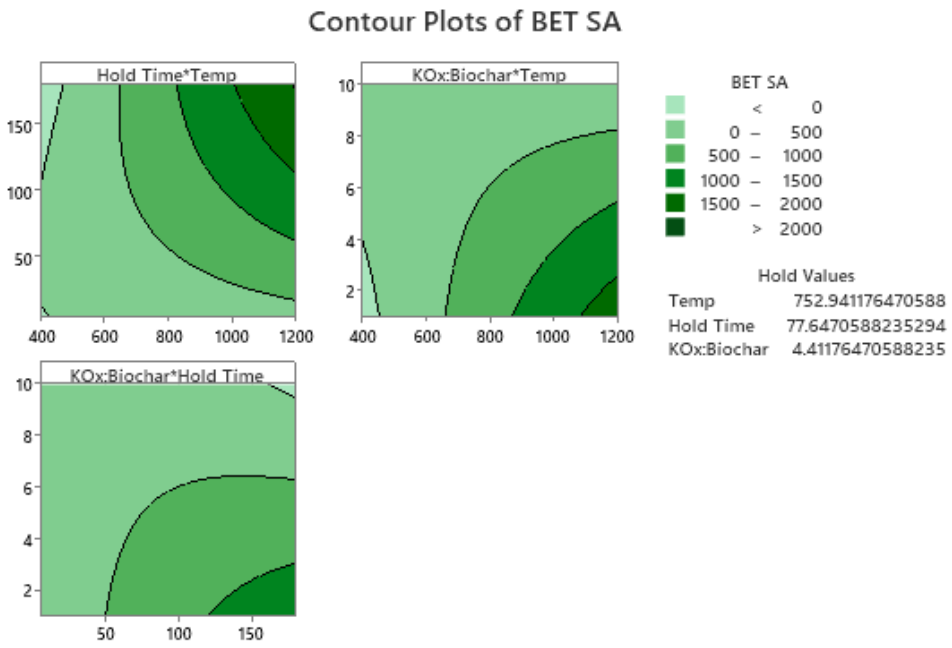

Figure 49 - Contour plots showing the effect of activation parameters on BET surface area.

Figure 49 presents the contour plots for **BET surface area**. The results show a consistent increase in surface area with temperature, particularly in the upper temperature range. While some enhancement is also observed with extended hold time and higher KOx dosage, the strongest effect appears to stem from thermal input. No distinct peak is visible, suggesting that the optimal surface area may lie beyond the current experimental window.

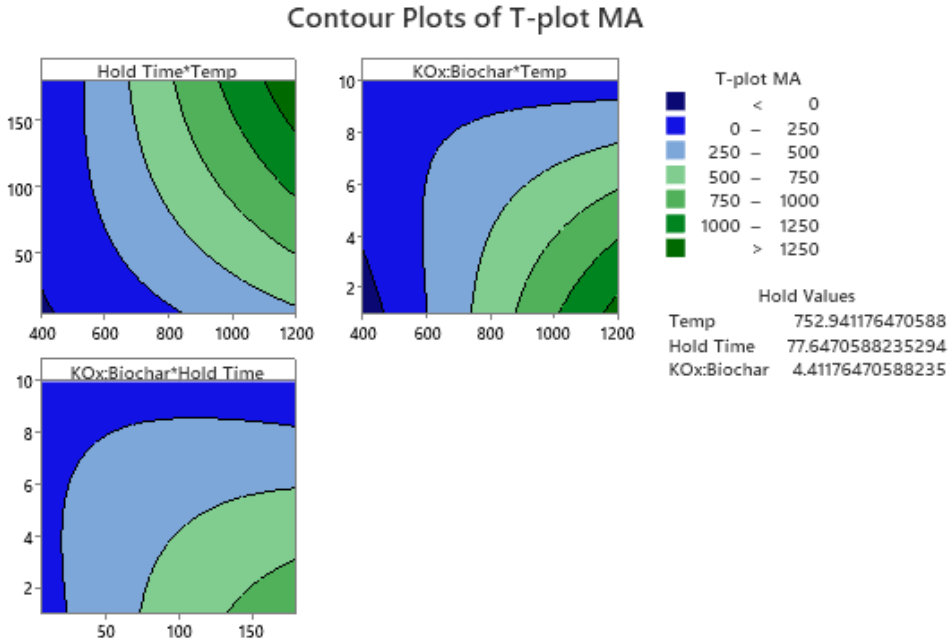

Figure 50 - Contour plots showing the influence of synthesis parameters on t-plot micropore area (MA).

Figure 50 shows the response surfaces for **t-plot micropore area (MA)**. The pattern broadly follows that of BET surface area, with a progressive increase across the temperature axis. This suggests that micropore development is primarily driven by temperature, with only minor modulation by hold time or KOx ratio.

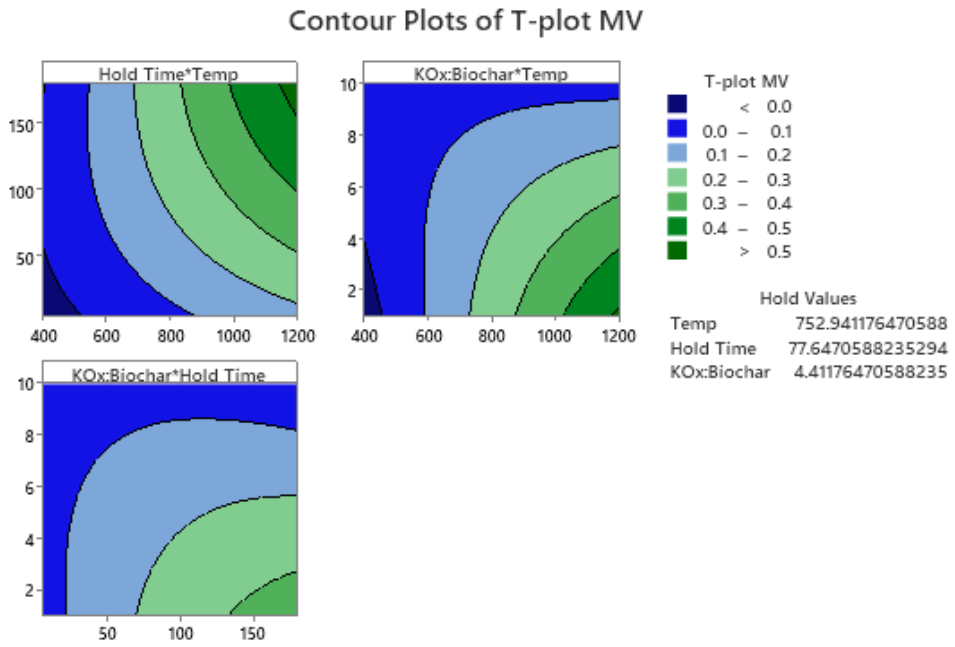

Figure 51 - Contour plots illustrating the dependence of t-plot micropore volume (MV) on activation conditions.

Figure 51 illustrates the trends for **t-plot micropore volume (MV)**. The plots show a similar shape to the micropore area, reinforcing the observation that temperature plays a key role in promoting microporosity. The gradual contours and consistent gradients imply that micropore formation increases steadily within the tested conditions.

Figure 52 presents the contour plots for **percentage microporosity (%MP)**. Unlike the previous responses, these plots show less defined patterns. While some regions of higher microporosity are visible, particularly at intermediate KOx ratios and hold times, the overall surfaces appear irregular. This may indicate that %MP is influenced by more complex or uncontrolled factors, or that the response is less sensitive within the tested range.

Overall, these plots illustrate coherent trends for most responses, particularly yield and surface area metrics, and offer a useful framework for identifying regions of interest for future optimisation.

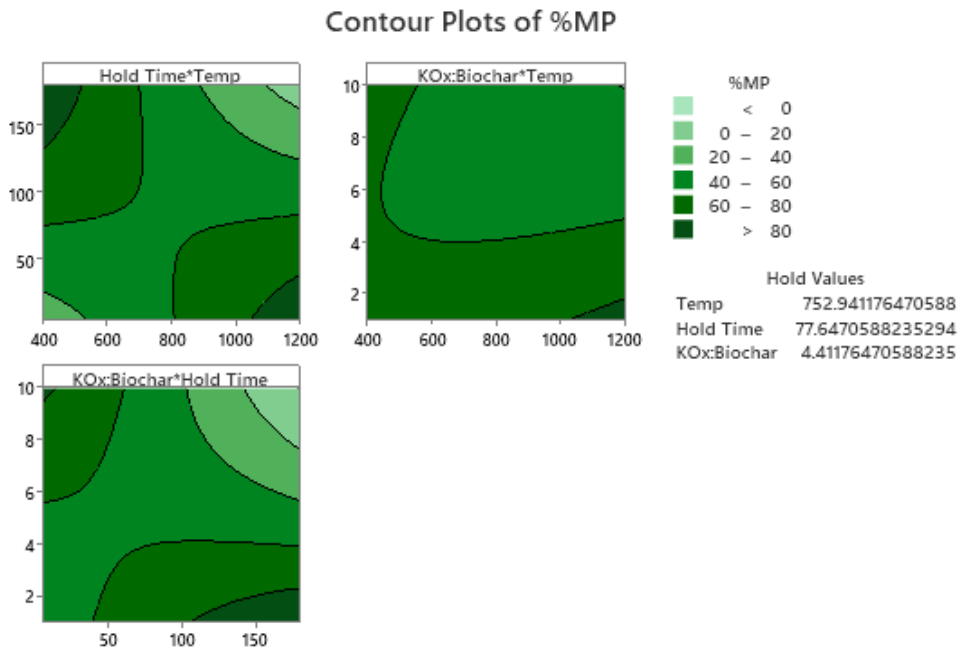

Figure 52 - Contour plots of percentage microporosity (%MP) in response to temperature, hold time, and KOx:biochar ratio.

Comparative Analysis of Activation Methods

Yield Comparison

The influence of activation method on biochar yield is summarised in Table 7, ANOVA

Table 17, Table 21, and Table 26. In general, the activation process markedly affected mass retention, with substantial differences observed between physical, chemical, and biological activation routes. Non-activated biochars pyrolysed under inert atmosphere at 500–900 °C exhibited yields between 21.8% and 24.2%, reflecting the mass loss associated with initial devolatilisation. These values establish a baseline against which the effects of post-pyrolysis activation can be assessed.

CO_2 activation led to moderate yield reductions at higher temperatures. Samples activated at 500–700 °C retained relatively high yields (21–25%), comparable to non-activated materials. However, activation at 800–900 °C resulted in significantly lower yields (approximately 4–6%), attributable to increased carbon burn-off through gasification reactions at elevated temperatures. This behaviour is consistent with the known tendency of CO_2 activation to selectively etch carbonaceous structures, with the extent of mass loss strongly dependent on activation temperature.

KOH activation resulted in more pronounced yield reductions, particularly under conditions of high reagent loading and extended hold-times. Samples activated with a 1:1 KOH:biochar

mass ratio exhibited yields ranging from 11% to 21%, whereas activation at a 1:8 ratio further reduced yields, with some experiments yielding as little as approximately 1.4%. It should be noted that these reported yields pertain solely to the activation step; when accounting for the initial pre-pyrolysis yield (~23%), the effective overall yield is considerably lower. Consequently, KOH activation imposes a significant penalty on material recovery, particularly under aggressive activation conditions. This outcome reflects the extensive carbon etching and volatilisation associated with KOH chemical activation.

Potassium oxalate (KOx) activation exhibited more variable effects on yield. For direct KOx activation (i.e., without pre-pyrolysis), yields were generally higher than those observed for KOH activation, ranging from approximately 14% to 22% depending on temperature and reagent ratio. However, for samples subjected to a two-step pre-pyrolysis and KOx activation process, the reported activation yields are artificially inflated due to exclusion of mass losses incurred during the initial pyrolysis step. Correcting for the pre-pyrolysis yield (~23%) indicates that the effective overall yields for these samples are approximately 4–5 times lower, making the process less competitive in practical terms. Nonetheless, KOx activation appears to be a less aggressive chemical activation strategy than KOH.

Fungal activation via *Pleurotus ostreatus* treatment led to relatively low yields overall, ranging from 8.9% to 21.1%, despite the biological nature of the pre-treatment. These values are broadly comparable to those of non-activated biochars and suggest that fungal pre-treatment does not substantially mitigate mass loss during subsequent pyrolysis. In some cases, fungal treatment even appeared to exacerbate yield loss, potentially due to partial degradation of the biomass matrix during the biological growth phase.

Yield comparisons indicate that CO_2 activation at moderate temperatures offers the best balance between preserving material mass and enhancing porosity. KOH activation, while effective at developing high surface areas, imposes substantial yield penalties, particularly at high KOH loadings. KOx activation represents an intermediate case, providing less aggressive activation than KOH but necessitating careful consideration of the overall mass balance, especially for two-step processes. Fungal activation does not appear advantageous with respect to yield preservation.

Surface Area and Porosity

The activation method used in the synthesis of the biochar samples had a pronounced effect on the development of surface area and microporosity in the SCG-derived biochars.

Non-activated samples exhibited negligible surface areas (<3 m^2/g) and no measurable microporosity, attributable to the high volatile retention and limited structural reorganisation during pyrolysis under inert atmosphere.

CO_2 activation moderately enhanced surface area and micropore development, particularly at elevated temperatures (850 °C) and with prolonged hold times. BET surface areas up to 736–737 m^2/g and micropore volumes of ~0.236 cm^3/g were achieved, corresponding to microporosities exceeding 84%. The activation mechanism involves the endothermic reaction between carbon and CO_2 ($C + CO_2 \rightarrow 2CO$), selectively etching the carbon matrix to create micropores. However, due to the relatively slow kinetics of this reaction and its strong dependence on temperature, the enhancement of porosity remained moderate compared to chemical activation routes.

KOH activation resulted in the highest surface areas observed, exceeding 3000 m^2/g in certain samples (e.g., sample EX30-800-2H-KOH-1:8 and sample EX31-900-2H-KOH-1:8 - EX31-900-2H-KOH-1:8). The activation mechanism involves several reactions, including dehydration, carbon oxidation, and the formation of metallic potassium, which intercalates into the carbon lattice. Upon washing, the embedded potassium leaves behind an extensively developed pore network. However, despite the high BET surface areas, many KOH-activated samples exhibited no measurable microporosity, indicating that activation under aggressive conditions (e.g., high KOH loadings, prolonged times) promotes the formation of mesopores and macropores at the expense of micropores. This is consistent with reports that excessive KOH activation leads to structural collapse or widening of initial micropores.

Potassium oxalate (KOx) activation also produced substantial surface area development, with BET surface areas reaching up to 1579 m^2/g (sample EX45-900-2H-KOx-1:1. Unlike KOH, KOx decomposes upon heating to release CO and CO_2 gases, promoting a combination of mild chemical etching and gasification. This resulted in materials with high microporosity (typically 80–90%) and balanced textural properties. Compared to KOH activation, KOx activation achieved slightly lower maximum surface areas but preserved microporosity to a greater extent, suggesting that KOx offers a gentler activation environment conducive to micropore retention.

Fungal (GO) activation proved comparatively ineffective, with BET surface areas remaining below 23 m^2/g and micropore volumes under 0.01 cm^3/g. Although fungal pre-treatment

partially degrades hemicellulose and lignin components, the subsequent pyrolysis does not significantly enhance porosity. These findings indicate that biological pre-treatment alone is insufficient to meaningfully modify the carbon matrix for the purposes of high surface area generation.

In direct comparison, KOH activation was most effective at producing extreme surface areas but often at the expense of microporosity. KOx activation offered a more balanced outcome, generating both high surface area and a high proportion of micropores. CO_2 activation was less aggressive but allowed for controlled micropore development with moderate surface area gains, while biological activation had minimal effect. Overall, chemical activation routes clearly outperformed physical and biological treatments in terms of textural enhancement, but trade-offs between surface area, micropore fraction, and material stability must be carefully considered.

Factor Significance

The statistical analyses conducted across the different activation methods reveal important contrasts in factor significance, reflecting fundamental differences in the underlying activation mechanisms.

KOH activation was dominantly governed by the biochar:KOH mass ratio. General factorial and linear regression consistently identified the activation ratio as the primary significant factor influencing micropore area, micropore volume, and microporosity percentage ($p < 0.01$). A higher KOH loading promoted extensive pore development, although excessive reagent quantities shifted the pore distribution towards mesoporosity and macroporosity, as evidenced by the decrease in microporosity. Hold-time was significant for yield ($p = 0.012$), with prolonged activation leading to greater mass loss due to enhanced carbon volatilisation. Temperature, surprisingly, did not emerge as a significant factor in yield or surface area development, suggesting that within the tested thermal window (500–1000 °C), chemical effects dominated over purely thermal processes. This highlights the aggressive and chemically driven nature of KOH activation, wherein reagent loading outweighs thermal activation effects.

In CO_2 activation, temperature emerged as the unequivocally dominant factor across all textural properties, with strong statistical significance ($p < 0.001$) for yield, BET surface area, micropore area, and micropore volume. Neither hold-time nor CO_2 flow rate had significant effects within the tested ranges, indicating that CO_2 activation is primarily

thermally controlled. The activation process relies on the endothermic Boudouard reaction ($C + CO_2 \rightarrow 2CO$), which proceeds slowly at moderate temperatures but becomes highly efficient at ≥800 °C. This explains the sharp increases in surface area and microporosity observed with rising temperature, and the negligible influence of residence time or gas flow rate. Unlike KOH activation, the CO_2 route requires precise thermal management to optimise porosity.

For fungal (GO) activation, no factors were statistically significant for any of the measured responses. Both temperature and hold-time had negligible influence, and regression models exhibited low explanatory power (adjusted $R^2 \approx 0\%$). This outcome reflects the weak activation potential of biological pre-treatment alone. The fungal modification of biomass composition, primarily through partial degradation of hemicellulose and lignin, was insufficient to enhance the carbon matrix during subsequent pyrolysis, confirming that fungal activation is not a viable method for significant porosity development under the conditions tested.

Potassium oxalate (KOx) activation demonstrated a more complex and nuanced behaviour. Temperature was moderately significant for BET surface area, micropore area, and micropore volume ($p \approx 0.1–0.15$), but no factors were highly significant at the 95% confidence level. General regression analysis suggested that interactions between temperature and KOx ratio may contribute to variations in porosity, albeit weakly. The decomposition of KOx into CO and CO_2 during pyrolysis likely promotes simultaneous mild gasification and chemical etching, resulting in less aggressive but more micropore-preserving activation than KOH. However, the relatively high variability and moderate model fits (adjusted $R^2 \approx 30–50\%$) indicate that further optimisation is necessary to robustly model the process. Compared to KOH, KOx activation appears more sensitive to subtle variations in process conditions.

The factor significance trends can be summarised as follows:

- KOH activation: Mass ratio dominates; temperature less critical; chemical effects prevail.
- CO_2 activation: Temperature dominates; hold-time and flow rate negligible; thermally driven activation.
- Fungal activation: No significant factors; limited impact on porosity.

- KOx activation: Temperature moderately significant; activation less aggressive, greater microporosity preservation; more complex factor interactions likely.

These distinctions highlight fundamental differences in activation mechanisms: chemical activation (KOH, KOx) is highly dependent on reagent dynamics and carbon-reactive chemistry, whereas physical activation (CO_2) is primarily governed by thermal energy input. Biological activation appears ineffective for pore development without subsequent chemical or physical treatment.

Overall, optimising SCG-derived biochar for CO_2 capture requires careful tuning of activation parameters specific to each method, balancing surface area enhancement against yield loss and micropore preservation.

Advantages and Limitations of the Activation Methods and Experimental Design

The comparative analysis of activation methods highlights several important advantages and limitations relevant to the development of SCG-derived biochars for CO_2 capture. Foremost among the advantages is the performance of CO_2 activation as a one-step**,** physically activated process. Unlike chemical activation methods such as KOH or potassium oxalate, CO_2 activation requires no chemical impregnation, no subsequent washing steps, and minimal reagent costs. It can be directly integrated with pyrolysis operations, offering a simple, continuous, and scalable route to porous biochar production. The ability to develop significant BET surface areas (over 700 m^2/g) and high microporosity (~84%) solely through thermal activation underscores its practicality for large-scale applications. Moreover, CO_2 activation generates no secondary waste streams and aligns well with sustainable manufacturing principles, positioning it as the most viable industrial strategy among the activation methods evaluated.

However, the current experimental approach is subject to important limitations. The statistical analysis was based solely on textural parameters—specifically, BET surface area, micropore area, micropore volume, and microporosity percentage—as the primary predictors of material performance. While these properties are strongly correlated with physical CO_2 uptake, they do not capture all relevant adsorption mechanisms. As will be discussed in subsequent chapters, the presence and nature of nitrogen surface functionalities**,** developed during pyrolysis and activation, significantly contribute to

enhancing CO_2 adsorption at low pressures through chemisorptive or acid-base interactions.

The exclusion of nitrogen surface functionality from the statistical framework restricts the ability to fully explain the observed adsorption behaviours. Although the statistical analysis effectively examined how reaction conditions influenced textural development, it did not account for chemical contributions due to the absence of CHN elemental analysis, X-ray Photoelectron Spectroscopy (XPS) data, or direct CO_2 adsorption measurements. As a result, the model evaluated the effects of reaction conditions on porosity in isolation, providing only a partial evaluation of the factors that contribute to CO_2 adsorption. This limitation arose not from a conceptual oversight but from budgetary and equipment constraints that precluded broader characterisation. While the emphasis on porosity metrics was justified given available resources, it necessarily yields an incomplete understanding of biochar performance, particularly under practical application conditions.

Thus, while the present study establishes valuable insights into activation effects on textural properties, it represents only part of the broader picture required for the comprehensive optimisation of SCG-derived biochars for post-combustion CO_2 capture applications.

Chapter 8. Characterisation of Biochar Samples

This chapter presents the comprehensive characterisation of SCG and derived biochar samples under various activation methods and pyrolysis conditions. The characterisation techniques employed include proximate analysis, ultimate analysis, Fourier Transform Infrared Spectroscopy (FTIR), X-ray Photoelectron Spectroscopy (XPS) and N_2 adsorption analysis. The objective is to elucidate the physical and chemical properties of the biochar samples, examining factors such as surface area, pore structure, elemental composition, and functional groups. These insights are critical for assessing the potential use of biochar in CO_2 adsorption. TGA proximate analysis curves can be found in Appendix D: Thermogravimetric Analysis (TGA) Proximate Analysis Curves

8.1. Proximate Analysis

Table 28 - Proximate Analysis Results

Sample	Final Temp (°C)	Hold Time (mins)	Activating method	Moisture (wt%)	Volatile matter (wt%)	Ash (wt%)	Fixed Carbon (wt%)
SCG	N/A	N/A	N/A	0.66	80.03	0.75	18.57
EX4-N2-500-2H	500	120	N/A	4.44	22.59	4.77	68.19
EX5-N2-700-2H	700	120	N/A	3.82	16.27	5.43	74.49
EX23-800-2H-KOH-1:1	800	120	KOH 1:1	7.03	18.23	2.53	72.2
EX25-900-2H-KOH-1:1	900	120	KOH 1:1	9.41	14.85	2.86	72.88
EX31-900-2H-KOH-1:8	900	120	KOH 1:8	3.59	23.47	3.77	69.18
EX42-700-15-KOH-1:1	700	15	KOH 1:1	15.53	22.1	6.09	56.28
EX37-850-15-CO_2-600	850	120	CO_2	7.23	22.6	7.33	62.84
EX53-900-2H-KOX-1:1 (pre-pyrolysed)	900	120	KOx 1:1	11.84	14.12	1.7	72.34
EX81-700-2H-GO	700	120	Fungal	7.01	26.09	20.39	46.51

The thermal analysis of SCG and derived biochar samples as seen in Table 28 reveals a multi-stage decomposition process, with distinct transitions at key temperatures. The initial moisture evaporation stage at ~120 °C ensures the removal of physically bound water, which is critical for further thermal treatments. The decomposition of volatile matter at ~920 °C indicates the presence of significant organic content, which is vital for understanding the behaviour of the material during pyrolysis or other high-temperature applications. Finally, the combustion of fixed carbon at ~820 °C under an air environment underscores the potential of biochars as carbonaceous adsorbents post-pyrolysis.

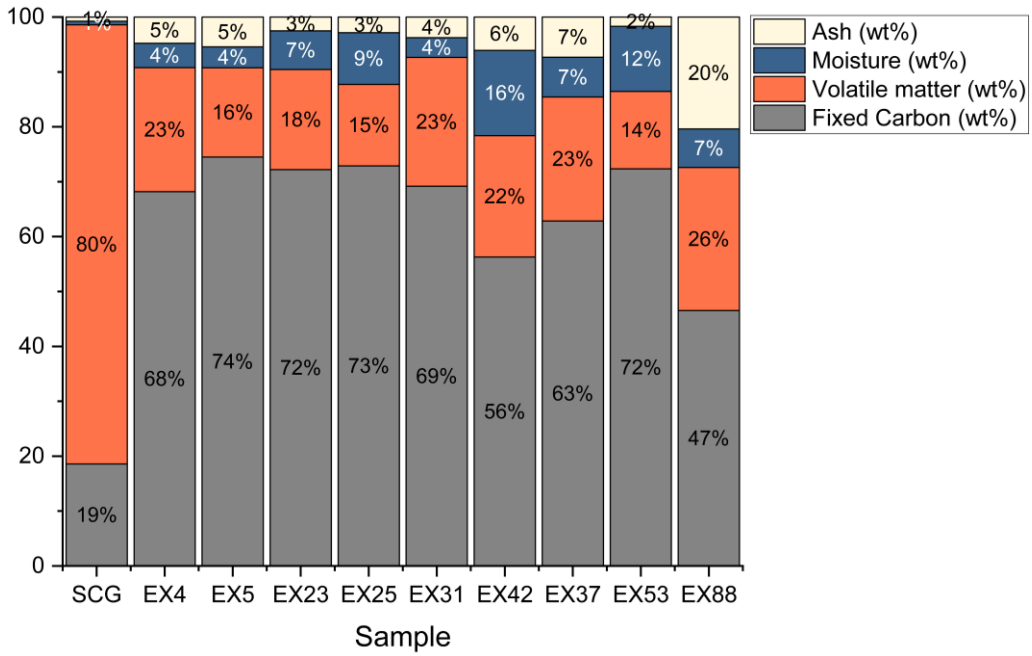

Figure 53 - Proximate composition of SCG and derived biochar samples, showing the distribution of fixed carbon, volatile matter, moisture, and ash contents.

The bar chart in Figure 53 provides a visual representation of the data presented in Table 28. This chart is designed to offer an intuitive comparison of the moisture, volatile matter, ash, and fixed carbon contents across the various biochar samples, highlighting the differences and trends more clearly than the tabulated data alone. As the final hold temperature increases during the production of our chars, we should see a decrease in the proportion of volatile matter, with a corresponding increase in fixed carbon and ash percentage. However, during the production of our chemically activated samples, the washing process results in a lower than expected ash content. This washing process removes some inorganic components, which can explain the lower ash content observed in these samples despite the higher final hold temperatures.

The SCG exhibited low ash and relatively high fixed carbon contents, consistent with literature values. This composition supports their suitability as a feedstock for biochar production, where high fixed carbon enhances adsorption potential and low ash content favours carbon yield. In this study, the raw SCG contained 0.75 wt% ash and 80.03 wt% volatile matter, closely matching reported values of 0.9 wt% and 81.2 wt% [340]. The fixed carbon content (18.57 wt%) was slightly higher than literature values (~14.6 wt%), likely due to variations in feedstock composition or processing. Combined with the abundance of SCG as a waste stream, these properties reinforce its potential as an economical and sustainable precursor for high-performance biochar production.

Biochars produced at higher temperatures showed the expected increase in fixed carbon and decrease in volatile matter. For example, EX5-N2-700-2H (700 °C) reached 74.49 wt% fixed carbon, surpassing the 64.3 wt% reported at 600 °C [340], with lower ash content. Chemically activated samples maintained high fixed carbon and low ash, likely due to post-treatment washing, in contrast to the ash accumulation typically seen at high pyrolysis temperatures.[167]

Compared to wood-derived biochars, which show variable ash content (0.2-6.7%) and generally lower fixed carbon contents (14-21%) [344,345], SCG biochars demonstrate comparable or superior carbon retention, supporting their suitability for high-performance adsorbent applications.

Samples EX42-700-15-KOH-1:1 and EX81-700-2H-GO exhibited compositional values that deviated significantly from expected trends. EX42-700-15-KOH-1:1 showed an unusually high moisture content (15.53%) and low fixed carbon (56.28%) despite being produced at 700 °C with KOH activation, while EX81-700-2H-GO displayed an atypically high ash content (20.39%) and low fixed carbon content (46.51%). These anomalies are inconsistent with the general behaviour observed across comparable samples and are likely the result of sample handling or analytical error. The affected results were retained in the dataset as the samples were not central to the study's key findings. Their influence on broader conclusions is minimal, and they were excluded from comparative or statistical analyses where appropriate.

8.2. Ultimate Analysis

Table 29 - Ultimate analysis results

Sample	Final Temp (°C)	Hold Time (mins)	Activating method	% Nitrogen	% Carbon	% Hydrogen
SCG	N/A	N/A	N/A	2.6	50.6	7.12
SCG	N/A	N/A	N/A	2.56	50.28	7.01
MSCG	N/A	N/A	N/A	3.38	40.39	5.28
MSCG	N/A	N/A	N/A	3.59	42.51	5.77
EX4-N2-500-2H	500	120	N/A	3.89	72.62	3.29
EX4-N2-500-2H	500	120	N/A	3.92	72.56	3.13
EX5-N2-700-2H	700	120	N/A	3.51	74.98	1.69
EX5-N2-700-2H	700	120	N/A	3.55	74.83	1.68
EX6-N2-900-2H	900	120	N/A	3.35	75.73	1.2
EX6-N2-900-2H	900	120	N/A	3.19	75.37	1.1
EX23-800-2H-KOH-1:1	800	120	KOH 1:1	0.88	79.54	0.99
EX23-800-2H-KOH-1:1	800	120	KOH 1:1	0.93	79.36	1.07
EX25-900-2H-KOH-1:1	900	120	KOH 1:1	0.69	73.67	1.1
EX25-900-2H-KOH-1:1	900	120	KOH 1:1	0.77	74.59	1.34
EX31-900-2H-KOH-1:8	900	120	KOH 1:8	0.71	84.93	1.17
EX31-900-2H-KOH-1:8	900	120	KOH 1:8	0.63	84.39	1
EX37-850-15-CO_2-600	850	15	CO_2 600	4.05	63.46	1.35
EX37-850-15-CO_2-600	850	15	CO_2 600	4.17	63.51	1.19
EX38-850-15-CO_2-100	850	15	CO_2 100	4.01	64.79	1.21
EX38-850-15-CO_2-100	850	15	CO_2 100	3.93	65.75	2.31

Sample	Final Temp (°C)	Hold Time (mins)	Activating method	% Nitrogen	% Carbon	% Hydrogen
EX42-700-15-KOH-1:1	700	15	KOH 1:1	2.42	71.69	2.27
EX42-700-15-KOH-1:1	700	15	KOH 1:1	2.56	72.23	2.37
EX45-900-2H-KOX-1:1	900	120	KOx 1:1	0.66	76.93	1.87
EX45-900-2H-KOX-1:1	900	120	KOx 1:1	0.63	75.56	1.9
EX53-900-2H-KOX-1:1 (pre-pyrolysed)	900	120	KOx 1:1	0.84	77.34	1.61
EX53-900-2H-KOX-1:1 (pre-pyrolysed)	900	120	KOx 1:1	0.84	76.87	1.65
EX77-900-15-GO	900	15	Fungal	3.33	65.65	1.47
EX77-900-15-GO	900	15	Fungal	3.34	66.11	1.61

All samples underwent elemental analysis to determine the compositional percentages of carbon, hydrogen, and nitrogen (CHN), which allowed us to assess the incorporation of nitrogen into the final biochar structure. The results, presented in Table 29, illustrate the impact of various activation methods on the elemental composition of the biochars. To ensure the reliability and accuracy of the data, duplicates of each sample were analysed. This approach helps to account for any variability and provides more robust data. Samples chosen for further characterisation were selected based on their BET surface area and micropore area, focusing on the highest-performing samples from each activation method category. However, due to financial constraints, not all samples could be characterised, which limits our ability to fully explore all trends in the data.

The trends observed in carbon, hydrogen, and nitrogen content across SCG-derived biochars are broadly consistent with literature reports on lignocellulosic biomass pyrolysis.

As pyrolysis severity increases, carbon content rises while hydrogen and nitrogen decline, reflecting progressive devolatilisation and aromatisation of the carbon matrix [36,239,340]. In this study, carbon contents above 84 wt% (e.g. EX31-900-2H-KOH-1:8) exceed those reported for SCG pyrolysed at 600 °C (81.5 wt%) [340], while hydrogen contents fall to ~1%, comparable with values observed at similar or higher pyrolysis temperatures [36,346]. These changes correspond to enhanced aromaticity and thermal stability, which are favourable for CO_2 adsorption performance. [65]

The nitrogen content was strongly influenced by activation strategy. Chemically activated samples (e.g. EX23-800-2H-KOH-1:1, EX53-900-2H-KOX-1:1 (pre-pyrolysed) exhibited substantially lower nitrogen content (<1 wt%), consistent with the removal of N-functional groups during aggressive KOH or KOx activation and subsequent washing. Similar nitrogen depletion has been reported in KOH- and H_3PO_4-activated wood chars [36,166,345]. In contrast, CO_2-activated (EX37-850-15-CO_2-600, ~4.1 wt%) and fungal-activated (EX77-900-15-GO, ~3.3 wt%) samples retained higher nitrogen content, comparable to nitrogen-rich biochars derived from proteinaceous precursors such as microalgae, chitosan, and zein, which can reach 4–13 wt% N depending on the feedstock and pyrolysis severity [35,346]. These nitrogen-rich biochars are especially relevant to CO_2 capture applications, where basic nitrogen functionalities (e.g. pyridinic, pyrrolic) enhance adsorption affinity under post-combustion conditions.[35]

8.2.1. Comparison of SCG and MSCG Results

The elemental analysis results reveal that MSCG (mycelium-spent coffee grounds) samples have a higher nitrogen content compared to SCG samples. Specifically, MSCG samples exhibit nitrogen percentages of 3.38% and 3.59%, whereas SCG samples have nitrogen percentages of 2.6% and 2.56%. This increase in nitrogen content is attributed to the metabolic activity of the mycelium, which breaks down and utilises the coffee grounds as a food source, releasing CO_2 in the process. This activity reduces the carbon content, as evidenced by the lower carbon percentages in MSCG samples (40.39% and 42.51%) compared to SCG samples (50.6% and 50.28%). Consequently, as the carbon content decreases, the relative proportion of nitrogen in the biomass increases, resulting in higher nitrogen content in the final biochar.

The higher nitrogen content in MSCG-derived biochars enhances their value as soil amendments or fertilisers, providing an additional nutrient source for plants. Moreover, the

increased nitrogen content may improve the adsorption properties of the biochar, particularly for CO_2, which is the focus of our study.

Using SCG as a substrate for mushroom cultivation before converting them to biochar also offers several other benefits. Although the increase in surface area of the resulting chars was small, it still enhances their physical properties. This process extracts more utility from the waste stream, adding both economic and calorific value. Additionally, it serves as a green, chemical-free method of nitrogen doping and enriching the feedstock, providing an environmentally friendly approach to managing coffee waste and turning it into a valuable resource for biochar production.

The results suggest that using SCG for mushroom cultivation is a beneficial strategy for producing nitrogen-enriched biochar. This approach not only adds value to the waste material but also enhances the properties of the final product, making it a sustainable and economically viable method. Further investigation could explore the specific mechanisms by which fungal growth influences biochar properties and how different fungal species or growth conditions might optimise this process. This could lead to improved methods for producing high-quality biochars from various biomass feedstocks, enhancing their effectiveness for various applications, including CO_2 capture.

8.2.2. Comparison of Non-activated Samples

The elemental analysis of non-activated samples reveals significant trends in the composition of nitrogen, hydrogen, and carbon as the final hold temperature increases. Specifically, we observe a decrease in both nitrogen (see Appendix H: Correlation of Synthesis Parameter Vs Nitrogen Content and hydrogen content with increasing temperature, while the carbon content correspondingly increases. These findings are corroborated by our TGA results, which confirm an increase in fixed carbon at higher temperatures.

As the final hold temperature rises, the thermal decomposition of organic matter in the biochar increases. This process, known as pyrolysis, results in the volatilisation of nitrogen- and hydrogen-containing compounds, leading to a reduction in their content within the biochar. For instance, at 500 °C, sample EX4-N2-500-2H shows an average nitrogen content of 3.91 % and hydrogen content of 3.21 %. However, at 900 °C, sample EX6-N2-900-2H shows reduced average nitrogen and hydrogen contents of 3.27 % and 1.15 %, respectively. Concurrently, the carbon content of the biochar increases as temperature rises due to the

relative concentration of carbon following volatile loss. The average carbon content increases from 72.59 % at 500 °C to 75.55 % at 900 °C.

These trends highlight the effect of temperature on the thermal stability and composition of biochar. Higher temperatures lead to more extensive carbonisation, resulting in biochars with higher fixed carbon and lower nitrogen and hydrogen contents. This behaviour is typical for biochars and indicates an increased degree of aromaticity and structural stability at higher pyrolysis temperatures. Understanding these thermal effects is crucial for optimising biochar production for specific applications. Biochars with higher carbon content and lower volatile matter are typically more stable and resistant to degradation, making them suitable for long-term carbon sequestration. On the other hand, biochars with higher nitrogen content and surface functionalities are more beneficial for CO_2 adsorption applications.

8.2.3. Comparison of Activated samples

The elemental analysis of chemically activated samples reveals a distinct trend of lower nitrogen content when compared to non-activated, CO_2 activated, and fungal activated samples. This observation can be attributed to several potential reasons inherent from the chemical activation process. Considering the chemically activated samples, particularly those treated with potassium hydroxide (KOH) and potassium oxalate (KOx), these consistently show significantly lower nitrogen percentages. For instance, KOH-activated samples such as EX23-800-2H-KOH-1:1 and EX25-900-2H-KOH-1:1 exhibit nitrogen contents of 0.88% and 0.69% respectively, while KOx-activated samples like EX45-900-2H-KOX-1:1 and EX53-900-2H-KOX-1:1 (pre-pyrolysed) have nitrogen contents of 0.66% and 0.84%. In contrast, non-activated samples like EX4-N2-500-2H and EX6-N2-900-2H have higher nitrogen contents of 3.89% and 3.35%, respectively, while CO_2 activated samples (EX37-850-15-CO_2-600 and EX38-850-15-CO_2-100) show nitrogen contents of 4.05% and 4.01%, and the fungal activated sample (EX77-900-15-GO) has a nitrogen content of 3.33%. One potential explanation for the lower nitrogen content in chemically activated samples is the harsh conditions of the chemical activation process. Chemical activators such as KOH and KOx facilitate the breakdown and removal of nitrogen-containing compounds during the activation process. These chemicals react with the biomass, promoting extensive dehydrogenation and decarboxylation, which not only removes volatile compounds but also disrupts nitrogenous structures within the biomass. As a result, nitrogen is volatilised and lost during the activation process, leading to lower nitrogen content in the final

biochar. Another contributing factor is the washing step that follows chemical activation. After activation with KOH or KOx, the samples are typically washed to remove residual chemicals. This washing process can further contribute to the loss of nitrogenous compounds, as soluble nitrogen-containing compounds may be washed away, resulting in lower nitrogen content in the final product.

In contrast, the CO_2 activation process is less aggressive. CO_2 activation primarily involves the gasification of carbon at high temperatures, which does not significantly disrupt nitrogen-containing structures. This results in higher nitrogen retention in CO_2 activated samples. Similarly, the fungal activation method involves the metabolic activity of fungi, which, while reducing the overall carbon content through CO_2 release, does not aggressively remove nitrogen. This allows for a higher proportion of nitrogen to remain in the biochar.

8.3. Fourier Transform Infrared Spectroscopy

Fourier Transform Infrared Spectroscopy (FTIR) is a widely used analytical technique for identifying and characterising the functional groups present on the surface of materials. The primary objective of using FTIR in this study was to screen biochar samples derived from SCG for their surface functionalities. Understanding these surface functionalities is crucial for evaluating the potential of biochars in applications such as carbon capture and adsorption. Initially, an ATR-FTIR spectrometer with a scanning range of 4000–400 cm^{-1} was employed to obtain the spectra of the biochar samples. Attenuated Total Reflectance (ATR) is a convenient sampling technique that allows direct analysis of solid samples without extensive preparation. However, during this initial screening, the spectra obtained from the non-activated biochar samples lacked distinct peak details, which posed a challenge for identifying specific functional groups. To address this issue, a Germanium (Ge) ATR with a scanning range of 5000–400 cm^{-1} was subsequently used. Ge ATR crystals are known for their ability to handle dark and highly absorbing materials more effectively than the standard ATR crystals, typically made of zinc selenide (ZnSe) or diamond. This higher refractive index allows for better internal reflection, which enhances the sensitivity of the FTIR analysis, particularly for dark or opaque samples that absorb more infrared light. Despite this adjustment, the FTIR spectra obtained using the Ge ATR crystal exhibited similar results, with minimal discernible peaks and reduced spectral detail. This suggested that the inherent properties of the biochar, such as its high carbon content and increased

absorptivity with pyrolysis temperature, significantly impacted the quality of the FTIR spectra. These findings highlighted the limitations of FTIR in analysing highly carbonaceous materials and underscored the need for complementary analytical techniques to fully characterise the surface functionalities of biochars.

8.3.1. Untreated Biochar FTIR trends

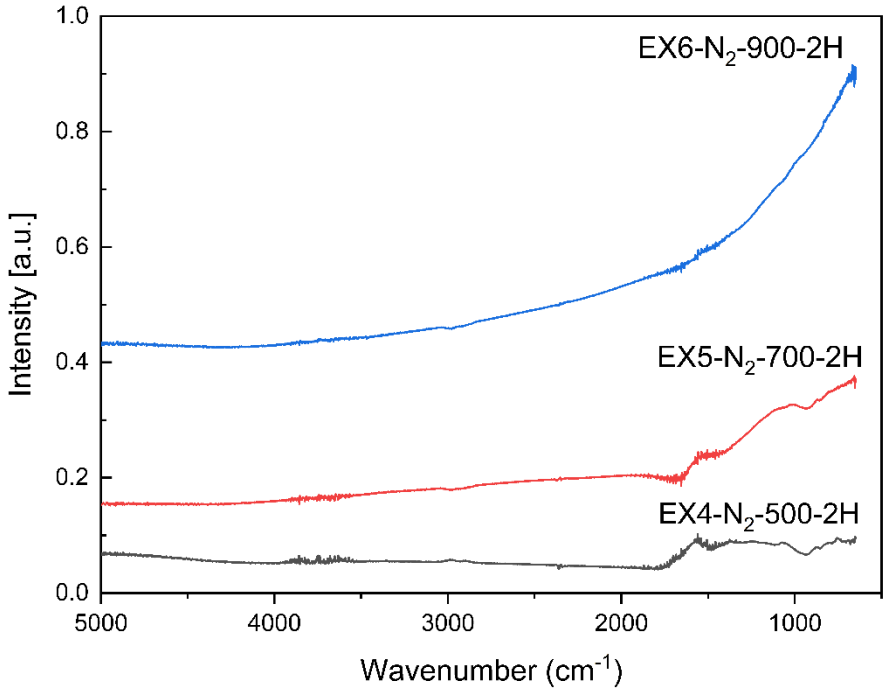

Figure 54 - Non-activated Biochar samples FTIR spectra

In the FTIR analysis of non-activated biochar samples shown in Figure 54, a clear trend of increased IR absorption and reduced spectral detail was observed with increasing pyrolysis temperature. This phenomenon can be explained by several factors:

1. **Increased Carbon Content and Aromaticity**: Higher pyrolysis temperatures result in greater carbonisation, increasing the carbon content and the aromatic nature of the biochar. These carbonaceous structures exhibit strong IR absorption, reducing the overall transmittance and peak visibility.
2. **Loss of Functional Groups**: Elevated temperatures cause the thermal decomposition of various functional groups, such as hydroxyl, carboxyl, and aliphatic groups, resulting in fewer distinct peaks in the FTIR spectrum.
3. **Higher Absorptivity and Surface Scattering**: The biochar becomes more absorptive to IR radiation due to its increased carbon content and more graphitic structure.

Additionally, the increased surface roughness and porosity scatter the IR beam, further diminishing spectral detail.

These findings suggest that the structural and compositional changes induced by higher pyrolysis temperatures significantly impact the IR absorption characteristics and the resulting FTIR spectra of biochar.

In the FTIR spectra of non-activated biochar samples, a few notable peaks are discernible despite the overall reduced spectral detail. A prominent peak is observed around 1550 cm^{-1}, which can be attributed to the aromatic C=C stretching vibrations [340]. This peak is indicative of the presence of aromatic structures within the biochar. Additionally, there is an anomalous peak around 3700 cm^{-1}, [340] which is likely due to the stretching vibrations of isolated surface hydroxyl (O-H) groups. The presence of this peak indicates that some hydroxyl groups remain on the surface of the biochar, even at elevated pyrolysis temperatures. The identification of these peaks provides valuable insights into the surface chemistry of the non-activated biochar and the changes that occur with increasing pyrolysis temperature.

8.3.2. Activated Biochar FTIR

The FTIR spectra of the activated biochar samples shown in Figure 55, similar to the untreated samples, suffer from a lack of discernible peaks due to the high absorptivity and carbon content of the biochars. Despite this, a few features are still observable.

Notably, a peak at approximately 1550 cm^{-1} is visible across all the spectra of activated samples, consistent with the aromatic C=C stretching vibrations. [340] This peak is labelled in both the KOH and KOx activated biochars, indicating the persistence of aromatic structures following activation. Additionally, faint peaks can be identified in the region of 1000-800 cm^{-1}. These peaks are likely associated with aromatic C-H out-of-plane bending vibrations, [340] which are characteristic of aromatic compounds. These features are particularly noticeable in the spectra of CO_2 and fungal activated biochar samples.

Despite the original plan to use FTIR for screening the surface functional groups of biochar samples, the lack of spectral detail, as previously discussed, rendered this approach ineffective. The high absorptivity, carbon content, and structural characteristics of the biochars significantly diminished the clarity of the FTIR spectra, making it difficult to identify specific functional groups. Consequently, alternative characterisation methods were employed to obtain a more comprehensive understanding of the surface chemistry of the

biochars.

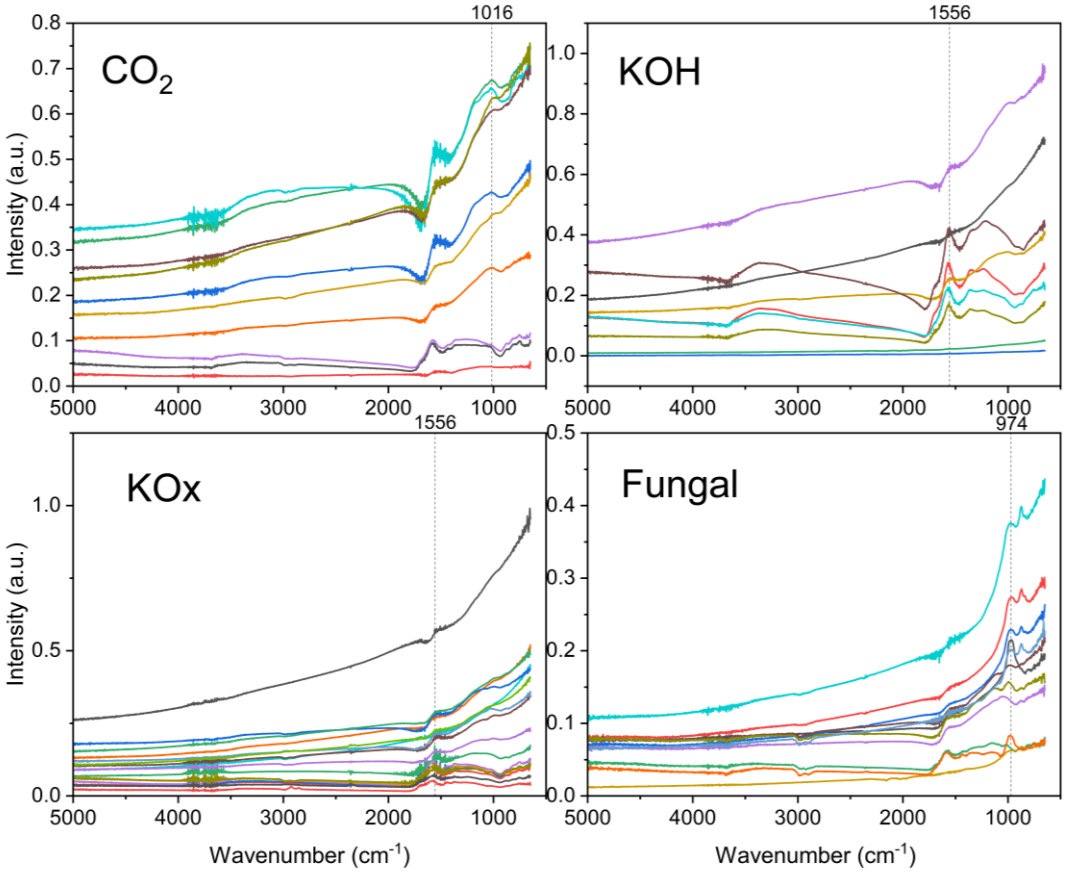

Figure 55 - CO_2, KOH, KOx and Fungal Activated Samples FTIR Spectra

8.4. X-Ray Photoelectron Spectroscopy

X-ray Photoelectron Spectroscopy (XPS) was utilised to analyse the chemical bonding states and the nature of various oxygenated and nitrogenated species present on the surface of biochar derived from SCG. The biochar samples were subjected to different activation methods, including chemical activation with potassium hydroxide (KOH), activation with carbon dioxide (CO_2), activation with potassium oxalate (KOx), and fungal activation using mycelium. These activation processes aim to enhance the surface properties and elemental composition of the biochar, improving its effectiveness for applications such as CO_2 adsorption. XPS survey data can be found in Appendix E: XPS Survey Spectra and Example element peak deconvolutions can be found in Appendix F: XPS Peak Deconvolution Spectra.

8.4.1. Elemental Analysis Results

The elemental composition of SCG-derived biochar samples, prepared under varying conditions, including final temperature, hold time, and activation method, is summarised in

Table 30. The data indicates significant differences in the carbon, oxygen, and nitrogen content among the samples, highlighting the influence of activation methods and pyrolysis conditions.

Table 30 - XPS Derived Surface Elemental Composition of Samples

Experiment	Final Temp (°C)	Hold Time (min)	Activation method	% Carbon	% Oxygen	% Nitrogen
MSCG	0	0	mycelium	64.93	20.77	14.30
SCG	0	0	none	84.22	14.10	1.67
EX4-N2-500-2H	500	120	none	85.74	11.65	2.62
EX5-N2-700-2H	700	120	none	85.13	9.94	4.93
EX6-N2-900-2H	900	120	none	82.96	13.56	3.48
EX23-800-2H-KOH-1:1	800	120	KOH 1:1	84.67	13.19	2.14
EX25-900-2H-KOH-1:1	900	120	KOH 1:1	85.89	13.72	0.39
EX31-900-2H-KOH-1:8	900	120	KOH 1:8	88.66	10.05	1.29
EX42-700-15-KOH-1:1	700	15	KOH 1:1	79.89	16.11	4.00
EX37-850-15-CO_2-600	850	15	CO_2 600 mL/min	86.76	9.76	3.49
EX38-850-15-CO_2-100	850	15	CO_2 600 mL/min	85.09	7.36	7.56
EX45-900-2H-KOX-1:1	900	120	KOx 1:1	87.02	12.53	0.45
EX53-900-2H-KOX-1:1 (pre-pyrolysed)	900	120	KOx 1:1	81.77	17.47	0.76
EX60-1200-68-KOx-1:4.5	1200	68	KOx 1:4.5	83.77	15.45	0.78
EX77-900-15-GO	900	15	Fungal	79.92	15.17	4.90

The XPS data shows that MSCG samples have a significantly higher nitrogen content (14.30%) compared to SCG samples (1.67%), consistent with the ultimate analysis. This increase in nitrogen proportion is attributed to carbon loss during fungal colonisation. As the fungus metabolises the substrate, it releases carbon as CO_2 through respiration, reducing the overall carbon content of the material. This selective depletion of carbon leads

to a relative enrichment of nitrogen in the remaining biomass, thereby explaining the elevated nitrogen levels observed in the MSCG-derived biochar.

The XPS data for non-activated samples shows an increase in nitrogen content from 2.62% at 500 °C (sample EX4-N2-500-2H) to 4.93% at 700 °C (sample EX5-N2-700-2H) and then a decrease to 3.48% at 900 °C (sample EX6-N2-900-2H). The carbon content shows a decrease from 85.74% (sample EX4-N2-500-2H) and 85.13% (sample EX5-N2-700-2H) to 82.96% (sample EX6-N2-900-2H), and oxygen content increases from 9.94% (sample EX5-N2-700-2H) to 13.56% (sample EX6-N2-900-2H). These findings disagree with the ultimate analysis results, which showed a consistent increase in carbon content and decrease in nitrogen content with higher temperatures, a trend that agrees with the literature. [146–148,152] The discrepancy likely arises from key differences between the two techniques. XPS measures only the surface chemistry of a material (the outer 1–10 nanometres), whereas ultimate analysis provides a bulk composition of the entire sample. Surface oxidation or contamination, particularly in porous materials, can therefore lead to differences between the two methods. In this case, the XPS measurements were also conducted in two separate sessions, with different sample batches and instrument settings. Although the data were corrected where possible, slight differences in calibration, detector response, or vacuum conditions between runs may have introduced additional variability. These discrepancies underscore the importance of using complementary analytical techniques to accurately characterise chemically and structurally heterogeneous carbon materials.

By contrast, the XPS data for chemically activated samples show lower nitrogen content compared to non-activated, CO_2-activated, and fungal-activated samples. For example, the KOH-activated sample (EX25-900-2H-KOH-1:1) contains 0.39% nitrogen, and the KOx-activated sample (EX45-900-2H-KOX-1:1) contains 0.45%. This trend agrees with prior studies reporting that chemical activation—especially with strong alkalis—can lead to significant nitrogen volatilisation due to high-temperature degradation of nitrogenous species such as amines, pyrroles, and amides.[347] It also aligns with the ultimate analysis and reflects the harsh reaction conditions driving off volatile nitrogen compounds.

Both KOH and KOx-activated samples exhibit elevated carbon content and a moderate increase in oxygen content, a trend that has been previously attributed to the removal of labile heteroatoms (e.g., nitrogen and hydrogen) and incorporation of oxygenated functional groups during activation [348,349]. For instance, KOH-activated samples EX25-900-

2H-KOH-1:1 and EX31-900-2H-KOH-1:8 show carbon contents of 85.89% and 88.66%, respectively, and oxygen contents of 13.72% and 10.05%. KOx-activated samples EX45-900-2H-KOX-1:1 and EX53-900-2H-KOX-1:1 (pre-pyrolysed) show comparable behaviour. These trends are consistent with reports indicating that KOH activation facilitates redox reactions that generate reactive oxygenated intermediates (e.g., CO, K_2CO_3), which in turn react with the carbon surface to introduce hydroxyl, carbonyl, and lactone functionalities [350]. Such oxygen incorporation has been widely observed in chemically activated carbons and contributes to enhanced surface reactivity and wettability. [199]

Fungal-activated samples (MSCG and EX77-900-15-GO) show significantly higher nitrogen contents, underscoring the potential of biological pre-treatment for nitrogen enrichment. The MSCG precursor exhibited 14.30% nitrogen, while the derived biochar (EX77-900-15-GO) retained 4.90%. Although literature on fungal pre-treatment is limited, this behaviour is consistent with studies on biologically enriched biomass where microbial metabolism leads to selective carbon loss and relative nitrogen enrichment, often resulting in elevated N-doping after pyrolysis. [222] The retention of nitrogen functionalities during pyrolysis is advantageous for applications such as CO_2 capture, where basic nitrogen sites can enhance sorption affinity via acid–base interactions. [36]

These findings reinforce that while XPS confirms several trends observed in the bulk elemental analysis, differences in depth sensitivity and measurement conditions can lead to discrepancies, particularly in surface-sensitive measurements of carbon and nitrogen.

8.4.2. Functional Group Analysis

To assign the complete bonding configurations of the heteroatoms (N1s and O1s), as well as the carbon (C1s) species, high-resolution XPS spectra were deconvoluted into different components representing various nitrogen-, oxygen-, and carbon-containing moieties on the biochar surface (Appendix F: XPS Peak Deconvolution Spectra**Error! Reference source not found.**). This analysis helps in understanding the distribution and chemical states of these elements, which play a critical role in the performance of the biochar, especially in applications like CO_2 adsorption.

High-Resolution C1s Spectrum

The high-resolution C1s spectrum for the biochar samples revealed various carbon species, which include graphitic/aliphatic carbon (sp2/sp3), characterised by peaks around 284.5 eV,

phenol/alcohol/ ether (285.7 eV), carbonyl/ketone or lactone (287.5 eV), carboxyl or ester linkages (289.0 eV), π-π* shake-up transition (292.0 eV).

The carbon functional groups in the biochar samples indicate significant variations in their surface chemistry. Graphitic or aliphatic carbon is dominant in most samples. The presence of phenol, alcohol, and ether groups is notable in samples like EX25-900-2H-KOH-1:1 and EX45-900-2H-KOX-1:1, highlighting the influence of the activation process on the surface chemistry of the biochar. The occurrence of carbonyl, ketone, and lactone groups is significant in samples such as EX42-700-15-KOH-1:1 and EX6-N2-900-2H, which can contribute to the reactivity and adsorption capacity of the biochar. The π-π* shake-up transitions observed in several samples, such as EX60-1200-68-KOx-1:4.5 and EX6-N2-900-2H, indicate the presence of aromatic structures.

SCG samples (P1, P2, P3) show a high proportion of graphitic/aliphatic carbon (sp^2/sp^3), with SCG(P2) and SCG(P3) containing over 96% graphitic carbon. In contrast, MSCG samples (P1, P2, P3) display significantly lower graphitic content, with the highest being 40.5% in MSCG(P2). These samples instead exhibit a much higher proportion of oxygenated surface functionalities—particularly phenol, alcohol, and ether groups (up to 58.5%), alongside substantial contributions from carbonyl, ketone, and lactone species.

The increased presence of oxygen-containing groups in MSCG samples is likely a result of fungal metabolism. As the fungus degrades the biomass, it oxidises part of the carbon to CO_2, leading to an overall decrease in carbon content and a relative increase in oxygen. In addition to this proportional effect, the specific increase in carbonyl-type groups indicates that fungal activity alters the chemical environment of the surface, introducing new functional groups via biochemical oxidation pathways. This suggests that fungal colonisation not only changes the elemental composition but also produces a distinct surface chemistry.

Samples activated with KOH (EX23-800-2H-KOH-1:1, EX25-900-2H-KOH-1:1, EX31-900-2H-KOH-1:8, EX42-700-15-KOH-1:1) generally show a reduction in graphitic content compared to non-activated samples and an increase in phenol/alcohol/ether groups. These groups likely form through oxidative reactions facilitated by KOH, which disrupt C–C and C–H bonds and favour rehydroxylation or oxidation of defect sites. KOH activation tends to introduce more carbonyl, ketone, or lactone groups, as seen in samples EX23-800-2H-KOH-

1:1 and EX42-700-15-KOH-1:1, which can enhance the adsorption capacity for gases like CO_2. [67]

CO_2 activated samples (EX37-850-15-CO_2-600, EX38-850-15-CO_2-100) maintain a significant graphitic content but also show increased presence of carbonyl and ketone groups. This may result from CO_2 gasification reactions introducing oxygen at reactive edge sites during activation.

KOx activated samples (EX45-900-2H-KOX-1:1, EX53-900-2H-KOX-1:1 (pre-pyrolysed), EX60-1200-68-KOx-1:4.5) exhibit a range of surface functionalities. While samples EX45-900-2H-KOX-1:1 and EX53-900-2H-KOX-1:1 (pre-pyrolysed) samples show a significant presence of phenol/alcohol/ether groups, sample EX60-1200-68-KOx-1:4.5 highlights a notable amount of π-π* shake-up transitions, indicating aromatic character. KOx activation appears effective in introducing a diverse set of functional groups, potentially enhancing the adsorption properties of the biochar for different applications.

Samples activated with mycelium (sample EX77-900-15-GO) show a high graphitic content, similar to non-activated samples, but with additional oxygenated functional groups like carboxyl or ester linkages. This is unique compared to other samples, as the fungal activation introduces carboxyl groups, which are beneficial for various adsorption applications. These may arise from biochemical precursors deposited by fungal metabolism prior to carbonisation. This method distinctly enhances the biochar by adding specific oxygenated functionalities that are not as prevalent in other activation methods. For example C1 peak deconvolutions see Figures 105, 107, 108 and 109, in Appendix F: XPS Peak Deconvolution Spectra.

Table 31 - Relative Area Percentage of Carbon Functional Groups (C1s)

Sample	Final Temp (°C)	Hold Time (mins)	Activation method	Graphitic/Aliphatic (sp2/sp3)	Phenol/Alcohol/ Ether	carbonyl, ketone or lactone	carboxyl or ester linkages	π-π* Shake-up Transition
SCG(P1)	0	0	none	79.7		4.3	16	
SCG(P2)				97.2	2.8			
SCG(P3)				96.7	3.3			
MSCG(P1)	0	0	mycelium	35	58.3	6.7		
MSCG(P2)				40.5	52.5	7		
MSCG(P3)				32	58.5	9.4		
EX4-N2-500-2H(P1)	500	120	none	61	16.3	16.2	-	6.1
EX4-N2-500-2H(P2)				59.8	17.2	9.8	-	13
EX5-N2-700-2H(P1)	700	120	none	77.1		22.9		
EX5-N2-700-2H(P2)				80.2		19.8		
EX5-N2-700-2H(P3)				84.7		15.3		
EX6-N2-900-2H(P1)	900	120	none	66.7		20.8		5.6
EX6-N2-900-2H(P2)				54.4		22.5		17.4
EX6-N2-900-2H(P3)				52.8		16.2		31
EX23-800-2H-KOH-1:1 (P1)	800	120	KOH 1:1	72.4	-	27.6	-	-
EX23-800-2H-KOH-1:1 (P2)				81.4	-	18.6	-	-

Sample	Final Temp (°C)	Hold Time (mins)	Activation method	Graphitic/Aliphatic (sp2/sp3)	Phenol/Alcohol/ Ether	carbonyl, ketone or lactone	carboxyl or ester linkages	π-π* Shake-up Transition
EX23-800-2H-KOH-1:1 (P3)				85.3	-	14.7	-	-
EX25-900-2H-KOH-1:1(P1)	900	120	KOH 1:1	65.3	34.6	-	-	-
EX25-900-2H-KOH-1:1(P2)				67.9	32	-	-	-
EX31-900-2H-KOH-1:8 (P1)	900	120	KOH 1:8	73.6		26.4		
EX31-900-2H-KOH-1:8 (P2)				72.1		27.9		
EX31-900-2H-KOH-1:8 (P3)				70.2		29.8		
EX42-700-15-KOH-1:1(P1)	700	15	KOH 1:1	88.2		11.8		
EX42-700-15-KOH-1:1(P2)				53.3	6.2	40.5		
EX42-700-15-KOH-1:1(P3)				61.6	9.1	29.2		
EX37-850-15-CO_2-600(P1)	850	15	CO_2 600mL/m	66.2	14.3	19.3	-	-
EX37-850-15-CO_2-600(P2)				48.8	31.7	19.3	-	-
EX38-850-15-CO_2-100(P1)	850	15	CO_2 600mL/m	80.3		19.7		
EX38-850-15-CO_2-100(P2)				80.7		19.3		
EX38-850-15-CO_2-100(P3)				74.9		25.1		

Sample	Final Temp (°C)	Hold Time (mins)	Activation method	Graphitic/Aliphatic (sp2/sp3)	Phenol/Alcohol/ Ether	carbonyl, ketone or lactone	carboxyl or ester linkages	π-π* Shake-up Transition
EX45-900-2H-KOX-1:1(P1)	900	120	KOx 1:1	70	29.9	-	-	-
EX45-900-2H-KOX-1:1(P2)				65.1	34.8	-	-	-
EX53-900-2H-KOX-1:1 (pre-pyrolysed)(P1)	900	120	KOx 1:1	62.5	37.3	-	-	-
EX53-900-2H-KOX-1:1 (pre-pyrolysed)(P2)				55.8	20	24	-	-
EX60-1200-68-KOx-1:4.5(P1)	1200	68	KOx 1:4.5	44.3	22.8	20.2	-	12.5
EX60-1200-68-KOx-1:4.5(P2)				35	28.8	21.7	-	14.3
EX77-900-15-GO(P1)	900	15	mycelium	79	2.4		18.6	
EX77-900-15-GO(P2)				78			22	
EX77-900-15-GO(P3)				79.4			20.6	

High-Resolution O1s Spectrum

The high-resolution O1s spectrum for the biochar samples revealed various oxygen species, which include carbonyl, ketone, or lactone (O-1), characterised by peaks around 531-532 eV, ether and alcohol (O-2; 532-533 eV), carboxyl or ester groups (O-3; 533-534 eV), and specific binding energies indicating adsorbed water molecules (H_2O).

SCG samples generally exhibit a balanced presence of carbonyl/ketone/lactone (O-1) and ether/alcohol (O-2) groups. For instance, SCG(P1) shows 29.4% carbonyl/ketone/lactone and 70.5% ether/alcohol groups. MSCG samples, on the other hand, predominantly feature carbonyl/ketone/lactone groups, with MSCG(P1) showing 97.9% carbonyl/ketone/lactone content. This difference indicates that the presence of mycelium significantly increases the carbonyl/ketone/lactone groups. This suggests oxidative processes driven by fungal enzymes produce highly functionalised precursors rich in carbonyl and ketone groups.

The KOH-activated samples (EX23-800-2H-KOH-1:1, EX25-900-2H-KOH-1:1, EX31-900-2H-KOH-1:8, EX42-700-15-KOH-1:1) exhibit a diverse range of oxygen functional groups, showcasing the ability to fine-tune surface chemistry based on the activation conditions.

Sample EX23-800-2H-KOH-1:1 (P1) demonstrates a significant presence of 71.5% carbonyl/ketone/lactone (O-1) groups and 28.5% ether/alcohol (O-2) groups. Similarly, sample EX25-900-2H-KOH-1:1(P1) contains 64.3% carbonyl/ketone/lactone (O-1) groups and 35.6% carboxyl/anhydrides/esters (O-3) groups. These samples indicate a dominant presence of O-1 groups, with a noteworthy proportion of O-3 groups in sample EX25-900-2H-KOH-1:1. This composition suggests high surface reactivity, which is beneficial for various adsorption applications, particularly where carbonyl and lactone functionalities enhance interaction with adsorbates.

In contrast, the heavily activated sample EX31-900-2H-KOH-1:8 shows a remarkable shift towards ether/alcohol (O-2) groups. Sample EX31-900-2H-KOH-1:8 (P1) exhibits 89.2% O-2 groups, sample EX31-900-2H-KOH-1:8 (P2) consists of 96.6% O-2 groups, and sample EX31-900-2H-KOH-1:8 (P3) displays 94.2% O-2 groups. These results indicate that the high KOH activation ratio (8:1) significantly promotes the formation of ether and alcohol groups, almost entirely shifting the surface chemistry towards O-2 functionalities. This specific tuning is likely to enhance the hydrophilic properties of the biochar, making it highly suitable for applications involving polar adsorbates. Sample EX42-700-15-KOH-1:1, with a reduced retention time and temperature, presents a nearly equal distribution of O-1 and O-

2 groups. Sample EX42-700-15-KOH-1:1(P1) exhibits 56.7% carbonyl/ketone/lactone (O-1) groups and 43.2% ether/alcohol (O-2) groups. sample EX42-700-15-KOH-1:1(P2) shows 41.2% O-1 and 55.5% O-2 groups, while sample EX42-700-15-KOH-1:1(P3) contains 45.8% O-1 and 54.1% O-2 groups. This balanced composition demonstrates the ability to create a biochar with both high surface reactivity and hydrophilicity, offering versatile adsorption properties for a variety of applications.

The KOH activation process clearly demonstrates the potential to dial in specific surface chemistries depending on the pyrolysis conditions. Lower KOH ratios and standard activation times favour the formation of carbonyl and lactone groups (O-1), which are beneficial for adsorption due to their high reactivity. Conversely, heavier activation ratios (8:1) favour the formation of ether and alcohol groups (O-2), enhancing the hydrophilic nature of the biochar. Samples like EX42-700-15-KOH-1:1, with adjusted retention times and temperatures, exhibit a balanced presence of O-1 and O-2 groups, indicating the possibility of tailoring the surface chemistry of the biochar to specific application needs through careful control of activation parameters. This flexibility in tuning surface functionalities underscores the versatility of KOH activation in producing biochars with targeted adsorption properties.

The CO_2-activated samples (EX37-850-15-CO_2-600, EX38-850-15-CO_2-100) display a distinct surface chemistry characterised by a significant presence of ether/alcohol (O-2) groups and an increase in carboxyl or ester (O-3) groups. For instance, sample EX37-850-15-CO_2-600(P1) shows 75.5% ether/alcohol (O-2) and 21.9% carboxyl or ester (O-3) content, highlighting a balanced surface chemistry that is beneficial for adsorption applications. Similarly, sample EX38-850-15-CO_2-100(P1) exhibits 61.8% ether/alcohol (O-2) and 38.1% carboxyl or ester (O-3), while sample EX38-850-15-CO_2-100(P3) shows 80.7% O-2 and 5.5% O-3, emphasising the variability and adaptability of the CO_2 activation process in producing functionalised biochar surfaces. Sample EX42-700-15-KOH-1:1, activated with KOH but with a similar retention time of 15 min, presents a notably different surface chemistry compared to the CO_2-activated samples. Sample EX42-700-15-KOH-1:1(P1) demonstrates a balanced distribution of 56.7% carbonyl/ketone/lactone (O-1) groups and 43.2% ether/alcohol (O-2) groups, while sample EX42-700-15-KOH-1:1(P2) shows 41.2% O-1 and 55.5% O-2 groups, and sample EX42-700-15-KOH-1:1(P3) exhibits 45.8% O-1 and 54.1% O-2 groups. This indicates a combination of high surface reactivity and hydrophilicity, in contrast to the

ether/alcohol and carboxyl/ester functionalities that were prevalent for the CO_2-activated samples.

The non-activated sample EX6-N2-900-2H provides a baseline for understanding the effects of activation. Sample EX6-N2-900-2H(P1) contains 31.6% carbonyl/ketone/lactone (O-1) groups and 68.4% ether/alcohol (O-2) groups, with no significant presence of carboxyl or ester (O-3) groups. Samples EX6-N2-900-2H(P2) and EX6-N2-900-2H(P3) similarly show predominant O-2 group content with minor O-1 group presence. This highlights the limited functionalisation of non-activated samples compared to the activated ones.

The CO_2 activation process results in biochars with a high content of ether/alcohol (O-2) groups and significant carboxyl/ester (O-3) groups, which can enhance adsorption properties due to the increased surface polarity and potential for hydrogen bonding. In comparison, sample EX42-700-15-KOH-1:1, activated with KOH and with a similar retention time, offers a mix of carbonyl/ketone/lactone (O-1) and ether/alcohol (O-2) groups, providing a balanced surface chemistry suitable for various adsorption applications. The non-activated sample EX6-N2-900-2H, in contrast, lacks the extensive functionalisation seen in activated samples, highlighting the importance of activation processes in enhancing the surface properties of biochar.

KOx-activated samples (EX45-900-2H-KOX-1:1, EX53-900-2H-KOX-1:1 (pre-pyrolysed), EX60-1200-68-KOx-1:4.5) exhibit a predominance of ether/alcohol (O-2) groups, which significantly enhance the surface functionalities and adsorption properties of the biochar. This may be due to the release of CO/CO_2 from oxalate decomposition, driving mild oxidation and formation of ether linkages. For instance, sample EX45-900-2H-KOX-1:1(P1) contains 91.4% ether/alcohol (O-2) groups, and sample EX45-900-2H-KOX-1:1(P2) has 90.3% O-2 groups, indicating the effectiveness of KOx activation in introducing these functional groups. Similarly, samples EX53-900-2H-KOX-1:1 (pre-pyrolysed)(P1) and EX53-900-2H-KOX-1:1 (pre-pyrolysed)(P2) show 86.3% and 90.7% O-2 groups, respectively, underscoring the high oxygenation level achieved through KOx activation. When comparing KOx-activated samples (EX45-900-2H-KOX-1:1, EX53-900-2H-KOX-1:1 (pre-pyrolysed) with KOH-activated samples (EX23-800-2H-KOH-1:1, EX25-900-2H-KOH-1:1), a clear difference in surface functionalities is observed. Samples EX23-800-2H-KOH-1:1 (P1) and EX23-800-2H-KOH-1:1 (P2) exhibit 71.5% and 100% carbonyl/ketone/lactone (O-1) groups, respectively, with minimal presence of ether/alcohol (O-2) groups. Similarly, sample EX25-900-2H-KOH-

1:1(P1) shows 64.3% O-1 groups and 35.6% carboxyl/anhydrides/esters (O-3) groups, while sample EX25-900-2H-KOH-1:1(P2) has 60.3% O-1 and 39.6% O-3 groups. This highlights that KOH activation tends to introduce more O-1 and O-3 groups compared to the O-2 groups prevalent in KOx-activated samples.

Non-activated samples, such as sample EX6-N2-900-2H, provide a baseline for understanding the extent of functionalisation achieved through activation. Sample EX6-N2-900-2H(P1) contains 31.6% O-1 groups and 68.4% O-2 groups, with no significant presence of O-3 groups. Samples EX6-N2-900-2H(P2) and EX6-N2-900-2H(P3) similarly show predominant O-2 group content with minor O-1 group presence, underscoring the limited functionalisation of non-activated samples compared to those activated with KOx or KOH. The comparison reveals that KOx activation (samples EX45-900-2H-KOX-1:1 and EX53-900-2H-KOX-1:1 (pre-pyrolysed) predominantly introduces ether/alcohol (O-2) groups, which are beneficial for enhancing hydrophilicity and adsorption properties of the biochar. In contrast, KOH activation (samples EX23-800-2H-KOH-1:1 and EX25-900-2H-KOH-1:1) results in a higher presence of carbonyl/ketone/lactone (O-1) and carboxyl/ anhydrides/esters (O-3) groups, providing a different surface chemistry profile. Non-activated samples, such as EX6-N2-900-2H, exhibit a relatively lower level of functionalisation, primarily composed of ether/alcohol (O-2) groups.

Samples activated with mycelium (EX77-900-15-GO) exhibit a unique presence of carboxyl or ester (O-3) groups compared to other samples. For instance, sample EX77-900-15-GO(P1) shows 7.9% O-3 content. This indicates that fungal activation significantly enhances the presence of carboxyl or ester functionalities, which are advantageous for adsorption applications due to their increased surface reactivity.

MSCG is the precursor for sample EX77-900-15-GO. Interestingly, the oxygen group composition remains relatively consistent between MSCG and sample EX77-900-15-GO, despite the pyrolysis process. MSCG samples (P1, P2, P3) exhibit a dominant presence of carbonyl/ketone/lactone (O-1) groups, with MSCG(P1) showing 97.9% O-1 groups, MSCG(P2) having 96.5% O-1 groups, and MSCG(P3) with 96.6% O-1 groups. Similarly, sample EX77-900-15-GO retain a high proportion of O-1 groups. For example, sample EX77-900-15-GO(P1) has 92% O-1 content. The lack of significant change in oxygen functionalities between MSCG and sample EX77-900-15-GO suggests that the fungal activation process preserves the existing oxygenated groups while introducing additional carboxyl or ester

functionalities. For example O1 peak deconvolutions see Figures 105-109, in Appendix F: XPS Peak Deconvolution Spectra.

Table 32 - Oxygen Functional Groups Distribution in Samples

Sample	Final Temp (°C)	Hold Time	Activation method	O-1 (Carbonyl/Ketone/Lactone)	O-2 (Ether/Alcohol)	O-3 (Carboxyl/Anhydrides/Esters)	water
SCG(P1)	0	0	none	29.4	70.5	-	
SCG(P2)				64.2	3.4	32.4	
SCG(P3)				36.8	63.1	-	
MSCG(P1)	0	0	mycelium	97.9	2.1		
MSCG(P2)				96.5	3.5		
MSCG(P3)				96.6	3.3		
EX4-N2-500-2H(P1)	500	120	none	100		-	
EX4-N2-500-2H(P2)				94.7	5.2		
EX5-N2-700-2H(P1)	700	120	none	95.8	4.2		
EX5-N2-700-2H(P2)				15.2	84.7	-	
EX5-N2-700-2H(P3)				17	71.5	11.4	
EX6-N2-900-2H(P1)	900	120	none	31.6	68.4		
EX6-N2-900-2H(P2)				26.5	73.4	-	
EX6-N2-900-2H(P3)				22.4	77.5	-	
EX23-800-2H-KOH-1:1 (P1)	800	120	KOH 1:1	71.5	28.5		
EX23-800-2H-KOH-1:1 (P2)				100			

Sample	Final Temp (°C)	Hold Time	Activation method	O-1 (Carbonyl/Ketone/Lactone)	O-2 (Ether/Alcohol)	O-3 (Carboxyl/Anhydrides/Esters)	water
EX23-800-2H-KOH-1:1 (P3)				95.7		4.2	
EX25-900-2H-KOH-1:1(P1)	900	120	KOH 1:1	64.3		35.6	
EX25-900-2H-KOH-1:1(P2)				60.3		39.6	
EX31-900-2H-KOH-1:8 (P1)	900	120	KOH 1:8	-	89.2		10.7
EX31-900-2H-KOH-1:8 (P2)				-	96.6		3.4
EX31-900-2H-KOH-1:8 (P3)				-	94.2		5.7
EX42-700-15-KOH-1:1(P1)	700	15	KOH 1:1	56.7	43.2	-	
EX42-700-15-KOH-1:1(P2)				41.2	55.5		3.1
EX42-700-15-KOH-1:1(P3)				45.8	54.1	-	
EX37-850-15-CO_2-600(P1)	850	15	CO_2 600mL/m	2.5	75.5	21.9	
EX37-850-15-CO_2-600(P2)				12.6	87.3	-	
EX38-850-15-CO_2-100(P1)	850	15	CO_2 600mL/m	-	61.8	38.1	
EX38-850-15-CO_2-100(P2)				-	61.5	38.5	
EX38-850-15-CO_2-100(P3)				13.6	80.7		5.5
EX45-900-2H-KOX-1:1(P1)	900	120	KOx 1:1	8.5	91.4	-	

Sample	Final Temp (°C)	Hold Time	Activation method	O-1 (Carbonyl/Ketone/Lactone)	O-2 (Ether/Alcohol)	O-3 (Carboxyl/Anhydrides/Esters)	water
EX45-900-2H-KOX-1:1(P2)				9.6	90.3	-	
EX53-900-2H-KOX-1:1 (pre-pyrolysed)(P1)	900	120	KOx 1:1	13.6	86.3	-	
EX53-900-2H-KOX-1:1 (pre-pyrolysed)(P2)				9.3	90.7		
EX60-1200-68-KOx-1:4.5(P1)	1200	68	KOx 1:4.5	38.2	61.6		
EX60-1200-68-KOx-1:4.5(P2)				48.5	51.4		
EX77-900-15-GO(P1)	900	15	mycelium	92		7.9	
EX77-900-15-GO(P2)				95.5		4.4	
EX77-900-15-GO(P3)				100			

SCG is the precursor for sample EX6-N2-900-2H. Similar to the MSCG and sample EX77-900-15-GO comparison, there is a notable lack of change in oxygen group composition between SCG and sample EX6-N2-900-2H. SCG samples (P1, P2, P3) have varied oxygen group compositions, with SCG(P1) showing 29.4% O-1 and 70.5% O-2, SCG(P2) having 64.2% O-1 and 3.4% O-2, and SCG(P3) with 36.8% O-1 and 63.1% O-2. Sample EX6-N2-900-2H maintains this trend, with sample EX6-N2-900-2H(P1) showing 31.6% O-1 and 68.4% O-2, sample EX6-N2-900-2H(P2) with 26.5% O-1 and 73.4% O-2, and sample EX6-N2-900-2H(P3) exhibiting 22.4% O-1 and 77.5% O-2. This consistency in oxygen group composition suggests that the pyrolysis conditions for sample EX6-N2-900-2H do not significantly alter the pre-existing oxygen functionalities of the SCG precursor.

High-Resolution N1s Spectrum

High-resolution N 1s spectra were acquired but not included in the final analysis due to the very low nitrogen concentrations present in most samples. Survey spectra indicated surface nitrogen contents close to the detection limit, resulting in weak N1s signals with low signal-to-noise ratios. Under these conditions, peak fitting and deconvolution are highly sensitive to background selection and fitting parameters, making quantitative speciation unreliable. To avoid over-interpretation of noisy data, detailed N1s deconvolution was not pursued.

Nevertheless, literature on nitrogen evolution in pyrolysed and activated carbons provides guidance on the likely nitrogen functionalities present. Biomass-derived carbons typically contain pyridinic-N and pyrrolic-N at moderate pyrolysis temperatures (≈500–800 °C), while higher temperatures (>800–900 °C) and strong activation treatments tend to favour the conversion toward more thermodynamically stable graphitic nitrogen, with concurrent overall nitrogen loss. Oxygen-containing nitrogen groups (e.g., N-oxides) are generally less stable at high temperatures and are expected to diminish under severe thermal or chemical activation. [35,346]

Accordingly, it is reasonable to infer that lower-temperature and mildly activated samples likely retain predominantly pyridinic and pyrrolic functionalities, whereas high-temperature or strongly activated biochars are more likely to contain small amounts of graphitic nitrogen as the dominant residual form. These inferences align with established nitrogen transformation pathways in carbon materials but are presented here as qualitative expectations rather than direct spectroscopic assignments. For example N1 peak deconvolutions see Figures 106 and 107, in Appendix F: XPS Peak Deconvolution Spectra.

8.5. N_2 adsorption analysis

N_2 adsorption analysis is a fundamental technique used to evaluate the surface area and porosity of biochar samples; examining the adsorption characteristics of both untreated and activated biochar samples, highlights the impact of different activation methods and pyrolysis temperatures on their textural properties. By analysing parameters such as BET surface area and micropore volume, this study aims to identify optimal conditions for producing biochars with high adsorption capacities, suitable for various environmental and industrial applications. N_2 isotherm data can be found in Appendix G: N_2 Isotherm Plots.

8.5.1. Pore Size Distribution

Although pore size distribution (PSD) analysis is widely reported in porous material studies, its application to the present work is constrained by both methodological and data limitations. The biochars produced in this study are predominantly microporous, as indicated by their Type I isotherm behaviour and high micropore fractions. In such systems, conventional nitrogen physisorption at 77 K has well-recognised limitations for resolving pore size distributions.

While micropore size and distribution are recognised as key determinants of CO_2 adsorption performance, reliable determination of micropore size distributions requires adsorption measurements specifically designed for this purpose. Nitrogen molecules at 77 K experience diffusion and kinetic limitations in ultramicropores (<0.7 nm) due to their kinetic diameter and reduced mobility at cryogenic temperatures. Consequently, N_2 adsorption often underestimates accessible ultramicroporosity and can distort PSD calculations. For microporous carbons, N_2-derived PSDs are therefore considered semi-quantitative at best.

Furthermore, classical PSD approaches such as the BJH model are fundamentally unsuitable for microporous materials because they rely on capillary condensation phenomena that occur only in mesopores. Applying BJH analysis to the present materials would violate its underlying assumptions and yield physically unrealistic distributions.

Advanced methods such as NLDFT or QSDFT can resolve micropore size distributions; however, these approaches require high-resolution adsorption data obtained with appropriate probe gases. Accurate micropore PSD determination is typically performed using CO_2 adsorption at 273 K or argon adsorption at 87 K, where diffusion limitations are significantly reduced. In this study, CO_2 adsorption measurements were conducted only on

selected samples and at limited temperatures (0, 25, and 60 °C) for performance evaluation rather than full isotherm acquisition suitable for PSD modelling. The dataset is therefore insufficient for robust DFT-based pore size analysis.

Deriving PSD from the available N_2 isotherms would risk producing artefactual or misleading results and could lead to over-interpretation of the textural data. For this reason, the present work focuses on BET surface area, micropore volume, and adsorption performance metrics, which provide more reliable and directly relevant indicators of CO_2 capture performance in microporous carbons.

Future studies employing dedicated CO_2 (273 K) or Ar (87 K) isotherms across appropriate pressure ranges could enable rigorous micropore PSD analysis. However, within the scope of the present study, omission of PSD analysis ensures methodological consistency and avoids reporting results that would not be statistically or physically robust.

8.5.2. Non-activated Samples

Untreated biochar samples, namely EX4-N2-500-2H, EX5-N2-700-2H, and 900-2H, (see Table 33) exhibited no porosity and contained a surprisingly high volatile content, with negligible adsorption uptakes and minimal surface areas, even under stringent degas conditions. Despite the aggressive pyrolysis conditions used, the presence of a high volatile content in these samples is unexpected. Literature suggests that untreated SCG samples, under comparable conditions, usually present moderate surface areas, reaching BET surface areas as high as 539 m^2/g, [43] [44] much higher than the results obtained here. Several factors could contribute to the disparity between these findings and those reported in the literature. These include slight variations in processing conditions, differences in SCG feedstock, potential equipment discrepancies, and differences in analytical methods. The results obtained here indicate a decrease in yield correlating with increasing temperature. However, given the prolonged residence time (2H), it may be anticipated that this effect would be rather insignificant, as the results demonstrate. This is primarily due to the ample time for volatiles to escape from the pyrolysed samples. [44] Corresponding Nitrogen isotherms can be found in Appendix G: N_2 Isotherm Plots, Figures 110-112.

Table 33 - Untreated Samples, conditions and Adsorption results

Biochar Identification	Final Temp (°C)	Activation Method	Yield (%)	BET Surface Area (m^2/g)	t-plot Micropore Area (m^2/g)	T-plot Micropore Volume (cm^3/g)
EX4-N2-500-2H	500	none	24.21	N/A	N/A	N/A

EX5-N2-700-2H	700	none	22.59	N/A	N/A	N/A
EX6-N2-900-2H	900	none	21.84	N/A	N/A	N/A

8.5.3. CO_2 Activated Samples

As outlined in the methodology section, CO_2 was used to physically activate the SCG samples with the aim of further developing the porous character of the materials. Table 34 illustrates the significant influence of pyrolysis temperature on biochar yield and porosity, corroborating earlier research in this area. A high yield of 25.59% is observed at 500 °C (sample EX15-500-2H-CO_2-100), although the BET surface area and micropore volume remain modest. However, as the temperature is increased to 700 °C, and subsequently to 800 °C, there is a marked increase in both surface area and micropore volume, albeit at the cost of overall yield. This trend persisted up until 900 °C, where total gasification of carbonaceous material was noted.

It was discovered that prolonging the hold time to 15 min (samples EX37-850-15-CO_2-600, EX38-850-15-CO_2-100) noticeably amplified yield, surface area, and microporosity. For instance, the BET surface area increased from 506 m^2/g (EX22-800-2H-CO_2-600) to 736 m^2/g (EX37-850-15-CO_2-600), and the micropore volume increased from 0.186 cm^3/g to 0.239 cm^3/g. This reveals a potential symbiotic relationship between hold time and pyrolysis temperature that warrants further optimisation. This observation aligns with established literature that reports an inverse correlation between microporosity development and residence time for CO_2-activated samples.

Contrary to the findings observed for temperature and hold time, the CO_2 flow rate exhibited negligible impact on yield, surface area, or porosity, thus aligning with previously published work. [45 46] This finding points to a crucial interaction between pyrolysis temperature and residence time, which is paramount for crafting high surface area, highly microporous materials. [28-31] Notably, samples EX37-850-15-CO_2-600 and EX38-850-15-CO_2-100 showed high BET surface areas (736 m^2/g and 722 m^2/g, respectively) and appreciable micropore volumes (~0.236 cm^3/g). Given that the microporosity of these samples exceeds 84%, they demonstrate exceptional potential for CO_2 sorption. Their yields also make them attractive for further exploration. Corresponding Nitrogen isotherms can be found in Appendix G: N_2 Isotherm Plots, Figures 113-118.

Table 34 - Activated Samples, Conditions and Adsorption results

Biochar Identification	Final Temp (°C)	Hold Time (mins)	Activating method	Yield (%)	BET Surface Area (m^2/g)	t-plot Micropore Area (m^2/g)	t-plot Micropore Volume (cm^3/g)	% micro-porosity
CO_2 Activated Samples			CO_2 Flow Rate (mL/m)					
EX15-500-2H-CO_2-100	500	120	100	25.5	0.1	5	0.002	N/A
EX16-700-2H-CO_2-100	700	120	100	23.7	N/A	N/A	N/A	N/A
EX17-900-2H-CO_2-100	900	120	100	1.0	N/A	N/A	N/A	N/A
EX18-800-2H-CO_2-100	800	120	100	5.92	535	366	0.189	68.4
EX20-500-2H-CO_2-600	500	120	600	24.3	5	9	0.005	N/A
EX21-700-2H-CO_2-600	700	120	600	21.2	208	181	0.093	87
EX22-800-2H-CO_2-600	800	120	600	5.1	506	361	0.186	71.3
EX37-850-15-CO_2-600	850	15	600	15.1	736	621	0.239	84.3
EX38-850-15-CO_2-100	850	15	100	15.7	722	614	0.236	84.9
EX39-700-15-CO_2-600	700	15	600	23.0	0.6	N/A	N/A	N/A
EX40-700-15-CO_2-100	700	15	100	23.6	0.6	N/A	N/A	N/A
KOH Activated Samples			Biochar:KOH Mass					
EX23-800-2H-KOH-1:1	800	120	KOH 1:1	13.6	1185	1066	0.551	89.9
EX25-900-2H-KOH-1:1	900	120	KOH 1:1	11.0	1217	996	0.511	81.8
EX26-500-2H-KOH-1:1	500	120	KOH 1:1	20.8	262	224	0.115	85.4
EX27-700-2H-KOH-1:1	700	120	KOH 1:1	17.2	845	745	0.385	88.1
EX28-500-2H-KOH-1:8	500	120	KOH 1:8	19.0	2	3	0.002	N/A
EX29-700-2H-KOH-1:8	700	120	KOH 1:8	4.2	2862	193	0.084	6.7
EX30-800-2H-KOH-1:8	800	120	KOH 1:8	5.1	3196	N/A	0	N/A
EX31-900-2H-KOH-1:8	900	120	KOH 1:8	1.37	3204	N/A	0	N/A
EX41-1000-15-KOH-1:1	1000	15	KOH 1:1	22.7	23	11	0.004	49.2
EX42-700-15-KOH-1:1	700	15	KOH 1:1	10.8	1085	943	0.361	86.9
EX43-1000-15-KOH-1:8	1000	15	KOH 1:8	44.2	478	415	0.159	86.7
EX44-700-15-KOH-1:8	700	15	KOH 1:8	61.8	28	24	0.009	86.7

Biochar Identification	Final Temp (°C)	Hold Time (mins)	Activating method	Yield (%)	BET Surface Area (m^2/g)	t-plot Micropore Area (m^2/g)	t-plot Micropore Volume (cm^3/g)	% micro-porosity
KOx activated samples			Biochar:KOx					
EX45-900-2H-KOx-1:1	900	120	KOx 1:1	15.4	1472	1232	0.476	83.6
EX46-500-2H-KOx-1:1	500	120	KOx 1:1	21.0	19	17	0.006	87.5
EX47-900-15-KOx-1:1	900	15	KOx 1:1	N/A	N/A	N/A	N/A	N/A
EX48-500-15-KOx-1:1	500	15	KOx 1:1	22.3	5	2	0.001	48.2
EX49-900-15-KOx-1:8	900	15	KOx 1:8	22.3	160	100	0.039	62.4
EX50-500-15-KOx-1:8	500	15	KOx 1:8	16.4	159	127	0	80.0
EX51-900-2H-KOx-1:8	900	120	KOx 1:8	N/A	N/A	N/A	N/A	N/A
EX52-500-2H-KOx-1:8	500	120	KOx 1:8	21.7	41	12	0.005	28.9
EX53-900-2H-KOX-1:1 (pre-pyrolysed)	900	120	KOx 1:1	15.6	1188	1099	0.419	92.5
EX54-700-2H-KOx-1:1 (pre-pyrolysed)	700	120	KOx 1:1	18.2	417	393	0.149	94.1
EX55-500-2H-KOx-1:1 (pre-pyrolyzed)	500	120	KOx 1:1	20.5	19	20.8	0.006	N/A
EX56-1000-2H-KOx-1:1	1000	120	KOx 1:1	12.6	1570	1082	0.430	68.9
EX58-1100-30-KOx-1:1	1100	30	KOx 1:1	19.7	774	731	0.278	94.5
EX59-700-68-KOx-1:4.5	700	68	KOx 1:4.5	22.0	504	450	0.172	89.2
EX60-1200-68-KOx-1:4.5	1200	68	KOx 1:4.5	14.9	1307	1061	0.413	81.2
EX61-400-68-KOx-1.45	400	68	KOx 1:4.5	21.2	20	7	0.002	36.1
EX62-700-5-KOx-1:4.5	700	5	KOx 1:4.5	27.2	5	N/A	0	N/A
EX63-700-68-KOx-1:4.5	700	68	KOx 1:4.5	22.4	558	509	0.194	91.2
EX64-700-180-KOx-1:4.5	700	180	KOx 1:4.5	18.8	847	758	0.289	89.4
EX65-700-68-KOx-1:10	700	68	KOx 1:10	23.8	599	496	0.191	82.8
Fungal activated samples								
EX75-500-15-GO	500	15	GO	8.8	1	4	0.001	N/A
EX77-900-15-GO	900	15	GO	9.9	23	24	0.009	N/A
EX78-500-2H-GO	500	120	GO	10.4	2	3	0.001	N/A
EX79-700-15-GO	700	15	GO	11.3	5	11	0.003	N/A
EX80-900-2H-GO	900	120	GO	11.8	3	0.7	0.000	N/A
EX81-700-2H-GO	700	120	GO	14.6	3	19	0.006	N/A

Biochar Identification	Final Temp (°C)	Hold Time (mins)	Activating method	Yield (%)	BET Surface Area (m^2/g)	t-plot Micropore Area (m^2/g)	t-plot Micropore Volume (cm^3/g)	% micro-porosity
EX82-700-15-GO	700	15	GO	13	15	17	0.006	N/A
EX83-500-60-GO	500	60	GO	21	8	9	0.003	N/A
EX84-900-60-GO	900	60	GO	9.7	0	N/A	N/A	N/A

8.5.4. KOH Activated samples

As outlined in the methodology section, KOH was used to chemically activate the SCG samples with the aim of significantly enhancing the porosity and surface area of the biochar. This activation method is known for its effectiveness in developing highly porous structures, making the biochar more suitable for applications such as CO_2 adsorption.

The results from the KOH activated samples are outlined in Table 34. An observed trend shows that an increase in final temperature from 500 °C to 900 °C (for samples with a 1:1 biochar mass ratio and a hold time of 120 min) typically results in an increase in BET surface area, micropore area, and micropore volume. For example, the BET surface area increased from 262 m^2/g (EX26-500-2H-KOH-1:1) to 1217 m^2/g (EX25-900-2H-KOH-1:1), and the micropore volume increased from 0.115 cm^3/g to 0.511 cm^3/g. However, this enhancement comes with a trade-off in terms of yield, which decreases under these conditions.

Additionally, when the biochar:KOH mass ratio was increased from 1:1 to 1:8 at a constant temperature (either 700 °C or 900 °C for a 120 min hold time), a significant increase in the BET surface area was observed. A maximum surface area of 3204 m^2/g was recorded for the sample EX31-900-2H-KOH-1:8 . Yet, this enhancement in surface area was accompanied by a considerable decrease in yield and a loss of microporosity.

These findings are in line with previous studies, which demonstrated that elevating pyrolysis temperature and activation intensity positively impacts surface area, but this often comes at the cost of yield and microporosity. [27-31]

Interestingly, the hold time appeared to have minimal effect on the proportion of microporosity, with samples obtained at dwell times of 15 and 120 mins exhibiting remarkably similar percentages of microporosity under comparable test conditions. Generally, hold time would influence the degree of activation, leading to an increased surface area and porosity. However, this can also result in a yield decrease due to more biochar being consumed or altered in the process. For example, when comparing the samples EX42-700-15-KOH-1:1 and EX27-700-2H-KOH-1:1, which have surface areas of 1085 m^2/g and 845 m^2/g respectively, similar microporosity was observed. In contrast, a dramatic difference in results is noted when comparing EX29-700-2H-KOH-1:8 and EX44-700-15-KOH-1:8, with surface areas of 2862 m^2/g and 28 m^2/g respectively. These observations suggest that the impact of hold time on the properties of activated biochar warrants further investigation. In terms of surface area and microporosity, the most

promising samples wereEX23-800-2H-KOH-1:1 and EX31-900-2H-KOH-1:8 , with biochar:KOH mass ratios of 1:1 and 1:8, respectively.

The results suggest that final temperature, biochar:KOH mass ratio, and hold time can significantly influence the properties of KOH-activated biochar. Among the tested conditions, a final temperature of 800 °C, a 1:1 biochar:KOH mass ratio, and a hold time of 120 min seem to provide a balance between yield, surface area, and microporosity. These conditions make the biochar a promising candidate for CO_2 adsorption applications. However, the highest surface area was obtained with a 1:8 biochar:KOH mass ratio at 900 °C, even though this led to a decrease in yield and either undefined or negative micropore volume. Further studies may help optimise these conditions to achieve the best balance of these properties for efficient CO_2 adsorption. Corresponding Nitrogen isotherms can be found in Appendix G: N_2 Isotherm Plots, Figures 119-133.

8.5.5. KOx Activated samples

As outlined in the methodology, potassium oxalate (KOx) was used to chemically activate the SCG-derived biochar in an effort to enhance surface area and develop a highly porous structure suitable for CO_2 adsorption. The performance outcomes for the KOx-activated series are summarised in Table 34.

Elevating the final activation temperature from 500 °C to 900 °C (for samples synthesised at a constant 1:1 biochar:KOx mass ratio with a 2-hour hold time) led to marked increases in BET surface area, micropore area, and micropore volume. These enhancements occurred alongside a corresponding reduction in yield. The sample synthesised at 900 °C under these conditions (EX45-900-2H-KOx-1:1 exhibited the highest measured micropore area, with a BET surface area of 1473 m^2/g, micropore area of 1232 m^2/g, micropore volume of 0.477 cm^3/g, and microporosity of 83.6%.

Increasing the KOx loading from 1:1 to 1:8 (at both 500 °C and 900 °C, with a 2-hour hold time) resulted in an unexpected reduction in BET surface area and micropore metrics. While a more aggressive activation regime would conventionally be expected to enhance pore development, the observed decline may be attributed to excessive burn-off and structural collapse, reducing accessible surface area. Yields under these conditions were either slightly higher or comparable to the lower-ratio samples, possibly due to the formation of inorganic residues. Additionally, some samples presented anomalous negative micropore volumes derived from *t*-plot analysis, likely resulting from model artefacts where

calculated external surface area exceeds total surface area, often caused by non-ideal isotherm behaviour or the presence of mesoporosity.

Retention time significantly affected the characteristics of the activated biochar. For example, reducing the hold time to 15 min (EX48-500-15-KOx-1:1 significantly increased the yield compared to samples held for 2 h at similar temperatures with the same biochar:KOx mass ratio. However, this resulted in a considerable decrease in surface area and micropore area.

A significant finding in this investigation was the impact of pre-pyrolysis on the properties of KOx-activated biochar. The pre-pyrolysed sample exhibited a higher fraction of micropores, despite a decrease in surface area and total micropore area. This suggests that pre-pyrolysis might be influencing the pore structure. In light of previous studies that showed enhanced formation of oxygen-containing functional groups on the biochar surface during KOH activation with pre-pyrolysis, it could be postulated that similar effects might occur with KOx activation. However, as this effect has not been extensively studied in the context of KOx activation, further exploration is needed.

The most promising samples in terms of surface area and microporosity were 900-2H-KOx-1:1 (with a 1:1 biochar:KOx mass ratio) and EX53-900-2H-KOX-1:1 (pre-pyrolysed) with a 1:1 biochar:KOx mass ratio). Comprehensive further analysis is required to fully understand their CO_2 adsorption potential.

The findings of this study corroborate previous research on KOx activation of biochar. For instance, the significant improvement in biochar surface area with an increase in pyrolysis temperature underscores the importance of this parameter in the production process. In contrast to the trend seen in KOH activations, an increase in the biochar:KOx ratio does not enhance the surface area, underscoring the distinct behaviour of different activating agents. [32-35] Notably, this study observed a significant increase in biochar microporosity with KOx activation across almost all conditions, peaking at 94%. This indicates the potential of KOx activation to produce highly microporous biochar, desirable for many applications.

The work conducted here demonstrates that the final temperature, biochar:KOx mass ratio, and retention time can significantly alter the properties of KOx-activated biochar. Among the conditions evaluated, a final temperature of 900 °C, a 1:1 biochar:KOx mass ratio, and a 2-h hold time provide a favourable balance between yield, surface area, and microporosity, suggesting its potential for CO_2 adsorption applications. Although the highest surface area

was achieved with a 1:8 biochar:KOx mass ratio at 500 °C, this was coupled with a decrease in yield and occasional instances of negative or undefined micropore volume. Future research will aim to optimise these conditions to maximise the efficiency of CO_2 adsorption. Corresponding Nitrogen isotherms can be found in Appendix G: N_2 Isotherm Plots, Figures 134-149.

8.5.6. Fungal Activated samples

As outlined in the methodology section, fungal activation was explored as a biological method to enhance the porosity and surface area of biochar. This innovative approach leverages the metabolic activity of fungi to introduce and modify functional groups on the biochar surface, potentially improving its adsorption capabilities in an environmentally friendly manner.

The fungal activation approach, in its current form, was found to be largely ineffective. Although the treated samples exhibited minor improvements in surface area and microporosity over untreated samples (see Table 34), these enhancements were not comparable to those achieved by physical and chemical activations.

Specifically, the EX77-900-15-GO sample processed at 900 °C for 15 min yielded a BET surface area of 23 m^2/g and a micropore area of 24 m^2/g. The resulting BET surface area and micropore area, while improved over untreated biochar, were significantly lower than those obtained through other activation methods such as CO_2, KOH or KOx activation.

It is important to consider that these modest enhancements may not be solely due to the fungal activation process. The biochar samples contained additional biomass components, specifically rye grain and hay. The rye grain was incorporated as grain spawn, while hay was utilised to aid in moisture retention during the preparation process.

As such, it is conceivable that these additional biomass constituents could be contributing to the slight increase in surface area and microporosity observed in the samples. As such, the precise impact of fungal activation on biochar properties remains uncertain. Further comprehensive studies are required to definitively ascertain the efficacy of this method. Low yields were observed across all samples, which can be attributed to the biochar not being dried prior to measurement. Notably, moisture content in biochar samples can significantly affect the yield measurements, and future studies could benefit from ensuring samples are thoroughly dried before measurement to provide more accurate data.

Another observation was the reported t-plot micropore areas, which in most cases were larger than the total BET surface areas. This discrepancy is likely due to the low overall surface areas of the samples, potentially leading to inaccurate readings when assessing microporosity. This highlights the need for further refinement of the measurement methods when dealing with biochars having such low surface areas.

Although the fungal activation of biochar presents a novel approach, the current methodology proved to be largely ineffective in comparison to other activation methods. Future research should focus on refining this method, ensuring samples are adequately prepared and dried, and possibly exploring other fungal strains or variations in the activation process to improve results. Corresponding Nitrogen isotherms can be found in Appendix G: N_2 Isotherm Plots, Figures 150-157.

8.5.7. Sample Selection

The present study employed several biochar activation methods, with the aim to compare their performance and feasibility for scale-up. The most promising samples from each method are compared in Table 35. Physical activation, particularly using CO_2, is often favoured due to its simplicity, cost-effectiveness, and minimal generation of harmful by-products. However, when compared to the other methods employed in this study, CO_2 activation, though environmentally benign, was not found to be competitive. The surface area and microporosity achieved were relatively lower, thus limiting its potential for applications requiring high adsorption capabilities.

Chemical activation, on the other hand, often achieves superior performance in terms of surface area and porosity, albeit with some significant drawbacks. Potassium hydroxide (KOH) is one of the most frequently used chemical activating agents due to its effectiveness in enhancing biochar porosity. Indeed, the results obtained with KOH-activated biochar demonstrated high surface areas and microporosity. However, the practicality of KOH for large-scale applications is constrained by its high toxicity, corrosiveness, and the generation of harmful by-products.

To address these limitations, this study also explored the use of potassium oxalate (KOx), a less corrosive and more manageable activating agent. The results indicate that KOx activation can yield biochar with a desirable balance of surface area, microporosity, and yield. Notably, KOx-activated biochars demonstrated a higher fraction of micropores, echoing previous studies, which is a desirable feature for CO_2 adsorption. However, despite

its advantages over KOH, KOx activation still entails significant costs and produces harmful by-products, presenting challenges for its adoption at scale. In another attempt to overcome the limitations of both physical and chemical activation methods, a novel biological activation approach using a fungus was explored. Regrettably, initial attempts using this method proved largely ineffective, with the resultant biochar exhibiting only minor improvements in surface area and microporosity.

While each activation method presents its own benefits and drawbacks, this study suggests that KOx activation could potentially offer a balanced performance in terms of yield, surface area, and microporosity.

Table 35 - Top-performing SCG-derived biochar samples based on yield, surface area, and microporosity. Key synthesis conditions and t-plot textural properties are shown for each candidate.

Biochar Identification	Final Temp (°C)	Hold Time (mins)	Yield (%)	BET Surface Area (m^2/g)	t-plot Micropore Area (m^2/g)	t-plot Micropore Volume (cm^3/g)	% micro-porosity
EX37-850-15-CO_2-600	850	15	15.1	736	621	0.239	84.3
EX38-850-15-CO_2-100	850	15	15.7	722	614	0.236	84.9
EX23-800-2H-KOH-1:1	800	120	13.6	1185	1066	0.551	89.9
EX42-700-15-KOH-1:1	700	15	10.8	1085	943	0.361	86.9
EX45-900-2H-KOx-1:1	900	120	15.4	1472	1232	0.476	83.6
EX53-900-2H-KOX-1:1 (pre-pyrolysed)	900	120	15.6	1188	1099	0.419	92.5

8.6. Summary

FTIR spectroscopy was largely ineffective due to the highly carbonised nature of the biochars. Despite using a Ge-ATR crystal to enhance resolution, most spectra showed limited peaks, with only weak signals from aromatic C=C and hydroxyl groups. This highlights the limitations of using FTIR to analyse highly carbon-rich materials and the need for complementary techniques. However, XPS offered a detailed view of surface composition and bonding. It confirmed elevated nitrogen in fungal-treated samples and nitrogen loss in chemically activated ones, aligning with CHN trends. High-resolution spectra identified pyridinic, pyrrolic, and graphitic nitrogen species, and various oxygen

groups, demonstrating that activation methods fundamentally alter surface chemistry. Discrepancies between XPS and CHN for non-activated samples may reflect surface sensitivity or batch variability when using XPS.

Proximate analysis showed that increasing pyrolysis temperature decreased volatile matter and increased fixed carbon, as expected. Chemically activated samples had unexpectedly low ash content, due to post-activation washing removing residual inorganics—highlighting the importance of post-treatment effects on proximate data. This was supported by CHN analysis, which showed that fungal pre-treatment via mushroom cultivation (yielding MSCG) substantially increased nitrogen content in the biomass, retained after pyrolysis. This points to fungal treatment as a viable, sustainable pre-treatment for nitrogen doping, combining food production with biochar enhancement in a circular economy model.

Samples for CO_2 adsorption analysis were selected based on surface area and microporosity from N_2 adsorption data. Non-activated SCG biochars had negligible porosity and surface area, even at high temperatures. CO_2 activation notably improved textural properties, especially at high temperatures with short hold times, enhancing microporosity and indicating suitability for post-combustion CO_2 capture. KOH activation achieved the highest BET surface areas (some over 3000 m^2/g), though often at the cost of microporosity and yield. KOx activation gave a more balanced performance, with high surface area and microporosity, using milder conditions and fewer hazards, making it more viable for scale-up.

Chapter 9. CO_2 Adsorption

Selected SCG-derived biochars were evaluated for their suitability in post-combustion carbon capture applications, using gravimetric determination of CO_2 adsorption capacity across a range of pressures, kinetic analysis to assess sorption rates and diffusion characteristics, and cycling tests to evaluate the stability and renderability of the materials over repeated use. Additionally, thermodynamic parameters (i.e. enthalpy and entropy of adsorption), as well as activation energies, from kinetic data, are calculated to provide deeper insight into the nature of the adsorption process.

Understanding these characteristics is essential for determining the feasibility of using biochar as a solid sorbent in industrial carbon capture systems. High capacity, favourable kinetics, low regeneration energy, and long-term cyclic stability are key attributes of viable sorbents. The results presented herein help elucidate how activation methods and pyrolysis conditions influence these performance metrics, thereby supporting the rational design of biochar-based materials for scalable and energy-efficient CO_2 capture technologies.

9.1. Sample Selection

Five biochar samples were selected for CO_2 adsorption studies based on their textural, chemical, and surface characteristics as established in preceding chapters. The selection aimed to represent a range of activation methods and material properties to assess their influence on CO_2 uptake performance and to test underlying assumptions regarding structure–function relationships in engineered sorbents.

Two KOx-activated samples—**EX45-900-2H-KOX-1:1** and **EX53-900-2H-KOX-1:1 (pre-pyrolysed)**—were selected due to their high BET surface areas (1473 and 1189 m^2/g, respectively) and significant microporous character (83.65% and 92.54%). These properties are critical for enhancing CO_2 adsorption at low partial pressures, typical of post-combustion flue gas conditions. Both samples exhibited a predominance of ether/alcohol (O–2) surface groups and diverse nitrogen functionalities, contributing to their potential affinity for CO_2.

Two KOH-activated samples were also selected: **EX23-800-2H-KOH-1:1** and **EX31-900-2H-KOH-1:8** . These were included to provide a comparative reference, despite the practical limitations of KOH activation—such as high cost, handling complexity, and environmental burden. Sample EX23-800-2H-KOH-1:1 was chosen for its high surface area (1185 m^2/g)

and microporous character (89.9%), enabling direct comparison with the KOx-activated materials. In contrast, sample EX31-900-2H-KOH-1:8 possessed a notably high BET surface area (3204 m^2/g) but negligible microporosity. Its inclusion facilitates evaluation of the hypothesis that microporosity is a key determinant of CO_2 adsorption capacity and selectivity at low partial pressures. Furthermore, its structural characteristics may be advantageous in high-pressure scenarios such as oxy-fuel combustion processes, where total surface area plays a more dominant role.

The final sample, **EX37-850-15-CO_2-600**, represents the best-performing CO_2-activated biochar in terms of adsorption per unit area and surface functionality. Although it exhibited a comparatively lower BET surface area (737 m^2/g) and microporous character (84.3%) than the KOx- and KOH-activated samples, it retained a substantially higher content of nitrogen-containing surface functionalities, as indicated by XPS and CHN analysis. Given the known affinity of basic nitrogen groups for acidic CO_2 molecules, this sample was selected to explore the influence of surface chemistry on selective CO_2 adsorption.

9.2. Gravimetric CO_2 Adsorption Capacity

Gravimetric CO_2 adsorption capacity was evaluated for the five selected biochar samples (EX23-800-2H-KOH-1:1, EX31-900-2H-KOH-1:8, EX37-850-15-CO_2-600, EX45-900-2H-KOX-1:1, EX53-900-2H-KOX-1:1 (pre-pyrolysed) across a range of pressures and temperatures to simulate conditions relevant to post-combustion and high-pressure carbon capture applications. The results are presented as a function of pressure in Figure 56, with comparative adsorption capacities at representative conditions shown in Figure 57. Corresponding numerical values are summarised in Table 36.

The isotherms (Figure 56) generally exhibit Type I(b) behaviour characteristic of microporous materials, with a steep initial uptake followed by a gradual plateau at higher pressures. This confirms the predominance of monolayer adsorption at lower pressures, especially in samples with significant microporosity (e.g. samples EX23-800-2H-KOH-1:1, EX45-900-2H-KOX-1:1, EX53-900-2H-KOX-1:1 (pre-pyrolysed) and suggests multilayer formation or pore filling at higher pressures.

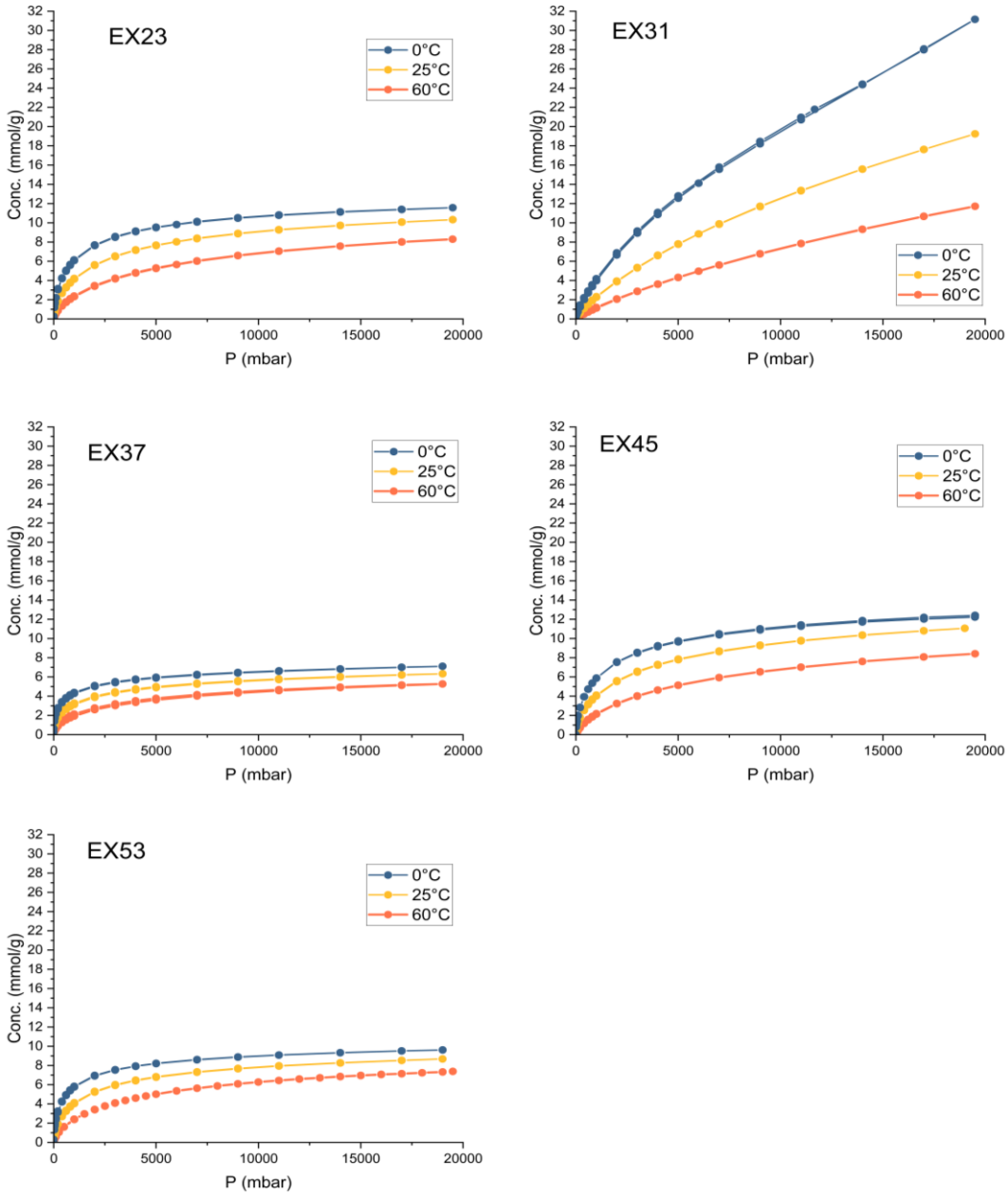

Figure 56 - Gravimetric CO_2 adsorption isotherms for SCG biochar samples EX23-800-2H-KOH-1:1, EX31-900-2H-KOH-1:8, EX37-850-15-CO_2-600, EX45-900-2H-KOX-1:1, and EX53-900-2H-KOX-1:1 (pre-pyrolysed) measured at 0 °C, 25 °C, and 60 °C.

Figure 57 presents comparative CO_2 adsorption capacities (mmol/g) under three relevant conditions:

- 0 °C and 19000 mbar (blue): simulating extreme pressure environments, such as oxy-fuel combustion systems.
- 25 °C and 1000 mbar (orange): representing standard laboratory conditions and a reference for comparing literature values.

- 60 °C and 150 mbar (red): mimicking typical post-combustion flue gas conditions.

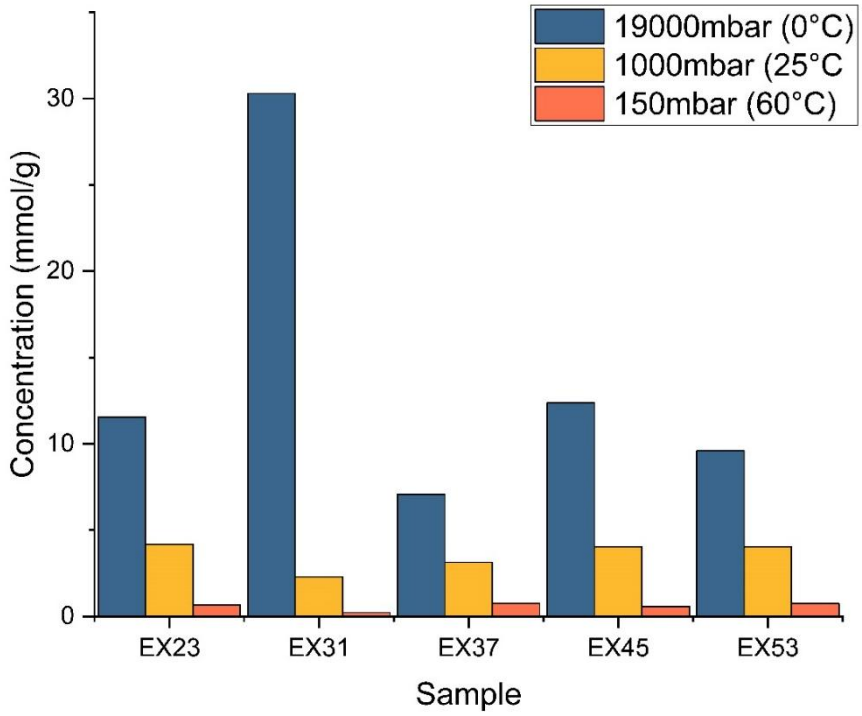

Figure 57 - Gravimetric CO_2 adsorption capacities (mmol/g) of biochar samples EX23-800-2H-KOH-1:1, EX31-900-2H-KOH-1:8, EX37-850-15-CO_2-600, EX45-900-2H-KOX-1:1, and EX53-900-2H-KOX-1:1 (pre-pyrolysed) at 19000 mbar (0 °C), 1000 mbar (25 °C), and 150 mbar (60 °C).

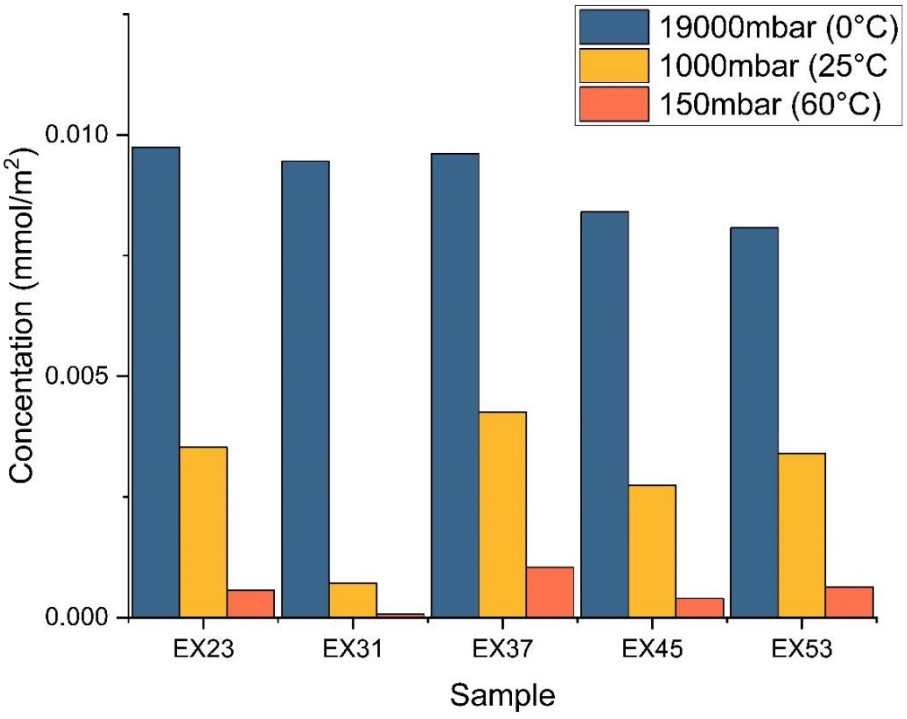

Figure 58 - Normalised CO_2 adsorption capacities (mmol/m²) of selected biochars at 19000 mbar (0 °C), 1000 mbar (25 °C), and 150 mbar (60 °C).

Under high-pressure conditions (0 °C, 19000 mbar), sample EX31-900-2H-KOH-1:8 significantly outperformed all other samples, achieving an uptake of 30.3 mmol/g, due to its exceptionally high BET surface area (3204 m^2/g) despite its negligible microporosity. This supports the notion that surface area dominates in multilayer adsorption regimes at very high pressures, whereas micropore volume becomes the controlling factor at lower pressures where pore confinement effects govern adsorption.

Notably, correlation analysis (found in Appendix H:) performed across the selected samples indicates that micropore volume is the strongest structural predictor of CO_2 uptake under near-ambient conditions. Samples with higher micropore volumes consistently exhibited greater adsorption capacities at 25 °C and 1000 mbar. This trend supports a micropore-filling mechanism as the dominant adsorption process in these carbons. In contrast, total BET surface area was found to be a poor predictor of uptake in this regime, particularly when mesoporosity dominates, as demonstrated by the behaviour of sample EX31-900-2H-KOH-1:8. These observations are consistent with established adsorption theory and highlight that accessible micropore volume, rather than total surface area, governs adsorption performance at sub-atmospheric CO_2 pressures.

At intermediate pressure (25 °C, 1000 mbar), sample EX23-800-2H-KOH-1:1 (4.18 mmol/g), sample EX45-900-2H-KOX-1:1 (4.03 mmol/g), and sample EX53-900-2H-KOX-1:1 (pre-pyrolysed) (4.04 mmol/g) demonstrated comparable and superior uptake, attributable to their combination of microporous structure and favourable surface chemistry. In contrast, the performance of sample EX31-900-2H-KOH-1:8 was diminished (2.28 mmol/g), highlighting its inefficiency in this regime and the limited utility of surface area alone without corresponding pore confinement or surface functionality effects.

The most critical condition for this study—60 °C and 150 mbar—reflects the CO_2 partial pressure and temperature typical of flue gas in post-combustion carbon capture. Under these conditions, sample EX37-850-15-CO_2-600 exhibited the highest uptake (0.76 mmol/g), closely followed by sample EX53-900-2H-KOX-1:1 (pre-pyrolysed) (0.75 mmol/g) and sample EX23-800-2H-KOH-1:1 (0.67 mmol/g). The performance of sample EX37-850-15-CO_2-600 is notable given its moderate surface area (737 m^2/g), suggesting that its high nitrogen content (4.1% by CHN, 3.5% by XPS), and well-developed micropore volume strongly enhances CO_2 adsorption affinity under dilute conditions. This is further corroborated in Figure 58, which normalises uptake by surface area ($mmol/m^2$) and

demonstrates superior surface affinity of sample EX37-850-15-CO_2-600 for CO_2 between 150 and 1000 mbar.

Notably, the influence of temperature is substantial across all samples, with increasing temperature leading to reduced uptake (Figure 56). This inverse temperature dependence is characteristic of physisorption and further confirms the exothermic nature of CO_2 adsorption on these materials. The temperature effect is most pronounced in microporous samples (EX45-900-2H-KOX-1:1, EX53-900-2H-KOX-1:1 (pre-pyrolysed)), consistent with enhanced pore-filling mechanisms at lower temperatures.

At high pressure (19000 mbar), the differences in normalised uptake (mmol/m²) between samples become negligible (Figure 58), suggesting that at elevated CO_2 concentrations, the adsorption mechanism shifts from site-specific interactions towards surface saturation and multilayer formation. This diminishes the relative influence of microporosity and surface chemistry, highlighting the importance of these features only under sub-atmospheric CO_2 concentrations.

The experimental error in gravimetric CO_2 uptake was estimated at ±0.003 mmol/g**,** based on IGA precision. Given the instrument's high sensitivity and consistent sample behaviour, this level of uncertainty is sufficiently low to support the observed trends and confidently distinguish between sample performances.

Table 36 - Gravimetric and surface-area-normalised CO_2 adsorption capacities of selected biochars under three representative conditions relevant to carbon capture (0 °C, 19000 mbar; 25 °C, 1000 mbar; 60 °C, 150 mbar).

	Concentration (mmol/g)			Concentration (mmol/m^2)		
	19000 @ 0 °C	1000 @ 25 °C	150 @ 60 °C	19000 @ 0 °C	1000 @ 25 °C	150@ 60 °C
EX23-800-2H-KOH-1:1	11.5	4.2	0.665684	0.00974	0.00353	0.000562
EX31-900-2H-KOH-1:8	30.3	2.3	0.220115	0.00946	0.000712	6.87E-05
EX37-850-15-CO_2-600	7.07	3.1	0.763579	0.00961	0.00426	0.00104
EX45-900-2H-KOX-1:1	12.4	4.03	0.575975	0.00841	0.00274	0.000391
EX53-900-2H-KOX-1:1 (pre-pyrolysed)	9.6	4.04	0.74566	0.00808	0.00340	0.000628

The gravimetric CO_2 adsorption capacities of the SCG-derived biochars developed in this study—particularly EX23-800-2H-KOH-1:1, EX45-900-2H-KOX-1:1, and EX53-900-2H-KOX-1:1 (pre-pyrolysed), which exhibited uptakes between 4.03 and 4.18 mmol g^{-1} at 25 °C and 1000 mbar—compare favourably with most biomass-derived sorbents reported in the literature. These values exceed those of CO_2-activated whitewood biochar (1.43 mmol g^{-1} at 25 °C, 1000 mbar), as well as ammoniated and CO_2/NH_3-treated soybean straw samples, which typically achieve maximum uptakes of 1.86–2.02 mmol g^{-1} at 30 °C and 1000 mbar. Similarly, cottonwood biochars modified with Mg, Al, or Fe generally fall in the range of 1.3 to 1.6 mmol g^{-1} under comparable conditions (25 °C, 1000 mbar). [36]

When benchmarked against the broader class of solid adsorbents, these SCG biochars perform comparably to several commercial and synthetic porous materials. Zeolite 13X achieves 3.64 mmol g^{-1} at 25 °C and 1013 mbar, while zeolite 5A records 3.5 mmol g^{-1} at 25 °C and 1060 mbar.[351] In contrast, metal–organic frameworks (MOFs) typically surpass these values, but only under significantly elevated pressures. For example, HKUST-1 reaches 4.16 mmol g^{-1} at 25 °C and 1000 mbar, whereas MOF-5 and IRMOF-3 exhibit uptakes of 14.0 and 14.7 mmol g^{-1} respectively, but at 25 °C and 12300 mbar. MIL-101 and NU-1000 achieve extremely high capacities of 40.0 and 46.4 mmol g^{-1}, though these are obtained at 31 °C and 50000 mbar, and 40 °C and 40000 mbar, respectively. Importantly, MOF-177, despite its exceptionally high BET surface area of 4500 m^2 g^{-1}, only reaches 0.77 mmol g^{-1} at 25 °C and 1000 mbar, illustrating that high surface area alone does not guarantee high performance under ambient pressure.

Under post-combustion-relevant conditions of 60 °C and 150 mbar, the performance of sample EX37-850-15-CO_2-600 is particularly noteworthy. With an uptake of 0.76 mmol g^{-1}, it exceeds the low-pressure performance of many benchmark sorbents, including the aforementioned MOF-177. This performance is attributable to the presence of nitrogen functionalities and favourable surface chemistry, which promote selective CO_2 uptake under dilute conditions. As such, the SCG-derived biochars developed here demonstrate performance characteristics that are competitive with, and in some cases superior to, many established materials, particularly when low-cost synthesis routes and operationally relevant pressures are taken into account.

9.2.1. Correlation of Structural and Compositional Properties with CO_2 Uptake

To further elucidate the factors governing CO_2 adsorption performance in SCG-derived biochars, a correlation analysis was conducted between key physicochemical properties and equilibrium CO_2 uptake at 1000 mbar and 25 °C. The parameters examined included elemental composition (C, O, N), BET surface area, micropore area, micropore volume, and percentage microporosity.

It is important to note that this analysis is based on a limited sample set (n = 5), comprising materials produced via different activation routes (KOH, KOx, and CO_2 activation). As such, the correlations presented here should be interpreted as indicative rather than definitive and are primarily used to identify dominant trends rather than establish strict predictive relationships. Additionally, sample EX31 exhibited negligible microporosity; therefore, its micropore area, micropore volume, and microporosity were assigned values of zero to reflect its essentially non-microporous character.

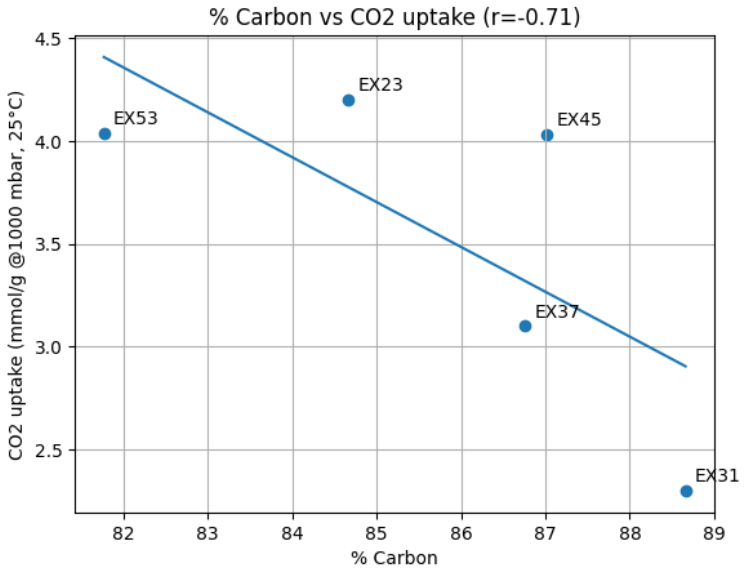

Figure 59 - Correlation between carbon content (%) and CO_2 uptake at 25 °C and 1000 mbar for selected SCG-derived biochars.

Carbon content showed a moderate inverse correlation with CO_2 uptake. This suggests that higher bulk carbon purity does not necessarily translate to higher adsorption capacity. This is consistent with adsorption being governed more strongly by pore structure than by elemental composition. High carbon content may reflect greater structural ordering or graphitisation, which does not inherently improve micropore availability for CO_2 adsorption.

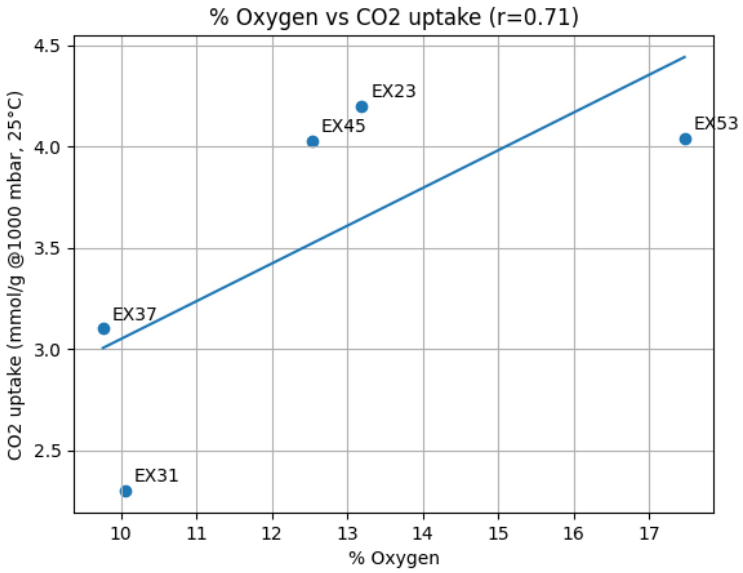

Figure 60 - Correlation between oxygen content (%) and CO_2 uptake at 25 °C and 1000 mbar.

Oxygen content exhibited a moderate positive correlation with CO_2 uptake. This trend may indicate a minor contribution from oxygen-containing surface functional groups, which can enhance CO_2 affinity via dipole–quadrupole interactions. However, the correlation was weaker than that observed for micropore characteristics, suggesting that oxygen functionality plays a secondary role relative to pore structure.

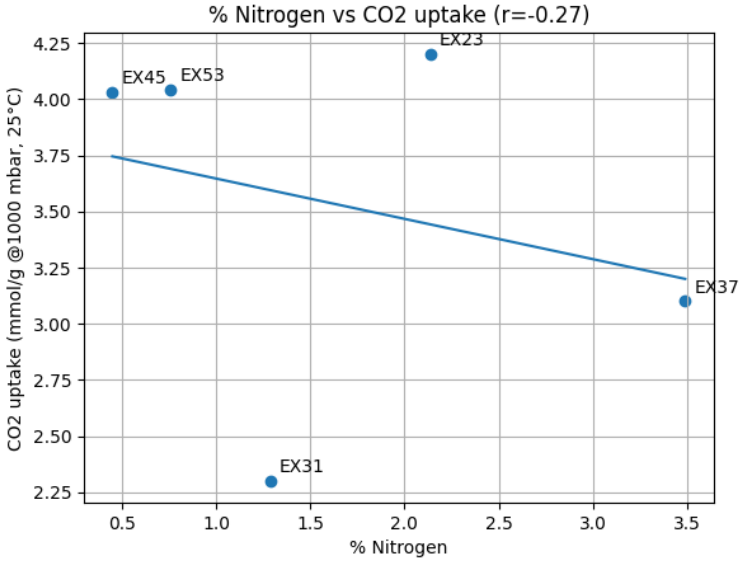

Figure 61 - Correlation between nitrogen content (%) and CO_2 uptake at 25 °C and 1000 mbar.

Nitrogen content showed only a weak relationship with CO_2 uptake. Despite the commonly reported benefits of nitrogen doping for CO_2 adsorption, these results indicate that nitrogen content alone was not a strong predictor of equilibrium uptake in this sample set.

This may reflect the dominance of physical adsorption in micropores under the conditions studied, as well as possible covariation between nitrogen retention and activation severity.

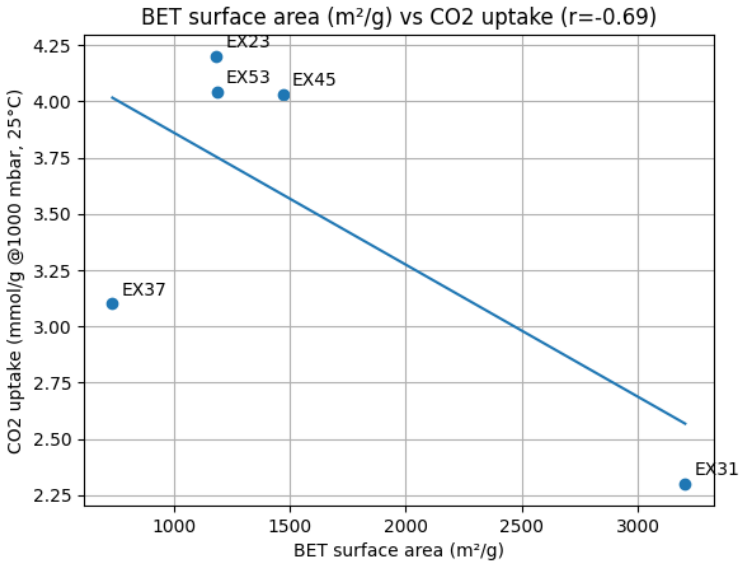

Figure 62 - Correlation between BET surface area and CO_2 uptake at 25 °C and 1000 mbar.

BET surface area displayed a negative correlation with CO_2 uptake once EX31 was included. This behaviour highlights a known limitation of BET surface area as a descriptor for CO_2 capture performance. EX31 possessed the highest BET surface area but exhibited poor adsorption capacity due to its lack of microporosity. This demonstrates that total surface area, particularly when dominated by mesopores, does not necessarily correspond to enhanced CO_2 adsorption.

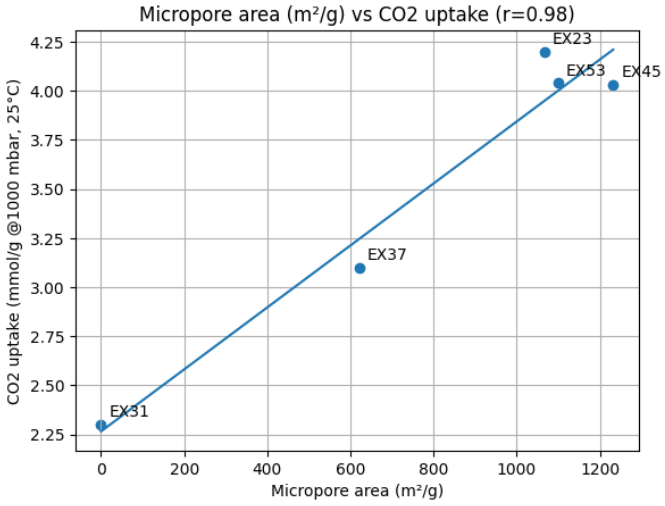

Figure 63 - Correlation between micropore area and CO_2 uptake at 25 °C and 1000 mbar.

Micropore area showed a very strong positive correlation with CO_2 uptake. This supports the well-established role of micropores as the primary adsorption sites for CO_2 in activated carbons. The trend suggests that increasing micropore development directly increases adsorption capacity.

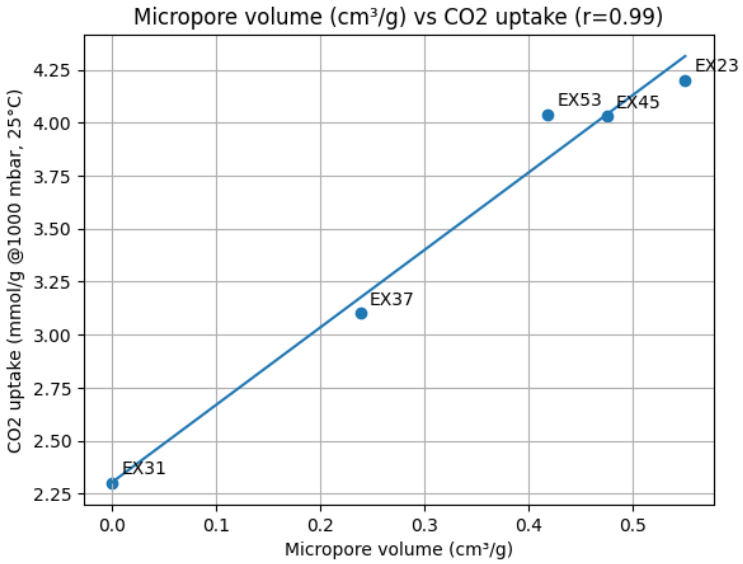

Figure 64 - Correlation between micropore volume and CO_2 uptake at 25 °C and 1000 mbar.

Micropore volume exhibited the strongest correlation with CO_2 uptake among all parameters examined. The near-linear relationship observed strongly supports a micropore-filling adsorption mechanism, consistent with classical Dubinin-based adsorption theory. This finding indicates that available micropore volume is a primary determinant of equilibrium CO_2 capacity in these materials.

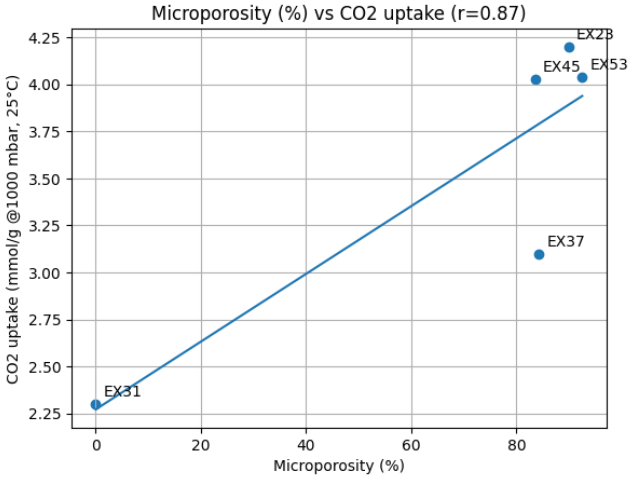

Figure 65 - Correlation between percentage microporosity and CO_2 uptake at 25 °C and 1000 mbar.

Percentage microporosity also showed a strong positive trend with CO_2 uptake once the non-microporous EX31 sample was included. This suggests that a higher fraction of micropores relative to total porosity is beneficial for CO_2 adsorption. However, this parameter was slightly less predictive than absolute micropore volume, indicating that total micropore development remains more important than relative pore distribution.

Across all parameters examined, micropore characteristics demonstrated the strongest relationships with CO_2 uptake. In particular:

- **Micropore volume showed the strongest correlation**
- Micropore area was similarly highly predictive
- BET surface area was not a reliable indicator of performance
- Elemental composition played a secondary role

These results collectively indicate that CO_2 adsorption in SCG-derived biochars is primarily governed by micropore development and follows a micropore-filling mechanism. Surface chemistry appears to modulate adsorption behaviour but does not dominate capacity under the conditions studied.

Given the limited sample size and diversity of activation methods, these trends should be interpreted cautiously. Nevertheless, the consistency of the observed relationships with established adsorption theory lends confidence to the mechanistic conclusions drawn.

9.3. Thermodynamics of Adsorption

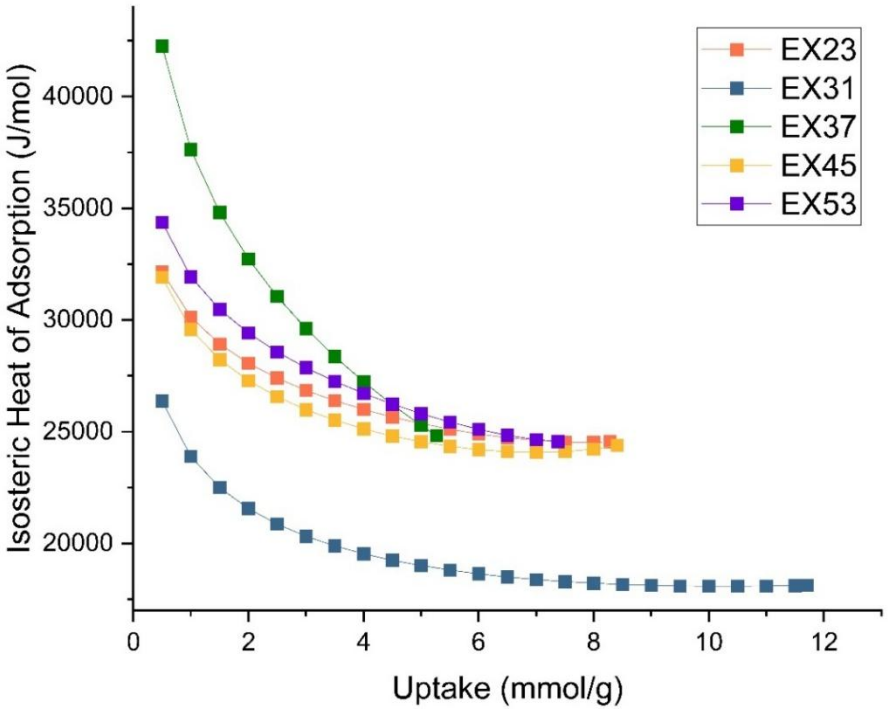

Figure 66 - Isosteric heat of CO_2 adsorption (ΔH_i) as a function of uptake for samples EX23-800-2H-KOH-1:1, EX31-900-2H-KOH-1:8, EX37-850-15-CO_2-600, EX45-900-2H-KOX-1:1, and EX53-900-2H-KOX-1:1 (pre-pyrolysed).

The isosteric heat (ΔH_i) and entropy (ΔS_i) of CO_2 adsorption were determined using the Clausius-Clapeyron method via the isostere approach, extracting values at constant uptake from experimental isotherms measured at 0 °C, 25 °C, and 60 °C. The results, presented in Figure 66 and Figure 67, provide insight into the energetic and entropic landscape of CO_2 adsorption for the five selected biochar samples: EX23-800-2H-KOH-1:1, EX31-900-2H-KOH-1:8, EX37-850-15-CO_2-600, EX45-900-2H-KOX-1:1, and EX53-900-2H-KOX-1:1 (pre-pyrolysed).

Figure 66 displays the variation in isosteric heat of adsorption as a function of uptake. All samples exhibit decreasing ΔH_i with increasing uptake, characteristic of physisorption. This trend reflects the initial occupation of high-energy adsorption sites followed by progressively weaker interactions as loading increases. At low coverage (0.5 mmol/g), sample EX37-850-15-CO_2-600 shows the highest heat of adsorption (42.3 kJ/mol), followed by sample EX53-900-2H-KOX-1:1 (pre-pyrolysed) (34.4 kJ/mol) and sample EX23-800-2H-KOH-1:1 (32.2 kJ/mol), indicating stronger CO_2 interactions. These samples also possess higher nitrogen content and more basic surface functionalities, which enhance interactions with the acidic CO_2 molecule.

The isosteric heats of CO_2 adsorption observed in this study, ranging from 42.3 kJ mol^{-1} at low coverage to 24–25 kJ mol^{-1} at higher uptake, are consistent with physisorption and reflect strong initial interactions followed by weaker multilayer adsorption. These values are notably higher than those typically reported for activated carbons, which exhibit initial heats of adsorption between 25 and 33 kJ mol^{-1}, [352] and broadly align with nitrogen-containing xerogels where ΔH_i falls in the range of 25–30 kJ mol^{-1}. [343] The elevated initial enthalpies observed for EX37-850-15-CO_2-600, EX53-900-2H-KOX-1:1 (pre-pyrolysed), and EX23-800-2H-KOH-1:1 suggest enhanced interactions due to surface nitrogen functionalities, while the convergence at higher loadings confirms a transition to weaker, non-specific adsorption modes.

Sample EX31-900-2H-KOH-1:8, despite its high surface area, exhibits the lowest initial ΔH_i (~26.4 kJ/mol), demonstrating that surface functionality and pore structure, rather than surface area alone, govern interaction strength at low coverage. At higher uptakes (q > 6 mmol/g), the valuess of ΔH_i converge toward 24–25 kJ/mol for all samples, suggesting a shift to weaker, non-specific interactions associated with multilayer adsorption or pore-filling. This convergence reflects the transition from specific adsorption to interactions resembling CO_2 liquefaction, with values around 17–18 kJ/mol aligning with the heat of condensation, and the slightly higher values (~24–25 kJ/mol) observed in microporous samples indicating stronger confinement effects within narrow pores.

Figure 67 shows the corresponding isosteric entropy values. A general increase in ΔS_i with uptake is observed for most samples, indicative of greater molecular disorder as CO_2 loading increases. However, sample EX37-850-15-CO_2-600 exhibits an initial decrease in entropy followed by a gradual increase, suggesting an initial ordering effect potentially linked to strong specific interactions or confinement within micropores, before transitioning to less ordered multilayer adsorption. At low uptake, sample EX31-900-2H-KOH-1:8 exhibits the lowest entropy (129 J/mol K), while sample EX37-850-15-CO_2-600 shows the highest peak entropy (162 J/mol K), consistent with its higher heterogeneity and surface functionality. Samples EX23-800-2H-KOH-1:1, EX45-900-2H-KOX-1:1, and EX53-900-2H-KOX-1:1 (pre-pyrolysed) display intermediate trends, rising from ~134 to 156 J/mol K. The increase in entropy with uptake (Figure 67) supports the view that adsorption initially restricts molecular motion but becomes less ordered as more CO_2 molecules populate available sites and interact with each other rather than with the surface.

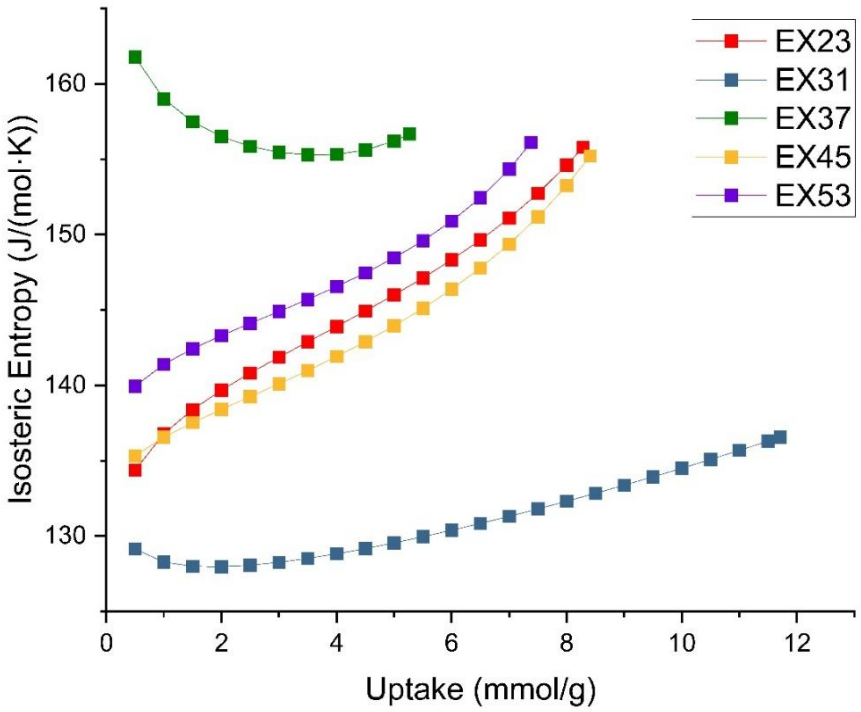

Figure 67 - Isosteric entropy of CO_2 adsorption (ΔS_i) as a function of uptake for samples EX23-800-2H-KOH-1:1, EX31-900-2H-KOH-1:8, EX37-850-15-CO_2-600, EX45-900-2H-KOX-1:1, and EX53-900-2H-KOX-1:1 (pre-pyrolysed).

Taken together, the thermodynamic data affirm that CO_2 adsorption across all samples is dominated by physisorption, with favourable enthalpic interactions at low coverage enhanced by nitrogen functionalities. The decline in ΔH_i and rise in ΔS_i with uptake are consistent with a transition from site-specific adsorption to multilayer physisorption. These findings further support the potential for energy-efficient regeneration and the utility of nitrogen-doped biochars in post-combustion carbon capture.

9.4. Kinetic Analysis

The pressure-dependent adsorption kinetics of CO_2 were evaluated for each sample using a stretched exponential (SE) model. This model is particularly appropriate for characterising systems where a distribution of adsorption or desorption rates is expected due to structural or energetic heterogeneities. The SE model provides two principal parameters: the effective rate constant *k*, which quantifies the overall rate of uptake or release of CO_2, and the dimensionless exponent β, which describes the breadth of the distribution of relaxation times within the system. When β approaches 1, the kinetic process can be interpreted as

largely homogeneous, dominated by a single rate-limiting mechanism such as surface adsorption or macropore diffusion. Conversely, values of β significantly below or above 1 indicate kinetic dispersion, often arising from variations in pore geometry, surface functionalisation, or diffusional resistances within the sorbent.

Kinetic data were collected across a wide pressure range, typically from 25 mbar up to 19500 mbar, at three different temperatures: 0 °C, 25 °C, and 60 °C. Fitting of the SE model was applied independently to the adsorption and desorption branches of each isotherm. This analysis aims to provide insight into how pressure and temperature influence the rate and uniformity of CO_2 transport within the porous matrices, and how these characteristics vary as a function of material structure and activation conditions. The following sections detail the extracted kinetic profiles for each sample, highlighting trends in *k* and β with respect to pressure and temperature.

9.4.1. Sample EX23-800-2H-KOH-1:1

Figure 68 displays the variation of the rate constant *k* with pressure during both adsorption and desorption at the three temperatures studied. At low pressures (25–100 mbar), the rate constants are relatively high, particularly at elevated temperatures. For instance, at 60 °C, the adsorption rate constant reaches 0.050 s^{-1} at 25 mbar, compared to 0.019 s^{-1} at 0 °C. This behaviour is consistent with thermally activated adsorption, where increased molecular mobility enhances the frequency of successful collisions with active sites. However, as pressure increases, k systematically decreases across all temperatures. Beyond 1000 mbar, rate constants generally stabilise in the range of 0.009–0.012 s^{-1}, suggesting a transition from surface-limited to diffusion-limited kinetics. In this regime, the primary resistance to mass transfer arises not from surface accessibility but from internal pore diffusion constraints. Notably, adsorption and desorption curves converge at higher pressures, implying that the adsorption–desorption dynamics are increasingly governed by similar diffusion processes under saturated conditions.

The corresponding variation in the stretching exponent β is shown in Figure 69. At low pressure, β values for both adsorption and desorption are generally below 1, particularly at 25 °C and 60 °C, where values as low as 0.13 and 0.19 are observed. This indicates the presence of multiple simultaneous kinetic processes with a broad distribution of timescales, likely attributable to the complex micro- and mesoporous structure of the material. As pressure increases, β tends to rise toward values between 0.9 and 1.1, particularly at 0 °C.

This convergence suggests a narrowing of the kinetic distribution and a dominance of a single rate-limiting step, most likely associated with intraparticle diffusion in partially saturated pores.

At very high pressures, however, the model begins to produce anomalously large values of β, particularly at 25 °C and 60 °C. At 17000 mbar and 60 °C, for instance, β reaches a value of 2.31, far outside the theoretical upper bound of 1 for the SE model. Such divergence is indicative of a poor model fit, likely arising from the breakdown of the assumptions underpinning the stretched exponential function. Several mechanisms may contribute to this deviation. First, as pressure increases, the sorbent approaches saturation, and additional uptake may involve cooperative effects, pore blocking, or structural rearrangements not well captured by models based on continuous diffusion. Second, at high loadings, the availability of active sites becomes increasingly restricted, and the adsorption front may propagate through the material in a non-uniform manner. Finally, experimental uncertainty increases with pressure due to reduced mass change gradients, which can amplify noise in model fitting and exaggerate the stretching exponent.

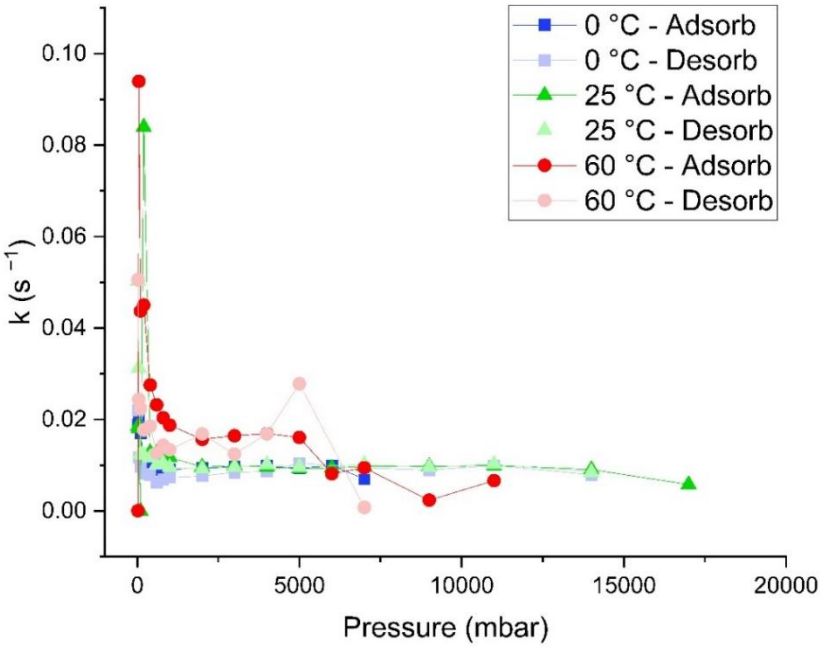

Figure 68 - Effective rate constant (k) for CO_2 adsorption and desorption as a function of pressure for sample EX23-800-2H-KOH-1:1 at 0 °C, 25 °C, and 60 °C.

Taken together, these results indicate that sample EX23-800-2H-KOH-1:1 exhibits relatively fast and heterogeneous adsorption kinetics at low pressure, with a clear transition to more homogeneous and diffusion-limited behaviour at intermediate

pressures. At high pressures, the kinetic model becomes less reliable, and the extracted parameters should be interpreted cautiously due to the likely presence of fitting artefacts and non-ideal adsorption phenomena.

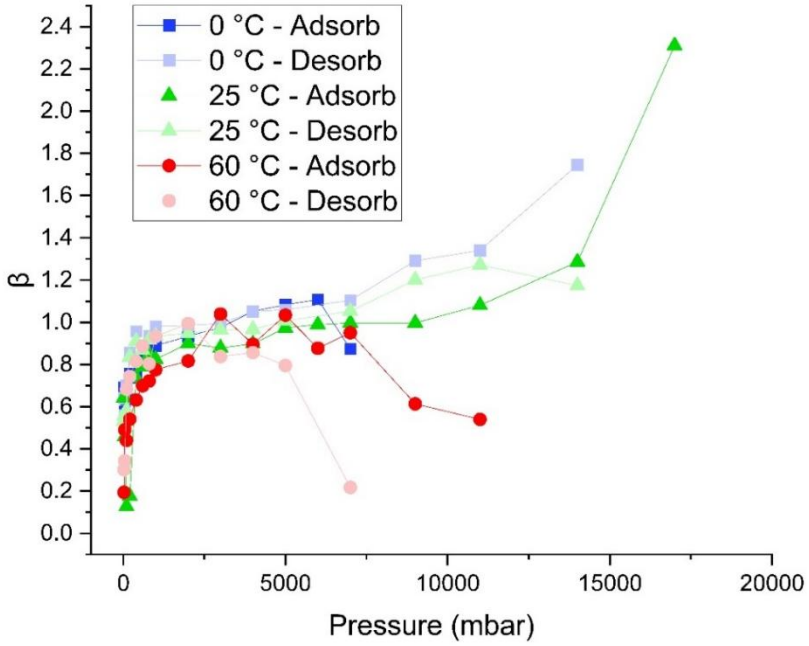

Figure 69 - Stretching exponent (β) for CO_2 adsorption and desorption in sample EX23-800-2H-KOH-1:1 .

9.4.2. Sample EX31-900-2H-KOH-1:8

The kinetic parameters extracted for sample EX31-900-2H-KOH-1:8 are presented in Figure 70 and

Figure 71 showing the pressure dependence of the rate coefficient *k* and the heterogeneity parameter β, respectively. Sample EX31-900-2H-KOH-1:8 is a high-surface-area mesoporous sample and thus provides an instructive contrast to the microporous sample (EX23-800-2H-KOH-1:1) discussed previously.

As shown in Figure 70, the adsorption and desorption *k* values follow a characteristic decay with increasing pressure. At low pressure, *k* exhibits elevated values across all temperatures, falling sharply within the first few hundred mbar before levelling off into a relatively stable plateau. This initial drop is consistent with a regime in which fast uptake into high-affinity sites dominates, followed by a transition to slower pore filling as pressure increases. Compared to sample EX23-800-2H-KOH-1:1, the *k* values for sample EX31-900-2H-KOH-1:8 are broadly similar in trend and magnitude, though a single desorption data point at 60 °C deviates markedly from the overall pattern. This outlier likely arises from

experimental or fitting error, as no systematic increase in fluctuation is observed across the rest of the dataset. Overall, the mesoporous character of sample EX31-900-2H-KOH-1:8 appears to promote consistent and rapid adsorption–desorption kinetics across the pressure range, without introducing significant artefacts or instabilities in *k*. The corresponding β values are plotted in

Figure 71.

As with sample EX23-800-2H-KOH-1:1, β increases rapidly with pressure at low loading, then approaches a more gradual ascent beyond ~1000 mbar. This trend is particularly evident for adsorption branches at 0 °C and 25 °C, which display a secondary rise at higher pressures, reaching values of approximately 1.5 and 1.4, respectively. At 60 °C, β shows more irregularity, likely reflecting greater sensitivity to small deviations in data at elevated temperatures. Unlike sample EX23-800-2H-KOH-1:1, however, desorption β values for sample EX31-900-2H-KOH-1:8 remain relatively consistent with their adsorption counterparts. This suggests that sample EX31-900-2H-KOH-1:8 does not exhibit kinetic hysteresis or restricted desorption pathways—an outcome consistent with its open mesoporous architecture, which should impose fewer energetic or diffusional constraints on gas release.

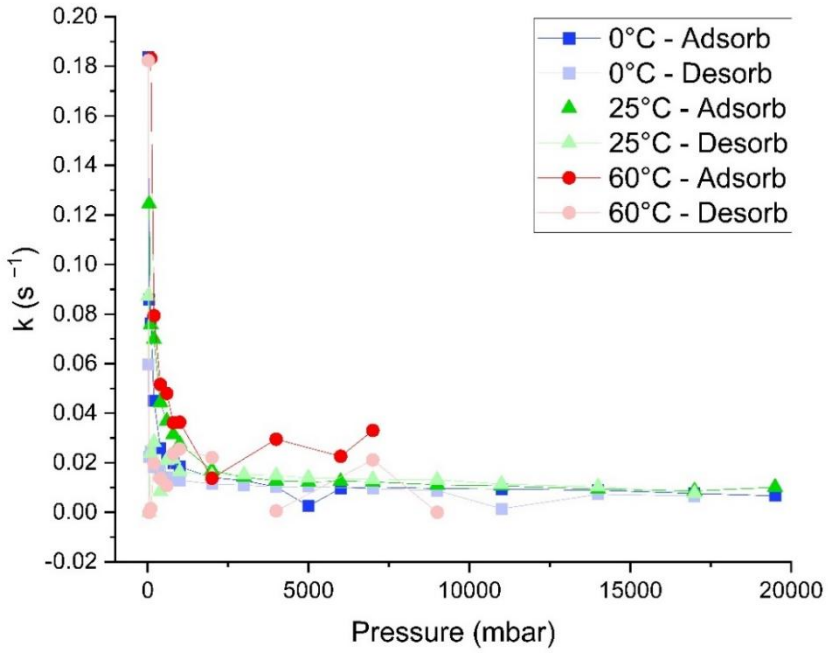

Figure 70 - Effective rate constant (k) for CO_2 adsorption and desorption as a function of pressure for sample EX31-900-2H-KOH-1:8 .

The apparent increase in β at higher pressures, particularly where uptake is nearly saturated, is likely an artefact of the dual-site fitting approach. As signal variation diminishes at high loading, the SE model becomes increasingly insensitive to changes in the isotherm curvature, exaggerating the role of the exponential term and thereby inflating β. This artefact appears consistently across both microporous and mesoporous samples and should not be interpreted as a real increase in surface heterogeneity or energetic disorder.

In summary, sample EX31-900-2H-KOH-1:8 displays kinetic trends in K and β that are consistent with rapid and efficient adsorption in a mesoporous matrix. Compared to sample EX23-800-2H-KOH-1:1, its desorption behaviour is more regular, and the pressure dependence of both parameters is smoother, reinforcing the influence of pore architecture on adsorption kinetics.

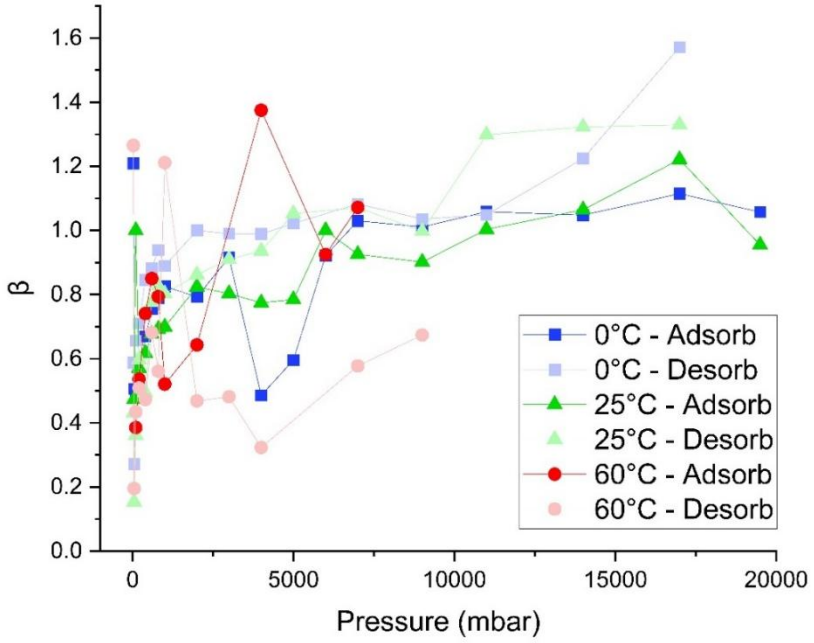

Figure 71 - Stretching exponent (β) for CO_2 adsorption and desorption in sample EX31-900-2H-KOH-1:8 .

9.4.3. Sample EX37-850-15-CO_2-600

For sample EX37-850-15-CO_2-600 (Figure 72), which was produced by CO_2 activation and contains nitrogen functionalities, the kinetic parameter *k* displays an initial decline with increasing pressure, followed by a plateau at values around 0.01. This trend reflects the expected reduction in the rate of adsorption as available high-energy adsorption sites become occupied at low pressures. Beyond approximately 2000 mbar, the rate of uptake

slows considerably and becomes more uniform, consistent with the transition from surface-controlled to diffusion-limited kinetics.

The evolution of the β parameter (Figure 73) shows convergence towards a value near 1 as pressure increases, in line with observations from the other samples. This transition indicates a shift from strongly cooperative adsorption mechanisms at low pressures to more linear, equilibrium-like uptake at higher pressures. The slight divergence observed at elevated pressures and higher temperatures likely reflects the reduced sensitivity of the fitting model in this regime, where changes in adsorption become increasingly subtle and the pressure–loading relationship flattens. Nonetheless, the general consistency across both adsorption and desorption branches suggests a reliable kinetic profile.

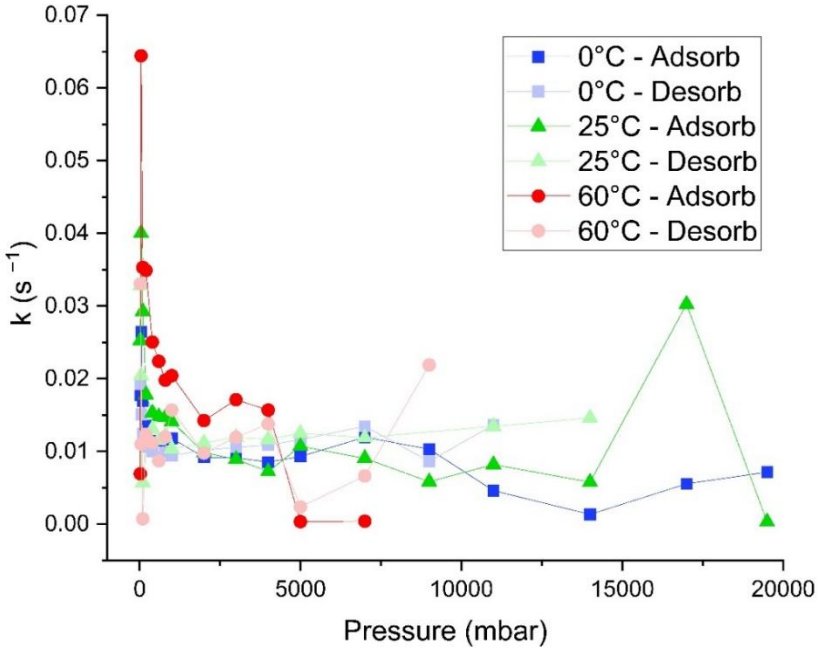

Figure 72 - Effective rate constant (k) for CO_2 adsorption and desorption as a function of pressure for sample EX37-850-15-CO_2-600.

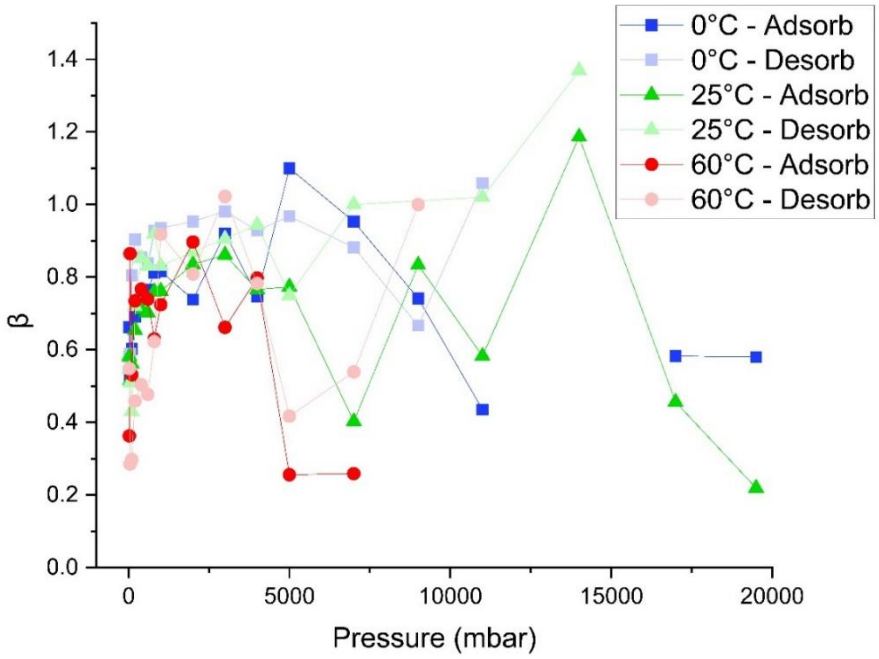

Figure 73 - Stretching exponent (β) for CO_2 adsorption and desorption in sample EX37-850-15-CO_2-600.

Compared to the microporous (EX23-800-2H-KOH-1:1) and mesoporous (EX31-900-2H-KOH-1:8) samples, sample EX37-850-15-CO_2-600 shows moderately lower *k* and β values, especially at intermediate pressures. This behaviour is attributed to its lower overall surface area and pore volume, a characteristic feature of CO_2 activation, as well as the presence of nitrogen functionalities, which may alter the interaction strength with CO_2. These differences highlight the role of surface chemistry and pore structure in modulating adsorption kinetics, while the broader trends remain consistent across all three samples.

9.4.4. Sample EX45-900-2H-KOX-1:1

The pressure dependence of the fitting parameters for sample EX45-900-2H-KOX-1:1 is shown in Figure 74 and Figure 75. The values of *k* exhibit the typical trend observed across previous samples, with relatively high values at low pressure followed by a rapid decline and subsequent stabilisation beyond approximately 2000 mbar. This behaviour reflects the initial dominance of Henry-type adsorption, followed by a transition to multilayer or pore-filling processes. The *k* values show some temperature dependence, particularly at 60 °C where the values are slightly elevated at low pressures, but this diminishes with increasing pressure.

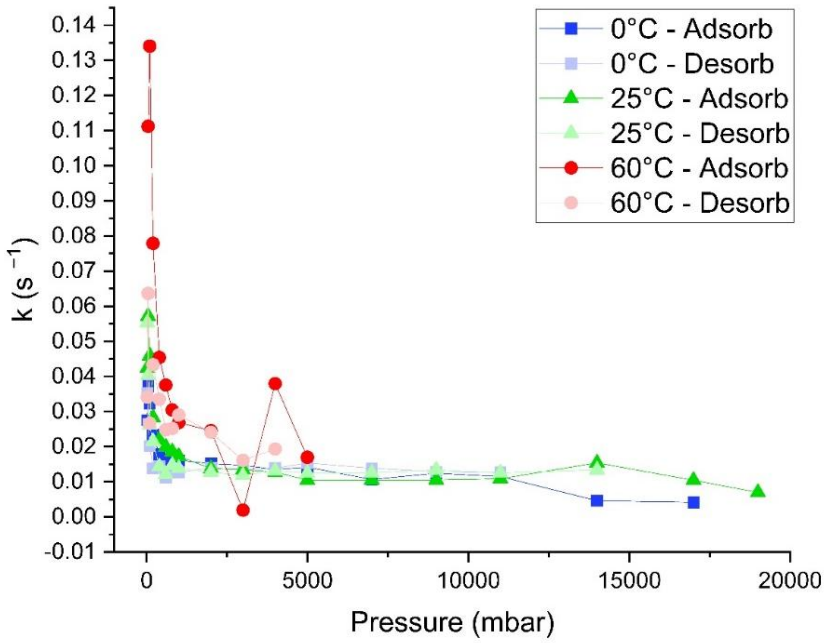

Figure 74 - Effective rate constant (k) for CO_2 adsorption and desorption as a function of pressure for sample EX45-900-2H-KOX-1:1.

The corresponding β values display a broadly consistent trend with earlier samples. As seen in Figure 75, β tends to increase towards approximately 1 with increasing pressure, though notable scatter is again present in the high-pressure region due to limitations in fitting accuracy. At lower pressures, particularly below 2000 mbar, β remains below 1 in most cases, indicating the prevalence of heterogeneous surface interactions or a distribution of binding energies. The general increase in β with pressure across all temperatures is consistent with a shift towards more homogeneous adsorption behaviour as higher energy sites become saturated.

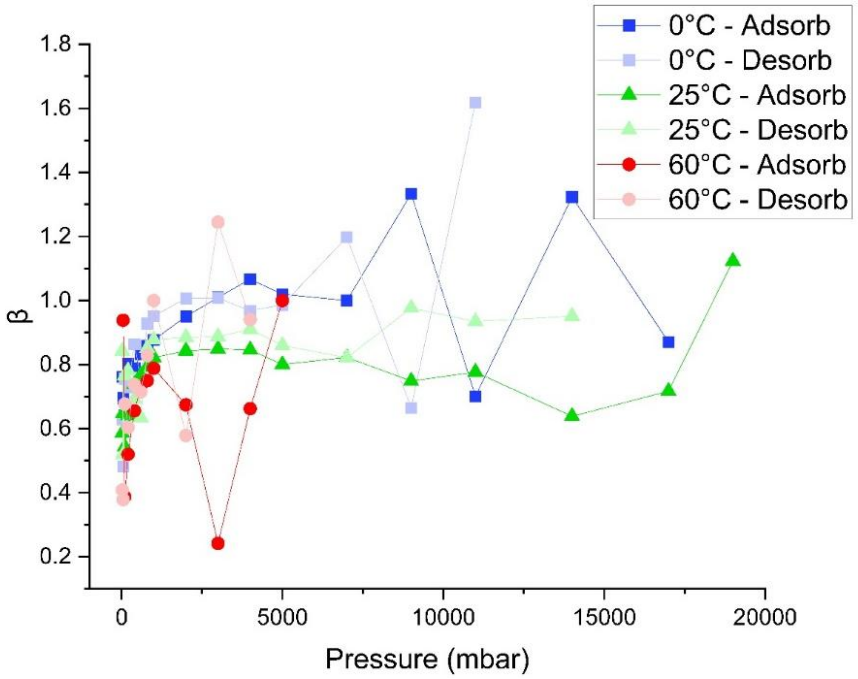

Figure 75 - Stretching exponent (β) for CO_2 adsorption and desorption in sample EX45-900-2H-KOX-1:1.

9.4.5. Sample EX53-900-2H-KOX-1:1 (pre-pyrolysed)

The pressure-dependent profiles of the fitted parameters for sample EX53-900-2H-KOX-1:1 (pre-pyrolysed) are shown in Figure 76 and Figure 77. As with samples EX45-900-2H-KOX-1:1 and EX23-800-2H-KOH-1:1, the values of *k* exhibit a steep decline at low pressures (0–500 mbar), after which they stabilise with only minor fluctuations. This behaviour reflects the higher sensitivity of *k* to the initial region of the isotherm, where small changes in uptake produce relatively large changes in the gradient. Above 1000 mbar, *k* remains relatively stable, with no clear evidence of hysteresis between adsorption and desorption branches.

The values of β mostly fall within the range of 0.6 to 1.1 and follow a trend broadly consistent with the other microporous samples. An initial increase with pressure is observed, followed by levelling behaviour at intermediate to high pressures. As before, some divergence appears at higher pressures, particularly in the desorption branches at elevated temperatures, which is likely due to reduced curvature in the isotherm and increased fitting uncertainty. Nevertheless, the overall pattern again suggests a gradual transition toward more homogeneous adsorption behaviour with increasing pressure.

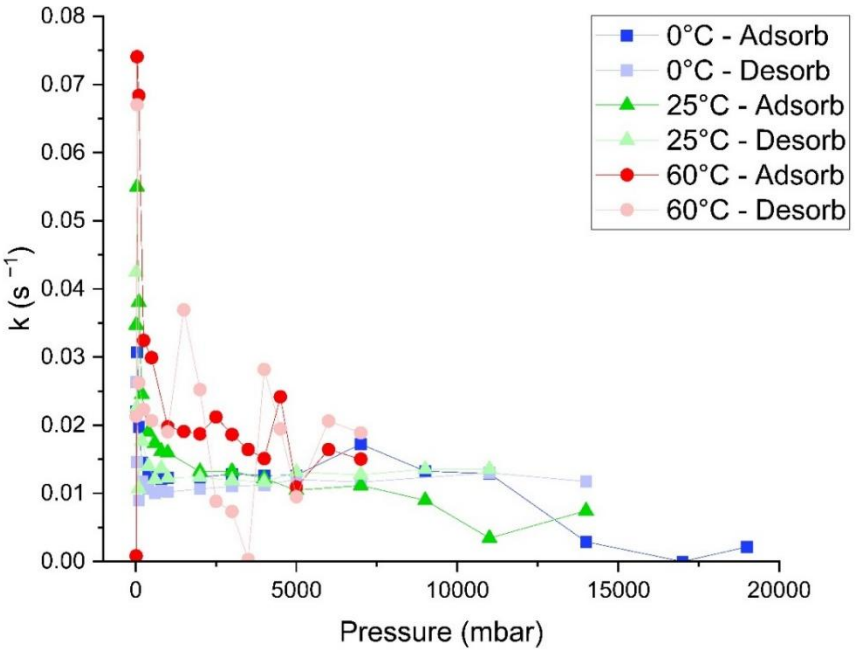

Figure 76 - Effective rate constant (k) for CO_2 adsorption and desorption as a function of pressure for sample EX53-900-2H-KOX-1:1 (pre-pyrolysed).

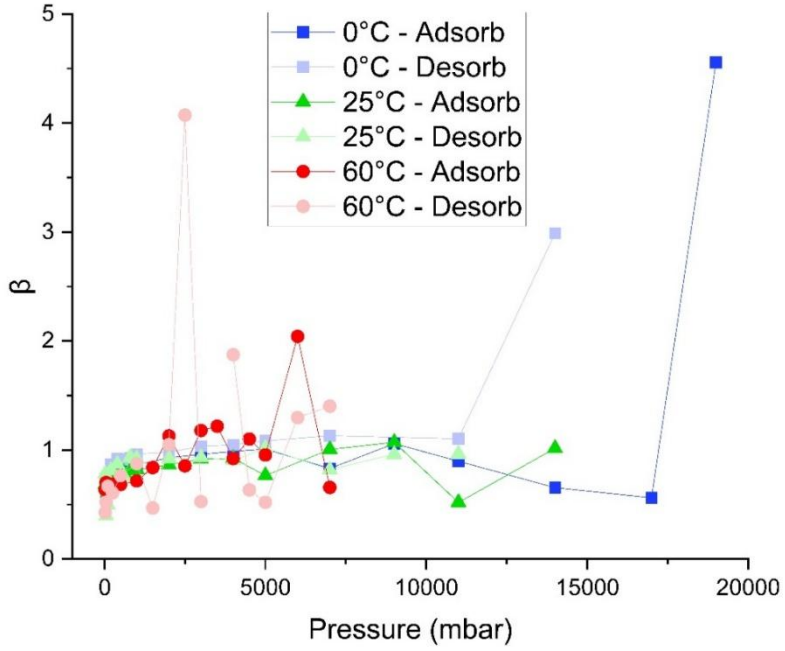

Figure 77 - Stretching exponent (β) for CO_2 adsorption and desorption in sample EX53-900-2H-KOX-1:1 (pre-pyrolysed).

9.4.6. Comparison of Samples

Across all five samples, the kinetic profiles extracted from stretched exponential (SE) model fitting reveal consistent underlying trends that reflect fundamental adsorption–diffusion behaviour in porous solids. The effective rate constant k exhibits a broadly similar

dependence on pressure for each material: initially elevated at low pressure, followed by a pronounced decline and eventual stabilisation into a plateau. This behaviour is most pronounced below 500–1000 mbar, a region where rapid uptake is expected due to the availability of high-affinity adsorption sites. As these sites become occupied, the rate of uptake slows, and the process becomes increasingly governed by slower transport into less accessible pores or lower-energy regions. The convergence of *k* values at higher pressures reflects this shift from surface-limited to diffusion-limited kinetics, a common feature of gas–solid adsorption systems.

The stretching exponent β shows a similarly consistent trend across the samples. At low pressure, β values are typically below 1, indicating a distribution of relaxation times arising from heterogeneities in pore size, surface functionality, and internal transport resistances. As pressure increases, β rises toward unity, signalling a narrowing of this distribution and the emergence of a dominant, rate-limiting process. In most cases, this asymptotic behaviour occurs between 1000 and 3000 mbar, corresponding to the point at which adsorption approaches pore-filling equilibrium and mass transfer becomes governed primarily by intraparticle diffusion. These results reinforce the physical interpretation of the SE model parameters and support their utility in capturing kinetic transitions across a broad loading range.

Among the samples studied, EX31-900-2H-KOH-1:8 —the high-surface-area mesoporous material—exhibited a notably higher initial rate constant *k* than the others. This enhancement is attributed to its open mesoporous structure, which facilitates rapid molecular diffusion and reduces the incidence of transport bottlenecks during the early stages of adsorption. Compared to the predominantly microporous samples (samples EX23-800-2H-KOH-1:1, EX37-850-15-CO_2-600, EX45-900-2H-KOX-1:1, and EX53-900-2H-KOX-1:1 (pre-pyrolysed), sample EX31-900-2H-KOH-1:8 enables faster equilibration with minimal restriction to gas ingress, supporting the conclusion that pore architecture plays a central role in controlling the rate of CO_2 uptake.

At higher pressures, an increase in parameter scatter—particularly for β—was consistently observed. This behaviour arises from the reduced sensitivity of the fitting model in regimes where the isotherm becomes increasingly flat. Under these conditions, the changes in mass with respect to pressure become small, reducing the information content available for fitting and amplifying the influence of experimental noise. As a result, fitted parameters

become less stable, and minor deviations in the data can cause disproportionately large changes in the calculated values of β. This effect is exacerbated at elevated temperatures and during desorption, where equilibrium gradients are often weakest.

To assess whether these fitting instabilities were a result of model limitations, a comparison was conducted using a double exponential model, which introduces an additional degree of flexibility by fitting two distinct kinetic components. However, this approach did not yield a systematic improvement in the fit quality or parameter stability. In some cases, it introduced additional ambiguity and overfitting, particularly in regions with limited signal. Given these findings, the stretched exponential model was retained as the preferred approach. Its single-equation form allows for efficient and consistent application across a wide range of conditions, avoids unnecessary model complexity, and provides parameters that are readily interpretable in the context of distributed kinetic processes. The simplicity and robustness of the SE model ultimately offered a more reliable basis for cross-sample comparison and for assessing the pressure- and temperature-dependent evolution of adsorption kinetics.

The kinetic values obtained in this study—namely the effective rate constant k and the stretching exponent β —are consistent with those reported for typical carbonaceous adsorbents used in post-combustion CO_2 capture. Across the samples, *k* values fall in the range of 0.01–0.05 s^{-1} at low pressures (25–100 mbar), declining to approximately 0.008–0.012 s^{-1} at higher pressures (>1 bar). This is well aligned with the expected range for physisorptive materials such as activated carbons and mesoporous silicas, where *k* is typically reported between 0.01 and 0.1 s^{-1} depending on structure, temperature, and pressure conditions. [69,353]

The observed β values, generally spanning 0.5–1.1, are similarly characteristic of carbon-based sorbents. [343] Microporous and disordered carbons often yield values below 0.8, while mesoporous materials and those with more regular pore networks tend to approach 1, reflecting more uniform transport mechanisms. [69] The trend toward $\beta \approx 1$ at higher pressures observed in this work is in line with reports that attribute this behaviour to the saturation of high-energy binding sites, which reduces kinetic heterogeneity.[354,355]

Overall, the kinetics exhibited by the studied biochars—especially in samples EX23-800-2H-KOH-1:1 and EX31-900-2H-KOH-1:8 —are excellent relative to other porous physisorbents. Their performance suggests rapid mass transport supported by accessible

pore structures and minimal diffusion constraints, making them highly suitable for dynamic CO_2 capture processes.

9.5. Adsorption Activation Energies

Activation energies (Ea) were extracted from temperature-dependent kinetic data using the Arrhenius equation applied to the effective rate constant *k* obtained from stretched exponential model fitting. These values were plotted as a function of pressure for both adsorption and desorption branches, as shown in Figure 78 (full pressure range) and Figure 79 (zoomed to 0–2000 mbar).

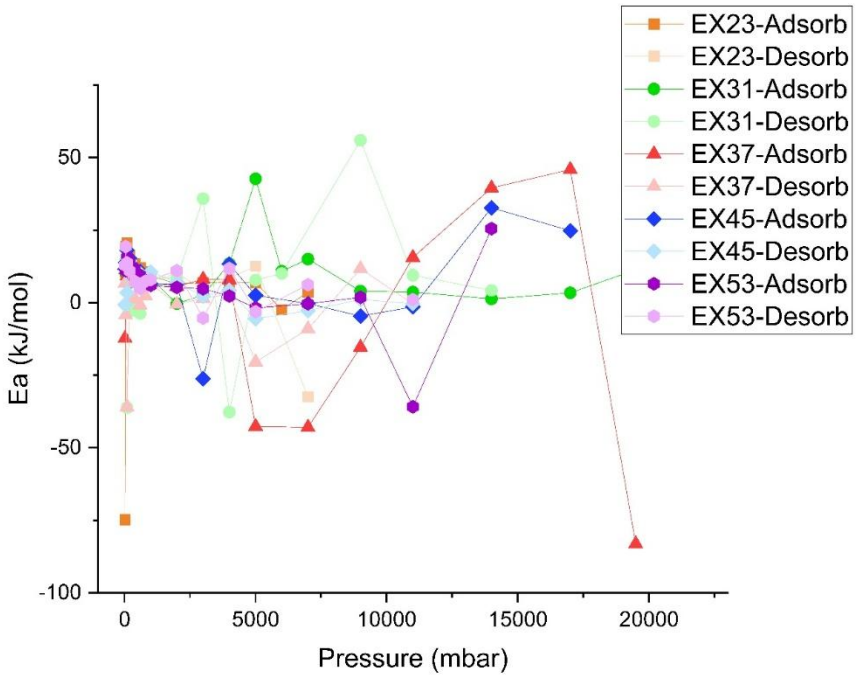

Figure 78 - Adsorption and desorption activation energy (Ea) as a function of pressure across the full range (0–20000 mbar) for samples EX23-800-2H-KOH-1:1, EX31-900-2H-KOH-1:8, EX37-850-15-CO_2-600, EX45-900-2H-KOX-1:1, and EX53-900-2H-KOX-1:1 (pre-pyrolysed).

Across all samples, activation energies generally remained within the range of 5–20 kJ/mol at low to intermediate pressures (25–1000 mbar), consistent with physisorption-dominated processes. Notably, deviations from this range were observed at both very low and very high pressures, suggesting the presence of fitting artefacts or shifts in adsorption mechanisms under non-ideal conditions. At low pressure (25–100 mbar), samples EX23-800-2H-KOH-1:1, EX45-900-2H-KOX-1:1, and EX53-900-2H-KOX-1:1 (pre-pyrolysed) showed consistently positive activation energies, with sample EX23-800-2H-KOH-1:1 reaching a maximum of 20.7 ± 2 kJ/mol. This trend aligns with a kinetically favourable uptake regime, where adsorption is driven by rapid diffusion into accessible micropores. The elevated

activation energy at these pressures reflects initial site-specific interactions with activated sites or surface functionalities. Samples EX31-900-2H-KOH-1:8 and EX37-850-15-CO_2-600, however, showed anomalously negative or near-zero activation energies at 25 mbar (e.g., –74.8 ± 40 kJ/mol for adsorption on sample EX23-800-2H-KOH-1:1, –312.9 ± 70 kJ/mol for desorption from sample EX31-900-2H-KOH-1:8 ; Figure 79). These negative values are physically implausible and most likely arise from noise in the kinetic fits at very low-pressure gradients, where adsorption rates become difficult to resolve accurately. These artefacts are exacerbated by low signal-to-noise ratios in mass change at such low loading.

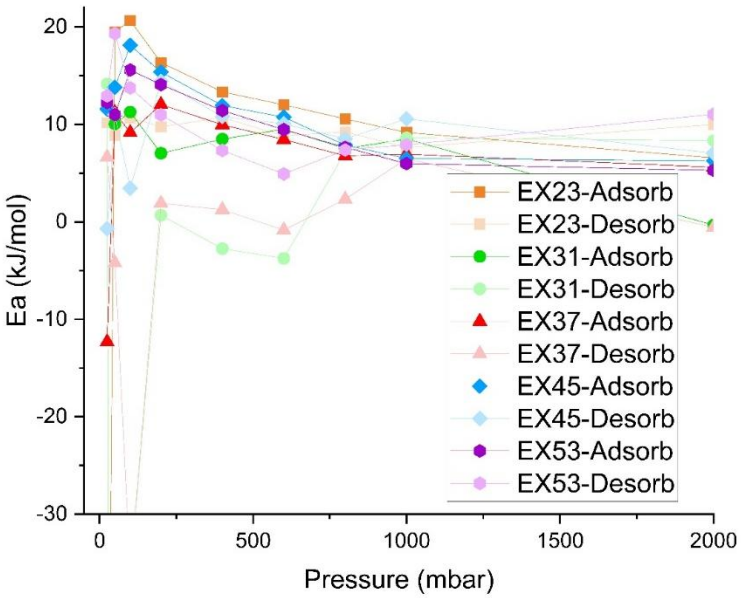

Figure 79 - Adsorption and desorption activation energy (Ea) as a function of pressure across the intermediate pressure (0–2000 mbar) for samples EX23-800-2H-KOH-1:1, EX31-900-2H-KOH-1:8, EX37-850-15-CO_2-600, EX45-900-2H-KOX-1:1, and EX53-900-2H-KOX-1:1 (pre-pyrolysed).

In the intermediate pressure regime (100–1000 mbar), all samples exhibited converging activation energies in the range of 8–15 kJ/mol. This consistency suggests a transition from site-specific interactions to pore-filling or multilayer physisorption mechanisms. Within this regime, samples EX23-800-2H-KOH-1:1 and EX45-900-2H-KOX-1:1 maintained the highest average Ea values (~12–14 kJ/mol), indicating persistent energy barriers to adsorption likely associated with narrow micropores or moderate steric constraints. Sample EX53-900-2H-KOX-1:1 (pre-pyrolysed) displayed slightly lower values (~10–12 kJ/mol), reflecting more accessible pore architecture and favourable diffusion characteristics.

Sample EX31-900-2H-KOH-1:8, a mesoporous high-surface-area material, exhibited the lowest overall activation energies across the full pressure range (Figure 78), with adsorption

Ea stabilising around 8–10 kJ/mol. This reflects reduced diffusional resistance due to its open pore structure, corroborating earlier kinetic analyses showing rapid equilibration and low heterogeneity ($\beta \approx 1$). However, its desorption Ea values were more erratic, including strongly negative values at 25 and 50 mbar, reinforcing the earlier interpretation of fitting instability under low-pressure conditions.

At high pressures (>1000 mbar), significant divergence in activation energy behaviour was observed, especially in the desorption branches (Figure 78). Samples EX37-850-15-CO_2-600 and EX45-900-2H-KOX-1:1 displayed increasing Ea values beyond 3000 mbar, with sample EX37-850-15-CO_2-600 reaching 45 kJ/mol and sample EX45-900-2H-KOX-1:1 exceeding 32 kJ/mol by 17000 mbar. Such elevated activation energies at high pressure are consistent with a transition from rapid surface adsorption to diffusion-limited transport in saturated pore networks. As the adsorbent approaches' full coverage, steric hindrance and pore blocking may contribute to a higher energetic cost for CO_2 diffusion and desorption. These increases are not universally observed, however, samples EX31-900-2H-KOH-1:8 and EX53-900-2H-KOX-1:1 (pre-pyrolysed) maintain relatively stable Ea values at high pressure, suggesting that these materials do not experience the same degree of kinetic constraint under saturation. This reinforces the hypothesis that pore architecture and functional group distribution significantly modulate adsorption energetics.

The activation energies observed (5–20 kJ/mol at 25–1000 mbar) are consistent with literature values for CO_2 physisorption on activated carbons and biochars, typically ranging from 5 to 25 kJ/mol.[356–360] The increase in Ea at high pressures (e.g., 30–45 kJ/mol for EX37-850-15-CO_2-600 and EX45-900-2H-KOX-1:1) aligns with reported diffusion limitations and pore saturation effects. Negative Ea values at very low pressures have also been noted in prior studies and are attributed to fitting artefacts under low signal conditions.[343] Overall, the trends are in good agreement with established behaviour for porous carbon sorbents.

Across all materials, desorption activation energies were generally comparable to or slightly lower than adsorption values. This is consistent with weakly bound physisorbed CO_2 and reversible uptake mechanisms. In a few cases (e.g. samples EX45-900-2H-KOX-1:1 and EX53-900-2H-KOX-1:1 (pre-pyrolysed), slightly elevated desorption Ea values at higher pressures may reflect cooperative effects or structural rearrangements during release.

9.5.1. Correlation Between Activation Energy and Pre-exponential Factor

To further examine the kinetic character of CO_2 adsorption on the studied biochars, the relationship between the activation energy (Ea) and the natural logarithm of the pre-exponential factor (lnA) was evaluated. This is shown in Figure 80, which plot lnA as a function of Ea for both adsorption and desorption processes across all samples.

These plots reveal a strong linear correlation between lnA and Ea, a relationship frequently observed in activated processes and commonly referred to as the compensation effect or the enthalpy–entropy compensation phenomenon. In physical terms, this indicates that increases in activation energy are often accompanied by proportional increases in entropy, reflected here in elevated pre-exponential factors.[361] As such, faster processes with lower Ea also exhibit lower A, while systems with higher energy barriers compensate through more frequent or favourable molecular configurations enabling adsorption. This trend supports the hypothesis that adsorption on these porous carbons is governed by distributed and heterogeneous energy landscapes, with surface chemistry and pore accessibility modulating both the energetic and entropic contributions to the adsorption rate.

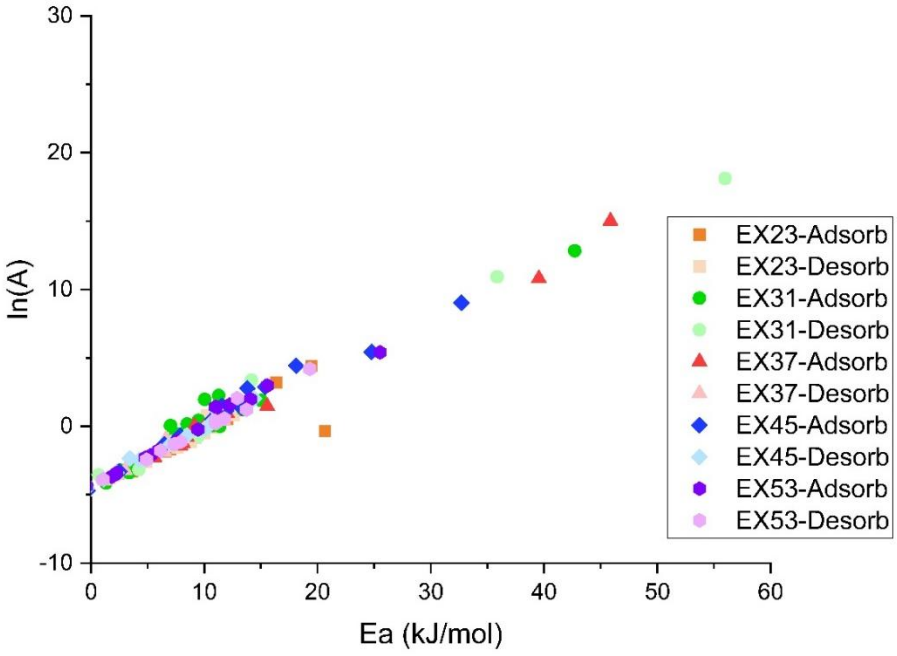

Figure 80 - Correlation between activation energy (Ea) and the natural logarithm of the Arrhenius pre-exponential factor (lnA) for samples EX23-800-2H-KOH-1:1, EX31-900-2H-KOH-1:8, EX37-850-15-CO_2-600, EX45-900-2H-KOX-1:1, and EX53-900-2H-KOX-1:1 (pre-pyrolysed).

The compensation effect observed here is particularly relevant in porous media, where a spectrum of binding environments exists. For instance:

- Samples such as EX31-900-2H-KOH-1:8 and EX53-900-2H-KOX-1:1 (pre-pyrolysed), which have more accessible pore structures, cluster tightly in the lower-left region of the plot (*Figure 8.4.2d*), showing modest activation energies and low-to-moderate A values—typical of systems dominated by fast, low-barrier physisorption.
- In contrast, samples EX37-850-15-CO_2-600 and EX45-900-2H-KOX-1:1 show points that extend into the higher Ea and lnA regime, particularly in their adsorption branches. This reflects the presence of energetically demanding adsorption sites, potentially due to constrained micropores or specific interactions with nitrogen-containing surface groups.

Importantly, the coherence of the linear trend across both adsorption and desorption branches suggests that the stretched exponential kinetic model captures a consistent kinetic signature across pressure and temperature variations, and that the underlying activation process is thermally activated and not strongly disrupted by hysteresis or irreversible structural changes. This analysis reinforces the physical validity of the kinetic parameters extracted and provides further confidence in the Arrhenius-based approach to characterising temperature-dependent adsorption kinetics.

The pressure- and temperature-dependent analysis of CO_2 adsorption activation energies has provided valuable insight into the kinetic and energetic behaviour of the five biochar samples under conditions relevant to post-combustion carbon capture. Activation energies predominantly fell within the 8–20 kJ/mol range at sub-atmospheric pressures, consistent with physisorption processes governed by diffusion and surface affinity. Materials with greater microporosity and surface functionalisation—such as samples EX23-800-2H-KOH-1:1, EX45-900-2H-KOX-1:1, and EX53-900-2H-KOX-1:1 (pre-pyrolysed)—exhibited elevated activation energies at low pressure, reflecting more constrained diffusion pathways and stronger adsorbate–surface interactions. In contrast, sample EX31-900-2H-KOH-1:8, a mesoporous material with minimal microporosity, consistently exhibited the lowest activation energies and desorption barriers, confirming its suitability for high-throughput adsorption under high-pressure conditions. At elevated pressures, samples EX37-850-15-

CO_2-600 and EX45-900-2H-KOX-1:1 displayed increasing activation energies, suggestive of steric hindrance and diffusion-limited desorption within saturated pore environments.

The observed linear correlation between Ea and lnA across all samples and processes confirms the presence of enthalpy–entropy compensation behaviour, reinforcing the physical validity of the kinetic model and the extracted parameters. This trend reflects the interplay between activation barriers and molecular freedom, highlighting the importance of pore structure and chemical heterogeneity in dictating adsorption dynamics. Overall, the activation energy analysis complements the kinetic and thermodynamic findings and supports the identification of samples EX53-900-2H-KOX-1:1 (pre-pyrolysed) and EX23-800-2H-KOH-1:1 as promising candidates for low-pressure CO_2 capture, with sample EX31-900-2H-KOH-1:8 better suited to high-capacity applications in pressurised environments. These results will inform the selection and further optimisation of biochar-based sorbents for integration into cyclic or continuous carbon capture systems.

9.6. CO_2 Cyclic Stability

Cyclic adsorption–desorption tests were performed to assess the stability, regenerability, and working capacity of selected biochars under dynamic conditions relevant to post-combustion CO_2 capture. Four materials — samples EX23-800-2H-KOH-1:1, EX37-850-15-CO_2-600, EX45-900-2H-KOX-1:1, and EX53-900-2H-KOX-1:1 (pre-pyrolysed)—were subjected to 60 consecutive cycles at 60 °C under pressure swing conditions. Adsorption was carried out at 1000 mbar, followed by desorption at 50 mbar, each phase involving a 100 mbar/min ramp rate and 15-min equilibration. The sample mass ranged from 40–60 mg, and uptake was recorded gravimetrically. Sample EX31-900-2H-KOH-1:8 was excluded due to its mesoporous structure and poor performance under the low-pressure conditions tested.

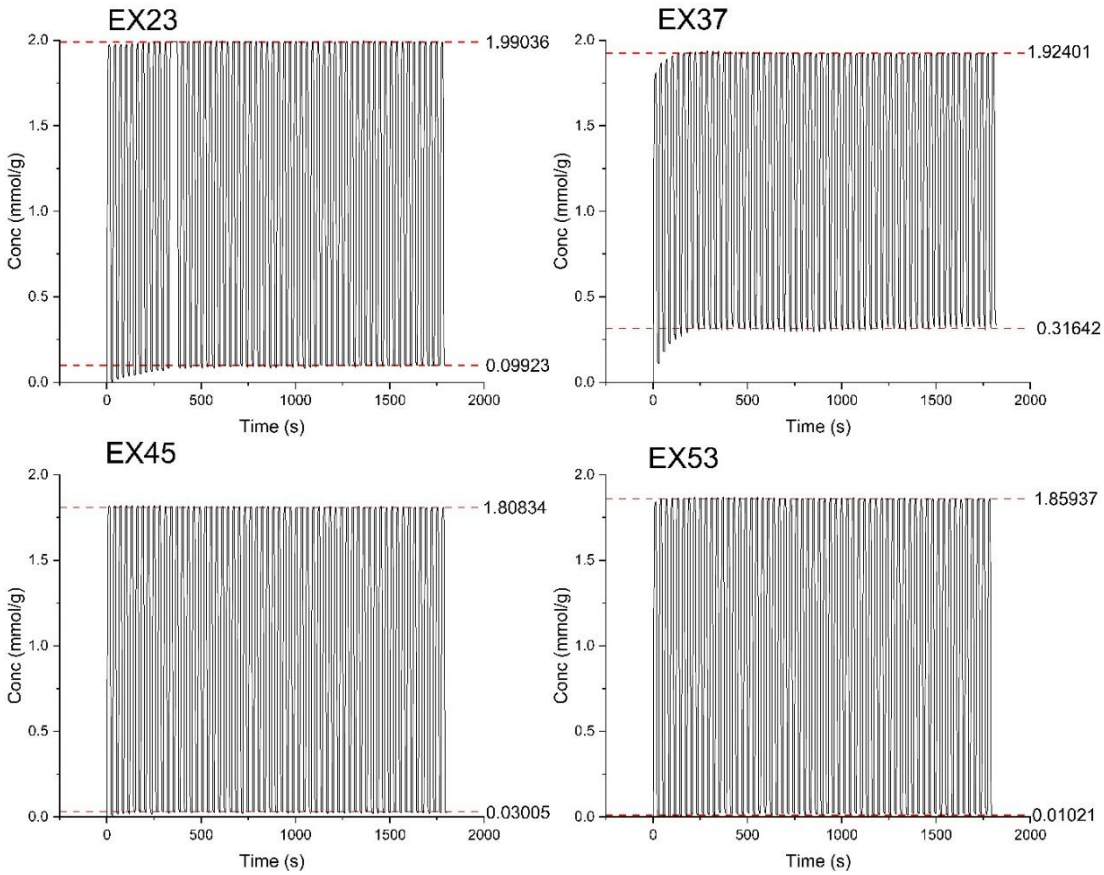

Figure 81 - Cyclic CO_2 adsorption–desorption profiles for samples EX23-800-2H-KOH-1:1, EX37-850-15-CO_2-600, EX45-900-2H-KOX-1:1, and EX53-900-2H-KOX-1:1 (pre-pyrolysed) over 60 cycles at 60 °C, between 1000 mbar and 50 mbar.

Time-resolved adsorption profiles are shown in Figure 81, demonstrating stable and reproducible cyclic behaviour for all four samples across the 60-cycle test. The working capacity—defined as the difference between maximum and minimum CO_2 uptake per cycle—was extracted from these profiles and is summarised in Table 37.

Table 37 - Working Capacity under 1000–50 mbar Cycling Conditions (mmol/g)

Sample	Working Capacity (mmol/g)
EX23-800-2H-KOH-1:1	1.89
EX37-850-15-CO_2-600	1.60
EX45-900-2H-KOX-1:1	1.79
EX53-900-2H-KOX-1:1 (pre-pyrolysed)	1.84

All samples exhibited high retention of capacity and minimal signal drift across cycles, indicating robust structural and functional stability under repeated operation. However, differences emerged in desorption completeness, which directly impacted usable capacity. Notably, sample EX37-850-15-CO_2-600—despite achieving a maximum uptake of 1.92 mmol/g—retained a substantial residual CO_2 loading after desorption (0.32 mmol/g),

leading to the lowest working capacity in the group. This behaviour is attributed to its elevated nitrogen content (3.49 at.% via XPS), which enhances CO_2 binding via strong acid–base interactions but hinders full desorption under modest pressure swings. Sample EX23-800-2H-KOH-1:1 also exhibited some residual retention (0.10 mmol/g), consistent with its intermediate nitrogen content (2.14 at.%). By contrast, samples EX45-900-2H-KOX-1:1 and EX53-900-2H-KOX-1:1 (pre-pyrolysed)—activated with potassium oxalate and possessing lower nitrogen contents (0.45 and 0.76 at.%, respectively)—showed near-complete desorption (<0.03 and <0.01 mmol/g, respectively) and therefore maximised their available working capacity under the tested conditions.

Although cyclic testing was performed at 1000 mbar to simulate standard laboratory regeneration protocols, it is important to note that the target operating range for post-combustion CO_2 capture lies between 150 mbar and 50 mbar. In this context, sample EX31-900-2H-KOH-1:8 was excluded from cycling tests due to its poor uptake performance under sub-atmospheric conditions, where its low microporosity renders it non-competitive despite high BET surface area. To better reflect the practical working conditions, a corrected estimate of working capacity was derived using the isotherm-derived CO_2 uptake at 150 mbar and 60 °C (from Table 37), subtracting the minimum cyclic uptake value observed in each test. These results are summarised in Table 38.

Table 38 - Estimated Working Capacity over 150–50 mbar Range (mmol/g)

Sample	Max Uptake (150 mbar, 60 °C)	Min Uptake (from cycle data)	Estimated Working Capacity
EX23-800-2H-KOH-1:1	0.666	0.099	0.566
EX37-850-15-CO_2-600	0.764	0.317	0.447
EX45-900-2H-KOX-1:1	0.576	0.031	0.545
EX53-900-2H-KOX-1:1 (pre-pyrolysed)	0.746	0.011	0.735

These corrected values illustrate a shift in performance ranking. While sample EX23-800-2H-KOH-1:1 exhibited the highest working capacity under 1000 mbar adsorption, the corrected analysis at 150 mbar reveals that sample EX53-900-2H-KOX-1:1 (pre-pyrolysed) offers the highest usable capacity (0.735 mmol/g) in the low-pressure regime most relevant to industrial flue gas conditions. This distinction arises from the combination of strong low-pressure uptake and excellent desorption behaviour for sample EX53-900-2H-KOX-1:1 (pre-pyrolysed), with virtually no CO_2 retained after regeneration.

These results emphasise the importance of evaluating working capacity under realistic process conditions. Although higher nitrogen content improves CO_2 affinity at low pressure, as seen in sample EX37-850-15-CO_2-600 and sample EX23-800-2H-KOH-1:1, this advantage can be offset by incomplete desorption under mild regeneration. The desorption conditions used in this study—1000 to 50 mbar pressure swing at 60 °C—are relatively gentle, and further improvements in working capacity for samples EX37-850-15-CO_2-600 and EX23-800-2H-KOH-1:1 could potentially be realised under more aggressive regeneration protocols, such as vacuum or temperature swing adsorption.

Although EX45 and EX53 exhibit higher total micropore volumes than EX37, adsorption performance at low CO_2 partial pressures is governed not only by micropore volume but also by the presence of ultramicropores (<0.7 nm), which provide enhanced adsorption potentials for CO_2. While detailed pore width distributions were not resolved in this study, the strong low-pressure affinity observed for EX37 suggests a higher fraction of ultramicropores, likely enhanced by nitrogen functionalities that increase local adsorption energies. This explains why EX37 can display high uptake despite a lower total micropore volume. However, when performance is evaluated based on working capacity and desorption reversibility under application-relevant conditions, EX53 ultimately provides the most practical performance.

The cyclic stability observed here aligns with studies on nitrogen-doped porous adsorbents. DES-functionalised activated carbons retained ~92% of their initial CO_2 capacity over 15 cycles under CO_2/N_2 mixtures, though gradual decline was observed due to incomplete desorption and structural degradation.[343] MRF xerogels similarly maintained reversible uptake over 60–500 cycles, with working capacities up to ~0.7 mmol/g under pressure swing conditions.[343] In this context, EX53-900-2H-KOX-1:1 (pre-pyrolysed)'s performance—demonstrating full reversibility and 0.735 mmol/g working capacity over 150–50 mbar—is comparable or superior, confirming that well-optimised biochars can rival or exceed more complex synthetic and functionalised sorbents under mild regeneration conditions.

Overall, all four biochars displayed excellent structural resilience and repeatable adsorption–desorption profiles over 60 pressure swing cycles. However, when evaluated against the application-relevant 150–50 mbar pressure window, sample EX53-900-2H-KOX-1:1 (pre-pyrolysed) emerged as the most effective and practical sorbent, offering the highest working capacity and near-complete desorption. Its balanced nitrogen content, high

microporosity, and robust regeneration behaviour support its suitability for deployment in pressure swing adsorption (PSA) systems under modest operating conditions. The remaining samples—EX45-900-2H-KOX-1:1, EX23-800-2H-KOH-1:1, and EX37-850-15-CO_2-600—demonstrated comparable cyclic stability and favourable performance, though with varying degrees of desorption efficiency. These findings underscore the importance of matching sorbent design to the specific pressure and temperature constraints of the intended capture process and support the selection of sample EX53-900-2H-KOX-1:1 (pre-pyrolysed) as the optimal biochar candidate for low-pressure post-combustion CO_2 capture applications.

9.7. Summary

The materials tested here were selected to represent a range of activation strategies and textural properties. Sample EX37-850-15-CO_2-600, a CO_2-activated sample, consistently exhibited strong intrinsic adsorption performance. It delivered the highest low-pressure uptake (0.76 mmol g^{-1} at 150 mbar and 60 °C), the greatest surface-normalised affinity, and the strongest initial enthalpic interactions (ΔH_i = 42.25 kJ mol^{-1}). These characteristics are attributable to its elevated nitrogen content and favourable surface functionality. Moreover, sample EX37-850-15-CO_2-600 is the only sample produced via a single-step CO_2 pyrolysis process, making it a lower-cost, more scalable, and environmentally preferable route compared to chemical activation.

However, under 60-cycle pressure swing tests (1000–50 mbar, 60 °C), sample EX53-900-2H-KOX-1:1 (pre-pyrolysed) demonstrated the best process-relevant performance. It exhibited the highest corrected working capacity in the target operating window of 150–50 mbar (0.735 mmol g^{-1}), with negligible residual CO_2 loading after desorption and excellent regeneration efficiency. The combination of high microporosity and lower nitrogen content in sample EX53-900-2H-KOX-1:1 (pre-pyrolysed) supports reversible physisorption and minimal retention.

While the production of sample EX53-900-2H-KOX-1:1 (pre-pyrolysed) involves a more complex two-step chemical activation process using potassium oxalate, this route is associated with higher reagent costs, chemical consumption, and extensive post-activation washing requirements, which introduce economic and environmental burdens at larger scale. In contrast, physical activation routes avoid chemical reagents and wastewater generation, making them inherently simpler to scale. As a result, although sample EX53-

900-2H-KOX-1:1 (pre-pyrolysed) shows superior cyclic performance, CO_2-only activation routes such as that used for sample EX37-850-15-CO_2-600 may offer advantages in terms of process simplicity, sustainability, and scalability.

Correlation analysis (found in Appendix H:) across the tested sorbents further demonstrated that micropore volume is the strongest structural predictor of equilibrium CO_2 uptake. Samples with greater micropore volumes consistently exhibited higher adsorption capacities, supporting a micropore-filling mechanism as the dominant adsorption process. In contrast, total BET surface area showed little predictive value, and in some cases an inverse relationship, highlighting that surface area alone is not a reliable descriptor for CO_2 capture performance. This finding aligns with established adsorption theory and reinforces that effective sorbent design should prioritise the development of accessible micropore volume over maximising total surface area.

In this context, sample EX37-850-15-CO_2-600 can be regarded as the strongest performer in terms of intrinsic adsorption affinity, process simplicity, and scalability, whereas sample EX53-900-2H-KOX-1:1 (pre-pyrolysed) is the most effective under realistic cyclic operating conditions.

The observed trade-off between CO_2 affinity and desorption efficiency highlights the impact of nitrogen content on sorbent performance. These findings underscore the importance of aligning sorbent design and activation method with the operational parameters and practical constraints of the intended capture process.

Chapter 10. Competitive Adsorption

The selective adsorption of CO_2 in the presence of N_2 is a key requirement for effective post-combustion carbon capture, where CO_2 concentrations are typically low (10–15%) and must be separated from a nitrogen-rich stream. To assess the performance of candidate materials under such realistic conditions, this study investigates the competitive adsorption behaviour of four SCG-derived biochars—EX37-850-15-CO_2-600, EX45-900-2H-KOX-1:1, EX53-900-2H-KOX-1:1 (pre-pyrolysed), and EX31-900-2H-KOH-1:8 —using a binary CO_2/N_2 mixture.

These four samples were selected to provide a broad representation of sorbent architectures and chemistries. Sample EX31-900-2H-KOH-1:8 is a KOH-activated material with high BET surface area but low microporosity, making it representative of mesoporous, surface-rich carbons. Samples EX45-900-2H-KOX-1:1 and EX53-900-2H-KOX-1:1 (pre-pyrolysed) are potassium oxalate (KOx)-activated samples, both exhibiting high microporosity but minimal surface functionalisation. Sample EX23-800-2H-KOH-1:1 was not included in these tests, has a similar performance to EX45-900-2H-KOX-1:1 and EX53-900-2H-KOX-1:1 (pre-pyrolysed) but relies on KOH activation, which is less viable for scale-up due to cost, handling, and regeneration limitations. Sample EX37-850-15-CO_2-600 is a CO_2-activated material with comparatively low surface area and microporosity but a high content of nitrogen-containing surface groups, offering an opportunity to explore the role of chemical functionality in CO_2 selectivity. The inclusion of sample EX31-900-2H-KOH-1:8, despite its poor performance in prior low-pressure adsorption tests, allows for a direct comparison against microporous and functionalised materials, thereby testing the underlying hypothesis that nitrogen functionalities and micropore confinement enhance CO_2 selectivity.

Pure component adsorption isotherms of CO_2 and N_2 were first measured for each sample at 60 °C to establish baseline adsorption characteristics. These data were subsequently used to calculate Ideal Adsorbed Solution Theory (IAST) predictions for competitive adsorption. In addition, direct mixed-gas adsorption measurements were performed using a binary gas mixture of 15% CO_2 and 85% N_2 at 60 °C, with total pressure incrementally varied from 0 to 1000 mbar in 100 mbar steps. These experiments provide experimental validation of the IAST predictions and enable detailed comparison of CO_2/N_2 selectivity across the tested biochars.

10.1. IAST Methodology

The Ideal Adsorbed Solution Theory (IAST) provides a thermodynamic framework for predicting multicomponent gas adsorption from pure component isotherms, assuming ideality in the adsorbed phase. Analogous to Raoult's law for vapour–liquid equilibria, IAST assumes that the spreading pressure of each component in the mixture is equivalent to that of its pure component at an adjusted (fictitious) pressure. By solving for this pressure and applying mass balance constraints, the total adsorbed amount and selectivity of the mixture can be predicted. In this study, IAST calculations were performed using GraphIAST, a user-friendly graphical interface built upon the pyIAST Python library, [362] which facilitates isotherm fitting and multicomponent prediction without the need for programming. Pure component isotherms for CO_2 and N_2 were fitted using the Langmuir model, which provided an adequate representation of the adsorption behaviour across all samples. While alternative models (e.g. interpolation, BET and Quadratic) were tested, the deviations in predicted selectivity were minimal, and the Langmuir model was retained for consistency and interpretability.

GraphIAST was configured to calculate binary adsorption loadings and selectivities across the same pressure range used in the experimental competitive adsorption tests (0–1000 mbar), under a fixed inlet composition of 15% CO_2 and 85% N_2. The fitting and calculation workflow ensured that all data were analysed under consistent thermodynamic assumptions and model constraints, supporting a rigorous comparison between predicted and experimental trends.

10.2. Mixed Gas Adsorption Results and IAST Predictions

Experimental and predicted mixed-gas adsorption behaviours were evaluated for four samples—EX31-900-2H-KOH-1:8, EX37-850-15-CO_2-600, EX45-900-2H-KOX-1:1, and EX53-900-2H-KOX-1:1 (pre-pyrolysed)—using a 15% CO_2/85% N_2 mixture at 60 °C. For each sample, experimental pure-component CO_2 and N_2 isotherms, IAST predictions based on fitted Langmuir models, and, where available, experimental mixed-gas isotherms were plotted together to assess CO_2 selectivity and the reliability of IAST predictions. To contextualise performance, a vertical line was drawn at 150 mbar on each pure CO_2 isotherm, corresponding to the CO_2 partial pressure in the gas mixture. In an idealised case of perfect CO_2 selectivity, the mixed-gas uptake would approximate the pure-component

CO_2 uptake at this pressure. Deviations from this benchmark offer qualitative insight into the degree of selective adsorption achieved.

It is important to recognise that while IAST remains the benchmark tool for predicting binary adsorption behaviours, it is predicated on ideal thermodynamic assumptions. IAST does not account for kinetic barriers, competitive effects, or heterogeneity in surface chemistry. Consequently, deviations between IAST predictions and experimental mixed-gas uptakes are common, particularly in systems with strong adsorbate–adsorbent interactions or significant textural complexity. Experimental validation thus remains critical, especially when surface functionalities or microporosity effects are significant.

10.2.1. Sample EX31-900-2H-KOH-1:8

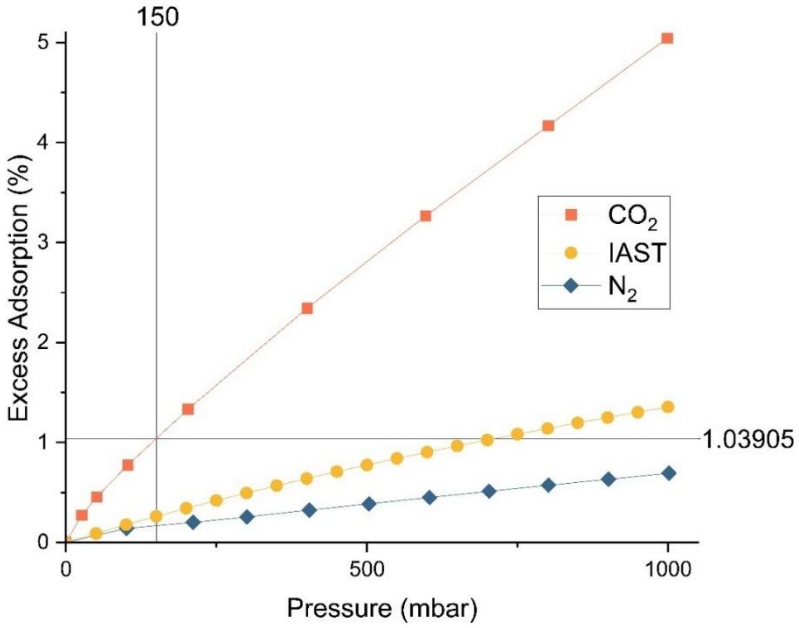

Figure 82 - Pure-component and IAST-predicted isotherms for sample EX31-900-2H-KOH-1:8 with CO_2/N_2 binary mixture at 60 °C. Experimental binary data unavailable.

The mixed-gas isotherm for sample EX31-900-2H-KOH-1:8 could not be successfully recorded due to a combination of material fragility and instrumentation limitations. During the initial experiment, the extremely fine nature of sample EX31-900-2H-KOH-1:8 — stemming from its aggressive KOH activation—caused physical displacement of the sample within the instrument under flow conditions. A second attempt, employing quartz wool to secure the sample bed, was unsuccessful due to a malfunction in the mass flow controller, resulting in the absence of N_2 in the gas stream. Given the limited experimental time available and the marginal relevance of sample EX31-900-2H-KOH-1:8 for low-pressure post-combustion capture—owing to its low uptake at 150 mbar and impractical activation

conditions—further reruns were deprioritised. Nevertheless, IAST predictions based on pure-component isotherms were still evaluated for comparative purposes.

As shown in the sample EX31-900-2H-KOH-1:8 plot (Figure 82), the IAST-predicted CO_2 uptake indicates significantly higher uptake relative to the pure CO_2 uptake at 150 mbar, consistent with poor selectivity. This behaviour is in line with expectations for a high surface area, mesoporous material like sample EX31-900-2H-KOH-1:8, where the lack of micropore confinement and the relatively low affinity for CO_2 under dilute conditions result in diminished competitive separation performance.

10.2.2. Sample EX37-850-15-CO_2-600

Sample EX37-850-15-CO_2-600, a CO_2-activated sample with relatively low surface area and microporosity but a high nitrogen content, displayed an interesting deviation from IAST predictions (Figure 83). The mixed gas isotherm significantly underperformed relative to the IAST-predicted values, particularly at lower pressures. At 1000 mbar, the measured binary uptake was approximately 2.38%, compared to an IAST-predicted value of ~2.61%.

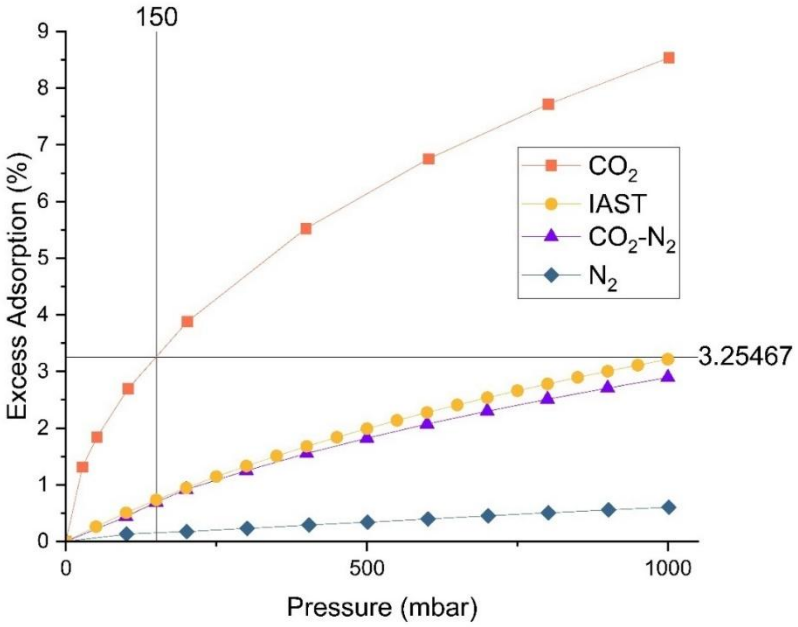

Figure 83 - Pure-component, experimental binary, and IAST-predicted isotherms for sample EX37-850-15-CO_2-600 under a CO_2/N_2 mixture at 60 °C.

This underprediction by IAST may reflect limitations of the model in capturing specific adsorbate–adsorbent interactions conferred by nitrogen surface functionalities, which are not accounted for in the ideal solution assumption. Furthermore, confinement effects within narrow micropores could result in cooperative or non-ideal behaviours during co-adsorption, deviating from the assumptions of homogenous surface energetics inherent to

IAST. The deviation suggests that sample EX37-850-15-CO_2-600 may exhibit lower-than-predicted CO_2 selectivity under binary conditions despite strong uptake in the pure-component isotherm.

10.2.3. Sample EX45-900-2H-KOX-1:1

Sample EX45-900-2H-KOX-1:1, a KOx-activated sample characterised by high microporosity and minimal surface nitrogen content, showed close agreement between IAST predictions and experimental results (Figure 84). At 1000 mbar, the experimental mixed-gas CO_2 uptake reached 2.93%, compared to an IAST prediction of approximately 2.61%.

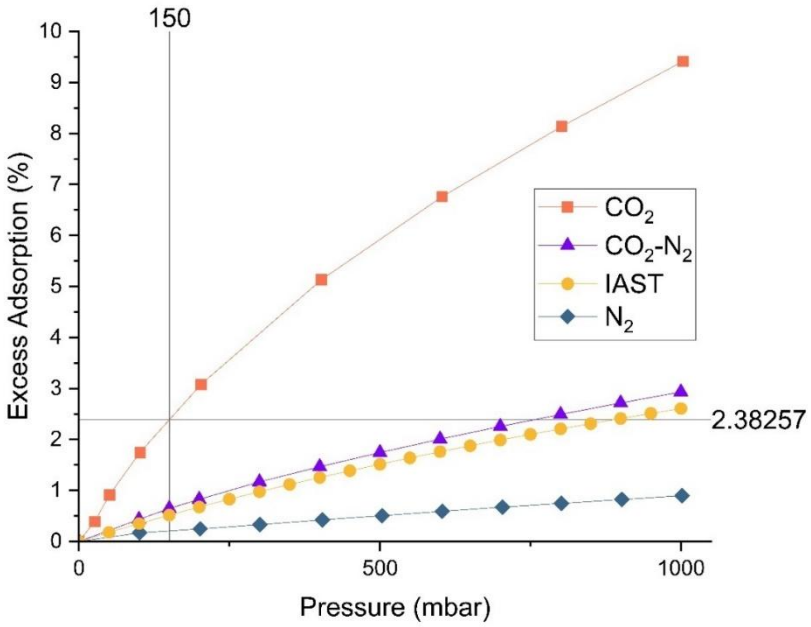

Figure 84 - Pure-component, experimental binary, and IAST-predicted isotherms for sample EX45-900-2H-KOX-1:1 under a CO_2/N_2 mixture at 60 °C.

The IAST predictions indicate that CO_2 uptake at 1000 mbar is significantly above the pure-component CO_2 uptake at 150 mbar (2.38%), suggesting that sample EX45-900-2H-KOX-1:1 does not achieve perfect selectivity but nevertheless strongly favours CO_2 adsorption over N_2. The small underprediction by IAST likely arises from the subtle effects of micropore confinement enhancing CO_2 adsorption relative to ideal assumptions. The close alignment of experimental and predicted uptakes confirms that IAST remains a robust predictive tool for chemically homogeneous, microporous materials, and the deviation from perfect selectivity is consistent with expectations under practical post-combustion capture conditions.

10.2.4. Sample EX53-900-2H-KOX-1:1 (pre-pyrolysed)

Sample EX53-900-2H-KOX-1:1 (pre-pyrolysed) exhibited the largest deviation between IAST predictions and experimental results (Figure 85). The experimental mixed-gas CO_2 uptake reached 3.62% at 1000 mbar, compared to an IAST prediction of 2.69%. This underprediction widening as the entire pressure increased.

Given the combination of high microporosity and minimal nitrogen surface functionality found in sample EX53-900-2H-KOX-1:1 (pre-pyrolysed), the enhanced experimental uptake likely reflects synergistic effects not captured by the idealised IAST framework. Specifically, cooperative interactions between adsorbed CO_2 molecules and preferential confinement within ultra-micropores could contribute to increased uptake beyond ideal predictions. However, the fact that the mixed-gas uptake exceeds the pure CO_2 uptake at 150 mbar suggests imperfect selectivity, highlighting the real-world trade-off between adsorption capacity and competitive sorption effects. This case further underscores the importance of complementing theoretical predictions with direct experimental validation, especially when evaluating materials with complex physicochemical characteristics.

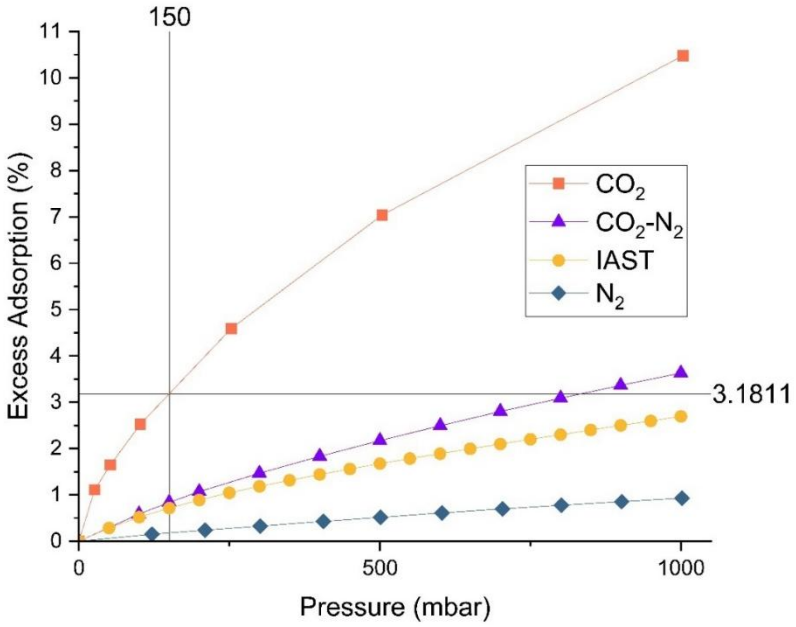

Figure 85 - Pure-component, experimental binary, and IAST-predicted isotherms for sample EX53-900-2H-KOX-1:1 (pre-pyrolysed) under a CO_2/N_2 mixture at 60 °C.

10.3. Selectivity Results and Discussion

Sample EX31-900-2H-KOH-1:8, a highly mesoporous, high surface area KOH-activated sample, exhibits the lowest CO_2 selectivity across the entire pressure range, as seen in Figure 86, with values increasing only marginally from 4.6 to 5.7 between 50 and

1000 mbar. The low and relatively flat selectivity profile is consistent with the physical characteristics of sample EX31-900-2H-KOH-1:8 : large pores, lack of strong adsorptive sites, and limited confinement effects. Such behaviour reflects poor competitive adsorption performance, as the material exhibits similar affinity for both CO_2 and N_2, undermining separation efficiency.

In stark contrast, sample EX37-850-15-CO_2-600 demonstrates the highest selectivity, rising from approximately 24 at 50 mbar to nearly 44 at 1000 mbar. This substantial and steadily increasing selectivity can be attributed to the pronounced nitrogen surface functionalities of sample EX37-850-15-CO_2-600, and their preferential interactions with CO_2 molecules. Nitrogen functionalities are known to enhance CO_2 adsorption through specific acid-base interactions, beyond the physisorption mechanisms dominant in microporous carbons lacking chemical heterogeneity. The high selectivity further supports the hypothesis that surface chemistry plays a critical role in determining competitive adsorption behaviour.

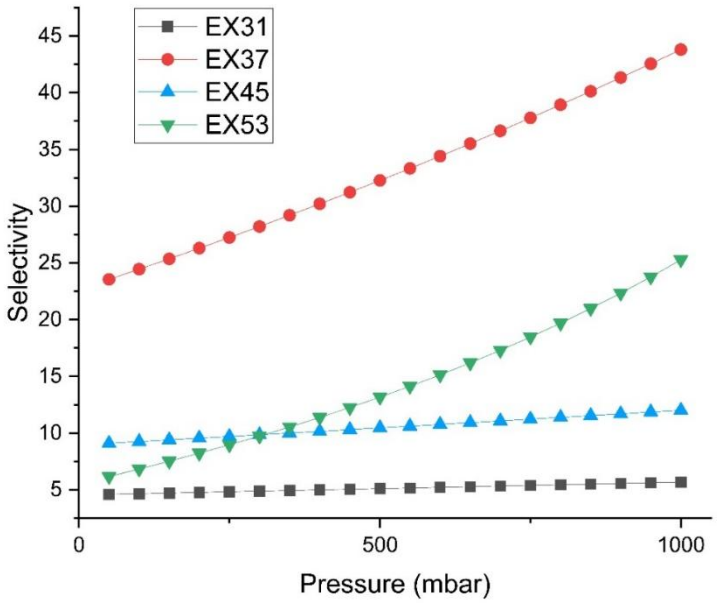

Figure 86 - IAST-predicted CO_2/N_2 selectivities as a function of pressure (50–1000 mbar) for the four samples (EX31-900-2H-KOH-1:8, EX37-850-15-CO_2-600, EX45-900-2H-KOX-1:1, and EX53-900-2H-KOX-1:1 (pre-pyrolysed).

Sample EX45-900-2H-KOX-1:1, the KOx-activated sample with high microporosity but minimal nitrogen functionalities, shows intermediate behaviour. Its selectivity increases modestly from around 9.1 to 12.0 over the pressure range studied. The relatively stable and moderate selectivity can be ascribed to the dominance of physical confinement effects within micropores, which favour CO_2 adsorption primarily through size and kinetic selectivity rather than chemical affinity. Notably, the flatness of the curve obtained for

sample EX45-900-2H-KOX-1:1 relative to that for sample EX37-850-15-CO_2-600 suggests that while microporosity enhances CO_2 uptake compared to mesoporous materials like sample EX31-900-2H-KOH-1:8, the absence of chemical functional groups limits the achievable selectivity.

Sample EX53-900-2H-KOX-1:1 (pre-pyrolysed) displays behaviour intermediate between samples EX37-850-15-CO_2-600 and EX45-900-2H-KOX-1:1. Selectivity increases from approximately 6.2 at 50 mbar to 25.3 at 1000 mbar, showing a much steeper slope than sample EX45-900-2H-KOX-1:1 but a lower ultimate selectivity than sample EX37-850-15-CO_2-600. This indicates that sample EX53-900-2H-KOX-1:1 (pre-pyrolysed) benefits from both significant microporosity and some degree of chemical enhancement, although to a lesser extent than sample EX37-850-15-CO_2-600. The substantial growth in selectivity with increasing pressure suggests that cooperative confinement effects within micropores increasingly dominate at higher loading levels. However, this steep increase is also likely caused by the growing divergence between IAST predictions and experimental uptake values observed across the pressure range, with IAST increasingly underpredicting gas uptake in EX53-900-2H-KOX-1:1 (pre-pyrolysed).

While the observed trends affirm the importance of microporosity and surface chemistry in enhancing CO_2 selectivity, several limitations and assumptions warrant scrutiny. Notably, the high BET surface area of EX31-900-2H-KOH-1:8 did not translate to meaningful selectivity, illustrating that surface area alone is a poor predictor of performance in competitive adsorption. This challenges a common assumption in sorbent development and highlights the need to prioritise micropore distribution and surface functionality over bulk textural metrics. Conversely, EX37-850-15-CO_2-600 exhibited exceptional selectivity despite its low surface area, underscoring the disproportionate impact of nitrogen functionalities.

Furthermore, the use of Ideal Adsorbed Solution Theory (IAST) introduces critical modelling limitations. IAST predictions increasingly diverged from experimental uptake with pressure, particularly in EX53-900-2H-KOX-1:1 (pre-pyrolysed), suggesting that ideal assumptions break down in materials with complex pore geometries or strong site-specific interactions. The model's inability to account for co-adsorption effects, kinetic barriers, or surface heterogeneity may lead to over- or underestimation of selectivity in real systems. Moreover, the binary CO_2/N_2 tests, while necessary for controlled analysis, oversimplify the multicomponent nature of flue gases. Without considering the influence of water, SO_x, and

NO_x, or assessing cyclic performance, the practical relevance of the selectivity values remains constrained. These findings indicate that a more holistic evaluation framework—incorporating chemical characterisation, multicomponent testing, and regeneration behaviour—is essential for assessing real-world suitability of carbon-based sorbents.

The best-performing sample in this study, EX37-850-15-CO_2-600, demonstrated CO_2/N_2 selectivity values ranging from ~24 at 50 mbar to ~44 at 1000 mbar, which favourably compares with several benchmark materials. At 1 bar and 25 °C, typical CO_2/N_2 selectivities for widely studied adsorbents such as Cu-BTC, BPL activated carbon, and ZIF-8 are significantly lower at 19, 10 and 7 respectively. [363] Even the high-surface-area mesoporous silica SBA-15 exhibits a CO_2/N_2 selectivity of only ~5.2, while some MOF composites such as Cu-BTC@SBA-15 achieve values around 26—comparable to the lower end of EX37-850-15-CO_2-600's performance range. Fe-BTC and MOF-5 also show selectivities in the range of 17–18, further reinforcing the competitiveness of the functionalised biochar. Although materials such as MIL-53-Al or certain microporous MOF hybrids (e.g., DEPO-2, Cu-BDC/MCM-41) can exceed selectivities of 40–60 under ideal conditions, these systems typically rely on crystalline order, specific metal-ligand coordination, or templated nanostructures, which are expensive and difficult to scale. [364] In contrast, EX37-850-15-CO_2-600 achieves comparable selectivity values with a far simpler synthesis from low-cost waste biomass and without the need for metallic precursors, offering a strong case for further development of chemically modified carbons as viable sorbents for post-combustion CO_2 separation.

Overall, the trends observed highlight the interplay between surface chemistry and pore structure in determining CO_2/N_2 selectivity. High surface area alone, as exemplified by sample EX31-900-2H-KOH-1:8, is insufficient to deliver meaningful separation performance without appropriate pore architecture or chemical functionality. Conversely, nitrogen functionalities (sample EX37-850-15-CO_2-600) and microporous structures (samples EX45-900-2H-KOX-1:1 and EX53-900-2H-KOX-1:1 (pre-pyrolysed) synergistically contribute to improved selectivity, with chemically active sites offering the most substantial enhancement. The comparative performance of the four materials underscores the importance of designing sorbents with both tailored microporosity and functionalised surfaces to optimise post-combustion carbon capture applications.

10.4. Summary

The competitive adsorption study of CO_2/N_2 mixtures across the four SCG-derived biochars provided several important conclusions regarding sorbent performance. The results demonstrated that nitrogen surface functionalities significantly enhance CO_2 selectivity, as most clearly evidenced by sample EX37-850-15-CO_2-600. This material, despite having the lowest surface area and microporosity among the samples, exhibited the highest and most pressure-responsive selectivity. This finding underscores the critical role of surface chemical properties, beyond textural characteristics alone, in promoting preferential CO_2 adsorption over N_2 in post-combustion conditions.

In contrast, samples EX45-900-2H-KOX-1:1 and EX53-900-2H-KOX-1:1 (pre-pyrolysed), both characterised by high microporosity but minimal nitrogen functionalities, achieved only moderate CO_2 selectivity. Their performance indicates that while microporous structures can favour CO_2 adsorption through kinetic and size-selective mechanisms, the absence of chemical affinity limits the magnitude of separation achievable. Between these two, sample EX53-900-2H-KOX-1:1 (pre-pyrolysed) showed a steeper pressure dependence in selectivity, suggesting that subtle differences in pore structure or surface chemistry still influence competitive adsorption behaviour even among nominally similar materials.

Sample EX31-900-2H-KOH-1:8, a highly mesoporous, high surface area sample, exhibited the poorest selectivity, with only marginal increases across the full pressure range studied. Its behaviour confirms that high surface area alone is insufficient to guarantee separation performance; appropriate pore size distributions and chemical functionalities are required to achieve strong selective adsorption under realistic operating conditions.

Finally, IAST proved to be a generally reliable predictive tool for assessing binary adsorption behaviour, with good agreement between predicted and experimental results for most samples. However, deviations observed particularly for samples EX37-850-15-CO_2-600 and EX53-900-2H-KOX-1:1 (pre-pyrolysed) highlight the limitations of the idealised assumptions underpinning IAST, particularly when surface-specific interactions and cooperative confinement effects are significant. These results emphasise the necessity of experimental validation to complement thermodynamic modelling, especially when evaluating functionalised or structurally complex adsorbents.

Collectively, the findings of this study reinforce that optimal sorbents for post-combustion CO_2 capture should integrate both microporosity and tailored surface chemistry to

maximise selective adsorption performance under competitive, low partial pressure conditions.

Chapter 11. Biochar Synthesis Limitations and Repeatability

11.1. Feedstock Selection

Feedstock selection plays a critical role in determining the physicochemical properties of the resulting biochar and must balance technical suitability with environmental and economic viability.[151] This study prioritised materials that align with principles of waste valorisation and circular economy by focusing exclusively on locally available biomass waste streams. SCG were selected as the feedstock due to their widespread availability, high lignin content, relatively low ash, and notable nitrogen content—all properties conducive to generating porous, high-carbon biochars with potential for CO_2 adsorption.[365] Their selection was further supported by the fact that SCG are largely underutilised as a resource, with limited competing industrial applications, in contrast to other residues such as spent grain and agricultural waste, which is already widely repurposed as animal feed.

From a technical perspective, SCG exhibit favourable pyrolytic behaviour. High lignin content enhances fixed carbon yield and thermal stability, while moderate cellulose and hemicellulose fractions contribute to pore development. Their intrinsic nitrogen facilitates the incorporation of nitrogen functionalities. The relatively low ash content is beneficial for surface area development, minimising pore obstruction.[366]

Nevertheless, several challenges are associated with the use of SCG at scale. These include the need for consistent pre-treatment (drying and particle size reduction), the diffuse nature of the waste stream, and the presence of residual oils and soluble compounds that may affect activation. Despite these challenges, SCG present a compelling case as a sustainable and strategic feedstock for advanced biochar production, supporting both performance and environmental objectives.

11.2. Activation Method Selection

The choice of activation method significantly influences the surface area, pore structure, and surface functionality of biochars, which are critical for adsorption applications. While various physical, chemical, and biological methods are available, the selection was guided by considerations of performance, scalability, and experimental feasibility.[164]

Physical activation methods are often preferable for scale-up due to their simplicity and reduced chemical usage. However, due to equipment constraints, only carbon dioxide (CO_2) activation was feasible in this study. Although alternative physical methods such as steam,

ammonia, ozone, or limited air activation are well-documented, they were not accessible under current laboratory conditions. CO_2 activation was selected not only for its proven effectiveness in enhancing microporosity, but also for its alignment with circular economy principles. Specifically, the CO_2 used in activation can be integrated into a carbon loop, transforming a captured waste stream into a process input. Furthermore, CO_2 activation enables the production of carbon monoxide (CO) via the Boudouard reaction, which has potential as a feedstock in chemical synthesis processes such as Fischer–Tropsch and methanol production.

Potassium hydroxide (KOH) activation was included as a benchmark chemical activation method due to its widespread application in the literature and its ability to produce high-surface-area activated carbons. Its inclusion allows for direct comparison with other feedstocks and activation methods. Potassium oxalate (KOx) was selected as a less commonly applied chemical activator that has been reported to yield materials with favourable microporosity while being less corrosive, easier to handle, and more environmentally benign than KOH.[349] Fungal activation was explored as a novel biological method. While included as an activation strategy, it is more accurately a pre-treatment that alters the biomass structure prior to pyrolysis. By partially degrading lignocellulosic components, fungal pre-treatment has the potential to lower the energy input required during pyrolysis and enhance porosity development. This approach exemplifies circular economy thinking by extracting additional utility from biomass waste prior to carbonisation and enabling potential integration with other activation techniques.

11.3. Overview of Experimental Conditions

A comprehensive series of biochar samples was synthesised to explore the effects of pyrolysis parameters, specifically temperature, residence time, ramp rate, and activation conditions. All samples were derived from SCG waste, chosen for its consistent particle size, local abundance, and relevance to sustainable waste valorisation. Prior to pyrolysis, the material was finely ground for espresso preparation, with sample textures ranging from granular at lower pyrolysis severities to extremely fine, dust-like residues at higher temperatures and activation intensities.

The experiments were designed within a structured framework using design of experiments (DoE) principles, employing screening and central composite design (CCD) approaches where appropriate. This allowed a systematic evaluation of activation conditions and their

effects on material properties. Further details of the DoE methodology and statistical analysis are provided in Chapter 7 Effects of Operating Parameters on Biochar Yield and Textural Properties.

The pyrolysis temperatures employed ranged from 400 °C to 1200 °C.[165] These limits were selected based on established literature guidance regarding the development of porosity, fixed carbon content, and thermal stability, while remaining within the operational constraints of the Carbolite Eurotherm horizontal tube furnace. High temperatures above 900 °C were specifically included to investigate potential structural collapse and pore merging at extreme conditions. [36]

All experiments were conducted in a Carbolite Eurotherm horizontal tube furnace operated under continuous N_2 flow. The furnace relied on its internal thermocouple for temperature control, and no independent external calibration was performed prior to the experimental campaign. While the furnace is factory-calibrated and routinely used for thermal treatments, minor spatial temperature gradients along the tube cannot be excluded. The sample boats were therefore positioned consistently in the central zone of the tube to maximise exposure to the most uniform thermal region.

The system was not equipped with a formally characterised isothermal zone measurement. Instead, consistency was maintained by fixing the sample position and gas flow conditions across all experiments. This approach prioritised reproducibility between runs rather than absolute temperature mapping.

Residence times varied from 5 to 180 min, selected to span both short and extended thermal exposures while remaining compatible with laboratory operating hours. Practical considerations, such as the need for full thermal cycling (heating, holding, cooling) within a certain window, influenced the choice of residence times.[165]

A consistent ramp rate of 20 °C/min was applied across all samples. This rate represented a balance between achieving reasonable thermal uniformity and ensuring the feasibility of conducting multiple runs within limited daily laboratory access. Although slower ramp rates may benefit pore development, logistical constraints (gas had to be turned off) necessitated a standardised and expedient heating protocol.[166]

Activation strategies were designed to explore a broad range of intensities. Physical activation with CO_2 was conducted at two flow rates (100 and 600 mL/min), offering insight

into the role of oxidising agent availability during activation. Chemical activation methods utilised potassium hydroxide (KOH) and potassium oxalate (KOx) at mass ratios from 1:1 to 1:10 relative to biochar. KOH was selected as a widely established activating agent to serve as a benchmark, whereas KOx was employed due to its milder chemical nature, reduced corrosivity, and easier handling. Activation ratios were based on values commonly reported in the literature and aimed to systematically vary activation severity to study effects on yield and pore development. [58,165]

Fungal pre-treatment was investigated as a biological activation method, representing a novel and less commonly studied approach. Due to the nature of biological growth, exact conditions such as cultivation duration could not be strictly controlled. Grey oyster mushrooms were chosen for their robust growth across a variety of biomass types. [367] The spent grounds were used until they ceased productive mushroom growth (typically after two to three flushes). Contamination issues, primarily with competing moulds, occasionally arose; only material from uncontaminated areas was harvested. While there are clear opportunities to improve growth conditions and reduce contamination, such process optimisations were beyond the scope of the current study.

Gas sealing at the tube ends was achieved using rubber bungs fitted to gas inlet and outlet lines. While these provided a practical laboratory seal, some wear over time may have reduced sealing efficiency. To mitigate potential air ingress, a continuous positive N_2 flow was maintained during operation.

A water-filled gas trap was connected downstream of the reactor outlet to act as a simple backflow barrier and to prevent atmospheric air from diffusing into the system during cooling. This trap also served as a precautionary scrubbing step for condensable pyrolysis vapours.

In summary, the chosen ranges of temperature, residence time, ramp rate, and activation intensity were designed to systematically investigate the synthesis-structure relationships in biochar production, while being inherently shaped by practical limitations regarding scalability, reactor configuration, and laboratory availability. These considerations defined the achievable diversity of the sample set and framed the experimental exploration of biochar development.

11.4. Limitations of Experimental Setup

Several constraints inherent to the experimental setup shaped the scope and direction of this work, particularly limiting the activation strategies and characterisation techniques available. These limitations should be considered when evaluating the reproducibility, scalability, and interpretability of the results.

Reactor Configuration and Activation Method Constraints

All experiments were conducted using a Carbolite Eurotherm horizontal tube furnace. While suitable for controlled pyrolysis, this system imposed several practical limitations. The limited volume of the furnace tube restricted the quantity of biomass that could be processed in a single run, thereby limiting scale-up assessment. Furthermore, the ceramic tube used in the system may have introduced thermal gradients due to its poor heat conductivity and lack of thermal contact optimisation—no heat sink compound was applied between the tube and furnace wall. These factors may have contributed to non-uniform heating and inconsistent activation, particularly across the sample bed.

Due to the equipment design, several physical activation methods—including steam, ozone, ammonia, and air-dilution activation—were not feasible. The system lacked the infrastructure to safely introduce or control such gases. Additionally, the reactor was not adequately sealed for methods requiring high gas-tightness, such as ammonia activation. As a result, only CO_2 activation was possible. While CO_2 activation is well studied and aligns with circular economy principles by valorising captured CO_2, this limitation precluded broader investigation into physical activation strategies. Operational restrictions also constrained temperature profiles. Experiments were conducted during standard lab hours (9:00–17:00), necessitating full heating and cooling cycles within a day to ensure safe gas handling and prevent water backflow into the furnace from the water gas trap. This imposed upper limits on final temperature, residence time, and ramp rate, which in turn limited exploration of extreme pyrolysis conditions.

Analytical Constraints

Fourier-transform infrared spectroscopy (FTIR) was used as a screening tool for identifying surface functional groups, including nitrogen-containing moieties. However, FTIR was found to be insufficiently sensitive for reliable detection of nitrogen functionalities at the levels expected in these samples. Alternative characterisation techniques, such as CHN elemental analysis and X-ray photoelectron spectroscopy (XPS) were considered. However, these

were not pursued due to the lack of in-house instrumentation, prohibitive cost, and long turnaround times, which would have impeded the progress of experimental work.

Nitrogen physisorption (BET) was employed as the primary screening method for assessing surface area and porosity across samples. While this technique is well-established and effective for evaluating mesoporous structures, it has known limitations when applied to microporous materials.[293] Specifically, the relatively large kinetic diameter and low polarizability of nitrogen at 77 K may restrict diffusion into ultra-micropores, potentially leading to underestimation of accessible pore volume. Additionally, the low measurement temperature does not reflect adsorption behaviour under realistic operating conditions. Nevertheless, nitrogen physisorption was selected due to its widespread acceptance, availability, and ability to provide comparative insight across the sample library. These limitations were considered in the interpretation of results and complemented by further adsorption studies using CO_2 as a probe molecule to better resolve microporosity.

Constraints on Nitrogen Doping Evaluation

Several nitrogen doping agents—including ammonium hydroxide, urea, and melamine—were trialled early in the study. However, due to the limitations described above, their incorporation could not be confirmed or quantified. This precluded the systematic development of nitrogen-doped sorbents and constrained the ability to explore relationships between surface chemistry and CO_2 adsorption.

Characterisation Scope

With CHN and XPS unavailable, the primary screening method for selecting promising adsorbents was nitrogen physisorption (BET). Only a subset of materials was taken forward for in-depth characterisation and CO_2 adsorption testing. This restriction limited the extent to which structure–function relationships could be generalised.

Collectively, these limitations highlight the need for more comprehensive reactor control and expanded analytical capabilities in future work, particularly when evaluating surface modifications and their influence on adsorption behaviour.

11.5. Preliminary Assessment of Repeatability

Given the extensive range of experimental conditions explored across different activation methods, it was not feasible within the scope of this study to conduct a full repeatability assessment for all samples. Instead, a preliminary evaluation of repeatability was carried out based on a subset of samples where duplications naturally occurred during

experimental planning. This approach provides an initial indication of the reproducibility of the synthesis methods without the requirement for a comprehensive and resource-intensive repeat study.

The duplicates assessed in this section cover chemical activation using KOH (sample EX31-900-2H-KOH-1:8 vs EX31.2-900-2H-KOH-1:8), chemical activation using potassium oxalate (KOx) (sample EX59-700-68-KOx-1:4.5 vs EX63), and grey oyster fungal activation (GO) (sample EX79 vs EX82). A summary of their synthesis conditions, yield, and textural properties is provided in Table 39.

For the KOH-activated samples, EX31-900-2H-KOH-1:8 and EX31.2-900-2H-KOH-1:8, moderate variation was observed. Sample EX31-900-2H-KOH-1:8 exhibited a BET surface area of 3204 m^2/g, whereas EX31.2-900-2H-KOH-1:8 measured 2513 m^2/g. The mean surface area was 2858.5 m^2/g, with a standard deviation of 488.6 m^2/g and a relative standard deviation (RSD) of 17.1%. Although both demonstrate high surface areas, the observed variation highlights the sensitivity of aggressive chemical activation processes—particularly under extreme activation ratios (1:8)—to minor inconsistencies in reagent distribution, sample homogeneity, or activation dynamics.

The KOx-activated samples (EX59 and EX63) showed closer agreement, with yields of 22.00% and 22.42% and BET surface areas of 505 m^2/g and 559 m^2/g, respectively. The mean surface area was 532.0 m^2/g with a standard deviation of 38.2 m^2/g and an RSD of 7.2%. This comparatively low variability suggests that KOx activation, under the conditions tested, is relatively robust and reproducible compared to the harsher KOH activation regime.

For fungal activation (samples EX79 and EX82), larger variability was again observed. Both samples exhibited low BET surface areas, with EX79 measuring 5 m^2/g and EX82 reaching 15 m^2/g. The mean value was 10.0 m^2/g with a standard deviation of 7.1 m^2/g and a notably high RSD of 70.7%. This degree of fluctuation is attributed to the inherent biological variability associated with fungal pre-treatment, including differences in fungal growth behaviour, biomass degradation extent, and possible minor contamination effects.

The values obtained in this preliminary repeatability assessment are broadly consistent with expectations for each activation strategy. For KOH activation, BET surface areas exceeding 2500 m^2/g are within the upper range reported for biochars synthesised with high reagent ratios (1:6 to 1:8) and elevated temperatures (≥800 °C), though they are

known to exhibit greater variability due to the aggressiveness of the activation process. In contrast, the BET surface areas of 505–559 m²/g recorded for KOx-activated samples fall within typical ranges for milder chemical activation using potassium salts, which often produce more moderate porosity with improved reproducibility.[349,368,369] For the fungal-activated samples (5–15 m²/g), no directly comparable literature values are available, as this approach represents a novel pre-treatment strategy; however, the low surface areas are not unexpected given the biological nature of the modification, which is likely to influence surface chemistry more than textural development. These comparisons suggest that while variability exists, particularly in KOH and fungal activation, the absolute values themselves are reasonable and in line with expectations for the respective methods.

Table 39 - Synthesis conditions, yield, and BET surface area of duplicate samples for preliminary repeatability assessment across KOH, KOx, and fungal activation methods.

Biochar Identification	Final Temp (°C)	Hold Time (mins)	CO_2 Flow Rate (mL/min)	Yield (%)	BET Surface Area (m^2/g)
EX31-900-2H-KOH-1:8	900	120	KOH 1:8	1.374	3204
EX31.2-900-2H-KOH-1:8	900	120	KOH 1:8	1.836	2513
EX59-700-68-KOx-1:4.5	700	68	KOx 1:4.5	22	505
EX63-700-68-KOx-1:4.5	700	68	KOx 1:4.5	22.42	559
EX79-700-15-GO	700	15	GO	11.35	5
EX82-700-15-GO	700	15	GO	13.01	15

It is important to emphasise that two-sample comparisons inherently limit the strength of conclusions that can be drawn. Nevertheless, this preliminary assessment provides useful insights into the general reproducibility trends across different activation strategies. A formal, targeted repeatability study focusing on the most promising CO_2-activated sample is presented in the next section, offering a more rigorous evaluation of synthesis reproducibility under optimised conditions.

11.6. Formal Assessment of Repeatability

To provide confidence in the reliability of subsequent adsorption analyses, a structured repeatability study was conducted on sample EX37-850-15-CO_2-600, which was identified during preliminary screening as a promising candidate based on its high BET surface area and significant microporosity. These initial metrics indicated strong potential for CO_2 capture applications, warranting further investigation of its synthetic reproducibility.

Table 40 - Experimental synthesis conditions and characterisation results for sample EX37-850-15-CO_2-600 replicates.

Biochar ID	Final Temp (°C)	Hold Time (min)	CO_2 Flow Rate (mL/min)	Yield (%)	BET Surface Area (m^2/g)	t-plot Micropore Area (m^2/g)	t-plot Micropore Volume (cm^3/g)	% Microporosity
EX37-850-15-CO_2-600	850	15	600	15.10	736	621	0.239	84.3
EX37.2-850-15-CO_2-600	850	15	600	16.96	676	581	0.220	85.9
EX37.3-850-15-CO_2-600	850	15	600	17.46	618	537	0.210	86.9
EX37.4-850-15-CO_2-600	850	15	600	16.90	676	579	0.220	85.7
EX37.5-850-15-CO_2-600	850	15	600	18.14	609	536	0.200	88.0

As discussed in later chapters, sample EX37-850-15-CO_2-600 ultimately demonstrated the highest CO_2 uptake in the low-pressure region and superior CO_2/N_2 selectivity among all samples tested. Additionally, its method of synthesis—physical activation using CO_2—offers practical advantages in terms of scalability, environmental compatibility, and operational simplicity. These factors reinforce the relevance of selecting sample EX37-850-15-CO_2-600 for a detailed repeatability assessment at this stage. By establishing the reproducibility of sample EX37-850-15-CO_2-600's synthesis and textural properties, this section underpins the robustness of the performance data presented in subsequent chapters.

Five independent synthesis replicates (samples EX37-850-15-CO_2-600 through EX37-850-15-CO_2-600.5) were produced under identical pyrolysis and activation conditions: 850 °C final temperature, 15 min hold time, and 600 mL/min CO_2 flow rate. The key synthesis and characterisation results are summarised in Table 40.

Descriptive statistics for the key properties are presented in Table 41.

Table 41 - Summary statistics and Shapiro-Wilk normality test p-values for sample EX37-850-15-CO_2-600 replicate series.

Property	Mean	Standard Deviation	Variance	Coefficient of Variation (%)	Shapiro-Wilk p-value
Yield (%)	16.91	1.13	1.27	6.67%	0.809
BET Surface Area (m^2/g)	663	51.78	2681.33	7.81%	0.830
Micropore Area (m^2/g)	570	35.62	1268.75	6.24%	0.944
Micropore Volume (cm^3/g)	0.218	0.0145	0.00021	6.64%	0.867
% Microporosity	86.16	1.38	1.92	1.61%	0.933

The results indicate that the synthesis method for sample EX37-850-15-CO_2-600 is highly repeatable within acceptable experimental error margins. Yield exhibited a coefficient of variation (CV) of 6.67%, demonstrating good consistency in mass retention. BET surface area showed slightly higher variability (CV = 7.81%), likely reflecting minor fluctuations in activation severity, such as differences in thermal gradients or gas distribution during CO_2 flow. Micropore area and micropore volume showed low variability (CVs of 6.24% and 6.64%, respectively), suggesting that micropore development was robust and reproducible under the given conditions. The microporosity percentage was particularly consistent, with a CV of just 1.61%, indicating that the relative proportion of microporosity remained highly stable across replicates. Normality of the datasets was confirmed using the Shapiro-Wilk test, with all p-values exceeding 0.05, indicating that the data distributions could be considered normal. Furthermore, no outliers were detected using the Z-score method, with all measurements falling within ±2 standard deviations of their respective means.

The textural properties observed for the EX37-850-15-CO_2-600 series are consistent with literature reports on CO_2-activated biochars derived from lignocellulosic biomass. BET surface areas in the range of 600–740 m^2/g and microporosity above 80% are characteristic of activation at high temperatures (≥800 °C) with moderate to high CO_2 flow rates. [347,348] The observed micropore volumes (0.20–0.24 cm^3/g) fall within expected ranges for physically activated carbons optimised for CO_2 capture applications.[36] These values support the validity of the activation protocol and confirm that the EX37-850-15-CO_2-600 samples possess the textural features typically associated with effective physisorbents for post-combustion CO_2 separation.

Overall, the reproducibility of sample EX37-850-15-CO_2-600 activation conditions is satisfactory. While some modest spread in BET surface area was observed, critical textural

properties governing CO_2 adsorption, particularly microporosity, were very stable. The variability is likely attributable to unavoidable minor differences in sample packing, furnace temperature homogeneity, or gas flow distribution in small-scale laboratory reactors. These findings strengthen confidence in the reliability of sample EX37-850-15-CO_2-600 samples for further adsorption analysis and suggest that the chosen activation protocol can serve as a reproducible and scalable basis for CO_2 capture technologies.

11.7. Design of Experiments and Parameter Screening

A preliminary Design of Experiments (DoE) campaign was conducted to systematically evaluate the influence of activation parameters—including temperature, hold time, and reagent ratio—on the textural properties of the SCG-derived biochars. This study aimed to identify significant factors governing surface area, microporosity, and yield across different activation methods. However, the statistical analyses revealed that while some factors showed consistent trends, the overall findings did not significantly impact the final sample selection for detailed adsorption studies. Consequently, these results, while informative for understanding process sensitivities, were not decisive in selecting the main samples discussed in this work.

11.8. Summary

A broad range of activation conditions was employed to generate a diverse library of samples, and a preliminary assessment of repeatability across selected duplicates provided initial insight into reproducibility trends. A structured reproducibility study conducted on the most promising CO_2-activated sample, EX37-850-15-CO_2-600, demonstrated good repeatability in terms of yield, surface area, micropore volume, and microporosity, with low variability and no significant outliers detected. These findings validate the robustness of the sample EX37-850-15-CO_2-600 synthesis protocol and underscore the scalability and environmental advantages of physical activation with CO_2 compared to chemical methods.

Chapter 12. Conclusions and Future Work

12.1. Summary

This research explored the synthesis, characterisation, and performance evaluation of biochar materials derived from spent coffee grounds (SCG) for post-combustion CO_2 capture applications. A range of activation methods—CO_2, KOH, potassium oxalate (KOx), and fungal pre-treatment—were systematically assessed to determine their effects on biochar yield, porosity, surface chemistry, and gas adsorption properties. Design of Experiments (DoE) methodology was applied to explore activation conditions, and a range of analytical tools including nitrogen adsorption, FTIR, XPS, CHN, and gravimetric CO_2 adsorption were used to evaluate material performance.

The following research objectives were comprehensively addressed, with findings that advance understanding of SCG-derived biochars for CO_2 capture:

Objective 1: A critical literature review identified spent coffee grounds (SCG) as a promising biomass precursor due to their high fixed carbon content, intrinsic nitrogen, and wide availability as a waste stream. The review also guided the selection of activation methods — CO_2, KOH, potassium oxalate, and fungal activation — based on their reported efficacy in developing microporosity, enhancing surface chemistry, and improving CO_2 affinity in biochar systems.

Objective 2: A diverse set of SCG-derived biochars was successfully synthesised using the selected activation strategies. These methods produced distinct textural and chemical profiles: CO_2 activation yielded highly microporous materials with minimal surface modification; KOH and potassium oxalate introduced mesoporosity and residual basic sites; fungal activation promoted nitrogen-rich surface functionalities via biological processing.

Objective 3: As shown in Chapter 7 revealed that key activation parameters had statistically significant effects on porosity and surface area. CO_2 activation performance was highly sensitive to temperature. In contrast, KOH activation was more strongly influenced by the mass ratio of activating agent, highlighting the importance of chemical loading over thermal input.

Objective 4: Gravimetric CO_2 adsorption studies indicated that samples possessing greater micropore development and nitrogen functionalities generally exhibited enhanced uptake and affinity at low partial pressures (80–150 mbar), relevant to post-combustion capture.

EX37-850-15-CO_2-600, a nitrogen-containing microporous sample, frequently showed among the highest uptakes under these conditions, although performance differences between samples also reflected variations in micropore volume and activation route.

Objective 5: Cyclic adsorption–desorption testing over multiple cycles demonstrated strong regeneration capacity in several samples. EX53-900-2H-KOX-1:1 (pre-pyrolysed) retained over 95% of its initial capacity after five cycles, despite lower affinity, indicating robustness suitable for pressure swing adsorption (PSA) applications. These findings support the feasibility of reusing certain SCG-derived adsorbents with minimal performance loss.

Objective 6: Ideal Adsorbed Solution Theory (IAST) modelling of competitive CO_2/N_2 adsorption confirmed that chemical functionality significantly enhanced CO_2 selectivity under flue gas conditions (15% CO_2, 60 °C). EX37-850-15-CO_2-600 again outperformed other samples, illustrating that textural properties alone were insufficient for selective separation. This underscores the importance of synergistic pore–surface design for binary gas capture.

12.2. Evaluation of Sorbents Against Literature Criteria

To contextualise the performance of the SCG-derived sorbents developed in this study, a critical evaluation was performed against established criteria for solid adsorbents used in post-combustion CO_2 capture. These include adsorption capacity, selectivity, kinetics, mechanical and chemical stability, regenerability, and cost.

CO_2 Adsorption Capacity: While the equilibrium capacities measured here fall below the 3–4 mmol/g benchmark established for competitiveness with MEA systems,[57] all sorbents in this study exceeded that range at 1000 mbar and 25 °C, with EX31-900-2H-KOH-1:8 reaching up to 4.04 mmol/g and EX37-850-15-CO_2-600 achieving 3.13 mmol/g. However, this comparison is complicated by the lack of standardised testing conditions in the literature. Though 1000 mbar and 25 °C is a common reporting standard, it does not reflect the low partial pressure and elevated temperatures encountered in post-combustion capture scenarios. As demonstrated in this study, performance at ambient conditions can significantly differ from performance under realistic flue gas conditions—particularly for microporous, functionalised sorbents such as EX37-850-15-CO_2-600. Consequently, low-pressure, high-temperature uptake and working capacity metrics remain more relevant for practical evaluation, where EX37-850-15-CO_2-600 also exhibited excellent performance.

Selectivity for CO_2 over N_2: EX37-850-15-CO_2-600 achieved the highest and most pressure-responsive selectivity, rising from approximately 24 at 50 mbar to nearly 44 at 1000 mbar. This places it among the top-performing carbonaceous sorbents reported in the literature, where values between 10 and 30 are typical for porous carbons without nitrogen doping under comparable conditions. Such a high and steadily increasing selectivity underscores the impact of nitrogen surface functionalities, which are known to enhance CO_2 capture via acid-base interactions beyond what is possible through physisorption alone. EX37-850-15-CO_2-600's performance supports growing evidence that surface chemistry—particularly pyridinic and pyrrolic nitrogen groups—is a key determinant in competitive adsorption behaviour and highlights its suitability for selective CO_2 separation in post-combustion gas streams.

Adsorption/Desorption Kinetics: Kinetic modelling showed that both EX37-850-15-CO_2-600 and EX53-900-2H-KOX-1:1 (pre-pyrolysed) adsorbed CO_2 rapidly, with time constants consistent with other porous carbons. This rapid uptake suggests suitability for PSA processes.

Mechanical and Chemical Stability: No direct tests of attrition or oxidative stability were conducted; however, the sorbents maintained structural integrity and consistent performance across multiple adsorption–desorption cycles. The absence of post-synthetic modification and high thermal resistance of carbon materials implies good resilience, though further tests with impurities like SOx and NOx are required.

Regenerability: EX53-900-2H-KOX-1:1 (pre-pyrolysed) showed excellent cycling stability over 60 PSA cycles, maintaining working capacity with negligible performance loss. The measured heats of adsorption fell within the expected physisorption range (25–45 kJ/mol), suggesting low energy costs for regeneration relative to chemisorbents.

Cost and Scalability: All sorbents were produced from waste SCG using relatively low-cost reagents and thermal processes. Notably, EX37-850-15-CO_2-600 was synthesised using a single-step CO_2 activation, eliminating chemical washing steps, lowering environmental burden and cost.

Comparison Against Other SCG-Derived Activated Carbons:

When compared specifically to previously reported SCG-derived activated carbons, the materials developed in this work fall within, and in several metrics exceed, established

performance ranges. Literature reports commonly cite CO_2 adsorption capacities of 3.0–4.5 mmol g^{-1} at 298 K and 1 bar for KOH-activated SCG carbons, with selectivity values typically between 10 and 30 under comparable IAST-derived conditions. Isosteric heats of adsorption are generally reported in the range of 20–40 kJ mol^{-1}, reflecting predominantly physisorptive behaviour strengthened by micropore confinement. [70–75]

The best-performing samples in this study align closely with these benchmarks in terms of absolute capacity, while demonstrating enhanced selectivity under flue gas-relevant conditions. In particular EX37-850-15-CO_2-600 achieved selectivity values approaching 44, exceeding many reported undoped SCG-derived carbons. Moreover, performance under elevated temperature and low partial pressure conditions—conditions more representative of industrial application—was explicitly evaluated here, whereas many literature studies report only ambient equilibrium uptake. The present work therefore not only confirms the competitiveness of SCG-derived carbons but extends prior studies through systematic activation comparison, kinetic modelling, and competitive adsorption analysis under realistic conditions.

Overall, while the materials do not surpass state-of-the-art synthetic adsorbents in absolute performance metrics, they offer a strong balance of selectivity, regenerability, and cost-effectiveness. This positions SCG-derived biochars as highly promising candidates for sustainable carbon capture technologies, particularly in contexts where circular resource use and low environmental impact are prioritised. The study confirms that SCG-derived biochars can serve as effective, low-cost sorbents for post-combustion CO_2 capture, but that performance is highly contingent on activation method and surface chemistry.

Textural Development: CO_2 and KOx activation offered the best balance between porosity enhancement and material yield. CO_2 activation achieved microporosities exceeding 80% without chemical reagents, positioning it as the most scalable and environmentally sustainable route.

Surface Chemistry: Nitrogen-containing functional groups—especially pyridinic and pyrrolic species identified via XPS—played a pivotal role in enhancing CO_2 affinity and selectivity. EX37-850-15-CO_2-600, with elevated nitrogen content and controlled microporosity, demonstrated the strongest performance under single-component and binary gas conditions.

Process Trade-offs: KOH activation generated the highest surface areas (>3000 m^2/g) but often lacked microporosity and imposed substantial yield penalties. Moreover, chemical activation routes such as KOH and KOx introduce higher material and operational costs, require post-synthesis washing, and increase process complexity—factors that can hinder scalability compared to simpler physical methods like CO_2 activation. Fungal pre-treatment increased nitrogen content in biomass and represents a sustainable, low-cost modification route. While ineffective alone in developing porosity, it holds promise when combined with other activation strategies to enhance surface chemistry in a more circular and environmentally friendly manner.

Adsorption Behaviour: A clear trade-off was observed between high-affinity adsorption (EX37-850-15-CO_2-600) and high regenerability (EX53-900-2H-KOX-1:1 (pre-pyrolysed). In this context, physisorptive sorbents like EX53-900-2H-KOX-1:1 (pre-pyrolysed) are better suited to PSA due to their lower regeneration energy requirements. Sorbents relying heavily on chemisorption, although often exhibiting higher initial CO_2 affinity, can incur significant energy penalties during regeneration, potentially undermining their economic viability for rapid-cycle operation.

Statistical Modelling: The DoE approach revealed clear trends in how activation parameters influenced porosity, with CO_2 activation being strongly temperature-dependent and KOH activation primarily governed by reagent loading. These mechanistic insights align well with the experimental observations and underpin the broader conclusions drawn from the factorial design. For further detail see Chapter 7.

Together, these findings demonstrate that both microporosity and targeted surface chemistry are essential to optimising biochar-based CO_2 sorbents.

12.3. Contributions to Knowledge

This research makes several original contributions to the field:

Comprehensive multi-route activation comparison: It is the first study to systematically compare physical (CO_2), chemical (KOH and KOx), and biological (fungal) activation of SCG-derived biochars under a Design of Experiments (DoE) framework. This provides a detailed comparative perspective on how activation conditions influence porosity, yield, and performance.

Integration of circular waste valorisation and sorbent development: By using spent coffee grounds and introducing fungal pre-treatment, this work highlights sustainable, low-cost approaches that align with circular economy principles. It explores the dual functionality of fungal treatment for both nitrogen enrichment and biochar pre-processing.

Detailed insights into activation–yield–structure relationships: This study provides detailed data on how activation severity influences not only biochar yield but also surface morphology and chemical functionality. High KOH loadings significantly increase surface area and mesoporosity but lead to extensive mass loss and reduced microporosity, while milder routes (e.g. KOx and CO_2) better preserve microporous structure and nitrogen-containing functional groups. These insights offer practical guidance for tuning activation strategies to optimise sorbent performance, stability, and scalability.

Comprehensive material characterisation and CO_2 performance evaluation: The study integrates a broad suite of analytical techniques—BET surface area analysis, FTIR, proximate analysis, and CO_2 adsorption measurements including capacity, kinetics, thermodynamics, and cycling stability. This holistic approach enables a well-rounded assessment of structure–function relationships across a diverse material set and supports more meaningful comparisons to other sorbents in the literature.

Demonstration of physisorption-chemistry trade-offs in cyclic performance: The study highlights a critical performance tension between materials with strong CO_2 affinity (e.g. EX37-850-15-CO_2-600) and those with superior regenerability (e.g. EX53-900-2H-KOX-1:1 (pre-pyrolysed)), contributing to a deeper understanding of how adsorption mechanisms affect PSA compatibility.

Detailed evaluation of CO_2/N_2 selectivity using IAST: The study includes a thorough assessment of competitive CO_2/N_2 adsorption using IAST predictions validated against experimental data. It provides strong evidence that nitrogen surface functionalities can significantly enhance CO_2 selectivity—even in materials with lower surface area—reinforcing the importance of chemical tuning alongside textural optimisation.

12.4. Suggested Future Work

Several immediate extensions to this work are recommended:

Optimisation of Activation Methods: Continued refinement of activation conditions—particularly for KOH and CO_2 routes—will be essential to maximise CO_2 uptake, selectivity,

and regenerability under post-combustion conditions. For KOH activation, research should aim to balance high surface area development with yield preservation and micropore control, while minimising reagent consumption and waste. For CO_2 activation, optimisation of parameters such as temperature, residence time, and gas flow can further enhance microporosity and sorbent performance while retaining scalability.

Advanced Nitrogen Doping Strategies: Future work should explore both in-situ and post-synthetic nitrogen doping methods to enhance CO_2 affinity through tailored surface chemistry. In-situ strategies—such as co-pyrolysis with ammonia or nitrogen-rich precursors—offer the potential for one-step functionalisation, improving nitrogen retention and simplifying processing. Post-synthetic treatments (e.g. with urea, melamine, or amine-functionalisation) may allow finer control over surface groups but require careful balance to avoid pore collapse or sorbent degradation. Evaluating the effect of each method on porosity, thermal stability, and adsorption performance will be essential for practical deployment.

Exploration of Physical Activation Methods: Further investigation is needed into the use of physical activation routes—such as steam, air, or CO_2 under varied pressures and residence times and combinations —as scalable, chemical-free alternatives. These methods may offer greater process simplicity, reduced environmental impact, and easier integration into continuous pyrolysis systems, especially when optimised for micropore development.

Realistic Process Simulation: Evaluate the most promising materials under conditions that closely mimic industrial flue gas—such as mixed-gas streams containing CO_2, N_2, water vapour, and common contaminants. This would help assess the robustness and practical efficacy of the sorbents beyond idealised lab conditions.

Extended Cyclic and Durability Testing: Perform long-term adsorption–desorption cycling (beyond 60 cycles) to assess mechanical and chemical stability under repeated PSA operation. Monitoring for signs of pore collapse, performance degradation, or surface fouling will be critical to determining commercial viability.

12.5. Recommendations for Future Research

Looking ahead, broader research efforts should explore the following strategic directions to accelerate the development and deployment of SCG-derived sorbents for post-combustion CO_2 capture:

Design of Experiments (DoE): Future work should employ a full factorial design with additional levels for activation ratio and hold-time, enabling interaction analysis. Nonlinear regression or response surface methodology (RSM) may also better capture complex dependencies. Further studies should also explore finer temperature increments and include additional variables, such as Heating rate or biochar pre-treatment, to enhance model robustness and relevance.

Comprehensive Optimisation of Sorbent Properties: Future research should aim to optimise both surface chemistry and textural properties to meet the specific demands of post-combustion CO_2 capture—particularly high uptake and selectivity at low partial pressures and elevated temperatures. This will require systematic synthesis parameter tuning supported by integrated characterisation (e.g., BET, pore structure, CHN, XPS) and ideally expanded within a multi-variable Design of Experiments (DoE) framework.

Techno-Economic and Life Cycle Assessments (LCA): Rigorous TEA and LCA are essential to evaluate the economic feasibility, environmental impact, and sustainability of large-scale production and deployment of biochar-based sorbents. This includes assessing costs of raw materials, activation processes, and regeneration energy alongside carbon offset potential.

Machine Learning for Sorbent Design: As data-driven modelling continues to advance, machine learning is poised to become an invaluable tool for accelerating sorbent development. These approaches could uncover complex, nonlinear relationships between synthesis conditions, material properties, and adsorption performance—enabling smarter experiment design and reducing the need for labour-intensive screening.

Quantum Simulation of Adsorbate–Surface Interactions: As quantum computing and first-principles modelling techniques evolve, they will play an increasingly critical role in guiding sorbent design. These tools offer the potential to reveal fundamental insights into CO_2 binding mechanisms, particularly in functionalised or doped biochars, and could inform the rational development of next-generation materials with optimised physisorption and chemisorption characteristics.

Hybrid and Composite Materials: Future work should explore the development of hybrid sorbents by combining biochar with other functional materials, such as amine groups, metal oxides, or polymers. Such composites may offer enhanced selectivity, humidity tolerance, or mechanical stability compared to biochar alone.

Process and Reactor Integration: Investigate opportunities to integrate activation and carbonisation steps directly into continuous pyrolysis or biochar production systems. Inline CO_2 or steam activation could simplify processing, reduce waste, and lower production costs while maintaining desirable porosity and functionality.

Continued Exploration of Waste Valorisation and Circular Economy Integration: Further research should expand the investigation of waste-derived precursors beyond spent coffee grounds, including other abundant organic residues such as agricultural waste, food processing by-products, and urban biowaste. Emphasis should be placed on developing scalable, low-impact processing methods that align with circular economy principles—maximising resource efficiency while contributing to carbon mitigation and material sustainability goals.

References

1. Masson-Delmotte, V. *et al. Climate Change and Land An IPCC Special Report on Climate Change, Desertification, Land Degradation, Sustainable Land Management, Food Security, and Greenhouse Gas Fluxes in Terrestrial Ecosystems Head of TSU (Operations) IT/Web Manager Senior Administrator*. www.ipcc.ch (2019).

2. *The Global Assessment Report on BIODIVERSITY AND ECOSYSTEM SERVICES SUMMARY FOR POLICYMAKERS SUMMARY FOR POLICYMAKERS OF THE IPBES GLOBAL ASSESSMENT REPORT ON BIODIVERSITY AND ECOSYSTEM SERVICES*. (2019).

3. (PDF) Global Energy and Climate Outlook 2019: Electrification for the low-carbon transition The role of electrification in low-carbon pathways, with a global and regional focus on EU and China. https://www.researchgate.net/publication/340298869_Global_Energy_and_Climate_Outlook_2019_Electrification_for_the_low-carbon_transition_The_role_of_electrification_in_low-carbon_pathways_with_a_global_and_regional_focus_on_EU_and_China?channel=doi&linkId=5e8324b24585150839af8c9b&showFulltext=true.

4. Trends in CO_2 - NOAA Global Monitoring Laboratory. https://gml.noaa.gov/ccgg/trends/global.html.

5. Masson-Delmotte, V. *et al. Climate Change and Land An IPCC Special Report on Climate Change, Desertification, Land Degradation, Sustainable Land Management, Food Security, and Greenhouse Gas Fluxes in Terrestrial Ecosystems Head of TSU (Operations) IT/Web Manager Senior Administrator*. www.ipcc.ch (2019).

6. UNDP Annual Report 2022 | United Nations Development Programme. https://www.undp.org/publications/undp-annual-report-2022.

7. Climate Change 2021: The Physical Science Basis | Climate Change 2021: The Physical Science Basis. https://www.ipcc.ch/report/ar6/wg1/.

8. Assessing the Global Climate in 2023 | News | National Centers for Environmental Information (NCEI). https://www.ncei.noaa.gov/news/global-climate-202312.

9. Nick Lunn, Kristin L. Laidre & Regehr, E. V. *IUCN SSC Polar Bear Specialist Group 2021 Report Mission Statement*. https://www.iucn-pbsg.org.

10. The State of World Fisheries and Aquaculture 2022. *The State of World Fisheries and Aquaculture 2022* https://doi.org/10.4060/CC0461EN (2022) doi:10.4060/CC0461EN.

11. *Crop Monitoring in Europe*. (2021).

12. *Economic Losses and Fatalities from Weather and Climate-Related Events in Europe Economic Losses and Fatalities from Weather-and Climate-Related Events in Europe*.

13. 2022 U.S. billion-dollar weather and climate disasters in historical context | NOAA Climate.gov. https://www.climate.gov/news-features/blogs/beyond-data/2022-us-billion-dollar-weather-and-climate-disasters-historical.

14. Global Report 2021 | Global Focus. https://reporting.unhcr.org/globalreport2021.

15. WHO Results Report 2020-2021. https://www.who.int/about/accountability/results/who-results-report-2020-2021.

16. Annual Report 2022 | UNEP - UN Environment Programme. https://www.unep.org/resources/annual-report-2022.

17. Global Warming of 1.5 ºC —. https://www.ipcc.ch/sr15/.

18. The Paris Agreement | UNFCCC. https://unfccc.int/process-and-meetings/the-paris-agreement.

19. Annual Report 2023 | Green Climate Fund. https://www.greenclimate.fund/document/annual-report-2023.

20. ASEAN-UK Dialogue Partnership: plan of action 2022 to 2026 - GOV.UK. https://www.gov.uk/government/publications/asean-uk-dialogue-partnership-plan-of-action-2022-to-2026.

21. Africa Climate Change Strategy. (2020).

22. The European Green Deal - European Commission. https://commission.europa.eu/strategy-and-policy/priorities-2019-2024/european-green-deal_en.

23. OECD Economic Outlook, Volume 2021 Issue 1. https://doi.org/10.1787/EDFBCA02-EN (2021) doi:10.1787/EDFBCA02-EN.

24. The ten point plan for a green industrial revolution - GOV.UK. https://www.gov.uk/government/publications/the-ten-point-plan-for-a-green-industrial-revolution.

25. Climate Change Act 2008.

26. Carbon capture, usage and storage (CCUS): business models - GOV.UK. https://www.gov.uk/government/publications/carbon-capture-usage-and-storage-ccus-business-models.

27. Acorn | Growing Our Decarbonised Future - The Acorn Project. https://theacornproject.uk/.

28. Figueroa, J. D., Fout, T., Plasynski, S., McIlvried, H. & Srivastava, R. D. Advances in CO_2 capture technology-The U.S. Department of Energy's Carbon Sequestration Program. *International Journal of Greenhouse Gas Control* vol. 2 9–20 Preprint at https://doi.org/10.1016/S1750-5836(07)00094-1 (2008).

29. Mondal, M. K., Balsora, H. K. & Varshney, P. Progress and trends in CO_2 capture/separation technologies: A review. *Energy* **46**, 431–441 (2012).

30. Sanz, W., Mayr, M. & Jericha, H. Thermodynamic and economic evaluation of an IGCC plant based on the Graz Cycle for CO_2 capture. *Proceedings of the ASME Turbo Expo* **3**, 493–503 (2010).

31. Wilberforce, T., Baroutaji, A., Soudan, B., Al-Alami, A. H. & Olabi, A. G. Outlook of carbon capture technology and challenges. *Science of the Total Environment* **657**, 56–72 (2019).

32. Romano, M. C., Chiesa, P. & Lozza, G. Pre-combustion CO_2 capture from natural gas power plants, with ATR and MDEA processes. *International Journal of Greenhouse Gas Control* **4**, 785–797 (2010).

33. Rao, A. B. & Rubin, E. S. A technical, economic, and environmental assessment of amine-based CO_2 capture technology for power plant greenhouse gas control. *Environ. Sci. Technol.* **36**, 4467–4475 (2002).

34. Ho, S. Low-Cost Adsorbents for the Removal of Phenol/Phenolics, Pesticides, and Dyes from Wastewater Systems: A Review. *Water (Switzerland)* **14**, (2022).

35. Leng, L. *et al.* Nitrogen containing functional groups of biochar: An overview. *Bioresource Technology* vol. 298 Preprint at https://doi.org/10.1016/j.biortech.2019.122286 (2020).

36. Dissanayake, P. D. *et al.* Biochar-based adsorbents for carbon dioxide capture: A critical review. *Renewable and Sustainable Energy Reviews* vol. 119 Preprint at https://doi.org/10.1016/j.rser.2019.109582 (2020).

37. Meisen, A. & Shuai, X. *RESEARCH AND DEVELOPMENT ISSUES IN* CO_2 *CAPTURE*. ~ *Pergamon Energy Convers. Mgrnt* vol. 38 (1997).

38. Ellison, C., Hoffman, J. & Shekhawat, D. Comparison of microwave and conventional heating for CO_2 desorption from zeolite 13X. *International Journal of Greenhouse Gas Control* **107**, 103311 (2021).

39. Font-Palma, C., Cann, D., Udemu, C. & García, O. Review of Cryogenic Carbon Capture Innovations and Their Potential Applications. *C 2021, Vol. 7, Page 58* **7**, 58 (2021).

40. Keshavarz, A. *et al.* Cryogenic CO_2 Capture. 251–277 (2019) doi:10.1007/978-3-030-29337-6_10.

41. Khalilpour, R. *et al.* Membrane-based carbon capture from flue gas: a review. *J. Clean. Prod.* **103**, 286–300 (2015).

42. Lee, J. & Aluru, N. R. Water-solubility-driven separation of gases using graphene membrane. *J. Memb. Sci.* **428**, 546–553 (2013).

43. Climate Change 2022: Impacts, Adaptation and Vulnerability | Climate Change 2022: Impacts, Adaptation and Vulnerability. https://www.ipcc.ch/report/ar6/wg2/.

44. Choi, S., Drese, J. H. & Jones, C. W. Adsorbent materials for carbon dioxide capture from large anthropogenic point sources. *ChemSusChem* vol. 2 796–854 Preprint at https://doi.org/10.1002/cssc.200900036 (2009).

45. Kwon, S. *et al.* CO_2 Sorption. in *Coal Gasification and Its Applications* 293–339 (Elsevier, 2011). doi:10.1016/b978-0-8155-2049-8.10010-5.

46. Sjostrom, S. & Krutka, H. Evaluation of solid sorbents as a retrofit technology for CO_2 capture. *Fuel* **89**, 1298–1306 (2010).

47. Glier, J. C. & Rubina, E. S. Assessment of solid sorbents as a competitive post-combustion CO 2 capture technology. in *Energy Procedia* vol. 37 65–72 (Elsevier Ltd, 2013).

48. Drage, T. C. *et al.* Materials challenges for the development of solid sorbents for post-combustion carbon capture. *J. Mater. Chem.* **22**, 2815–2823 (2012).

49. Sayari, A., Belmabkhout, Y. & Serna-Guerrero, R. Flue gas treatment via CO_2 adsorption. *Chemical Engineering Journal* **171**, 760–774 (2011).

50. Li, M., Liu, X., Sun, C., Stevens, L. & Liu, H. Synthesis and characterization of advanced bio-carbon materials from Kraft lignin with enhanced CO_2 capture properties. *J. Environ. Chem. Eng.* **10**, 107471 (2022).

51. Zhang, Z. *et al.* Critical role of small micropores in high CO_2 uptake. *Physical Chemistry Chemical Physics* **15**, 2523–2529 (2013).

52. Sajjadi, B., Chen, W. Y. & Egiebor, N. O. A comprehensive review on physical activation of biochar for energy and environmental applications. *Reviews in Chemical Engineering* **35**, 735–776 (2019).

53. Fletcher, A. J., Yüzak, Y. & Thomas, K. M. Adsorption and desorption kinetics for hydrophilic and hydrophobic vapors on activated carbon. *Carbon N. Y.* **44**, 989–1004 (2006).

54. Gargiulo, V. *et al.* Assessing the Potential of Biochars Prepared by Steam-Assisted Slow Pyrolysis for CO_2 Adsorption and Separation. *Energy and Fuels* **32**, 10218–10227 (2018).

55. Oschatz, M. & Antonietti, M. A search for selectivity to enable CO_2 capture with porous adsorbents. *Energy and Environmental Science* vol. 11 57–70 Preprint at https://doi.org/10.1039/c7ee02110k (2018).

56. Joos, L., Huck, J. M., Van Speybroeck, V. & Smit, B. Cutting the cost of carbon capture: A case for carbon capture and utilization. *Faraday Discussions* vol. 192 391–414 Preprint at https://doi.org/10.1039/c6fd00031b (2016).

57. Samanta, A., Zhao, A., Shimizu, G. K. H., Sarkar, P. & Gupta, R. Post-combustion CO 2 capture using solid sorbents: A review. *Ind. Eng. Chem. Res.* **51**, 1438–1463 (2012).

58. Crombie, K., Mašek, O., Sohi, S. P., Brownsort, P. & Cross, A. The effect of pyrolysis conditions on biochar stability as determined by three methods. *GCB Bioenergy* **5**, 122–131 (2013).

59. Kim, D. *et al.* Rate of CO_2 adsorbent attrition induced by gas jets on perforated plate distributors in bubbling fluidized beds. *Advanced Powder Technology* **31**, 4411–4419 (2020).

60. Lee, S.-K., Jiang, X., Keener, T. C. & Khang, S. J. *Attrition of Lime Sorbents during Fluidization in a Circulating Fluidized Bed Absorber*. *Ind. Eng. Chem. Res* vol. 32 https://pubs.acs.org/sharingguidelines (1993).

61. Severino, M. I., Gkaniatsou, E., Nouar, F., Pinto, M. L. & Serre, C. MOFs industrialization: A complete assessment of production costs. *Faraday Discuss.* **231**, 326–341 (2021).

62. Pardakhti, M. *et al.* Trends in Solid Adsorbent Materials Development for CO_2 Capture. *ACS Appl. Mater. Interfaces* **11**, 34533–34559 (2019).

63. Wang, Q., Luo, J., Zhong, Z. & Borgna, A. CO_2 capture by solid adsorbents and their applications: Current status and new trends. *Energy and Environmental Science* vol. 4 42–55 Preprint at https://doi.org/10.1039/c0ee00064g (2011).

64. Yu, C. H., Huang, C. H. & Tan, C. S. A review of CO_2 capture by absorption and adsorption. *Aerosol and Air Quality Research* vol. 12 745–769 Preprint at https://doi.org/10.4209/aaqr.2012.05.0132 (2012).

65. Zhao, H. *et al.* Carbon-based adsorbents for post-combustion capture: a review. *Greenhouse Gases: Science and Technology* vol. 8 11–36 Preprint at https://doi.org/10.1002/ghg.1758 (2018).

66. Marsh, H. & Rodriguez-Reinoso, F. *Activated Carbon*. *Elsevier Science and Technology Books* vol. 16 (2006).

67. Panwar, N. L. & Pawar, A. Influence of activation conditions on the physicochemical properties of activated biochar: a review. https://doi.org/10.1007/s13399-020-00870-3/Published doi:10.1007/s13399-020-00870-3/Published.

68. Omidi, Y. *et al.* Adsorption of 4-chlorophenol from aqueous solution using activated carbon synthesized from aloe vera green wastes. *Journal of Advances in Environmental Health Research* **3**, 120–129 (2015).

69. Samanta, A., Zhao, A., Shimizu, G. K. H., Sarkar, P. & Gupta, R. Post-combustion CO 2 capture using solid sorbents: A review. *Ind. Eng. Chem. Res.* **51**, 1438–1463 (2012).

70. Liu, S. H. & Huang, Y. Y. Valorization of coffee grounds to biochar-derived adsorbents for CO_2 adsorption. *J. Clean. Prod.* **175**, 354–360 (2018).

71. González, A. S., Plaza, M. G., Pis, J. J., Rubiera, F. & Pevida, C. Post-combustion CO_2 capture adsorbents from spent coffee grounds. *Energy Procedia* **37**, 134–141 (2013).

72. Plaza, M. G., González, A. S., Pevida, C., Pis, J. J. & Rubiera, F. Valorisation of spent coffee grounds as CO_2 adsorbents for postcombustion capture applications. *Appl. Energy* **99**, 272–279 (2012).

73. González, A. S., Plaza, M. G., Pis, J. J., Rubiera, F. & Pevida, C. Post-combustion CO_2 capture adsorbents from spent coffee grounds. *Energy Procedia* **37**, 134–141 (2013).

74. Wang, H. *et al.* Coffee grounds derived N enriched microporous activated carbons: Efficient adsorbent for post-combustion CO_2 capture and conversion. *J. Colloid Interface Sci.* **578**, 491–499 (2020).

75. Kim, M. J., Choi, S. W., Kim, H., Mun, S. & Lee, K. B. Simple synthesis of spent coffee ground-based microporous carbons using K2CO3 as an activation agent and their application to CO_2 capture. *Chemical Engineering Journal* **397**, 125404 (2020).

76. Wang, C. *et al.* Fabrication of Highly Ordered Carbon Networks as Catalyst Supports for Aerobic Oxidation of Glucose. *Adv. Mat. Res.* **476–478**, 1186–1192 (2012).

77. Ashourirad, B., Sekizkardes, A. K., Altarawneh, S. & El-Kaderi, H. M. Exceptional Gas adsorption properties by nitrogen-doped porous carbons derived from benzimidazole-linked polymers. *Chemistry of Materials* **27**, 1349–1358 (2015).

78. Kumar, K. V., Preuss, K., Lu, L., Guo, Z. X. & Titirici, M. M. Effect of Nitrogen Doping on the CO_2 Adsorption Behavior in Nanoporous Carbon Structures: A Molecular Simulation Study. *Journal of Physical Chemistry C* **119**, 22310–22321 (2015).

79. Vasiliev, L., TSITOVICH, A. & Zhuravlyov, A. Solod Sorption Cooler with Composite Sorbent Bed and Heat Pipe Thermal Control. *Polska Energetyka Sloneczna* 12–18 (2012).

80. Yoon, S. H. *et al.* KOH activation of carbon nanofibers. *Carbon N. Y.* **42**, 1723–1729 (2004).

81. Lee, S. Y. & Park, S. J. Determination of the optimal pore size for improved CO 2 adsorption in activated carbon fibers. *J. Colloid Interface Sci.* **389**, 230–235 (2013).

82. Díez, N. *et al.* CO_2 adsorption capacity and kinetics in nitrogen-enriched activated carbon fibers prepared by different methods. *Chemical Engineering Journal* **281**, 704–712 (2015).

83. Chiang, Y. C., Hsu, W. L., Lin, S. Y. & Juang, R. S. Enhanced CO_2 adsorption on activated carbon fibers grafted with nitrogen-doped carbon nanotubes. *Materials* **10**, (2017).

84. Di Biase, E. & Sarkisov, L. Systematic development of predictive molecular models of high surface area activated carbons for adsorption applications. *Carbon N. Y.* **64**, 262–280 (2013).

85. Di Biase, E. & Sarkisov, L. Molecular simulation of multi-component adsorption processes related to carbon capture in a high surface area, disordered activated carbon. *Carbon N. Y.* **94**, 27–40 (2015).

86. Imaging and Analyzing Graphene Layers | JEOL Resources. https://www.jeolusa.com/RESOURCES/Electron-Optics/Documents-Downloads/imaging-and-analyzing-graphene-layers.

87. Garcia-Gallastegui, A. *et al.* Graphene oxide as support for layered double hydroxides: Enhancing the CO_2 adsorption capacity. *Chemistry of Materials* **24**, 4531–4539 (2012).

88. Ghosh, A. *et al.* Uptake of H2 and CO_2 by graphene. *Journal of Physical Chemistry C* **112**, 15704–15707 (2008).

89. Chandra, V. *et al.* Highly selective CO_2 capture on N-doped carbon produced by chemical activation of polypyrrole functionalized graphene sheets. *Chemical Communications* **48**, 735–737 (2012).

90. Takeuchi, K. *et al.* Adsorption of CO_2 on Graphene: A Combined TPD, XPS, and vdW-DF Study. *Journal of Physical Chemistry C* **121**, 2807–2814 (2017).

91. Khakpay, A., Rahmani, F., Nouranian, S. & Scovazzo, P. Molecular Insights on the CH4/CO_2 Separation in Nanoporous Graphene and Graphene Oxide Separation Platforms: Adsorbents versus Membranes. *Journal of Physical Chemistry C* **121**, 12308–12320 (2017).

92. Garaga, M. N., Persson, M., Yaghini, N. & Martinelli, A. Local coordination and dynamics of a protic ammonium based ionic liquid immobilized in nano-porous silica micro-particles probed by Raman and NMR spectroscopy. *Soft Matter* **12**, 2583–2592 (2016).

93. Fayaz, M. & Sayari, A. Long-Term Effect of Steam Exposure on CO_2 Capture Performance of Amine-Grafted Silica. *ACS Appl. Mater. Interfaces* **9**, 43747–43754 (2017).

94. Quang, D. V., Dindi, A. & Abu-Zahra, M. R. M. One-Step Process Using CO_2 for the Preparation of Amino-Functionalized Mesoporous Silica for CO_2 Capture Application. *ACS Sustain. Chem. Eng.* **5**, 3170–3178 (2017).

95. Zhao, P., Zhang, G., Sun, Y. & Xu, Y. CO_2 Adsorption Behavior and Kinetics on Amine-Functionalized Composites Silica with Trimodal Nanoporous Structure. *Energy and Fuels* **31**, 12508–12520 (2017).

96. Gunathilake, C., Gangoda, M. & Jaroniec, M. Mesoporous Alumina with Amidoxime Groups for CO_2 Sorption at Ambient and Elevated Temperatures. *Ind. Eng. Chem. Res.* **55**, 5598–5607 (2016).

97. Yuan, Z. H., Sun, S. Q., Duan, Y. Q. & Wang, D. J. Fabrication of densely packed AlN nanowires by a chemical conversion of Al 2O 3 nanowires based on porous anodic alumina film. *Nanoscale Res. Lett.* **4**, 1126–1129 (2009).

98. Feist, B. J. & Hill, J. M. CO_2 and H2S Adsorption on γ-Al2O3-Supported Lanthanum Oxide. *Energy and Fuels* **29**, 6049–6056 (2015).

99. Sakwa-Novak, M. A. & Jones, C. W. Steam induced structural changes of a poly(ethylenimine) impregnated γ-alumina sorbent for CO_2 extraction from ambient air. *ACS Appl. Mater. Interfaces* **6**, 9245–9255 (2014).

100. Marakatti, V. S. & Halgeri, A. B. Metal ion-exchanged zeolites as highly active solid acid catalysts for the green synthesis of glycerol carbonate from glycerol. *RSC Adv.* **5**, 14286–14293 (2015).

101. Zeolite, SEM - Stock Image - C043/7633 - Science Photo Library. https://www.sciencephoto.com/media/1003512/view/zeolite-sem.

102. Coudert, F. X. & Kohen, D. Molecular Insight into CO_2 'trapdoor' Adsorption in Zeolite Na-RHO. *Chemistry of Materials* **29**, 2724–2730 (2017).

103. Tomoyuki Inui, Masaki Yasuda & Yoshitaka Okugawa. *Relationship between Properties of Various Zeolites and Their Carbon Dioxide Adsorption Behaviors in Pressure Swing Adsorption OperationClick to Copy Article Link*. *General Electric Co., Technical Bulletin* vol. 27 https://pubs.acs.org/sharingguidelines (1988).

104. Bonelli, B., Onida, B., Fubini, B., Otero Areán, C. & Garrone, E. Vibrational and thermodynamic study of the adsorption of carbon dioxide on the zeolite Na - ZSM-5. *Langmuir* **16**, 4976–4983 (2000).

105. Wirawan, S. K. & Creaser, D. CO_2 adsorption on silicalite-1 and cation exchanged ZSM-5 zeolites using a step change response method. *Microporous and Mesoporous Materials* **91**, 196–205 (2006).

106. Díaz, E., Muñoz, E., Vega, A. & Ordóñez, S. Enhancement of the CO_2 retention capacity of y zeolites by Na and Cs treatments: Effect of adsorption temperature and water treatment. *Ind. Eng. Chem. Res.* **47**, 412–418 (2008).

107. Gallei, E. & Stumpf, G. *Infrared Spectroscopic Studies of the Adsorption of Carbon Dioxide and the Coadsorption of Carbon Dioxide and Water on CaY-and NiY-Zeolites 1*.

108. Herm, Z. R., Swisher, J. A., Smit, B., Krishna, R. & Long, J. R. Metal-organic frameworks as adsorbents for hydrogen purification and precombustion carbon dioxide capture. *J. Am. Chem. Soc.* **133**, 5664–5667 (2011).

109. Decoste, J. B. & Peterson, G. W. Metal-organic frameworks for air purification of toxic chemicals. *Chemical Reviews* vol. 114 5695–5727 Preprint at https://doi.org/10.1021/cr4006473 (2014).

110. Chen, C. X. *et al.* A Robust Metal–Organic Framework Combining Open Metal Sites and Polar Groups for Methane Purification and CO_2/Fluorocarbon Capture. *Chemistry - A European Journal* **23**, 4060–4064 (2017).

111. Lin, J. Y. S. Synthesis and High Pressure Gas Separation Properties of Thin Metal-Organic Framework Membranes.

112. Walton, K. S. *et al.* Understanding inflections and steps in carbon dioxide adsorption isotherms in metal-organic frameworks. *J. Am. Chem. Soc.* **130**, 406–407 (2008).

113. Grant Glover, T., Peterson, G. W., Schindler, B. J., Britt, D. & Yaghi, O. MOF-74 building unit has a direct impact on toxic gas adsorption. *Chem. Eng. Sci.* **66**, 163–170 (2011).

114. Demessence, A., D'Alessandro, D. M., Foo, M. L. & Long, J. R. Strong CO_2 binding in a water-stable, triazolate-bridged metal-organic framework functionalized with ethylenediamine. *J. Am. Chem. Soc.* **131**, 8784–8786 (2009).

115. Britt, D., Furukawa, H., Wang, B., Glover, T. G. & Yaghi, O. M. *Highly Efficient Separation of Carbon Dioxide by a Metal-Organic Framework Replete with Open Metal Sites*. www.pnas.org/cgi/content/full/.

116. Couck, S. *et al.* An amine-functionalized MIL-53 metal-organic framework with large separation power for CO_2 and CH4. *J. Am. Chem. Soc.* **131**, 6326–6327 (2009).

117. Keskin, S., van Heest, T. M. & Sholl, D. S. Can metal-organic framework materials play a useful role in large-scale carbon dioxide separations? *ChemSusChem* vol. 3 879–891 Preprint at https://doi.org/10.1002/cssc.201000114 (2010).

118. Deacon, A. *et al.* Understanding the ZIF-L to ZIF-8 transformation from fundamentals to fully costed kilogram-scale production. *Commun. Chem.* **5**, 1–10 (2022).

119. Krishna, R. & Van Baten, J. M. In silico screening of metal-organic frameworks in separation applications. *Physical Chemistry Chemical Physics* vol. 13 10593–10616 Preprint at https://doi.org/10.1039/c1cp20282k (2011).

120. Pérez-Pellitero, J. *et al.* Adsorption of CO_2, CH4, and N2 on zeolitic imidazolate frameworks: Experiments and simulations. *Chemistry - A European Journal* **16**, 1560–1571 (2010).

121. Al-Maythalony, B. A. *et al.* Tuning the interplay between selectivity and permeability of ZIF-7 mixed matrix membranes. *ACS Appl. Mater. Interfaces* **9**, 33401–33407 (2017).

122. Ramos-Fernandez, E. V., Grau-Atienza, A., Farrusseng, D. & Aguado, S. A water-based room temperature synthesis of ZIF-93 for CO_2 adsorption. *J. Mater. Chem. A Mater.* **6**, 5598–5602 (2018).

123. Ban, Y. *et al.* Confinement of Ionic Liquids in Nanocages: Tailoring the Molecular Sieving Properties of ZIF-8 for Membrane-Based CO 2 Capture . *Angewandte Chemie* **127**, 15703–15707 (2015).

124. Phan, A. *et al.* Synthesis, structure, and carbon dioxide capture properties of zeolitic imidazolate frameworks. *Acc. Chem. Res.* **43**, 58–67 (2010).

125. Li, W., Samarasinghe, S. A. S. C. & Bae, T. H. Enhancing CO_2/CH4 separation performance and mechanical strength of mixed-matrix membrane via combined use of graphene oxide and ZIF-8. *Journal of Industrial and Engineering Chemistry* **67**, 156–163 (2018).

126. Huang, N., Wang, P. & Jiang, D. Covalent organic frameworks: a materials platform for structural and functional designs. *Nat. Rev. Mater.* **1**, 16068 (2016).

127. Chen, X. *et al.* Towards covalent organic frameworks with predesignable and aligned open docking sites. *Chemical Communications* **50**, 6161–6163 (2014).

128. Liu, Y., Liu, D., Yang, Q., Zhong, C. & Mi, J. Comparative Study of Separation Performance of COFs and MOFs for CH4/CO_2/H2 Mixtures. *Ind. Eng. Chem. Res.* **49**, 2902–2906 (2010).

129. Covalent Organic Framework-TpPa-1 (COF-TpPa-1) - Covalent Organic Frameworks - Materials - Molecular Sieves. https://www.acsmaterial.com/covalent-organic-framework-tppa-1-cof-tppa-1.html.

130. Dey, S. *et al.* Two linkers are better than one: enhancing CO_2 capture and separation with porous covalent triazine-based frameworks from mixed nitrile linkers. *J. Mater. Chem. A Mater.* **5**, 3609–3620 (2017).

131. Lan, J., Cao, D., Wang, W. & Smit, B. Doping of Alkali, Alkaline-Earth, and Transition Metals in Covalent-Organic Frameworks for Enhancing CO_2 Capture by First-Principles Calculations and Molecular Simulations. *ACS Nano* **4**, 4225–4237 (2010).

132. Hani M. El-Kaderi *et al.* Designed Synthesis of 3D Covalent Organic Frameworks. *Science (1979).* **316**, 265–268 (2007).

133. Zeng, Y., Zou, R. & Zhao, Y. Covalent Organic Frameworks for CO_2 Capture. *Advanced Materials* **28**, 2855–2873 (2016).

134. Chen, W., Huang, L., Yi, X. F. & Zheng, A. M. Lithium doping on 2D squaraine-bridged covalent organic polymers for enhancing adsorption properties: a theoretical study. *PHYSICAL CHEMISTRY CHEMICAL PHYSICS* **20**, 6487–6499 (2018).

135. Essien, E. R., Atasie, V. N., Okeafor, A. O. & Nwude, D. O. Biogenic synthesis of magnesium oxide nanoparticles using Manihot esculenta (Crantz) leaf extract. *Int. Nano Lett.* **10**, 43–48 (2020).

136. Bhagiyalakshmi, M., Lee, J. Y. & Jang, H. T. Synthesis of mesoporous magnesium oxide: Its application to CO_2 chemisorption. *International Journal of Greenhouse Gas Control* **4**, 51–56 (2010).

137. Yu, F.-C., Phalak, N., Sun, Z. & Fan, L.-S. Activation Strategies for Calcium-Based Sorbents for CO_2 Capture: A Perspective. *Ind. Eng. Chem. Res.* **51**, 2133–2142 (2012).

138. Gupta, H. & Fan, L.-S. Carbonation−Calcination Cycle Using High Reactivity Calcium Oxide for Carbon Dioxide Separation from Flue Gas. *Ind. Eng. Chem. Res.* **41**, 4035–4042 (2002).

139. Sayyah, M., Ito, B. R., Rostam-Abadi, M., Lu, Y. & Suslick, K. S. CaO-based sorbents for CO_2 capture prepared by ultrasonic spray pyrolysis. *RSC Adv.* **3**, 19872–19875 (2013).

140. Chen, H., Zhao, C. & Yu, W. Calcium-based sorbent doped with attapulgite for CO_2 capture. *Appl. Energy* **112**, 67–74 (2013).

141. Liu, M. Y., Vogt, C., Chaffee, A. L. & Chang, S. L. Y. Nanoscale Structural Investigation of Cs_2CO_3-Doped MgO Sorbent for CO_2 Capture at Moderate Temperature. *JOURNAL OF PHYSICAL CHEMISTRY C* **117**, 17514–17520 (2013).

142. Duan, Y. H. & Sorescu, D. C. CO_2 capture properties of alkaline earth metal oxides and hydroxides: A combined density functional theory and lattice phonon dynamics study. *JOURNAL OF CHEMICAL PHYSICS* **133**, (2010).

143. Harada, T. & Hatton, T. A. Colloidal Nanoclusters of MgO Coated with Alkali Metal Nitrates/Nitrites for Rapid, High Capacity CO_2 Capture at Moderate Temperature. *CHEMISTRY OF MATERIALS* **27**, 8153–8161 (2015).

144. Qiao, Y. Q. *et al.* Alkali Nitrates Molten Salt Modified Commercial MgO for Intermediate-Temperature CO_2 Capture: Optimization of the Li/Na/K Ratio. *Ind. Eng. Chem. Res.* **56**, 1509–1517 (2017).

145. Lee, S.-Y. & Park, S.-J. A review on solid adsorbents for carbon dioxide capture. *Journal of Industrial and Engineering Chemistry* **23**, 1–11 (2015).

146. Tomczyk, A., Sokołowska, Z. & Boguta, P. Biochar physicochemical properties: pyrolysis temperature and feedstock kind effects. *Reviews in Environmental Science and Biotechnology* vol. 19 191–215 Preprint at https://doi.org/10.1007/s11157-020-09523-3 (2020).

147. Li, Y., Xing, B., Ding, Y., Han, X. & Wang, S. A critical review of the production and advanced utilization of biochar via selective pyrolysis of lignocellulosic biomass. *Bioresource Technology* vol. 312 Preprint at https://doi.org/10.1016/j.biortech.2020.123614 (2020).

148. Yaashikaa, P. R., Kumar, P. S., Varjani, S. & Saravanan, A. A critical review on the biochar production techniques, characterization, stability and applications for circular bioeconomy. *Biotechnology Reports* **28**, e00570 (2020).

149. The State of Carbon Dioxide Removal. https://www.stateofcdr.org/.

150. Macías, F. & Arbestain, M. C. Soil carbon sequestration in a changing global environment. *Mitig. Adapt. Strateg. Glob. Chang.* **15**, 511–529 (2010).

151. Tomczyk, A., Sokołowska, Z. & Boguta, P. Biochar physicochemical properties: pyrolysis temperature and feedstock kind effects. *Reviews in Environmental Science and Biotechnology* vol. 19 191–215 Preprint at https://doi.org/10.1007/s11157-020-09523-3 (2020).

152. Leng, L. *et al.* An overview on engineering the surface area and porosity of biochar. *Science of the Total Environment* vol. 763 Preprint at https://doi.org/10.1016/j.scitotenv.2020.144204 (2021).

153. Pujol, D. *et al.* The chemical composition of exhausted coffee waste. *Ind. Crops Prod.* **50**, 423–429 (2013).

154. Taleb, F., Ammar, M., Mosbah, M. ben, Salem, R. ben & Moussaoui, Y. Chemical modification of lignin derived from spent coffee grounds for methylene blue adsorption. *Sci. Rep.* **10**, 11048 (2020).

155. Andrade, T. S., Vakros, J., Mantzavinos, D. & Lianos, P. Biochar obtained by carbonization of spent coffee grounds and its application in the construction of an energy storage device. *Chemical Engineering Journal Advances* **4**, 100061 (2020).

156. Kondamudi, N., Mohapatra, S. K. & Misra, M. Spent Coffee Grounds as a Versatile Source of Green Energy. *J. Agric. Food Chem.* **56**, 11757–11760 (2008).

157. Tsai, W.-T. Chapter 10 - The potential of pyrolysing exhausted coffee residue for the production of biochar. in *Handbook of Coffee Processing By-Products* (ed. Galanakis, C. M.) 299–322 (Academic Press, 2017). doi:https://doi.org/10.1016/B978-0-12-811290-8.00010-4.

158. Liu, S.-H. & Huang, Y.-Y. Valorization of coffee grounds to biochar-derived adsorbents for CO_2 adsorption. *J. Clean. Prod.* **175**, 354–360 (2018).

159. Li, C. *et al.* Impact of heating rates on the evolution of function groups of the biochar from lignin pyrolysis. *J. Anal. Appl. Pyrolysis* **155**, 105031 (2021).

160. Wulandari, Y. R. *et al.* Effect of N2 flow rate on kinetic investigation of lignin pyrolysis. *Environ. Res.* **190**, 109976 (2020).

161. tBJ:The 55 uses of biochar. https://www.biochar-journal.org/en/ct/2.

162. tBJ:The use of biochar in cattle farming. https://www.biochar-journal.org/en/ct/9.

163. Biochar Market Size, Share & Analysis | Growth Report [2032]. https://www.fortunebusinessinsights.com/industry-reports/biochar-market-100750.

164. Akhil, D. *et al.* Production, characterization, activation and environmental applications of engineered biochar: a review. *Environ. Chem. Lett.* **19**, 2261–2297 (2021).

165. Panwar, N. L. & Pawar, A. Influence of activation conditions on the physicochemical properties of activated biochar: a review. *Biomass Convers. Biorefin.* **12**, 925–947 (2022).

166. Cha, J. S. *et al.* Production and utilization of biochar: A review. *Journal of Industrial and Engineering Chemistry* vol. 40 1–15 Preprint at https://doi.org/10.1016/j.jiec.2016.06.002 (2016).

167. Dalai, A. K. & Azargohar, R. Production of Activated Carbon from Biochar Using Chemical and Physical Activation: Mechanism and Modeling. in *MATERIALS, CHEMICALS, AND ENERGY FROM FOREST BIOMASS* (ed. Argyropoulos, D. S.) vol. 954 463–476 (2007).

168. Lussier, M. G., Zhang, Z. & Miller, D. J. Characterizing rate inhibition in steam/hydrogen gasification via analysis of adsorbed hydrogen. *Carbon N. Y.* **36**, 1361–1369 (1998).

169. Feng, D. D., Zhao, Y. J., Zhang, Y., Gao, J. M. & Sun, S. Z. Changes of biochar physiochemical structures during tar H_2O and CO_2 heterogeneous reforming with biochar. *FUEL PROCESSING TECHNOLOGY* **165**, 72–79 (2017).

170. Feng, D. D., Zhang, Y., Zhao, Y. J., Sun, S. Z. & Gao, J. M. Improvement and maintenance of biochar catalytic activity for in-situ biomass tar reforming during pyrolysis and H_2O/CO_2 gasification. *FUEL PROCESSING TECHNOLOGY* **172**, 106–114 (2018).

171. Jung, S. H. & Kim, J. S. Production of biochars by intermediate pyrolysis and activated carbons from oak by three activation methods using CO_2. *J. Anal. Appl. Pyrolysis* **107**, 116–122 (2014).

172. Guo, S. H. *et al.* Effects of CO_2 activation on porous structures of coconut shell-based activated carbons. *Appl. Surf. Sci.* **255**, 8443–8449 (2009).

173. Zhang, T. Y. *et al.* Preparation of activated carbon from forest and agricultural residues through CO_2 activation. *CHEMICAL ENGINEERING JOURNAL* **105**, 53–59 (2004).

174. Demiral, H., Demiral, I., Karabacakoglu, B. & Tümsek, F. Production of activated carbon from olive bagasse by physical activation. *CHEMICAL ENGINEERING RESEARCH & DESIGN* **89**, 206–213 (2011).

175. Rajapaksha, A. U. *et al.* Enhanced sulfamethazine removal by steam-activated invasive plant-derived biochar. *J. Hazard. Mater.* **290**, 43–50 (2015).

176. Koltowski, M., Hilber, I., Bucheli, T. D. & Oleszczuk, P. Effect of steam activated biochar application to industrially contaminated soils on bioavailability of polycyclic aromatic hydrocarbons and ecotoxicity of soils. *SCIENCE OF THE TOTAL ENVIRONMENT* **566**, 1023–1031 (2016).

177. Ippolito, J. A. *et al.* Macroscopic and Molecular Investigations of Copper Sorption by a Steam-Activated Biochar. *J. Environ. Qual.* **41**, 1150–1156 (2012).

178. Chen, W. *et al.* Influence of NH3 concentration on biomass nitrogen-enriched pyrolysis. *Bioresour. Technol.* **263**, 350–357 (2018).

179. Zhang, X. *et al.* Preparation of nitrogen-doped microporous modified biochar by high temperature CO_2–NH3 treatment for CO_2 adsorption: effects of temperature. *RSC Adv.* **6**, 98157–98166 (2016).

180. Xiong, Z. *et al.* Influence of NH3/CO_2 Modification on the Characteristic of Biochar and the CO_2 Capture. *Bioenergy Res.* **6**, 1147–1153 (2013).

181. Kastner, J. R., Miller, J. & Das, K. C. Pyrolysis conditions and ozone oxidation effects on ammonia adsorption in biomass generated chars. *J. Hazard. Mater.* **164**, 1420–1427 (2009).

182. Jimenez-Cordero, D., Heras, F., Alonso-Morales, N., Gilarranz, M. A. & Rodriguez, J. J. Ozone as oxidation agent in cyclic activation of biochar. *FUEL PROCESSING TECHNOLOGY* **139**, 42–48 (2015).

183. Valdés, H., Sánchez-Polo, M., Rivera-Utrilla, J. & Zaror, C. A. Effect of ozone treatment on surface properties of activated carbon. *LANGMUIR* **18**, 2111–2116 (2002).

184. Py, X., Guillot, A. & Cagnon, B. Activated carbon porosity tailoring by cyclic sorption/decomposition of molecular oxygen. *Carbon N. Y.* **41**, 1533–1543 (2003).

185. Suliman, W. *et al.* Modification of biochar surface by air oxidation: Role of pyrolysis temperature. *Biomass Bioenergy* **85**, 1–11 (2016).

186. Chu, G. *et al.* Phosphoric acid pretreatment enhances the specific surface areas of biochars by generation of micropores. *Environmental Pollution* **240**, 1–9 (2018).

187. Peng, P., Lang, Y.-H. & Wang, X.-M. Adsorption behavior and mechanism of pentachlorophenol on reed biochars: pH effect, pyrolysis temperature, hydrochloric acid treatment and isotherms. *Ecol. Eng.* **90**, 225–233 (2016).

188. Li, Y. *et al.* Characterization of Modified Biochars Derived from Bamboo Pyrolysis and Their Utilization for Target Component (Furfural) Adsorption. *Energy & Fuels* **28**, 5119–5127 (2014).

189. Yakout, S. M., El Hakim Daifullah, A. M. & El-Reefy, S. A. *PORE STRUCTURE CHARACTERIZATION OF CHEMICALLY BIOCHAR DERIVED FROM RICE STRAW*. vol. 14 http://omicron.ch.tuiasi.ro/EEMJ/ (2015).

190. Liu, D. *et al.* A green technology for the preparation of high capacitance rice husk-based activated carbon. *J. Clean. Prod.* **112**, 1190–1198 (2016).

191. Wang, J. & Kaskel, S. KOH activation of carbon-based materials for energy storage. *J. Mater. Chem.* **22**, 23710–23725 (2012).

192. Jin, H. *et al.* Biochar pyrolytically produced from municipal solid wastes for aqueous As(V) removal: Adsorption property and its improvement with KOH activation. *Bioresour. Technol.* **169**, 622–629 (2014).

193. Cazetta, A. L. *et al.* NaOH-activated carbon of high surface area produced from coconut shell: Kinetics and equilibrium studies from the methylene blue adsorption. *Chemical Engineering Journal* **174**, 117–125 (2011).

194. Fan, Y. *et al.* Adsorptive removal of chloramphenicol from wastewater by NaOH modified bamboo charcoal. *Bioresour. Technol.* **101**, 7661–7664 (2010).

195. Shen, Y. & Zhang, N. Facile synthesis of porous carbons from silica-rich rice husk char for volatile organic compounds (VOCs) sorption. *Bioresour. Technol.* **282**, 294–300 (2019).

196. Zheng, Y. *et al.* Insight into the KOH/KMnO4 activation mechanism of oxygen-enriched hierarchical porous biochar derived from biomass waste by in-situ pyrolysis for methylene blue enhanced adsorption. *J. Anal. Appl. Pyrolysis* **158**, 105269 (2021).

197. Huang, D. *et al.* Influence of morphological and chemical features of biochar on hydrogen peroxide activation: implications on sulfamethazine degradation. *RSC Adv.* **6**, 73186–73196 (2016).

198. Mo, Z. *et al.* Efficient removal of Cd(II) from aqueous environment by potassium permanganate-modified eucalyptus biochar. *Biomass Convers. Biorefin.* **14**, 77–89 (2024).

199. Huff, M. D. & Lee, J. W. Biochar-surface oxygenation with hydrogen peroxide. *J. Environ. Manage.* **165**, 17–21 (2016).

200. Xue, Y. *et al.* Hydrogen peroxide modification enhances the ability of biochar (hydrochar) produced from hydrothermal carbonization of peanut hull to remove aqueous heavy metals: Batch and column tests. *Chemical Engineering Journal* **200–202**, 673–680 (2012).

201. Wang, H. Y. *et al.* Removal of Pb(II), Cu(II), and Cd(II) from aqueous solutions by biochar derived from $KMnO_4$ treated hickory wood. *Bioresour. Technol.* **197**, 356–362 (2015).

202. Wang, C. & Liu, T. Nori-based N, O, S, Cl co-doped carbon materials by chemical activation of ZnCl2 for supercapacitor. *J. Alloys Compd.* **696**, 42–50 (2017).

203. Tian, W., Gao, Q., Tan, Y. & Li, Z. Unusual interconnected graphitized carbon nanosheets as the electrode of high-rate ionic liquid-based supercapacitor. *Carbon N. Y.* **119**, 287–295 (2017).

204. Chu, G. *et al.* Phosphoric acid pretreatment enhances the specific surface areas of biochars by generation of micropores. *Environmental Pollution* **240**, 1–9 (2018).

205. Deng, J. *et al.* Inspired by bread leavening: one-pot synthesis of hierarchically porous carbon for supercapacitors. *Green Chemistry* **17**, 4053–4060 (2015).

206. Sevilla, M., Al-Jumialy, A. S. M., Fuertes, A. B. & Mokaya, R. Optimization of the Pore Structure of Biomass-Based Carbons in Relation to Their Use for CO_2 Capture under Low- and High-Pressure Regimes. *ACS Appl. Mater. Interfaces* **10**, 1623–1633 (2018).

207. Sevilla, M., Ferrero, G. A. & Fuertes, A. B. One-Pot Synthesis of Biomass-Based Hierarchical Porous Carbons with a Large Porosity Development. *CHEMISTRY OF MATERIALS* **29**, 6900–6907 (2017).

208. Gong, Y., Li, D., Luo, C., Fu, Q. & Pan, C. Highly porous graphitic biomass carbon as advanced electrode materials for supercapacitors. *Green Chemistry* **19**, 4132–4140 (2017).

209. Rudakiya, D. M. & Gupte, A. Degradation of hardwoods by treatment of white rot fungi and its pyrolysis kinetics studies. *Int. Biodeterior. Biodegradation* **120**, 21–35 (2017).

210. Yang, X., Ma, F., Yu, H., Zhang, X. & Chen, S. Effects of biopretreatment of corn stover with white-rot fungus on low-temperature pyrolysis products. *Bioresour. Technol.* **102**, 3498–3503 (2011).

211. Zhang, J. *et al.* Selective fungal pretreatment favored pyrolysis products of wheat straw based on pyrolytic polygeneration system. *Fuel Processing Technology* **215**, 106749 (2021).

212. Yu, H., Liu, F., Ke, M. & Zhang, X. Thermogravimetric analysis and kinetic study of bamboo waste treated by Echinodontium taxodii using a modified three-parallel-reactions model. *Bioresour. Technol.* **185**, 324–330 (2015).

213. Yang, X., Dey Laskar, D., Ma, F., Zhang, X. & Chen, S. Medium-temperature pyrolysis of corn stover improved by biopretreatment with white-rot fungi. *Bioresources* **8**, 6383–6394 (2013).

214. Lou, R. & Wu, S. Products properties from fast pyrolysis of enzymatic/mild acidolysis lignin. *Appl. Energy* **88**, 316–322 (2011).

215. Zeng, Y. L., Yang, X. W., Yu, H. B., Zhang, X. Y. & Ma, F. Y. Comparative Studies on Thermochemical Characterization of Corn Stover Pretreated by White-Rot and Brown-Rot Fungi. *J. Agric. Food Chem.* **59**, 9965–9971 (2011).

216. Wu, J. *et al.* Thermogravimetric kinetics of corn stalk pretreated by oleaginous fungi Cunninghamella echinulata. *Bioresour. Technol.* **102**, 5255–5258 (2011).

217. Ma, F. *et al.* Influence of fungal pretreatment on thermogravimetric characteristics and fast pyrolysis vapors of corn stover. *Biofuels* **2**, 557–567 (2011).

218. You, T., Li, X., Wang, R., Zhang, X. & Xu, F. Effects of synergistic fungal pretreatment on structure and thermal properties of lignin from corncob. *Bioresour. Technol.* **272**, 123–129 (2019).

219. Mushroom magic: 5 ways fungus-based technology will change the world - BBC Science Focus Magazine. https://www.sciencefocus.com/nature/fungus-technology.

220. Liu, Z. *et al.* Trichoderma bridges waste biomass and ultra-high specific surface area carbon to achieve a high-performance supercapacitor. *J. Power Sources* **497**, 229880 (2021).

221. Chai, Y. *et al.* Valorization of waste biomass through fungal technology: Advances, challenges, and prospects. *Ind. Crops Prod.* **188**, 115608 (2022).

222. Wan, C. & Li, Y. Fungal pretreatment of lignocellulosic biomass. *Biotechnol. Adv.* **30**, 1447–1457 (2012).

223. Vasco-Correa, J. & Shah, A. Techno-Economic Bottlenecks of the Fungal Pretreatment of Lignocellulosic Biomass. *Fermentation* **5**, (2019).

224. Sankaran, S. *et al.* Use of Filamentous Fungi for Wastewater Treatment and Production of High Value Fungal Byproducts: A Review. *Crit. Rev. Environ. Sci. Technol.* **40**, 400–449 (2010).

225. Kainthola, J., Podder, A., Fechner, M. & Goel, R. An overview of fungal pretreatment processes for anaerobic digestion: Applications, bottlenecks and future needs. *Bioresour. Technol.* **321**, 124397 (2021).

226. López, M. J., Elorrieta, M. A., Vargas-García, M. C., Suárez-Estrella, F. & Moreno, J. The effect of aeration on the biotransformation of lignocellulosic wastes by white-rot fungi. *Bioresour. Technol.* **81**, 123–129 (2002).

227. Inyang, M. *et al.* Removal of heavy metals from aqueous solution by biochars derived from anaerobically digested biomass. *Bioresour. Technol.* **110**, 50–56 (2012).

228. Zhang, K. *et al.* High-performance supercapacitor energy storage using a carbon material derived from lignin by bacterial activation before carbonization. *J. Mater. Chem. A Mater.* **7**, 26838–26848 (2019).

229. Tian, S. *et al.* Anisotropic reed-stem-derived hierarchical porous biochars supported paraffin wax for efficient solar-thermal energy conversion and storage. *J. Energy Storage* **56**, 106153 (2022).

230. Wei, H. *et al.* Biomass-derived nitrogen-doped porous carbon with superior capacitive performance and high CO_2 capture capacity. *Electrochim. Acta* **266**, 161–169 (2018).

231. Xu, L. *et al.* Nitrogen-doped porous carbon spheres derived from d-glucose as highly-efficient CO_2 sorbents. *RSC Adv.* **5**, 37964–37969 (2015).

232. Wang, J. *et al.* Highly porous nitrogen-doped polyimine-based carbons with adjustable microstructures for CO_2 capture. *J. Mater. Chem. A Mater.* **1**, 10951–10961 (2013).

233. Hao, G.-P., Li, W.-C., Qian, D. & Lu, A.-H. Rapid Synthesis of Nitrogen-Doped Porous Carbon Monolith for CO_2 Capture. *Advanced Materials* **22**, 853–857 (2010).

234. Zhang, Z. *et al.* Rational design of tailored porous carbon-based materials for CO_2 capture. *J. Mater. Chem. A Mater.* **7**, 20985–21003 (2019).

235. Wan, Z. *et al.* Customised fabrication of nitrogen-doped biochar for environmental and energy applications. *Chemical Engineering Journal* **401**, 126136 (2020).

236. Shafeeyan, M. S., Daud, W. M. A. W., Houshmand, A. & Arami-Niya, A. Ammonia modification of activated carbon to enhance carbon dioxide adsorption: Effect of pre-oxidation. *Appl. Surf. Sci.* **257**, 3936–3942 (2011).

237. Bamdad, H., Hawboldt, K. & Macquarrie, S. Nitrogen Functionalized Biochar as a Renewable Adsorbent for Efficient CO_2 Removal. *Energy and Fuels* **32**, 11742–11748 (2018).

238. Tang, Y. *et al.* Influence of pyrolysis temperature on production of digested sludge biochar and its application for ammonium removal from municipal wastewater. *J. Clean. Prod.* **209**, 927–936 (2019).

239. Chellappan, S., Nair, V., V., S. & K., A. Synthesis, optimization and characterization of biochar based catalyst from sawdust for simultaneous esterification and transesterification. *Chin. J. Chem. Eng.* **26**, 2654–2663 (2018).

240. Maliutina, K., Tahmasebi, A. & Yu, J. Pressurized entrained-flow pyrolysis of microalgae: Enhanced production of hydrogen and nitrogen-containing compounds. *Bioresour. Technol.* **256**, 160–169 (2018).

241. Yuan, S., Tan, Z. & Huang, Q. Migration and transformation mechanism of nitrogen in the biomass–biochar–plant transport process. *Renewable and Sustainable Energy Reviews* **85**, 1–13 (2018).

242. Chen, W. *et al.* Co-pyrolysis of lignocellulosic biomass and microalgae: Products characteristics and interaction effect. *Bioresour. Technol.* **245**, 860–868 (2017).

243. Khosrowshahi, M. S. *et al.* The role of surface chemistry on CO_2 adsorption in biomass-derived porous carbons by experimental results and molecular dynamics simulations. *Sci. Rep.* **12**, 8917 (2022).

244. Zhao, P., Zhang, G., Yan, H. & Zhao, Y. The latest development on amine functionalized solid adsorbents for post-combustion CO_2 capture: Analysis review. *Chin. J. Chem. Eng.* **35**, 17–43 (2021).

245. Saha, D. & Kienbaum, M. J. Role of oxygen, nitrogen and sulfur functionalities on the surface of nanoporous carbons in CO_2 adsorption: A critical review. *Microporous and Mesoporous Materials* **287**, 29–55 (2019).

246. Saha, D. & Kienbaum, M. J. Role of oxygen, nitrogen and sulfur functionalities on the surface of nanoporous carbons in CO_2 adsorption: A critical review. *Microporous and Mesoporous Materials* **287**, 29–55 (2019).

247. Mashhadimoslem, H. *et al.* Development of Predictive Models for Activated Carbon Synthesis from Different Biomass for CO_2 Adsorption Using Artificial Neural Networks. *Ind. Eng. Chem. Res.* **60**, 13950–13966 (2021).

248. Ma, X. *et al.* Highly Nitrogen-Doped Porous Carbon Derived from Zeolitic Imidazolate Framework-8 for CO_2 Capture. *Chem. Asian J.* **13**, 2069–2076 (2018).

249. Lim, G., Lee, K. B. & Ham, H. C. Effect of N-Containing Functional Groups on CO_2 Adsorption of Carbonaceous Materials: A Density Functional Theory Approach. *JOURNAL OF PHYSICAL CHEMISTRY C* **120**, 8087–8095 (2016).

250. Ma, X. *et al.* Heteroatom-doped nanoporous carbon derived from MOF-5 for CO 2 capture. *Appl. Surf. Sci.* **435**, 494–502 (2018).

251. Saha, D. *et al.* CO_2 capture in lignin-derived and nitrogen-doped hierarchical porous carbons. *Carbon N. Y.* **121**, 257–266 (2017).

252. Sevilla, M., Valle-Vigón, P. & Fuertes, A. B. N-Doped Polypyrrole-Based Porous Carbons for CO_2 Capture. *Adv. Funct. Mater.* **21**, 2781–2787 (2011).

253. Xu, X. C., Song, C. S., Miller, B. G. & Scaroni, A. W. Influence of moisture on CO_2 separation from gas mixture by a nanoporous adsorbent based on

polyethylenimine-modified molecular sieve MCM-41. *Ind. Eng. Chem. Res.* **44**, 8113–8119 (2005).

254. Hao, G. P. *et al.* Structurally Designed Synthesis of Mechanically Stable Poly(benzoxazine-co-resol)-Based Porous Carbon Monoliths and Their Application as High-Performance CO_2 Capture Sorbents. *J. Am. Chem. Soc.* **133**, 11378–11388 (2011).

255. Honig, J. M. ADSORBENT-ADSORBATE INTERACTIONS AND SURFACE HETEROGENEITY IN PHYSICAL ADSORPTION. *Ann. N. Y. Acad. Sci.* **58**, 741–797 (1954).

256. London, F. Zur Theorie und Systematik der Molekularkräfte. *Zeitschrift für Physik* **63**, 245–279 (1930).

257. Gregg, S. J. & Sing, K. S. W. *Adsorption, Surface Area, and Porosity*. (Academic Press, 1991).

258. Fontana, F. Memorie Mat. *Fis. Soc. Ital Sci* **1**, 679 (1777).

259. von Saussure, T. Beobachtungen über die Absorption der Gasarten durch verschiedene Körper. *Ann. Phys.* **47**, 113–183 (1814).

260. Webb, P. Introduction to Chemical Adsorption Analytical Techniques and their Applications to Catalysis. (2003).

261. Kayser, H. Ueber die Verdichtung von Gasen an Oberflächen in ihrer Abhängigkeit von Druck und Temperatur. *Ann. Phys.* **248**, 526–537 (1881).

262. Langmuir, I. THE ADSORPTION OF GASES ON PLANE SURFACES OF GLASS, MICA AND PLATINUM. *J. Am. Chem. Soc.* **40**, 1361–1403 (1918).

263. Langmuir, I. THE CONSTITUTION AND FUNDAMENTAL PROPERTIES OF SOLIDS AND LIQUIDS. II. LIQUIDS.1. *J. Am. Chem. Soc.* **39**, 1848–1906 (1917).

264. Langmuir, I. THE CONSTITUTION AND FUNDAMENTAL PROPERTIES OF SOLIDS AND LIQUIDS. PART I. SOLIDS. *J. Am. Chem. Soc.* **38**, 2221–2295 (1916).

265. Adsorption. in *Physics and Chemistry of Interfaces* 177–205 (2003). doi:https://doi.org/10.1002/3527602313.ch9.

266. Surface Tension - What is surface tension - Kibron. https://www.kibron.com/surface-tension.

267. Liquid Surfaces. in *Physics and Chemistry of Interfaces* 4–25 (2003). doi:https://doi.org/10.1002/3527602313.ch2.

268. Physical and chemical adsorption[5]. | Download Scientific Diagram. https://www.researchgate.net/figure/Physical-and-chemical-adsorption5_fig1_357746714.

269. Chatelier, H. L. *Recherches Expérimentales et Théoriques Sur Les Équilibres Chimiques*. (Dunod, 1888).

270. Brunauer, S. & Hugh Emmett, P. Introduction ϖ BET ¬ Gas adsorption or Nitrogen adsorption.

271. Cheremisinoff, N. P. & Cheremisinoff, P. N. *Carbon Adsorption for Pollution Control*. (New York, NY (United States); PTR Prentice Hall, United States, 1993).

272. Surface Chemistry and Adsorption - Chemistry for JEE Main and Advanced PDF. https://edurev.in/t/93338/Adsorption-and-Absorption-Surface-Chemistry--CBSE-.

273. 1. Esquema de sólido poroso (Rouquerol, y otros, 1994). | Download Scientific Diagram. https://www.researchgate.net/figure/Esquema-de-solido-poroso-Rouquerol-y-otros-1994_fig1_308892892.

274. Oschatz, M. & Antonietti, M. A search for selectivity to enable CO_2 capture with porous adsorbents. *Energy and Environmental Science* vol. 11 57–70 Preprint at https://doi.org/10.1039/c7ee02110k (2018).

275. Noked, M., Avraham, E., Soffer, A. & Aurbach, D. The Rate-Determining Step of Electroadsorption Processes into Nanoporous Carbon Electrodes Related to Water Desalination. *The Journal of Physical Chemistry C* **113**, 21319–21327 (2009).

276. Arruda, T. M. *et al.* In situ tracking of the nanoscale expansion of porous carbon electrodes. *Energy Environ. Sci.* **6**, 225–231 (2013).

277. Zhao, Y., Liu, X. & Han, Y. Microporous carbonaceous adsorbents for CO_2 separation via selective adsorption. *RSC Adv.* **5**, 30310–30330 (2015).

278. Millward, A. R. & Yaghi, O. M. Metal−Organic Frameworks with Exceptionally High Capacity for Storage of Carbon Dioxide at Room Temperature. *J. Am. Chem. Soc.* **127**, 17998–17999 (2005).

279. Thermodynamics of Interfaces. in *Physics and Chemistry of Interfaces* 26–41 (2003). doi:https://doi.org/10.1002/3527602313.ch3.

280. Clausius, R. Ueber die bewegende Kraft der Wärme und die Gesetze, welche sich daraus für die Wärmelehre selbst ableiten lassen. *Ann. Phys.* **155**, 500–524 (1850).

281. Thommes, M. *et al.* Physisorption of gases, with special reference to the evaluation of surface area and pore size distribution (IUPAC Technical Report). *Pure and Applied Chemistry* **87**, 1051–1069 (2015).

282. Thommes, M. *et al.* IUPAC Technical Report Physisorption of gases, with special reference to the evaluation of surface area and pore size distribution (IUPAC Technical Report). https://doi.org/10.1515/pac-2014-1117 (2015) doi:10.1515/pac-2014-1117.

283. Serafin, J. & Dziejarski, B. Application of isotherms models and error functions in activated carbon CO_2 sorption processes. *Microporous and Mesoporous Materials* **354**, 112513 (2023).

284. Swenson, H. & Stadie, N. P. Langmuir's Theory of Adsorption: A Centennial Review. *Langmuir* **35**, 5409–5426 (2019).

285. Brunauer, S., Emmett, P. H. & Teller, E. Adsorption of Gases in Multimolecular Layers. *J. Am. Chem. Soc.* **60**, 309–319 (1938).

286. Freundlich, H. *Kapillarchemie: Eine Darstellung Der Chemie Der Kolloide Und Verwandter Gebiete*. (Akademische verlagsgesellschaft m.b.h., 1909).

287. Temkin, M. I. The Kinetics of Some Industrial Heterogeneous Catalytic Reactions. in *Advances in Catalysis* (eds. Eley, D. D., Pines, H. & Weez, P. B.) vol. 28 173–291 (Academic Press, 1979).

288. Chu, K. H. Revisiting the Temkin Isotherm: Dimensional Inconsistency and Approximate Forms. *Ind. Eng. Chem. Res.* **60**, 13140–13147 (2021).

289. Tóth, J. State equation of the solid-gas interface layers. *Acta chim. hung.* **69**, 311–328 (1971).

290. Tóth, J. Calculation of the BET-Compatible Surface Area from Any Type I Isotherms Measured above the Critical Temperature. *J. Colloid Interface Sci.* **225**, 378–383 (2000).

291. Tóth, J. Uniform interpretation of gas/solid adsorption. *Adv. Colloid Interface Sci.* **55**, 1–239 (1995).

292. Sips, R. On the structure of a catalyst surface. *J. Chem. Phys.* **16**, 490–495 (1948).

293. Rouquerol, J., Llewellyn, P. & Rouquerol, F. Is the BET equation applicable to microporous adsorbents? *Stud. Surf. Sci. Catal.* **160**, 49–56 (2007).

294. Dubinin, A. M. M. A study of the porous structure of active carbons using a variety of methods. *Quarterly Reviews, Chemical Society* **9**, 101–114 (1955).

295. Bering, B. P., Dubinin, M. M. & Serpinsky, V. V. Theory of volume filling for vapor adsorption. *J. Colloid Interface Sci.* **21**, 378–393 (1966).

296. Polanyi, M. The Potential Theory of Adsorption. *Science (1979).* **141**, 1010–1013 (1963).

297. Talu, O. & Myers, A. L. Rigorous thermodynamic treatment of gas adsorption. *AIChE Journal* **34**, 1887–1893 (1988).

298. Marsh, H. & Rand, B. The characterization of microporous carbons by means of the dubinin-radushkevich equation. *J. Colloid Interface Sci.* **33**, 101–116 (1970).

299. Hacskaylo, J. J. & LeVan, M. D. Correlation of adsorption equilibrium data using a modified Antoine equation: a new approach for pore-filling models. *Langmuir* **1**, 97–100 (1985).

300. Brunauer, S. & Hugh Emmett, P. Introduction ϖ BET ¬ Gas adsorption or Nitrogen adsorption.

301. Yang, M. & Wang, Y. D-BJH: The Intrinsic Model for Characterizing the Pore Size Distribution of Porous Materials. *Langmuir* **40**, 20368–20378 (2024).

302. Barrett, E. P., Joyner, L. G. & Halenda, P. P. The Determination of Pore Volume and Area Distributions in Porous Substances. I. Computations from Nitrogen Isotherms. *J. Am. Chem. Soc.* **73**, 373–380 (1951).

303. Skinner, L. M. & Sambles, J. R. The Kelvin equation—a review. *J. Aerosol Sci.* **3**, 199–210 (1972).

304. Lippens, B. C. & de Boer, J. H. Studies on pore systems in catalysts: V. The t method. *J. Catal.* **4**, 319–323 (1965).

305. Harkins, W. D. & Jura, G. Surfaces of Solids. XIII. A Vapor Adsorption Method for the Determination of the Area of a Solid without the Assumption of a Molecular Area, and the Areas Occupied by Nitrogen and Other Molecules on the Surface of a Solid. *J. Am. Chem. Soc.* **66**, 1366–1373 (1944).

306. *Standard Test Method for Carbon Black-Total and External Surface Area by Nitrogen Adsorption*. https://standards.iteh.ai/catalog/standards/sist/1d74758b-e118-4416-ac45-8f334fcf8770/astm-d6556-01.

307. Ketabchi, M. R., Babamohammadi, S., Davies, W. G., Gorbounov, M. & Masoudi Soltani, S. Latest advances and challenges in carbon capture using bio-based sorbents: A state-of-the-art review. *Carbon Capture Science & Technology* **6**, 100087 (2023).

308. Fletcher, A. J. *et al.* Adsorption Dynamics of Gases and Vapors on the Nanoporous Metal Organic Framework Material Ni2(4,4‘-Bipyridine)3(NO3)4: Guest Modification of Host Sorption Behavior. *J. Am. Chem. Soc.* **123**, 10001–10011 (2001).

309. Fletcher, A. J., Cussen, E. J., Bradshaw, D., Rosseinsky, M. J. & Thomas, K. M. Adsorption of Gases and Vapors on Nanoporous Ni2(4,4‘-Bipyridine)3(NO3)4 Metal−Organic Framework Materials Templated with Methanol and Ethanol: Structural Effects in Adsorption Kinetics. *J. Am. Chem. Soc.* **126**, 9750–9759 (2004).

310. Fletcher, A. J., Uygur, Y. & Thomas, K. M. Role of Surface Functional Groups in the Adsorption Kinetics of Water Vapor on Microporous Activated Carbons. *The Journal of Physical Chemistry C* **111**, 8349–8359 (2007).

311. Klafter, J. & Shlesinger, M. F. On the relationship among three theories of relaxation in disordered systems. *Proceedings of the National Academy of Sciences* **83**, 848–851 (1986).

312. Shlesinger, M. F. & Montroll, E. W. On the Williams—Watts function of dielectric relaxation. *Proceedings of the National Academy of Sciences* **81**, 1280–1283 (1984).

313. Reid, C. R. & Thomas, K. M. Adsorption of Gases on a Carbon Molecular Sieve Used for Air Separation: Linear Adsorptives as Probes for Kinetic Selectivity. *Langmuir* **15**, 3206–3218 (1999).

314. Reid, C. R., O'koy, I. P. & Thomas, K. M. Adsorption of Gases on Carbon Molecular Sieves Used for Air Separation. Spherical Adsorptives as Probes for Kinetic Selectivity. *Langmuir* **14**, 2415–2425 (1998).

315. Fletcher, A. J. & Thomas, K. M. Compensation Effect for the Kinetics of Adsorption/Desorption of Gases/Vapors on Microporous Carbon Materials. *Langmuir* **16**, 6253–6266 (2000).

316. Webster, C. E., Drago, R. S. & Zerner, M. C. Molecular Dimensions for Adsorptives. *J. Am. Chem. Soc.* **120**, 5509–5516 (1998).

317. Aktivační energie (článek) | Khan Academy. https://cs.khanacademy.org/science/fyzikalni-chemie/xecb1a3ac274b46c2:chemicka-kinetika/xecb1a3ac274b46c2:activation-energy-and-reaction-rate/a/activation-energy.

318. Valadi, F. M. *et al.* Competitive adsorption of CO_2, N2, and CH4 in coal-derived asphaltenes, a computational study. *Sci. Rep.* **14**, 7664 (2024).

319. Hand, D. W., Loper, Scott., Ari, Metin. & Crittenden, J. C. Prediction of multicomponent adsorption equilibria using ideal adsorbed solution theory. *Environ. Sci. Technol.* **19**, 1037–1043 (1985).

320. Chen, J., Loo, L. S. & Wang, K. An Ideal Absorbed Solution Theory (IAST) Study of Adsorption Equilibria of Binary Mixtures of Methane and Ethane on a Templated Carbon. *J. Chem. Eng. Data* **56**, 1209–1212 (2011).

321. Krishna, R. & van Baten, J. M. How Reliable Is the Ideal Adsorbed Solution Theory for the Estimation of Mixture Separation Selectivities in Microporous Crystalline Adsorbents? *ACS Omega* **6**, 15499–15513 (2021).

322. Radke, C. J. & Prausnitz, J. M. Thermodynamics of multi-solute adsorption from dilute liquid solutions. *AIChE Journal* **18**, 761–768 (1972).

323. Hand, D. W., Loper, S. W., Ari, M. & Crittenden, J. C. Prediction of multicomponent adsorption equilibria using ideal adsorbed solution theory. *Environ. Sci. Technol.* **19 11**, 1037–43 (1985).

324. Smith, B. C. *Fundamentals of Fourier Transform Infrared Spectroscopy, Second Edition*. *Fundamentals of Fourier Transform Infrared Spectroscopy, Second Edition* (2011).

325. IR (Infra-red Spectroscopy) (A-Level) | ChemistryStudent. https://www.chemistrystudent.com/IRspectroscopy.html.

326. Schematic sketch of the essential features of a Fourier transform... | Download Scientific Diagram. https://www.researchgate.net/figure/Schematic-sketch-of-the-essential-features-of-a-Fourier-transform-infrared-FTIR_fig1_225065938.

327. Palik, E. D. Handbook of Optical Constants of Solids, Five-Volume Set. 3224 (1997).

328. Choosing the right ATR crystal for FTIR analysis - Specac Ltd. https://specac.com/theory-articles/choosing-the-right-atr-crystal/.

329. *Carbon Black Analysis Using FT-IR with Germanium and Diamond ATR*. www.thermoscientific.com.

330. Stevie, F. A. & Donley, C. L. Introduction to x-ray photoelectron spectroscopy. *Journal of Vacuum Science & Technology A* **38**, 063204 (2020).

331. Photoelectron_Spectroscopy.

332. Gibson, L. T. Archaeometry and Antique Analysis - Metallic and Ceramic Objects. *Encyclopedia of Analytical Science: Second Edition* 117–123 (2004) doi:10.1016/B0-12-369397-7/00020-0.

333. An Editorial About Elemental Analysis. *Organometallics* **35**, 3255–3256 (2016).

334. Kuveke, R. E. H. *et al.* An International Study Evaluating Elemental Analysis. *ACS Cent. Sci.* **8**, 855–863 (2022).

335. Kandioller, W., Theiner, J., Keppler, B. K. & Kowol, C. R. Elemental analysis: an important purity control but prone to manipulations. *Inorg. Chem. Front.* **9**, 412–416 (2022).

336. Bird, M., Keitel, C. & Meredith, W. Analysis of biochars for C,H,N,O and S by elemental analyser. in (2017).

337. Shadangi, K. P., Sarangi, P. K. & Behera, A. K. Chapter 3 - Characterization techniques of biomass: physico-chemical, elemental, and biological. in *Bioenergy Engineering* (eds. Shadangi, K. P., Sarangi, P. K., Mohanty, K., Deniz, I. & Kiran Gollakota, A. R.) 51–66 (Woodhead Publishing, 2023). doi:https://doi.org/10.1016/B978-0-323-98363-1.00022-3.

338. Racero-Galaraga, D., Rhenals-Julio, J. D., Sofan-German, S., Mendoza, J. M. & Bula-Silvera, A. Proximate analysis in biomass: Standards, applications and key characteristics. *Results Chem.* **12**, 101886 (2024).

339. Thermogravimetric Analysis - Particle Technology Labs. https://particletechlabs.com/analytical-testing/thermogravimetric-analysis/.

340. Mukherjee, A., Borugadda, V. B., Dynes, J. J., Niu, C. & Dalai, A. K. Carbon dioxide capture from flue gas in biochar produced from spent coffee grounds: Effect of surface chemistry and porous structure. *J. Environ. Chem. Eng.* **9**, 106049 (2021).

341. ASAP 2460 & 2425 - Micromeritics. https://micromeritics.com/products/asap-2460-2425/.

342. Broom, D. P. Gas Sorption Measurement Techniques. *Green Energy and Technology* **27**, 117–139 (2011).

343. Ivan Alejandro. *Development of Nitrogen Doped Resorcinol-Formaldehyde Gels for Carbon Capture*.

344. Afrina Sianturi, H. *et al.* Activated carbon production from bagasse and banana stem at various times of carbonization. *IOP Conf. Ser. Mater. Sci. Eng.* **309**, 012064 (2018).

345. Danish, M. & Ahmad, T. A review on utilization of wood biomass as a sustainable precursor for activated carbon production and application. *Renewable and Sustainable Energy Reviews* **87**, 1–21 (2018).

346. Qiao, Y. & Wu, C. Nitrogen enriched biochar used as CO_2 adsorbents: a brief review. *Carbon Capture Science & Technology* **2**, 100018 (2022).

347. Mukherjee, A., Saha, B., Niu, C. & Dalai, A. K. Preparation of activated carbon from spent coffee grounds and functionalization by deep eutectic solvent: Effect of

textural properties and surface chemistry on CO_2 capture performance. *J. Environ. Chem. Eng.* **10**, 108815 (2022).

348. Li, Z., Guo, D., Liu, Y., Wang, H. & Wang, L. Recent advances and challenges in biomass-derived porous carbon nanomaterials for supercapacitors. *Chemical Engineering Journal* **397**, 125418 (2020).

349. Guerrera, J. V. *et al.* Evaluation of Two Potassium-Based Activation Agents for the Production of Oxygen- A nd Nitrogen-Doped Porous Carbons. *Energy and Fuels* **34**, 6101–6112 (2020).

350. Kikuchi, K. *et al.* Double layer properties of spent coffee grounds-derived carbon activated with potassium hydroxide (koh). *Electrochemistry* **81**, 828–832 (2013).

351. Rashid, H. & Rafey, A. Solid adsorbents for carbon dioxide capture: a review. *Chemistry and Ecology* **39**, 775–791 (2023).

352. Choma, J., Stachurska, K., Marszewski, M. & Jaroniec, M. Equilibrium isotherms and isosteric heat for CO_2 adsorption on nanoporous carbons from polymers. *Adsorption* **22**, 581–588 (2016).

353. Gautam, Sah, R. P. & Sahoo, S. A review on adsorption isotherms and kinetics of CO_2 and various adsorbent pairs suitable for carbon capture and green refrigeration applications. *Sādhanā 2023 48:1* **48**, 1–37 (2023).

354. Ji, G. *et al.* Recent advances on kinetics of carbon dioxide capture using solid sorbents at elevated temperatures. *Appl. Energy* **267**, 114874 (2020).

355. Zhao, H. *et al.* Carbon-based adsorbents for post-combustion capture: a review. *Greenhouse Gases: Science and Technology* **8**, 11–36 (2018).

356. Raganati, F., Chirone, R. & Ammendola, P. Thermodynamic and kinetic study of CO_2 adsorption on a fine activated carbon in a sound assisted fluidized bed.

357. Zhang, Z., Zhang, W., Chen, X., Xia, Q. & Li, Z. Adsorption of CO_2 on Zeolite 13X and Activated Carbon with Higher Surface Area. *Sep. Sci. Technol.* **45**, 710–719 (2010).

358. Sarker, A. I., Aroonwilas, A. & Veawab, A. Equilibrium and Kinetic Behaviour of CO_2 Adsorption onto Zeolites, Carbon Molecular Sieve and Activated Carbons. *Energy Procedia* **114**, 2450–2459 (2017).

359. Wei, M. *et al.* Kinetics studies of CO_2 adsorption and desorption on waste ion-exchange resin-based activated carbon. *Int. J. Hydrogen Energy* **42**, 27122–27129 (2017).

360. Lahuri, A. H. *et al.* Comparative studies on adsorption isotherm and kinetic for CO_2 capture using iron oxide impregnated activated carbon. *Catal. Today* **418**, 114111 (2023).

361. Fletcher, A. J. & Thomas, K. M. Compensation effect for the kinetics of adsorption/desorption of gases/vapors on microporous carbon materials. *Langmuir* **16**, 6253–6266 (2000).

362. Dautzenberg, E., van Hurne, S., Smulders, M. M. J. & de Smet, L. C. P. M. GraphIAST: A graphical user interface software for Ideal Adsorption Solution Theory (IAST) calculations. *Comput. Phys. Commun.* **280**, 108494 (2022).

363. Dalakoti, S. *et al.* Cu-trimesate and mesoporous silica composite as adsorbent showing enhanced CO_2/CH4 and CO_2/N2 selectivity for biogas and flue gas separation. *Microporous and Mesoporous Materials* **381**, 113354 (2025).

364. Singh, N. *et al.* Shaping of MIL-53-Al and MIL-101 MOF for CO_2/CH4, CO_2/N2 and CH4/N2 separation. *Sep. Purif. Technol.* **341**, 126820 (2024).

365. Liu, S. H. & Huang, Y. Y. Valorization of coffee grounds to biochar-derived adsorbents for CO_2 adsorption. *J. Clean. Prod.* **175**, 354–360 (2018).

366. Tsai, W. T. The potential of pyrolysing exhausted coffee residue for the production of biochar. in *Handbook of Coffee Processing By-Products: Sustainable Applications* 299–322 (Elsevier Inc., 2017). doi:10.1016/B978-0-12-811290-8.00010-4.

367. Stamets, P. GROWING GOURMET and MEDICINAL MUSHROOMS a companion guide to The Mushroom Cultivator. (2000).

368. Padilla-Martínez, E. D., Pérez-Buendía, S. K., López-Sandoval, R. & Sánchez-Rodríguez, C. E. Electrochemical energy storage from spent coffee grounds-derived carbon by KOH activation. *J. Energy Storage* **71**, 108115 (2023).

369. Lionetti, V. *et al.* Optimized activation of coffee-ground carbons for hydrogen storage. *Int. J. Hydrogen Energy* **136**, 1029–1040 (2025).

370. Help Online - Origin Help - Theory of Nonlinear Curve Fitting. https://www.originlab.com/doc/origin-help/nlfit-theory#ANOVA_Table.

371. Press, W. H., Teukolsky, S. A., Vetterling, W. T. & Flannery, B. P. Nonlinear Models. in *Numerical Recipes in C: The Art of Scientific Computing* 681–690 (Cambridge University Press, Cambridge, 1992).

372. Press, W. H. . *Downhill Simplex Method In*. (Cambridge University Press, 1992).

373. Nelder, J. A. & Mead, R. A simplex method for function minimization. *Comput. J.* **7**, 308–313 (1965).

374. Watson, L., Boggs, P. & Zwolak, J. A weighted orthogonal distance regression code with bound constraints. (2005).

Appendices

Appendix A: Intermolecular Interactions

London Dispersion Forces

London dispersion forces are the most ubiquitous form of intermolecular attraction. They arise from transient fluctuations in electron density that create instantaneous dipoles, which in turn induce dipoles in neighbouring molecules. The strength of these interactions increases with molecular size and polarizability. While individually weak, dispersion forces collectively contribute significantly to cohesion in nonpolar systems and govern the behaviour of many molecular assemblies and surface interfaces. [256]

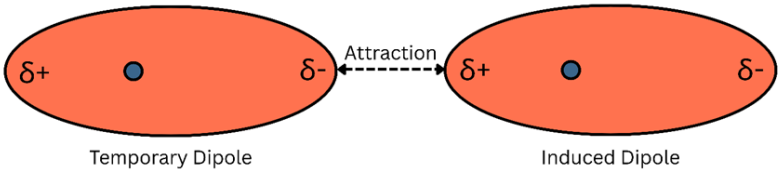

Figure 87 - London dispersion interaction arising from a transient dipole inducing a dipole in a neighbouring molecule.

Dipole–Dipole Interactions

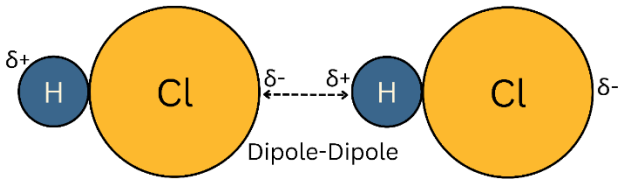

Figure 88 - Dipole–Dipole interaction between two HCl molecules.

Dipole–dipole interactions occur between molecules possessing permanent dipole moments. These forces are directional, arising from the electrostatic attraction between partial charges on adjacent polar molecules. The strength and nature of the interaction depend on molecular orientation and distance, influencing the alignment and organisation of polar species in condensed phases or on polar surfaces.

Dipole-Induced Dipole Interactions

Dipole–induced dipole interactions result when a polar molecule distorts the electron cloud of a nearby nonpolar molecule, inducing a temporary dipole. Although weaker than permanent dipole–dipole interactions, they play an important role in systems involving

both polar and nonpolar species, allowing for broader compatibility and interaction versatility in complex environments. [257]

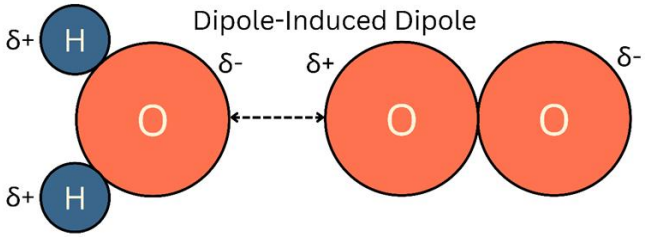

Figure 89- Dipole–induced dipole interaction between water and oxygen molecules.

Hydrogen Bonding

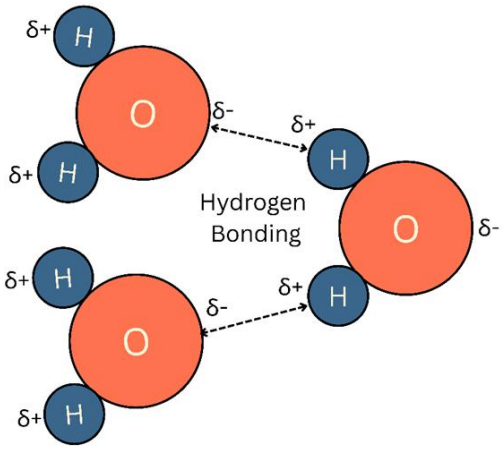

Figure 90 - Hydrogen bonding between water molecules.

Hydrogen bonding is a specialised form of dipole–dipole interaction in which a hydrogen atom covalently bonded to a strongly electronegative element (typically nitrogen, oxygen, or fluorine) interacts with another electronegative atom bearing a lone pair of electrons. These bonds are stronger than other van der Waals forces and contribute significantly to the structural organisation and stability of molecular systems, particularly those involving water, alcohols, or amines. [257]

Quadrupole Interactions

Quadrupole interactions arise from anisotropic charge distributions in molecules or molecular assemblies that possess a quadrupole moment, such as carbon dioxide or certain aromatic compounds. These interactions depend on the spatial orientation and symmetry of the molecules and can influence the arrangement and alignment of quadrupolar species near surfaces or within confined environments. [257]

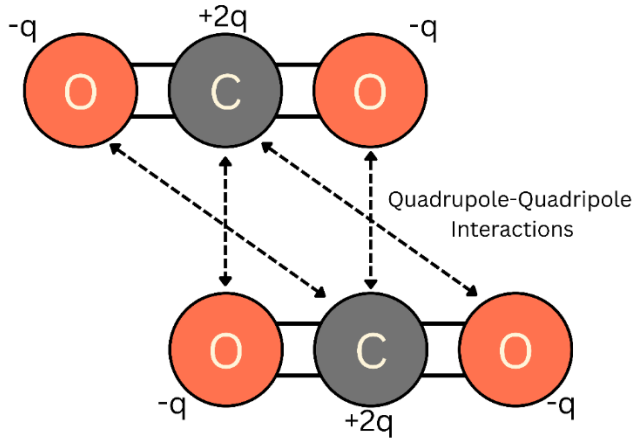

Figure 91 - Quadrupole–quadrupole interaction between carbon dioxide molecules.

π–π Interactions

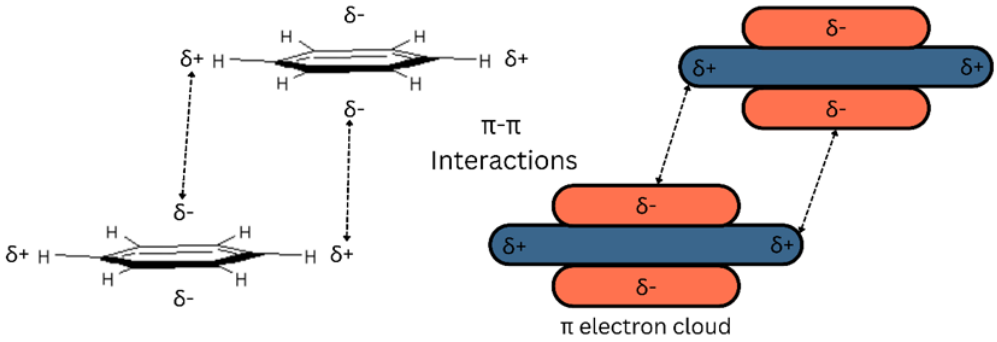

Figure 92 - π–π interactions between aromatic rings via overlapping electron clouds.

π–π interactions occur between aromatic rings due to the overlap of π-electron clouds. These interactions are non-covalent yet can exert significant influence on molecular assembly, especially in planar, conjugated systems. π–π stacking plays a prominent role in supramolecular chemistry, molecular recognition, and the structural arrangement of aromatic compounds on surfaces. [257]

Cation–π and Anion–π Interactions

Cation–π and anion–π interactions involve electrostatic attractions between charged species and π-electron-rich systems. These interactions are highly specific and can contribute to ion selectivity, molecular recognition, and surface complexation phenomena, particularly in materials and systems designed to engage with charged species or functional groups. [257]

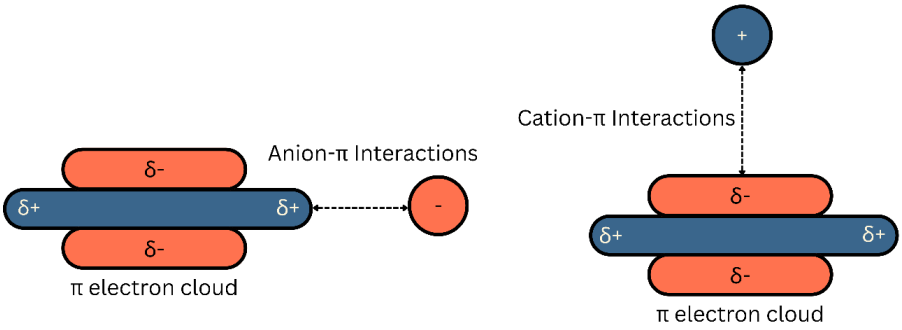

Figure 93 - Cation–π and anion–π interactions involving electrostatic attraction to π-electron systems.

Comparison of Interaction Strengths

The strength of intermolecular interactions spans several orders of magnitude. Table 42 summarises typical energy ranges and general roles of each interaction type in molecular and surface systems.

Table 42 - Approximate energy ranges and roles of key intermolecular interactions.

Interaction Type	**Energy Range (kJ/mol)**	**General Role**
London Dispersion Forces	0.05–40	Dominant in nonpolar systems; universally present
Dipole–Dipole	2–25	Significant for polar molecules and orientational structuring
Dipole–Induced Dipole	1–15	Enables interactions between polar and nonpolar species
Hydrogen Bonding	10–40	Provides specificity and structural directionality
Quadrupole Interactions	~5–15	Important for molecules with anisotropic charge distributions (e.g. CO_2)
π–π Interactions	5–50	Critical in aromatic systems and molecular stacking
Cation–π / Anion–π	10–80	Specific electrostatic binding in charged and π-conjugated systems

The collective action of these intermolecular forces governs a wide range of surface-related phenomena, including molecular alignment, selective binding, wetting, and surface self-assembly. Their reversibility and tunable strength make them especially important in reversible surface processes, where weak interactions can enable dynamic equilibrium or multilayer formation. The balance between different interaction types—determined by the chemical nature of the surface and interacting species—ultimately dictates selectivity, strength, and kinetics in any surface-mediated process.

Appendix B: Adsorption Characterisation and Techniques

BET Surface Area Calculation

1. **Collect the Adsorption Isotherm Data**
    - Measure the volume of gas adsorbed at different relative pressures (P/P^0) at a constant temperature (typically 77 K for nitrogen adsorption).
2. **Select the Appropriate Pressure Range**
    - Identify the linear region of the BET plot, usually within a relative pressure range of 0.05 to 0.3.
    - Apply the Rouquerol criteria to ensure a positive intercept and continuous increase in the adjusted term.
3. **Construct the BET Plot**
    - Plot $\boldsymbol{P/V\left(P^0 - P\right)}$ against $\boldsymbol{P/P^0}$ to obtain a straight-line fit.
    - The slope (S) and intercept (I) of the linear portion allow determination of the monolayer capacity: $V_m = \frac{1}{S+I}$ where V_m is the monolayer adsorption volume.
4. **Calculate the Surface Area**
    - Using the equation:

$$S = \frac{V_m N_A A_m}{M} \qquad \textit{Equation 67}$$

    where:
        - A_m is the cross-sectional area of the adsorbate molecule (e.g., 16.2 Å² for nitrogen),
        - N_A is Avogadro's number,
        - M is the mass of the adsorbent.
5. **Account for Microporosity**
    - Use the t-plot method or αs-method to differentiate between monolayer adsorption and micropore filling.
    - Estimate the external surface area by fitting the data to a reference isotherm for a non-porous analogue.
    - Subtract the estimated non-microporous contribution from the total BET surface area to obtain the micropore contribution.

Step-by-Step BJH Pore Volume and Pore Size Distribution Determination

1. **Collect the Adsorption-Desorption Isotherm Data**
    - Perform nitrogen adsorption measurements at 77 K to obtain the adsorption-desorption isotherm.
    - Ensure that the relative pressure range includes the region where capillary condensation occurs (typically $0.35 < P/P_o < 0.99$ for mesopores).
2. **Identify the Desorption Branch for Analysis**
    - The BJH method is typically applied to the desorption isotherm, as it provides a more accurate representation of pore emptying processes.
    - The hysteresis loop observed in mesoporous materials is analysed to determine pore size distribution.
3. **Apply the BJH Equation for Pore Volume and Pore Size Computation**
    - The BJH method determines pore size distribution by considering the relationship between desorbed volume and decreasing relative pressure:

$$V_p = \sum \left(\frac{\Delta V_n}{A_p} \right) \qquad \textit{Equation 68}$$

where:

- V_p is the total pore volume,
- ΔV_n is the differential volume of adsorbate desorbed,
- A_p is the area of each pore.

    - The full BJH pore size distribution equation is given by:

$$V_{p,n} = \frac{V_n - \sum_{j=n+1}^{N} (t_j - t_{j-1}) A_j}{t_n - t_{n-1}} \qquad \textit{Equation 69}$$

where:

- $V_{p,n}$ is the pore volume for a given radius,
- V_n is the total desorbed volume at step n,
- t_j is the film thickness at step j,
- A_j is the pore surface area at step j.

- The reduction of relative pressure from $(\mathrm{P}/\mathrm{P}_0)_1$ to $(P/P_0)_2$ allows measurement of the differential volume ΔV_n, which is related to the area of each pore A_p.
- The desorption process also reduces the thickness of the physically adsorbed layer by Δt_1, which is factored into the computation.

4. **Apply the Kelvin Equation for Capillary Condensation**
   - The Kelvin equation plays a central role in determining the pore radius from the relative pressure at which desorption occurs. It expresses the relationship between vapor pressure and curvature of the meniscus formed inside the pore:

$$r = -\frac{2\gamma V_m}{RT\ln(P/P_0)} \qquad \textit{Equation 70}$$

where:

- r is the pore radius,
- γ is the surface tension of the adsorbate,
- V_m is the molar volume of the adsorbed liquid,
- R is the universal gas constant,
- T is the absolute temperature.

   - The Kelvin equation highlights how vapor pressure is lower over curved liquid surfaces in pores than over bulk liquid, leading to capillary condensation. This is critical for interpreting adsorption-desorption isotherms and deriving pore size distributions.

5. **Compute the Pore Volume and Pore Size Distribution**
   - The pore volume is calculated from the amount of gas desorbed at each pressure step.
   - The pore size distribution is obtained by differentiating the pore volume with respect to pore radius, typically resulting in a Gaussian-like distribution.

Application of the t-Method

Selection of the Linear Region of the V–t Plot

- Generate a plot of V_{liq} versus t.
- Identify the linear region corresponding to multilayer adsorption on the external (non-microporous) surface.
- An extrapolation of this linear region to the *t*-axis: if it passes through the origin, no microporosity is present; a positive intercept indicates additional adsorption due to micropores.

Calculation of Surface Areas and Pore Volumes

- Total Surface Area (S_{total}) is determined from the slope of the linear region of the $V - t$ plot (after applying the appropriate conversion factors to convert from volume per unit thickness to m²/g).
- Micropore Volume (V_{mp}) is obtained from the intercept of the linear region.
- External (Non-Microporous) Surface Area (S_{ext}) is derived from the adjusted slope:

$$S_{ext} = \frac{V_{liq} - V_{mp}}{t} \qquad \textit{Equation 71}$$

- **Micropore Surface Area** ($\boldsymbol{S_{micro}}$) is then calculated as:

$$S_{micro} = S_{total} - S_{ext} \qquad \textit{Equation 72}$$

Alternative Approach Using Low Partial Pressure Data

If high-quality data at low P/P_0 are available, the micropore surface area may also be estimated by the difference in slopes at low and high relative pressures:

$$S_{micro} = \left(\frac{dV}{dt}\right)_{lowP/P_0} - \left(\frac{dV}{dt}\right)_{highP/P_0} \qquad \textit{Equation 73}$$

Measurement Process

The adsorption capacity of CO_2 was determined using an Intelligent Gravimetric Analyzer (IGA), a high-precision gravimetric system. The measurement follows these key steps:

1. **Sample Preparation**: Adsorbent materials are pre-treated by degassing under vacuum to remove moisture and any pre-adsorbed gases.
2. **Adsorption Measurement**:
    - The sample is exposed to CO_2 at controlled pressures and temperatures.
    - Pressure is increased stepwise, and adsorption is monitored in real-time until equilibrium is reached at each step.
3. **Equilibration**: The system ensures that equilibrium adsorption is achieved before recording data, allowing precise measurement of the mass change due to CO_2 uptake.
4. **Data Recording**:
    - The amount of CO_2 adsorbed is recorded as a function of pressure, generating adsorption isotherms.
    - Measurements are performed at multiple temperatures to understand the effect of thermal conditions on adsorption behaviour.

Calculation and Standard Units of CO_2 Adsorption Capacity

The CO_2 adsorption capacity is calculated from the raw mass change data using the following equation:

$$q = \frac{\Delta m}{M_{CO_2} \times m_{adsorbent}} \qquad \textit{Equation 74}$$

where:

- q is the adsorption capacity in mmol/g,
- Δm is the mass of CO_2 adsorbed (mg),
- M_{CO_2} is the molar mass of CO_2 (44.01 g/mol),
- $m_{adsorbent}$ is the mass of the adsorbent (g).

This calculation ensures accurate and consistent reporting of adsorption capacities across different materials and experimental conditions. The standard unit of mmol/g is preferred

because it allows direct comparison of adsorption efficiency irrespective of material density or surface area.

Step-by-Step IAST Calculation Procedure

1. Fit Pure Component Isotherms
    - Obtain adsorption isotherms for pure CO_2 and N_2.
    - Fit these isotherms using appropriate models (e.g., Langmuir, Freundlich, or Sips) to extract key parameters such as the adsorption equilibrium constant (K) and the monolayer capacity (C_m). These parameters serve as inputs for IAST.
2. Calculate Spreading Pressure for Each Component
    - For each pure component, calculate the spreading pressure (ω) by integrating the isotherm data. Although the specific form of the integration may vary with the model used, a general expression is: $\omega = \int_0^P \frac{q(P')}{A_S} dP'$ where $q(P')$ is the molar uptake at pressure P' and A_S is the surface area of the adsorbent.
    - This step converts the pure component data into a thermodynamic parameter used to predict the behaviour of the adsorbed mixture.
3. Determine Equilibrium Adsorbed Phase Composition
    - Apply the condition that, at equilibrium, the spreading pressures for each component in the mixture equal those in the pure systems.
    - Solve the resulting set of coupled, nonlinear equations iteratively (typically using numerical methods) to obtain the adsorbed phase mole fractions X_{CO_2} and X_{N_2}.
4. Compute Adsorbed Amounts
    - With the mole fractions determined, calculate the adsorbed amount for each component using: $q_i = X_i \times q_{\text{total}}$ where q_{total} is the total amount adsorbed.
5. Calculate Selectivity
    - The selectivity for CO_2 over N_2 is defined as the ratio of the normalized adsorbed amounts. In this formulation, selectivity is given by: $S_{CO_2/N_2} = \frac{(q_{CO_2}/q_{N_2})}{(y_{CO_2}/y_{N_2})}$ where q_{CO_2} and q_{N_2} are the molar amounts adsorbed of CO_2 and N_2, respectively, and y_{CO_2} and y_{N_2} are their corresponding gas-phase mole

fractions. This metric quantifies the sorbent's preferential adsorption of CO_2.

Appendix C: Model Fitting Algorithms and Error Functions

Error Functions for Isotherm Model Fitting

Error functions play a crucial role in evaluating the accuracy of adsorption isotherm models by quantifying the deviation between experimental data and predicted values. By minimizing these errors, researchers can determine the most suitable model for describing a specific adsorption system. Various statistical criteria are employed to assess the quality of fit, ensuring that the chosen model accurately represents adsorbate-adsorbent interactions. In this study, we utilize Origin software for model fitting, applying multiple error functions to evaluate adsorption isotherm models. [283,370]

Since different error functions emphasize various aspects of data fitting, no single criterion is universally superior. Therefore, multiple methods are often used in combination to enhance reliability. [283,370]

Degrees of Freedom

Degrees of freedom (df) refer to the number of independent data points available for model fitting after accounting for the number of parameters being estimated. It is calculated as:

$$df = N - p \qquad \textit{Equation 75}$$

where:

- N is the total number of experimental data points,
- p is the number of parameters in the model.

Degrees of freedom are crucial in statistical analysis because they determine the robustness of model predictions. A lower df value (i.e., a higher number of parameters relative to data points) increases the risk of overfitting, whereas a higher df value suggests a more generalizable model.

Coefficient of Determination (R^2)

The coefficient of determination measures how well the model explains the variability in the data. It is given by:

$$R^2 = 1 - \frac{RSS}{TSS} \qquad \textit{Equation 76}$$

where:

- RSS is the **Residual Sum of Squares**,
- TSS is the **Total Sum of Squares**.

An R^2 value close to 1 indicates a strong correlation between the predicted and experimental data. However, it should not be the sole criterion for model selection, as it does not account for overfitting.

Adjusted R²

The adjusted R^2 compensates for the number of parameters in the model, providing a more accurate measure of fit for models with different numbers of parameters:

$$\overline{R^2} = 1 - \frac{RSS/df_{Error}}{TSS/df_{Total}} \qquad \textit{Equation 77}$$

This metric prevents artificially high R^2 values due to overfitting by incorporating the degrees of freedom into the calculation.

Residual Sum of Squares (RSS)

The Residual Sum of Squares (RSS) quantifies the total squared deviation between the experimental and predicted values:

$$RSS = \sum_{i=1}^{N} w_i \left(q_{e,exp} - q_{e,mod}\right)^2 \qquad \textit{Equation 78}$$

where:

- $q_{e,exp}$ is the experimentally measured adsorbed amount,
- $q_{e,mod}$ is the model-predicted adsorbed amount,
- w_i is the weight assigned to each data point.

A lower RSS value indicates a better model fit, but it does not consider the number of parameters, potentially leading to overfitting.

Reduced Chi-Square (χ^2_{red})

The reduced chi-square error function accounts for the degrees of freedom in the system and is defined as:

$$\chi^2_{red} = \frac{RSS}{df_{Error}} \qquad \textit{Equation 79}$$

where df_{Error} is the number of degrees of freedom. This function helps compare models with different numbers of parameters, ensuring that improvements in fit are not due to overfitting.

Sum of Squares Error (SSE or ERRSQ)

SSE is a widely used error function but has the drawback of amplifying errors at higher adsorption pressures:

$$SSE = \sum_{i=1}^{N} \left(q_{e,exp} - q_{e,mod}\right)^2 \qquad \textit{Equation 80}$$

This metric is sensitive to outliers and may disproportionately favour models that fit high-pressure data points better.

Sum of Absolute Errors (SAE)

SAE is similar to SSE but measures absolute deviations instead of squared deviations:

$$SAE = \sum_{i=1}^{N} \left|q_{e,exp} - q_{e,mod}\right| \qquad \textit{Equation 81}$$

This function reduces the influence of large outliers, making it useful for systems where extreme deviations should not dominate the error evaluation.

Hybrid Fractional Error Function (HYBRID)

HYBRID improves upon SSE by normalizing errors at lower pressures, ensuring a more balanced fit across the full range of data:

$$HYBRID = \frac{100}{N-p} \sum_{i=1}^{N} \frac{\left(q_{e,exp} - q_{e,mod}\right)^2}{q_{e,exp}} \qquad \textit{Equation 82}$$

where $N - p$ represents the degrees of freedom. This function provides a more representative error distribution.

Marquardt's Percent Standard Deviation (MPSD)

$MPSD$ is based on the geometric mean of the error distribution and considers the degrees of freedom:

$$MPSD = \sqrt{\frac{1}{N-p}\sum_{i=1}^{N}\left(\frac{q_{e,exp}-q_{e,mod}}{q_{e,exp}}\right)^2} \times 100 \qquad \textit{Equation 83}$$

This metric is particularly useful in adsorption studies, as it ensures error minimization across all pressure ranges.

Average Relative Error (ARE)

ARE distributes errors more evenly over the entire dataset by focusing on relative deviations:

$$RE = \frac{100}{N}\sum_{i=1}^{N}\left|\frac{q_{e,exp}-q_{e,mod}}{q_{e,exp}}\right| \qquad \textit{Equation 84}$$

This function is effective for datasets with large variations in adsorption values.

Model Fitting Algorithms

Determining the optimal parameters for adsorption isotherms and kinetic models is a critical step in data analysis, and model fitting algorithms play an essential role in this process. These algorithms iteratively adjust the parameters of a model so that the predicted values best match the experimental data. In our work, we use Origin software, which offers several robust algorithms for nonlinear curve fitting. [370]

How Origin Fits Models

The general fitting procedure in Origin involves three key steps:

1. **Initial Guess:**
   An initial curve is generated using a set of starting parameter values. This guess serves as the starting point for the iterative process.
2. **Iterative Refinement:**
   The algorithm adjusts the parameter values step by step, reducing the differences between the experimental data and the model prediction.
3. **Convergence (Stopping Criteria):**
   The iteration stops when further adjustments no longer yield significant improvements in the fit, as defined by pre-set convergence criteria.

Least-Squares Algorithm

The foundation of most fitting routines is the least-squares method. This method minimizes the sum of the squared differences between the experimental data points and the values

predicted by the model. The objective function, often represented as the chi-square (χ^2) value, is given by [370]:

$$\chi^2 = \sum_{i=1}^{N} \left[\frac{Y_i - f(X_i, \beta)}{\sigma_i} \right]^2 \qquad \textit{Equation 85}$$

where:

- Y_i represents the experimental measurement at the i-th data point,
- $f(X_i, \beta)$ is the model's predicted value based on the independent variable X_i and the parameter set β,
- σ_i denotes the uncertainty (or standard deviation) associated with Y_i.

A smaller χ^2 indicates a closer match between the model and the experimental data.

Levenberg-Marquardt (L-M) Algorithm

The Levenberg-Marquardt (L-M) algorithm is the most commonly used method in Origin for nonlinear curve fitting. It combines two approaches:

- Gauss-Newton Method: Efficient when the initial parameter guess is already close to the optimum.
- Steepest Descent Method: Provides robustness when the initial guess is far from the optimum.

This hybrid approach iteratively updates the parameter vector β\betaβ to minimize χ^2, making it suitable for many nonlinear adsorption models. [371]

Downhill Simplex Algorithm

Also known as the Nelder-Mead algorithm, the Downhill Simplex method is a derivative-free optimization technique. Instead of relying on gradient information, it adjusts a geometrical shape (a "simplex") formed by $N + 1$ points in an N-dimensional parameter space. This method is particularly useful when derivatives are difficult to compute or when the initial guess is uncertain. However, it generally converges more slowly compared to the L-M algorithm. [372,373]

Orthogonal Distance Regression (ODR)

The Orthogonal Distance Regression (ODR) algorithm takes a different approach by minimizing the orthogonal (i.e., perpendicular) distances between the data points and the

fitted curve. This is especially important when both the independent variable (e.g., pressure) and the dependent variable (e.g., adsorption amount) contain measurement errors. The ODR algorithm adjusts both the parameter values and the independent variable values. Its objective function can be expressed as [374]:

$$\min_{\beta,\,\delta_i,\,\epsilon_i} \sum_{i=1}^{N} \left(w_{xi}\,\delta_i^2 + w_{yi}\,\epsilon_i^2 \right) \qquad \textit{Equation 86}$$

subject to the constraint for each data point:

$$Y_i = f(X_i + \delta_i, \beta) - \epsilon_i \qquad \textit{Equation 87}$$

Here, δ_i and ϵ_i represent the adjustments (or residuals) for the independent and dependent variables, respectively, while w_{xi} and w_{yi} are the corresponding weighting factors.

Table 43 - Comparison of Fitting Algorithms

Algorithm	Strengths	Weaknesses
Levenberg-Marquardt (L-M)	Fast convergence when starting near the optimum; widely used and reliable.	Can be sensitive to poor initial guesses.
Downhill Simplex (Nelder-Mead)	Does not require derivatives; robust when the initial guess is uncertain.	Typically, slower convergence and may be less precise near the optimum.
Orthogonal Distance Regression (ODR)	Accounts for errors in both independent and dependent variables.	More computationally intensive and complex.

Choosing the Right Algorithm

- **Levenberg-Marquardt (L-M):**
  Ideal when you have a good initial parameter estimate and when a standard nonlinear least-squares fit is sufficient.
- **Downhill Simplex:**
  Preferable when derivative information is not available or reliable, or when the initial parameter estimates are uncertain.
- **Orthogonal Distance Regression (ODR):**
  Best suited for cases where measurement errors in both the independent and dependent variables need to be considered.

By carefully selecting the appropriate algorithm, we can achieve accurate model fits, thereby enhancing the reliability and interpretability of adsorption studies.

Appendix D: Thermogravimetric Analysis (TGA) Proximate Analysis Curves

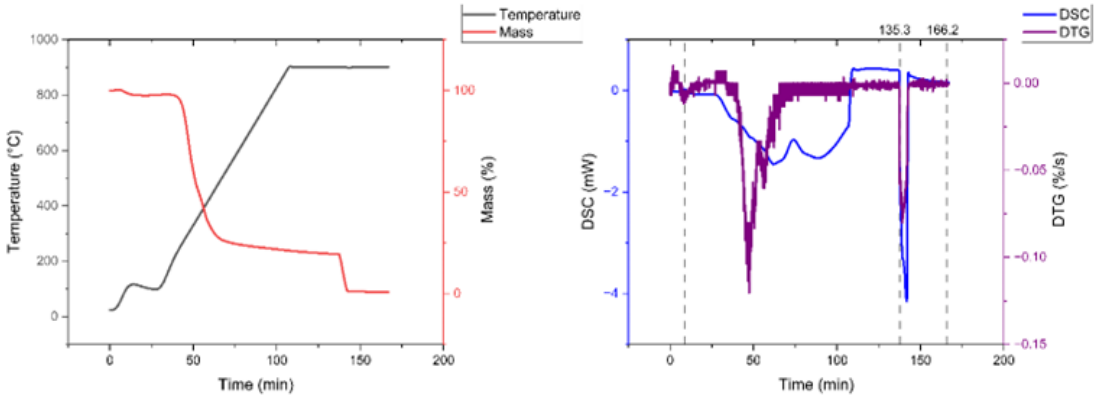

Figure 94 - TG and Derivative Thermogravimetry (DTG) curves from TGA proximate analysis of SCG sample. Dashed vertical lines mark the temperature intervals used for determination of proximate analysis fractions.

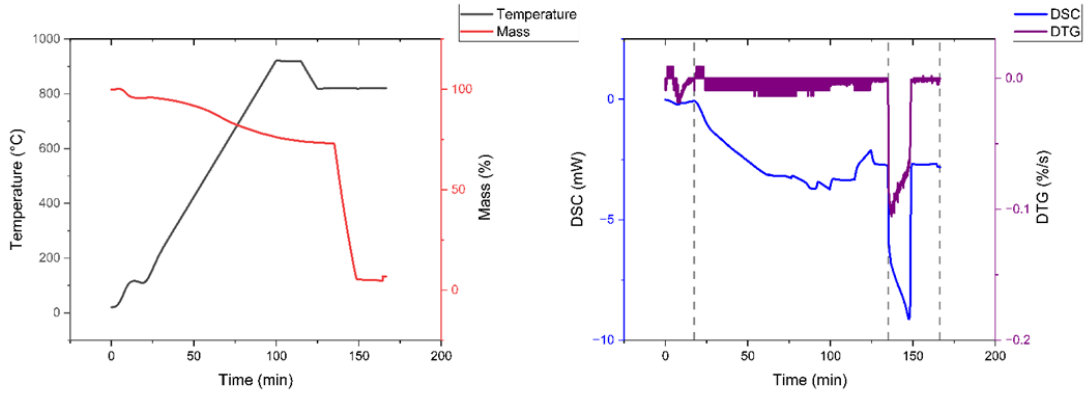

Figure 95 - TG and DTG curves from TGA proximate analysis of sample EX4-N2-500-2H. Dashed vertical lines mark the temperature intervals used for determination of proximate analysis fractions.

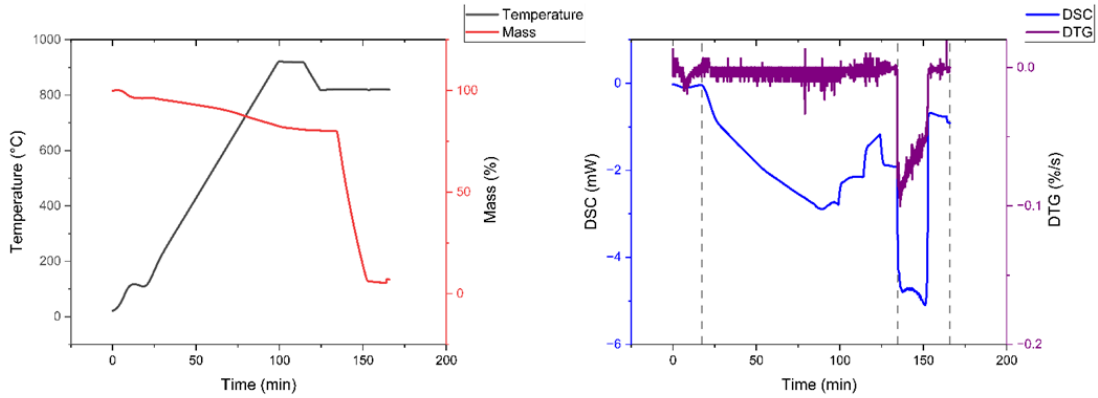

Figure 96 - TG and DTG curves from TGA proximate analysis of sample EX5-N2-500-2H. Dashed vertical lines mark the temperature intervals used for determination of proximate analysis fractions.

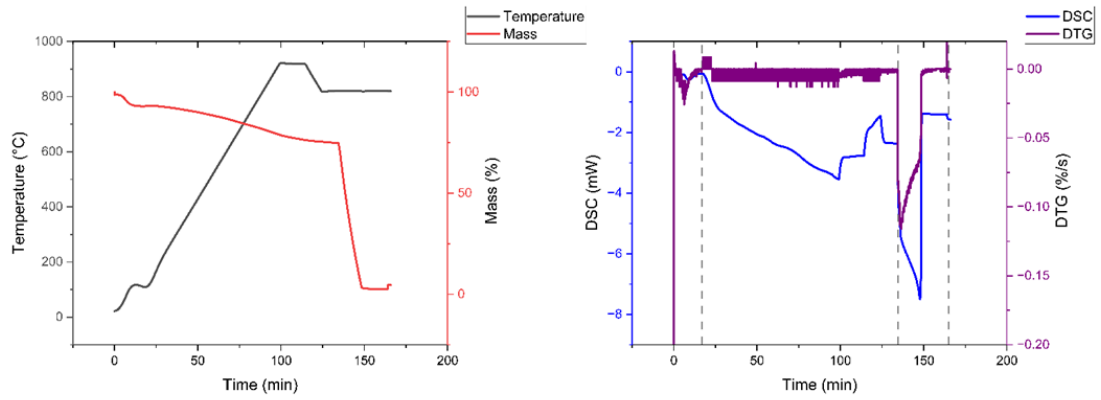

Figure 97 - TG and DTG curves from TGA proximate analysis of sample EX23-800-2H-KOH-1:1. Dashed vertical lines mark the temperature intervals used for determination of proximate analysis fractions.

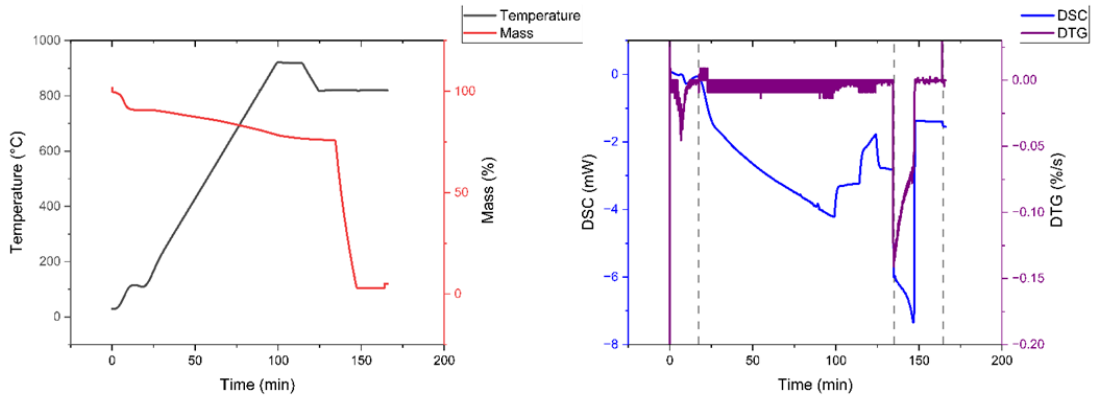

Figure 98 - TG and DTG curves from TGA proximate analysis of sample EX25-900-2H-KOH-1:1. Dashed vertical lines mark the temperature intervals used for determination of proximate analysis fractions

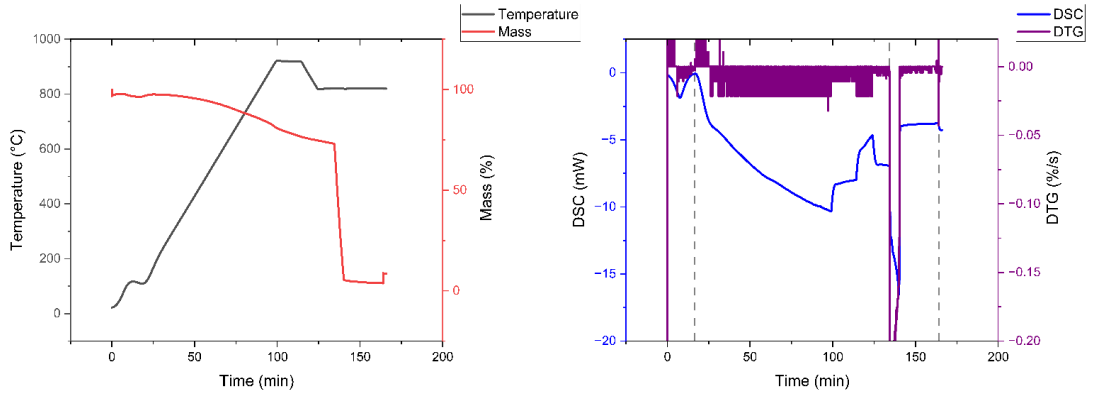

Figure 99 - TG and DTG curves from TGA proximate analysis of sample EX31-900-2H-KOH-1:8. Dashed vertical lines mark the temperature intervals used for determination of proximate analysis fractions.

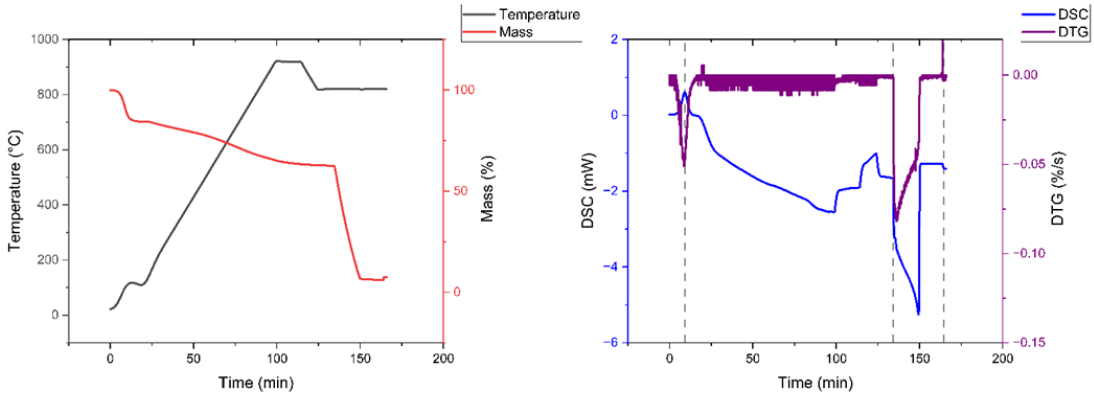

Figure 100 - TG and DTG curves from TGA proximate analysis of sample EX42-700-15-KOH-1:1. Dashed vertical lines mark the temperature intervals used for determination of proximate analysis fractions.

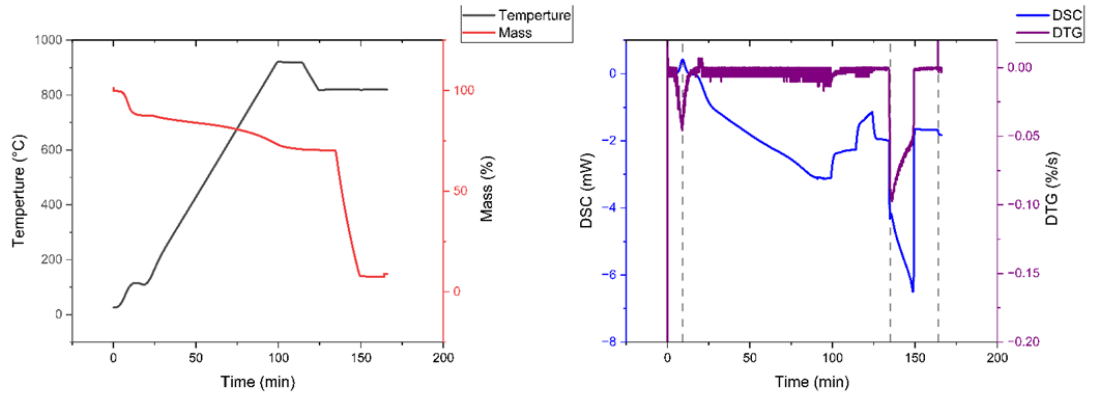

Figure 101 - TG and DTG curves from TGA proximate analysis of sample EX37-850-15-CO2-600. Dashed vertical lines mark the temperature intervals used for determination of proximate analysis fractions.

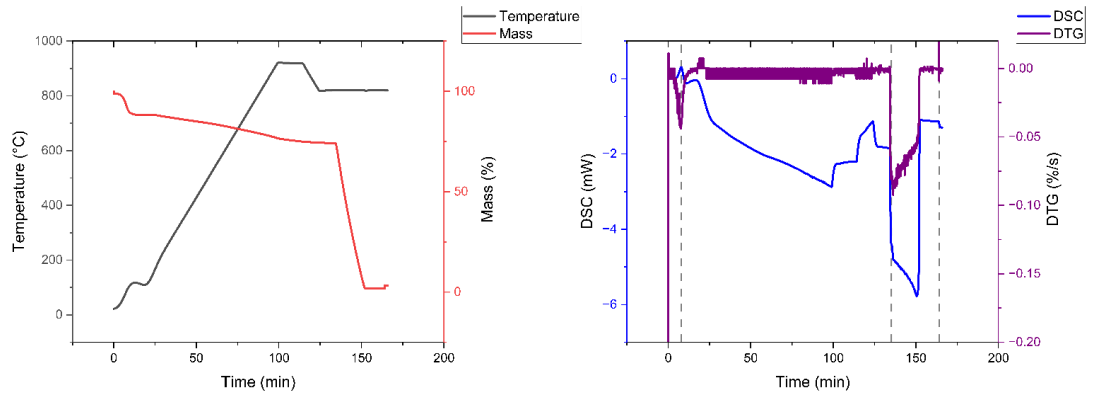

Figure 102 - TG and DTG curves from TGA proximate analysis of sample EX53-900-2H-KOx-1:1 (pre-pyrolyzed). Dashed vertical lines mark the temperature intervals used for determination of proximate analysis fractions.

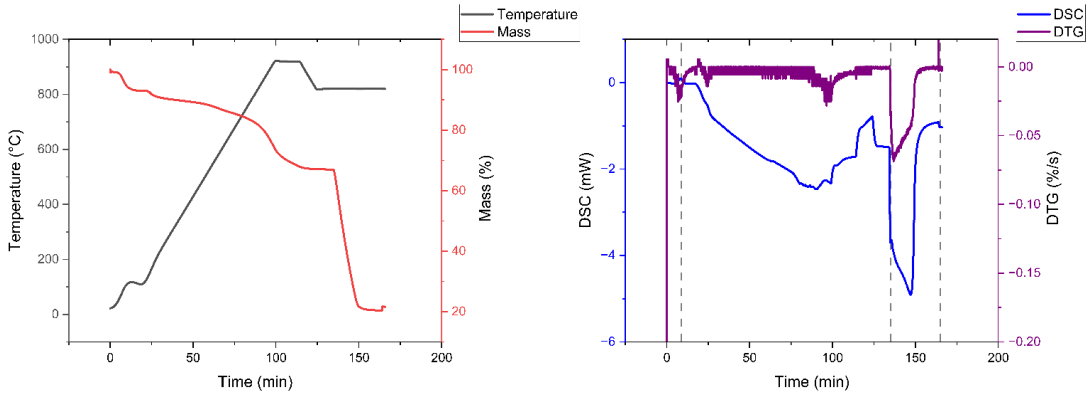

Figure 103 - TG and DTG curves from TGA proximate analysis of sample EX81-700-2H-GO. Dashed vertical lines mark the temperature intervals used for determination of proximate analysis fractions.

Appendix E: XPS Survey Spectra

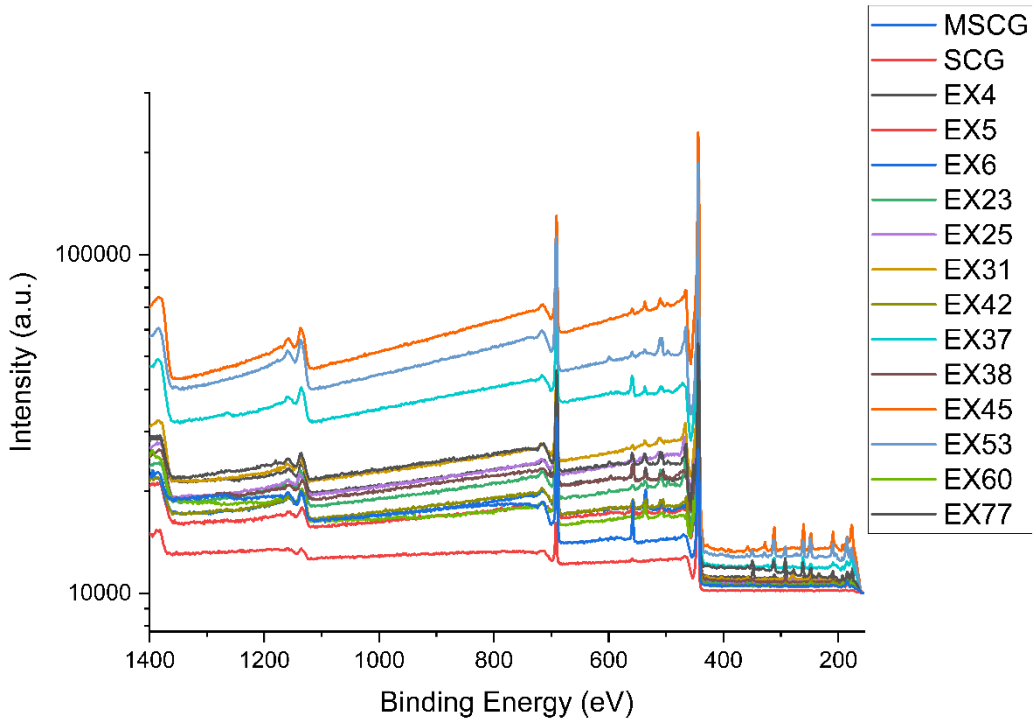

Figure 104 - Stacked X-ray photoelectron spectroscopy (XPS) survey spectra of raw spent coffee grounds (SCG), MSCG, and selected biochar samples. Spectra are displayed with vertical offsets for clarity.

Appendix F: XPS Peak Deconvolution Spectra

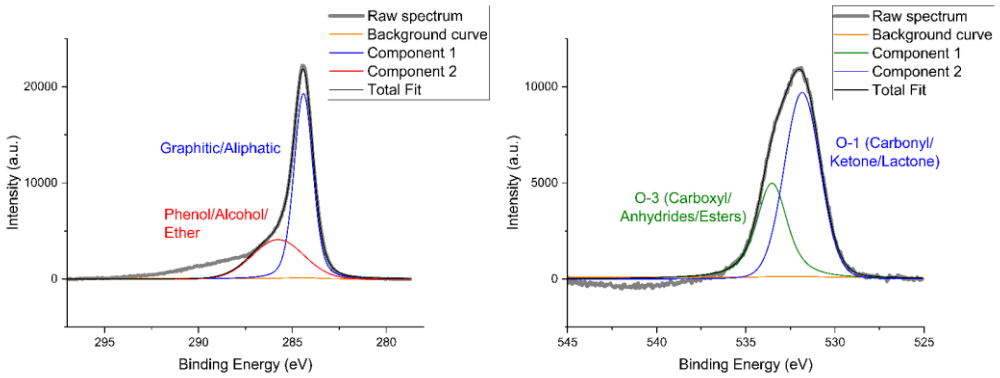

Figure 105 - High-resolution XPS spectra of EX25-900-2H-KOH-1:1 showing (a) C1s and (b) O1s core-level regions with peak deconvolution. The C1s spectrum was resolved into graphitic/aliphatic carbon (C–C/C–H) and oxygenated carbon species (phenol/alcohol/ether).

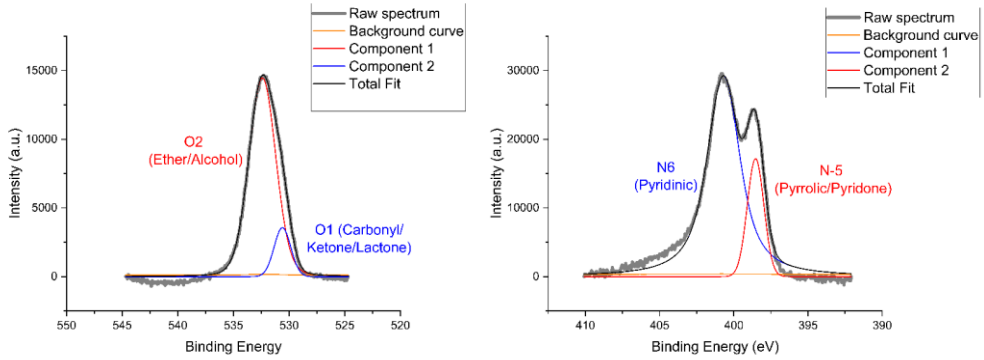

Figure 106 - High-resolution XPS spectra of EX37-850-15-CO_2-600 showing (a) O1s and (b) N1s core-level regions with peak deconvolution. The O1s spectrum was fitted with components attributed to ether/alcohol (C–O) and carbonyl/lactone (C=O) functionalities. The N1

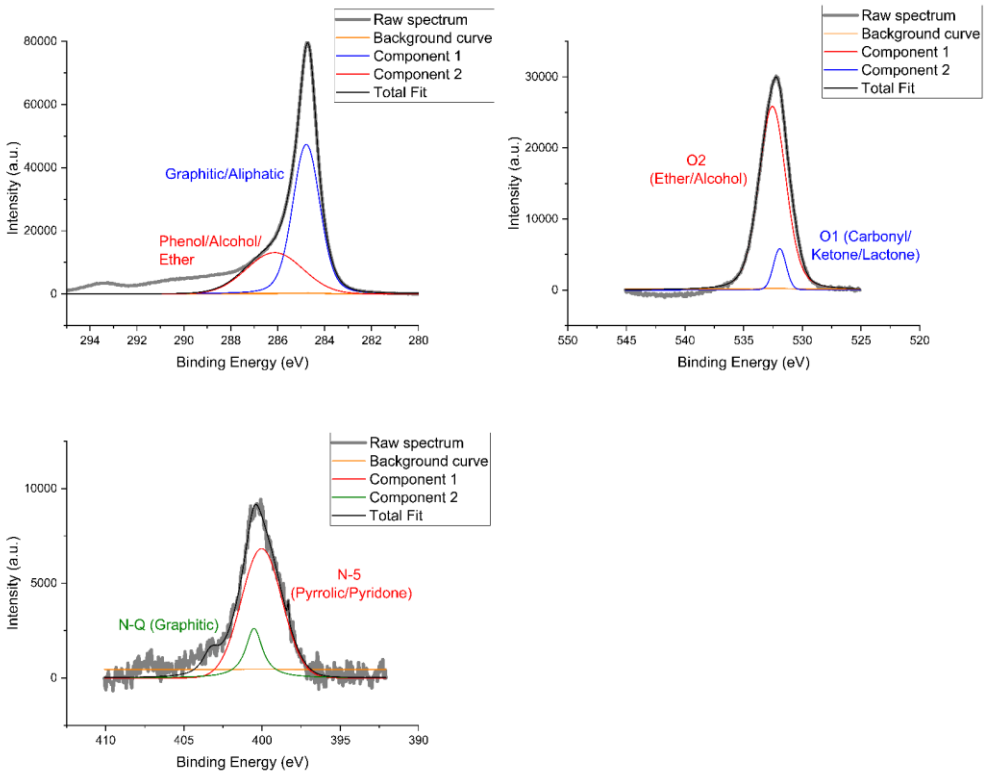

Figure 107 - High-resolution XPS spectra of theEX45-900-2H-KOx-1:1 showing peak deconvolution of the (a) C1s, (b) O1s, and (c) N1s core-level regions. The C1s spectrum was resolved into C–C/C–H (graphitic/aliphatic carbon) and C–O (phenolic/alcohol/ether) contri

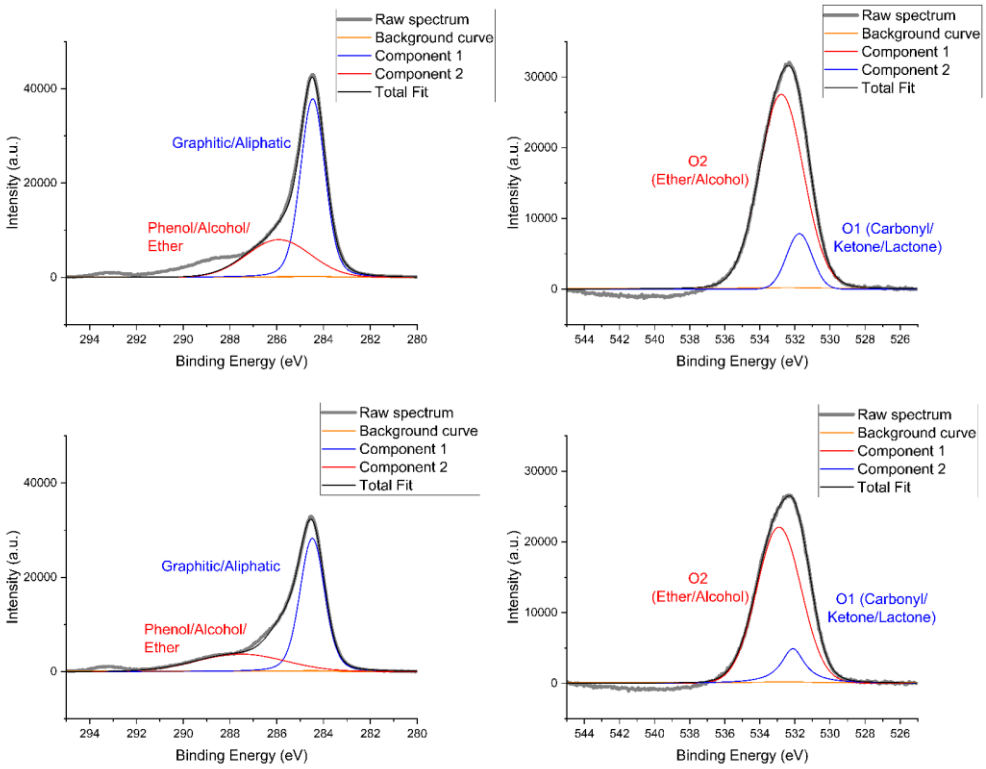

Figure 108 - High-resolution XPS spectra showing peak deconvolution of EX53-900-2H-KOx-1:1 (pre-pyrolyzed). C1s (left) and O1s (right) core-level regions for two representative samples (top and bottom). The C1s spectra were resolved into C–C/C–H (graphitic/aliphatic carbon) and C–O (phenolic/alcohol/ether) contributions. The O1s spectra were fitted with components attributed to C–O (ether/alcohol) and C=O (carbonyl/ketone/lactone) functionalities. A Shirley background was applied in all cases, and the total fit is shown together with the individual component peaks.

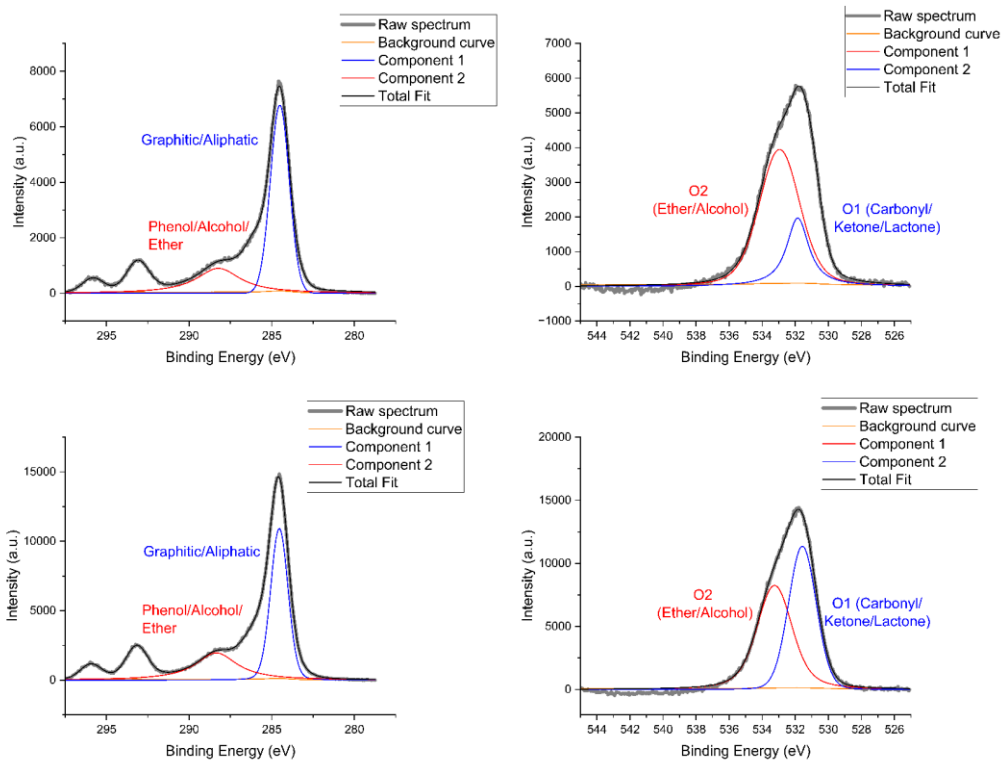

Figure 109 - High-resolution XPS spectra of EX60-1200-68-KOx-1:4.5 showing peak deconvolution of the C1s (left) and O1s (right) core-level regions for two measurements (top and bottom). The C1s spectra were resolved into C–C/C–H (graphitic/aliphatic carbon) and C–O (phenolic/alcohol/ether) contributions. The O1s spectra were fitted with components attributed to C–O (ether/alcohol) and C=O (carbonyl/ketone/lactone) functionalities. A Shirley background was applied in all cases, and the total fit is shown together with the individual component peaks.

Appendix G: N_2 Isotherm Plots

Non-Activated Samples

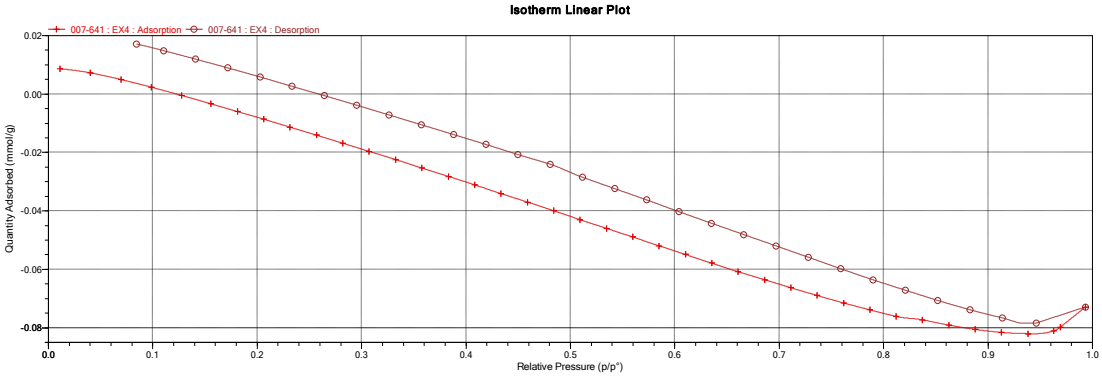

Figure 110 - N_2 adsorption–desorption isotherm of EX4-N_2-500-2H. The negligible uptake across the relative pressure range indicates minimal porosity development. The slight downward trend arises from buoyancy and baseline correction effects that become prominent at very low adsorption capacities, consistent with a non-activated, low-surface-area carbon.

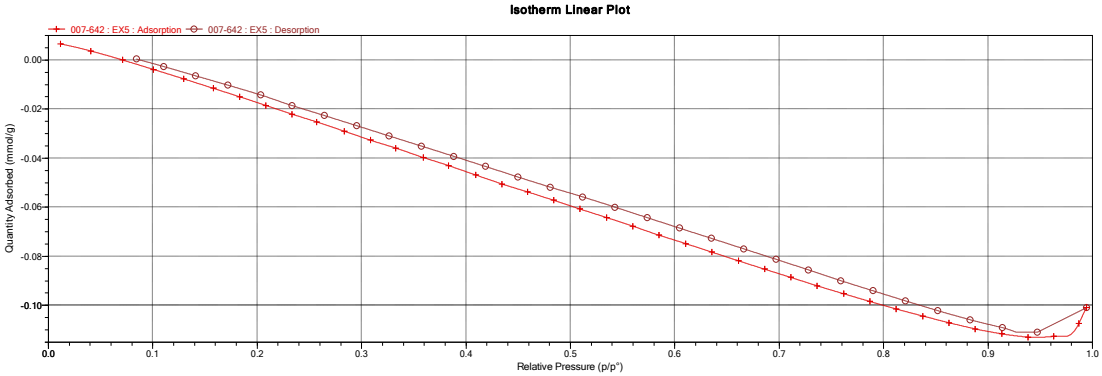

Figure 111 - N_2 adsorption–desorption isotherm of EX5-N_2-700-2H. Very limited nitrogen uptake is observed, confirming the absence of significant pore development without activation. The apparent negative slope reflects baseline and buoyancy correction artefacts typical of ultra-low surface area materials.

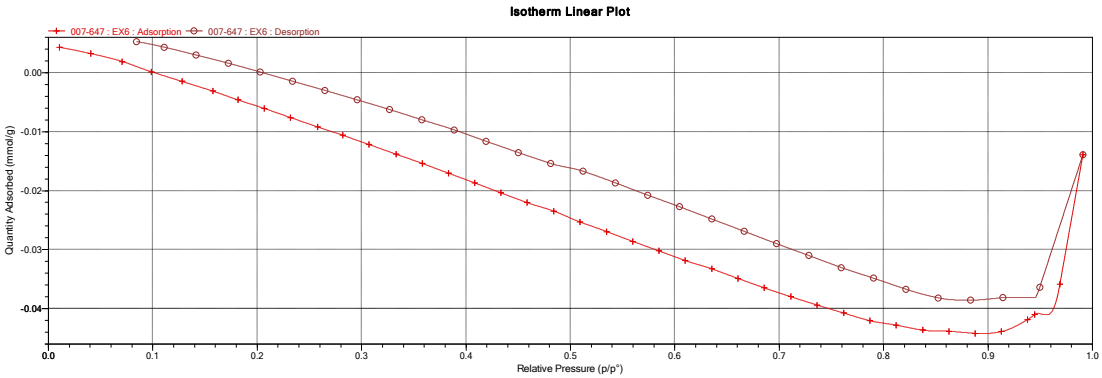

Figure 112 - N_2 adsorption–desorption isotherm of EX6-N_2-900-2H. The near-flat isotherm and minimal adsorption indicate negligible accessible porosity. Minor signal drift is attributed to buoyancy correction effects, which dominate when adsorption capacity is extremely low.

CO_2 Activated Samples

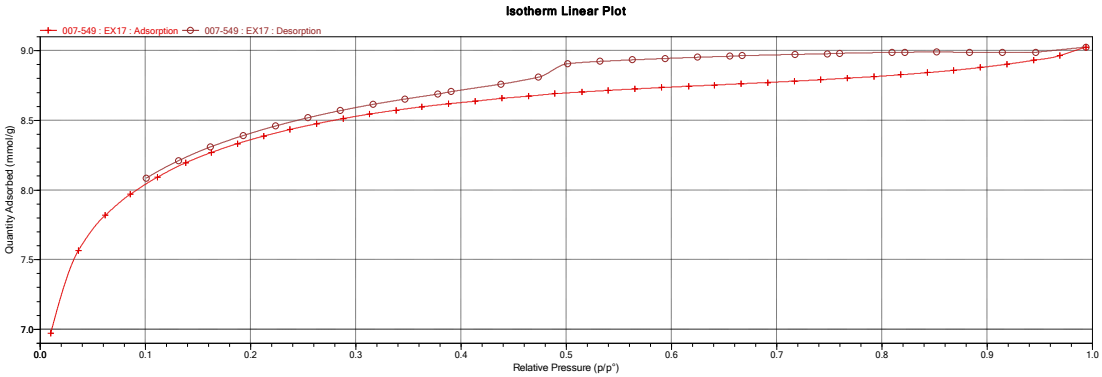

Figure 113 – N_2 adsorption–desorption isotherm of EX17-900-2H-CO_2-100 exhibiting Type I(b) behaviour.

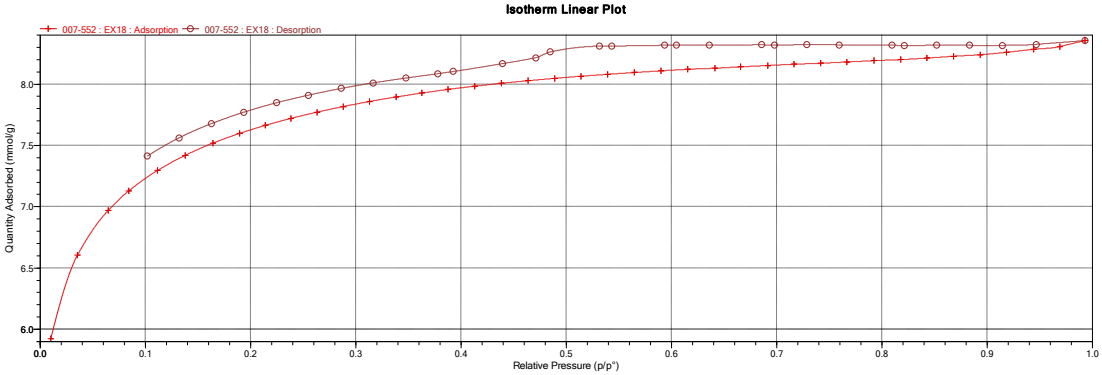

Figure 114 – N_2 adsorption–desorption isotherm of EX18-800-2H-CO_2-100 exhibiting Type I(b) behaviour.

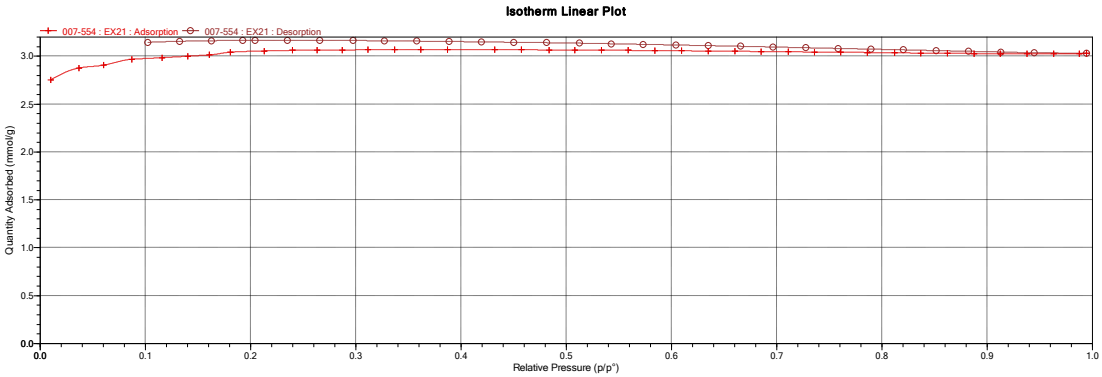

Figure 115 - N_2 adsorption–desorption isotherm (Type I(a) of EX21-700-2H-CO_2-600, indicating a predominantly microporous structure.

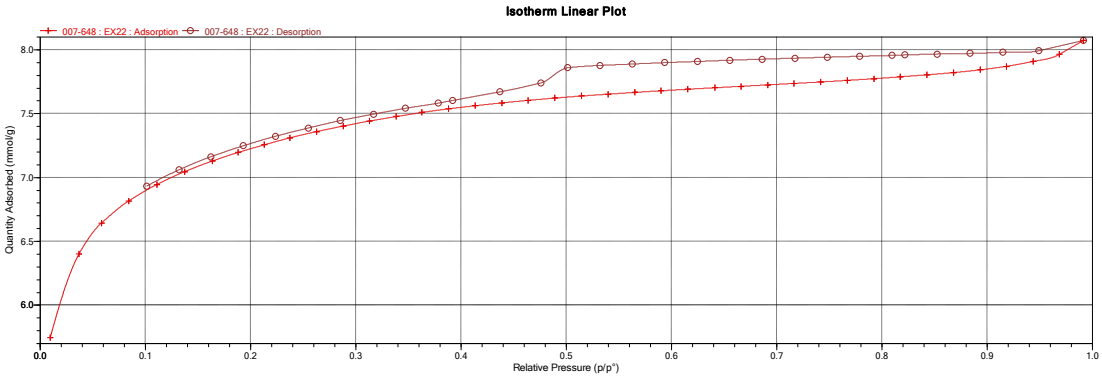

Figure 116 - N_2 adsorption–desorption isotherm of EX22-800-2H-CO_2-600 exhibiting Type I(b) behaviour.

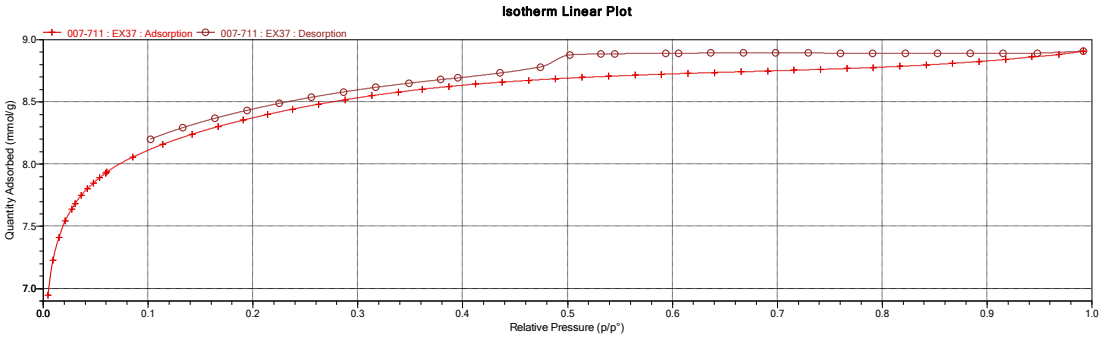

Figure 117 - N_2 adsorption–desorption isotherm of EX37-850-15-CO_2-600 exhibiting Type I(b) behaviour.

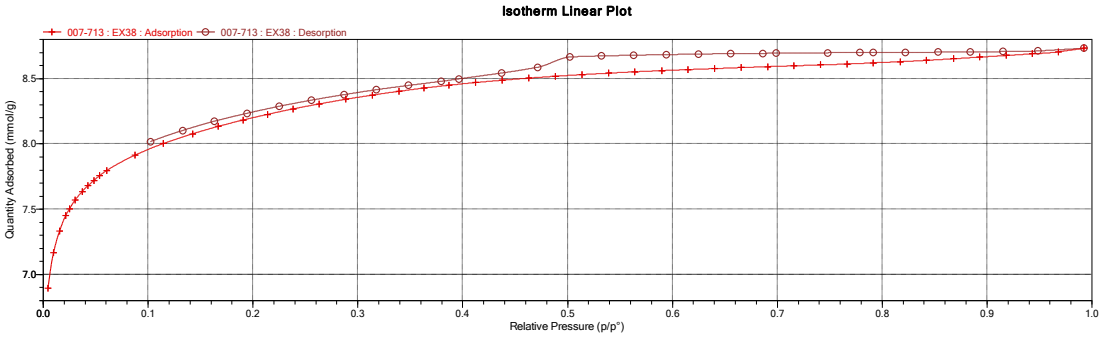

Figure 118 - N_2 adsorption–desorption isotherm of EX38-850-15-CO_2-100 exhibiting Type I(b) behaviour.

KOH Activated Samples

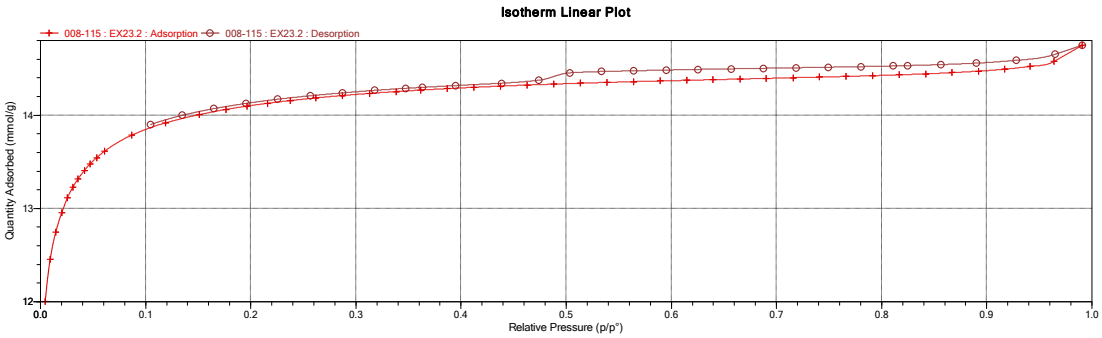

Figure 119 - N_2 adsorption–desorption isotherm of EX23-800-2H-KOH-1:1 showing Type I(b) behaviour with minor hysteresis, indicating a predominantly microporous structure with limited narrow mesoporosity.

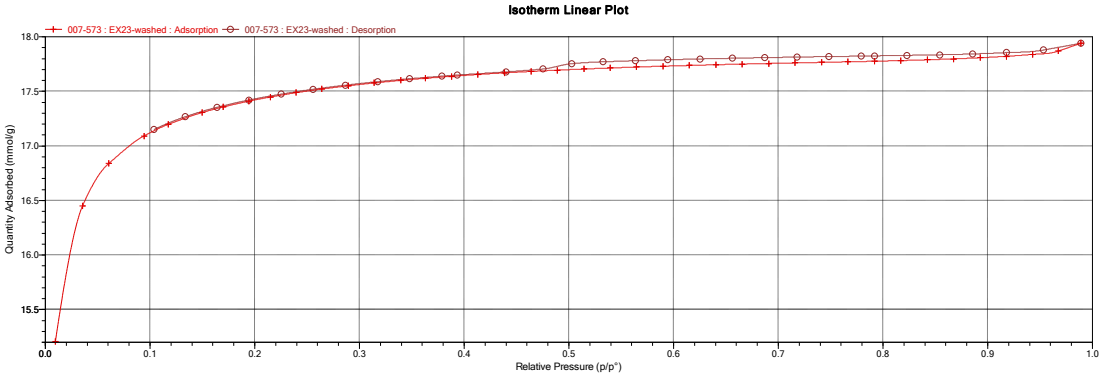

Figure 120 - N_2 adsorption–desorption isotherm of EX23.2-800-2H-KOH-1:1 showing Type I(b) behaviour with minor hysteresis, indicating a predominantly microporous structure with limited narrow mesoporosity.

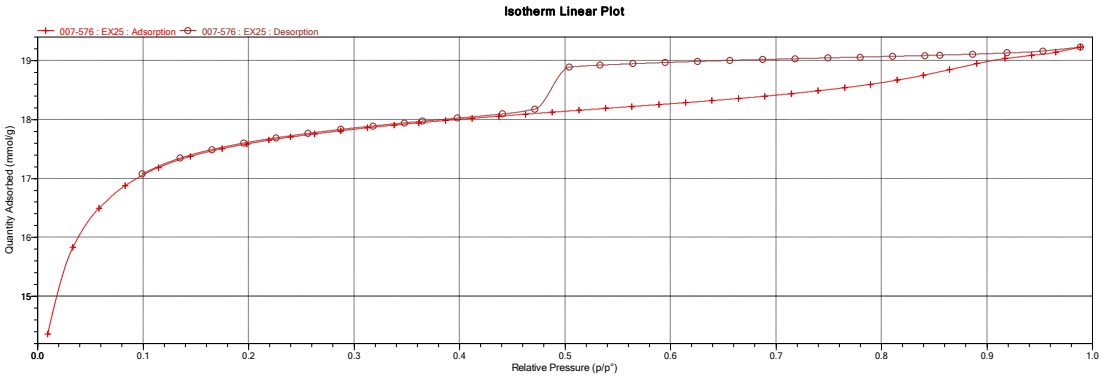

Figure 121 - N_2 adsorption–desorption isotherm of EX25-900-2H-KOH-1:1 showing Type I(b) behaviour with minor hysteresis, indicating a predominantly microporous structure with limited narrow mesoporosity

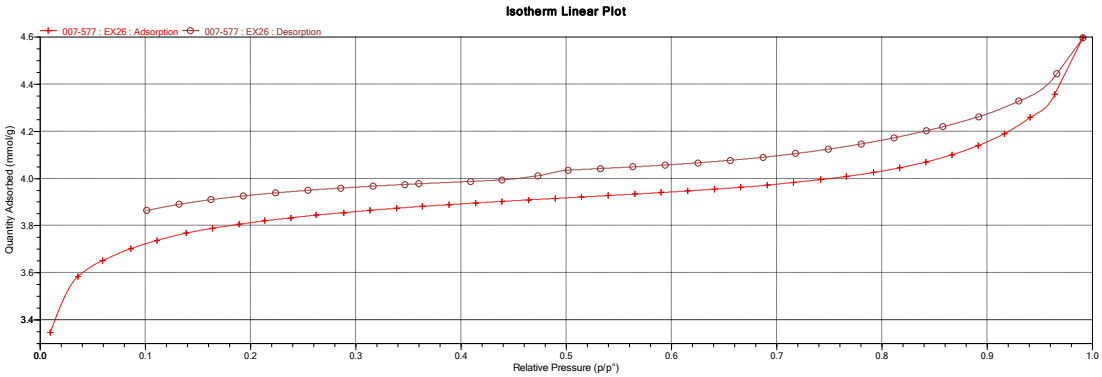

Figure 122 - N_2 adsorption–desorption isotherm of EX26-500-2H-KOH-1:1 showing Type IV(a) behaviour with hysteresis, indicating combined micro–mesoporosity.

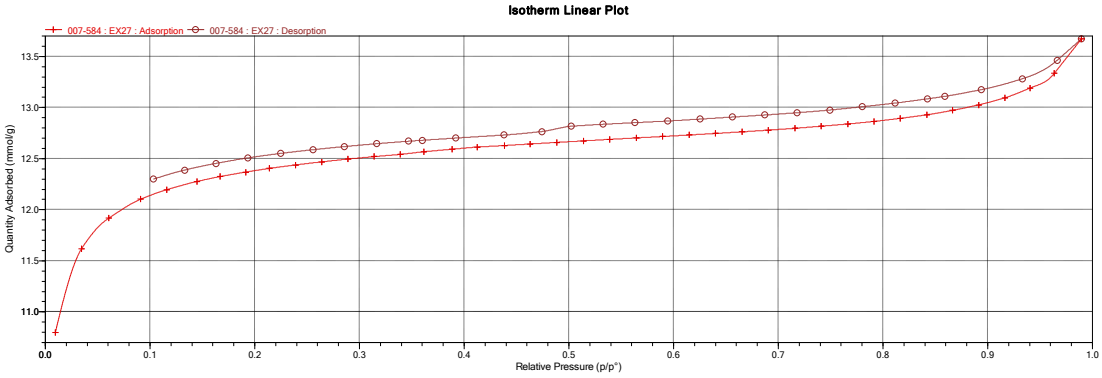

Figure 123 - N_2 adsorption–desorption isotherm of EX27-700-2H-KOH-1:1 showing Type IV(a) behaviour with hysteresis, indicating combined micro–mesoporosity.

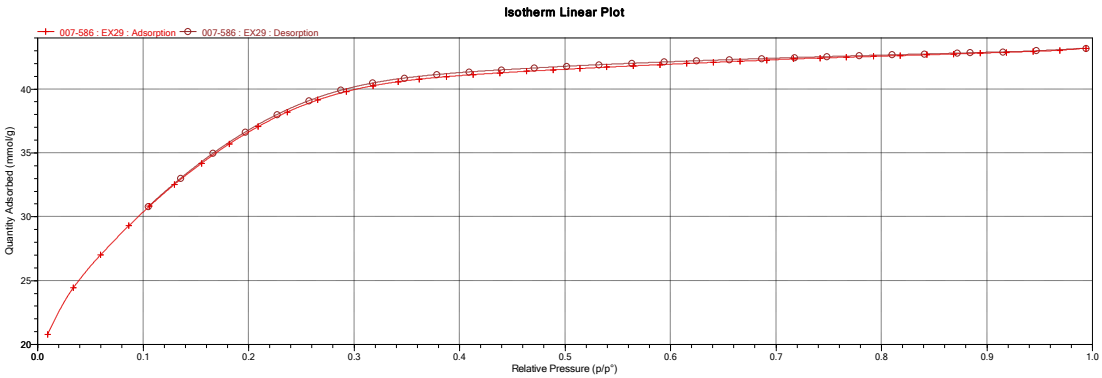

Figure 124 - N_2 adsorption–desorption isotherm of EX29-700-2H-KOH-1:8 exhibiting Type I(b) behaviour, indicating predominantly microporous structure with some wider micropores.

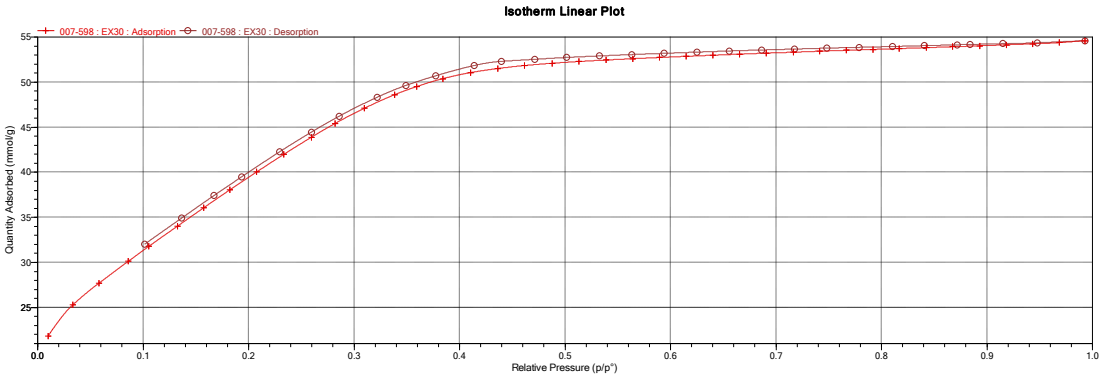

Figure 125 - N_2 adsorption–desorption isotherm of EX30-800-2H-KOH-1:8 exhibiting Type I(b) behaviour, indicating predominantly microporous structure with some wider micropores.

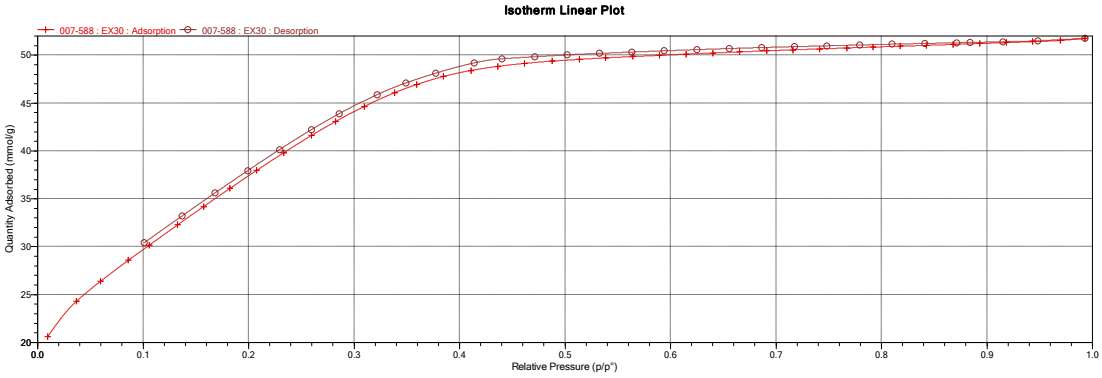

Figure 126 - N_2 adsorption–desorption isotherm of EX30.2-800-2H-KOH-1:8exhibiting Type I(b) behaviour, indicating predominantly microporous structure with some wider micropores.

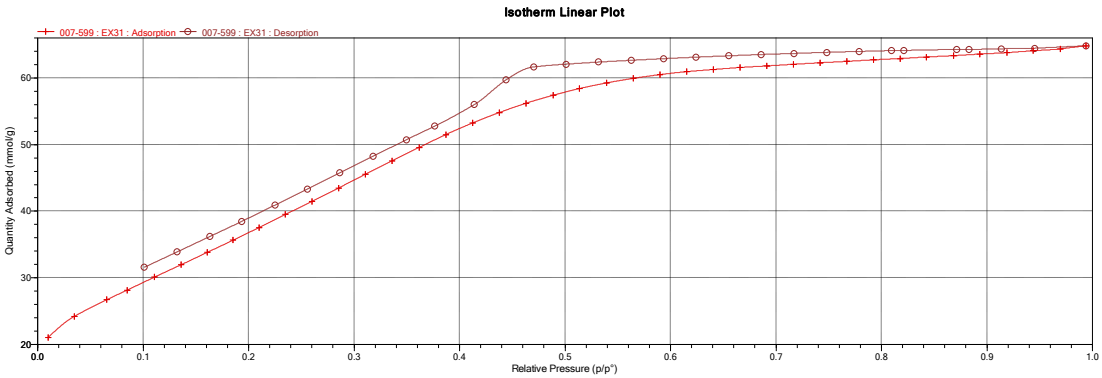

Figure 127 - N_2 adsorption–desorption isotherm of EX31-900-2H-KOH-1:8 showing Type IV(a) behaviour with minor hysteresis, indicating combined micro–mesoporosity.

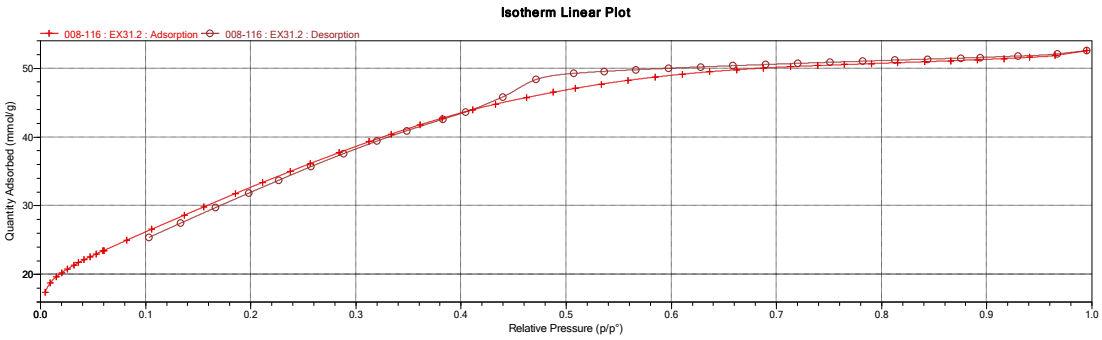

Figure 128 - N_2 adsorption–desorption isotherm of EX31.2-900-2H-KOH-1:8 showing Type IV(a) behaviour with minor hysteresis, indicating combined micro–mesoporosity.

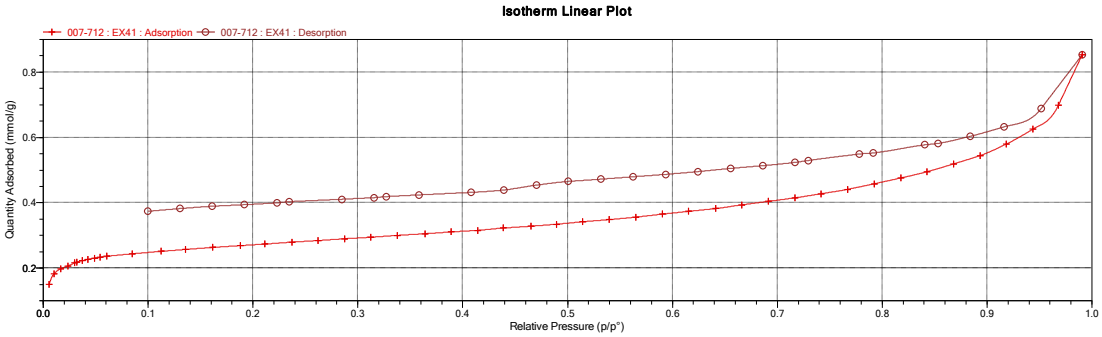

Figure 129 - N_2 adsorption–desorption isotherm of EX41-1000-15-KOH-1:1 exhibiting Type IV(a) behaviour with hysteresis, indicating combined micro–mesoporosity with significant mesopore contribution.

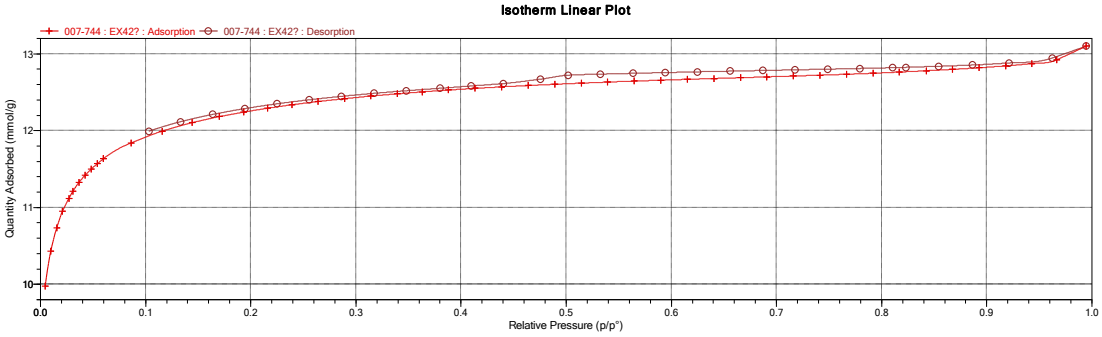

Figure 130 - N_2 adsorption–desorption isotherm of EX42-700-15-KOH-1:1 exhibiting Type I(b) behaviour, indicating predominantly microporous structure with some wider micropores.

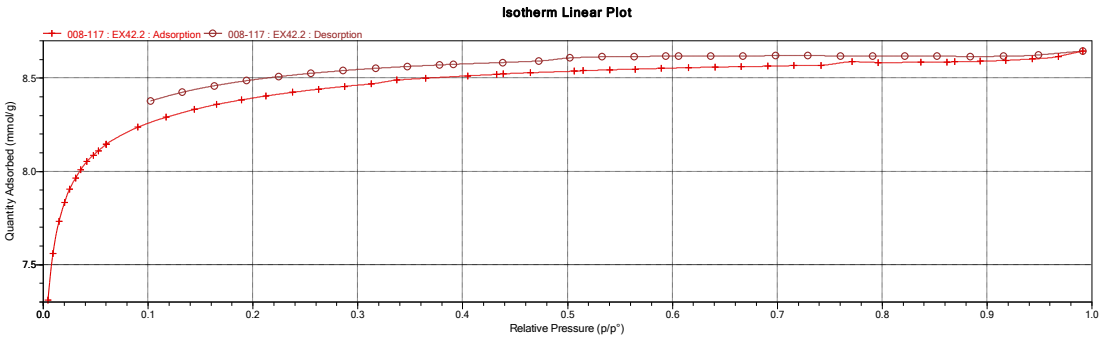

Figure 131 - N_2 adsorption–desorption isotherm of EX42.2-700-15-KOH-1:1 exhibiting Type I(b) behaviour, indicating predominantly microporous structure with some wider micropores.

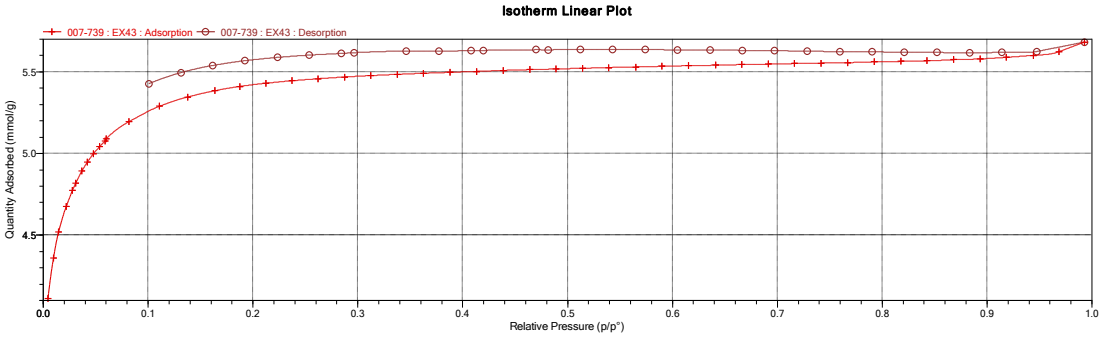

Figure 132 - N_2 adsorption–desorption isotherm EX43-1000-15-KOH-1:8 exhibiting Type I(b) behaviour, indicating predominantly microporous structure with some wider micropores.

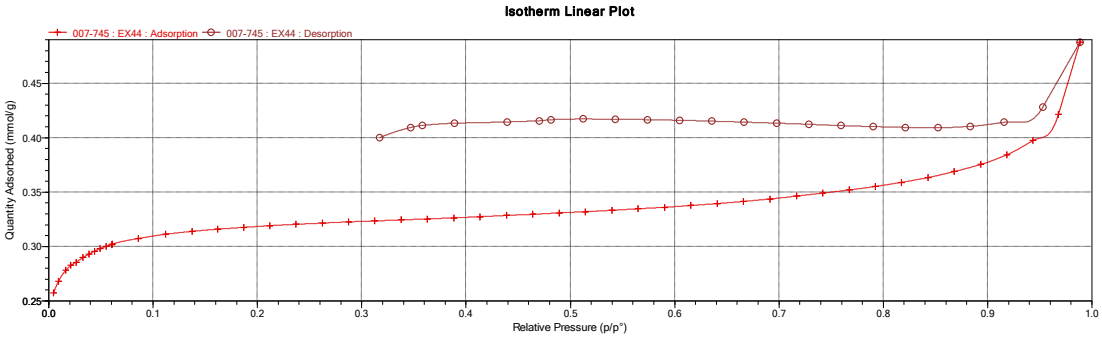

Figure 133 - adsorption–desorption isotherm of EX44-700-15-KOH-1:8 exhibiting Type IV(a) behaviour with hysteresis, indicating combined micro–mesoporosity with significant mesopore contribution.

KOx Activated Sample

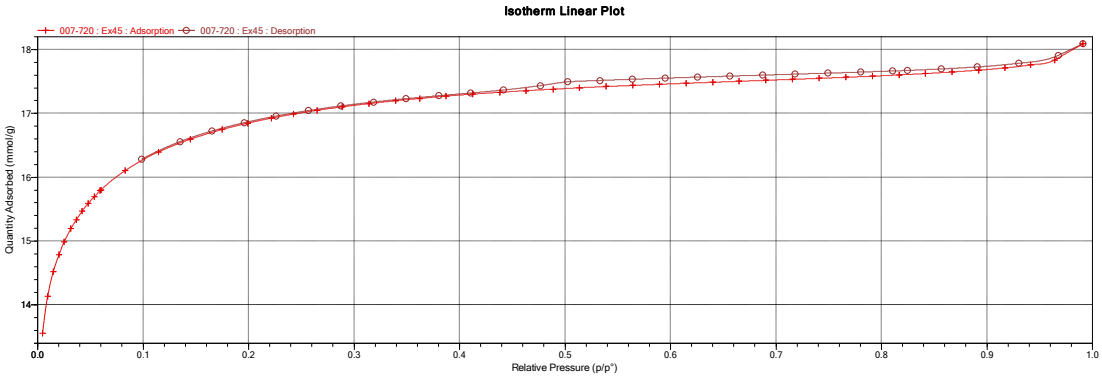

Figure 134 - N_2 adsorption–desorption isotherm EX45-900-2H-KOx-1:1 exhibiting Type I(b) behaviour, indicating predominantly microporous structure with some wider micropores.

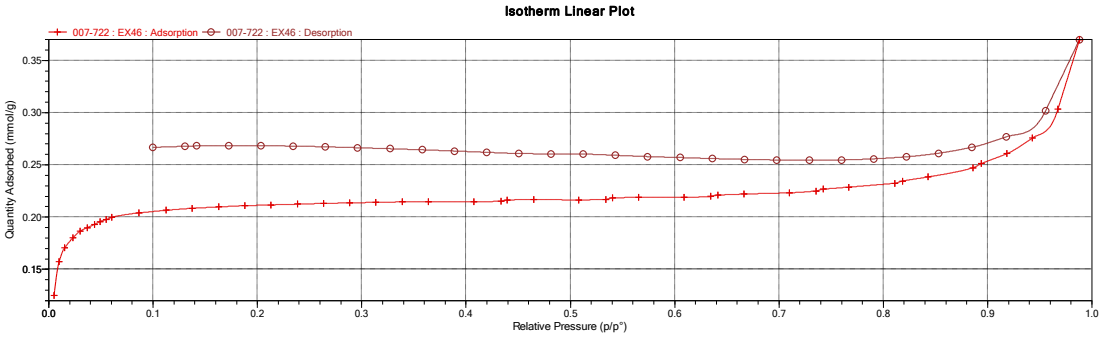

Figure 135 - N_2 adsorption–desorption isotherm of EX46-500-2H-KOx-1:1 exhibiting Type IV(a) behaviour with hysteresis, indicating combined micro–mesoporosity with significant mesopore contribution.

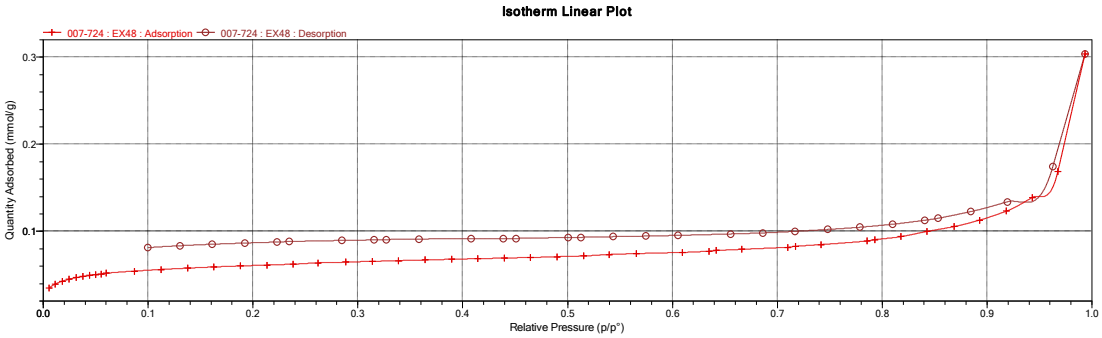

Figure 136 - N_2 adsorption–desorption isotherm of EX48-500-15-KOx-1:1 exhibiting Type IV(a) behaviour with hysteresis, indicating combined micro–mesoporosity with significant mesopore contribution.

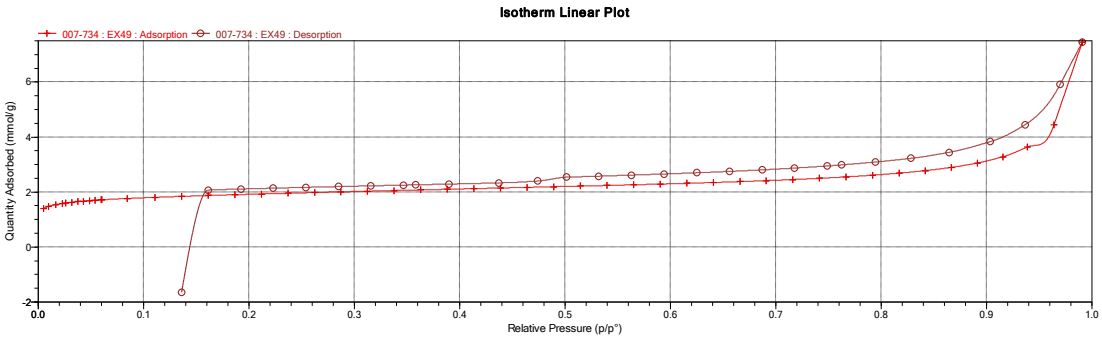

Figure 137 - N_2 adsorption–desorption isotherm of EX49-900-15-KOx-1:8 exhibiting Type IV(a) behaviour with hysteresis, indicating combined micro–mesoporosity with significant mesopore contribution.

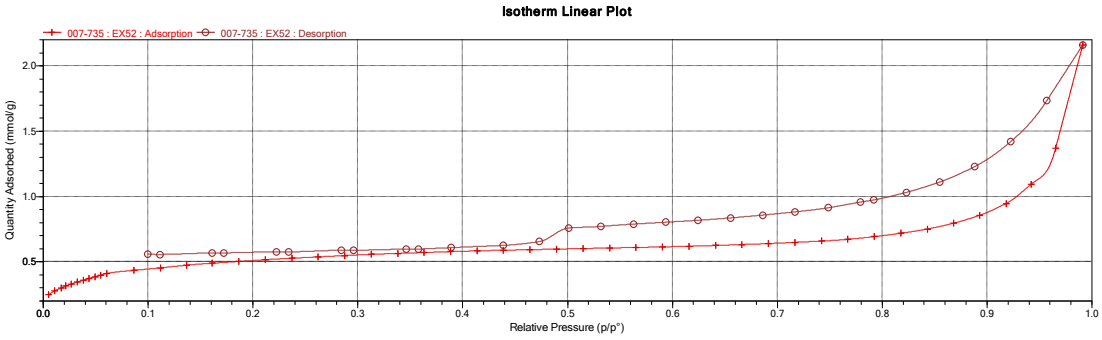

Figure 138 - N_2 adsorption–desorption isotherm of EX52-500-2H-KOx-1:8 exhibiting Type IV(a) behaviour with hysteresis, indicating combined micro–mesoporosity with significant mesopore contribution.

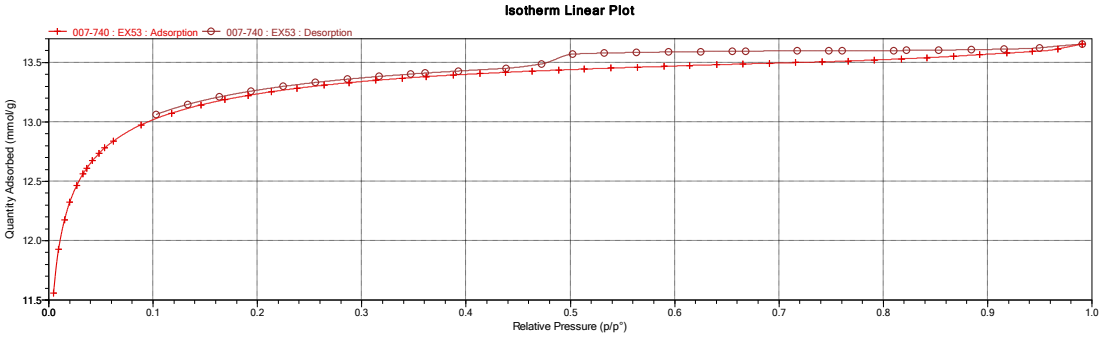

Figure 139 - N_2 adsorption–desorption isotherm EX53-900-2H-KOx-1:1 (pre-pyrolyzed) exhibiting Type I(b) behaviour, indicating predominantly microporous structure with some wider micropores.

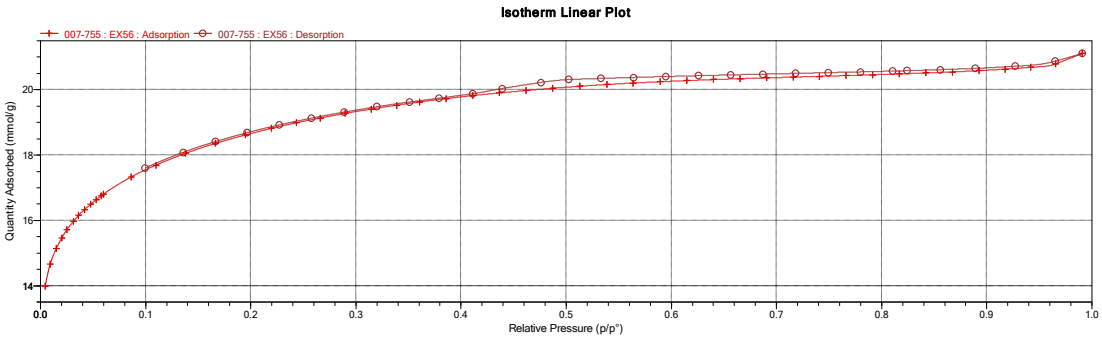

Figure 140 - N_2 adsorption–desorption isotherm EX56-1000-2H-KOx-1:1 exhibiting Type I(b) behaviour, indicating predominantly microporous structure with some wider micropores.

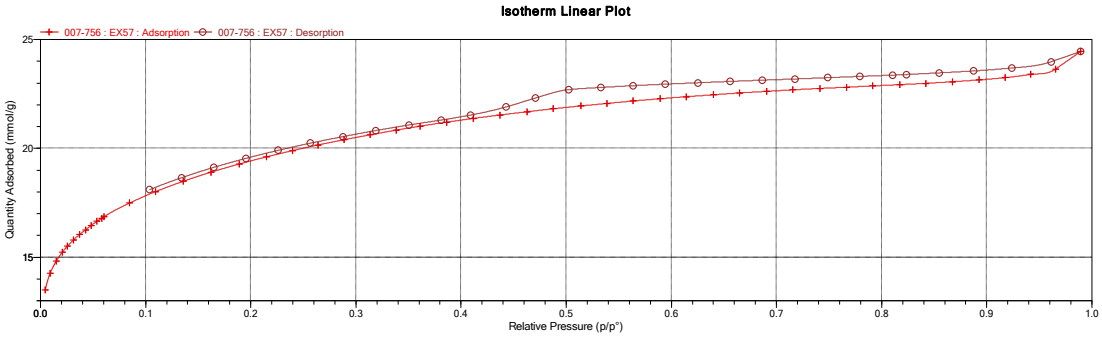

Figure 141 - N_2 adsorption–desorption isotherm EX57-900-2H-KOx-1:1 exhibiting Type I(b) behaviour, indicating predominantly microporous structure with some wider micropores.

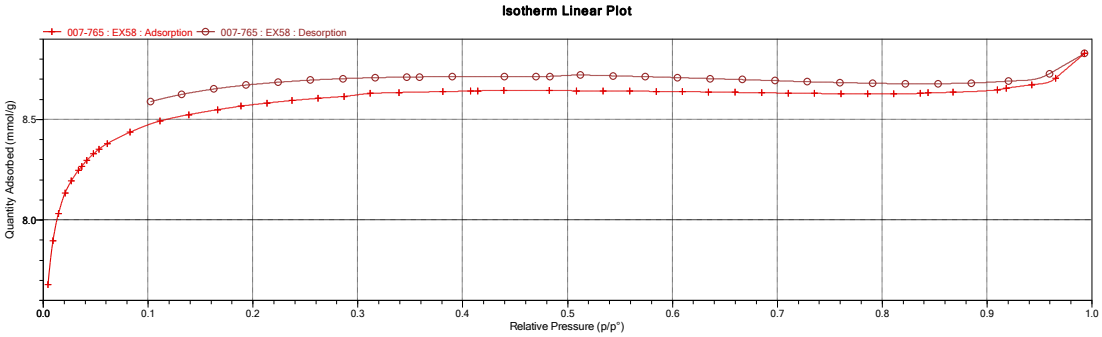

Figure 142 - N_2 adsorption–desorption isotherm of EX58-1100-30-KOx-1:1 exhibiting Type IV(a) behaviour with hysteresis, indicating combined micro–mesoporosity with significant mesopore contribution.

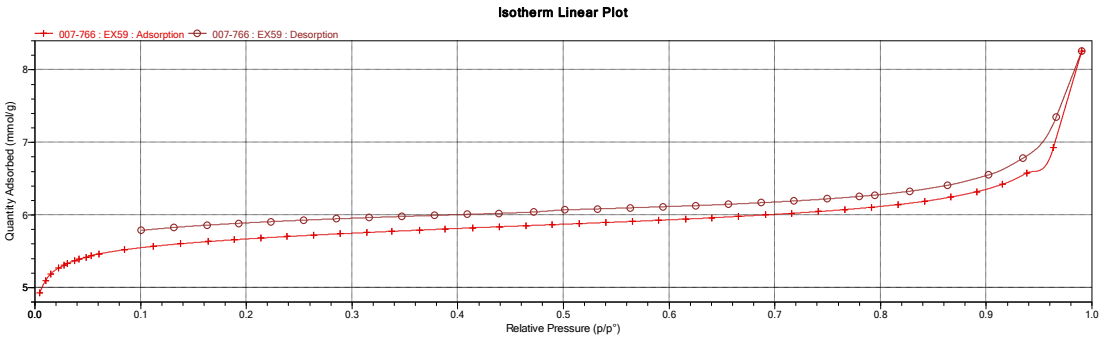

Figure 143 - N_2 adsorption–desorption isotherm of EX59-700-68-KOx-1:4.5 exhibiting Type IV(a) behaviour with hysteresis, indicating combined micro–mesoporosity with significant mesopore contribution.

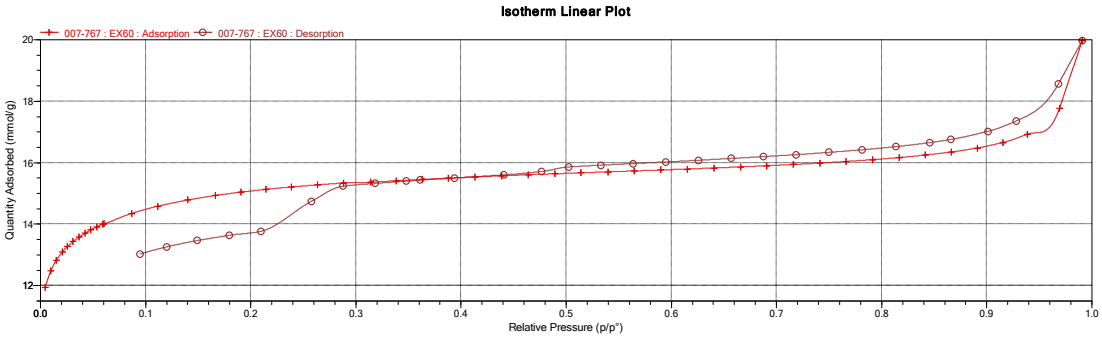

Figure 144 - N_2 adsorption–desorption isotherm of EX60-1200-68-KOx-1:4.5 exhibiting Type IV(a) behaviour with hysteresis, indicating combined micro–mesoporosity with significant mesopore contribution.

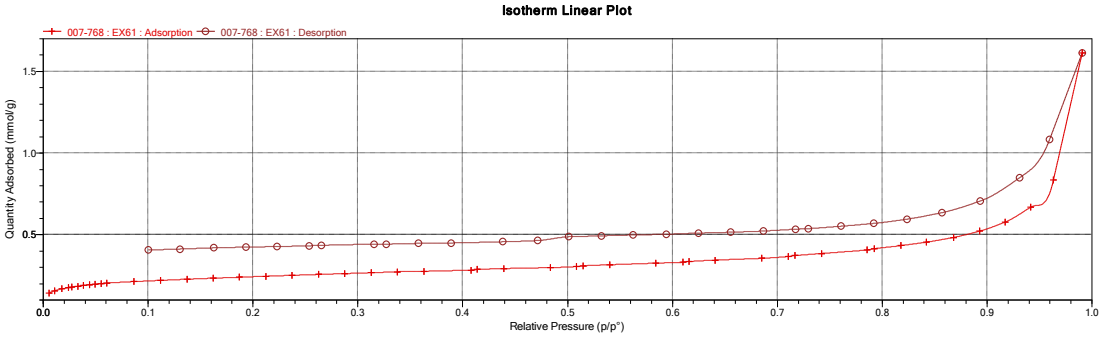

Figure 145 - N_2 adsorption–desorption isotherm of EX61-400-68-KOx-1:4.5 exhibiting Type IV(a) behaviour with hysteresis, indicating combined micro–mesoporosity with significant mesopore contribution.

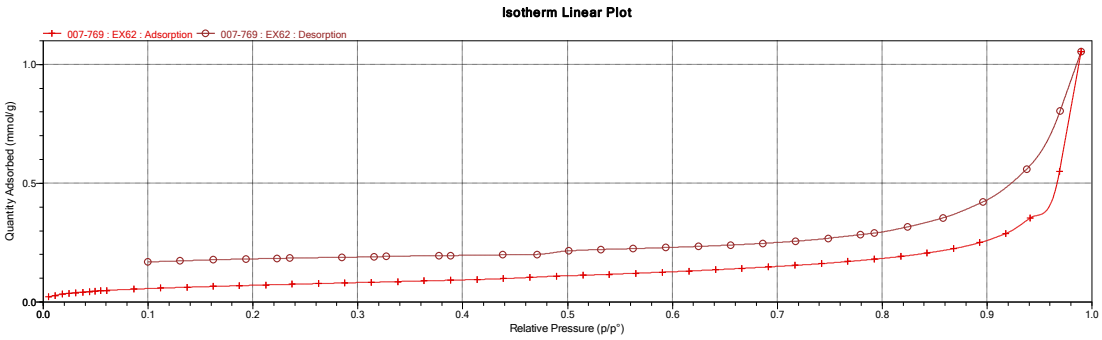

Figure 146 - N_2 adsorption–desorption isotherm of EX62-700-5-KOx-1:4.5 exhibiting Type IV(a) behaviour with hysteresis, indicating combined micro–mesoporosity with significant mesopore contribution.

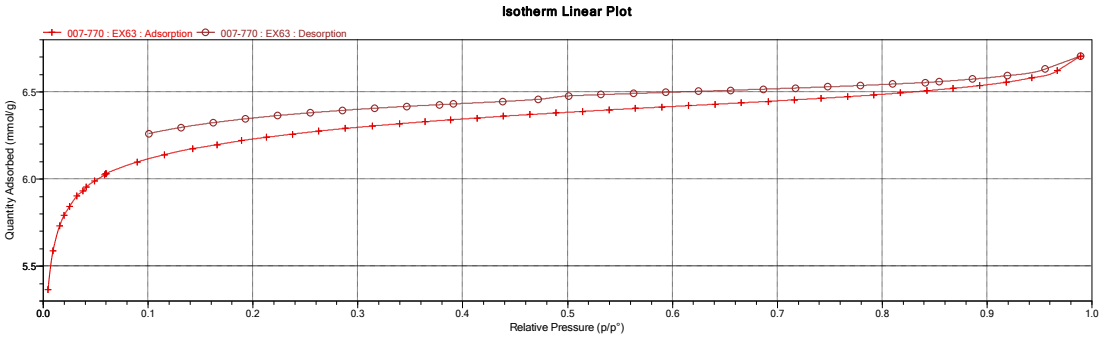

Figure 147 - N_2 adsorption–desorption isotherm of EX63-700-68-KOx-1:4.5 exhibiting Type IV(a) behaviour with hysteresis, indicating combined micro–mesoporosity with significant mesopore contribution.

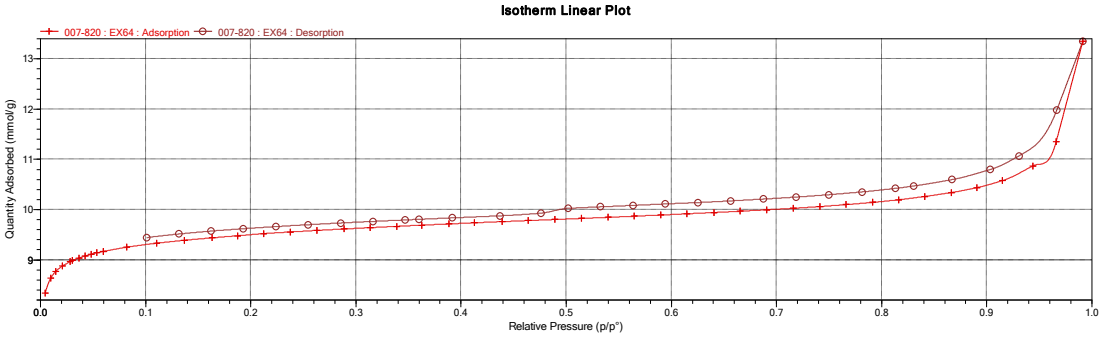

Figure 148 - N_2 adsorption–desorption isotherm of EX64-700-180-KOx-1:4.5 exhibiting Type IV(a) behaviour with hysteresis, indicating combined micro–mesoporosity with significant mesopore contribution.

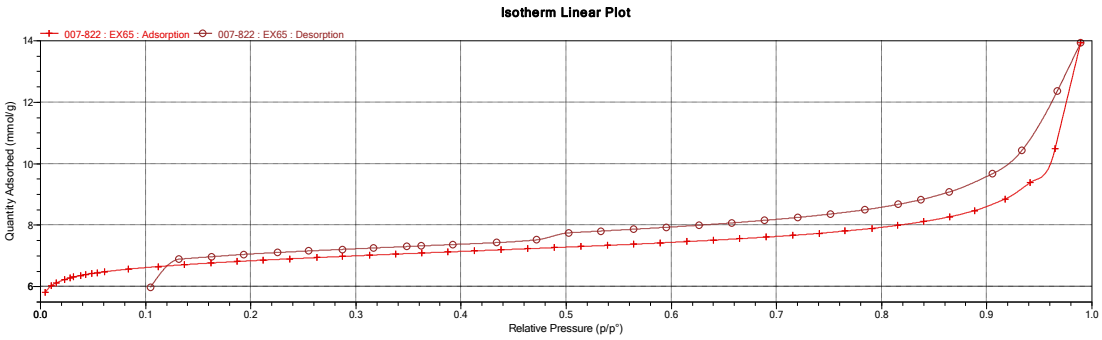

Figure 149 - N_2 adsorption–desorption isotherm of EX65-700-68-KOx-1:10 exhibiting Type IV(a) behaviour with hysteresis, indicating combined micro–mesoporosity with significant mesopore contribution.

Fungal Activated Samples

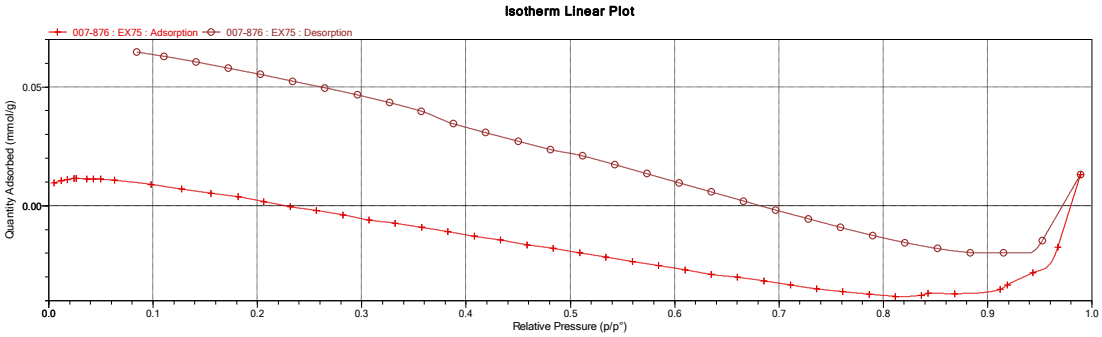

Figure 150 - N_2 adsorption–desorption isotherm of EX75-500-15-GO showing negligible nitrogen uptake. The apparent negative slope arises from buoyancy and baseline correction effects that dominate at extremely low adsorption capacities, consistent with a non-porous material.

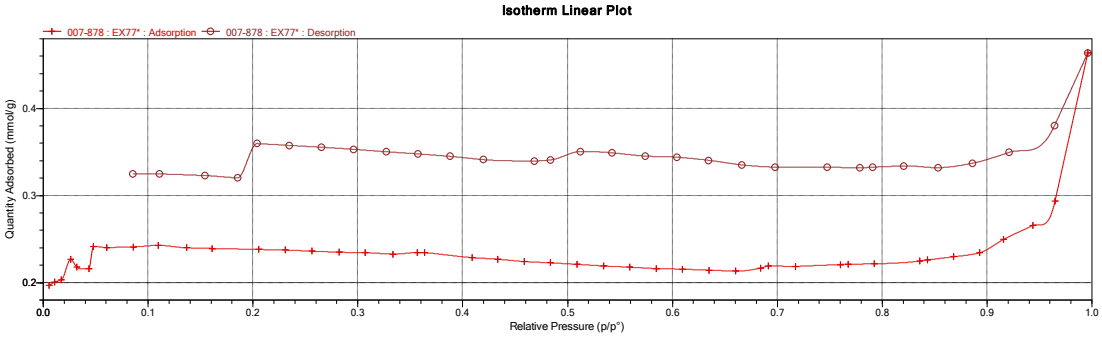

Figure 151 - N_2 adsorption–desorption isotherm of EX77-900-15-GO showing negligible nitrogen uptake. The apparent negative slope arises from buoyancy and baseline correction effects that dominate at extremely low adsorption capacities, consistent with a non-porous material.

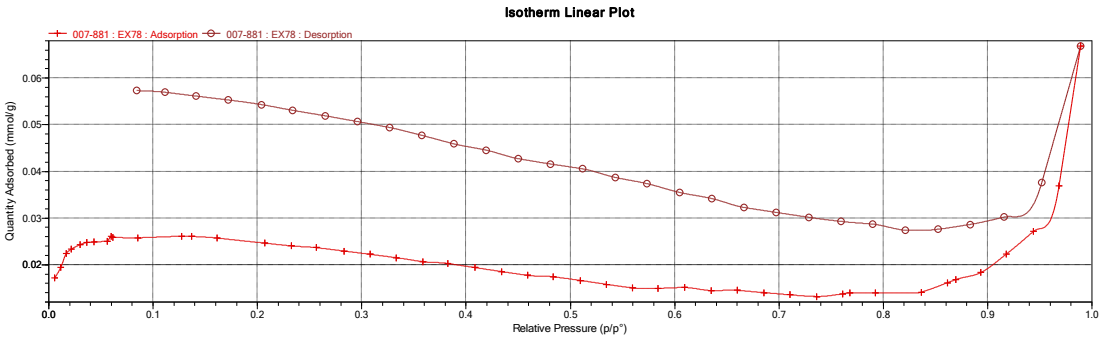

Figure 152 - N_2 adsorption–desorption isotherm of EX78-500-2H-GO showing negligible nitrogen uptake. The apparent negative slope arises from buoyancy and baseline correction effects that dominate at extremely low adsorption capacities, consistent with a non-porous material.

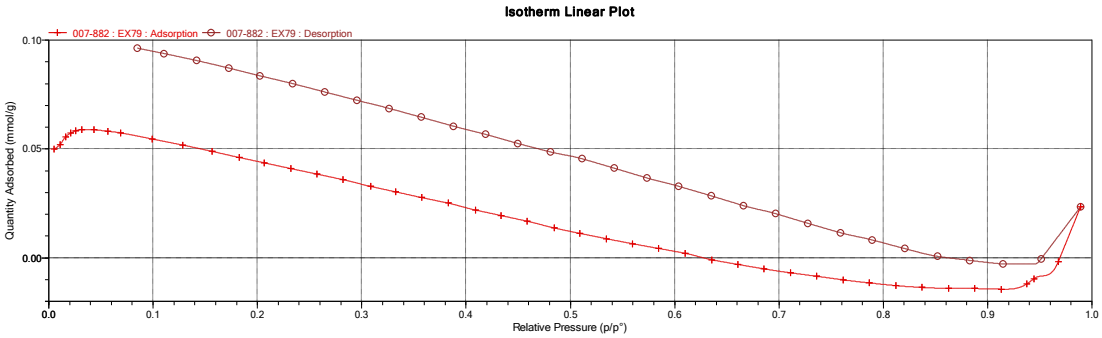

Figure 153 - N_2 adsorption–desorption isotherm of EX79-700-15-GO showing negligible nitrogen uptake. The apparent negative slope arises from buoyancy and baseline correction effects that dominate at extremely low adsorption capacities, consistent with a non-porous material.

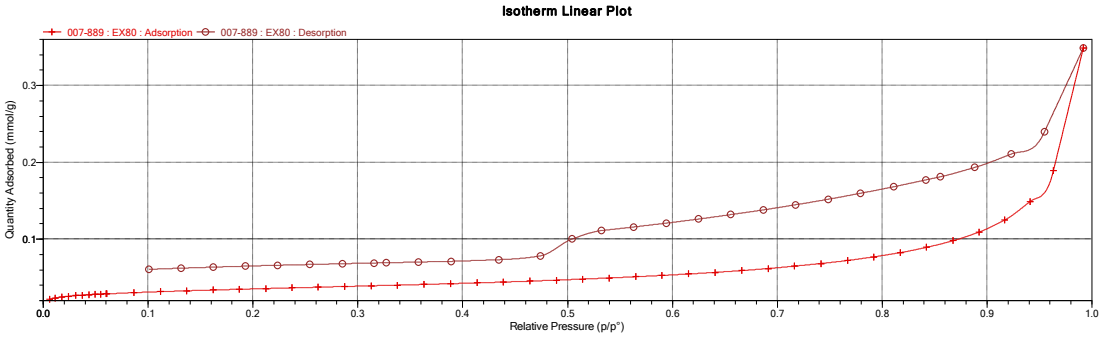

Figure 154 - N_2 adsorption–desorption isotherm of EX80-900-2H-GO exhibiting Type IV(a) behaviour with hysteresis, indicating combined micro–mesoporosity with significant mesopore contribution.

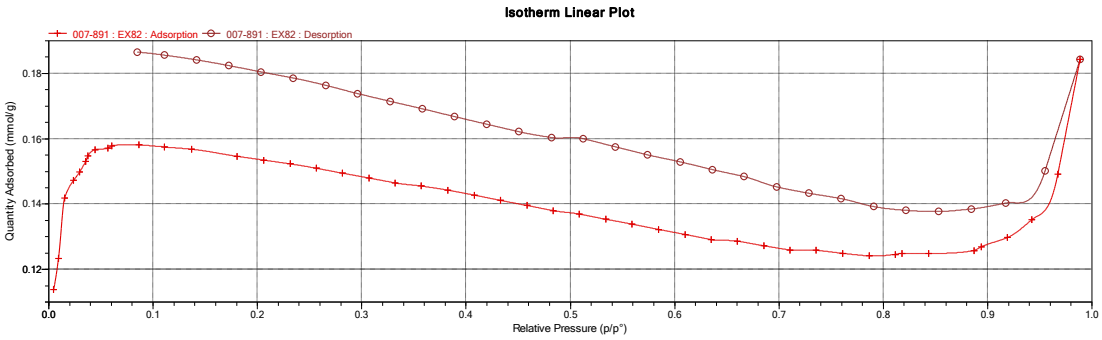

Figure 155 - N_2 adsorption–desorption isotherm of EX82-700-15-GO showing negligible nitrogen uptake. The apparent negative slope arises from buoyancy and baseline correction effects that dominate at extremely low adsorption capacities, consistent with a non-porous material.

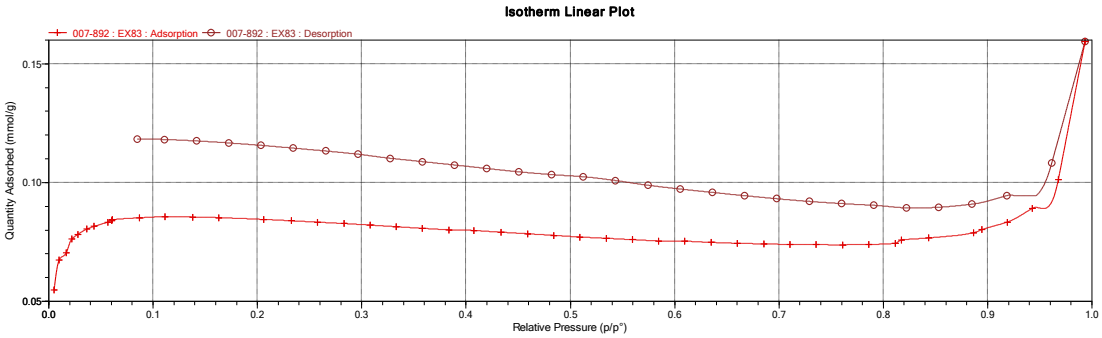

Figure 156 - N_2 adsorption–desorption isotherm of EX83-500-60-GO showing negligible nitrogen uptake. The apparent negative slope arises from buoyancy and baseline correction effects that dominate at extremely low adsorption capacities, consistent with a non-porous material.

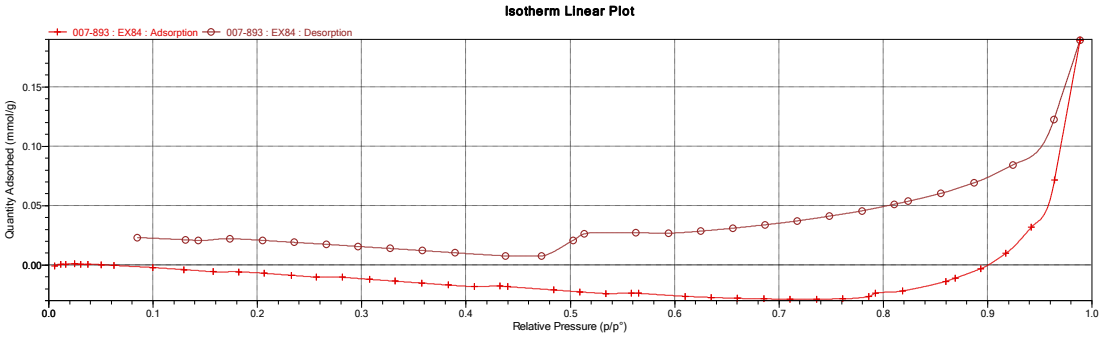

Figure 157 - N_2 adsorption–desorption isotherm of EX84-900-60-GO showing negligible nitrogen uptake. The apparent negative slope arises from buoyancy and baseline correction effects that dominate at extremely low adsorption capacities, consistent with a non-porous material.

Appendix H: Correlation of Synthesis Parameter Vs Nitrogen Content

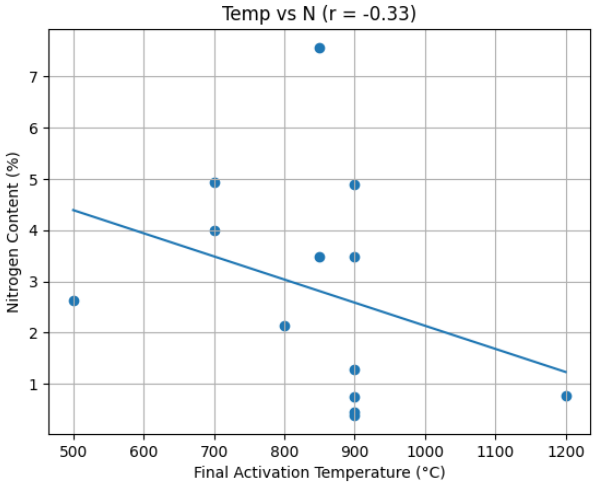

Figure 158 - Corrlation between final hold temp (°C) and Nitrogen Content (%)

A weak inverse correlation (r = –0.33) was observed between final activation temperature and nitrogen content, consistent with progressive thermal degradation of nitrogen functionalities. However, the poor correlation suggests that activation route and chemical environment exert a stronger influence on nitrogen retention than temperature alone.

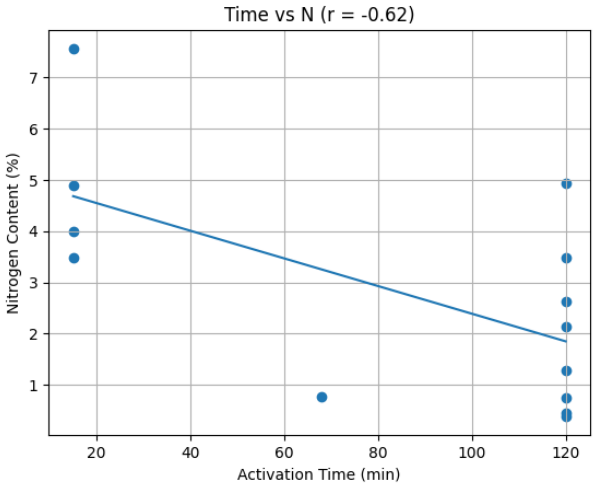

Figure 159 - Corrlation between final hold time (mins) and Nitrogen Content (%)

A statistically significant inverse correlation was observed between activation time and nitrogen content ($r = –0.62$, $p < 0.05$), indicating that prolonged activation promotes progressive loss of nitrogen functionalities. This trend is consistent with increased thermal and gasification-driven degradation of nitrogen-containing surface groups during extended treatment.